

# **Organ-on-Chip Systems Integrating Human Adipose Tissues**

## **Dissertation**

der Mathematisch-Naturwissenschaftlichen Fakultät  
der Eberhard Karls Universität Tübingen  
zur Erlangung des Grades eines  
Doktors der Naturwissenschaften  
(Dr. rer. nat.)

vorgelegt von  
Julia Rogal  
aus Ueckermünde

Tübingen  
2021

Gedruckt mit Genehmigung der Mathematisch-Naturwissenschaftlichen Fakultät der Eberhard Karls Universität Tübingen.

Tag der mündlichen Qualifikation:

16.11.2021

Dekan:

Prof. Dr. Thilo Stehle

1. Berichterstatterin:

Prof. Dr. Katja Schenke-Layland

2. Berichterstatter:

Prof. Dr. Andreas Stahl

3. Berichterstatter:

PD Dr. Alexander S. Mosig





# Table of Content

<b>Table of Content</b> .....	<b>I</b>
<b>Abstract</b> .....	<b>V</b>
<b>Zusammenfassung</b> .....	<b>VII</b>
<b>Abbreviations</b> .....	<b>IX</b>
<b>List of Figures</b> .....	<b>XIII</b>
<b>List of Tables</b> .....	<b>XIII</b>
<b>List of Publications</b> .....	<b>XV</b>
<i>a. Accepted Publications</i> .....	<i>XV</i>
<i>a. Submitted Manuscripts</i> .....	<i>XVI</i>
<b>Candidate’s Contribution to Publications</b> .....	<b>XVII</b>
<b>1. Introduction</b> .....	<b>3</b>
1.1 <i>Organ-on-Chip Technology</i> .....	3
1.1.1 General Process for Developing an OoC Model .....	5
1.2 <i>Human Adipose Tissue</i> .....	8
1.2.1 Types of Adipose Tissues and Their Functions.....	9
1.2.2 Malfunctioning Adipose Tissue & Adipose-Immune Interactions.....	15
1.3 <i>Research Landscape of Human Adipose Tissue</i> .....	17
1.3.1 <i>In vivo</i> Research on Adipose Tissue .....	17
1.3.2 Conventional <i>in vitro</i> Adipose Tissue Models.....	18
1.3.3 Organ-on-Chip Systems Integrating Adipose Tissue .....	19
<b>2. Objective of the Thesis</b> .....	<b>23</b>
<b>3. Materials &amp; Methods</b> .....	<b>27</b>
3.1 <i>Fabrication and Characterization of Third-Generation Microfluidic Platform</i> .....	27
3.1.1 Chip Design and Dimensions .....	27
3.1.2 Chip Fabrication .....	28
3.1.3 Comparison of Absorption Characteristics: PET-G vs. PDMS .....	30
3.1.4 Characterization of on-Chip Diffusive Transport.....	30
3.1.5 Computational Fluid Dynamic (CFD) Modeling .....	30
3.2 <i>Setup and Characterization of a Beige Adipocytes-on-Chip Model</i> .....	32
3.2.1 Preparation and Injection of Human Preadipocytes .....	32
3.2.2 On-Chip Differentiation of Preadipocytes into Beige Adipocytes.....	33
3.2.3 Monitoring of Viability on-Chip.....	34
3.2.4 Morphological Characterization of Beige Adipocytes on-Chip.....	35
3.2.5 Gene Expression Analysis of Beige Adipocytes on-Chip .....	36
3.2.6 Fatty acid uptake monitoring of beige adipocytes-on-chip .....	37

3.2.7	Image processing and statistical analysis .....	37
3.3	<i>Materials and Devices</i> .....	38
<b>4.</b>	<b>Results &amp; Discussion</b> .....	<b>45</b>
4.1	<i>Technological Development of Tailored Adipose Tissue-on-Chip Platforms</i> .....	45
4.1.1	First-Generation Platform .....	46
4.1.2	Second-Generation Platform .....	47
4.1.3	Third-Generation Platform .....	48
4.2	<i>Cell Sources for Adipose Tissue-on-Chip Systems</i> .....	52
4.3	<i>Monoculture Models Towards Adipose Tissue-on-Chip Systems</i> .....	53
4.3.1	Human Mature White Adipocytes-on-Chip .....	53
4.3.2	On-Chip Differentiation of Beige Adipocytes .....	58
4.3.3	Recreating Barriers on Chip .....	69
4.4	<i>Full Complexity Adipose Tissue-on-Chip Models</i> .....	74
4.4.1	Co-Culture Logistics and Considerations .....	76
4.4.2	Mix-and-Match Toolbox for Autologous WAT-on-Chip Models .....	76
4.4.3	Immunocompetency of the WAT-on-Chip Systems.....	78
<b>5.</b>	<b>Conclusion</b> .....	<b>83</b>
<b>6.</b>	<b>Outlook</b> .....	<b>89</b>
	<b>References</b> .....	<b>93</b>
	<b>Acknowledgements</b> .....	<b>111</b>
	<b>Declaration</b> .....	<b>113</b>
	<b>Curriculum Vitae</b> .....	<b>115</b>
	<b>Appendices</b> .....	<b>119</b>





## Abstract

Adipose tissue constitutes about one fourth of a healthy adult human's body mass and is involved in a large variety of (patho-)physiological processes. Especially in the era of 'diabesity', a thorough understanding of human adipose tissue has become more important than ever. Yet, research on human adipose biology is hampered by a lack of predictive model systems. Even though many valuable insights could be gained from animal models, they often fall short of predicting human physiology. Then again, unusual characteristics of mature adipocytes, such as buoyancy, fragility, and large size, make conventional cell culture approaches challenging. In recent years, organ-on-chip (OoC) technology has emerged from a synergy of tissue engineering and microfluidics approaches. OoC systems integrate engineered tissues into physiological microenvironments supplied by a vasculature-like perfusion. Yet even though OoC technology is thriving regarding other organ systems, there has only been very little focus on adipose tissue so far. Hence, the objectives of this thesis were to design, develop and characterize adipose tissue-on-chip models. To achieve this, designs, biomaterials and fabrication approaches were developed leading to three generations of microfluidic platforms specifically tailored to the needs of human adipose tissues. Moreover, protocols and logistics for sourcing, isolating, and utilizing almost all adipose tissue cell types from one donor were established. Together, this enabled the generation of white and beige adipose tissues (WAT and bAT, respectively) on chip either by injecting mature adipose cell types (in case of WAT) or by inducing adipogenesis on chip (in case of bAT). Along the way towards a highly complex, immunocompetent autologous model integrating almost all adipose-associated cell types, a mix-and-match strategy was established allowing for a flexible combination of cellular modules to fit-for-purpose models serving a specific scientific question. Moreover, a toolbox of readout methods was compiled that enabled a comprehensive characterization of on-chip adipose tissue structure and function, demonstrating functional on-chip WAT culture times beyond one month. Case studies on compound screening and immune responses highlighted the models' suitability as tools for target identification in drug discovery or for studies on immunometabolism. All in all, the developed models hold great potential for mechanistic studies on adipose tissue biology or disease modelling in the context of obesity and diabetes, as well as for personalized or precision medicine due to its fully autologous character.



## Zusammenfassung

Fettgewebe macht etwa ein Viertel des Körpergewichts eines gesunden, erwachsenen Menschen aus und ist an einer Vielzahl von (patho-)physiologischen Prozessen beteiligt. Vor allem im Zeitalter der „Diabesity“ ist ein gründliches Verständnis des menschlichen Fettgewebes wichtiger denn je. Studien an menschlichem Fettgewebe werden jedoch durch einen Mangel an prädiktiven Modellsystemen erschwert. Obwohl viele wertvolle Erkenntnisse aus Tiermodellen gewonnen werden konnten, können diese oft nicht die menschliche Physiologie vorhersagen. Hinzu kommt, dass der Auftrieb, die Fragilität und die Größe reifer Fettzellen eine Herausforderung für herkömmliche Zellkulturansätze sind. Im letzten Jahrzehnt ist die Organ-on-Chip (OoC)-Technologie an der Grenzfläche des Tissue Engineering und der Mikrofluidik entstanden. OoC-Systeme integrieren künstlich hergestellte Gewebe, durch eine gefäßähnliche Perfusion versorgt, in physiologische Mikroumgebungen. Obwohl es viele Beispiele für OoC-Modelle anderer Organsysteme gibt, gibt es bisher wenige Ansätze für Fettgewebe. Ziel dieser Arbeit war es daher, Fettgewebe-on-chip-Modelle zu konzipieren, zu entwickeln und zu charakterisieren. Dazu wurden Designs, Biomaterialien und Mikrostrukturierungsansätze entwickelt, die in drei Generationen von speziell auf die Bedürfnisse des menschlichen Fettgewebes zugeschnittenen, mikrofluidischen Plattformen resultierten. Darüber hinaus wurden Protokolle und Logistik für die Beschaffung, Isolierung und Verwendung fast aller Fettgewebe-Zelltypen von einem/r Spender/in etabliert. Dies ermöglichte die Erzeugung von weißem und beigem Fettgewebe (WAT bzw. bAT) „on-chip“, entweder durch Injektion reifer Fettzelltypen (für WAT) oder durch Adipogenese „on-chip“ (für bAT). Neben einem komplexen, immunkompetenten autologen Modell, das fast alle Fettgewebe-assoziierten Zelltypen integriert, wurde eine „Mix-and-Match“-Strategie entwickelt, die eine flexible Kombination zellulärer Module zu „fit-for-purpose“ Modellen, maßgeschneidert für die jeweilige wissenschaftliche Fragestellung, ermöglicht. Zusätzlich wurde eine Toolbox von Analysemethoden etabliert, die eine umfassende Charakterisierung der Struktur und Funktion des Fettgewebes „on-chip“ ermöglichte. Fallstudien zum Wirkstoffscreening und zu Immunreaktionen betonten die Eignung der Modelle als Werkzeuge für die Arzneimittelforschung und für Studien zum Immunmetabolismus. Für die Zukunft bieten die entwickelten Modelle großes Potenzial für mechanistische Studien zur Fettgewebe-Biologie, für die Modellierung von Krankheiten sowie für die personalisierte Medizin.



## Abbreviations

$\beta$ -AR, e.g., $\beta$ 1-AR	$\beta$ -adrenoreceptor, e.g., $\beta$ -adrenoreceptor type 1
12,13-diHOME	12,13-dihydroxy-9Z-octadecenoic acid
3D	Three-dimensional
AC	Adenylyl cyclase
Ac-LDL	Acetylated low-density lipoprotein
AdMSC	Adipose-derived mesenchymal stem cell
ADP	Adenosine diphosphate
APTES	(3-Aminopropyl)triethoxysilane
ASC-1	Asc-1 neutral amino acid transporter [also: Solute carrier family 7 member 10 (SLC7A10)]
ATGL	Adipose triglyceride lipase
ATM	Adipose tissue macrophage
ATP	Adenosine triphosphate
bAT	Beige/brite adipose tissue
BAT	Brown adipose tissue
BCAA	Branched-chain amino acids
bFGF	Basic fibroblast growth factor
BMI	Body mass index
BSA	Bovine serum albumin
C	Cytochrome c
CAD	Computer-aided design
cAMP	cyclic adenosine monophosphate
CD106	Cluster of differentiation 106 [also: vascular cell adhesion molecule 1 (VCAM-1)]
CD137	Cluster of differentiation 137 [also: TNF receptor superfamily member 9 (TNFRSF9)]
CD309	Cluster of differentiation 309 [also: vascular endothelial growth factor receptor 2 (VEGFR-2)]
CD31	Cluster of differentiation 31 [also: platelet endothelial cell adhesion molecule 1 (PECAM-1)]
CD4/8/...	Cluster of differentiation 4/8/...
CD41	Cluster of differentiation 41 [also: integrin subunit alpha 2b (ITGA2B)]
cDNA	Complementary DNA
CFD	Computational Fluid Dynamic
CO <sub>2</sub>	Carbon dioxide
C <sub>q</sub>	Quantification cycle
CREB	cAMP response element-binding protein
CXCL14	C-X-C motif chemokine ligand 14
DAG	Diacylglycerol
DAPI	4', 6-diamidino-2-phenylindole
DIO2	Iodothyronine deiodinase 2
DMEM/F-12	Dulbecco's Modified Eagle Medium/Nutrient Mixture F-12
DMSO	Dimethyl sulfoxide
DNA	Deoxyribonucleic acid

ECM	Extracellular matrix
eNOS	endothelial nitric oxide synthase
EPA	Environmental Protection Agency
EUROoCS	European Organ-on-Chip Society
f-actin	Filamentous actin
FA	Fatty acid
FABP4	Fatty acid binding protein 4
FADH <sub>2</sub> /FAD	Reduced/oxidized form of flavin adenine dinucleotide (FAD)
FATP1	Fatty acid transport protein 1
FCS	Fetal calf serum
FDA	Fluorescein diacetate
FDG-PET/CT	<sup>18</sup> F-fluorodeoxyglucose positron emission tomography combined with computed tomography
FEM	Finite element method
FFA	Free fatty acid
FGF21	Fibroblast growth factor 21
FITC-dextran	Fluorescein isothiocyanate-dextran
FLIM	Fluorescence lifetime imaging microscopy
g-actin	globular actin
GLUT, e.g., GLUT4	Glucose transporter, e.g., glucose transporter type 4
GLUT4	Glucose transporter type 4
GM-CSF	Granulocyte-macrophage colony-stimulating factor
GWAS	genome-wide association studies
H <sup>+</sup>	Hydrogen cation
H <sub>2</sub> O	Water
HEPES	(4-(2-hydroxyethyl)-1-piperazineethanesulfonic acid)
HIF-1 $\alpha$	Hypoxia inducible factor 1 $\alpha$ subunit
HSL	Hormone-sensitive lipase
HUVEC	Human umbilical vein endothelial cell
HyA	Hyaluronic acid
I-IV	respiratory complexes I-IV (electron transport chain)
IBMX	3-Isobutyl-1-methylxanthine
IFN- $\gamma$	Interferon $\gamma$
IL-4/6/...	Interleukin 4/6/...
iPSC	Induced pluripotent stem cell
LAM	Lipid-associated macrophage
LCFA	Long-chain fatty acid
LDH	Lactate dehydrogenase
LHX8	LIM homeobox 8
LogP	N-octanol/water partition coefficient
LPL	Lipoprotein lipase
LPS	Lipopolysaccharide
MACS	Magnetic activated cell sorting
MAG	Monoacylglycerol
MCFA	Medium-chain fatty acid

MCP1	Monocyte chemoattractant protein 1 [also: C-C motif chemokine ligand 2 (CCL2)]
MGL	Monoacylglycerol lipase
MPS	Microphysiological system
mRNA	Messenger ribonucleic acid
mvEC	Microvascular endothelial cell
NADH/NAD <sup>+</sup>	Reduced/oxidized form of nicotinamide adenine dinucleotide (NAD)
NE	Norepinephrine
NRG4	Neuregulin 4
O <sub>2</sub>	Oxygen
OoC	Organ-on-Chip
PBS <sup>-</sup>	Dulbecco's phosphate-buffered saline without calcium chloride and without magnesium chloride
PBS <sup>+</sup>	Dulbecco's Phosphate Buffered Saline with magnesium chloride and calcium chloride
PC	Polycarbonate
PCR	Polymerase chain reaction
PDMS	Polydimethylsiloxane
PECAM-1	Platelet endothelial cell adhesion molecule 1 [also: CD31]
Pen/Strep	Penicillin/Streptomycin
PET	Polyethylene terephthalate
PET-G	Polyethylene terephthalate glycol-modified
PGC-1 $\alpha$	peroxisome proliferator activated receptor $\gamma$ coactivator 1 $\alpha$
PI	Propidium iodide
Pi	Inorganic phosphate
PKA	Protein kinase A
PMMA	Poly(methyl methacrylate)
pO <sub>2</sub>	Partial pressure of oxygen
PPAR $\gamma$	Peroxisome proliferator activated receptor $\gamma$
PPIA	Peptidylprolyl isomerase A
PRDM16	PR/SET domain 16
Q	Coenzyme Q/ubiquinone
qPCR	Quantitative polymerase chain reaction
RBP4	Retinol binding protein 4
rhEGF	Recombinant human epidermal growth factor
RNA	Ribonucleic acid
ROI	Region of interest
RPE	Retinal pigment epithelium
RT	Reverse Transcription
SARS-CoV-2	Severe acute respiratory syndrome coronavirus-2
SEM	Standard error of mean
SNS	Sympathetic nervous system
SVF	Stromovascular fraction
T3	3,3',5-Triiodo-L-thyronine
TAG	triacylglyceride
TE	Tissue engineering

TEER	Transepithelial/endothelial electrical resistance
Th1	T helper 1 cell
Th2	T helper 2 cell
TLR4	Toll-like receptor 4
Tmem26	Transmembrane protein 26
TNF- $\alpha$	Tumor necrosis factor $\alpha$
TPE	Thermoplastic elastomer
TRL	TAG-rich lipoprotein
UCP1	Uncoupling protein 1
VCAM-1	Vascular cell adhesion molecule 1 [also: CD106]
VEGFR-2	Vascular endothelial growth factor receptor 2 [also: CD309]
WAT	White adipose tissue
ZIC1	Zic family member 1

## List of Figures

Figure 1	General concept of OoC systems.	4
Figure 2	Typical development process of a fit-for-purpose OoC model.	8
Figure 3	Schematic of human adipose tissue anatomy.	9
Figure 4	Main types of adipocytes and their origins.	10
Figure 5	Overview of WAT storage- (left) and endocrine functions (right).	12
Figure 6	Overview of key functions of bAT.	14
Figure 7	Maladaptation of adipose tissue in obesity.	16
Figure 8	Key fabrication steps of 3 <sup>rd</sup> -generation microfluidic device.	29
Figure 9	Engineering of tailored adipose tissue-on-chip microfluidic platforms.	42
Figure 10	Characterization of the 3 <sup>rd</sup> -generation adipose tissue microfluidic platform.	47
Figure 11	Toolbox of on-chip analysis of human mature white adipocytes.	50
Figure 12	General concept of the human beige adipocyte-on-chip model.	54
Figure 13	Cell viability during beige adipocyte differentiation on chip.	55
Figure 14	Gene expression analysis of on-chip differentiation into beige adipocytes.	57
Figure 15	Morphological characterization of beige adipocytes on chip.	60
Figure 16	Analysis of beige adipocyte functionality on chip.	62
Figure 17	Patient-specific bAT-on-chip model (d10).	65
Figure 18	Toolbox of on-chip analysis of human endothelial barriers.	68
Figure 19	Concept of high-complexity WAT-on-chip models.	71

## List of Tables

Table 1	Dimensions of the 3 <sup>rd</sup> -generation microfluidic adipose tissue-on-chip platform.	27
Table 2	Overview of cell culture media used for the beige adipocyte-on-chip model.	32
Table 3	Materials and chemicals for PDMS-thermoplastic hybrid microfluidic device fabrication and characterization.	89
Table 4	Cells, media and supplements for (on-chip) differentiation, culture and monitoring of beige adipocytes.	89
Table 5	Materials and Chemicals for Gene Expression Analysis.	91
Table 6	Materials and Chemicals for Staining.	91
Table 7	Devices used for PDMS-thermoplastic hybrid chip fabrication and beige adipocyte-on-chip characterization.	92



## List of Publications

### a. Accepted Publications

# = authors contributed equally

#### 2017

- [1] **J. Rogal**<sup>#</sup>, C. Probst<sup>#</sup>, P. Loskill. “Integration concepts of multi-organ-chips: How to keep your flexibility?!”*, Future Science OA* 3, FSO180 (2017), <http://www.dx.doi.org/10.4155/fsoa-2016-0092>

#### 2018

- [2] **J. Rogal**<sup>#</sup>, A. Zbinden<sup>#</sup>, K. Schenke-Layland, P. Loskill. “Stem-cell based organ-on-a-chip models for diabetes research”, *Adv. Drug. Deliv. Rev.* 140, 101-128 (2018), <https://dx.doi.org/10.1016/j.addr.2018.10.010>
- [3] J. Nawroth<sup>#</sup>, **J. Rogal**<sup>#</sup>, M. Weiss, S. Y. Brucker, P. Loskill. “Organ-on-a-chip systems for women’s health”, *Adv. Healthc. Mater.* 7, 1700550 (2018), <http://www.dx.doi.org/10.1002/adhm.201700550>

#### 2019

- [4] K. Achberger<sup>#</sup>, C. Probst<sup>#</sup>, J. C. Haderspeck<sup>#</sup>, S. Bolz, **J. Rogal**, J. Chuchuy, M. Nikolova, V. Cora, L. Antkowiak, W. Haq, N. Shen, K. Schenke-Layland, M. Ueffing, S. Liebau, P. Loskill. “Human retina-on-a-chip: merging organoid and organ-on-a-chip technology to generate complex multi-layer tissue models”, *eLife* 8, e46188 (2019), <https://dx.doi.org/10.7554/eLife.46188>

#### 2020

- [5] **J. Rogal**, C. Binder, E. Kromidas, S. Schneider, C. Probst, K. Schenke-Layland, P. Loskill. “WAT-on-a-chip integrating human mature white adipocytes for mechanistic research and pharmaceutical applications”, *Sci. Rep.* 10, 6666 (2020), <https://dx.doi.org/10.1038/s41598-020-63710-4>
- [6] **J. Rogal**, M. Cipriano, P. Loskill. “Organ-on-Chip: Playing LEGO® with mini-organs to reduce animal testing and make medicines safer”, *Front. Young Minds* 8, 544390 (2020), <https://dx.doi.org/10.3389/frym.2020.544390>

2021

- [7] **J.Rogal**<sup>#</sup>, J. Roosz<sup>#</sup>, P.Loskill. “Isolation, Integration, and Culture of Human Mature Adipocytes Leveraging Organ-on-Chip Technology”, *Methods Mol. Biol.*, in press (2021), [https://dx.doi.org/10.1007/978-1-0716-1693-2\\_18](https://dx.doi.org/10.1007/978-1-0716-1693-2_18)
- [8] J. Chuchuy, **J. Rogal**, T. Ngo, K. Stadelmann, L. Antkowiak, S. Liebau, K. Schenke-Layland, P. Loskill. “Integration of electrospun membranes into low-absorption thermoplastic organ-on-chip“, *ACS Biomater. Sci. Eng.* 7, 3006–3017 (2021), <https://dx.doi.org/10.1021/acsbiomaterials.0c01062>
- [9] F. Hornung, **J. Rogal**, P. Loskill, B. Löffler, S. Deinhardt-Emmer. “The inflammatory profile of obesity and the role on pulmonary bacterial and viral infections”, *Int. J. Mol. Sci.* 22, 3456 (2021), <https://dx.doi.org/10.3390/ijms22073456>
- [10] S. Schneider, M. Bubeck, **J. Rogal**, H. Weener, C. Rojas, M. Weiss, M. Heymann, A. D. van der Meer, P. Loskill. „Peristaltic on-chip pump for tunable media circulation and whole blood perfusion in PDMS-free organ-on-chip and organ-disc systems“, *Lab Chip Ahead of Print* (2021), <https://dx.doi.org/10.1039/D1LC00494H>

a. Submitted Manuscripts

2021

- [11] **J. Rogal**, R. Xu, J. Roosz, C. Teufel, M. Cipriano, W. Eisler, M. Weiss, K. Schenke-Layland, P.Loskill. “Autologous human immunocompetent white adipose tissue-on-chip”, *under review* (2021) (available at bioRxiv <https://dx.doi.org/10.1101/2021.08.08.455559>)

## Candidate's Contribution to Publications

B.C. = Book chapter; R. = Review

Publication No.	1	2	3	4	5	6	7	8	9	10	11
Accepted for publication	yes	yes	yes	yes	no						
Manuscript submitted	-	-	-	-	-	-	-	-	-	-	yes
Number of authors	3	4	5	15	7	3	3	8	5	9	9
Position of the candidate in the list of authors	1	1	1	5	1	1	1	2	2	3	1
Scientific ideas of candidate (%)	R.	R.	R.	10	60	R.	B. C.	10	R.	10	70
Data generation by candidate (%)	R.	R.	R.	10	65	R.	B. C.	20	R.	10	70
Interpretation and analysis by candidate (%)	R.	R.	R.	0	75	R.	B. C.	10	R.	10	70
Paper writing by candidate (%)	45	50	40	0	70	80	50	10	30	10	70



# Chapter 1

## Introduction



## 1. Introduction

### 1.1 Organ-on-Chip Technology

Organ-on-chip (OoC) systems, more broadly called microphysiological systems (MPS), are microfluidic devices capable of reflecting physiological functions of human (or other animals') organs or tissues at the smallest biologically acceptable scale. Living cells are cultured in continuously perfused, micrometer-sized chambers in order to create *in vitro* minimal functional units emulating the tissue- or organ-level functions at question<sup>1,2</sup>. A detailed definition of OoCs was drafted by the European Organ-on-Chip Society (EUROoCS) delineating an OoC as a „fit-for-purpose microfluidic device, containing living engineered organ substructures in a controlled microenvironment, that recapitulates one or more aspects of the organ's dynamics, functionality and (patho) physiological response *in vivo* under real-time monitoring"<sup>3</sup>.

The OoC technology emerged from the convergence of the research fields of tissue engineering (TE) and microfluidic technologies, such as the lab-on-a-chip technology<sup>4</sup>. TE broadly focuses on recreating organs, or parts of organs, mainly for their application in regenerative medicine, and comprises the following three fundamental aspects: engineering of (i) cells, (ii) tissue architectures and (iii) extracellular matrix (ECM) or ECM-like biomaterials<sup>5</sup>. Microfluidics is defined as the science and technology of manipulating, processing or analyzing small volumes of fluidics in microscale channel structures<sup>6</sup>. Most advantageous, thereby, are the demand of only small quantities of samples and/or reagents and associated low costs, high sensitivity and resolution, shorter analysis times as well as smaller footprints of analytical devices<sup>6,7</sup>. Moreover, due to the microscale dimensions, flow regimes are almost exclusively laminar<sup>6</sup>. Over the last two decades, the lab-on-a-chip technologies has prospered immensely and finds many (bio-)medical applications<sup>8,9</sup>, including point-of-care diagnostics<sup>10</sup>, single cell analysis<sup>11</sup>, and, likewise, OoCs. Notably, the term "chip" in OoC and lab-on-a-chip might be misleading; the platforms differ significantly from computer microchips. The term "chip" originates from the originally applied fabrication methods to generate microfluidic platforms, which are modified versions of photolithographic etching used to manufacture computer microchips<sup>1</sup>. Together, the microfabrication approaches, microfluidic characteristics and tailored biomaterials enable the reflection of a physiological microenvironment *in vitro*, which permits a precise control over physicochemical cues and cell- and tissue organization.

A key feature of OoC platforms, facilitated by their organization in microchannels (and -chambers), is the mimicry of vascularization<sup>12</sup> – one of the biggest challenges impeding traditional TE<sup>13</sup>. The vascular-like perfusion channels implement physiological transport processes, including nutrient supply and clearance of metabolized or secreted factors, such as signaling molecules, and provide travelling routes for circulating immune cells, for instance. Besides the *in vitro* imitation of individual organs (or organ-substructures), another unique potential of the OoC technology is the capability to combine various OoC systems to so-called multi-organ chips<sup>2,14–17</sup>, which can reflect interorgan crosstalk or even systemic effects. Strategies, and associated considerations, for creating flexible mix-and-match toolboxes for combining individual OoC devices into multi-organ chips were proposed in a perspective drafted within the framework of this thesis (see **Publication [1]**). Thus, by merging complex tissue architecture featuring vascular-like perfusion, human genetic background of integrated tissues and even the opportunity to reflect organ-organ interactions, the OoC technology unites the advantages of both conventional cell-based assays and animal models (**Figure 1**). Importantly, OoCs have become a powerful potential alternative for animal models, since they have the potential to be the more predictive models of human physiology obviating the need for interspecies translation of findings<sup>2</sup>.

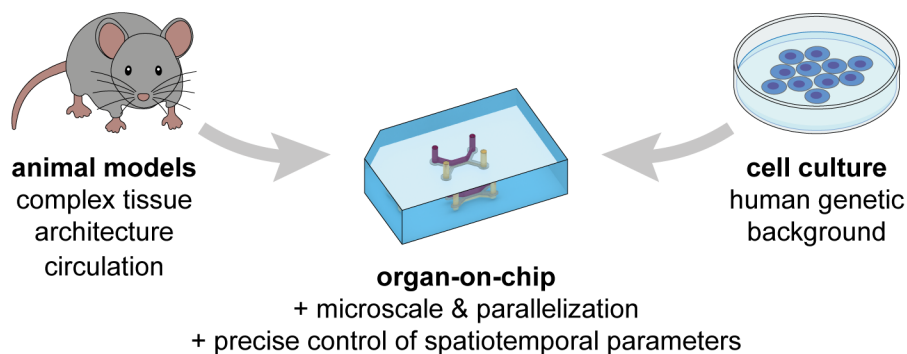


**Figure 1: General concept of OoC systems.** OoCs combine the advantages of both animal models and conventional cell culture in a microphysiological *in vitro* environment. Microfabrication techniques and biomaterial engineering allow for the generation of highly controllable physicochemical cues and spatiotemporal parameters. Integration of co-cultures of human cells enables the formation of human-relevant complex tissue models.

Even though the technology is still in its infancy, OoCs are up to bringing about game-changing benefits to a plethora of biomedical applications, including more human-centered drug/compound discovery and development<sup>2,18,19</sup> as well as toxicity screening of chemicals<sup>20</sup> or environmental toxins<sup>21</sup>, for instance. Moreover, OoCs are broadly

applicable for basic mechanistic research and disease modelling<sup>22,23</sup>. Upon combination with patient-specific cells, OoCs can become powerful tools in the field of personalized medicine and precision medicine<sup>24</sup>, focusing on individual patients or specific patient populations stratified by genetic predisposition, age (e.g., children vs. adults), ethnicity or simply sex (comprehensively reviewed in **Publication [3]**), for instance.

### 1.1.1 General Process for Developing an OoC Model

The developmental process of a new, fit-for-purpose OoC model (**Figure 2**) takes off with the overall idea. Generally, the human body, specifically the targeted organ and tissue, serves as a structural template for the OoC system's architecture and microenvironment. Moreover, it may either directly serve as a source, or at least as a reference, for cells or tissues. An integration of the tissue into the microfluidic platform then yields the tailored OoC model.

One of the first steps is the structural design of the microfluidic platform. This is typically done using computer-aided design (CAD) software. Next, the drafted design needs to be translated into an actual microfluidic platform. At first, the choice of chip material must be considered; depending on the future purpose of the developed model, some materials might be superior to others. Polydimethylsiloxane (PDMS) is one of the most commonly used materials for chip fabrication, since it features advantages for both fabrication and cell culture: rapid prototyping of PDMS can easily be implemented using photolithography and replica molding. Moreover it is long-term biocompatible, permeable to oxygen, optically transparent and relatively inexpensive<sup>25</sup>. However, the application of PDMS can become problematic because it readily absorbs small hydrophobic molecules<sup>26–29</sup>, which might impact the availability of substances in the medium for the on-chip tissues, or, vice versa, distort measurements of substances secreted from the tissues, requiring simulations to predict absorption of specific molecules<sup>30</sup>. Moreover, uncured oligomers might leach from the bulk of the polymer<sup>29</sup>, which can alter cell behavior<sup>31</sup>. From a fabrication perspective, PDMS has only a limited capacity for manufacturing scale-up making it an unfavorable material for chip production at industrial proportions<sup>26,32</sup>. Hence, alternative, non-absorbing materials and associated fabrication processes for OoCs are sought after; one promising alternative is the use of thermoplastic polymers, such as poly(methyl methacrylate) (PMMA), polycarbonate (PC) or glycol-modified polyethylene terephthalate (PET-G). They are less absorbing and less prone to leaching of monomers, but still long-term biocompatible and easy to use for rapid prototyping. However, one of

the biggest challenges of using thermoplastics for OoC applications is their compromised oxygen permeability posing the challenge of oxygen availability for tissues on-chip.<sup>32</sup> A class of materials that has recently been discovered for OoC fabrication are thermoplastic elastomers (TPEs)<sup>33</sup>, which combine certain advantages of both PDMS and thermoplastics (e.g. better oxygen permeability than thermoplastics but less absorbing than PDMS<sup>34</sup>), but up until recently they tended to have laborious handling protocols<sup>33</sup>. After deciding for a chip material, protocols for chip fabrication must be established. Moreover, prior to tissue integration, the microfluidic platform itself should be characterized in terms of flow profiles and transport processes that can be accompanied by finite element method (FEM)-based modeling.

In parallel to engineering the microfluidic platforms, biological OoC preparations include identification and characterization of suitable cell sources and bioactive scaffolds or coatings. So far, many biomedical studies have relied on cell lines; while they are inexpensive, standardizable and capable to proliferate indefinitely, they are often animal- and/or tumor-derived and thereby not (fully) resembling original organ-specific cell types. Primary cells, as an alternative, perform much better in recapitulating desired phenotypes and functions, but they are often not proliferative and tough to source resulting in limited cell quantities and, by association, limited availability for experiments. Another promising alternative is the use of stem cells. Especially induced pluripotent stem cells (iPSCs), which harbor the advantages of both cell lines (proliferation and standardizable) and primary cells (human, physiological function and morphology), turned out to be an asset for the OoC technology<sup>35</sup>, potentially even with organoids as intermediate step<sup>36</sup>. Alongside the cellular aspect, the mechanical properties and chemical composition of on-chip used scaffolds should resemble that of the native ECM. *In vivo*, the ECM composition and the portion of the main components – collagen and elastin fibers, glycoproteins and polysaccharides – varies depending on its organ-specific functions, among them being mechanical support, regulation of cell shape, resistance to external forces or signal transduction<sup>37</sup>. To model the ECM *in vitro*, many TE approaches make use of hydrogels, i.e., crosslinked (bio-)polymer networks holding high water contents<sup>38</sup>. They can be engineered from a broad range of natural and/or synthetic materials and usually offer tunable properties regarding mechanical strength and chemical composition<sup>39</sup>, making them favorable, and broadly utilized scaffold materials for three-dimensional (3D) tissues in microfluidic platforms<sup>40–42</sup>.

The next step, tissue integration, combines the biological- and engineering branches of OoC development. It involves the development of customized tissue injection and on-chip culture protocols, which lead to the generation of the target structures (monolayer/barrier tissues vs. 3D volumetric constructs) and the preservation of viability and functionality of the on-chip tissues. Further, the proliferation state of the cells needs consideration; while proliferating cells require proper confinements by the device to prevent overgrowth, post-mitotic cells already need to be injected at physiological (high) densities. To be able to assess the quality of the established procedures, the development of on-chip tissue readout methods is essential. While many readouts must be organ-specific, they also need to address more general aspects such as the monitoring of on-chip viability, morphology and structure. The monitoring can happen on different levels: (i) online (also frequently labeled as 'in-line' or '*in situ*') monitoring usually implies non-invasive real-time assessment of the on-chip situation realized through optical interrogation or the integration of sensors; (ii) at-line measurements are based on analyses of samples removed from the perfusion medium after contact with the on-chip tissues (i.e., the 'effluent medium') and thereby generate discrete data points; (iii) off-line measurements occur at the end of the process and usually involve invasive methods<sup>43,44</sup>. When a versatile spectrum of on-chip tissue readout methods is established allowing for an evaluation of different key aspects of organ functionality and structures, the last stage before model application is its functional validation; one of the most crucial steps, resolving the question of whether the model will serve its specific, intended application purpose.

Importantly, OoC models are usually developed to serve a defined purpose. Before utilizing this model for another application, all the aspects of the OoC development should be carefully re-considered in terms of their reasonableness for the new purpose. At each stage of the process, one should be prepared to take one or more steps back to re-iterate the process. Following this strategy, many prominent OoC models emulating either barrier tissues, such as lung-on-chip<sup>45</sup>, gut-on-chip<sup>46</sup>, or kidney-on-chip<sup>47</sup> devices, or complex 3D tissues such as heart-on-chip<sup>48</sup>, liver-on-chip<sup>49</sup> and even brain-on-chip<sup>50</sup> platforms have been successfully proposed. Concerning adipose tissue research, however, the attempts of adipose tissue-on-chip platforms are scarce and marked by challenging demands of this special type of tissue.

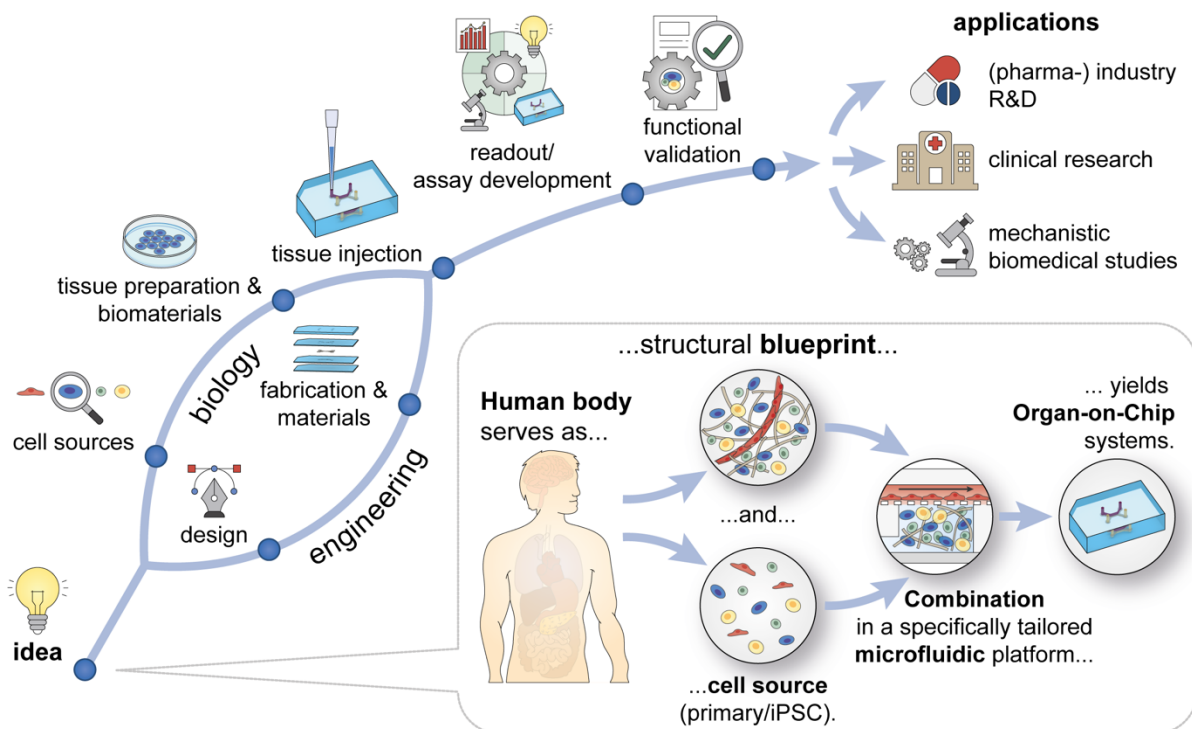


**Figure 2: Typical development process of a fit-for-purpose OoC model.** The cellular composition and architecture of the microfluidic platform are designed to emulate the human *in vivo* situation. Alongside designing the chip architecture, developing the microfluidic platform involves evaluating a chip material (and fabrication methods thereof) suitable for the model's intended purpose. Similarly, the biological components, including cells and biomaterials (e.g., ECM), are selected. Next, tissue injection and on-chip culture protocols are established. To assure preservation of tissue viability and functionality, a range of tailored readout methods is developed. Finally, before the OoC model can be applied, its functionality needs to be confirmed via the assays established in the previous step. OoCs' applications are broad ranging from drug testing and toxicity screening to clinical research, including the fields of personalized and precision medicine, and mechanistic biomedical research, such as disease modeling. R&D: research and development.

## 1.2 Human Adipose Tissue

For a long time, the physiology of adipose tissue was of little interest, and the tissue was simply labeled as passive storage site for fats. However, the increasing prevalence of obesity, and its associated co-morbidities, has caught researchers' interests in understanding physiological mechanisms underlying adipose tissue (dys-)functions. Nowadays, adipose tissue is a well-recognized master regulator of energy balance and nutritional homeostasis, not only through storage of fuels but also in functioning as an endocrine organ secreting signaling molecules that control systemic functions. Moreover, adipose tissue can exert non-shivering thermogenesis, i.e., generation of heat, to prevent hypothermia.

The functional diversity of adipose tissue is reflected in its cellular heterogeneity (**Figure 3**). Adipocytes are the main parenchymal cell type and make up around 90% of adipose tissue volume but less than 50% of the cellular content<sup>51</sup>. The stromovascular fraction

(SVF) encompasses all adipose tissue-associated cell types except for adipocytes themselves, and thereby is a dynamic, heterogeneous cell population with changing degrees of maturity and diverse functions. It includes adipose-derived mesenchymal stem cells (AdMSCs), vascular and adipocyte precursor cells, mature vascular cells, fibroblasts, and several types of tissue-resident immune cells.

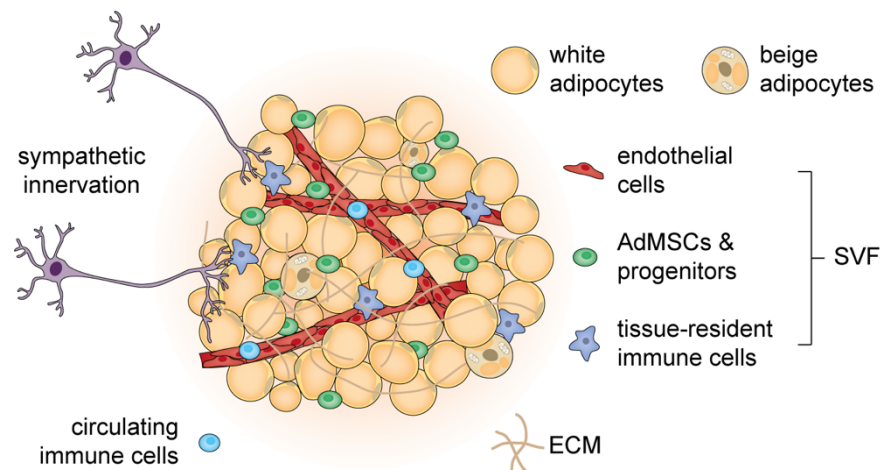


**Figure 3: Schematic of human adipose tissue anatomy.** Adipocytes are the main parenchymal cell type in adipose tissue. Yet, adipose tissue exhibits a great cellular heterogeneity owing to its dense vascularization (endothelial cells), innervation (sympathetic neurons) and contribution of the immune system (circulating and tissue-resident immune cells).

Given adipose tissue's prominent heterogeneity regarding function and cellular composition, it goes without saying that an abnormal amount or metabolic dysfunction of adipose tissue may lead to, or at least predispose to, the development of various disorders, including cardiovascular complications<sup>52</sup>, hepatic diseases<sup>53</sup>, diabetes mellitus<sup>54</sup> or cancer<sup>55,56</sup>. Moreover, excessive, malfunctioning adipose tissue – the clinical picture of obesity – directly impacts the immune system's capacity to respond to infections, e.g., to severe acute respiratory syndrome coronavirus-2 (SARS-CoV-2) threats (discussed at length in **Publication [9]**).

### 1.2.1 Types of Adipose Tissues and Their Functions

In line with the multifaceted functions of adipose tissue, there are different types of adipose tissues, distinguished by their morphology, specific functions, and location: white adipose tissue (WAT), beige or brite adipose tissue (bAT), and brown adipose tissue (BAT) (**Figure 4**). Their distinct morphologies are closely linked to their functions.

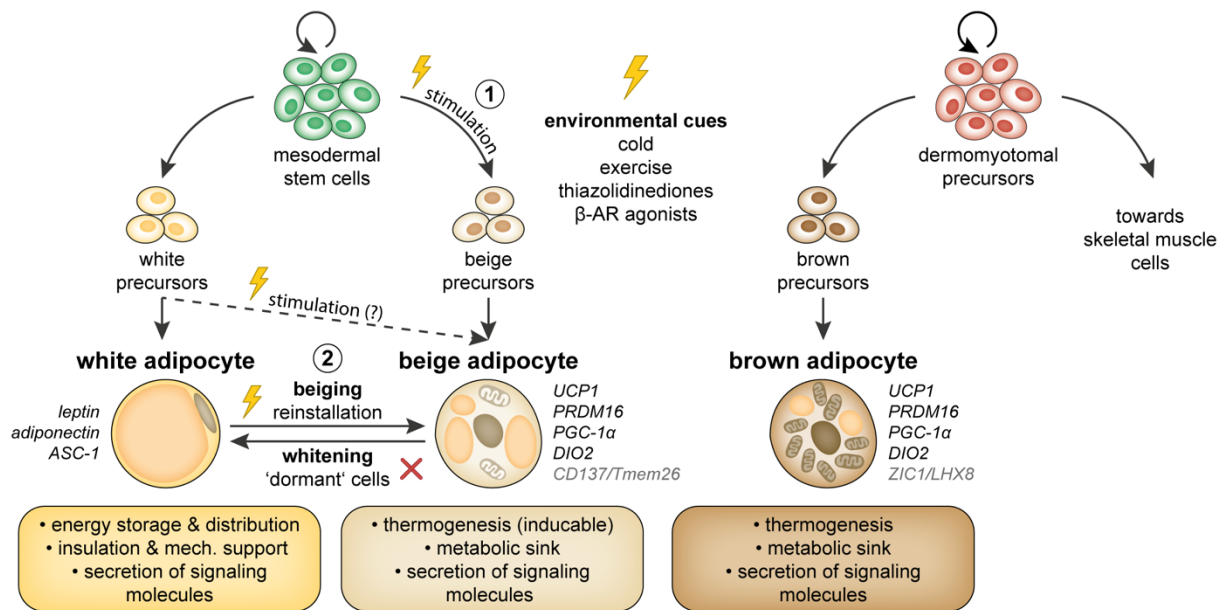


**Figure 4: Main types of adipocytes and their origins.** Adipocytes are classified into three morphologically and functionally distinct subtypes: white, beige and brown adipocytes (examples of cell type-specific markers presented in italic; putative, beige-/brown-exclusive markers in gray<sup>57–61</sup>). All three subtypes are endocrinologically active and play major roles in systemic metabolic homeostasis. One of the key functions of white adipocytes is storage and distribution of energy; beige and brown adipocytes dissipate energy through thermogenesis. White and beige adipocytes develop in WAT depots from mesodermal stem cells. Brown adipocytes, by contrast, develop during embryonic development from the dermomyotome and thereby have common precursors with skeletal muscle cells. Beige adipocytes develop upon stimulation through various environmental cues; their biogenesis happens *de novo* from precursors (pathway 1) or through *transdifferentiation/reinstallation* from 'dormant', white-like adipocytes (pathway 2). It is still under debate whether white precursors – when stimulated – can give rise to beige adipocytes (dashed line).

ASC-1: Asc-1 neutral amino acid transporter; UCP1: uncoupling protein 1; PRDM16: PR/SET domain 16; PGC-1 $\alpha$ : peroxisome proliferator activated receptor  $\gamma$  coactivator 1 $\alpha$ ; DIO2: Iodothyronine deiodinase 2; CD137: cluster of differentiation 137; Tmem26: Transmembrane protein 26; ZIC1: Zic family member 1; LHX8: LIM homeobox 8.

White adipocytes contribute to metabolic homeostasis by storing excess dietary energy in the form of fat and redistributing this stored energy upon the body's needs. To perform this function best, white adipocytes are equipped with a single large lipid vacuole. The large (25–200  $\mu\text{m}$ ) spherical cells arise in visceral and subcutaneous fat depots. Beige and brown adipocytes contribute to homeostasis through thermogenesis; to do so, they comprise large numbers of mitochondria, the sites where most of the thermogenic mechanisms occur. They are smaller than white adipocytes and contain multiple (small) lipid droplets. While beige adipocytes are dispersed within WAT depots, brown adipocytes are located in cervical, axillary, mediastinal, paraspinal and abdominal depots in the adult human body<sup>62,63</sup>. Because of its high metabolic activity, depots of thermogenic adipocytes can be radiologically detected *in vivo* via <sup>18</sup>F-fluorodeoxyglucose positron emission tomography combined with computed tomography (FDG-PET/CT) (i.e., radiolabeled

glucose uptake)<sup>64</sup>. Importantly, BAT is innate and develops from dermomyotomal progenitors while bAT is adaptive and arises through *de novo* differentiation of distinct beige precursor cells<sup>65–67</sup> or through *transdifferentiation* of white adipocytes, upon stimulation<sup>57,68–71</sup>. After withdrawal of the beiging stimulus, beige adipocytes directly acquire a white-like morphology (i.e., without involvement of a dedifferentiation step); one hallmark of beige-to-white transition is autophagy, the loss of mitochondria<sup>72</sup>. Although sharing several functions and phenotypic characteristics, brown and beige are considered distinct cell types because of different developmental origin, location and regulation<sup>57</sup>. Of note, Giordano *et al.* recently described a new subset of adipocytes – milk-producing pink adipocytes, which presumably arise from *transdifferentiation* of subcutaneous mammary white adipocytes during pregnancy and lactation<sup>73,74</sup>. Since the focus of this thesis was the development of white and beige *in vitro* models, these two types of adipose tissue are discussed in greater detail in the next sections.

#### 1.2.1.1 White Adipose Tissue

In healthy human adults, WAT comprises approximately 20-25% of total body mass. In obese individuals, the contribution of WAT to total body mass can become as high as 50%.<sup>75</sup> WAT is a key regulator of systemic energy homeostasis; not only does it constitute the main storage site of excess dietary energy, it also takes on endocrine functions (**Figure 5**). In their role as energy depots, white adipocytes sense the body's energy condition and respond by either storing fuel (in the postprandial state) or mobilizing and releasing it (in the fasting state). In the fed state, white adipocytes take up glucose – mainly through glucose transporter type 4 (GLUT4), the most abundant glucose transporter in adipocytes<sup>76,77</sup> – and long-chain fatty acids (LCFAs) from the circulation, which are then, after *de novo* lipogenesis, stored in the form of triacylglycerides (TAGs)<sup>78</sup>. In fasting states, white adipocytes receive signals from the sympathetic nervous system (SNS) to release fuel for the supply of peripheral organs. In sequential hydrolysis mediated by lipases (**Figure 5**), TAG is broken down to three free fatty acid (FFA) molecules and one glycerol molecule, which are then liberated into the circulation.<sup>79</sup> Naturally, lipolysis is triggered by SNS' release of catecholamines, such as norepinephrine (NE), which bind to  $\beta$ -adrenoreceptors ( $\beta$ -ARs) on the adipocytes' plasma membranes. However, lipolysis can also be induced artificially by administration of synthetic NE-derivates, such as isoproterenol.

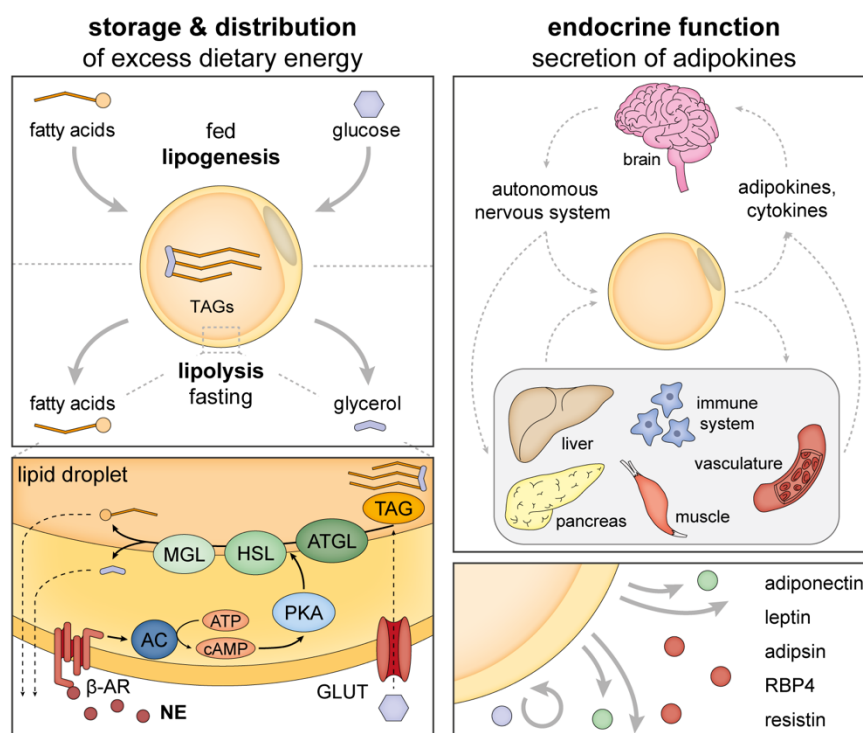


**Figure 5: Overview of WAT storage- (left) and endocrine functions (right).** White adipocytes can sense the body's energy status and respond accordingly, either by storing or releasing fuel. In the fed state, white adipocytes take up fatty acids (FAs) and glucose from the circulation by converting them to TAGs. Upon signals inducing lipolysis, i.e., the hydrolysis of TAG into three FA and one glycerol molecules, liberated fatty acids enter the circulation to supply peripheral tissue. The most common mechanism of lipolysis (lower left panel) is triggered by catecholamines, such as NE, released from sympathetic neurons in response to fasting. Binding of NE to  $\beta$ -ARs initiates a signaling cascade, in which adenylyl cyclase (AC) converts adenosine triphosphate (ATP) to cyclic adenosine monophosphate (cAMP). Elevated cAMP levels drive the protein kinase A (PKA)-dependent phosphorylation of adipose triglyceride lipase (ATGL) – converts TAG to diacylglycerol (DAG) – and hormone-sensitive lipase (HSL) – converts DAG to monoacylglycerol (MAG). In the final hydrolysis step, monoacylglycerol lipase (MGL) converts MAG to glycerol and FFAs.<sup>79</sup> GLUT: glucose transporter; RBP4: retinol binding protein 4.

The classical energy storage and distribution function of WAT already implies an extensive crosstalk with other organs; yet WAT's inter-organ communication goes way beyond simple feedback loops of fasted- vs. fed states (**Figure 5**). Only less than 30 years ago, with the discovery of leptin<sup>80</sup>, adipose tissue was established as an endocrine organ. By now, it is well-recognized that white adipocytes, and other WAT-resident cell types, secrete a plethora of signaling molecules, including adipokines (i.e., adipose-associated cytokines), bioactive lipids (lipokines), and exosomal microRNAs<sup>81</sup>. By affecting brain, liver, pancreas and immune system, amongst others, the impact of WAT is not limited to regulating energy expenditure, appetite control, glucose homeostasis, and insulin sensitivity, but includes also contributions to inflammatory events and tissue repair<sup>81,82</sup>. Leptin, adiponectin, adipsin, fatty acid binding protein 4 (FABP4), and neuregulin 4

(NRG4), amongst others, are factors exclusively produced in adipose tissues with important functions in systemic homeostasis<sup>81</sup>. Many of them act only locally (i.e., paracrine), but especially the adipokines derived from the adipocytes themselves, act on a systemic level. Notably, the secretion of signaling molecules depends on energy and adipose disease states.<sup>81</sup> Adipose dysfunction and adipose-immune interactions are covered in section 1.2.2 in greater detail.

#### 1.2.1.2 Beige Adipose Tissue

Thermogenic biogenesis and -activity of fat are regulated by cold (especially *de novo* adipogenesis) or by chronic  $\beta$ -AR signaling (especially reprogramming of white adipocytes)<sup>71,83–85</sup>. Concerning the  $\beta$ -AR signaling, however, contradictory findings from human studies exist; while  $\beta$ 3-AR signaling has been reported to induce a reprogramming of subcutaneous white adipocytes to beige adipocytes<sup>83,84</sup>, a recent study identified  $\beta$ 1-AR and not  $\beta$ 3-AR (the predominant  $\beta$ -AR in mice) as the predominant  $\beta$ -AR in human bAT<sup>59</sup>. This suggests that thermogenic fat might be regulated differently in humans and mice<sup>59</sup>. Further regulation activities haven been ascribed to systemic hormonal cues<sup>86</sup> and immune cells<sup>87</sup>.

Even though they have the machinery to store and distribute lipids, beige adipocytes' main business is not storage of fuel but thermogenesis. They contain abundant mitochondria, which feature the distinct skills to oxidize fatty acids at a great pace. To fuel thermogenesis, thermogenic adipocytes harness, for instance, metabolites, which would typically be stored by white adipocytes. This is made possible by a complex machinery of proteins, which is unique to thermogenic adipocytes. This protein complex is predominantly controlled by the transcriptional regulator PR/SET domain 16 (PRDM16) and co-factor peroxisome proliferator activated receptor  $\gamma$  coactivator 1 $\alpha$  (PGC1 $\alpha$ ) – the two master regulators of mitochondrial biogenesis, including expression of thermogenic proteins, and oxidative metabolism<sup>88–93</sup>.

The best-characterized thermogenic mechanism in beige adipocytes is mitochondrial uncoupling through uncoupling protein 1 (UCP1)<sup>78</sup> (**Figure 6**). Located at the inner mitochondrial membrane, UCP1 dissipates the proton gradient that was formed across the inner mitochondrial membrane by the electron transport chain. Thereby, heat, instead of ATP, is generated. The thermogenic signal can be propagated among beige adipocytes through connexin 43, a gap junction channel<sup>94</sup>. Interestingly, besides provoking thermogenic activity,  $\beta$ -adrenergic stimulation leads to biomechanical signaling in brown

and beige adipocytes; the actomyosin-mediated tension that was generated upon  $\beta$ -AR signaling was found critical for metabolic activation, mitochondrial uncoupling and the preservation of UCP1 expression<sup>95</sup>.

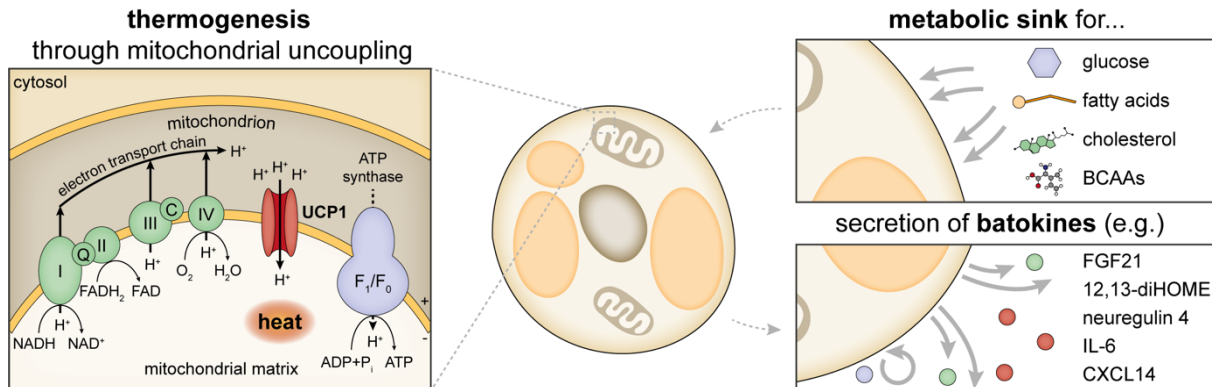


**Figure 6: Overview of key functions of bAT.** Upon induction, beige adipocytes become thermogenic. Exemplarily depicted is one mechanism of thermogenesis involving the mitochondrial uncoupling of the respiratory chain from ATP production through UCP1. Moreover, beige adipocytes act as a metabolic sink for glucose, FAs, cholesterol and BCAAs and thereby contribute to their clearance from circulation. Beige adipocytes also produce messenger molecules, i.e., batokines, which act autocrine, paracrine, or endocrine and are involved in bAT-immune interactions, for instance.

NADH/NAD<sup>+</sup>: reduced/oxidized form of nicotinamide adenine dinucleotide (NAD); FADH<sub>2</sub>/FAD: reduced/oxidized form of flavin adenine dinucleotide (FAD); H<sup>+</sup>: hydrogen cation; H<sub>2</sub>O: water; ADP: adenosine diphosphate P<sub>i</sub>: inorganic phosphate; I-IV: respiratory complexes I-IV; Q: coenzyme Q/ubiquinone; C: cytochrome c; FGF21: fibroblast growth factor 21; 12,13-diHOME: 12,13-dihydroxy-9Z-octadecenoic acid; CXCL14: C-X-C motif chemokine ligand 14.

Besides this UCP1-dependent thermogenic process, there are a couple of UCP1-independent processes: futile metabolic cycling mechanisms that depend on two simultaneous reactions – one ATP consuming reaction and another, inverse energetic reaction – which effectively do not lead to net loss of ATP, but still to the generation of heat. A number of thermogenic futile cycling mechanisms have been reported: Ca<sup>2+</sup>-cycling across the membrane of the endoplasmic reticulum<sup>96</sup>, creatine-driven futile substrate cycling (i.e., phosphorylation and dephosphorylation of creatine)<sup>97</sup>, as well as interconversion between TAG and fatty acids. Since beige adipocytes have a higher ATP production capacity than brown adipocytes, bAT can even maintain thermogenesis in the absence of UCP1 just by ATP-dependent futile cycling<sup>96,98</sup>. Consequently, UCP1 cannot be classified as universal marker for thermogenic adipocytes, since it is not necessarily expressed by all beige adipocytes.<sup>71</sup> Interestingly, beige adipocytes display heterogeneity not only regarding mechanisms of thermogenesis, but also regarding their source of fuel (e.g., ‘g-beige adipocytes’ featuring high glucose catabolism for metabolic fuel – instead of FAs).<sup>99</sup>

Importantly, beige adipocytes also take on roles beyond thermogenesis, contributing to metabolic homeostasis in several ways (**Figure 6**). Through their highly active oxidative metabolism, for example, beige adipocytes act as ‘metabolic sink’ by clearing substances, such as FAs, glucose, cholesterol and branched-chain amino acids (BCAAs), from the systemic circulation. Moreover, similar to their white counterparts, beige adipocytes secrete a myriad of signaling molecules, called batokines, mediating local (paracrine) or systemic and peripheral (endocrine) communication to other organs.<sup>71</sup>

Since there is a positive correlation between bAT prevalence and activity, respectively, and metabolic health, therapeutic strategies that target thermogenic adipocytes to regulate systemic energy homeostasis are becoming increasingly popular. On the one hand, this includes the induction of thermogenic adipose tissue through pharmaceuticals; on the other hand, options for tissue-based therapies based on implanting *ex vivo* generated grafts are being explored<sup>100,101</sup>.

### 1.2.2 Malfunctioning Adipose Tissue & Adipose-Immune Interactions

Obesity and its sequelae (see section 1.2) are one of the greatest health burdens nowadays. In 2016, approximately 13% percent of adults qualified as obese (defined by the World Health Organization by a body mass index (BMI) > 30)<sup>102</sup>. While this number likely has continued to rise, the increasing prevalence of childhood obesity is even more worrisome<sup>102</sup>.

A positive energy balance, caused by overnutrition, leads to enormous accumulation of fat in adipocytes (**Figure 7**). At first, they adapt to this overload by expanding in size (hypertrophy) and in number (hyperplasia), and finally by initiating an inflammatory response which is intended to alleviate the homeostatic stress.<sup>103</sup> However, prolonged anabolic stress eventually unleashes a pathological (maladaptive) response, which is marked by ‘metaflammation’, i.e., a low-grade chronic inflammation triggered by an altered metabolism<sup>104,105</sup>. In spite of its low-grade condition, adipose inflammation impacts organ function on a systemic level, especially through proinflammatory signaling and the strong involvement of the immune system. Even though the initial trigger of the inflammatory reaction remains unknown<sup>105</sup>, it is hypothesized that a rapid expansion of adipose tissue, which is accompanied by hypoxia, adipocyte death and changes in ECM deposition, could kick off the inflammatory response<sup>103</sup>. Reams of proinflammatory immune cells infiltrate the tissue, among them M1 macrophages<sup>106</sup>, T helper 1 (Th1) and CD8<sup>+</sup> cytotoxic T cells<sup>107–109</sup>. Together with the inflammatory adipocytes, they secrete

many proinflammatory signaling molecules, especially proinflammatory cytokines and chemoattractants, which are further exacerbating the malfunction. Insulin sensitivity becomes impaired, and so do mitochondrial function, beige fat biogenesis and consequently thermogenesis. At the same time, fibrosis and “spillover” of lipids due to adipocytes dysfunctional storage increase.<sup>78,103,105,110</sup>

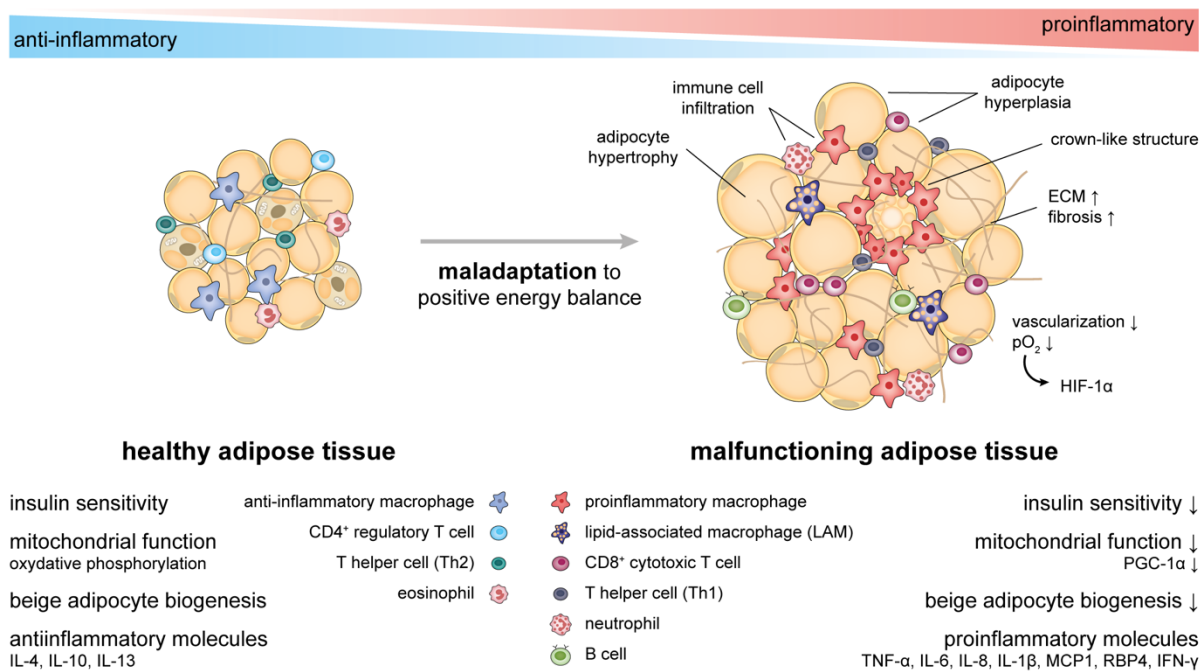


**Figure 7: Maladaptation of adipose tissue in obesity.** Schematic of healthy adipose tissue (left) and malfunctioning adipose tissue (right) with their associated (immuno-)phenotypes. Healthy adipose tissue is sensitive to insulin and possesses thermogenic beige adipocytes. Immune cells associated with healthy adipose tissue have an anti-inflammatory and regulatory character. In response to overnutrition, adipose tissue can become malfunctioning. The cells are insulin resistant, and mitochondrial- and beige adipocyte biogenesis are impaired. ECM is produced excessively leading to fibrosis, which is further aggravated by hypoxia caused by vascular rarefaction. In response, plenty of proinflammatory immune cells infiltrate the adipose tissue releasing a plethora of pro-inflammatory molecules. Figure inspired by references<sup>78,105</sup>. CD4/8: cluster of differentiation 4/8; IL-4/6/8/...: interleukin 4/6/8...; MCP1: monocyte chemoattractant protein 1; IFN-γ: interferon γ; pO<sub>2</sub>: partial pressure of oxygen; HIF-1α: Hypoxia inducible factor 1 α subunit.

Macrophages are the master regulators of adipose tissue inflammation<sup>105</sup>. Adipose tissue macrophages (ATMs) exhibit a high degree of plasticity and their activation state is more multifaceted than the binary M1/M2 classification<sup>106,111</sup>. Alongside their phenotypic diversity, obese ATMs further exhibit a dual bioenergetic profile by utilizing both glycolysis (classically M1) and oxidative phosphorylation (classically M2) simultaneously<sup>106</sup>. This heterogeneity is further reflected in their functions: one of their key tasks upon adipose tissue inflammation seems to be engulfing, or scavenging, of dead adipocytes (often by the formation of crown-like structures). Hypertrophic adipocytes are prone to pyroptosis

(a proinflammatory form of programmed cell death), a process that specifically attracts macrophages with substrate buffering capacities. Of note, ATMs are not only well equipped for handling lipids, they can also incorporate other substrates, such as catecholamines or iron, to clear, or modulate the availability, of these substrates in the microenvironment.<sup>106,112,113</sup> Moreover, an active, direct crosstalk between adipocytes and ATMs has been documented: adipocytes were found to release exosome-sized, lipid-laden vesicles, which directly modulate ATM activity by inducing a differentiation of macrophage precursors<sup>114</sup>. A further interesting example of adipocyte-macrophage interaction was recently reported by Brestoff *et al.*: in mice, adipocytes were shown to transfer their mitochondrial contents to neighboring macrophages, potentially to regulate adipose tissue homeostasis. In obesity, this mechanism was impaired.<sup>115</sup>

The close connection of adipose tissue to the immune system is not limited to disease states: lean adipose tissue, too, is populated with a variety of immune cells, which surveil and maintain tissue functions through regulatory, anti-inflammatory activities. Among them are M2 macrophages releasing interleukin 10 (IL-10) to maintain adipocytes' insulin sensitivity<sup>116</sup>, T helper 2 (Th2)<sup>117,118</sup> cells promoting activation of eosinophils and type 2 innate lymphoid cells which release interleukin 4 (IL-4) leading, e.g., to beige adipocyte differentiation<sup>119,120</sup>. Therefore, it is not only the inflammatory pathways that are potential therapeutic targets for future obesity/metabolic disease treatments. More attention could also be paid to mechanisms supporting the maintenance, or restoration, of the original anti-inflammatory mediators.

### 1.3 Research Landscape of Human Adipose Tissue

#### 1.3.1 *In vivo* Research on Adipose Tissue

In light of the severe global 'diabesity' burden, obtaining human-relevant detailed mechanistic insights in adipose (patho-)physiology are of great importance for the development of prevention strategies and therapeutic interventions. However, *in vivo* human studies on mechanistic levels are associated with unacceptable health risks, which is why most of our knowledge of human adipose tissue arose from clinical observations and genome-wide association studies (GWAS). By comparison, animal models allow for more flexibility regarding experimental interventions and mechanistic investigations. Hence, a great part of our current understanding of adipose tissue lead back to research on animal models. In order to study adipose mechanisms and to mimic human pathologies such as obesity, a variety of rodent models have been developed: the

“AdipoChaser” mouse exhibiting inducible, permanent mature adipocyte labeling for studying adipogenesis<sup>121</sup>, the *ob/ob* mouse as a monogenic model of obesity lacking leptin on protein level<sup>122,123</sup>, and the diet-induced obese mouse, which, as a polygenic model, resembles human obesity closer than monogenic models<sup>124</sup>. However, despite humanization efforts of rodent models, in many cases, findings from animal models cannot be translated to human biology. Especially with regard to metabolism and immunology, there are immense differences between the different species<sup>125–130</sup>.

### 1.3.2 Conventional *in vitro* Adipose Tissue Models

Even though human WAT, as compared to other types of tissue, is quite readily available for research as a byproduct from cosmetic surgery, working with mature human adipocytes *in vitro* is troubled by culturability challenges: mature adipocytes are non-proliferating and cannot be cryopreserved, which makes large-scale donor-specific studies impractical. Moreover, they are buoyant, large, and extremely fragile, and hence cannot be cultured using conventional cell culture methods. Moreover, the use of adipose tissue explants as a tissue source is frequently hampered by issues of hypoxia or inflammation<sup>131,132</sup>. To circumvent these obstacles, most studies on adipose tissue rely on an *in vitro* differentiation of stem cells or adipose progenitors. The most commonly used, and characterized, cell line in adipose tissue research is the murine 3T3-L1 line<sup>133</sup>. Unlike white adipocytes, human thermogenic adipocytes are not readily available, and *in vitro* research depends on differentiation strategies. Brown adipocytes have been differentiated from human pluripotent stem cells recently<sup>134</sup>; beige adipocytes can be derived from human AdMSCs, for instance<sup>135</sup>.

Yet, despite rapid progress in the field of stem cell differentiation, maturity of adipocytes differentiated *in vitro* is still inadequate: differentiated adipocytes hardly reach the stage of unilocularity and show different cytokine secretion profiles than their *in vivo* as well as mature *in vitro* counterparts<sup>136–138</sup>, an important hurdle when studying adipose tissue endocrine function. Consequently, as long as differentiation protocols are insufficient, the use of isolated mature adipocytes is indispensable for building a physiologically relevant WAT *in vitro* model, which is not specifically designed for adipogenesis research.

Overall, the landscape of *in vitro* adipose models is rather sparse, in comparison to the one of other organ systems. Moreover, a large part of adipose tissue engineering approaches attempts to generate large-scale tissue grafts for regenerative medicine instead of focusing on models of adipose (patho-)physiology. A commonly used method

to maintain mature white adipocytes *in vitro* is the concept of ceiling culture. It exploits the adipocytes floating properties by presenting them with an adhesion surface at the ceiling of the culture vessel; the media supply is assured from below.<sup>139–141</sup> However, this culture method has its limitation since it induces dedifferentiation of mature adipocytes within a few days<sup>142–144</sup>. Over recent years, a few advanced adipose tissue *in vitro* models have been introduced that enable long-term culture of mature adipocytes by overcoming the challenges in mature adipocyte handling and culturability. First, to offer protection and ensure structural stability for the buoyant adipocytes, 3D biomaterial scaffolds are broadly used<sup>145–150</sup>. Similarly, other strategies to achieve structural support of adipocytes and prevent them from floating have been implemented by sandwiching adipocytes between SVF sheets<sup>151</sup> or by advanced versions of ceiling culture<sup>152</sup>. Even though these studies present valuable first steps towards the longevity of mature adipocytes *in vitro*, their physiological relevance is limited due to the absence of vascular perfusion or (mostly) interactions with other cell types, such as immune cells, for instance.

### 1.3.3 Organ-on-Chip Systems Integrating Adipose Tissue

The OoC technology offers the potential to integrate the missing piece of a physiological adipose 3D microenvironment. Especially the integration of a vascular component is of utmost importance for a physiologically relevant adipose tissue model in the light of its high metabolic and endocrine activity.

Yet, just like conventional adipose *in vitro* models, adipose tissue-on-chip systems are rare, at least compared to other OoC systems, and they are marked by *in vitro* differentiated adipocytes and their shortcomings (see above)<sup>136,137,153</sup>: although trying to recapitulate adipocyte insulin resistance or even adipose tissue immunomodulatory function, all existing adipose tissue-on-chip models, to the best of my knowledge, resort to differentiating human AdMSCs/preadipocytes<sup>154–157</sup> or even murine preadipocytes<sup>158–162</sup> as a cell source. There is a collection of microanalytical fluidic systems targeting adipocyte investigation based on microfluidic approaches<sup>163–165</sup>, which all integrate mature adipocytes. However, the devices were specifically designed to measure adipocyte secretions at very high resolutions and are less suited for long-term culture of adipocytes and recapitulation of physiological microenvironments. Notably, all adipose tissue microfluidic systems discussed above aimed to integrate white adipocytes. No reports on BAT- or bAT-on-chip platforms were found.



# Chapter 2

## Objective of the Thesis



## 2. Objective of the Thesis

The overall objective of this thesis is to develop human adipose tissue-on-chip systems capable of reflecting adipose tissue's miscellaneous functions in order to address the urgent need for physiological, human-relevant *in vitro* models for adipose tissues research. Owing to the enormous heterogeneity of adipose tissue, two distinct types of adipose tissue-on-chip models are targeted:

- i. WAT-on-chip models that recapitulate the complex structure and cellular composition of WAT in its entirety and in an autologous manner
- ii. bAT-on-chip models that facilitate the process of thermogenic adipocyte biogenesis on chip

To develop these models, a number of intermediate sub-objectives need to be achieved, representative of all stages of the OoC development process (**Figure 2**), ranging from conceptualization, design, and fabrication of microfluidic platforms, over development of logistics and protocols for cell sourcing, isolation, and chip integration, to functional validation of the models via case studies.

Specifically, the first sub-objective is the **technological development of microfluidic platforms** particularly tailored to the needs of adipose tissue. On the one hand, the challenging characteristics of mature white adipocytes, above all buoyancy and fragility, have to be addressed. On the other hand, the demands of other WAT-associated cells, such as the endothelium, need to be considered. Along the same line, the specific demands of differentiation protocols regarding chip materials have to be taken into account to enable on-chip beige adipogenesis.

The second sub-objective is the **evaluation and establishment of suitable tissue sources**. This includes the development of tailored isolation, preparation, and injection procedures as well as setting up logistics to source autologous materials.

The third sub-objective is the **establishment of a toolbox of readout methods** specifically tailored for OoC application and adipose tissue functionalities, including online, at-line and off-line analysis tools.

The fourth sub-objective is the **generation and characterization of monoculture on-chip models** incorporating key parenchymal adipose cells such as mature white adipocytes and beige adipocytes as well as endothelial barriers.

Finally, the fifth sub-objective is the **increase in physiological relevance of the WAT-on-chip model** by adding complexity regarding cellular heterogeneity via integration of almost all WAT-associated cell types (adipocytes, endothelial barriers, adipose progenitors, and tissue-resident immune cells).

# Chapter 3

## Materials & Methods



### 3. Materials & Methods

**Most methods applied to perform the research experiments of this thesis are covered at length in the appended publications and manuscripts, respectively.** The following chapter describes the methods applied to fabricate and characterize the third-generation silicone-thermoplastic hybrid adipose tissue microfluidic platform as well as the protocols to build and read out beige adipocytes-on-chip models. Materials and device utilized for performing these experiments are listed in **Table 3 - Table 7** in '*Materials and Devices*'.

#### 3.1 Fabrication and Characterization of Third-Generation Microfluidic Platform

##### 3.1.1 Chip Design and Dimensions

The 3<sup>rd</sup>-generation adipose tissue-on-chip device consists of two microstructured layers – one layer contains tissue compartment structures while the other contains microscale channels for constant media perfusion – separated by a porous membrane (**Figure 9a**). The design of the microstructures was customized to the integration of human adipocytes and drafted using CorelCAD [Corel Corporation, Ottawa, Ontario, Canada]. Table 1 provides an overview of key chip dimensions and associated volumes.

**Table 1: Dimensions of the 3<sup>rd</sup>-generation microfluidic adipose tissue-on-chip platform.**

<b>Tissue compartment</b>		
Entire compartment (incl. channels)	Area	37.90 mm <sup>2</sup>
	Volume	7.54 µL
Individual tissue chamber	Radius	0.60 mm
	Area	1.13 mm <sup>2</sup>
	Height	0.20 mm
	Volume	0.23 µL
Sum of 16 chambers	Area	18.10 mm <sup>2</sup>
	Volume	3.62 µL
<b>Media compartment</b>		
Entire compartment	Area	125.32 mm <sup>2</sup>
	Height	0.20 mm
	Volume	25.06 µL

### 3.1.2 Chip Fabrication

The microfluidic platform is fabricated from multiple different materials tailored to meet the requirements of the respective layers, including (i) a glass (to provide optimal optical accessibility), (ii) a PDMS tissue compartment layer (to allow for oxygen diffusion through the chip's bulk material) as well as interface layer (to allow tubing connection), (iii) a porous polyethylene terephthalate (PET) (to fluidically connect media and tissue compartments) and (iv) a PET-G media layer (to limit absorption of small hydrophobic molecules from perfused media) (**Figure 10a**). To microstructure the parts and assemble the devices, we used standard soft lithography and replica molding, hot embossing as well as wet-chemical- and oxygen plasma surface functionalization (**Figure 8**).

Patterned silicon wafers served as positive molding templates for PDMS casting; the wafers were produced by common soft lithography (process described in detail in attached **Publication [7]**). The production of PDMS tissue compartment layers, and their bonding to glass coverslips (**Figure 8b**) or microscope slides (in the case of gene expression analysis experiments) was performed as described in attached **Publications [7] and [11]**. PDMS interface layers for connection to the external pumping system were produced by engraving the chip's footprint in a ~4 mm thick, unstructured PDMS slab using a lasercutter with a 10 W carbon dioxide (CO<sub>2</sub>)-laser (8% power, 10% speed, and 1000 pixel per inch). The chip pieces were cut using a scalpel. Inlet and outlet ports were punched using a biopsy punch.

PET-G media channel layers were produced by hot embossing. First, the structured silicon master wafer was used to create a PDMS slab with the indented features. This PDMS slab was silanized (2 h exposure to trichloro(1H,1H,2H,2H-perfluorooctyl)silane in an evacuated desiccator) and served as a negative molding template for another PDMS slab with protruding features. This slab was cut to the footprints of individual chips, and the pieces were placed at 150°C overnight to further harden the PDMS. The resulting PDMS pieces served as stamps for the hot embossing process (**Figure 8a**): A 500 µm thick PET-G piece, slightly larger than the final design, was cleaned with isopropanol, placed onto the PDMS stamp and clamped between two clean microscope slides using foldback clips. The clamped stack was placed for 30 min in a convection oven (preheated to 130°C) and subsequently let cool down at RT for at least 30 min. Afterwards, the structured PET-G was released from the PDMS stamp. Finally, the PET-G piece was cut to the correct size, and all in- and outlet ports were punched open using the biopsy punch. For final chip bonding, silane-functionalization and O<sub>2</sub>-plasma activation was used: first,

the PET-G layer was activated with O<sub>2</sub>-plasma (60 s, 50 W, 0.2 cm<sup>3</sup>m<sup>-1</sup> O<sub>2</sub>) from both sides and immediately submerged in a preheated (50°C) 4% APTES (3-Aminopropyl)triethoxysilane solution (in ultrapure water) for 20 min. In the meantime, after ~15 min, the tissue layer (bonded to the coverslip), membrane and PDMS top layer were activated with O<sub>2</sub>-plasma (30 s, 50 W, 0.2 cm<sup>3</sup>m<sup>-1</sup> O<sub>2</sub>). After the incubation in APTES, the PET-G layer was transferred to ultrapure water, and then blow-dried with nitrogen. Finally, the membrane was bonded to the tissue layer (activated membrane side facing the PDMS), the prepared PET-G layer was placed onto the tissue layer/membrane and the entire module eventually closed off by aligning the top layer (**Figure 8b**). The layers were pressed together by applying manual pressure and placed in a convection oven (60°C) overnight to enhance bonding strength.

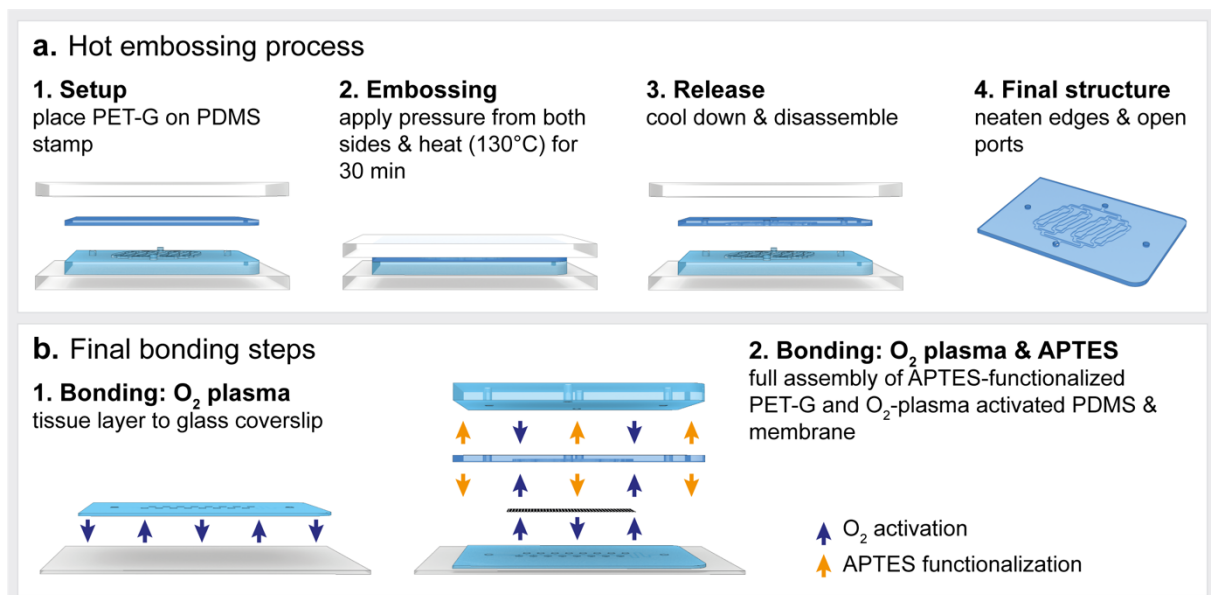


**Figure 8: Key fabrication steps of 3<sup>rd</sup>-generation microfluidic device.** **a.** Media channel features are created via hot embossing of a PET-G sheet using a PDMS template. **b.** Chip assembly includes two subsequent bonding steps: the PDMS tissue layer is bonded to glass substrate using O<sub>2</sub> plasma bonding. The final assembly is based on O<sub>2</sub> plasma activation (PDMS pieces and PET membrane) and APTES functionalization (PET-G piece).

On the next day, the chips' bonding quality was tested by flushing DI water into the channels and observing the fluid flow for any leakages or discontinuities. Preparation for tissue injection, as well as preparation of supplies for connection to the external pumping system, was performed as reported in attached **Publication [11]**.

### 3.1.3 Comparison of Absorption Characteristics: PET-G vs. PDMS

To study the differences in the partitioning of small molecules into the chip material, chips of the same design made entirely from PDMS were fabricated in addition to the hybrid chips. In both types of chips, a 100  $\mu\text{M}$  solution of rhodamine 6G in Dulbecco's phosphate-buffered saline without calcium chloride and without magnesium chloride (PBS<sup>-</sup>) was perfused through the media channels (20  $\mu\text{L}/\text{h}$ ) and monitored using a fluorescence microscope [Leica DMI8]. Image sections were chosen to capture two media channels (one at each side of the image) bordering bulk material. Using Fiji [ImageJ version 1.53c]<sup>166</sup>, the vertically averaged pixel intensity (specifically, the mean gray value) was plotted against the horizontal distance through the image for timepoints 30 min, 60 min, 90 min and 120 min of dye perfusion.

### 3.1.4 Characterization of on-Chip Diffusive Transport

To visualize the diffusion of compounds from the media channels across the membrane into the tissue chamber, we perfused a PBS<sup>-</sup> solution containing 100  $\mu\text{g}/\text{mL}$  fluorescein isothiocyanate (FITC)-dextran (3-5 kDa) through the system (20  $\mu\text{L}/\text{h}$ ). Prior to perfusion of the tracer, the tissue compartment was filled with hydrogel (HyStem<sup>®</sup>-C) to keep the microenvironment consistent with cell experiments. Six tissue chambers were monitored – three that were closer and three that were farther from the media inlet port (i.e., second in row of the serial media perfusion). Each position was imaged every 60 s, and in two different focal planes – in the lower part of the tissue chamber and in the media channel above the same tissue chamber – using a confocal laser scanning microscope [Zeiss LSM 710]. For each image, fluorescence intensity (specifically, mean gray value in Fiji software) was determined in an ROI (region of interest) in the chamber/media channel as well as for the background. After subtraction of background signal, fluorescence intensity values were averaged for the three replicates per chamber location and plotted against the time of image acquisition.

### 3.1.5 Computational Fluid Dynamic (CFD) Modeling

For numerical modeling of on-chip fluid flow, transport of diluted species as well as oxygen supply and consumption, COMSOL Multiphysics [COMSOL Vers.5.5, Stockholm, Sweden] was used. We used the model described in attached **Publications [5] and [11]** with slight modifications: In brief, the membrane as well as the hydrogel were treated as porous media. With the 'Free and Porous Media Flow' module, the free flow was solved

by employing the Navier-Stokes equation and the porous media flow by employing Darcy's law. To simultaneously assess the diffusion properties of small molecules solved in the media across the membrane and through the hydrogel, the 'Transport of Diluted Species in Porous Media' module was added. For the membrane with a pore radius  $r_p = 1.5 \times 10^{-6}$  m and a pore density of  $6 \times 10^9$  m<sup>-2</sup>, the porosity was calculated to  $\rho = 4.24\%$ . Using Dagan's equation<sup>167</sup>,

$$Rp = \frac{\mu}{r_p^3} \left( 3 + \frac{8L}{\pi r_p} \right)$$

with fluid viscosity  $\mu$ , and pore length  $L$ , the fluidic resistance of the pores was calculated to  $R_p = 5.9 \times 10^{15}$  Ns/m<sup>6</sup>. Further, using

$$\kappa = \frac{\mu L \rho}{\pi r_p^2 R_p}$$

the hydraulic permeability  $\kappa$  was calculated to  $\kappa = 1.07 \times 10^{-14}$  m<sup>-2</sup>. Diffusion coefficient was assumed to be  $1 \times 10^{-9}$  m<sup>2</sup>/s<sup>168</sup>.

For the hydrogel, we used the following parameters<sup>169</sup>: porosity  $\rho = 0.99$ , hydraulic permeability  $\kappa = 1.5 \times 10^{-16}$  m<sup>2</sup> and a diffusion coefficient of  $1 \times 10^{-11}$  m<sup>2</sup>/s.

The flow rate was set to  $5.56 \times 10^{-12}$  m<sup>3</sup>/s (20  $\mu$ L/h) for simulations including the entire chip, or to  $6.95 \times 10^{-13}$  m<sup>3</sup>/s (2.5  $\mu$ L/h) for simulations focusing on one of the eighth split media channel supplying two tissue chambers.

For modeling oxygen consumption by the tissue compartment and oxygen supply through media flow and diffusion through the chips bulk material, we calculated the oxygen consumption to  $4.128 \times 10^{-5}$  mol/s m<sup>3</sup> assuming a beige adipocyte O<sub>2</sub> consumption of  $4.3 \times 10^{-10}$  mol/s per mg of deoxyribonucleic acid (DNA)<sup>170</sup>, a DNA mass of 6 pg per cell<sup>171</sup> and a loading cell density of  $1.6 \times 10^{13}$  cells/m<sup>3</sup>. The O<sub>2</sub> concentration was assumed to be saturated (i.e., 0.2 mol/m<sup>3</sup>) in the perfused media at the chip's inlet and at the surfaces of the chip. The diffusion coefficient of O<sub>2</sub> in medium was chosen as  $D_{O_2} = 3 \times 10^{-9}$  m<sup>2</sup>/s<sup>172</sup>, through PDMS as  $D_{O_2} = 3.25 \times 10^{-9}$  m<sup>2</sup>/s<sup>173</sup>, and through PET-G as  $D_{O_2} = 1 \times 10^{-12}$  m<sup>2</sup>/s<sup>174</sup>. Of note, the simulations should merely be treated as approximations to the actual situation; when modeling O<sub>2</sub> availability, for instance, the solubility of O<sub>2</sub> in the different materials was not taken into the account for calculations. Since its solubility in PDMS is higher than in water<sup>175</sup>, the actual O<sub>2</sub> concentrations on-chip might be higher.

### 3.2 Setup and Characterization of a Beige Adipocytes-on-Chip Model

Given the scarcity of human sources for mature beige adipocytes, preadipocytes were differentiated on-chip to generate a human beige adipocyte-on-chip model. Preadipocytes were expanded in cell culture flasks prior to chip injection. On-chip differentiation was conducted over the course of 8 days by administration of different differentiation media (**Table 2**, adapted from<sup>176</sup>). Endpoint analyses were performed on day 0 (d0), d3, and d7.

**Table 2: Overview of cell culture media used for the beige adipocyte-on-chip model.**

DMEM-F-12: Dulbecco's Modified Eagle Medium/Nutrient Mixture F-12; HEPES: (4-(2-hydroxyethyl)-1-piperazineethanesulfonic acid); FCS: fetal calf serum; bFGF: basic fibroblast growth factor; rhEGF: recombinant human epidermal growth factor; IBMX: 3-Isobutyl-1-methylxanthine; T3: 3,3',5-Triiodo-L-thyronine.

Name of medium	Time of administration	Purpose	Ingredients
<i>ZBSQ base</i>	-	Basis for other media	DMEM/F-12 + 10 $\mu$ M HEPES + 10% (v/v) FCS + 100 U/mL Pen/Strep
<i>ZBSQ growth</i>	Off-chip: expansion On-chip: d-1 to d0		<i>ZBSQ base</i> + 5 ng/mL bFGF + 5 ng/mL rhEGF
<i>ZBSQ BAT induction</i>	On-chip: d0 to d3 (off-chip pre-diff.: d0 to d3)	Initiating differentiation into beige adipocytes	<i>ZBSQ base</i> + 597 nM human insulin + 2 $\mu$ g/mL dexamethasone + 500 $\mu$ M IBMX + 500 nM Rosiglitazone + 1 nM T3 + 125 $\mu$ M indomethacin
<i>ZBSQ BAT maintenance</i>	On-chip: d3 to d7	Maintaining and promoting differentiation	<i>ZBSQ base</i> + 597 nM human insulin + 500 nM Rosiglitazone + 1 nM T3

#### 3.2.1 Preparation and Injection of Human Preadipocytes

Cryopreserved primary subcutaneous human preadipocytes were purchased from Zen-Bio [SP-F-SL, lots: SL0064 and SL0065, both lots are cells pooled from several female donors with BMI 25.0-29.99]. Alternatively, stromovascular cells were isolated from human skin biopsies with subcutaneous adipose tissue as described in attached **Publication [11]**. Prior to injection, cells were expanded using standard cell culture procedures: in brief, preadipocytes were thawed by placing the vial in a 37°C water bath. Upon reaching a liquid state, the cell suspension was immediately transferred to prewarmed *ZBSQ growth* medium (**Table 2**) in a T175 cell culture flask. Seeding densities

ranged from 2850 – 6000 cells/cm<sup>2</sup>. Cells were expanded to a confluency of ~90%. The preadipocytes were detached by first rinsing the growth surface with PBS<sup>-</sup> and subsequently incubating for 3 min with TrypLE™ Select Enzyme. The dissociation reaction was stopped by adding 10% (v/v) fetal calf serum (FCS). The cell suspension was centrifuged at 209 rcf while cells were counted using a hemocytometer. After the cell pellet was resuspended to the desired concentration, the preadipocyte solution was either split (not more than five times), cryopreserved (1 x 10<sup>6</sup> cells/mL in FCS with 10% (v/v) dimethyl sulfoxide (DMSO) using a freezing container with a cooling rate of -1°C/min), or prepared for chip injection.

The mvECs for patient-specific beige adipocyte-endothelium co-culture chips were isolated, expanded and seeded as described in attached **Publication [11]**. Anthropometric data of the donor in (**Figure 17**): 41-year-old female with BMI = 30 (at maximum weight BMI = 52). Biopsy origin was gluteal.

### 3.2.2 On-Chip Differentiation of Preadipocytes into Beige Adipocytes

Preadipocyte injection into the microfluidic platform was performed similar to the injection process introduced in attached **Publication [11]**. In brief, the microfluidic platforms were prepared by filling microchannels and -chambers with PBS<sup>-</sup> and creating a liquid droplet on top of the tissue inlet port. Hydrogel (HyStem<sup>®</sup>-C) components were reconstituted and mixed according to manufacturer's instructions (except for addition of the hydrogel crosslinker). Two chips were injected in one injection round; injection rounds were repeated until the desired amount of chips was injected. For each round, 0.5 x 10<sup>6</sup> cells were transferred to a 1.5 mL microcentrifuge tube and centrifuged at 209 rcf for 5 min. The cell pellet was then thoroughly resuspended in 25 µL of the hydrogel components (i.e., 12.5 µL thiol-modified hyaluronan (Glycosil) and 12.5 µL thiol-modified denatured collagen (Gelin-S<sup>®</sup>)). When the cells were suspended homogenously among the hydrogel, 6.25 µL of thiol-reactive crosslinker, PEGDA (Extralink) was mixed to the cell-hydrogel mixture. Quickly, 15 µL of the mixture was injected into each of the two chips by (i) removing the filled pipette tip from the pipette, (ii) creating a small droplet of cell-hydrogel mixture at the tip, (iii) letting the liquid droplets on top of the tissue inlet port and at the apex of the pipette tip coalesce, (iv) inserting the pipette tip into the tissue inlet port and (v) injecting the cell-hydrogel mixture by applying gentle manual pressure on top of the pipette tip. When all tissue chambers were filled, the tissue injection channels were cleared from preadipocytes by flushing with a hydrogel mixture without cells as described

above. Afterwards, the tissue in- and outlet ports were plugged using cut sterile wire, and the chips were supplied by intermediate, hydrostatic pressure-driven media flow by inserting an empty pipette tip into the media outlet port and a tip filled with 100  $\mu$ L of *ZBSQ growth* medium in the media inlet port. After all chips were successfully loaded, they were mounted to a constant media perfusion actuated by external syringe pumps connected via tubing infrastructure as described in attached **Publications [7] and [11]** (flow rate set to 20  $\mu$ L/h at all times). After overnight perfusion of *ZBSQ growth* medium, the medium was changed to *ZBSQ bAT induction* medium to initiate differentiation (denoted d0 of on-chip differentiation). On d1 and d2, the perfusing *ZBSQ bAT induction* medium was refreshed. On d3, medium was fully changed to *ZBSQ bAT maintenance* medium, which was in the following exchanged every other day. Importantly, when changing media, the medium in both syringe and tubing was replaced.

Alternatively, to reduce on-chip cell death typically occurring after initiation of differentiation, preadipocytes were pre-differentiated until d3 in tissue culture flasks, detached and injected as described above. With this method, the cells that died in response to initiation of beige differentiation were eliminated prior to injection. After injection, the chips were cultured for 5 more days (day of injection was excluded from differentiation timeline) with *ZBSQ bAT maintenance* perfusion (see above).

### 3.2.3 Monitoring of Viability on-Chip

On chip viability was determined by measuring the lactate dehydrogenase (LDH) concentration from media effluents using the CytoTox 96<sup>®</sup> Non-Radioactive Cytotoxicity Assay (Promega GmbH). Media effluents from the chips were collected every 24 h and immediately analyzed with the Cytotoxicity Assay in 384 well plate format according to manufacturer's instructions. To determine the possible maximum target LDH release, we lysed three of the chips directly after injection for 2 h using 1X Lysis Solution provided with the kit in *ZBSQ growth* medium. Following lysis, the effluents were collected thoroughly, diluted to 480  $\mu$ L (volume expected for 24 h perfusion at 20  $\mu$ L/h), and analyzed. Resulting absorbance values were averaged and used for the normalization of the other samples.

We further performed live-/dead staining on d7 of on-chip culture for differentiated beige adipocytes as well as undifferentiated preadipocytes. The cytosol of live cells was visualized by fluorescein diacetate (FDA) while propidium iodide (PI) intercalated into the DNA of dead cells (with damaged plasma membrane). As counterstain, nuclei of all cells

were visualized using Hoechst 33342 staining. The staining procedure was performed as described in attached **Publication [11]**, whereby Hoechst solution was added at a concentration of 20  $\mu\text{M}$  to the FDA/PI-solution.

### 3.2.4 Morphological Characterization of Beige Adipocytes on-Chip

For visualization of the morphological changes during differentiation, lipid droplets and mitochondria as well as nuclei and cytoskeleton were stained on d3 and d7. Unless stated otherwise, all washing and staining steps were performed via hydrostatic pressure-driven flow: an empty pipette tip was inserted into the media outlet, a pipette tip filled with 100  $\mu\text{L}$  of the respective solution was inserted into the media inlet, and the solution perfused for at least 5 min. All steps were conducted protected from light to prevent bleaching of fluorophores.

Mitochondria were visualized by incubating 2  $\mu\text{M}$  MitoTracker<sup>®</sup> Deep Red FM in cell culture medium (as defined by differentiation state of stained sample) for 1 h at 37°C, 5% CO<sub>2</sub> and 95% relative humidity (rH). Afterwards, the chips were washed with Dulbecco's Phosphate Buffered Saline with magnesium chloride and calcium chloride (PBS<sup>+</sup>) twice and fixed with ROTI<sup>®</sup>Histofix 4% for 30 min on ice. Then, the chips were washed twice with PBS<sup>-</sup> and permeabilized/blocked for 15 min with 0.1% (v/v) Triton-X and 0.3% (w/v) bovine serum albumin (BSA) in PBS<sup>-</sup>. For subsequent staining, the chips were incubated for 60 min in Antibody Diluent with Background-Reducing Components with 1  $\mu\text{g}/\text{mL}$  (2.85  $\mu\text{M}$ ) 4',6-diamidino-2-phenylindole (DAPI), 132 nM Alexa Fluor<sup>™</sup> 546 Phalloidin and 1  $\mu\text{g}/\text{mL}$  (3.82  $\mu\text{M}$ ) BODIPY<sup>™</sup> 493/503 dye. Finally, the chips were washed three more times with PBS<sup>-</sup>, stored submerged in PBS<sup>-</sup> in 50 mL centrifuge tubes and imaged within 14 days.

To monitor lipid droplet formation, mitochondria biogenesis, cell number and cytoskeletal changes throughout progressing beige differentiation in a quantitative way, all 16 chambers of all chips were imaged with a fluorescence microscope (Leica DMI8) whereby imaging parameters were set for the d7 sample and kept unchanged for imaging of the d3 samples. For analysis, mean gray values of image sections within the tissue chambers were calculated using Fiji, averaged per day of analysis and plotted against the respective day.

Moreover, fluorescence images were acquired using laser scanning microscopes [Zeiss LSM 710 and LSM 880 with Airyscan]. Airyscan images were acquired with the kind help

of Aline Zbinden and Daniel Alejandro Carvajal Berrio, both members of the Schenke-Layland Lab at Eberhard Karls University Tübingen.

Images were processed using Fiji for adjustment of brightness and contrast, for creating maximum intensity projections or orthogonal views of Z-stacks and for insertion of scale bars.

### 3.2.5 Gene Expression Analysis of Beige Adipocytes on-Chip

To monitor the beige differentiation on a transcriptional level, gene expression of general adipogenesis and beige/brown adipose tissue-specific markers was analyzed on d0, d3 and d7 of differentiation as well as in response to  $\beta$ -adrenergic stimulation on d7 (with 5  $\mu$ M, 10  $\mu$ M and 20  $\mu$ M (-)-Isoproterenol hydrochloride for 5 h). Therefore, the messenger ribonucleic acid (mRNA) levels of FABP4 and peroxisome proliferator activated receptor  $\gamma$  (PPAR $\gamma$ ) (both adipogenesis in general), as well as UCP1, PRDM16 and PGC-1 $\alpha$  (all beige/brown specific markers) were measured relative to peptidylprolyl isomerase A (PPIA) (housekeeping gene) levels.

For ribonucleic acid (RNA) extraction and isolation, the ReliaPrep™ RNA Miniprep Systems Kit (Promega GmbH) was used. Since the kit is for well plate format experiments, a protocol for on-chip lysis and lysate retrieval was established: chips were washed with 100  $\mu$ L ice-cold PBS<sup>-</sup> via hydrostatic pressure-driven flow. Then, the chips were cut apart at the interface between PDMS tissue layer and PET-G media layer using a scalpel. Media layer and PDMS top were discarded. The membrane was carefully removed from the tissue layer and placed upside-down in a disposable petri dish. Then, 50  $\mu$ L of lysis buffer each (prepared according to the kit's instructions) were added onto the open tissue compartment layer and onto the membrane. The lysis buffer was incubated for 10 min on ice. Afterwards, the lysis buffer was thoroughly collected from inside the tissue chambers as well as the membrane and collected in an RNase-free microcentrifuge tube. Fresh lysis buffer was applied to the tissue layer and membrane once more, and lysis was enhanced by carefully mixing lysis buffer with the contents of the tissue chambers. The process was monitored using an inverted bright field microscope to ensure cell lysis. When all cells were lysed, the lysis buffer was added to the RNase-free microcentrifuge tube. RNA isolation was then performed according to the manufacturer's instructions. When adding isopropanol to the lysate, 70  $\mu$ L of isopropanol were added to 200  $\mu$ L chip-derived lysate. In the final step of the protocol, purified RNA was eluted into 15  $\mu$ L of nuclease-free water. RNA concentrations and purity were

determined using a NanoDrop™ 2000/2000c Spectrophotometer. The samples were stored at -80°C until proceeding with reverse transcription (RT).

To synthesize complementary DNA (cDNA) molecules from the RNA templates, the iScript™ Reverse Transcription Supermix for RT-qPCR (Bio-Rad Laboratories, Inc.) was used according to the provided manual; 150 ng of RNA were utilized for each sample. Final cDNA samples were kept at -20°C until proceeding with the quantitative polymerase chain reaction (qPCR).

For the qPCR, the Applied Biosystems™ TaqMan™ Universal Master Mix II (no UNG) (Thermo Fisher Scientific) was used according to manufacturer's instructions in combination with the probes listed in

**Table 5.** The qPCR was performed in a 96 well plate with a reaction volume of 20 µL in technical triplicates for each sample and further analyzed with a CFX Connect Real-Time PCR Detection System (Bio-Rad Laboratories, Inc.).

Relative gene expression was calculated from the qPCR data by using the  $\Delta\Delta C_q$  calculation method<sup>177,178</sup>. In brief, quantification cycle ( $C_q$ ) values of the house keeping gene were subtracted from the  $C_q$  values of the target gene to form  $\Delta C_q$ . This value was then transformed to the exponential expression  $2^{-\Delta C_q}$ , replicates were averaged and finally normalized to the exponential expression of the treatment control to form  $\Delta\Delta C_q$ . The treatment control was either gene expression of the target gene before differentiation (d0) for the differentiation monitoring experiments, or non-stimulated samples, in case of  $\beta$ -adrenergic stimulation.

### 3.2.6 Fatty acid uptake monitoring of beige adipocytes-on-chip

To evaluate FA uptake properties of beige adipocytes on-chip, we monitored the uptake of a fluorescently tagged medium-chain fatty acid (Dodecanoic Acid, C12; BODIPY™ 500/510 C1, C12; Thermo Fisher Scientific Inc.). In general, the FA uptake assay was performed and quantified as described in attached **Publication [11]**. Yet, here, each of the 16 individual tissue chambers were imaged every 10 min for 360 min.

### 3.2.7 Image processing and statistical analysis

Images were processed using Fiji [Image J version 1.53c]<sup>166</sup> to adjust brightness and contrast, create maximum intensity projections or orthogonal views of Z-stacks and to insert scale bars. Calculations of mean gray values as a measure of fluorescence intensity and profile plots were also performed using Fiji.

If not stated otherwise, all data is presented as mean  $\pm$  standard error of mean (SEM) with sample sizes (n) stated for each case individually. In case of readouts feasible on chamber level, such as optical readout, n denotes number of individual chambers covered by the analyse. In case of readouts feasible on chip-level only, i.e., all kinds of effluent analyses, n denotes number of chip replicates. Graphs, descriptive statistics and hypothesis testing were compiled using OriginPro [Version 2021, OriginLab Corporation]. For testing statistical significance, we performed Two Sample *t*-Tests with the null hypothesis mean1 - mean2 = 0 [for gene expression comparison between different lots and different differentiation strategies (**Figure 14ab**); for gene expression comparison between untreated and isoproterenol-stimulated cells (**Figure 16b**) and for comparison of morphological beige adipocyte features on d3 and d7 (**Figure 15a**)] or with null hypothesis mean2 - mean1  $\geq$  0 [for testing if gene expression on d7 was higher than gene expression on d0 (**Figure 14c**)]. P values are denoted with \* for  $p < 0.05$ , \*\* for  $p < 0.01$ , and \*\*\* for  $p < 0.001$ .

### 3.3 Materials and Devices

In this section, all specific materials and devices utilized for PDMS-thermoplastic hybrid chip fabrication as well as within the scope of the beige adipocyte-on-chip project are listed. All other equipment and material utilized for projects of this thesis are covered in the appended publications and manuscripts, respectively.

**Table 3: Materials and chemicals for PDMS-thermoplastic hybrid microfluidic device fabrication and characterization.**

Name	Catalog number	Provider
3-Aminopropyltriethoxysilan	440140	Merck KGaA, Darmstadt, Germany
3M Scotchpak™ (Coated-foil)	1022 Release Liner Fluoropolymer Coated	3M, Saint Paul, MN, USA
Biopsy punch; 0.75 mm diameter	504529	World Precision Instruments, Friedberg, Germany
FITC dextran, 3-5 kDa	FD4	Merck KGaA, Darmstadt, Germany
Foldback clips	2141999	Jakob Maul GmbH, Bad König, Germany
PDMS Silicone Elastomer Base and Curing Agent	SYLGARD™ 184; 5498840000	Biesterfeld Spezialchemie GmbH, Hamburg, Germany

PET-G transparent, colourless, 0.5 mm thickness	3011211-ST	Modulor GmbH, Berlin, Germany
Rhodamine 6G	83697	Merck KGaA, Darmstadt, Germany
Trichloro(1H,1H,2H,2H-perfluorooctyl)silane	448931	Merck KGaA, Darmstadt, Germany

**Table 4: Cells, media and supplements for (on-chip) differentiation, culture and monitoring of beige adipocytes.**

<b>Name</b>	<b>Catalog number</b>	<b>Provider</b>
21 GA stainless steel plastic hub dispensing needles	400-3895 (Kahnetics - KDS2112P)	RS Components GmbH, Frankfurt am Main, Germany
23 GA stainless steel plastic hub dispensing needles	400-8272 (Kahnetics - KDS2312P)	RS Components GmbH, Frankfurt am Main, Germany
3-Isobutyl-1-methylxanthine (IBMX)	I5879	Merck KGaA, Darmstadt, Germany k
3,3',5-Triiodo-L-thyronine (T3)	T2877	Merck KGaA, Darmstadt, Germany
Cryopreserved, Subcutaneous Preadipocytes, POOLED Lot (2 million cells/vial) BMI 25.0-29.99	SP-F-SL Lots: SL0064 and SL0065	ZenBio Inc., Durham, NC, USA
Cytiva HyClone™ FetalClone™ II Serum (USA)	10326762	Thermo Fisher Scientific, Inc., Waltham, MA, USA
CytoTox 96® Non-Radioactive Cytotoxicity Assay	G1780	Promega GmbH, Walldorf, Germany
Dexamethasone	D1756	Merck KGaA, Darmstadt, Germany
Disposable syringe Injekt® With Luer-Lock fitting, 2 ml (from B. Braun)	EP95.1	Carl Roth GmbH + Co. KG, Karlsruhe, Germany
DMEM/F-12, no phenol red	21041025	Thermo Fisher Scientific, Inc., Waltham, MA, USA
Dulbecco's Phosphate Buffered Saline with magnesium chloride and calcium chloride (PBS <sup>+</sup> )	D8662	Merck KGaA, Darmstadt, Germany
Dulbecco's Phosphate Buffered Saline: without Magnesium, without Calcium (PBS <sup>-</sup> )	MS00SG1001	Biowest, Nuaille, France
Gibco™ TrypLE™ Select Enzyme (1X), no phenol red	50-591-419	Thermo Fisher Scientific, Inc., Waltham, MA, USA

HEPES 1 M	15630056	Thermo Fisher Scientific, Inc., Waltham, MA, USA
Human EGF Recombinant Protein	PHG0311L	Thermo Fisher Scientific, Inc., Waltham, MA, USA
Human FGF-basic (FGF-2/bFGF) Recombinant Protein	13256-029	Thermo Fisher Scientific, Inc., Waltham, MA, USA
HyStem®-C	GS313	CellSystems® GmbH, Troisdorf, Germany
Indomethacin	I7378	Merck KGaA, Darmstadt, Germany
Insulin solution human	I9278	Merck KGaA, Darmstadt, Germany
(-)-Isoproterenol hydrochloride	16504	Merck KGaA, Darmstadt, Germany
Penicillin-Streptomycin (10,000 U/mL)	15140122	Thermo Fisher Scientific, Inc., Waltham, MA, USA
Rosiglitazone	R2408	Merck KGaA, Darmstadt, Germany
TYGON® tubing ND-100-80/	5205508	OMNILAB-LABORZENTRUM GmbH & Co. KG, Bremen, Germany

**Table 5: Materials and Chemicals for Gene Expression Analysis.**

<b>Name</b>	<b>Catalog number</b>	<b>Provider</b>
Applied Biosystems™ TaqMan™ Universal Master Mix II, no UNG	44-400-40	Thermo Fisher Scientific, Inc., Waltham, MA, USA
iScript™ Reverse Transcription Supermix for RT-qPCR	1708841	Bio-Rad Laboratories, Inc., Hercules, CA, USA
Microseal 'B' PCR Plate Sealing Film, adhesive, optical	MSB1001	Bio-Rad Laboratories, Inc., Hercules, CA, USA
Multiplate® PCR Plates™ 96-well, clear	MLL9601	Bio-Rad Laboratories, Inc., Hercules, CA, USA
PrimePCR™ Probe Assay: FABP4, Human	qHsaCEP0058579	Bio-Rad Laboratories, Inc., Hercules, CA, USA
PrimePCR™ Probe Assay: PPARG, Human	qHsaCEP0051687	Bio-Rad Laboratories, Inc., Hercules, CA, USA
PrimePCR™ Probe Assay: PPARGC1A, Human	qHsaCIP0026151	Bio-Rad Laboratories, Inc., Hercules, CA, USA
PrimePCR™ Probe Assay: PPIA, Human	qHsaCEP0041342	Bio-Rad Laboratories, Inc., Hercules, CA, USA
PrimePCR™ Probe Assay: PRDM16, Human	qHsaCEP0052327	Bio-Rad Laboratories, Inc., Hercules, CA, USA
PrimeTime® Std qPCR Assay; UCP1 Homo Sapiens	Hs.PT.53a.2489606	Integrated DNA Technologies, Inc., Coralville, IA, USA

ReliaPrep™ RNA Miniprep Systems	Z6011	Promega GmbH, Walldorf, Germany
---------------------------------	-------	---------------------------------

**Table 6: Materials and Chemicals for Staining.**

Name	Catalog number	Provider
Alexa Fluor™ 546 Phalloidin	A22283	Thermo Fisher Scientific, Inc., Waltham, MA, USA
Antibody Diluent, Background Reducing	S302283-2	Agilent Technologies, Inc., Santa Clara, CA, USA
BODIPY™ 493/503 dye	D3922	Thermo Fisher Scientific, Inc., Waltham, MA, USA
BODIPY™ 500/510 C1, C12	D3823	Thermo Fisher Scientific, Inc., Waltham, MA, USA
Bovine serum albumin (BSA)	P6154	VWR International, LLC., Radnor, PA, USA
DAPI solution	MBD0015	Merck KGaA, Darmstadt, Germany
Fluorescein diacetate	F7378	Merck KGaA, Darmstadt, Germany
Hoechst 33342 Solution (20 mM)	62249	Thermo Fisher Scientific, Inc., Waltham, MA, USA
MitoTracker® Deep Red FM	8778S	Cell Signaling Technology, Inc., Danvers, MA, USA
Propidium iodide	P4170	Merck KGaA, Darmstadt, Germany
ROTI®Histofix 4%	P087.4	Carl Roth GmbH + Co. KG, Karlsruhe, Germany
Triton™ X-100	X100	Merck KGaA, Darmstadt, Germany

**Table 7: Devices used for PDMS-thermoplastic hybrid chip fabrication and beige adipocyte-on-chip characterization.**

Device	Model	Provider
Fluorescence microscope	DMi8	Leica Microsystems CMS GmbH, Wetzlar, Germany
Laser cutter with 10 W CO <sub>2</sub> laser	VLS2.30	Universal Laser Systems, Inc., Scottsdale, AZ, USA
Laser scanning microscope	LSM 710	Carl Zeiss Microscopy GmbH, Jena, Germany
Laser scanning microscope with Airyscan detector	LSM 880 with Airyscan	Carl Zeiss Microscopy GmbH, Jena, Germany
Nanodrop™ Spectrophotometer	2000	Peqlab Biotechnologie GmbH, Erlangen, Germany
Plasma unit	Zepto One	Diener electronic GmbH & Co KG, Ebhausen,

## Materials & Methods

---

Syringe pump	LA-190, 12-channel	Landgraf Laborsysteme HLL GmbH, Langenhagen, Germany
Thermocycler/qRT-PCR device	CFX96™ Real-Time PCR Detection System	Bio-Rad Laboratories, Inc., Hercules, CA, USA

# Chapter 4

## Results & Discussion

Content is based on the following appendices:

### Publication [4]:

K. Achberger<sup>#</sup>, C. Probst<sup>#</sup>, J. C. Haderspeck<sup>#</sup>, S. Bolz, **J. Rogal**, J. Chuchuy, M. Nikolova, V. Cora, L. Antkowiak, W. Haq, N. Shen, K. Schenke-Layland, M. Ueffing, S. Liebau, P. Loskill. “Human retina-on-a-chip: merging organoid and organ-on-a-chip technology to generate complex multi-layer tissue models“, *eLife* 8, e46188 (2019), <https://dx.doi.org/10.7554/eLife.46188>

### Publication [5]:

**J. Rogal**, C. Binder, E. Kromidas, S. Schneider, C. Probst, K. Schenke-Layland, P. Loskill. “WAT-on-a-chip integrating human mature white adipocytes for mechanistic research and pharmaceutical applications“, *Sci. Rep.* 10, 6666 (2020), <https://dx.doi.org/10.1038/s41598-020-63710-4>

### Publication [7]:

**J. Rogal**<sup>#</sup>, J. Roosz<sup>#</sup>, P. Loskill. “Isolation, Integration, and Culture of Human Mature Adipocytes Leveraging Organ-on-Chip Technology“, *Methods Mol. Biol.*, in press (2021), [https://dx.doi.org/10.1007/978-1-0716-1693-2\\_18](https://dx.doi.org/10.1007/978-1-0716-1693-2_18)

### Publication [8]:

J. Chuchuy, **J. Rogal**, T. Ngo, K. Stadelmann, L. Antkowiak, S. Liebau, K. Schenke-Layland, P. Loskill. “Integration of electrospun membranes into low-absorption thermoplastic organ-on-chip“, *ACS Biomater. Sci. Eng.* 7, 3006–3017 (2021), <https://dx.doi.org/10.1021/acsbiomaterials.0c01062>

### Publication [10]:

S. Schneider, M. Bubeck, **J. Rogal**, H. Weener, C. Rojas, M. Weiss, M. Heymann, A. D. van der Meer, P. Loskill. „Peristaltic on-chip pump for tunable media circulation and whole blood perfusion in PDMS-free organ-on-chip and organ-disc systems“, *Lab Chip Ahead of Print* (2021), <https://dx.doi.org/10.1039/D1LC00494H>

### Publication [11]:

**J. Rogal**, R. Xu, J. Roosz, C. Teufel, M. Cipriano, W. Eisler, M. Weiss, K. Schenke-Layland, P. Loskill. “Autologous human immunocompetent white adipose tissue-on-chip“, *under review* (2021) (available at bioRxiv <https://dx.doi.org/10.1101/2021.08.08.455559>)



## 4. Results & Discussion

### 4.1 Technological Development of Tailored Adipose Tissue-on-Chip Platforms

A microfluidic platform specifically equipped for housing human adipose tissue needs to account for the unique characteristics and resulting demands of human mature adipocytes, including buoyancy, fragility and size. Throughout the course of developing a tailored adipose tissue-on-chip featuring a microphysiological environment, different generations of microfluidic platforms were designed based on a constant optimization and re-iteration of chip architecture and associated materials. A key feature of all adipose tissue-on-chip platforms is a tissue chamber compartment separated from a constantly perfused media channel by a semipermeable membrane (**Figure 9a**). The direct connection of tissue chambers and media flow across the membrane pores ensured a continuous supply with nutrients and removal of waste products. At the same time, the membrane ensured that tissues were shielded from non-physiological shear forces caused by media flow. The restriction of convective flow to media channels could be confirmed via CFD approaches. The diffusive transport of dissolved molecules across the membrane's pores was studied by computational modeling and on-chip tracking of a fluorescent dye, both demonstrating a quick diffusion that reached the entire tissue chamber (see **Figure 10d**, attached **Publication [5] figure 2b**, and attached **Publication [11] figure 2b,d**).

In all developed adipose tissue-on-chip platforms, the cells were injected via common injection channels opening into the individual tissue chambers. To compensate for adipocyte buoyancy and ensure uniform, 3D filling of tissue chambers, injection channels were designed shallower than tissue chambers; when entering the tissue chamber, adipocytes thereby fill the chamber from the top to the bottom. Moreover, channel and chamber structures were designed without edges to protect fragile adipocytes. Additional protection from the shear forces during the injection process was achieved by encapsulating the cells in a hydrogel matrix prior to injection into the tissue chambers. The hydrogel further assures a 3D tissue formation by providing anchorage and supports a proper adipose tissue functionality by generating a physiological ECM-like surrounding. *In vivo*, the ECM comprises about 5% of adipose tissue volume<sup>179</sup> and supports adipose tissue homeostasis, e. g., by remodeling to adapt to nutritional cues or by controlling TAG storage and insulin sensitivity<sup>180–182</sup>. Unbalanced ECM remodeling, particularly fibrosis, can be a principal contributor to adipose tissue pathogenesis in obesity<sup>183,184</sup>.

Since collagens, especially collagen type I, are the most abundant components in adipose tissue ECM *in vivo*<sup>181,185</sup>, the hydrogels utilized for the adipose tissue-on-chip models were all either collagen-based or incorporated collagens.

The three chip generations developed (**Figure 9b**) are presented in the following paragraphs.

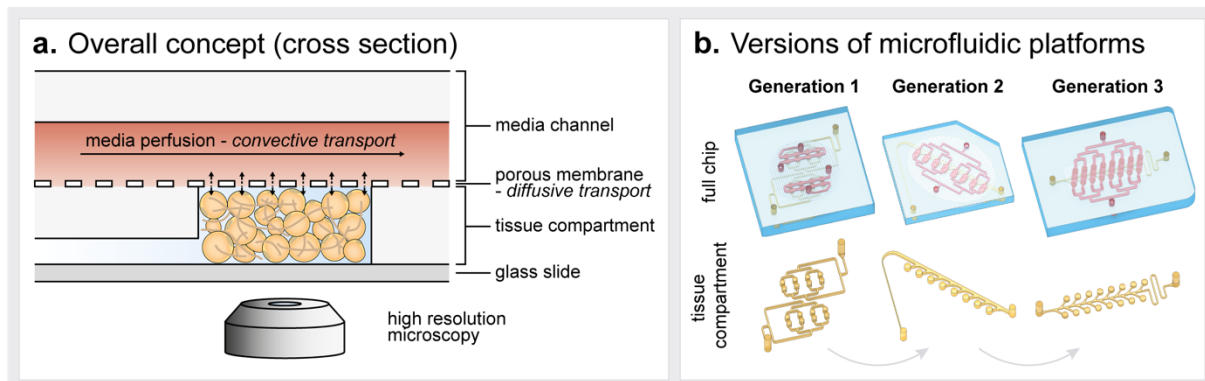


**Figure 9: Engineering of tailored adipose tissue-on-chip microfluidic platforms. a.** General concept of adipose tissue-on-chip devices in cross-sectional view. **b.** Schematic of the three successive generations of microfluidic devices used in this thesis. Illustration adapted from attached **Publications [5] and [11]**.

#### 4.1.1 First-Generation Platform

The first version of the microfluidic platform to house human adipose tissue was adapted from the lab's pre-existing murine WAT-on-chip system,<sup>158</sup> and is comprehensively described in attached **Publications [5] and [7]**. The platform was fabricated from two microstructured PDMS-layers – one featuring tissue channels and chambers and the other featuring a media channel for perfusion – that sandwich an isoporous, semipermeable PET membrane. Major adjustments regarding size of the chamber- and channel features had to be made for converting the platform from a device capable of integrating murine preadipocytes to one specifically tailored to house the much larger, and more fragile human mature adipocytes. Moreover, the fabrication process was optimized to enable advanced optical accessibility for high resolution imaging: the tissue layer compartment was generated by an 'exclusion molding' process, which lead to tissue chamber structures opened to both sides (see attached **Publication [5] figure S1**). During chip assembly, the tissue chamber structures were encased by a glass coverslip on the bottom side and the porous membrane providing a barrier to the adjacent vascular-like perfusion channel on the top side (**Figure 9a**).

The resulting first generation of the human adipose tissue-on-chip platform contains two independent, identical systems, which each feature eight individual tissue chambers and

a serial media perfusion. Although the suitability of this device to maintain white adipocyte viability and functionality for over a month could be confirmed (see attached **Publication [5]**), a variety of design- and material-derived challenges were encountered:

The design of the tissue compartment – a quite long, arborizing injection channel leading to dead-end tissue chambers – presented major difficulties: For once, the length of the injection channel made a complete, uniform filling of tissue chambers before onset of hydrogel gelation considerably hard, and often required higher pressures. The narrow time window made a parallelization of the injection process impossible. Even more serious consequences were provoked by the adipocytes remaining in the injection channel after loading. Distant from the media perfusion, cells are exposed to low to zero nutrient concentrations compared to cells close to the perfusion. If under severe metabolic stress, such as nutrient deprivation, cells might become necrotic<sup>186</sup> and impact the other cells through the release of damage-associated molecular patterns<sup>187,188</sup>. Another, related design issue was the serial media perfusion: Creating nutrient- and waste product gradients along the supply route could interfere with the comparability of individual tissue chambers. Finally, the choice of rat tail collagen I as adipocyte encapsulation matrix for the first adipose tissue-on-chip generation was revised carefully: through its natural origin, a batch-to-batch variability was frequently observed.

#### 4.1.2 Second-Generation Platform

The second generation of the adipose-tissue microfluidic system was optimized regarding the abovementioned challenges that manifested throughout application of the first-generation platform; it is comprehensively described in attached **Publication [11]**. A pivotal advancement was the re-design of the tissue compartment structures: eight individual tissue chambers branched off one common injection channel, which ended in a thin, high-resistance tissue outlet channel (**Figure 9b**). Given free flow in the superjacent media channel, the injected cell suspension followed the path of lowest fluidic resistance filling each chamber sequentially (see attached **Publication [11] figure 2a**). Since resistance grew with increasing chamber filling and eventually led to a diversion of flow along another route, the injection process was inherently protected from high pressures or ‘overloading’ of chambers. Moreover, by flushing the injection channel with hydrogel after injection of the cell suspension, surplus cells could be removed from the injection channel through the tissue outlet port. In addition, the media channel was re-designed to enable a parallel media perfusion ensuring comparable media properties for

the eight individual tissue chambers. To achieve higher control and reproducibility compared to natural alternatives, a hydrogel matrix with a synthetic backbone was used for the second generation of *in vitro* adipose tissue microenvironment: HyStem<sup>®</sup>-C hydrogel featuring denatured collagens and a hyaluronic acid (HyA) backbone. HyA can signal through direct binding of cell receptors and regulates signaling pathways of inflammation, angiogenesis or cell migration<sup>183,189</sup>. Moreover, the hydrogel scaffold kit allows for the adjustment of stiffness to best suit the ECM-like environment to the respective cell type.

### 4.1.3 Third-Generation Platform

Finally, the 2<sup>nd</sup>-generation microfluidic platform was further upgraded by revisiting the choice of material for the microfluidic system. As covered in the introduction, PDMS absorbs small hydrophobic molecules – a potential complication especially for adipose tissue research. Throughout the WAT studies, no obvious problems due to the choice of PDMS as the chips' bulk material were encountered. However, key substances required for the differentiation of beige adipocytes classify as 'small hydrophobic molecules' predestined to PDMS absorption. A measure to estimate a substance's absorption is its n-octanol/water partition coefficient (LogP). LogP describes the ratio of a chemical's concentration in the n-octanol phase to its concentration in water (at equilibrium at a specified temperature). Especially 3,3',5-Triiodo-L-thyronine (T3) (predicted logP ~ 3.98; MW = 650.97 g/mol) and indomethacin (predicted logP ~ 3.9; MW = 357.79 g/mol) have logP values higher than the previously defined threshold of 2.62<sup>27</sup> and their MWs are similar to those of substances shown to be considerably absorbed by PDMS such as estrogen (experimental logP = 3.67; MW = 296.41 g/mol)<sup>29</sup>, Nile red (predicted logP ~ 3.98; MW = 318.376 g/mol)<sup>28</sup> or rhodamine 6G (logP = 2.62; MW = 479.02 g/mol)<sup>27</sup>. Rosiglitazone, another important substance for beige adipogenesis, comes close to the cut-off, too (predicted logP ~ 2.49; MW = 357.43 g/mol). (All logP values and MWs according to the U.S. Environmental Protection Agency's (EPA) web-based CompTox Chemistry Dashboard<sup>190–192</sup>). Of note, recent studies have shown that molecule absorption is not exclusively determined by hydrophobicity, but potentially also by the substance's topological polar surface area<sup>193</sup> and hydrogen-bond donor number<sup>194</sup>.

Hence, an alternative, less absorbing material, such as a thermoplastic<sup>32</sup>, should be not only the material of choice for a platform able to recapitulate beige adipogenesis but

generally for all studies involving small hydrophobic substances. However, thermoplastics are considerably less permeant to oxygen than PDMS<sup>32</sup>. To leverage the benefits of both materials, i.e., low absorption of thermoplastics and high oxygen permeability of PDMS, a PDMS-thermoplastic hybrid microfluidic platform was developed; the media channel layer was made from the thermoplastic PET-G while the tissue compartment layer was made from PDMS. In addition to the material adaptations for the 3<sup>rd</sup>-generation device, the amount of tissue chambers in one chip was doubled to 16 tissues per chip to increase throughput (**Figure 10a**).

Tight and leak-free bonding between the different layers of the platform was achieved via a tailored fabrication- and assembly process combining multiple previously reported approaches<sup>195–197</sup>. The final fabrication protocol (cf. '*Chip Fabrication*') included (i) hot embossing techniques to imprint channel structures into PET-G sheets and (ii) silane functionalization of the thermoplastic for covalent bonding to O<sub>2</sub> plasma-treated PDMS (**Figure 8**). PET-G is more commonly used in 3D printing of microfluidic devices<sup>198–200</sup>, but it is also amenable to hot embossing strategies<sup>195,201</sup>. The surface chemical bonding using silane functionalization enables facile bonding with good tensile strength, high burst resistance and hydrolytic stability at room temperature and atmospheric pressure<sup>196–198,202,203</sup>. All in all, the developed fabrication process is a robust, easy-to-implement approach.

Upon successful chip fabrication, the key properties of the platform were characterized experimentally as well as by CFD simulations. Importantly, the chip's media layer compartment made of PET-G was indeed much less absorbing of rhodamine 6G (used as a representative for small hydrophobic molecules) than a media layer compartment made from PDMS (**Figure 10b**). Perfusion of the rhodamine solution was monitored for 120 min by fluorescence microscopy. The partitioning of the dye into the bulk material was quantified by creating plot profiles of the vertically averaged pixel intensity against the horizontal distance. The O<sub>2</sub> supply and consumption on chip was modeled for devices made from (i) a combination of PDMS and thermoplastic, (ii) all-PDMS or (iii) all-thermoplastic (**Figure 10c**). The simulations demonstrated a much higher O<sub>2</sub> supply for the hybrid version compared to the all-thermoplastic version, indicating that platforms entirely made from thermoplastics might be beneficial in terms of absorption characteristics but would not be able to maintain viability and functionality of adipose tissue. The hybrid version, however, featured minimal O<sub>2</sub> concentrations of 0.15–0.16 mol/m<sup>3</sup> (different from the all-PDMS version, a gradient in O<sub>2</sub> concentration between

the two serially connected tissue chambers could be detected in the hybrid version: in the tissue chambers closer to the media inlet, the lowest O<sub>2</sub> concentration was approximately 0.16 mol/m<sup>3</sup> while the tissue chamber farther from the media inlet could drop to approximately 0.15 mol/m<sup>3</sup>). This oxygen availability is slightly higher than values determined for human subcutaneous adipose tissue in upper arm and abdomen, where the O<sub>2</sub> concentration ranged between 0.6 – 0.12 mol/m<sup>3</sup> <sup>204,205</sup>.

Finally, the general on-chip transport processes of the 3<sup>rd</sup>-generation platform were analyzed (**Figure 10d**) and confirmed the confinement of convective flow to the media channels while nutrients still diffused across the membrane and reach the entire tissue chamber. Of note, as already shown in the O<sub>2</sub> simulations, the time lag of transport between the two serially connected chambers could be confirmed experimentally as well. Hence, in a future version of the chip, a re-design of the media channels back to an exclusively parallel media perfusion, as for the 2<sup>nd</sup>-generation adipose tissue-on-chip platform, might be worthwhile.

With the development of the PDMS-thermoplastic hybrid microfluidic platform, an important step towards a device with enhanced material properties was taken.

Hybrid material devices do not only profit from optimized absorption properties, but they might also exploit the differences in material rigidity or flexibility, respectively, which qualifies them for the OoC technology as much as for microfluidic bioassays such as polymerase chain reaction (PCR)<sup>206</sup>, or the creation of membrane valves<sup>207</sup>. For use within the OoC technology, however, only very few examples on hybrid devices have been reported, such as a TPE-PMMA device integrating endothelial cells<sup>208</sup>, a glass-polycarbonate OoC which has been tested in combination with intestinal epithelium<sup>209</sup> as well as a hybrid PMMA-PDMS microdevice for studying glioblastoma migration under electrical stimulation<sup>210,211</sup>.

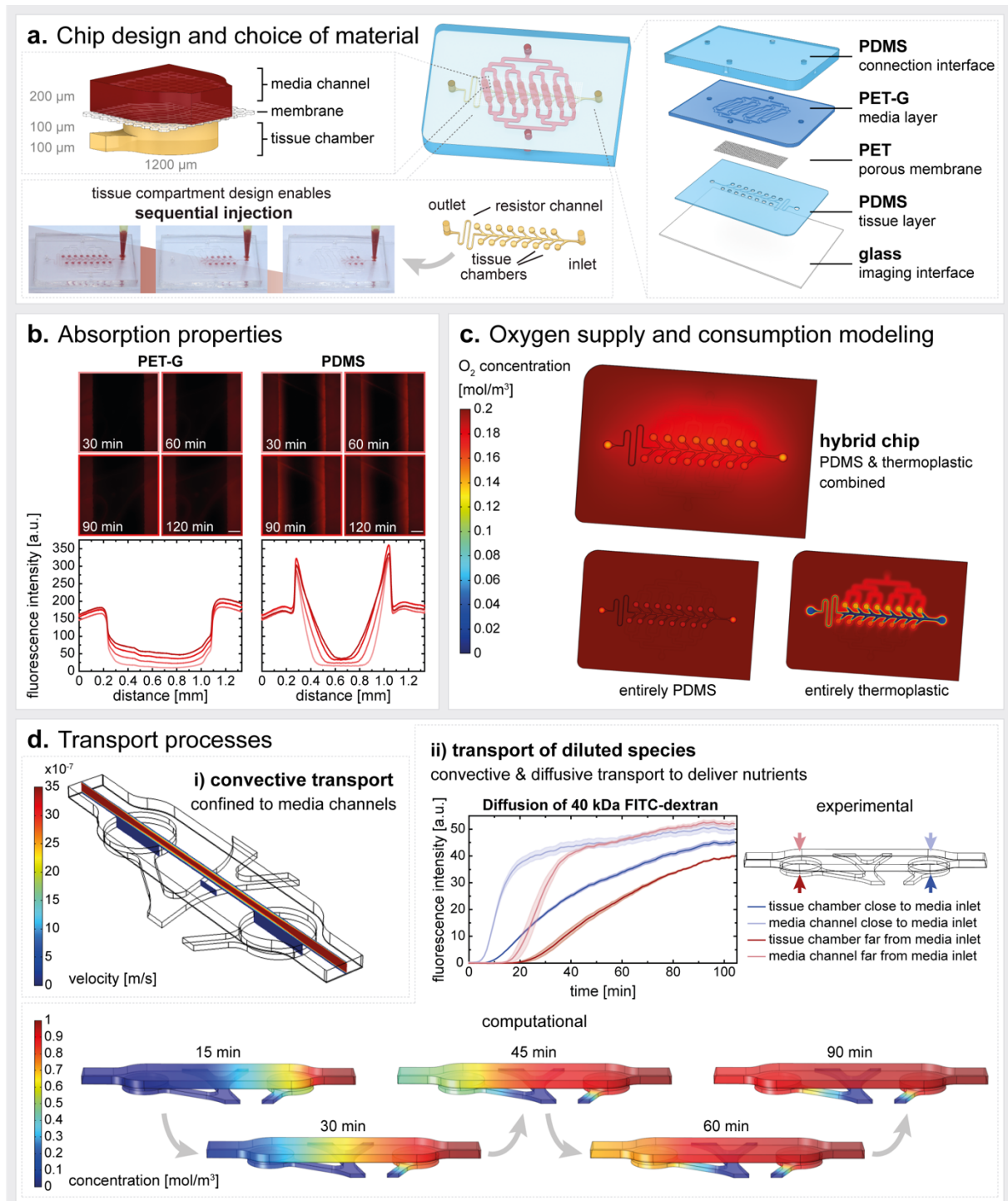


**Figure 10: Characterization of the 3<sup>rd</sup>-generation adipose tissue microfluidic platform.** **a.** The device consists of a microstructured tissue compartment layer separated from a perfused media channel by a porous membrane. The tissue compartment, featuring 16 individual tissue chambers, was designed to enable sequential injection. The chip was fabricated from PDMS and a thermoplastic (PET-G) to ensure oxygen supply while at the same time minimize absorption of small hydrophobic molecules. **b.** Absorption of Rhodamine 6G in media channel layers fabricated from PET-G (left) or PDMS (right). Fluorescence imaging and extracted corresponding plot profiles of fluorescence intensity (bottom), revealed increased absorption of Rhodamine into PDMS bulk material. Bulk material captured in the middle of each image section, flanked by dye-filled media channels to left and right. Scale bar equals 200  $\mu\text{m}$ . **c.** CFD modeling of on-chip oxygen concentration considering oxygen supply (through diffusive and convective transport) as well as consumption (by cells in the tissue compartment). **d.** On-chip transport processes were analyzed experimentally and via CFD modeling. Convective transport is confined to the media

channels. Diluted species (e.g., nutrients), delivered through a combination of convective and diffusive transport, reach the tissue chambers quickly. Both CFD modeling and experimental monitoring of the diffusion of a fluorescent tracer molecule (40 kDa FITC-dextran) revealed a time lag between the tissue chamber closer to the media inlet compared to the tissue chamber further from the media inlet. For experimental condition,  $n=3$  chambers per media channel position. Error bars represent  $\pm$  SEM.

### 4.2 Cell Sources for Adipose Tissue-on-Chip Systems

The second major component for a functional and human-relevant adipose-tissue-on-chip model besides a platform that provides the microphysiological environment is the integration of physiologically relevant cell types. All the different adipose-associated cell types used in this thesis were primary human cells, which were derived from human tissue samples of subcutaneous adipose tissue with skin. Circulating immune cells, such as monocytes and T cells, were isolated from fresh whole blood that was derived from the same donor (see attached **Publication [11]** *Figure 1b*).

Choosing a human cell source is an essential part for human-centered research. Although discoveries from animal models have elucidated many aspects of adipose tissue (patho-)physiology in the past, they reach their limits regarding human-relevance with increased regularity. Despite efforts on humanization of animal models, there are still dominant discrepancies between mice and men, especially concerning metabolism and functioning of the immune system<sup>125–130</sup>. For example, mouse adipose tissue contains more active bAT/BAT, which leads to very different lipolytic activity, especially in reaction to lipolysis stimulation<sup>127</sup>. Moreover, there are substantial differences between rodents and humans in the active bAT/BAT distribution, cellular composition and responsiveness to  $\beta$ 3-adrenergic stimulation<sup>212</sup>. Likewise, the many intricate immunological interspecies discrepancies span from innate to adaptive immunity and include both cellular and humoral defense mechanisms. Among many other disparities, macrophages in mice express different markers (such as F4/80, which is absent in humans), and a rodent equivalent of IL-8 does not exist<sup>128</sup>.

Besides the choice of species, the specific origin of the adipose tissue in the human body plays a major role. Different WAT depots, such as visceral (in the abdominal cavity), subcutaneous or perivascular WAT, perform different functions and are marked by differential cellular compositions<sup>213,214</sup>. Even regional differences, for instance in subcutaneous abdominal versus gluteal adipose tissue, show distinct gene expression profiles<sup>215</sup>. Hence, particularly when focusing on intercellular crosstalk, cells should be organotypic. The focus of the WAT parts of this thesis was on recapitulating

subcutaneous adipose tissue. The general concept, the developed microfluidic platforms and the established processes, however, would likely also enable the generation of models for different types of WAT depots.

Importantly, the tissue donor's health state needs to be considered carefully since the biopsies arise from cosmetic surgeries. Some basic anthropometric information was gathered from the tissue donors (see attached **Publication [11] Table 2**); most of them received surgery after massive weight loss, and despite being normal weight or pre-obese at the time of surgery, many of them were morbidly obese before losing weight. Despite returning to a normal BMI, the so-called 'obesogenic memory' poses a risk of prevailing adipose tissue inflammation and other obesity-associated dysfunctions<sup>216–218</sup>. In the studies performed throughout this thesis, the potential disease state of integrated cells did not seem to impact the functional validation of our model. However, tissue origin should be closely re-evaluated when applying the model for profound mechanistic studies such as disease modeling.

### 4.3 Monoculture Models Towards Adipose Tissue-on-Chip Systems

In a first step towards physiological adipose tissue-on-chip models, the suitability of the developed microenvironments for culturing individual adipose tissue-associated cell types such as human adipocytes and endothelial cells was evaluated, before progressing towards on-chip co- and multi-culture adipose tissue models. On the one hand, on-chip 3D monocultures of human primary mature white adipocytes were established and characterized. On the other hand, to develop an *in vitro* model of bAT, the *de novo* differentiation of human primary preadipocytes into functional beige adipocytes on chip was investigated. Additionally, protocols for creating and characterizing endothelial linings to create vasculature-like media channels were developed.

#### 4.3.1 Human Mature White Adipocytes-on-Chip

Human mature white adipocytes were isolated from skin biopsies with subcutaneous adipose tissue and injected into 1<sup>st</sup>- and 2<sup>nd</sup>-generation adipose tissue-on-chip platforms [comprehensively described in attached **Publication [5]** (1<sup>st</sup>-generation) and in attached **Publication [11]** (2<sup>nd</sup> generation)] no later than 24 h after isolation. Given their unique characteristics such as buoyancy and fragility, specially tailored handling- and injection methods and protocols had to be developed to maintain viability and integrity of the cells (described in detail in attached **Publication [7]**). The white adipocytes-on-chip model was

then thoroughly evaluated with respect to its capability to emulate white adipocyte *in vivo* functionality. To this end, the white adipocytes on chip were characterized comprehensively by assessing viability, morphology and functionality. Thereby, not only basal conditions were portrayed but the adipocytes were also challenged by drug administration or by inducing acute inflammatory stimuli (**Figure 11**).

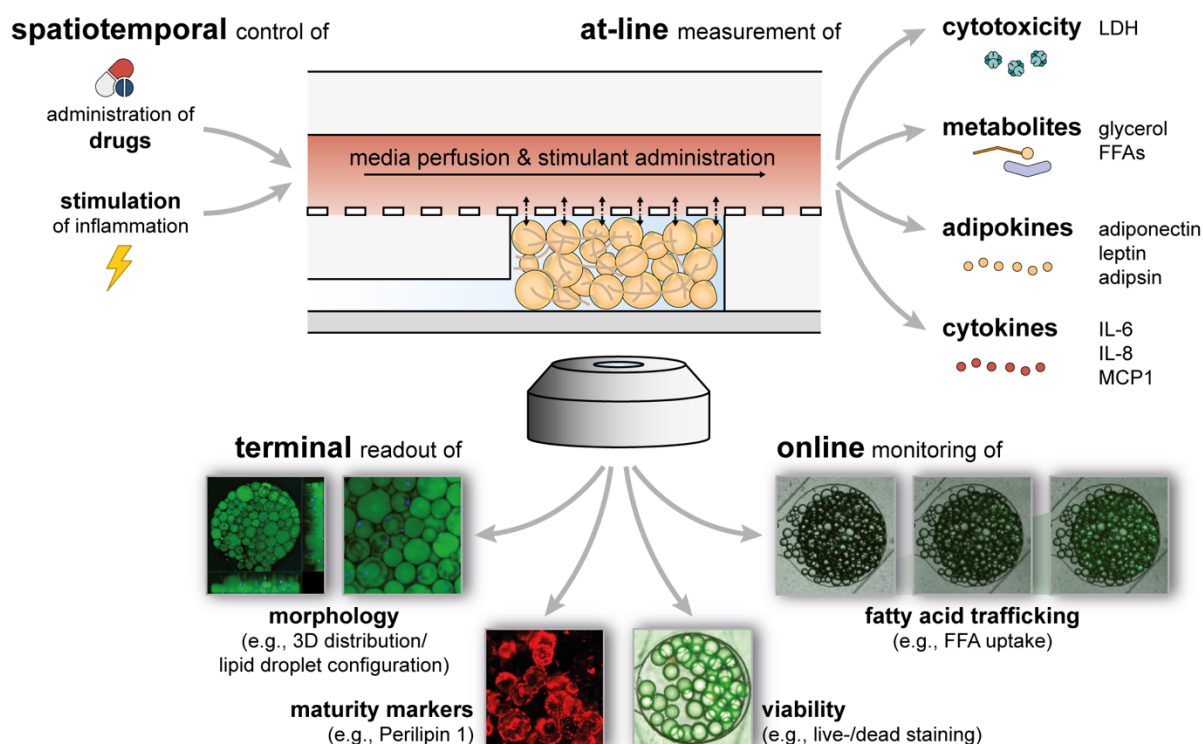


**Figure 11: Toolbox of on-chip analysis of human mature white adipocytes.** Adipocyte structure, viability and functionality was assessed via a comprehensive toolbox of readouts: non-invasive online monitoring of optical readouts, at-line measurements of adipocyte secretome in the media perfusion as well as terminal staining for structural analysis and identification of white adipocyte markers. Adipocytes were assessed both at basal conditions and in response to drug exposure or inflammatory stimulation. Images adapted from figures in attached **Publications [5] and [11]**.

Cell viability was confirmed non-invasively by quantification of LDH from media effluents (see attached **Publication [5] Figure 5a** and **Publication [11] Figure S1**) as well as via live-/dead staining based on FDA/PI (see attached **Publication [5] Figures 4a & 5b**). Especially the LDH assay is a convenient means to continuously control the tissues' quality complementary to other readouts, due to its non-invasive character. LDH is a ubiquitous cytosolic enzyme, and it is released from cells upon disruption of the plasma membrane. Since LDH is stable in common cell culture media, extracellular LDH is an indicator of cell damage induced by both endogenously or through exogenous

injury.<sup>219,220</sup> Alongside LDH concentration, adipocyte morphology was regularly monitored using brightfield microscopy.

For a structural analysis of adipocytes on chip, intracellular lipid vacuoles were visualized. Confocal imaging allowed for a close evaluation of the 3D arrangement of adipocytes within the tissue chamber (see attached **Publication [5] Figure 3a** and **Publication [11] Figure 3a**), which confirmed a homogeneous distribution of the adipocytes throughout the entire volume of the tissue chamber. More importantly though, this staining showed how the lipid content was intracellularly organized; unilocularity, i.e., the storage of lipids in one large vacuole, as compared to multilocularity (several smaller lipid vacuoles), is a key hallmark of white adipocyte maturity. White adipocytes are prone to dedifferentiate to fibroblast-like progenitor states when presented with unfavorable culture conditions exposing them to physical stressors<sup>221,222</sup> In ceiling culture, a commonly used method for culturing mature white adipocytes<sup>139–141</sup>, the adhesion surface seems to constitute such a physical stressor, since adipocytes begin to dedifferentiate within a few days<sup>142–144</sup>. While these dedifferentiated adipocytes have great potential and application areas in regenerative medicine, a dedifferentiation would be detrimental when studying mechanisms occurring in mature adipocytes. One of the first steps in the dedifferentiation process is lipid loss accompanied by a reorganization of the lipid content into several smaller lipid vacuoles<sup>222</sup>. Another important question, which was tackled by intracellular lipid staining, was whether the microfluidic devices were able to reflect the *in vivo* heterogeneity of mature white adipocytes or whether they exhibit adipocyte selectivity in terms of size or structure. Owing to their unilocularity, quantifying lipid droplet size is an indirect measure for adipocytes' size. Comparing on-chip adipocytes to adipocytes in donor-specific explants revealed that both average adipocyte size and distribution of individual cell sizes were highly similar between chip and explant (see attached **Publication [5] Figure 3b**).

Another morphological feature of mature adipocytes is the coating of lipid droplet vacuoles with perilipin 1. Perilipin 1 stabilizes larger lipid droplets (> 10  $\mu\text{m}$ ) and was ascribed a dual role in the regulation of lipolysis: it suppresses basal lipolysis by controlling the access of lipases to lipid vacuoles<sup>223–225</sup>, but enhances lipolysis upon its phosphorylation, which is induced by  $\beta$ -adrenergic stimulation<sup>223,226</sup>. Interestingly, the distribution of perilipin 1 on lipid vacuoles has recently been shown to be dynamic and dependent on the adipocyte's lipolytic state: under basal conditions, perilipin 1 localized to microdomains/clusters on the lipid droplet (as found attached **Publication [11] Figure**

3a), which are quickly dispersed upon stimulation of lipolysis<sup>227</sup>. Consequently, visualization and localization of perilipin 1 could not only serve as adipocyte maturity marker but might also be a readout of lipolytic state when comparing different stimulatory states in future experiments.

Generally, the superior optical accessibility of the adipose tissue-on-chip devices makes confocal imaging of (immuno-)fluorescent staining a powerful readout of on-chip adipocytes which goes beyond mere marker identification; the organization of intracellular lipid droplets reveals adipocyte maturity state, and the localization of adipose-associated proteins allows for conclusions on metabolic activity. However, conventional 3D volumetric imaging of adipose tissue is unusually complicated: obscuring effects from light scattering extensively occur at lipid-aqueous interfaces. Accordingly, adipose tissue imaging is highly susceptible to these effects, particularly in deeper layers of the tissue. Implementing adipose tissue clearing techniques<sup>228,229</sup> for application within OoC modules<sup>230</sup> could be a strategy to address this issue and achieve good imaging quality even in deeper layers of the tissue.

The optical accessibility of the adipose tissue on-chip further qualifies the microfluidic platform for microscopy-based online monitoring of adipocyte functionality: Addition of fluorescent FA-analogs to the perfused media allows for real-time assessment of FFA trafficking. Thereby it could be demonstrated that on-chip white adipocytes were able to take up and release medium-chain fatty acid (MCFA)- as well as LCFA-analogs (see attached **Publication [5] Figure 4b** and **Publication [11] Figure 3b**). These experiments provided valuable insights into the functionality of the white adipocytes on chip: MCFAs and especially LCFAs, the most common type of FAs in humans<sup>231</sup>, cannot merely diffuse across the plasma membrane; alongside a diffusive component, their uptake depends on protein-mediated entry into the plasma membrane as well as desorption at the inner side of the membrane<sup>232–235</sup>. The FA trafficking assay demonstrated that the FA uptake or release of the white adipocytes-on-chip could be modulated by providing different glucose concentrations (see attached **Publication [11] Figure 3b**) or through compound-induced lipolysis (see attached **Publication [5] Figure 6** and **Publication [11] Figure 3b**). The ability to reflect increased FA content in response to higher glucose concentrations indicates the utilization of glucose of the adipocytes on-chip for generating glycerol backbones of TAGs in lipogenesis<sup>236</sup> and a decreased FA release through uptake of glucose<sup>237</sup>. To further confirm the white adipocytes' metabolic activity, the concentration of adipose-derived metabolites was determined from the effluent media. On-chip

adipocytes secreted stable levels of both glycerol and FFAs at baseline conditions (see attached **Publication [5] Figure 4** and **Publication [11] Figure S3**), or at elevated levels when lipolysis was stimulated (see attached **Publication [11] Figure 3b**).

Aside from energy storage/-release functions, the on-chip white adipocytes' endocrine function was investigated by quantifying the concentration of adipokines from the effluent media (see attached **Publication [11] Figure 3b**). Interestingly, only the release of retinol binding protein 4 (RBP4) and adiponectin was detectable in effluent media; neither leptin nor adiponectin secretion could be attested from the white adipocyte-on-chip cultures. Yet, as will be addressed in section 4.4, when co-cultured with other adipose-associated cell types in the full complexity WAT-on-chip models, adipocytes of the same donor did release both adipokines.

In view of WAT's role in immunometabolism, the white adipocyte-on-chip model was investigated regarding the cells' response to inflammatory stimulation. White adipocytes reacted to both tumor necrosis factor  $\alpha$  (TNF- $\alpha$ ) or lipopolysaccharide (LPS) threats, as expected<sup>238–240</sup>, by increasing their release of the proinflammatory cytokines monocyte chemoattractant protein 1 (MCP-1), IL-6 and IL-8 (see attached **Publication [11] Figure 3c**).

Finally, the capability of the developed platforms for enabling long-term culture of adipose tissue was investigated. All abovementioned endpoint analyses were performed by day 12 on chip at latest. While a 12-day culture period is already quite substantial, compared to conventional adipocyte *in vitro* cultures, it is not sufficient to study mechanisms of chronic exposures or effects of complex, prolonging hormone dynamics, for instance. Therefore, viability and FFA uptake capability of white adipocyte-on-chip systems cultured for 36 days was confirmed (see attached **Publication [5] Figure 5**), demonstrating the ability of the platform to maintain viable and functional tissue for more than one month.

Following this comprehensive functional validation of white adipocytes on chip under basal and challenged conditions, the applicability of the microfluidic model for drug testing was examined. In response to isoproterenol, utilized as a tool compound, white adipocytes became lipolytic as reflected by altered FA trafficking dynamics (see attached **Publication [5] Figure 6**) as well as by increased glycerol release in a dose-dependent manner (see attached **Publication [11] Figure 3b**). This proof of concept successfully demonstrated the applicability of the model for drug testing and provided a reference point for the assessment of compounds with so far unknown effects on FA metabolism.

Further, white adipocyte-on-chip experiments hinted to an applicability of the model in the fields of personalized- and precision medicine: comparing experimental outcomes from different donors implied that the platform was able to capture inter-donor variations not only under basal conditions (see attached **Publication [11] Figure 3b & S3**) but also in response to inflammatory stimulation (see attached **Publication [11] Figure 3c**).

#### 4.3.2 On-Chip Differentiation of Beige Adipocytes

Unlike white adipocytes, primary human beige adipocytes are not readily available. Therefore, the development of a human beige adipocyte-on-chip model requires a differentiation process, either by *de novo* differentiation of precursor cells (**Figure 12**) or by *transdifferentiation* of mature white adipocytes. To serve as microfluidic platform for beige adipocyte differentiation, the 3<sup>rd</sup>-generation PDMS-thermoplastic hybrid chip (**Figure 10**) was chosen. By injecting human primary preadipocytes into the microfluidic platform and exposing them to differentiation media via the perfusion channels, beige adipocytes could be generated within 8 days. Prior to injection, the preadipocytes were encapsulated in a HyA-based ECM-like hydrogel matrix (HyStem<sup>®</sup>-C). HyA-hydrogels have been successfully used as a scaffold for *de novo* differentiation of beige adipocytes before<sup>100</sup>. Moreover, the HyStem<sup>®</sup>-C scaffold kit allows for adjustment of the hydrogel stiffness; since ECM stiffness has been shown to regulate differentiation into beige adipocytes with stiffer matrices leading to best results<sup>241</sup>, a hydrogel matrix that is more rigid compared to experiments with white adipocytes was generated.

The beige adipocytes differentiated on-chip were subsequently monitored in terms of viability, gene expression, morphology and functionality, as presented in the following sections. The data presented are not covered in any of the attached manuscripts.

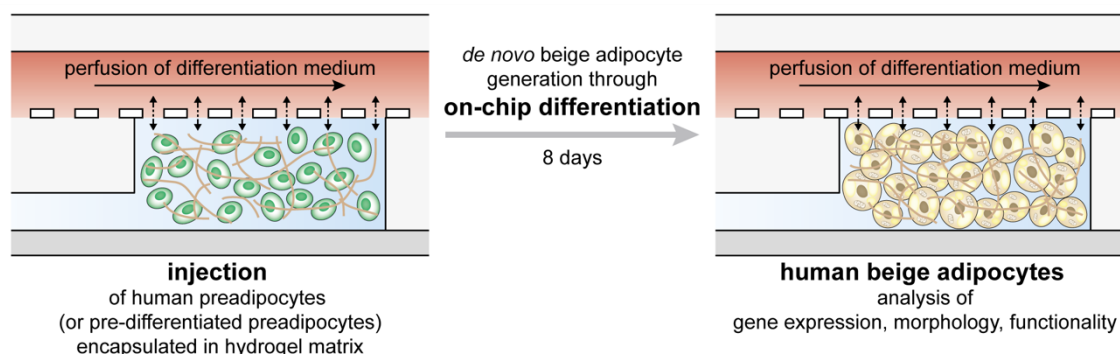


**Figure 12: General concept of the human beige adipocyte-on-chip model.** Human preadipocytes, or pre-differentiated beige preadipocytes (i.e., three days after initiation of beige differentiation) were encapsulated in an ECM-like hydrogel and injected into the microfluidic platform. Cells were differentiated on-chip to create human beige adipocyte-on-chip models.

#### 4.3.2.1 Cell Viability Throughout Beige Adipocyte Differentiation on Chip

First, the on-chip cell viability by determining LDH concentration in media effluents was analyzed non-invasively every 24 h (**Figure 13a**). Upon rupture of plasma membranes, LDH leaks from cytosol into the medium and thereby indicates cell death. On d3 and d4 of on-chip differentiation, LDH concentrations were always elevated (data from two independent runs of beige differentiation on-chip shown exemplarily in **Figure 13a** with ~25-60% LDH peaks compared to the expected maximum target LDH release). To exclude any viability-compromising effects of the newly developed hybrid material microfluidic device (e.g., potential leaching of toxic substances from bulk material), the LDH release of preadipocytes cultured in preadipocyte expansion medium was additionally examined ('no differentiation' condition in **Figure 13b**). Since the LDH levels detected from this culture condition remained low throughout the entire culture period, it could be concluded that the d3/d4 peaks in LDH release were likely caused by the differentiation process but not by the microfluidic platform. A live-/dead staining comparing differentiated beige adipocytes to non-differentiated preadipocytes on d7 of on-chip culture further supported an increased cell death during differentiation (**Figure 13b**).

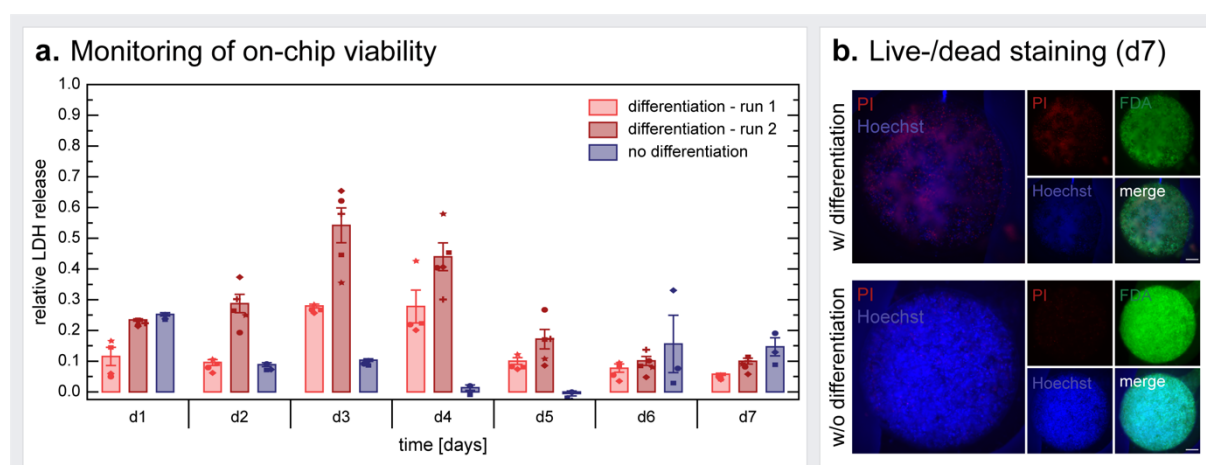


**Figure 13: Cell viability during beige adipocyte differentiation on chip.** **a.** Cytotoxicity was analyzed non-invasively by determining LDH concentration in media effluents every 24 h. LDH release (relative to the expected maximum target LDH release) was measured from two independent runs of on-chip differentiation into beige adipocytes. In addition, LDH release from cells which did not undergo differentiation but were supplied with standard preadipocyte expansion medium instead was analyzed ('no differentiation', run in parallel to 'differentiation – run 2'). **b.** Live-/dead staining using PI (marks nuclei of dead cells), FDA (stains cytosol of live cells) and Hoechst 33342 (marks all nuclei) indicated increased on-chip cell death for differentiating beige adipocytes as compared to non-differentiating preadipocytes. Scale bars equal 200 μm.

Error bars represent  $\pm$  SEM.

Cell death through apoptosis is a naturally occurring event in development and cell differentiation<sup>242–244</sup>. Apoptosis is essential to initiate adipogenesis since apoptotic cells provide lipophilic components that activate expression of PPAR $\gamma$  and other principal regulators of adipogenesis. Moreover, they facilitate lipid droplet formation.<sup>242</sup> Despite being an inherent part of adipogenesis, the considerable amount of apoptosis during the early adipogenesis lowered the final yield of beige adipocytes when the differentiation was initiated on-chip, since, in contrast to well plate culture, dead cells are not easily cleared in the confined tissue arrangement on-chip. Therefore, the injection- and differentiation process was adapted from a full on-chip differentiation to an off-chip initiation of differentiation for three days followed by cell injection and on-chip continuation of adipogenesis from d3. This approach ensured the injection of mostly preadipocytes committed to the beige lineage but not apoptotic cells and should thereby increase the amount of functional beige adipocytes per tissue chamber.

#### *4.3.2.2 Monitoring of On-chip Beige Adipocyte Differentiation on a Transcriptome Level*

Next, gene expression analysis of on-chip beige differentiation was conducted. The expression of PPAR $\gamma$  and FABP4 (representatives for general adipogenic markers<sup>91,245,246</sup>) as well as of UCP1, PRDM16 and PGC-1 $\alpha$  (representative for beige/brown adipocyte markers<sup>57–59</sup>) relative to PPIA (housekeeping gene) on d7 as well as on d0 (prior to differentiation) was analyzed (**Figure 14**).

The first step towards gene expression analysis experiments was to establish suitable protocols for retrieving the cell's transcripts from the microenvironment, i.e., microfluidic device and hydrogel. Because of the dead-end character of the tissue chambers, cell disruption could not be simply achieved by flushing the media channel with lysis solution but needed more complex handling. Comparison of different strategies revealed the following steps as most successful: (i) removal of the media channel and top layer, (ii) application of lysis buffer directly into the tissue chambers and onto the membrane and (iii) subsequent mechanical destruction of the cell-hydrogel constructs by trituration. Afterwards, RNA was isolated from the lysates using a spin column-based nucleic acid purification kit. Thereby, it was possible to retrieve ~ 900 ng of purified RNA from all 16 microtissues on one chip.

First, the beige differentiation capacity of two different preadipocyte batches was compared (ZenBio Inc., SP-F-SL Lots SL0064, '64', and SL0065, '65') (**Figure 14a**). All analyzed markers were upregulated relative to d0. Yet, while the expression of the

general adipose markers PPAR $\gamma$  and FABP4 presented comparable among the two batches, expression of UCP1 (higher for '64') and PGC-1 $\alpha$  (higher for '65') showed considerable differences. All further experiments were conducted using preadipocytes from '64'.

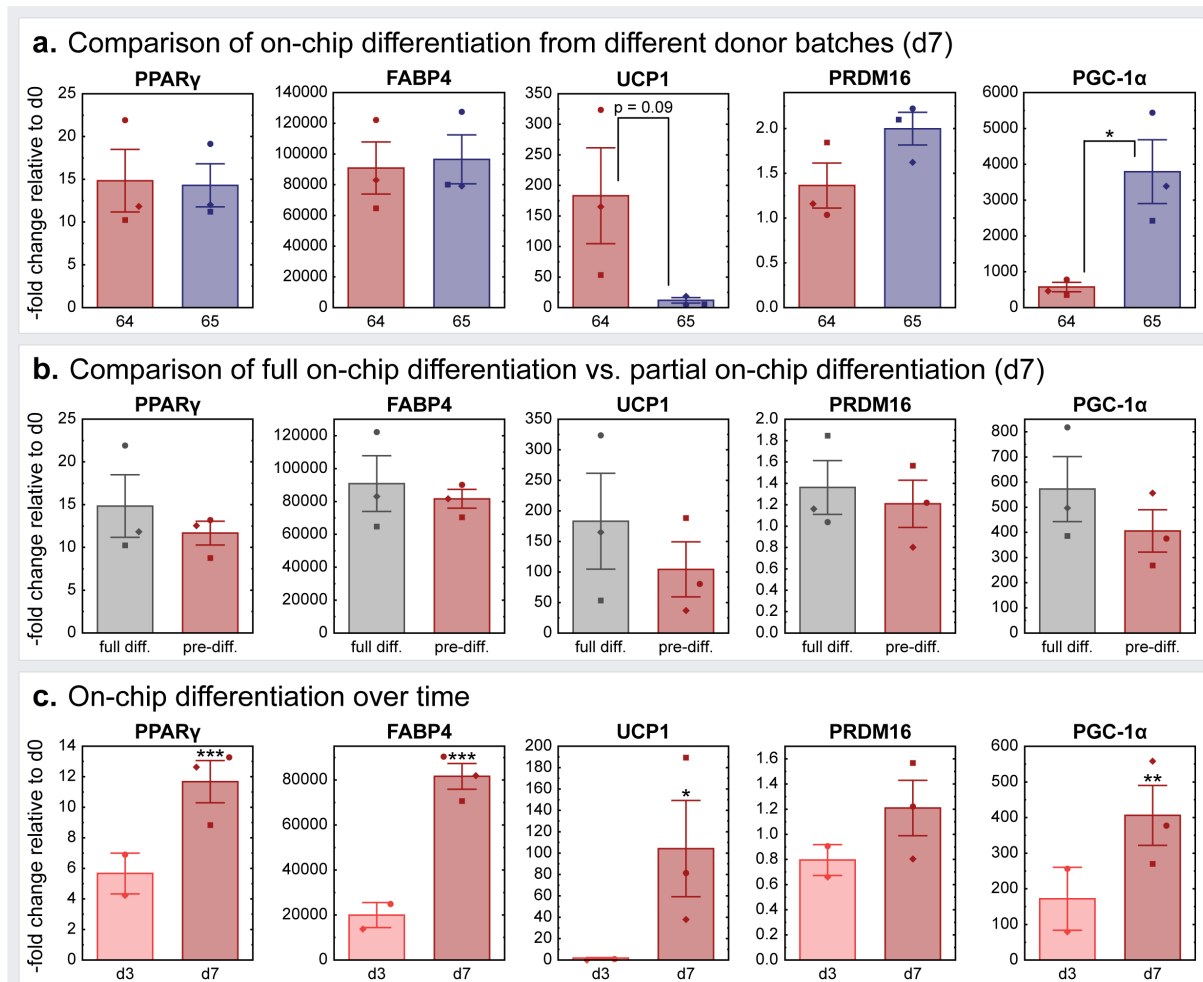


**Figure 14: Gene expression analysis of on-chip differentiation into beige adipocytes.** Expression of FABP4 and PPAR $\gamma$  (general markers of adipogenesis) and UCP1, PRDM16 and PGC-1 $\alpha$  (beige/brown adipocyte markers) was analyzed relative to expression of PPIA (housekeeping gene) and to respective gene expression on d0. D0 samples were produced for three individual chips in a culture format-specific and donor batch-specific manner. **a.** Comparison of marker gene expression for two different donor batches on d7. Due to low UCP1 expression after differentiation of the preadipocytes from batch SL0065 ('65'), all further experiments were conducted with cells from batch SL0064 ('64'). **b.** Comparison of gene expression from fully on-chip differentiated beige adipocytes vs. partial on-chip differentiation (i.e., pre-differentiation in well plate format; chip injection on d3 after initiation of differentiation). **c.** Monitoring adipogenesis and brown/beige marker expression over the course of differentiation. All genes of interest were expressed higher on d7 as compared to d3. Statistical analysis comparing d7 gene expression to d0 gene expression.

Error bars represent  $\pm$  SEM. \* $p < 0.05$ , \*\* $p < 0.01$ , and \*\*\* $p < 0.001$ .

Further, the d7 gene expression of cells that were pre-differentiated off-chip and then terminally differentiated on-chip was compared to the one of cells that were differentiated

on-chip without interruption (**Figure 14b**). Since none of the genes of interest showed significant differences in the expression, all following experiments were conducted according to the off-chip pre-differentiation protocol. This way, on-chip cell death in response to differentiation induction could be avoided (cf. '*Cell Viability Throughout Beige Adipocyte Differentiation*'). Finally, the gene expression signature throughout the course of differentiation was monitored by analyzing the genes of interest on d0 (prior to differentiation), on d3 (i.e., after the differentiation induction phase) and on d7 (**Figure 14c**). Transcripts of all genes increased over time indicating a successful differentiation into beige adipocytes. The increase in PPAR $\gamma$ , FABP4, UCP1 and PGC-1 $\alpha$  levels on d7 was significant compared to d0. Except for PRDM16 expression, which was lower than expected, the change in expression of the selected genes of interest after beige differentiation resembled gene expression profiles obtained by others differentiating human SVF or stem cells into beige adipocytes<sup>247,248</sup>. Given the small sample size, gene expression levels on d3 were not included in statistical analyses.

Overall, the transcriptional signatures obtained from the beige adipocyte differentiation experiments demonstrated an effective development of preadipocytes into beige adipocytes. The adipocytes were enriched in key beige/brown adipocyte markers verifying the suitability of the PDMS-thermoplastic hybrid OoC platform for on-chip beige adipogenesis. Given the recently discovered cellular complexity of beige adipocytes<sup>71</sup>, the spectrum of beige markers used for beige adipocyte characterization could be extended in future experiments: iodothyronine deiodinase 2 (DIO2), e.g., is another common marker for beige and brown adipocytes<sup>57-59</sup>. Moreover, it would be interesting to assess whether the on-chip beige adipocytes express CD137 and transmembrane protein 26 (Tmem26), two markers which are currently assumed to be beige-exclusive<sup>58,61</sup>. Yet, a considerable variability concerning the extent of marker expression from individual chips of the same condition could be registered, especially regarding the beige markers. Hence, the present findings should be backed by expanding sample size in future experiments. Additionally, beige differentiation efficiency could be further underpinned by expanding the assessment to a translational level. The typical approach of utilizing western blot, however, would be difficult to apply due to the required cell volume.

As a matter of fact, the OoC technology is not predestined to be combined with readout methods based on the disruption of cells/tissues: for once, OoCs are designed for integrating microscale cell- or tissue constructs, and thereby often do not meet the tissue

volume requirements needed to isolate sufficient nucleic acid or protein for further analysis. More importantly though, a tissue readout downstream of tissue disruption leads to loss of information on the morphological and structural context. Since the preservation of tissue structure and cellular relationship in a 3D environment are two of the key advantages of OoCs, optical readout-based methods, such as fluorescence microscopy, for detecting and quantifying transcripts and proteins would be more favorable. One such method, which might be a valuable tool for assessing beige adipocytes' transcriptional activity on-chip, could be RNA *in situ* hybridization since it combines the detection of mRNA without loss of spatial information. The RNAscope™ *in situ* hybridization assay has recently been successfully implemented on an OoC system<sup>249</sup>. However, especially concerning 3D volumetric imaging, the quantification of fluorescence intensity signals depends on many external parameters, amongst others microscope settings, detector, specimen preparation, and is less accurate and precise than qPCR or western blot results. Therefore, a combination of both, conventional, tissue disruption-based gene of interest/protein of interest expression analysis methods and fluorescence-based detection methods, will most likely be the best way to further characterize the on-chip beige differentiation in future experiments. Besides studying beige adipocytes derived from *de novo* adipogenesis, future beige adipocyte-on-chip experiments could also investigate whether a *trans*differentiation of white adipocyte into beige adipocytes can be induced in the microfluidic platform, too.

#### 4.3.2.3 Morphological Characterization of Beige Adipocytes on Chip

Next, the morphological changes throughout the differentiation of preadipocytes into beige adipocytes were monitored. Lipid droplets (via a neutral lipid dye), mitochondrial content (via MitoTracker®-labelling), filamentous actin (f-actin) (via phalloidin staining) and nuclei (via DAPI counterstaining) were visualized on-chip (**Figure 15a-b**). Quantification of the fluorescence intensities of the different morphological features revealed that lipid droplet- and mitochondria signals were significantly increased on d7 compared to d3. F-actin and nuclei signals, on the other side, significantly decreased from d3 to d7. High-resolution imaging using a confocal scanning microscope with an Airyscan detector revealed physiological intracellular distribution of lipid droplets (**Figure 15b**). Moreover, the presence of perilipin on the membranes of the lipid droplets could be confirmed (**Figure 15c**).

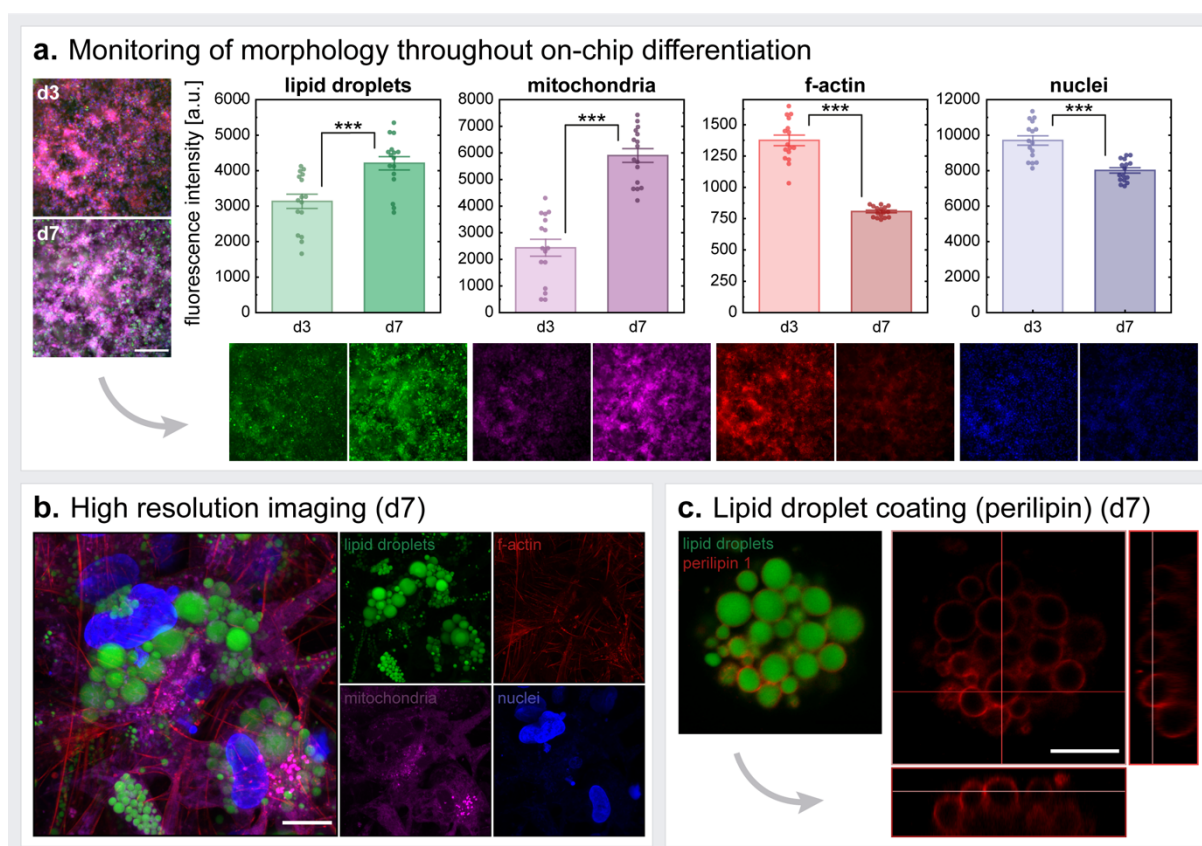


**Figure 15: Morphological characterization of beige adipocytes on chip.** **a.** Visualization and quantification of key bAT phenotypic features on d3 and d7 of differentiation ( $n = 16$  chambers per day of analysis). Fluorescence intensity from lipids and mitochondria staining significantly increased with progressing differentiation; f-actin and nuclei signal decreased from d3 to d7. Scale bar equals  $200 \mu\text{m}$ . **b.** High-resolution imaging of beige adipocytes on chip on d7. Scale bar equals  $10 \mu\text{m}$ . **c.** Verification of lipid droplet's perilipin 1 coating of on-chip adipocytes on d7. Scale bar equals  $10 \mu\text{m}$ .

All morphological characterization experiments were performed with partial on-chip differentiation (i.e., pre-differentiation in well plate format; chip injection on d3 after initiation of differentiation). Error bars represent  $\pm$  SEM. \*\*\* $p < 0.001$ .

Two morphological hallmarks of mature beige adipocytes are their multilocular lipid content and their enrichment in mitochondria. Hence, the increase in lipid- and mitochondria content from d3 to d7 of beige differentiation is a close reflection of the natural morphological changes. To accumulate and organize lipids inside the differentiating adipocytes, the cell shape must be adapted through cytoskeletal rearrangement. These morphological changes in the progress from a fibroblastic shape to the rounded adipocyte morphology are governed by dynamics of the actin skeleton<sup>250</sup>. More specifically, the ratio of f-actin fibers to monomeric globular actin (g-actin) plays a decisive role: to achieve a rounded shape, adipogenesis requires the disruption of F-actin stress fibers to g-actin<sup>250–253</sup>, which explains the decrease in f-actin signal registered with progressing beige differentiation. Yet, f-actin is not lost entirely; especially the high-resolution imaging performed on d7 displayed pronounced actin fibers. Unlike unilocular

white adipocytes, brown and beige adipocytes were reported previously to maintain an extensive cytoskeletal network; on the one hand, this network supports and organizes the multilocular lipid droplets and many mitochondria<sup>95</sup>. On the other hand, actin skeleton dynamics were linked to various metabolic adipocyte functions, such as glucose uptake, utilization of fat or insulin signaling<sup>254,255</sup>. A well-developed f-actin framework, for instance, is crucial for GLUT4 translocation from storage vesicles to the plasma membrane<sup>256–258</sup>. As discussed in attached **Publication [11]** (cf. *'Human Mature White Adipocytes-on-Chip'*), the presence of perilipin 1 on the multilocular lipid droplets brought another proof of mature adipocyte identity<sup>224</sup>.

#### 4.3.2.4 Functional Characterization of Beige Adipocytes on Chip

Finally, the functionality of beige adipocytes on chip was assessed. By administering a fluorescently tagged FA analog (dodecanoic acid with two BODIPY<sup>TM</sup> 500/510 fluorophores in the C1 and C12 position), it was possible to monitor the uptake of the FA in real-time by measuring the increase in fluorescence intensity. Thereby, the capability of the on-chip differentiated beige adipocytes to take up FAs could be demonstrated (**Figure 16a**), a process that is essential for thermogenesis<sup>259</sup>. LCFAs are required to activate UCP1's H<sup>+</sup> transport activity<sup>260,261</sup>; i.e., only upon LCFA binding, UCP1 increases the conductance of the inner mitochondrial membrane, which leads to generation of heat rather than ATP<sup>261</sup>. Moreover, free FAs are an important substrate for fueling thermogenesis: not only mitochondrial uncoupling (through maintaining the electrical gradient), but also UCP1-independent substrate futile cycling mechanisms (through dependency on active ATP synthesis) generate high energetic demands<sup>259</sup>. While the required FAs can be derived from the thermogenic adipocytes' lipid contents, recent studies from mice suggest WAT-derived FAs as main FA source<sup>262,263</sup>. FAs arrive at the thermogenic adipocytes through TAG-rich lipoprotein-(TRL-) and lipoprotein lipase-(LPL-) mediated processes or as free FFAs from serum; they are taken up by fatty acid transport proteins, e.g., CD36 or fatty acid transport protein 1 (FATP1)<sup>264–266</sup>. Of note, lipids are not only the preferred source of fuel, but also important for development, intercellular signaling and as structural components of thermogenic adipocytes<sup>259</sup>. Since the FA demand is elevated when thermogenesis is stimulated, a future FA-uptake experiment comparing unstimulated versus stimulated beige adipocytes could be interesting.



which leads to the release of FAs fueling  $\beta$ -oxidation in the mitochondria.<sup>264</sup> Hence, the ascending trend in the registered UCP1 expression was expected and confirms previous findings<sup>133,268</sup>; the expected increase in PGC-1 $\alpha$ , however, did not occur on-chip. PRDM16, which also didn't show elevated expression on-chip, is involved in the activation of UCP1 and PGC-1 $\alpha$  in response to isoproterenol<sup>269</sup>; yet, its gene expression level was not expected to change in response to isoproterenol<sup>133</sup>. FABP4 expression levels might be increased for handling the increased FA uptake for fueling the thermogenic response. Moreover, FABP4 has been shown to be secreted from lipolytic adipocytes with isoproterenol stimulation<sup>270</sup>.

Generally, this set of experiments should only be regarded as preliminary assessment of the on-chip beige adipocytes' responsiveness to  $\beta$ -adrenergic stimulation. In future experiments, the sample size must be increased to get a clearer picture of beige adipocyte stimulation. Moreover, beige adipocyte metabolic functions should be further investigated by other readout methods that harness the advantages of the OoC technology. On the one hand, this includes non-invasive optical readout methods to preserve spatial information: Enhanced thermogenesis could be monitored using mitochondrial membrane potential probes, which sense the polarization of the mitochondrial membrane<sup>271</sup>. Metabolic changes in response to stimulation in real-time could be monitored marker-free using fluorescence lifetime imaging microscopy (FLIM) by assessing the momentary proportions of glycolysis and oxidative phosphorylation<sup>272</sup>. Another imaging method that can non-invasively track metabolic changes, and has been successfully implemented for OoCs<sup>273</sup>, is Raman microspectroscopy and imaging, which provides *in situ* molecular information through a spectral fingerprint. On the other hand, future experiments should exploit the precise temporal control over the media perfusion, which allows high-resolution sampling of cells' secretions into, or consumptions from, the media. More specifically, the release of glycerol and fatty acids could be compared for unstimulated versus stimulated beige adipocytes. Furthermore, the consumption of glucose in response to treatments could be explored by determining glucose concentrations from medium before and after the tissue chambers.

Another strategy to assess beige adipocyte activity on-chip would be the integration of in-line sensors determining the local oxygen concentration. First trials with adipocyte-on-chip experiments featuring integrated optical O<sub>2</sub> sensors, applied to the bottoms of tissue chambers prior to chip assembly, were successfully conducted and demonstrated the

potential of this approach to detect changes on O<sub>2</sub> concentration when thermogenesis is induced.

### 4.3.2.5 *Towards a Patient-Specific Beige Adipose Tissue-on-Chip Model*

Besides a deeper and more detailed characterization of the beige adipocytes on chip, a future bAT-on-chip model should integrate further adipose tissue-associated cellular components such as vascularization through endothelial cells or immune cell integration. (Multi-cell type adipose tissue-on-chip models of WAT are discussed specifically in the chapter '*Full Complexity Adipose Tissue-on-Chip Models*'.) Additionally, a future application of the model might be in personalized medicine. In particular, the platform could be utilized to test a patients' stem cells' potential for beige adipogenesis in general, or, specifically, the effect of being compounds. In a preliminary experiment towards a patient-specific adipose tissue-on-chip model, an autologous endothelial lining of the media channel was added to on-chip differentiated beige adipocytes of the same donor (**Figure 17**). To do so, SVF was isolated from a skin biopsy with subcutaneous adipose tissue, expanded in preadipocyte growth medium and later injected into the chips and differentiated as done for the previous beige adipocyte-on-chip experiments. Following beige differentiation, patient-specific microvascular endothelial cells were seeded onto the membrane in the media channel according to protocols described in chapter '*Recreating Barriers on Chip*'. The beige adipocyte-mvEC co-culture chips were then constantly perfused for another three days using a 1:1 mixture of bAT maintenance medium and endothelial cell growth medium. On d10, the on-chip morphology was assessed by staining intracellular lipid droplets (using BODIPY), endothelial cells (with anti-CD31 staining) and nuclei: differentiated adipocytes had formed extensive lipid droplets and endothelial cells completely covered the membrane above the tissue chambers. Of note, for imaging the endothelial coverage of the membrane directly above the tissue chambers, the chips had to be inverted. Even though this first experiment on patient-specific beige adipocyte-endothelial co-culture was successful regarding on-chip morphology after differentiation, there are many more steps to take towards a full complexity donor-specific human bAT-on-chip model. One of the first steps would be to characterize the differentiation capacity of the donor-derived SVF; there are inter-donor variabilities and especially SVF from patients with overweight and insulin resistance showed markedly reduced beige differentiation<sup>247</sup>. Next, it should be investigated whether the presence of endothelial cells, or their respective culture medium, has any impact on

the beige adipocytes' functionality, and vice versa. After confirmation of beige adipocyte- and mvEC identity and functionality, other bAT-relevant cell types could be added to the model.

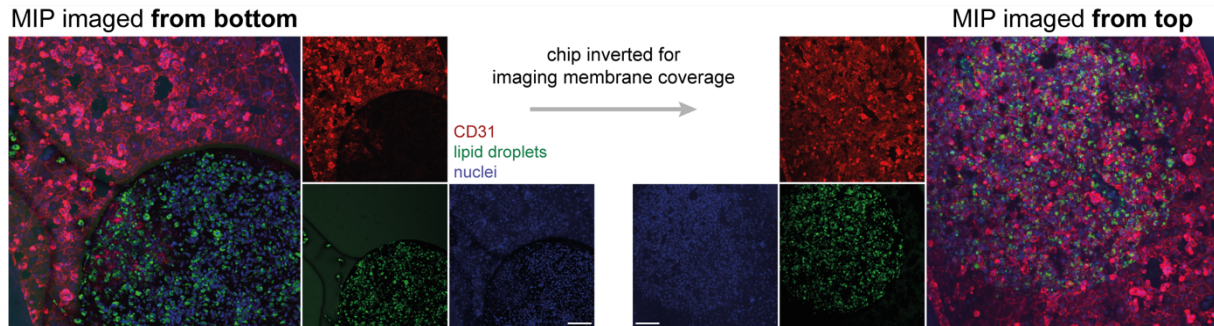


**Figure 17: Patient-specific bAT-on-chip model (d10).** SVF was isolated from one donor and differentiated on-chip into beige adipocytes. After differentiation (d7), autologous endothelial cells were seeded into the media channel and covered the membrane. The co-culture was reconnected to media perfusion for another three days with a 1:1 mixture of bAT maintenance medium and endothelial growth medium. Lipid droplets, endothelial cells (marked by an anti-CD31 antibody) and nuclei were visualized by (immuno-)fluorescent staining. For imaging the membrane coverage above the tissue chambers, the chips had to be inverted. Otherwise, the 'shade' of beige adipocytes in the tissue chamber obscured the view of the membrane. Z-stacks were acquired for the same tissue chamber from the bottom and from the top of the chip. Images represent maximum intensity projections (MIPs) of the stacks. Scale bars equal 200  $\mu\text{m}$ .

#### 4.3.3 Recreating Barriers on Chip

The human body comprises a multitude of barrier tissues, which either separate the internal from the external environment or delineate different compartments inside the body. These barriers are formed by epithelial tissues consisting of closely packed continuous cell sheets in single or multiple layers. Epithelia serve as selective barriers actively modulating the transfer of substances, protect against abrasive effects from the environment and secrete different kinds of signaling molecules. Owing to the different demand and wide-ranging functions, there are many different types of epithelia, which can be classified by their arrangement of cell layers and the shapes of the cells.<sup>274</sup> Since many OoC platforms feature compartmentalized designs, interfaces and barriers play a major role and a physiological recapitulation of barrier function *in vitro* is essential<sup>275,276</sup>. Besides requiring an appropriate design of chip architecture, a successful integration of epithelial linings in OoC platforms entails the establishment of epithelial cell type- and platform-specific seeding protocols. Important parameters to be evaluated include (i) the necessity of membrane coating to promote cell adhesion, (ii) appropriate cell seeding densities to achieve dense cell layers, (iii) optimal adhesion times and (iv) the best ways to connect to constant media perfusion.

The capability to generate physiological epithelia was demonstrated in a tailored OoC platform specifically designed to integrate an human iPSC-derived retinal pigment epithelium (RPE)-layer that separates a media flow from a compartment into which iPSC-derived retinal organoids could be integrated (see attached **Publication [4]**). The RPE is a single layer of cuboidal epithelial cells and, being located between light-sensitive photoceptors and the choroid (vascular layer of the eye), an integral part of the blood-retinal barrier and crucial for maintenance of visual function<sup>277,278</sup>. Together with Jasmin Haderspeck (Institute of Neuroanatomy & Developmental Biology, University of Tübingen), a tailored chip platform was designed and cell seeding as well as cultivation processes established that enabled the generation of a physiological iPSC-RPE barrier on-chip (which served as an integral part of the final, complex retina-on-chip platform): Prior to RPE integration, the membranes of the microfluidic devices had to be coated with laminin solution. Upon seeding, RPE cells formed a densely packed monolayer within 24 h. (see attached **Publication [4] Figure 3**).

Experiences gained from the establishment of the RPE barrier could then be transferred to integrate a physiological barrier in the adipose tissue-on-chip models. Here, a specialized type of the epithelium is of main interest, the endothelium. In a single layer of squamous cells, the endothelium is the innermost lining of all blood and lymphatic vessels forming a barrier between vessel lumen and the rest of the tissue. Since the microchannels of OoC platforms are designated to mimic *in vivo* vascular structures, lining these channels with endothelial cells is a crucial step towards higher physiological relevance by recapitulating not only the perfusion aspect of the vasculature but also key barrier- and regulatory functionality of the endothelium.

In the human body, the endothelium performs both systemic and organ-specific tasks. On systemic level, endothelial cells handle oxygen and nutrient supply, immune cell trafficking and inflammation<sup>279</sup>, hemostasis and coagulation<sup>280</sup> and angiogenesis<sup>281</sup>, amongst others. Especially the endothelial cells' control of bidirectional transport of a wide variety of molecules across the endothelial barrier is important for OoC applications: covering artificial porous membranes with endothelial cells shifts the transport from merely diffusive to active transport with endothelial cells operating as metabolic gate keeper by regulating and modulating the transport rates of gases, nutrients and hormones, including FAs, glucose and insulin<sup>282</sup>. Of course, for studies involving immune cell perfusion, the endothelium is crucial for a physiological recruitment of circulating

immune cells to the target tissue. Induced by an inflammatory response, endothelial cells express leukocyte adhesion molecules, such as vascular cell adhesion molecule 1 (VCAM-1)<sup>279</sup>, which capture circulating leukocytes and initiate their transendothelial migration via a process called diapedesis, i.e., paracellular or transcellular leukocyte extravasation<sup>283</sup>. Besides their systemic functions, endothelial cells take on organ-specific tasks which are induced by the organ-specific microenvironment (e.g., shear stress or hypoxia)<sup>284</sup>. Murine studies exploring endothelial cell heterogeneity through single-cell transcriptome analyses found that among all endothelial cells (arterial, venous, lymphatic), the capillary endothelial cells had the highest heterogeneity<sup>285</sup>.

Due to adipose tissues' considerable plasticity, adipogenesis is highly reliant on angiogenesis, governed by active endothelium<sup>286</sup>. However, functions performed by quiescent endothelial cells are as important for adipose tissue function and homeostasis: adipose microvascular endothelial cells (mvECs) communicate with adipocytes to oversee PPAR $\gamma$ -associated pathways and thereby directly impact the adipocytes' capacity to take up and store lipids<sup>287</sup>. Adipose-associated mvECs can even take up a limited amount of lipids themselves; however, they cannot undergo adipogenic differentiation upon exposure to adipogenesis factors<sup>287</sup>. Hence, the integration of an endothelial barrier is highly important for physiologically relevant adipose tissue *in vitro* models.

In a first step towards an endothelialization of the adipose tissue-on-chip models, monoculture models of endothelial barriers were created and characterized inside the 2<sup>nd</sup>-generation microfluidic platform (comprehensively described in attached **Publication [11]**).

Microvascular endothelial cells (mvECs) were isolated from the dermal part of the subcutaneous adipose/skin biopsy since the adipose tissue itself was required as a source for donor-specific adipocytes, SVF and tissue-resident immune cells. Yet, despite originating from neighboring but different tissue types, previous reports indicated that adipose- and skin-derived mvECs demonstrate high similarity exhibiting, amongst others, identical endothelial marker expression and inflammatory response<sup>288</sup>. After isolation, mvECs were expanded for at least seven days to allow for proliferation and purification from non-endothelial cell types. Prior to injection into the microfluidic platform, the tissue compartment needed to be filled with the HyStem<sup>®</sup>-C hydrogel, to maintain on-chip mechanical properties and to provide adhesion sites for the endothelial cells. Best results

of endothelial lining were obtained when letting endothelial cells adhere to the media channel's membrane overnight before connecting the media perfusion and by subsequently ramping up the flow rate in a stepwise manner. As for adipocyte characterization, a toolbox of endothelial readout methods was established to appraise on-chip viability, endothelial identity and function, as well as barrier integrity under basal and inflammatory conditions (**Figure 18**).

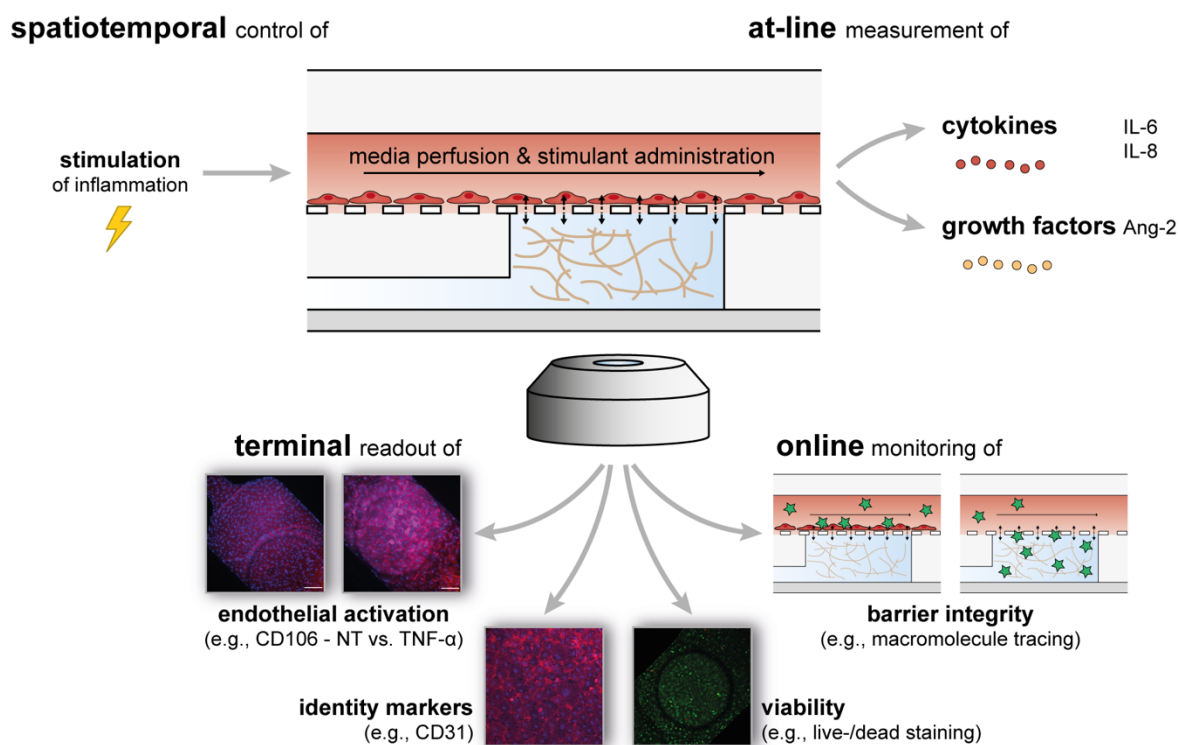


**Figure 18: Toolbox of on-chip analysis of human endothelial barriers.** Endothelial structure, viability and functionality was assessed via a comprehensive toolbox of readouts: non-invasive online monitoring of optical readouts, at-line measurements of EC secretome in the media perfusion as well as terminal staining for structural analysis and identification of EC markers. Endothelial barriers were assessed both at basal conditions and in response to inflammatory stimulation. Images adapted from figures in attached **Publication [11]**.

As can be seen in the live-/dead staining of the endothelium on chip, the mvECs formed dense layers which were viable for at least one week (attached **Publication [11] Figure S2**). Moreover, the endothelial identity of the cell barrier was confirmed by visualizing the expression of CD31 [also: platelet endothelial cell adhesion molecule 1 (PECAM-1); a junctional molecule highly expressed on the surface of endothelial cells], CD309 [also: vascular endothelial growth factor receptor 2 (VEGFR-2)] and endothelial nitric oxide synthase (eNOS) (attached **Publication [11] Figure 4a & S4a-b**). Importantly, the anti-CD31 staining not only verified identity but also demonstrated a tight barrier formation throughout the entire media channel.

As one of the most important intercellular junction proteins in endothelial cells, CD31 was reported to maintain endothelial integrity, to control leukocyte trafficking and to act as mechano-sensor<sup>289,290</sup>. An alignment of endothelial cells in the direction of media flow could not be observed but was also not expected since the shear forces on the 2<sup>nd</sup>-generation microfluidic platform (approx.  $4 \times 10^{-3}$  dyn/cm<sup>2</sup>, attached **Publication [11] Figure 2c**) are considerably lower than physiological shear forces (usually 0.1–60 dyn/cm<sup>2</sup>)<sup>291</sup>. An increase in flow rate to increase shear forces was not possible in the scope of this study, because it would dilute secreted molecules significantly hampering their detection in the media effluents. Future design generations of the microfluidic platform could focus on creating more physiological shear stress, e. g., by modifying media channel heights, since fluid shear stress is an important modulator of endothelial cell structure and function<sup>292–294</sup>.

Analysis of the permeability of the endothelial barrier on chip was conducted using macromolecular tracers: the transendothelial flux of differently sized, fluorescently labeled molecules across the endothelial barrier was assessed in comparison to the transport across acellular membranes (attached **Publication [11] Figure 4b & S4c**). An equilibrium in fluorescence signal between media channel and tissue chamber occurred much slower in the presence of a vascular barrier, indicating a retention of molecules in the media channel mediated by the endothelial cells. Although measuring the permeation of fluorescent macromolecules to assess barrier integrity is an easy and robust methods, it is not sensitive to rapid or transient changes in barrier function<sup>295</sup>. Hence, when studying mechanisms eliciting these rapid or transient changes, alternative methods for assessing permeability should be utilized. Transepithelial/endothelial electrical resistance (TEER) measurements, especially in combination with impedance spectroscopy<sup>296</sup>, can sensitively and non-invasively quantify barrier integrity and can be integrated into OoCs<sup>275,297</sup>.

Finally, in light of the endothelium's crucial role in inflammatory processes, the on-chip vascular barrier's response to proinflammatory stimuli was studied. Upon proinflammatory activation, e.g., through TNF- $\alpha$ , endothelial cells respond *in vivo* by altering their angiocrine profile<sup>279</sup>, growth factor expression and surface expression of leukocyte adhesion molecules<sup>279,298</sup>. The endothelium in the adipose tissue-on-chip platform demonstrated a matching response (attached **Publication [11] Figure 4c & S4d**): after 24 h exposure to TNF- $\alpha$ , the endothelial cells expressed significantly more VCAM-1 and released the proinflammatory cytokines IL-6 and IL-8 as well as the

endothelial activation-associated growth factor angiopoietin 2. Moreover, the capacity to take up, or to retain, acetylated low-density lipoprotein (Ac-LDL) was diminished with TNF- $\alpha$  stimulation.

Furthermore, the established concepts and methods to create, and characterize, on-chip endothelial barriers for adipose tissue-on-chip platforms could be successfully transferred to other microfluidic platforms:

As described in detail in attached **Publication [10]**, channels of organ-disc systems were lined with endothelium (human umbilical vein endothelial cells, HUVECs) and perfused via a newly developed, integrated peristaltic pump which allowed for closed loop perfusion (developed by Stefan Schneider; MicroOrganoLab, Fraunhofer IGB/Eberhard Karls University Tübingen). In cooperation with Stefan Schneider, a set of experiments exploring the on-disc endothelia's responsiveness to pro-inflammatory stimuli, a successful activation of the endothelium, as reflected by increase in VCAM-1 expression and elevated levels of the proinflammatory secretions IL-6, IL-8 and angiopoietin 2, could be shown. Moreover, it could be shown that, upon perfusion of whole blood through the channels of the organ-disc, platelets adhered to the endothelial lining as visualized by labelling platelets with an anti-CD41 antibody prior to perfusion (attached **Publication [10]** *Figure 4d-g*).

As described in detail in attached **Publication [8]**, electrospun membranes were integrated into OoC modules by Johanna Chuchuy (MicroOrganoLab, Fraunhofer IGB/Eberhard Karls University Tübingen) in an effort to create on-chip barrier properties which resemble *in vivo* ECM and basement membrane better than the commonly used, artificial PDMS- or PET-membranes. To confirm the electrospun membrane chips' suitability for cell culture mvECs were seeded onto the membranes and their viability and identity assessed on-chip. By adopting processes and protocols established for the adipose tissue-on-chip platforms, mvECs formed a viable endothelium that stained positive for CD31 (attached **Publication [8]** *Figure 4ab & 5a*).

#### 4.4 Full Complexity Adipose Tissue-on-Chip Models

In view of adipose tissue's considerable heterogeneity, adipocytes-on-chip alone do not make a well-rounded model. To obtain a model that recapitulates WAT in its entirety, a high-complexity WAT-on-chip was developed integrating almost all WAT-relevant cell

types (**Figure 19**). The model is based on the 2<sup>nd</sup>-generation microfluidic platform (cf. ‘*Second-Generation Platform*’). Autologous and organotypic stromovascular cells were isolated from the same tissue biopsy as adipocytes themselves. SVF was either co-injected in its entirety or served as a source for tissue-resident immune cells. In addition, mvECs were isolated from subcutaneous adipose tissue-attached dermis to line the chips’ media channels with endothelium.

Readout methods established within the scope of monoculture experiments on the white adipocytes-on-chip (cf. ‘*Human Mature White Adipocytes-on-Chip*’) and the endothelial barrier-on-chip systems (cf. ‘*Recreating Barriers on Chip*’), were successfully transferred to assess the complex adipose tissue-on-chip co- or multi-culture models. The range of methods was further extended by SVF- and immune cell-specific readouts (covered in detail in attached **Publication [11]**).

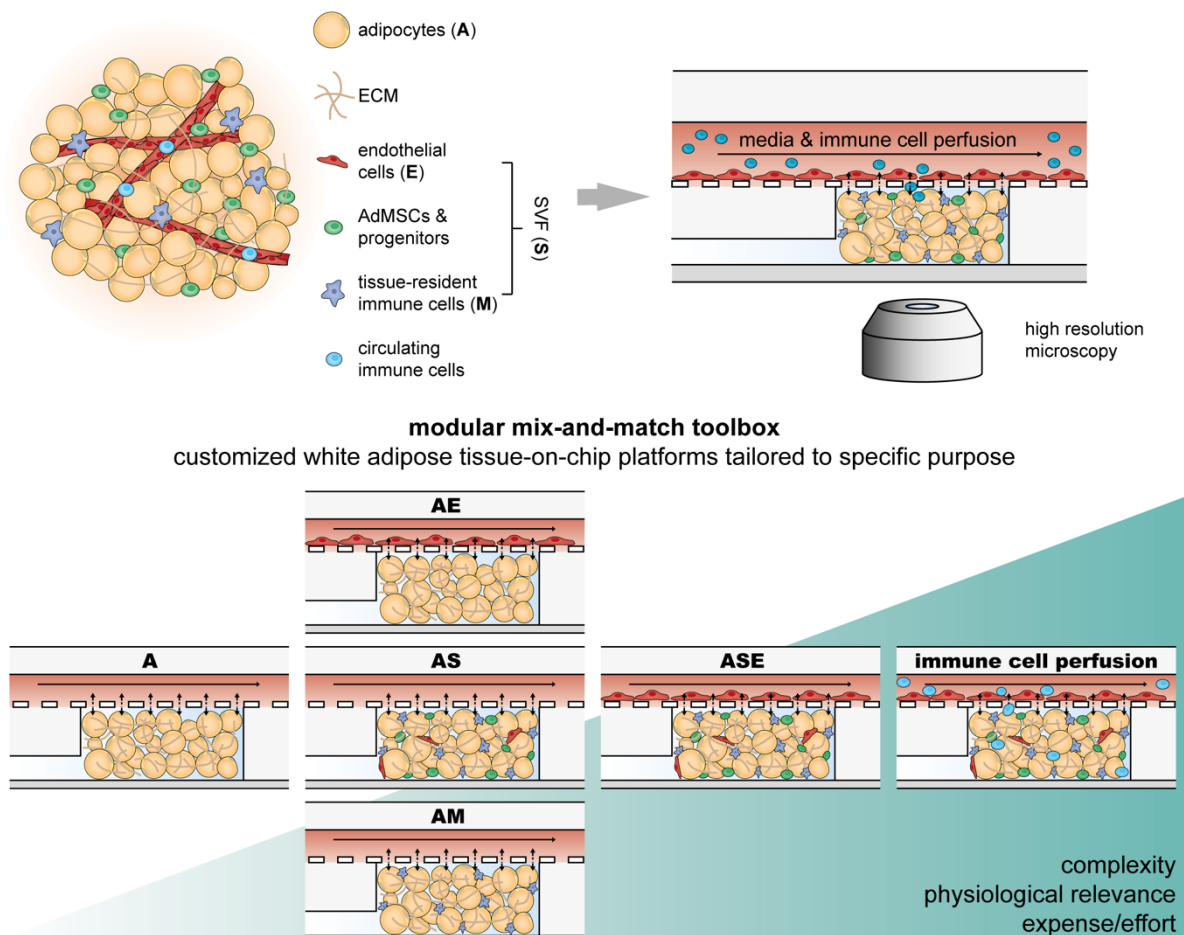


**Figure 19: Concept of high-complexity WAT-on-chip models.** Almost all WAT-relevant cell types (except for sympathetic innervation components) were integrated into the microfluidic platform. To tailor the WAT-on-chip models to fit a specific purpose, a modular mix-and-match approach was established. Degree of complexity can thereby be flexibly adjusted by choosing only scientific question-relevant cellular components. Adapted from attached **Publication [11]**.

### 4.4.1 Co-Culture Logistics and Considerations

Since each individual cell type brings along its individual culture requirements, several logistics- and cell handling-related aspects had to be taken into consideration when setting up high-complexity WAT-on-chip models (see attached **Publication [11] Figure 7**): as discussed above (cf. *'Human Mature White Adipocytes-on-Chip'*), mature white adipocytes require sophisticated *in vitro* culturing strategies that provide structural support while at the same time prevent physical stressors. Hence, adipocytes had to be injected no later than 24 h post isolation. Stromovascular cells (or tissue-resident immune cells) were injected the day after isolation, too, because their cellular composition was reported to change immensely with culturing and passaging<sup>299–301</sup>; therefore, they were encapsulated in the injected hydrogel together with the adipocytes. Patient-specific endothelial cells, however, had to be expanded and purified from other, non-endothelial cell types, such as fibroblasts, for instance, in traditional adherent cell culture for at least seven days. Consequently, autologous endothelial barriers were established on d7 of adipocyte (-SVF-) on-chip culture.

Another aspect that had to be considered was the choice of culture media to meet the needs of all the different cell types. For this study, each cell type was cultured in their cell-type specific media as long as they were in monoculture. Upon combination with other cell types, cell type specific media were mixed in a 1:1 ratio. Whenever tissue-resident immune cells were present in the culture systems, i.e., as part of the SVF or by themselves, media were supplemented with granulocyte-macrophage colony-stimulating factor (GM-CSF) to support viability and induce differentiation of monocytes to macrophages. Even though the established approach for media preparation allowed the establishment of the model systems and the conduction of a broad range of experiments, future experiments could focus on the influence of individual media components onto each cell type and on the optimization towards a universal medium. Generally, the concentrations of ingredients should be revised in terms of reflection of physiological states: most commercially available cell culture media, for instance, were designed for static cell culture and not continuous perfusion and hence contain, e.g., very high glucose concentrations to compensate for consumption.

### 4.4.2 Mix-and-Match Toolbox for Autologous WAT-on-Chip Models

By uniting mature white adipocytes, SVF and endothelial barriers, all derived from the same tissue donor, on the 2<sup>nd</sup>-generation microfluidic platform, a physiologically highly

relevant *in vitro* model of human WAT was generated. Yet, the increase in model complexity at the same time increases the associated amount of work and costs and thereby limits throughput. Moreover, when focusing on specific bilateral interaction of two distinct adipose-associated cell types, for instance, the presence of multiple other cell types might interfere. Thus, to allow researchers to choose the cell types of interest and individually adjust the level of complexity to fit their specific research question, a flexible mix-and-match toolbox was established, including the following co- and multi-culture platforms (**Figure 19**): white adipocyte-only systems ('A'; cf. '*Human Mature White Adipocytes-on-Chip*'), white adipocyte-endothelial barrier co-culture systems ('AE'), white adipocyte-SVF co-culture systems ('AS'), and white adipocyte-SVF-endothelial barrier multi-culture systems ('ASE'). Owing to WAT's important contributions to the immune functions, white adipocyte-CD14<sup>+</sup> cells co-culture systems ('AM') were established to allow for focused studies on adipocyte-monocyte/macrophage crosstalk. Moreover, a further layer of complexity was added by perfusion of circulating immune cells in the media channels allowing to study immune cell recruitment and infiltration.

The various co- and multi-culture WAT-on-chip models were characterized by assessing on-chip viability, cell identity, tissue morphology and structure, release of signaling molecules as well as FA trafficking properties.

An overall low LDH release into the effluent media indicated that the 2<sup>nd</sup>-generation microfluidic device could preserve the viability of all integrated cell types for at least 12 days (attached **Publication [11] Figure S1**). Physiological tissue structure on chip was confirmed by (immuno-)fluorescent staining approaches, e.g., on day 12 of an ASE on-chip culture (attached **Publication [11] Figure 5b**): mvECs formed a tight cell layer on the media channel's membrane (visualized by anti-CD31 staining), white adipocytes were unilocular and evenly distributed throughout the tissue chamber (visualized by lipid droplet staining using a neutral lipid dye), and SVF (labeled with a cell tracker prior to injection) were dispersed among the adipocytes.

Time-lapse monitoring of SVF after injection indicated the presence of a heterogeneous cell population with part of the cells dynamically moving throughout the tissue chamber while the other part remained settled among the white adipocytes. Leveraging the established FA trafficking assay, differences in FA uptake rates were registered for the different culture conditions (attached **Publication [11] Figure 5c**): In the presence of on-chip endothelial barriers (exemplarily shown for AE systems), FA uptake by adipocytes was approximately 50% less compared to endothelium-free systems (shown for AS and

A) suggesting an actively controlled transendothelial FA transport. Endothelial cells actually have been shown to specifically regulate FA and lipoprotein transport<sup>302,303</sup>, and they can even incorporate the FAs themselves<sup>287</sup>.

Finally, adipokine secretion profiles by four different culture systems (*ASE*, *AS*, *AE* and *A*) were analyzed after 12 days of on-chip culture (see attached **Publication [11] Figure 5d**). Interestingly, even though no other adipose-related cell type besides the white adipocytes themselves has been reported to release any of the analyzed adipokines in significant quantities<sup>81</sup>, the *ASE* condition showed the highest release for all four adipokines – adiponectin, leptin, adipsin and RBP4. Especially for the *A* and *AE* culture systems, adiponectin and leptin were hardly detectable. Provided that the analyzed adipokines indeed are exclusively released by the adipocytes, these results emphasize the importance of interactions between all adipose-associated cell types for an optimal functioning of adipocytes.

#### 4.4.3 Immunocompetency of the WAT-on-Chip Systems

To demonstrate the immunocompetency of the developed high-complexity WAT-on-chip model, first, the release of immunomodulatory cytokines and the impact of proinflammatory stimulation were characterized. As demonstrated in *sections 4.3.1* and *4.3.3*, white adipocytes and endothelial barriers on chip respond to TNF- $\alpha$  or LPS stimuli in the media perfusion by upregulating proinflammatory cytokine release. By analyzing donor-specific *ASE*, *AS*, *AE* and *A* culture systems, the contribution of the other WAT cellular components as well as of the intercellular crosstalk to immune responses could be investigated (see attached **Publication [11] Figure 6a-b**). Again IL-6, IL-8 and MCP1 releases were analyzed. IL-6 performs context-dependent roles and approximately 35% of basally circulating IL-6 levels *in vivo* are derived from adipocytes and AdMSCs<sup>304,305</sup>. IL-8 and MCP1 elevation is usually associated with proinflammatory responses and obesity<sup>306,307</sup>. Surprisingly, there were already differences in the baseline (unstimulated) cytokine release between the different culture systems: overall, cytokine release was lowest from adipocyte-only (*A*) systems demonstrating the important contribution of the other cellular components in the *ASE*, *AS* and *AE* systems. Moreover, considerable differences were found in the basal release of IL-6 and IL-8, which were highest for the *AS* condition. Interestingly, *ASE* models comprising the same cellular composition plus an additional endothelial barrier featured much lower release of IL-6 and IL-8, indicating an inhibiting effect of the endothelial cells on IL-6/IL-8 release into the media

compartments; this presents a prime example for the need for models that are as complete as possible when studying mechanisms orchestrated by multiple cell types. As anticipated, in response to 24 h-treatments with TNF- $\alpha$  or LPS, cytokine release was elevated in all different culture systems compared to the respective unstimulated systems. Interestingly, the response was most pronounced in culture systems with endothelial barrier (i.e., ASE and AE), implying a strong contribution of endothelial cells to the inflammatory response.

Next, white adipocytes were co-cultured with patient-specific CD14<sup>+</sup>-cells ('AM' culture condition), i.e., mainly monocytes and tissue-resident macrophages, which were isolated via MACS from the SVF. As a co-receptor to the LPS receptor, toll-like receptor 4 (TLR4), CD14 is strongly expressed on monocytes and macrophages. Yet, due to absence of a cytoplasmic domain, binding of the antibody does not activate signal transduction. ATMs rank among the key regulators of adipose tissue inflammation<sup>105</sup>. In response to inflammation, monocytes/macrophages infiltrate WAT through classical recruitment mechanisms, but there are also reports on mechanisms of local macrophage proliferation in WAT itself, mainly located to crown-like structures<sup>308,309</sup>. ATMs feature a high degree of plasticity, which goes beyond the typical binary M1/proinflammatory- versus M2/anti-inflammatory classification; many ATMs were found to exhibit mixed activation states holding on to both M1 and M2 traits, e.g., hybrid CD11c<sup>+</sup> (classically M1) CD206<sup>+</sup> (classically M2) ATMs, which were correlated with insulin resistance<sup>310</sup>. Moreover, distinct ATM subpopulations have been reported, such as metabolically activated ATMs (MMe) or oxidized ATMs (Mox)<sup>311,312</sup>. Importantly, Jaitin *et al.* recently discovered a new subset of lipid-associated macrophages (LAMs), which were accredited protective functions in obese humans by counteracting adipocyte hypertrophy and inflammation. The lipid receptor Trem2, which was highly expressed on the new subset of LAMs, was found accountable for these protective properties<sup>313</sup>.

To provide access to the phenotypic states of ATMs in co-culture with white adipocytes on chip, immunofluorescent staining was performed after five days: in addition to visualizing CD11c<sup>+</sup>-, CD206<sup>+</sup>- and CD86<sup>+</sup>-cells (all commonly occurring human ATM markers), Trem2<sup>+</sup>-LAMs and generally all leukocytes (CD45<sup>+</sup>) were uncovered (see attached **Publication [11] Figure 5e**). The staining revealed that the ATMs were located 3-dimensionally among the adipocytes. Oftentimes, they formed clusters attaching to single adipocytes, potentially even enwrapping them as crown-like structures. Lipid droplets, visualized by neutral lipid stain as well as by brightfield microscopy, were not

only located in adipocytes but also within ATMs indicating lipid scavenging activity. This highlights that although the dysregulated metabolism of adipocytes might still be the main driver of low-grade chronic inflammation in obesity<sup>236</sup>, the activity of ATMs should not in the least be disregarded. Showing the WAT-on-chip model's capacity to reflect adipocyte-macrophage interactions is, hence, not only of interest for investigating these interactions in greater detail, but also for studying ATMs as therapeutic target.

Moreover, to reflect monocyte/macrophage recruitment and infiltration into WAT on chip, PBMC-derived, fluorescently labeled CD14<sup>+</sup>-cells were perfused with the medium. Circulating CD14<sup>+</sup>-cells were not able to transmigrate through 3  $\mu\text{m}$  wide pores but could infiltrate the adipose tissue compartment in chips built with membranes featuring 5  $\mu\text{m}$  wide pores (see attached **Publication [11] Figure S6**). However, recruitment was scarce and the experiments should be repeated using the *AM* culture systems to provide circulating monocytes with chemotactic cues from tissue-resident ATMs, which are a key source of proinflammatory mediators<sup>314,315</sup> and have been shown to affect circulating levels of monocytes<sup>316</sup>.

Yet, monocytes and macrophages are not the only immune cells infiltrating WAT upon states of chronic inflammation. T cells play a major role in immunometabolism, too, and WAT has recently been identified as a hub for various T cell populations, such as tissue-resident memory T cells with distinct functionality and metabolic profiles<sup>118</sup>, and adaptive CD8<sup>+</sup> cytotoxic T cells, which reside in obese WAT<sup>107</sup>. Therefore, the recruitment of autologous CD3/CD28 co-stimulated and fluorescently labeled T cells was studied. T cells were perfused with the medium for 18 h, and their infiltration was assessed by confocal imaging. Comparing *ASE*, *AS* and *AE* culture conditions, the highest recruitment was registered for *AS* systems. This might be due to the increased release of IL-6 and IL-8, since both interleukins were shown to strongly mediate local T cell attraction<sup>238,317–319</sup>. These results show that the developed WAT-on-chip platforms were capable of recapitulating T cell infiltration into WAT and therefore are amenable for studying interactions of different T cell populations and WAT in greater detail.

# Chapter 5

## Conclusion



## 5. Conclusion

By combining innovative microfabrication approaches and adipose tissue engineering, two major classes of novel adipose tissue *in vitro* models were successfully established within the framework of this thesis: (i) the first human, fully autologous immunocompetent WAT-on-chip platform integrating virtually all *in vivo* WAT-associated cell types as well as (ii) a microfluidic model for *de novo* beige adipocyte biogenesis (beiging) on-chip.

Throughout the process leading to these two major results, various new procedures and protocols were established, which allowed to gain new insights for adipose tissue engineering on different levels. Generally, these achievements can be characterized into (i) technological development, (ii) cell sourcing processes, (iii) establishment of new models and (iv) *in vitro* recapitulation of human adipose biology.

*Technological development of customized adipose tissue-on-chip platforms:* Three generations of microfluidic devices tailored to the specific needs of adipose tissue resulted from a continuous revision- and optimization process regarding designs and materials. Consequentially, fabrication processes and microfluidic protocols had to be constantly adjusted.

With respect to chip design, several novel features have proven particularly favorable for the injection and culture of adipose tissue: the sequential loading process, the shielding from shear forces and the overall rounded architectures of the chip's tissue compartment. Thereby, the systems are well equipped to overcome the two major challenges arising from working with human mature adipocytes – buoyancy and fragility. The WAT-on-chip platform was initially fabricated from two PDMS layers sandwiching a PET membrane using conventional photolithography and replica molding techniques. To improve on-chip tissue accessibility by microscopy and entirely separate injection channels (but not tissue chambers) from media channels, a custom, exclusion molding process of PDMS was established. In terms of materials, the PDMS' absorption of small hydrophobic molecules can become a problem when working with adipose tissue. Thermoplastic alternatives, however, raise concerns in terms of oxygen supply for the tissues on chip. Here, hybrid devices that balance oxygen availability and bio-inertness of material can be a solution. Therefore, new concepts and fabrication approaches for long-term stable hybrid material microfluidic platform combining low-absorbing media layers and oxygen permeable tissue layers were established.

*Cell sourcing and logistics:* As long as the emerging technology of induced pluripotent stem cells cannot yet achieve the differentiation of adipocytes featuring fully mature phenotypes and functionality, primary cells are the most physiologically relevant cell type for *in vitro* culture. Moreover, not only complex tissue models integrating immune components will benefit strongly from autologous sources. Hence, as an integral milestone for building a complex WAT *in vitro* model, logistics, isolation protocols and handling procedures were successfully developed, allowing to source sufficient amounts of all required cell types. Here, a key advantage of OoC technology proved particularly useful: The microscale footprint of the platforms enabled the generation of a large number of models from a relatively small number of cells, allowing the study of many different conditions on tissues from only one individual. On the one hand, this allowed to address the challenge that only a limited number of cells can be derived from biopsies; on the other hand, it enabled the conduction of entire studies on cells from one donor, which paves the way for both circumventing inter-donor variation as well as addressing heterogeneities in patient populations.

*Establishment of new models:* On the way towards a highly complex, immunocompetent autologous model integrating almost all WAT-associated cell types, a modular mix-and-match strategy was established allowing for a tailorable complexity to build fit-for-purpose models serving a specific scientific question. The first cell component integrated into the microfluidic platforms were mature adipocytes. After successfully demonstrating tissue-specific morphology and functionality of on-chip mature white adipocytes and endothelial barriers, complexity of the models was gradually increased by addition of further cell types. The final, highly elaborate WAT-on-chip model accommodated mature white adipocytes, an endothelial barrier, adipose precursor cells, as well as tissue-resident and circulating immune cells. In parallel, strategies to obtain beige adipocytes from *de novo* adipogenesis on the microfluidic platform were established.

*In vitro recapitulation of adipose biology:* To assess on-chip functionality and structure, a comprehensive toolbox of readouts tailored for adipose tissue as well as on-chip application was established. This toolbox includes optical readouts, such as (immuno-)fluorescent staining of key adipose tissue features or monitoring of tracer molecules, analysis of molecules secreted into effluent media, as well as gene expression analysis.

Utilizing this toolbox, a range of key adipose tissue functions could be validated: long-term (> 1 month) viability and functionality on chip (WAT); functional lipid metabolism of adipose tissue, particularly uptake and release of different types of FAs (WAT & bAT); release of adipokines (WAT); tight, actively selective barrier formation by endothelial cells (WAT); cytokine secretion in response to inflammatory stimulation (WAT); responsiveness to  $\beta$ -AR stimulation (WAT & bAT); lipid formation and mitochondria biogenesis (bAT); gene expression of (beige) markers (bAT). Overall, the results obtained from these experiments highlighted that tissue function is not just the sum of the contributions from individual cell types but a result of the synergistic interactions occurring in the complex interplay of all the different cells in the tissue.

Importantly, all experiments performed within the scope of this thesis served the purpose of characterizing and validating the functionality of the developed adipose tissue *in vitro* models with respect to a physiological recapitulation of *in vivo* structure and function; an extensive, comprehensive description of the models' advantages and drawbacks regarding its different applications is of utmost importance for future studies addressing unexplored (patho)physiological mechanisms.



# Chapter 6

## Outlook



## 6. Outlook

The different models, processes and assays developed in the framework of this thesis open up a variety of possibilities for follow-up projects, pave the way for applications in different fields ranging from biological and clinical to toxicological and pharmaceutical research as well as lay the foundation for future technology transfer. Some of these potential next steps as well as possible further developments to refine the models will be addressed in the following, categorized in next generation platforms, future bAT-on-chip directions, and future WAT-on-chip directions.

*Next generation platforms:* While the latest versions of the developed adipose tissue-on-chip microfluidic platforms bring along tissue compartment design features highly favorable to the demand of adipocytes, the design of the media channel compartment could benefit from further refinement. First, the 3<sup>rd</sup>-generation platform's media perfusion was realized through a combination of parallel and serial channel connections. However, since a considerable solute gradient between the two serially connected tissue chambers was registered, future design adaptations should aim at an entirely parallelized media channel design. Another potential media flow-related advancement could be the generation of higher shear forces on the endothelial layer. Since the media perfusion flow rates were optimized with respect to metabolite secretion, both the 2<sup>nd</sup>- and 3<sup>rd</sup>-generation microfluidic platforms fell short on recapitulating physiological shear stresses in the perfusion channels. While a functional endothelium was achieved although the shear stress in the media channels was below physiological values, tailoring shear stresses to reflect physiological conditions for endothelial barriers can be of interest for studies focusing, e.g., on obesity-induced endothelial dysfunction<sup>320</sup> or perivascular adipose tissue characteristics.

Moreover, increasing adipose tissue volume per chip by increasing the number of tissue chambers might be a valuable design refinement, since it will increase tissue output (i.e., lower dilution of metabolites in effluent media, more cell lysate for gene expression analysis – especially for large white adipocytes).

In general, a future combination with enabling technologies and scale-up strategies to increase throughput might be worthwhile; e.g., the adipose tissue-on-chip design could be transferred to the organ-on-disc platform<sup>321</sup>: besides increasing throughput, this device manages media perfusion without the need for external pumps<sup>321</sup> (see attached

**Publication [10]**). Furthermore, future advancements should focus on the integration of on-chip sensor technology to enable in-line monitoring of AT secretions<sup>43,162,164,322</sup>.

*Future bAT-on-chip directions:* Since the beige adipocytes-on-chip model was not the main focus of the thesis and, hence, less comprehensively studied than the WAT-on-chip models, the presented model characterization should be complemented by further interrogations of the beige adipocyte functionality on chip. Their response to  $\beta$ -adrenergic stimulation, for instance, should be investigated in greater detail; potentially shedding further light into differences in  $\beta$ -AR signaling between human and murine bAT. Moreover, baseline analysis of beige adipocyte secretions into the perfusing media and the impact of different kind of stimuli on the batokine levels remain to be conducted. In a next step, the complexity, and physiological relevance, of the model could be increased by adding further cell types upgrading the model from a monoculture beige adipocyte-on-chip to a multi-culture bAT-on-chip model. Just like white adipocytes, beige adipocyte actively interact with other adipose tissue-resident cell types, especially immune cells<sup>87,323</sup>.

Further, as touched on in preliminary experiments, the concept of beige *de novo* adipogenesis could be transformed into a patient-specific model. This model would be a powerful tool for studying patient-specific beige differentiation capacity in general or in response to therapeutic beiging agents.

*Future WAT-on-chip directions:* In the first instance, future refinements of the developed WAT-on-chip models should revise the choice of cell culture media. In the present study, cell culture media that were originally designed for static adipose tissue culture approaches were used despite the differences that come along with perfused culture. Even though this issue did not pose any obvious challenges, the concentrations of media ingredients should be compared to physiological values, and, if necessary, adapted. Moreover, in the case of multi-culture models, efforts towards a universal medium serving all cell types should be conducted.

In terms of further addition of biological complexity to the multi-cell type WAT-on-chip model, the integration of sympathetic neurons would be of high interest. Innervation is the only component missing to a full complexity WAT *in vitro* model. *In vivo*, WAT is in close contact to the central nervous system, not only through leptin, but also through a heavily arborized network of afferent and efferent nerves, which densely pervade adipose tissue<sup>267</sup>. Since the interplay between neuroimmunology and immunometabolism is

particularly prevalent in adipose tissue, such a model could be an ideally suited stage for the up-and-coming field of neuroimmunometabolism<sup>324</sup>.

Already without the added aspect of innervation, the WAT-on-chip model can be a powerful tool for a broad spectrum of applications.

One of the greatest advantages, and anticipated future applications, of the OoC technology is precision medicine. Owing to the fully autologous character of the developed WAT-on-chip model, it fulfills the necessary prerequisites for this field. Within the experiments of this thesis, the topic of patient-specific WAT responses could be successfully introduced. As a next step, to merge the advantages of this patient-specific approach with the ready availability of cell lines, the primary cells in the model could be replaced by iPSC-derived ones provided that robust differentiation protocols are available that allow differentiation of all adipose tissue-associated cell types in a mature state.

The immunocompetency of the WAT-on-chip model integrating both tissue-resident as well as circulating immune cells allows to study aspects of innate and adaptive immune responses. Especially since it is becoming increasingly apparent that adipose tissue plays an important role for immune responses by, e.g., serving as a T cell hub and featuring unique sub-types of macrophages (ATMs), studies focusing on immune-adipose interactions can be of high interest either in the context of investigating the response to threats or of pharmaceutical assessment of biologicals.

The capability of reflecting adipose tissue inflammation, particularly regarding endocrine and immunomodulatory activity, makes the platform also a powerful tool for modelling adipose tissue-associated diseases, focusing, e.g., on adipocyte insulin resistance or dysregulated immune cell infiltration. Given the systemic character of many metabolic diseases, an integration into a multi-organ platform as a future application would open up even more opportunities. A connection of adipose tissue, liver and pancreas, for instance, might constitute a valuable first approach towards identification of treatment options for type 2 diabetes mellitus (reviewed in more detail in **Publication [2]**).

Another promising disease modelling application is in cancer research: there is a strong association between obesity and the incidence as well as mortality of cancer. Potential reasons for this correlation are (i) a metabolic symbiosis between cancer-associated adipocytes and cancer cells and (ii) the changes in adipose tissue microenvironment – two aspects which were found to be very favorable for cancer development and progression<sup>325,326</sup>. Moreover, adipocytes have been shown to sequester and metabolize chemotherapeutics eventually making the treatment less effective<sup>327</sup>.

In general, adipose tissue energy metabolism, thermogenesis and immunomodulatory functions have become therapeutic targets for combating adipose tissue-associated diseases. Controlling FA release from WAT, for instance, has presented a good way to achieve higher insulin sensitization. However, since there have been many off-target effects when targeting adipose activities so far, it is necessary to find therapeutics aiming at pathways exclusive to adipocytes.<sup>236</sup> Besides setting sight on the adipocytes themselves, other obesity-favorable mechanisms, such as the immune-cell mediated inflammatory response, could be targeted using the developed repertoire of adipose-on-chip models and assays.

## References

1. Bhatia, S. N. & Ingber, D. E. Microfluidic organs-on-chips. *Nat Biotechnol* **32**, 760–772 (2014).
2. Marx, U. *et al.* Biology-inspired microphysiological systems to advance patient benefit and animal welfare in drug development. *ALTEX* **37**, 364–394 (2020).
3. Mastrangeli, M., Millet, S., The ORCHID partners & van den Eijnden-van Raaij, J. Organ-on-chip in development: Towards a roadmap for organs-on-chip. *ALTEX* **36**, 650–668 (2019).
4. Ahadian, S. *et al.* Organ-On-A-Chip Platforms: A Convergence of Advanced Materials, Cells, and Microscale Technologies. *Advanced Healthcare Materials* **7**, 1700506 (2018).
5. *Principles of tissue engineering.* (Elsevier, 2020).
6. Whitesides, G. M. The origins and the future of microfluidics. *Nature* **442**, 368–373 (2006).
7. Manz, A. *et al.* Planar chips technology for miniaturization and integration of separation techniques into monitoring systems. *Journal of Chromatography A* **593**, 253–258 (1992).
8. Sackmann, E. K., Fulton, A. L. & Beebe, D. J. The present and future role of microfluidics in biomedical research. *Nature* **507**, 181–189 (2014).
9. Wu, J., Dong, M., Rigatto, C., Liu, Y. & Lin, F. Lab-on-chip technology for chronic disease diagnosis. *npj Digital Med* **1**, 7 (2018).
10. Jung, W., Han, J., Choi, J.-W. & Ahn, C. H. Point-of-care testing (POCT) diagnostic systems using microfluidic lab-on-a-chip technologies. *Microelectronic Engineering* **132**, 46–57 (2015).
11. Zare, R. N. & Kim, S. Microfluidic Platforms for Single-Cell Analysis. *Annu. Rev. Biomed. Eng.* **12**, 187–201 (2010).
12. Sohn, L. L. *et al.* How Can Microfluidic and Microfabrication Approaches Make Experiments More Physiologically Relevant? *Cell Systems* **11**, 209–211 (2020).
13. Novosel, E. C., Kleinhans, C. & Kluger, P. J. Vascularization is the key challenge in tissue engineering. *Advanced Drug Delivery Reviews* **63**, 300–311 (2011).
14. Rogal, J., Probst, C. & Loskill, P. Integration concepts for multi-organ chips: how to maintain flexibility?! *Future Science OA* **3**, FSO180 (2017).
15. Esch, M. B. *et al.* How multi-organ microdevices can help foster drug development. *Advanced Drug Delivery Reviews* **69–70**, 158–169 (2014).
16. Edington, C. D. *et al.* Interconnected Microphysiological Systems for Quantitative Biology and Pharmacology Studies. *Scientific Reports* **8**, 4530 (2018).
17. Picollet-D'hahan, N., Zuchowska, A., Lemeunier, I. & Le Gac, S. Multiorgan-on-a-Chip: A Systemic Approach To Model and Decipher Inter-Organ Communication. *Trends in Biotechnology* **39**, 788–810 (2021).
18. Esch, E. W., Bahinski, A. & Huh, D. Organs-on-chips at the frontiers of drug discovery. *Nature reviews. Drug discovery* **14**, 248–260 (2015).
19. Franzen, N. *et al.* Impact of Organ-on-a-Chip on pharmaceutical research and development costs. *Drug Discovery Today* **24**, 1720–1724 (2019).
20. Heringa, M., Park, M. V. D. Z., Kienhuis, A. S., & Rob J. Vandebriel. The value of organs-on-chip for regulatory safety assessment. *ALTEX* **37**, 208–222 (2020).
21. Cho, S. & Yoon, J.-Y. Organ-on-a-chip for assessing environmental toxicants. *Current Opinion in Biotechnology* **45**, 34–42 (2017).
22. Ingber, D. E. Reverse Engineering Human Pathophysiology with Organs-on-Chips. *Cell* **164**, 1105–1109 (2016).

23. Benam, K. H. *et al.* Engineered In Vitro Disease Models. *Annu. Rev. Pathol. Mech. Dis.* **10**, 195–262 (2015).
24. Peck, R. W., Hinojosa, C. D. & Hamilton, G. A. Organs-on-Chips in Clinical Pharmacology: Putting the Patient Into the Center of Treatment Selection and Drug Development. *Clin. Pharmacol. Ther.* **107**, 181–185 (2020).
25. Radisic, M. & Loskill, P. Beyond PDMS and Membranes: New Materials for Organ-on-a-Chip Devices. *ACS Biomater. Sci. Eng.* **7**, 2861–2863 (2021).
26. Mukhopadhyay, R. When PDMS isn't the best. *Anal. Chem.* **79**, 3248–3253 (2007).
27. Wang, J. D., Douville, N. J., Takayama, S. & ElSayed, M. Quantitative Analysis of Molecular Absorption into PDMS Microfluidic Channels. *Ann Biomed Eng* **40**, 1862–1873 (2012).
28. Toepke, M. W. & Beebe, D. J. PDMS absorption of small molecules and consequences in microfluidic applications. *Lab Chip* **6**, 1484 (2006).
29. Regehr, K. J. *et al.* Biological implications of polydimethylsiloxane-based microfluidic cell culture. *Lab Chip* **9**, 2132 (2009).
30. Grant, J. *et al.* Simulating drug concentrations in PDMS microfluidic organ chips. *Lab Chip* (2021) doi:10.1039/D1LC00348H.
31. Carter, S.-S. D. *et al.* PDMS leaching and its implications for on-chip studies focusing on bone regeneration applications. *Organs-on-a-Chip* **2**, 100004 (2020).
32. Campbell, S. B. *et al.* Beyond Polydimethylsiloxane: Alternative Materials for Fabrication of Organ-on-a-Chip Devices and Microphysiological Systems. *ACS Biomater. Sci. Eng.* **7**, 2880–2899 (2021).
33. Schneider, S., Brás, E. J. S., Schneider, O., Schlünder, K. & Loskill, P. Facile Patterning of Thermoplastic Elastomers and Robust Bonding to Glass and Thermoplastics for Microfluidic Cell Culture and Organ-on-Chip. *Micromachines* **12**, 575 (2021).
34. Roy, E., Galas, J.-C. & Veres, T. Thermoplastic elastomers for microfluidics: Towards a high-throughput fabrication method of multilayered microfluidic devices. *Lab Chip* **11**, 3193 (2011).
35. Wnorowski, A., Yang, H. & Wu, J. C. Progress, obstacles, and limitations in the use of stem cells in organ-on-a-chip models. *Advanced Drug Delivery Reviews* **140**, 3–11 (2018).
36. Takebe, T., Zhang, B. & Radisic, M. Synergistic Engineering: Organoids Meet Organs-on-a-Chip. *Cell Stem Cell* **21**, 297–300 (2017).
37. Verhulsel, M. *et al.* Biomaterials A review of microfabrication and hydrogel engineering for micro-organs on chips. *Biomaterials* **35**, 1816–1832 (2014).
38. Tibbitt, M. W. Hydrogels as extracellular matrix mimics for 3D cell culture - Tibbitt - 2009 - Biotechnology and Bioengineering - Wiley Online Library. *Biotechnology and Bioengineering* **103**, 655–663 (2009).
39. Lee, K. Y. & Mooney, D. J. Hydrogels for Tissue Engineering. *Chem. Rev.* **101**, 1869–1880 (2001).
40. Terrell, J. A., Jones, C. G., Kabandana, G. K. M. & Chen, C. From cells-on-a-chip to organs-on-a-chip: scaffolding materials for 3D cell culture in microfluidics. *J. Mater. Chem. B* **8**, 6667–6685 (2020).
41. Liu, H. *et al.* Advances in Hydrogels in Organoids and Organs-on-a-Chip. *Adv. Mater.* **31**, 1902042 (2019).
42. Lee, S. H., Shim, K. Y., Kim, B. & Sung, J. H. Hydrogel-based three-dimensional cell culture for organ-on-a-chip applications. *Biotechnol Progress* **33**, 580–589 (2017).
43. Fuchs, S. *et al.* In-Line Analysis of Organ-on-Chip Systems with Sensors: Integration, Fabrication, Challenges, and Potential. *ACS Biomater. Sci. Eng.* **7**, 2926–2948 (2021).

44. Gruber, P., Marques, M. P. C., Szita, N. & Mayr, T. Integration and application of optical chemical sensors in microbioreactors. *Lab Chip* **17**, 2693–2712 (2017).
45. Huh, D. *et al.* Reconstituting organ-level lung functions on a chip. *Science* **328**, 1662–1668 (2010).
46. Nikolaev, M. *et al.* Homeostatic mini-intestines through scaffold-guided organoid morphogenesis. *Nature* **585**, 574–578 (2020).
47. Lin, N. Y. C. *et al.* Renal reabsorption in 3D vascularized proximal tubule models. *Proc Natl Acad Sci USA* **116**, 5399–5404 (2019).
48. Mathur, A. *et al.* Human iPSC-based Cardiac Microphysiological System For Drug Screening Applications. *Scientific Reports* **5**, 8883 (2015).
49. Rennert, K. *et al.* A microfluidically perfused three dimensional human liver model. *Biomaterials* **71**, 119–131 (2015).
50. Cho, A.-N. *et al.* Microfluidic device with brain extracellular matrix promotes structural and functional maturation of human brain organoids. *Nat Commun* **12**, 4730 (2021).
51. Corvera, S. Cellular Heterogeneity in Adipose Tissues. *Annu. Rev. Physiol.* **83**, 257–278 (2021).
52. Berg, A. H. & Scherer, P. E. Adipose tissue, inflammation, and cardiovascular disease. *Circulation Research* **96**, 939–949 (2005).
53. Marra, F. & Bertolani, C. Adipokines in liver diseases. *Hepatology* **50**, 957–969 (2009).
54. Hajer, G. R., van Haeften, T. W. & Visseren, F. L. J. Adipose tissue dysfunction in obesity, diabetes, and vascular diseases. *European Heart Journal* **29**, 2959–2971 (2008).
55. Zhang, Z. & Scherer, P. E. Adipose tissue: The dysfunctional adipocyte — a cancer cell's best friend. *Nature Reviews Endocrinology* **14**, 132–134 (2018).
56. Pérez-Hernández, A. I., Catalán, V., Gómez-Ambrosi, J., Rodríguez, A. & Frühbeck, G. Mechanisms linking excess adiposity and carcinogenesis promotion. *Frontiers in Endocrinology* **5**, (2014).
57. Ikeda, K., Maretich, P. & Kajimura, S. The Common and Distinct Features of Brown and Beige Adipocytes. *Trends in Endocrinology & Metabolism* **29**, 191–200 (2018).
58. Pilkington, A.-C., Paz, H. A. & Wankhade, U. D. Beige Adipose Tissue Identification and Marker Specificity—Overview. *Front. Endocrinol.* **12**, 599134 (2021).
59. Riis-Vestergaard, M. J. *et al.* Beta-1 and Not Beta-3 Adrenergic Receptors May Be the Primary Regulator of Human Brown Adipocyte Metabolism. *The Journal of Clinical Endocrinology & Metabolism* **105**, e994–e1005 (2020).
60. Ussar, S. *et al.* ASC-1, PAT2, and P2RX5 are cell surface markers for white, beige, and brown adipocytes. *Sci. Transl. Med.* **6**, 247ra103-247ra103 (2014).
61. Cypess, A. M. *et al.* Anatomical localization, gene expression profiling and functional characterization of adult human neck brown fat. *Nat Med* **19**, 635–639 (2013).
62. Heaton, J. M. The distribution of brown adipose tissue in the human. *J Anat* **112**, 35–39 (1972).
63. Leitner, B. P. *et al.* Mapping of human brown adipose tissue in lean and obese young men. *Proc Natl Acad Sci USA* **114**, 8649–8654 (2017).
64. Virtanen, K. A. *et al.* Functional Brown Adipose Tissue in Healthy Adults. *N Engl J Med* **360**, 1518–1525 (2009).
65. Wu, J. *et al.* Beige Adipocytes Are a Distinct Type of Thermogenic Fat Cell in Mouse and Human. *Cell* **150**, 366–376 (2012).
66. Shinoda, K. *et al.* Genetic and functional characterization of clonally derived adult human brown adipocytes. *Nat Med* **21**, 389–394 (2015).
67. Oguri, Y. *et al.* CD81 Controls Beige Fat Progenitor Cell Growth and Energy Balance via FAK Signaling. *Cell* **182**, 563-577.e20 (2020).

68. Bartelt, A. & Heeren, J. Adipose tissue browning and metabolic health. *Nat Rev Endocrinol* **10**, 24–36 (2014).
69. Harms, M. & Seale, P. Brown and beige fat: development, function and therapeutic potential. *Nat Med* **19**, 1252–1263 (2013).
70. Kajimura, S., Spiegelman, B. M. & Seale, P. Brown and Beige Fat: Physiological Roles beyond Heat Generation. *Cell Metabolism* **22**, 546–559 (2015).
71. Cohen, P. & Kajimura, S. The cellular and functional complexity of thermogenic fat. *Nat Rev Mol Cell Biol* **22**, 393–409 (2021).
72. Altshuler-Keylin, S. *et al.* Beige Adipocyte Maintenance Is Regulated by Autophagy-Induced Mitochondrial Clearance. *Cell Metabolism* **24**, 402–419 (2016).
73. Giordano, A., Smorlesi, A., Frontini, A., Barbatelli, G. & Cinti, S. MECHANISMS IN ENDOCRINOLOGY: White, brown and pink adipocytes: the extraordinary plasticity of the adipose organ. *European Journal of Endocrinology* **170**, R159–R171 (2014).
74. Cinti, S. Pink Adipocytes. *Trends in Endocrinology & Metabolism* **29**, 651–666 (2018).
75. Young, B., O’Dowd, G. & Woodford, P. *Wheater’s functional histology: a text and colour atlas*. (Churchill Livingstone/Elsevier, 2014).
76. Chadt, A. & Al-Hasani, H. Glucose transporters in adipose tissue, liver, and skeletal muscle in metabolic health and disease. *Pflugers Arch - Eur J Physiol* **472**, 1273–1298 (2020).
77. Kahn, B. B. Adipose Tissue, Inter-Organ Communication, and the Path to Type 2 Diabetes: The 2016 Banting Medal for Scientific Achievement Lecture. *Diabetes* **68**, 3–14 (2019).
78. Chouchani, E. T. & Kajimura, S. Metabolic adaptation and maladaptation in adipose tissue. *Nat Metab* **1**, 189–200 (2019).
79. Duncan, R. E., Ahmadian, M., Jaworski, K., Sarkadi-Nagy, E. & Sul, H. S. Regulation of Lipolysis in Adipocytes. *Annu. Rev. Nutr.* **27**, 79–101 (2007).
80. Zhang, Y. *et al.* Positional cloning of the mouse obese gene and its human homologue. *Nature* **372**, 425–432 (1994).
81. Scheja, L. & Heeren, J. The endocrine function of adipose tissues in health and cardiometabolic disease. *Nat Rev Endocrinol* **15**, 507–524 (2019).
82. Fasshauer, M. & Blüher, M. Adipokines in health and disease. *Trends in Pharmacological Sciences* **36**, 461–470 (2015).
83. Finlin, B. S. *et al.* The  $\beta$ 3-adrenergic receptor agonist mirabegron improves glucose homeostasis in obese humans. *Journal of Clinical Investigation* **130**, 2319–2331 (2020).
84. Finlin, B. S. *et al.* Human adipose beiging in response to cold and mirabegron. *JCI Insight* **3**, e121510 (2018).
85. Shao, M. *et al.* Cellular Origins of Beige Fat Cells Revisited. *Diabetes* **68**, 1874–1885 (2019).
86. Sidossis, L. & Kajimura, S. Brown and beige fat in humans: thermogenic adipocytes that control energy and glucose homeostasis. *J. Clin. Invest.* **125**, 478–486 (2015).
87. Villarroya, F., Cereijo, R., Villarroya, J., Gavaldà-Navarro, A. & Giralt, M. Toward an Understanding of How Immune Cells Control Brown and Beige Adipobiology. *Cell Metabolism* **27**, 954–961 (2018).
88. Ishibashi, J. & Seale, P. Functions of Prdm16 in thermogenic fat cells. *Temperature* **2**, 65–72 (2015).
89. Seale, P. *et al.* PRDM16 controls a brown fat/skeletal muscle switch. *Nature* **454**, 961–967 (2008).
90. Seale, P. *et al.* Transcriptional Control of Brown Fat Determination by PRDM16.

*Cell Metabolism* **6**, 38–54 (2007).

91. Lin, J. Z. & Farmer, S. R. Morphogenetics in brown, beige and white fat development. *Adipocyte* **5**, 130–135 (2016).
92. Hondares, E. *et al.* Peroxisome Proliferator-activated Receptor  $\alpha$  (PPAR $\alpha$ ) Induces PPAR $\gamma$  Coactivator 1 $\alpha$  (PGC-1 $\alpha$ ) Gene Expression and Contributes to Thermogenic Activation of Brown Fat. *Journal of Biological Chemistry* **286**, 43112–43122 (2011).
93. Boström, P. *et al.* A PGC1- $\alpha$ -dependent myokine that drives brown-fat-like development of white fat and thermogenesis. *Nature* **481**, 463–468 (2012).
94. Zhu, Y. *et al.* Connexin 43 Mediates White Adipose Tissue Beiging by Facilitating the Propagation of Sympathetic Neuronal Signals. *Cell Metabolism* **24**, 420–433 (2016).
95. Tharp, K. M. *et al.* Actomyosin-Mediated Tension Orchestrates Uncoupled Respiration in Adipose Tissues. *Cell Metabolism* **27**, 602-615.e4 (2018).
96. Ikeda, K. *et al.* UCP1-independent signaling involving SERCA2b-mediated calcium cycling regulates beige fat thermogenesis and systemic glucose homeostasis. *Nat Med* **23**, 1454–1465 (2017).
97. Kazak, L. *et al.* A Creatine-Driven Substrate Cycle Enhances Energy Expenditure and Thermogenesis in Beige Fat. *Cell* **163**, 643–655 (2015).
98. Ukropec, J., Anunciado, R. P., Ravussin, Y., Hulver, M. W. & Kozak, L. P. UCP1-independent Thermogenesis in White Adipose Tissue of Cold-acclimated Ucp1-/- Mice. *Journal of Biological Chemistry* **281**, 31894–31908 (2006).
99. Chen, Y. *et al.* Thermal stress induces glycolytic beige fat formation via a myogenic state. *Nature* **565**, 180–185 (2019).
100. Tharp, K. M. *et al.* Matrix-Assisted Transplantation of Functional Beige Adipose Tissue. *Diabetes* **64**, 3713–3724 (2015).
101. Tharp, K. M. & Stahl, A. Bioengineering Beige Adipose Tissue Therapeutics. *Front. Endocrinol.* **6**, (2015).
102. WHO. Obesity and overweight. <https://www.who.int/news-room/fact-sheets/detail/obesity-and-overweight> (2020).
103. Reilly, S. M. & Saltiel, A. R. Adapting to obesity with adipose tissue inflammation. *Nat Rev Endocrinol* **13**, 633–643 (2017).
104. Hotamisligil, G. S. Inflammation and metabolic disorders. *Nature* **444**, 860–867 (2006).
105. Kawai, T., Autieri, M. V. & Scalia, R. Adipose tissue inflammation and metabolic dysfunction in obesity. *American Journal of Physiology-Cell Physiology* **320**, C375–C391 (2021).
106. Caslin, H. L., Bhanot, M., Bolus, W. R. & Hasty, A. H. Adipose tissue macrophages: Unique polarization and bioenergetics in obesity. *Immunol Rev* **295**, 101–113 (2020).
107. Wang, L., Sun, P., Wu, Y. & Wang, L. Metabolic tissue-resident CD8<sup>+</sup> T cells: A key player in obesity-related diseases. *Obesity Reviews* **22**, e13133 (2021).
108. Porsche, C. E., Delproposto, J. B., Geletka, L., O'Rourke, R. & Lumeng, C. N. Obesity results in adipose tissue T cell exhaustion. *JCI Insight* **6**, e139793 (2021).
109. Misumi, I. *et al.* Obesity Expands a Distinct Population of T Cells in Adipose Tissue and Increases Vulnerability to Infection. *Cell Reports* **27**, 514-524.e5 (2019).
110. Winn, N. C., Cottam, M. A., Wasserman, D. H. & Hasty, A. H. Exercise and Adipose Tissue Immunity: Outrunning Inflammation. *Obesity* **29**, 790–801 (2021).
111. Morris, D. L., Singer, K. & Lumeng, C. N. Adipose tissue macrophages: phenotypic plasticity and diversity in lean and obese states. *Current Opinion in Clinical Nutrition and Metabolic Care* **14**, 341–346 (2011).
112. Giordano, A. *et al.* Obese adipocytes show ultrastructural features of stressed cells and die of pyroptosis. *Journal of Lipid Research* **54**, 2423–2436 (2013).
113. Caspar-Bauguil, S. *et al.* Fatty acids from fat cell lipolysis do not activate an

- inflammatory response but are stored as triacylglycerols in adipose tissue macrophages. *Diabetologia* **58**, 2627–2636 (2015).
114. Flaherty, S. E. *et al.* A lipase-independent pathway of lipid release and immune modulation by adipocytes. *Science* **363**, 989–993 (2019).
  115. Brestoff, J. R. *et al.* Intercellular Mitochondria Transfer to Macrophages Regulates White Adipose Tissue Homeostasis and Is Impaired in Obesity. *Cell Metabolism* **33**, 270–282.e8 (2021).
  116. Fujisaka, S. *et al.* Regulatory Mechanisms for Adipose Tissue M1 and M2 Macrophages in Diet-Induced Obese Mice. *Diabetes* **58**, 2574–2582 (2009).
  117. Moro, K. *et al.* Innate production of T(H)2 cytokines by adipose tissue-associated c-Kit(+)Sca-1(+) lymphoid cells. *Nature* **463**, 540–544 (2010).
  118. Han, S.-J. *et al.* White Adipose Tissue Is a Reservoir for Memory T Cells and Promotes Protective Memory Responses to Infection. *Immunity* **47**, 1154–1168.e6 (2017).
  119. Lee, M.-W. *et al.* Activated Type 2 Innate Lymphoid Cells Regulate Beige Fat Biogenesis. *Cell* **160**, 74–87 (2015).
  120. Brestoff, J. R. *et al.* Group 2 innate lymphoid cells promote beiging of white adipose tissue and limit obesity. *Nature* **519**, 242–246 (2015).
  121. Wang, Q. A. & Scherer, P. E. The AdipoChaser mouse: A model tracking adipogenesis in vivo. *Adipocyte* **3**, 146–150 (2014).
  122. Frederich, R. C. *et al.* Expression of ob mRNA and its encoded protein in rodents. Impact of nutrition and obesity. *J. Clin. Invest.* **96**, 1658–1663 (1995).
  123. Ingalls, A. M., Dickie, M. M. & Snell, G. D. OBESE, A NEW MUTATION IN THE HOUSE MOUSE\*. *Journal of Heredity* **41**, 317–318 (1950).
  124. Nilsson, C., Raun, K., Yan, F., Larsen, M. O. & Tang-Christensen, M. Laboratory animals as surrogate models of human obesity. *Acta Pharmacol Sin* **33**, 173–181 (2012).
  125. Greek, R. & Menache, A. Systematic Reviews of Animal Models: Methodology versus Epistemology. *Int. J. Med. Sci.* **10**, 206–221 (2013).
  126. Mestas, J. & Hughes, C. C. W. Of Mice and Not Men: Differences between Mouse and Human Immunology. *J Immunol* **172**, 2731–2738 (2004).
  127. Reitman, M. L. Of mice and men - environmental temperature, body temperature, and treatment of obesity. *FEBS Lett* **592**, 2098–2107 (2018).
  128. Remick, D. G. Interleukin-8: *Critical Care Medicine* **33**, S466–S467 (2005).
  129. van der Worp, H. B. *et al.* Can Animal Models of Disease Reliably Inform Human Studies? *PLoS Med* **7**, e1000245 (2010).
  130. Svensson, P. *et al.* Gene expression in human brown adipose tissue. *Int J Mol Med* **27**, 227–232 (2011).
  131. Fain, J. N., Cheema, P., Madan, A. K. & Tichansky, D. S. Dexamethasone and the inflammatory response in explants of human omental adipose tissue. *Molecular and Cellular Endocrinology* **315**, 292–298 (2010).
  132. Gesta, S. *et al.* Culture of Human Adipose Tissue Explants Leads to Profound Alteration of Adipocyte Gene Expression. *Horm Metab Res* **35**, 158–163 (2003).
  133. Miller, C. N. *et al.* Isoproterenol Increases Uncoupling, Glycolysis, and Markers of Beiging in Mature 3T3-L1 Adipocytes. *PLoS ONE* **10**, e0138344 (2015).
  134. Zhang, L. *et al.* Generation of Functional Brown Adipocytes from Human Pluripotent Stem Cells via Progression through a Paraxial Mesoderm State. *Cell Stem Cell* **27**, 784–797.e11 (2020).
  135. Singh, A. M. *et al.* Human beige adipocytes for drug discovery and cell therapy in metabolic diseases. *Nat Commun* **11**, 2758 (2020).
  136. Bahmad, H. F. *et al.* Modeling Adipogenesis: Current and Future Perspective. *Cells* **9**, 2326 (2020).
  137. Li, X. & Easley, C. J. Microfluidic systems for studying dynamic function of

- adipocytes and adipose tissue. *Anal Bioanal Chem* **410**, 791–800 (2018).
138. Volz, A.-C., Omengo, B., Gehrke, S. & Kluger, P. J. Comparing the use of differentiated adipose-derived stem cells and mature adipocytes to model adipose tissue in vitro. *Differentiation* **110**, 19–28 (2019).
139. Sugihara, H. *et al.* A simple culture method of fat cells from mature fat tissue fragments. *Journal of Lipid Research* **30**, 1987–1995 (1989).
140. Zhang, H., Kumar, S., Barnett, A. & Eggo, M. Ceiling culture of mature human adipocytes: use in studies of adipocyte functions. *Journal of Endocrinology* **164**, 119–128 (2000).
141. Fernyhough, M. E. *et al.* Primary Adipocyte Culture: Adipocyte Purification Methods May Lead to a New Understanding of Adipose Tissue Growth and Development. *Cytotechnology* **46**, 163–172 (2004).
142. Wei, S., Bergen, W. G., Hausman, G. J., Zan, L. & Dodson, M. V. Cell culture purity issues and DFAT cells. *Biochemical and Biophysical Research Communications* **433**, 273–275 (2013).
143. Lessard, J. *et al.* Characterization of Dedifferentiating Human Mature Adipocytes from the Visceral and Subcutaneous Fat Compartments: Fibroblast-Activation Protein Alpha and Dipeptidyl Peptidase 4 as Major Components of Matrix Remodeling. *PLoS ONE* **10**, e0122065 (2015).
144. Shen, J., Sugawara, A., Yamashita, J., Ogura, H. & Sato, S. Dedifferentiated fat cells: an alternative source of adult multipotent cells from the adipose tissues. *Int J Oral Sci* **3**, 117–124 (2011).
145. Abbott, R. D. *et al.* Variability in responses observed in human white adipose tissue models. *J Tissue Eng Regen Med* **12**, 840–847 (2018).
146. Abbott, R. D. *et al.* The Use of Silk as a Scaffold for Mature, Sustainable Unilocular Adipose 3D Tissue Engineered Systems. *Adv. Healthcare Mater.* **5**, 1667–1677 (2016).
147. Abbott, R. D., Kimmerling, E. P., Cairns, D. M. & Kaplan, D. L. Silk as a Biomaterial to Support Long-Term Three-Dimensional Tissue Cultures. *ACS Appl. Mater. Interfaces* **8**, 21861–21868 (2016).
148. Huber, B. *et al.* Integration of Mature Adipocytes to Build-Up a Functional Three-Layered Full-Skin Equivalent. *Tissue Engineering Part C: Methods* **22**, 756–764 (2016).
149. Louis, F., Kitano, S., Mano, J. F. & Matsusaki, M. 3D collagen microfibers stimulate the functionality of preadipocytes and maintain the phenotype of mature adipocytes for long term cultures. *Acta Biomaterialia* **84**, 194–207 (2019).
150. Bender, R. *et al.* Human Adipose Derived Cells in Two- and Three-Dimensional Cultures: Functional Validation of an In Vitro Fat Construct. *Stem Cells International* **2020**, 1–14 (2020).
151. Lau, F. H. *et al.* Sandwiched White Adipose Tissue: A Microphysiological System of Primary Human Adipose Tissue. *Tissue Engineering Part C: Methods* **24**, 135–145 (2018).
152. Harms, M. J. *et al.* Mature Human White Adipocytes Cultured under Membranes Maintain Identity, Function, and Can Transdifferentiate into Brown-like Adipocytes. *Cell Reports* **27**, 213-225.e5 (2019).
153. McCarthy, M. *et al.* Fat-On-A-Chip Models for Research and Discovery in Obesity and Its Metabolic Comorbidities. *Tissue Engineering Part B: Reviews* **26**, 586–595 (2020).
154. Kongsuphol, P. *et al.* In vitro micro-physiological model of the inflamed human adipose tissue for immune-metabolic analysis in type II diabetes. *Sci Rep* **9**, 4887 (2019).
155. Liu, Y. *et al.* Adipose-on-a-chip: a dynamic microphysiological in vitro model of the human adipose for immune-metabolic analysis in type II diabetes. *Lab Chip* **19**, 241–253 (2019).
156. Yang, F., Cohen, R. N. & Brey, E. M. Optimization of Co-Culture Conditions for a

- Human Vascularized Adipose Tissue Model. *Bioengineering* **7**, 114 (2020).
157. Yang, F. *et al.* A 3D human adipose tissue model within a microfluidic device. *Lab Chip* **21**, 435–446 (2021).
158. Loskill, P. *et al.* WAT-on-a-chip: a physiologically relevant microfluidic system incorporating white adipose tissue. *Lab Chip* **17**, 1645–1654 (2017).
159. Tanataweethum, N. *et al.* Establishment and characterization of a primary murine adipose tissue-chip. *Biotechnology and Bioengineering* **115**, 1979–1987 (2018).
160. Tanataweethum, N. *et al.* Towards an Insulin Resistant Adipose Model on a Chip. *Cel. Mol. Bioeng.* **14**, 89–99 (2021).
161. Tanataweethum, N. *et al.* Differentiation of primary pre-adipocytes into adipose tissue in a microfluidic chip. *The FASEB Journal* **31**, 886.8-886.8 (2017).
162. Zhu, J. *et al.* An integrated adipose-tissue-on-chip nanoplasmonic biosensing platform for investigating obesity-associated inflammation. *Lab Chip* **18**, 3550–3560 (2018).
163. Godwin, L. A. *et al.* A microfluidic interface for the culture and sampling of adiponectin from primary adipocytes. *Analyst* **140**, 1019–1025 (2015).
164. Hu, J., Li, X., Judd, R. L. & Easley, C. J. Rapid lipolytic oscillations in ex vivo adipose tissue explants revealed through microfluidic droplet sampling at high temporal resolution. *Lab Chip* **20**, 1503–1512 (2020).
165. Li, X., Hu, J. & Easley, C. J. Automated microfluidic droplet sampling with integrated, mix-and-read immunoassays to resolve endocrine tissue secretion dynamics. *Lab Chip* **18**, 2926–2935 (2018).
166. Schindelin, J. *et al.* Fiji: an open-source platform for biological-image analysis. *Nat Methods* **9**, 676–682 (2012).
167. Dagan, Z., Weinbaum, S. & Pfeffer, R. Theory and experiment on the three-dimensional motion of a freely suspended spherical particle at the entrance to a pore at low Reynolds number. *Chemical Engineering Science* **38**, 583–596 (1983).
168. Hazel, J. R. & Sidell, B. D. A method for the determination of diffusion coefficients for small molecules in aqueous solution. *Analytical Biochemistry* **166**, 335–341 (1987).
169. Shirure, V. S. *et al.* Tumor-on-a-chip platform to investigate progression and drug sensitivity in cell lines and patient-derived organoids. *Lab Chip* **18**, 3687–3702 (2018).
170. Vijgen, G. H. E. J. *et al.* Increased Oxygen Consumption in Human Adipose Tissue From the “Brown Adipose Tissue” Region. *The Journal of Clinical Endocrinology & Metabolism* **98**, E1230–E1234 (2013).
171. Genomic DNA amount in diploid cell - Human Homo sapiens - BNID 111206. *Bionumbers - The Database Of Useful Biological Numbers* <https://bionumbers.hms.harvard.edu/bionumber.aspx?id=111206>.
172. Buchwald, P. FEM-based oxygen consumption and cell viability models for avascular pancreatic islets. *Theor Biol Med Model* **6**, 5 (2009).
173. Markov, D. A., Lillie, E. M., Garbett, S. P. & McCawley, L. J. Variation in diffusion of gases through PDMS due to plasma surface treatment and storage conditions. *Biomed Microdevices* **16**, 91–96 (2014).
174. Michaels, A. S., Vieth, W. R. & Barrie, J. A. Diffusion of Gases in Polyethylene Terephthalate. *Journal of Applied Physics* **34**, 13–20 (1963).
175. Kim, M.-C., Lam, R. H. W., Thorsen, T. & Asada, H. H. Mathematical analysis of oxygen transfer through polydimethylsiloxane membrane between double layers of cell culture channel and gas chamber in microfluidic oxygenator. *Microfluid Nanofluid* **15**, 285–296 (2013).
176. Liisberg Aune, U., Ruiz, L. & Kajimura, S. Isolation and Differentiation of Stromal Vascular Cells to Beige/Brite Cells. *JoVE* **73**, 50191 (2013).
177. Livak, K. J. & Schmittgen, T. D. Analysis of Relative Gene Expression Data Using

- Real-Time Quantitative PCR and the  $2^{-\Delta\Delta CT}$  Method. *Methods* **25**, 402–408 (2001).
178. Haimes, J. & Kelley, M. Demonstration of a  $\Delta\Delta Cq$  Calculation Method to Compute Relative Gene Expression from qPCR Data. *Thermo Scientific Tech Note* (2010).
179. Choi, J. S. *et al.* Decellularized extracellular matrix derived from human adipose tissue as a potential scaffold for allograft tissue engineering. *J. Biomed. Mater. Res.* **97A**, 292–299 (2011).
180. Buechler, C., Krautbauer, S. & Eisinger, K. Adipose tissue fibrosis. *WJD* **6**, 548 (2015).
181. Ruiz-Ojeda, Méndez-Gutiérrez, Aguilera, & Plaza-Díaz. Extracellular Matrix Remodeling of Adipose Tissue in Obesity and Metabolic Diseases. *IJMS* **20**, 4888 (2019).
182. Lin, D., Chun, T.-H. & Kang, L. Adipose extracellular matrix remodelling in obesity and insulin resistance. *Biochemical Pharmacology* **119**, 8–16 (2016).
183. Crewe, C., An, Y. A. & Scherer, P. E. The ominous triad of adipose tissue dysfunction: inflammation, fibrosis, and impaired angiogenesis. *Journal of Clinical Investigation* **127**, 74–82 (2017).
184. Sun, K., Tordjman, J., Clément, K. & Scherer, P. E. Fibrosis and Adipose Tissue Dysfunction. *Cell Metabolism* **18**, 470–477 (2013).
185. Chun, T.-H. Peri-adipocyte ECM remodeling in obesity and adipose tissue fibrosis. *Adipocyte* **1**, 89–95 (2012).
186. Caro-Maldonado, A. & Muoz-Pinedo, C. Dying for Something to Eat: How Cells Respond to Starvation. *Open Cell Signal J* **3**, 42–51 (2011).
187. Garcia-Martinez, I., Shaker, M. E. & Mehal, W. Z. Therapeutic Opportunities in Damage-Associated Molecular Pattern-Driven Metabolic Diseases. *Antioxidants & Redox Signaling* **23**, 1305–1315 (2015).
188. Roh, J. S. & Sohn, D. H. Damage-Associated Molecular Patterns in Inflammatory Diseases. *Immune Netw* **18**, e27 (2018).
189. Clause, K. C. & Barker, T. H. Extracellular matrix signaling in morphogenesis and repair. *Current Opinion in Biotechnology* **24**, 830–833 (2013).
190. Williams, A. J. *et al.* The CompTox Chemistry Dashboard: a community data resource for environmental chemistry. *J Cheminform* **9**, 61 (2017).
191. Lowe, C. N. & Williams, A. J. Enabling High-Throughput Searches for Multiple Chemical Data Using the U.S.-EPA CompTox Chemicals Dashboard. *J. Chem. Inf. Model.* **61**, 565–570 (2021).
192. CompTox Chemicals Dashboard. *United States Environmental Protection Agency - CompTox Chemicals Dashboard* <https://comptox.epa.gov/dashboard> (2021).
193. van Meer, B. J. *et al.* Small molecule absorption by PDMS in the context of drug response bioassays. *Biochemical and Biophysical Research Communications* **482**, 323–328 (2017).
194. Auner, A. W., Tasneem, K. M., Markov, D. A., McCawley, L. J. & Hutson, M. S. Chemical-PDMS binding kinetics and implications for bioavailability in microfluidic devices. *Lab Chip* **19**, 864–874 (2019).
195. Mehta, G. *et al.* Hard Top Soft Bottom Microfluidic Devices for Cell Culture and Chemical Analysis. *Anal. Chem.* **81**, 3714–3722 (2009).
196. Sunkara, V. *et al.* Simple room temperature bonding of thermoplastics and poly(dimethylsiloxane). *Lab Chip* **11**, 962–965 (2011).
197. Sunkara, V. & Cho, Y.-K. Investigation on the Mechanism of Aminosilane-Mediated Bonding of Thermoplastics and Poly(dimethylsiloxane). *ACS Appl. Mater. Interfaces* **4**, 6537–6544 (2012).
198. Mehta, V., Vilikkathala Sudhakaran, S. & Rath, S. N. Facile Route for 3D Printing of Transparent PETg-Based Hybrid Biomicrofluidic Devices Promoting Cell Adhesion. *ACS Biomater. Sci. Eng.* **7**, 3947–3963 (2021).

199. Guima, K.-E., Coelho, P.-H. L., Trindade, M. A. G. & Martins, C. A. 3D-Printed glycerol microfluidic fuel cell. *Lab Chip* **20**, 2057–2061 (2020).
200. Romanov, V. *et al.* FDM 3D Printing of High-Pressure, Heat-Resistant, Transparent Microfluidic Devices. *Anal. Chem.* **90**, 10450–10456 (2018).
201. Cui, F. *et al.* Batch fabrication of electrochemical sensors on a glycol-modified polyethylene terephthalate-based microfluidic device. *Biosensors and Bioelectronics* **167**, 112521 (2020).
202. Sivakumar, R. & Lee, N. Y. Chemically robust succinimide-group-assisted irreversible bonding of poly(dimethylsiloxane)–thermoplastic microfluidic devices at room temperature. *Analyst* **145**, 6887–6894 (2020).
203. Chow, W. W. Y., Lei, K. F., Shi, G., Li, W. J. & Huang, Q. Microfluidic channel fabrication by PDMS-interface bonding. *Smart Mater. Struct.* **15**, S112–S116 (2005).
204. Hodson, L. Adipose tissue oxygenation: Effects on metabolic function. *Adipocyte* **3**, 75–80 (2014).
205. Goossens, G. H. & Blaak, E. E. Adipose Tissue Dysfunction and Impaired Metabolic Health in Human Obesity: A Matter of Oxygen? *Front. Endocrinol.* **6**, (2015).
206. Sivakumar, R., Trinh, K. T. L. & Lee, N. Y. Heat and pressure-resistant room temperature irreversible sealing of hybrid PDMS–thermoplastic microfluidic devices *via* carbon–nitrogen covalent bonding and its application in a continuous-flow polymerase chain reaction. *RSC Adv.* **10**, 16502–16509 (2020).
207. Suzuki, Y., Yamada, M. & Seki, M. Sol–gel based fabrication of hybrid microfluidic devices composed of PDMS and thermoplastic substrates. *Sensors and Actuators B: Chemical* **148**, 323–329 (2010).
208. Busek, M. *et al.* Thermoplastic Elastomer (TPE)–Poly(Methyl Methacrylate) (PMMA) Hybrid Devices for Active Pumping PDMS-Free Organ-on-a-Chip Systems. *Biosensors* **11**, 162 (2021).
209. Pocock, K. J. *et al.* Low-temperature bonding process for the fabrication of hybrid glass–membrane organ-on-a-chip devices. *J. Micro/Nanolith. MEMS MOEMS* **15**, 044502 (2016).
210. Tsai, H.-F., Toda-Peters, K. & Shen, A. Q. Glioblastoma adhesion in a quick-fit hybrid microdevice. *Biomed Microdevices* **21**, 30 (2019).
211. Tsai, H.-F., IJspeert, C. & Shen, A. Q. Voltage-gated ion channels mediate the electrotaxis of glioblastoma cells in a hybrid PMMA/PDMS microdevice. *APL Bioengineering* **4**, 036102 (2020).
212. Liu, X., Cervantes, C. & Liu, F. Common and distinct regulation of human and mouse brown and beige adipose tissues: a promising therapeutic target for obesity. *Protein Cell* **8**, 446–454 (2017).
213. Ibrahim, M. M. Subcutaneous and visceral adipose tissue: structural and functional differences. *Obesity Reviews* **11**, 11–18 (2010).
214. Peinado, J. R. *et al.* The stromal-vascular fraction of adipose tissue contributes to major differences between subcutaneous and visceral fat depots. *Proteomics* **10**, 3356–3366 (2010).
215. Passaro, A. *et al.* Gene expression regional differences in human subcutaneous adipose tissue. *BMC Genomics* **18**, 202 (2017).
216. Schmitz, J. *et al.* Obesogenic memory can confer long-term increases in adipose tissue but not liver inflammation and insulin resistance after weight loss. *Molecular Metabolism* **5**, 328–339 (2016).
217. Sun, M., Zheng, S., Gao, X. & Lin, Z. The role of immune cells in obesogenic memory. *Cell Mol Immunol* **17**, 884–886 (2020).
218. Zou, J. *et al.* CD4+ T cells memorize obesity and promote weight regain. *Cell Mol Immunol* **15**, 630–639 (2018).

219. Decker, T. & Lohmann-Matthes, M.-L. A quick and simple method for the quantitation of lactate dehydrogenase release in measurements of cellular cytotoxicity and tumor necrosis factor (TNF) activity. *Journal of Immunological Methods* **115**, 61–69 (1988).
220. Kaja, S., Payne, A. J., Naumchuk, Y. & Koulen, P. Quantification of Lactate Dehydrogenase for Cell Viability Testing Using Cell Lines and Primary Cultured Astrocytes. *Current Protocols in Toxicology* **72**, (2017).
221. Li, Y. *et al.* Compression-induced dedifferentiation of adipocytes promotes tumor progression. *Sci. Adv.* **6**, eaax5611 (2020).
222. Côté, J. A., Ostinelli, G., Gauthier, M.-F., Lacasse, A. & Tchernof, A. Focus on dedifferentiated adipocytes: characteristics, mechanisms, and possible applications. *Cell Tissue Res* **378**, 385–398 (2019).
223. Sztalryd, C. & Brasaemle, D. L. The perilipin family of lipid droplet proteins: Gatekeepers of intracellular lipolysis. *Biochimica et Biophysica Acta (BBA) - Molecular and Cell Biology of Lipids* **1862**, 1221–1232 (2017).
224. Itabe, H., Yamaguchi, T., Nimura, S. & Sasabe, N. Perilipins: a diversity of intracellular lipid droplet proteins. *Lipids Health Dis* **16**, 83 (2017).
225. Sohn, J. H. *et al.* Perilipin 1 (Plin1) deficiency promotes inflammatory responses in lean adipose tissue through lipid dysregulation. *Journal of Biological Chemistry* **293**, 13974–13988 (2018).
226. Brasaemle, D. L., Subramanian, V., Garcia, A., Marcinkiewicz, A. & Rothenberg, A. Perilipin A and the control of triacylglycerol metabolism. *Mol Cell Biochem* **326**, 15–21 (2009).
227. Hansen, J. S., de Maré, S., Jones, H. A., Göransson, O. & Lindkvist-Petersson, K. Visualization of lipid directed dynamics of perilipin 1 in human primary adipocytes. *Sci Rep* **7**, 15011 (2017).
228. Chi, J., Crane, A., Wu, Z. & Cohen, P. Adipo-Clear: A Tissue Clearing Method for Three-Dimensional Imaging of Adipose Tissue. *JoVE* **137**, e58271 (2018).
229. Chung, K. *et al.* Structural and molecular interrogation of intact biological systems. *Nature* **497**, 332–337 (2013).
230. Chen, Y. Y. *et al.* Clarifying intact 3D tissues on a microfluidic chip for high-throughput structural analysis. *Proc Natl Acad Sci USA* **113**, 14915–14920 (2016).
231. Schönfeld, P. & Wojtczak, L. Short- and medium-chain fatty acids in energy metabolism: the cellular perspective. *Journal of Lipid Research* **57**, 943–954 (2016).
232. Glatz, JanF. C. & Luiken, JoostJ. F. P. Dynamic role of the transmembrane glycoprotein CD36 (SR-B2) in cellular fatty acid uptake and utilization. *Journal of Lipid Research* **59**, 1084–1093 (2018).
233. Glatz, J. F. C. & Luiken, J. J. F. P. Time for a détente in the war on the mechanism of cellular fatty acid uptake. *Journal of Lipid Research* **61**, 1300–1303 (2020).
234. Jay, A. G., Simard, J. R., Huang, N. & Hamilton, J. A. SSO and other putative inhibitors of FA transport across membranes by CD36 disrupt intracellular metabolism, but do not affect FA translocation. *Journal of Lipid Research* **61**, 790–807 (2020).
235. Thompson, B. R., Lobo, S. & Bernlohr, D. A. Fatty acid flux in adipocytes: The in's and out's of fat cell lipid trafficking. *Molecular and Cellular Endocrinology* **318**, 24–33 (2010).
236. Morigny, P., Boucher, J., Arner, P. & Langin, D. Lipid and glucose metabolism in white adipocytes: pathways, dysfunction and therapeutics. *Nat Rev Endocrinol* **17**, 276–295 (2021).
237. Wolfe, R. R. Metabolic interactions between glucose and fatty acids in humans. *The American Journal of Clinical Nutrition* **67**, 519S-526S (1998).
238. Bruun, J. M., Pedersen, S. B. & Richelsen, B. Regulation of Interleukin 8

- Production and Gene Expression in Human Adipose Tissue in Vitro<sup>1</sup>. *The Journal of Clinical Endocrinology & Metabolism* **86**, 1267–1273 (2001).
239. Hoch, M. *et al.* LPS induces interleukin-6 and interleukin-8 but not tumor necrosis factor- $\alpha$  in human adipocytes. *Cytokine* **41**, 29–37 (2008).
240. Meijer, K. *et al.* Human Primary Adipocytes Exhibit Immune Cell Function: Adipocytes Prime Inflammation Independent of Macrophages. *PLoS ONE* **6**, e17154 (2011).
241. Takata, K. *et al.* Stiffness of the extracellular matrix regulates differentiation into beige adipocytes. *Biochemical and Biophysical Research Communications* **532**, 205–210 (2020).
242. Hou, W. *et al.* The metabolic footprint during adipocyte commitment highlights ceramide modulation as an adequate approach for obesity treatment. *EBioMedicine* **51**, 102605 (2020).
243. Chen, Q. *et al.* Fate decision of mesenchymal stem cells: adipocytes or osteoblasts? *Cell Death Differ* **23**, 1128–1139 (2016).
244. Morrow, B. A., Roth, R. H., Redmond, D. E., Sladek, J. R. & Elsworth, J. D. Apoptotic natural cell death in developing primate dopamine midbrain neurons occurs during a restricted period in the second trimester of gestation. *Experimental Neurology* **204**, 802–807 (2007).
245. Furuhashi, M., Saitoh, S., Shimamoto, K. & Miura, T. Fatty Acid-Binding Protein 4 (FABP4): Pathophysiological Insights and Potent Clinical Biomarker of Metabolic and Cardiovascular Diseases. *Clin Med Insights Cardiol* **8s3**, CMC.S17067 (2014).
246. Rosen, E. D. & MacDougald, O. A. Adipocyte differentiation from the inside out. *Nat Rev Mol Cell Biol* **7**, 885–896 (2006).
247. Rodriguez-López, L. A. *et al.* The capacity of differentiation of stromal vascular fraction cells into beige adipocytes is markedly reduced in subjects with overweight/obesity and insulin resistance: effect of genistein. *Int J Obes* (2021) doi:10.1038/s41366-021-00921-3.
248. Guénantin, A.-C. *et al.* Functional Human Beige Adipocytes From Induced Pluripotent Stem Cells. *Diabetes* **66**, 1470–1478 (2017).
249. Thacker, V. V. *et al.* Rapid endotheliitis and vascular damage characterize SARS-CoV-2 infection in a human lung-on-chip model. *EMBO Rep* **22**, (2021).
250. Jaffe, A. B. & Hall, A. RHO GTPASES: Biochemistry and Biology. *Annu. Rev. Cell Dev. Biol.* **21**, 247–269 (2005).
251. Schiller, Z. A., Schiele, N. R., Sims, J. K., Lee, K. & Kuo, C. K. Adipogenesis of adipose-derived stem cells may be regulated via the cytoskeleton at physiological oxygen levels in vitro. *Stem Cell Res Ther* **4**, 79 (2013).
252. Nobusue, H. *et al.* Regulation of MKL1 via actin cytoskeleton dynamics drives adipocyte differentiation. *Nat Commun* **5**, 3368 (2014).
253. McDonald, M. E. *et al.* Myocardin-Related Transcription Factor A Regulates Conversion of Progenitors to Beige Adipocytes. *Cell* **160**, 105–118 (2015).
254. Yang, W. *et al.* Arp2/3 complex regulates adipogenesis by controlling cortical actin remodelling. *Biochemical Journal* **464**, 179–192 (2014).
255. Lim, C.-Y. *et al.* Tropomodulin3 is a novel Akt2 effector regulating insulin-stimulated GLUT4 exocytosis through cortical actin remodeling. *Nat Commun* **6**, 5951 (2015).
256. Kim, J. I. *et al.* During Adipocyte Remodeling, Lipid Droplet Configurations Regulate Insulin Sensitivity through F-Actin and G-Actin Reorganization. *Mol Cell Biol* **39**, (2019).
257. Leto, D. & Saltiel, A. R. Regulation of glucose transport by insulin: traffic control of GLUT4. *Nat Rev Mol Cell Biol* **13**, 383–396 (2012).

258. Kanzaki, M., Furukawa, M., Raab, W. & Pessin, J. E. Phosphatidylinositol 4,5-Bisphosphate Regulates Adipocyte Actin Dynamics and GLUT4 Vesicle Recycling. *Journal of Biological Chemistry* **279**, 30622–30633 (2004).
259. Verkerke, A. R. P. & Kajimura, S. Oil does more than light the lamp: The multifaceted role of lipids in thermogenic fat. *Developmental Cell* **56**, 1408–1416 (2021).
260. Winkler, E. & Klingenberg, M. Effect of fatty acids on H<sup>+</sup> transport activity of the reconstituted uncoupling protein. *Journal of Biological Chemistry* **269**, 2508–2515 (1994).
261. Fedorenko, A., Lishko, P. V. & Kirichok, Y. Mechanism of Fatty-Acid-Dependent UCP1 Uncoupling in Brown Fat Mitochondria. *Cell* **151**, 400–413 (2012).
262. Schreiber, R. *et al.* Cold-Induced Thermogenesis Depends on ATGL-Mediated Lipolysis in Cardiac Muscle, but Not Brown Adipose Tissue. *Cell Metabolism* **26**, 753–763.e7 (2017).
263. Shin, H. *et al.* Lipolysis in Brown Adipocytes Is Not Essential for Cold-Induced Thermogenesis in Mice. *Cell Metabolism* **26**, 764–777.e5 (2017).
264. Hoeke, G., Kooijman, S., Boon, M. R., Rensen, P. C. N. & Berbée, J. F. P. Role of Brown Fat in Lipoprotein Metabolism and Atherosclerosis. *Circ Res* **118**, 173–182 (2016).
265. Bartelt, A. *et al.* Brown adipose tissue activity controls triglyceride clearance. *Nat Med* **17**, 200–205 (2011).
266. Wu, Q. *et al.* Fatty Acid Transport Protein 1 Is Required for Nonshivering Thermogenesis in Brown Adipose Tissue. *Diabetes* **55**, 3229–3237 (2006).
267. Guilherme, A., Henriques, F., Bedard, A. H. & Czech, M. P. Molecular pathways linking adipose innervation to insulin action in obesity and diabetes mellitus. *Nat Rev Endocrinol* **15**, 207–225 (2019).
268. Bartesaghi, S. *et al.* Thermogenic Activity of UCP1 in Human White Fat-Derived Beige Adipocytes. *Molecular Endocrinology* **29**, 130–139 (2015).
269. Seale, P. *et al.* Prdm16 determines the thermogenic program of subcutaneous white adipose tissue in mice. *J. Clin. Invest.* **121**, 96–105 (2011).
270. Mita, T. *et al.* FABP4 is secreted from adipocytes by adenyl cyclase-PKA- and guanylyl cyclase-PKG-dependent lipolytic mechanisms: FABP4 Secretion from Adipocytes and Lipolysis. *Obesity* **23**, 359–367 (2015).
271. Cottet-Rousselle, C., Ronot, X., Leverve, X. & Mayol, J.-F. Cytometric assessment of mitochondria using fluorescent probes. *Cytometry* **79A**, 405–425 (2011).
272. Zbinden, A. *et al.* Fluorescence lifetime metabolic mapping of hypoxia-induced damage in pancreatic pseudo-islets. *J. Biophotonics* **13**, e202000375 (2020).
273. Zbinden, A. *et al.* Non-invasive marker-independent high content analysis of a microphysiological human pancreas-on-a-chip model. *Matrix Biology* **85–86**, 205–220 (2020).
274. Tortora, G. J. & Nielsen, M. T. *Principles of human anatomy*. (John Wiley & Sons, 2012).
275. Arik, Y. B. *et al.* Barriers-on-chips: Measurement of barrier function of tissues in organs-on-chips. *Biomicrofluidics* **12**, 042218 (2018).
276. Yeste, J., Illa, X., Alvarez, M. & Villa, R. Engineering and monitoring cellular barrier models. *J Biol Eng* **12**, 18 (2018).
277. Strauss, O. The Retinal Pigment Epithelium in Visual Function. *Physiological Reviews* **85**, 845–881 (2005).
278. R. Sparrow, J., Hicks, D. & P. Hamel, C. The Retinal Pigment Epithelium in Health and Disease. *CMM* **10**, 802–823 (2010).
279. Al-Soudi, A., Kaaij, M. H. & Tas, S. W. Endothelial cells: From innocent bystanders to active participants in immune responses. *Autoimmunity Reviews* **16**, 951–962 (2017).
280. Yau, J. W., Teoh, H. & Verma, S. Endothelial cell control of thrombosis. *BMC Cardiovasc Disord* **15**, 130 (2015).

281. Chen, W. *et al.* The endothelial tip-stalk cell selection and shuffling during angiogenesis. *J. Cell Commun. Signal.* **13**, 291–301 (2019).
282. Hasan, S. S. & Fischer, A. The Endothelium: An Active Regulator of Lipid and Glucose Homeostasis. *Trends in Cell Biology* **31**, 37–49 (2021).
283. Muller, W. A. Getting Leukocytes to the Site of Inflammation. *Vet Pathol* **50**, 7–22 (2013).
284. Ricard, N., Bailly, S., Guignabert, C. & Simons, M. The quiescent endothelium: signalling pathways regulating organ-specific endothelial normalcy. *Nat Rev Cardiol* **18**, 565–580 (2021).
285. Kalucka, J. *et al.* Single-Cell Transcriptome Atlas of Murine Endothelial Cells. *Cell* **180**, 764–779.e20 (2020).
286. Augustin, H. G. & Koh, G. Y. Organotypic vasculature: From descriptive heterogeneity to functional pathophysiology. *Science* **357**, eaal2379 (2017).
287. Gogg, S., Nerstedt, A., Boren, J. & Smith, U. Human adipose tissue microvascular endothelial cells secrete PPAR $\gamma$  ligands and regulate adipose tissue lipid uptake. *JCI Insight* **4**, e125914 (2019).
288. Monsuur, H. N. *et al.* Extensive Characterization and Comparison of Endothelial Cells Derived from Dermis and Adipose Tissue: Potential Use in Tissue Engineering. *PLoS ONE* **11**, e0167056 (2016).
289. Privratsky, J. R. & Newman, P. J. PECAM-1: regulator of endothelial junctional integrity. *Cell Tissue Res* **355**, 607–619 (2014).
290. Chen, Z. & Tzima, E. PECAM-1 Is Necessary for Flow-Induced Vascular Remodeling. *ATVB* **29**, 1067–1073 (2009).
291. Park, J. Y. *et al.* Responses of endothelial cells to extremely slow flows. *Biomicrofluidics* **5**, 022211 (2011).
292. Tzima, E. *et al.* A mechanosensory complex that mediates the endothelial cell response to fluid shear stress. *Nature* **437**, 426–431 (2005).
293. Jin, Z.-G. *et al.* Ligand-Independent Activation of Vascular Endothelial Growth Factor Receptor 2 by Fluid Shear Stress Regulates Activation of Endothelial Nitric Oxide Synthase. *Circulation Research* **93**, 354–363 (2003).
294. Baeyens, N. Fluid shear stress sensing in vascular homeostasis and remodeling: Towards the development of innovative pharmacological approaches to treat vascular dysfunction. *Biochemical Pharmacology* **158**, 185–191 (2018).
295. Bischoff, I. *et al.* Pitfalls in assessing microvascular endothelial barrier function: impedance-based devices versus the classic macromolecular tracer assay. *Sci Rep* **6**, 23671 (2016).
296. Benson, K., Cramer, S. & Galla, H.-J. Impedance-based cell monitoring: barrier properties and beyond. *Fluids Barriers CNS* **10**, 5 (2013).
297. Srinivasan, B. *et al.* TEER Measurement Techniques for In Vitro Barrier Model Systems. *Journal of laboratory automation* **20**, 107–126 (2015).
298. Pober, J. S. & Sessa, W. C. Evolving functions of endothelial cells in inflammation. *Nat Rev Immunol* **7**, 803–815 (2007).
299. Nunes, S. S. *et al.* Generation of a functional liver tissue mimic using adipose stromal vascular fraction cell-derived vasculatures. *Sci Rep* **3**, 2141 (2013).
300. Sun, Y., Chen, S., Zhang, X. & Pei, M. Significance of Cellular Cross-Talk in Stromal Vascular Fraction of Adipose Tissue in Neovascularization. *ATVB* **39**, 1034–1044 (2019).
301. Szöke, K., Beckstrøm, K. J. & Brinchmann, J. E. Human Adipose Tissue as a Source of Cells with Angiogenic Potential. *Cell Transplant* **21**, 235–250 (2012).
302. Mehrotra, D., Wu, J., Papangeli, I. & Chun, H. J. Endothelium as a gatekeeper of fatty acid transport. *Trends in Endocrinology & Metabolism* **25**, 99–106 (2014).

303. Pi, X., Xie, L. & Patterson, C. Emerging Roles of Vascular Endothelium in Metabolic Homeostasis. *Circ Res* **123**, 477–494 (2018).
304. Wueest, S. & Konrad, D. The controversial role of IL-6 in adipose tissue on obesity-induced dysregulation of glucose metabolism. *American Journal of Physiology-Endocrinology and Metabolism* **319**, E607–E613 (2020).
305. Blaber, S. P. *et al.* Analysis of in vitro secretion profiles from adipose-derived cell populations. *J Transl Med* **10**, 172 (2012).
306. Cimini, F. A. *et al.* Circulating IL-8 levels are increased in patients with type 2 diabetes and associated with worse inflammatory and cardiometabolic profile. *Acta Diabetol* **54**, 961–967 (2017).
307. Kim, C.-S. *et al.* Circulating levels of MCP-1 and IL-8 are elevated in human obese subjects and associated with obesity-related parameters. *Int J Obes* **30**, 1347–1355 (2006).
308. Haase, J. *et al.* Local proliferation of macrophages in adipose tissue during obesity-induced inflammation. *Diabetologia* **57**, 562–571 (2014).
309. Jenkins, S. J. *et al.* Local Macrophage Proliferation, Rather than Recruitment from the Blood, Is a Signature of TH2 Inflammation. *Science* **332**, 1284–1288 (2011).
310. Wentworth, J. M. *et al.* Pro-Inflammatory CD11c+CD206+ Adipose Tissue Macrophages Are Associated With Insulin Resistance in Human Obesity. *Diabetes* **59**, 1648–1656 (2010).
311. Li, Y., Yun, K. & Mu, R. A review on the biology and properties of adipose tissue macrophages involved in adipose tissue physiological and pathophysiological processes. *Lipids Health Dis* **19**, 164 (2020).
312. Russo, L. & Lumeng, C. N. Properties and functions of adipose tissue macrophages in obesity. *Immunology* **155**, 407–417 (2018).
313. Jaitin, D. A. *et al.* Lipid-Associated Macrophages Control Metabolic Homeostasis in a Trem2-Dependent Manner. *Cell* **178**, 686–698.e14 (2019).
314. Weisberg, S. P. *et al.* Obesity is associated with macrophage accumulation in adipose tissue. *J. Clin. Invest.* **112**, 1796–1808 (2003).
315. Xu, H. *et al.* Chronic inflammation in fat plays a crucial role in the development of obesity-related insulin resistance. *J. Clin. Invest.* **112**, 1821–1830 (2003).
316. Nagareddy, P. R. *et al.* Adipose Tissue Macrophages Promote Myelopoiesis and Monocytosis in Obesity. *Cell Metabolism* **19**, 821–835 (2014).
317. McLoughlin, R. M. *et al.* IL-6 trans-signaling via STAT3 directs T cell infiltration in acute inflammation. *Proceedings of the National Academy of Sciences* **102**, 9589–9594 (2005).
318. Taub, D. D., Anver, M., Oppenheim, J. J., Longo, D. L. & Murphy, W. J. T lymphocyte recruitment by interleukin-8 (IL-8). IL-8-induced degranulation of neutrophils releases potent chemoattractants for human T lymphocytes both in vitro and in vivo. *J. Clin. Invest.* **97**, 1931–1941 (1996).
319. Weissenbach, M. *et al.* Interleukin-6 is a direct mediator of T cell migration. *Eur. J. Immunol.* **34**, 2895–2906 (2004).
320. Li, M., Qian, M., Kyler, K. & Xu, J. Adipose Tissue-Endothelial Cell Interactions in Obesity-Induced Endothelial Dysfunction. *Front. Cardiovasc. Med.* **8**, 681581 (2021).
321. Schneider, S., Erdemann, F., Schneider, O., Hutschalik, T. & Loskill, P. Organ-on-a-disc: A platform technology for the centrifugal generation and culture of microphysiological 3D cell constructs amenable for automation and parallelization. *APL Bioengineering* **4**, 046101 (2020).
322. Zhu, Y. *et al.* State of the art in integrated biosensors for organ-on-a-chip applications. *Current Opinion in Biomedical Engineering* **19**, 100309 (2021).
323. Villarroya, F., Cereijo, R., Gavaldà-Navarro, A., Villarroya, J. & Giralt, M.

- Inflammation of brown/beige adipose tissues in obesity and metabolic disease. *J Intern Med* **284**, 492–504 (2018).
324. Larabee, C. M., Neely, O. C. & Domingos, A. I. Obesity: a neuroimmunometabolic perspective. *Nat Rev Endocrinol* **16**, 30–43 (2020).
325. Park, J., Morley, T. S., Kim, M., Clegg, D. J. & Scherer, P. E. Obesity and cancer—mechanisms underlying tumour progression and recurrence. *Nat Rev Endocrinol* **10**, 455–465 (2014).
326. Quail, D. F. & Dannenberg, A. J. The obese adipose tissue microenvironment in cancer development and progression. *Nat Rev Endocrinol* **15**, 139–154 (2019).
327. Sheng, X. *et al.* Adipocytes Sequester and Metabolize the Chemotherapeutic Daunorubicin. *Mol Cancer Res* **15**, 1704–1713 (2017).





## Acknowledgements

### Thank you...

... to all those who have supported me in any way throughout the making of this thesis!

First and foremost, I would like to express my sincere gratitude to **Prof. Dr. Katja Schenke-Layland** and **Prof. Dr. Andreas Stahl** for giving me the opportunity to pursue this PhD thesis. I very much appreciate your ideas, support, and enthusiasm, and I could have not asked for better PhD supervisors. I am beyond grateful!

Moreover, I would like to thank **Prof. Dr. Peter Loskill** and **Dr. Madelana Zincke Dos Reis Fernandes Cipriano** for being outstanding mentors. Peter, thank you very much, for making me a member of your marvelous lab, and for introducing me to the OoC community. Madalena, obrigado – your enthusiasm for research is merely amazing (and highly contagious). My gratitude towards the two of you is beyond words, and I am very much looking forward to all the exiting scientific journeys we will embark on together in the future.

Thank you to the entire MicroOrganoLab! I would particularly like to thank **Dr. Christopher Probst**, **Dr. Claudia Teufel**, **Johanna Chuchuy**, **Oliver Schneider**, **Ibrahim Tengku Maulana**, **Katharina Schlünder** and **Stefan Schneider** – I sincerely hope that you could learn as much from me as I have learnt from you. Furthermore, I would like to thank **Julia Roosz**, **Raylin Xu**, **Carina Binder**, **Elena Kromidas**, **Lydia Moll** and **Verena Haug** who I had the honor of mentoring and working with on the fat team. In general, thanks to all (former) lab members for many valuable scientific discussions, motivation, feedback and support. I am happy, and proud, that I could be part of such a great interdisciplinary and international research environment in the past five years. Keep exploring and keep fighting those airbubbles!

Many thanks to all of the members of the Stahl Lab, especially to **Pete Zushin** and **Ching Fang Chang**. I had two magnificent summers at UC Berkeley, and I am so grateful for the warm welcome to the lab, and especially for how incredibly much I learnt about molecular and adipose biology from you.

Moreover, a big thank you to my friends and (former) colleagues Johanna, Oli, Aline, Silke, Julia, Katrin, Lisa, Cris and Jasmin for many (non-) scientific adventures,

## Acknowledgements

---

Thanks to my brother, my mother, my grandparents and Rici, Iris and Domi for always being there no matter what.

Last but not least, I would like to thank Kodi for his endless mental support.

## Declaration

Ich erkläre hiermit, dass ich die zur Promotion eingereichte Arbeit mit dem Titel: „*Organ-on-Chip Systems Integrating Human Adipose Tissues*“ selbständig verfasst, nur die angegebenen Quellen und Hilfsmittel benutzt und wörtlich oder inhaltlich übernommene Zitate als solche gekennzeichnet habe. Ich erkläre, dass die Richtlinien zur Sicherung guter wissenschaftlicher Praxis der Universität Tübingen (Beschluss des Senats vom 25.5.2000) beachtet wurden. Ich versichere an Eides statt, dass diese Angaben wahr sind und dass ich nichts verschwiegen habe. Mir ist bekannt, dass die falsche Abgabe einer Versicherung an Eides statt mit Freiheitsstrafe bis zu drei Jahren oder mit Geldstrafe bestraft wird.

Tübingen, 03.09.2021

Julia Rogal





## Publication [4]

**Human retina-on-a-chip: merging organoid and organ-on-a-chip technology to generate complex multi-layer tissue models**

K. Achberger, C. Probst, J. C. Haderspeck, S. Bolz, **J. Rogal**, J. Chuchuy, M. Nikolova, V. Cora, L. Antkowiak, W. Haq, N. Shen, K. Schenke-Layland, M. Ueffing, S. Liebau, P. Loskill

*eLife* **8**, e46188 (2019) <https://dx.doi.org/10.7554/eLife.46188>

**Abstract:**

The devastating effects and incurable nature of hereditary and sporadic retinal diseases such as Stargardt disease, age-related macular degeneration or retinitis pigmentosa urgently require the development of new therapeutic strategies. Additionally, a high prevalence of retinal toxicities is becoming more and more an issue of novel targeted therapeutic agents. Ophthalmologic drug development, to date, largely relies on animal models, which often do not provide results that are translatable to human patients. Hence, the establishment of sophisticated human tissue-based in vitro models is of utmost importance. The discovery of self-forming retinal organoids (ROs) derived from human embryonic stem cells (hESCs) or human induced pluripotent stem cells (hiPSCs) is a promising approach to model the complex stratified retinal tissue. Yet, ROs lack vascularization and cannot recapitulate the important physiological interactions of matured photoreceptors and the retinal pigment epithelium (RPE). In this study, we present the retina-on-a-chip (RoC), a novel microphysiological model of the human retina integrating more than seven different essential retinal cell types derived from hiPSCs. It provides vasculature-like perfusion and enables, for the first time, the recapitulation of the interaction of mature photoreceptor segments with RPE in vitro. We show that this interaction enhances the formation of outer segment-like structures and the establishment of in vivo-like physiological processes such as outer segment phagocytosis and calcium dynamics. In addition, we demonstrate the applicability of the RoC for drug testing, by reproducing the retinopathic side-effects of the anti-malaria drug chloroquine and the antibiotic gentamicin. The developed hiPSC-based RoC has the potential to promote drug development and provide new insights into the underlying pathology of retinal diseases.



# Merging organoid and organ-on-a-chip technology to generate complex multi-layer tissue models in a human retina-on-a-chip platform

Kevin Achberger<sup>1†</sup>, Christopher Probst<sup>2†</sup>, Jasmin Haderspeck<sup>1†</sup>, Sylvia Bolz<sup>3</sup>, Julia Rogal<sup>2,4</sup>, Johanna Chuchuy<sup>2,4</sup>, Marina Nikolova<sup>1</sup>, Virginia Cora<sup>1</sup>, Lena Antkowiak<sup>1</sup>, Wadood Haq<sup>3</sup>, Nian Shen<sup>4</sup>, Katja Schenke-Layland<sup>4,5,6</sup>, Marius Ueffing<sup>3</sup>, Stefan Liebau<sup>1\*</sup>, Peter Loskill<sup>2,4\*</sup>

<sup>1</sup>Institute of Neuroanatomy & Developmental Biology (INDB), Eberhard Karls University Tübingen, Tübingen, Germany; <sup>2</sup>Fraunhofer Institute for Interfacial Engineering and Biotechnology IGB, Stuttgart, Germany; <sup>3</sup>Centre for Ophthalmology, Institute for Ophthalmic Research, Eberhard Karls University Tübingen, Tübingen, Germany; <sup>4</sup>Department of Women's Health, Research Institute for Women's Health, Eberhard Karls University Tübingen, Tübingen, Germany; <sup>5</sup>Natural and Medical Sciences Institute (NMI), Reutlingen, Germany; <sup>6</sup>Department of Medicine/Cardiology, Cardiovascular Research Laboratories, David Geffen School of Medicine, Los Angeles, United States

\*For correspondence: stefan.liebau@uni-tuebingen.de (SL); peter.loskill@igb.fraunhofer.de (PL)

†These authors contributed equally to this work

**Competing interests:** The authors declare that no competing interests exist.

**Funding:** See page 24

**Received:** 18 February 2019  
**Accepted:** 06 August 2019  
**Published:** 27 August 2019

**Reviewing editor:** Milica Radisic, University of Toronto, Canada

© Copyright Achberger et al. This article is distributed under the terms of the [Creative Commons Attribution License](https://creativecommons.org/licenses/by/4.0/), which permits unrestricted use and redistribution provided that the original author and source are credited.

**Abstract** The devastating effects and incurable nature of hereditary and sporadic retinal diseases such as Stargardt disease, age-related macular degeneration or retinitis pigmentosa urgently require the development of new therapeutic strategies. Additionally, a high prevalence of retinal toxicities is becoming more and more an issue of novel targeted therapeutic agents. Ophthalmologic drug development, to date, largely relies on animal models, which often do not provide results that are translatable to human patients. Hence, the establishment of sophisticated human tissue-based in vitro models is of utmost importance. The discovery of self-forming retinal organoids (ROs) derived from human embryonic stem cells (hESCs) or human induced pluripotent stem cells (hiPSCs) is a promising approach to model the complex stratified retinal tissue. Yet, ROs lack vascularization and cannot recapitulate the important physiological interactions of matured photoreceptors and the retinal pigment epithelium (RPE). In this study, we present the retina-on-a-chip (RoC), a novel microphysiological model of the human retina integrating more than seven different essential retinal cell types derived from hiPSCs. It provides vasculature-like perfusion and enables, for the first time, the recapitulation of the interaction of mature photoreceptor segments with RPE in vitro. We show that this interaction enhances the formation of outer segment-like structures and the establishment of in vivo-like physiological processes such as outer segment phagocytosis and calcium dynamics. In addition, we demonstrate the applicability of the RoC for drug testing, by reproducing the retinopathic side-effects of the anti-malaria drug chloroquine and the antibiotic gentamicin. The developed hiPSC-based RoC has the potential to promote drug development and provide new insights into the underlying pathology of retinal diseases.

DOI: <https://doi.org/10.7554/eLife.46188.001>

### Introduction

Retinal diseases such as Stargardt disease, age-related macular degeneration, diabetic retinopathies or retinitis pigmentosa are amongst the leading causes of vision loss in humans (Croze et al., 2014; Buch et al., 2004). Unfortunate for patients suffering from those diseases, there are currently no cures available (Shintani et al., 2009; Fine et al., 2000). Moreover, the complex neuro-retinal organization and the vast blood-supply make retinal tissue susceptible for side effects of compounds delivered intravitreally or systemically (Penha et al., 2010; Renouf et al., 2012). Retinal toxicities are a major issue for a wide range of therapeutic substances, especially for targeted anticancer agents since many of the targets are also expressed in ocular tissues (Renouf et al., 2012). Although animal models that are used to explore new therapeutic options and assess retinal toxicities resemble the human (patho-)physiology of vision in certain aspects, they fail to reflect fundamental characteristics including trichromacy or a fovea centralis, responsible for high visual acuity (Figure 1). In vitro cell culture assays, on the other hand, are typically based on non-physiological 2D cell cultures, which cannot reflect the complex architecture and cell-cell interactions as well as the blood perfusion. More complex approaches such as retinal explants from human donors provide a full-featured model; however, the limited availability and culturability as well as inter-donor variabilities make it unsuited for drug development and testing. The invention of physiologically relevant in vitro models

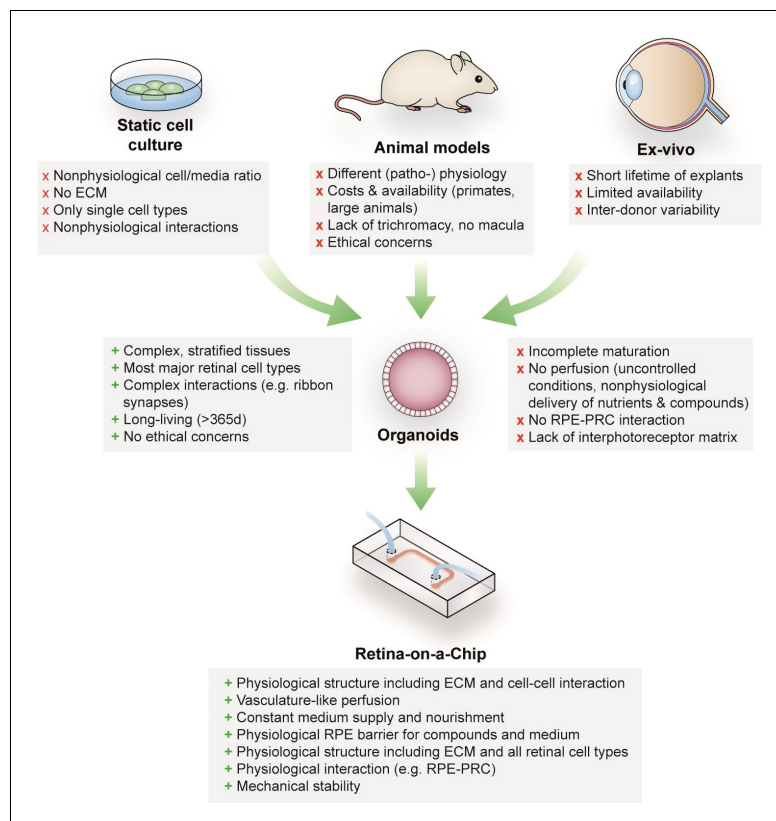


**Figure 1.** Advantages and limitations of retinal models for drug development and mechanistic research. DOI: <https://doi.org/10.7554/eLife.46188.002>

capable of mimicking the human retinal biology is hence of crucial importance. Recent progress in the generation of 3-dimensional (3D) organoids derived from human pluripotent stem cells (hPSC) (derived from both induced (hiPSC) as well as embryonic (hESC) stem cells) enabled the reflection of distinct types of tissues, such as subsystems of the central nervous system including the retina. Retinal organoids (ROs), also called 'eyes in the dish', resemble rudimentary optic vesicle-like structures with a retinal layering similar to in vivo conditions (Nakano *et al.*, 2012; Zhong *et al.*, 2014). These ROs contain most relevant retinal cell types in a physiological layering such as ganglion cells, amacrine cells, horizontal cells, bipolar cells, Müller glia as well as rods and cones. Nevertheless, hPSC-ROs are still facing a variety of drawbacks limiting predictive research on for example human retinal development, function or drug response. Some of the major hurdles are (i) the functional maturation of differentiated cells, (ii) lack of essential cell types (e.g. microglia), (iii) lack of a physiological interplay of the various retinal cell types especially of photoreceptors and retinal pigment epithelia (RPE), as well as (iv) a missing vascularization (reviewed in Achberger *et al.*, 2019; Yin *et al.*, 2016). Due to the lack of a physiological perfusion, the delivery of compounds to ROs is uncontrolled and entirely artificial. Here, general limitations of static cell culture apply including non-physiological cell-to-media ratio, uncontrolled shear forces during media exchanges, as well as highly variable conditions between media exchanges. In recent years, the short-comings of conventional static cell culture has led to the emergence of microphysiological systems (MPS), specifically Organ-on-a-Chip (OoC) platforms. MPSs have evolved into a powerful alternative for classical cell culture and animal models by providing physiological microenvironments embedded in a vascular-like microfluidic perfusion (reviewed in Wikswo, 2014; Zhang *et al.*, 2018). This new and promising technology has the potential to revolutionize drug development and usher into a new era of personalized medicine. Over the past years, a variety of MPSs have been developed, mimicking, for instance, cardiac (Mathur *et al.*, 2015; Agarwal *et al.*, 2013), lung (Huh *et al.*, 2010), renal (Wilmer *et al.*, 2016), and hepatic tissue (Bhise *et al.*, 2016; Nakao *et al.*, 2011). In the context of ophthalmologic research, a variety of approaches have been introduced that represent partial layers of the cornea (Puleo *et al.*, 2009) or the retina (Chen *et al.*, 2017; Dodson *et al.*, 2015; Su *et al.*, 2015; Jeon *et al.*, 2016; Mishra *et al.*, 2015). So far, however, no MPS has been able to successfully recapitulate the complex 3D architecture of the human retina.

In this study, we developed a physiologically relevant 3D in vitro model of the human retina by combining hiPSC-ROs with hiPSC-derived RPE in a retina-on-a-chip (RoC). This novel microphysiological platform enables enhanced inner and outer segment formation and preservation, a direct interplay between RPE and photoreceptors as well as a precisely controllable vasculature-like perfusion. In order to provide a high-content platform for basic and applied research, we established a toolbox comprising in situ analysis approaches as well as terminal endpoints enabling the monitoring of functionality as well as molecular mechanisms. To demonstrate the applicability for drug screening, the system was exposed to the drugs chloroquine and gentamicin, which are known to have retinopathic side effects (Elman *et al.*, 1976; Ding *et al.*, 2016; Yusuf *et al.*, 2017; Zemel *et al.*, 1995; McDonald *et al.*, 1986).

## Results

### Retinal organoids show rod and cone diversity and simple inner and outer segment formation

ROs derived from hiPSCs harbor all known major retinal subtypes such as ganglion cells, bipolar cells, horizontal cells, amacrine cells, Müller glia and photoreceptors (Zhong *et al.*, 2014; Figure 2—figure supplement 1). Using immunostaining and gene expression analysis, the presence of the retinal cell types, as well as crucial retinal morphological cues such as inner and outer photoreceptor segment formation, a tightly formed outer limiting membrane (OLM) and a correct layering, was verified (Figure 2—figure supplement 1). In order to reach a suitable maturation, ROs were differentiated for 180 days. ROs of that age harbor matured photoreceptors which have simple forms of inner and outer segments, situated on the surface of the ROs, visible in bright field microscopy or by immunostaining of respective markers (Figure 2b–f). Immunostaining of the respective organoids demonstrates the presence of a mixed population of rods and cones, identified by specific markers (rhodopsin for rods and Arrestin-3 for cones, Figure 2c–e, Figure 2—figure supplement 1). In order

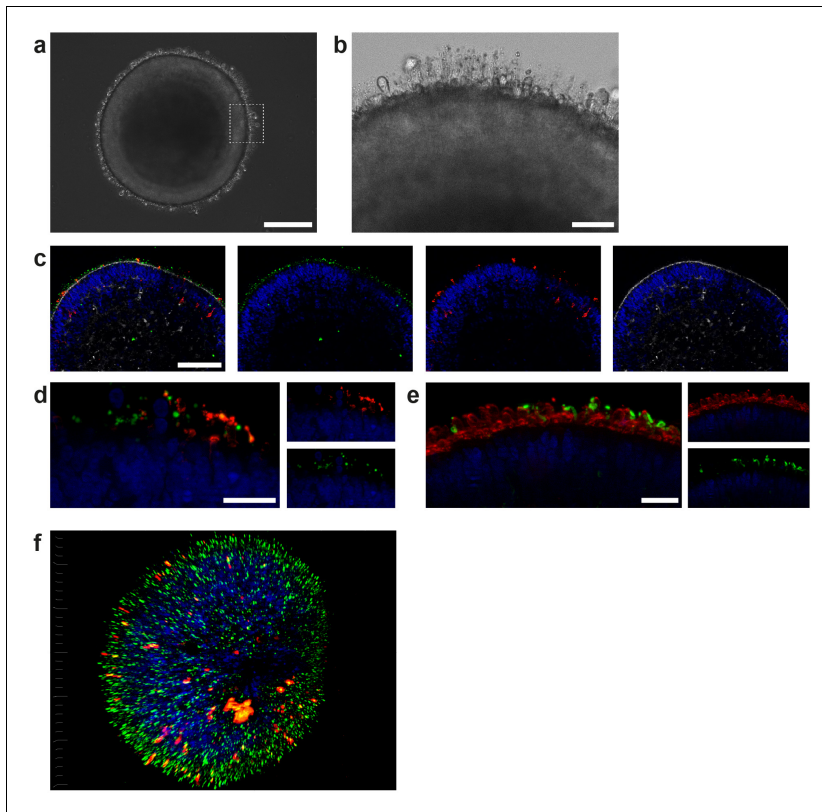


**Figure 2.** Characterization of retinal organoids. (a) Brightfield image of a day 180 RO in dish culture. (b) Magnified area of a highlighting inner and outer segment-like structures. (c) Day 180 ROs cryosectioned and immunostained for the rod marker rhodopsin (red), the outer segment marker ROM1 (green) and phalloidin (white) visualizing the outer limiting membrane. (d) Day 180 ROs sectioned and immunostained for the rod marker rhodopsin (red) and the outer segment marker ROM1 (green). (e) Day 180 ROs sectioned and immunostained for the rod marker rhodopsin (green) and for PNA lectin (red). (f) 3D visualization of whole-mount staining of day 180 RO stained for rhodopsin (red) and ROM1 (green). Bars indicate a) 250  $\mu\text{m}$  b) 50  $\mu\text{m}$  c) 100  $\mu\text{m}$  d-f) 20  $\mu\text{m}$ . Blue: DAPI.

DOI: <https://doi.org/10.7554/eLife.46188.003>

The following figure supplement is available for figure 2:

**Figure supplement 1.** Cell types in dish cultured hiPSC-derived retinal organoids.

DOI: <https://doi.org/10.7554/eLife.46188.004>

to analyze segment formation, we used ROM1 as it has been previously shown as specific outer segment marker (Datta *et al.*, 2015) and verified the segment specificity by co-staining with the rod marker rhodopsin (Figure 2c–d,f). Further, we tested the previously described protein PNA lectin, which was delineated to specifically bind to cone photoreceptor segments (Blanks and Johnson, 1984). Co-staining of rhodopsin with PNA lectin exhibited that not only cone but also rod segments in ROs are labeled with PNA lectin (Figure 2e).

### Microphysiological retina-on-a-chip

To recapitulate the complex *in vivo* anatomy of the human retina *in vitro* (Figure 3a), we developed a microfluidic platform that enables the culture of hiPSC-derived RPE and ROs in a defined

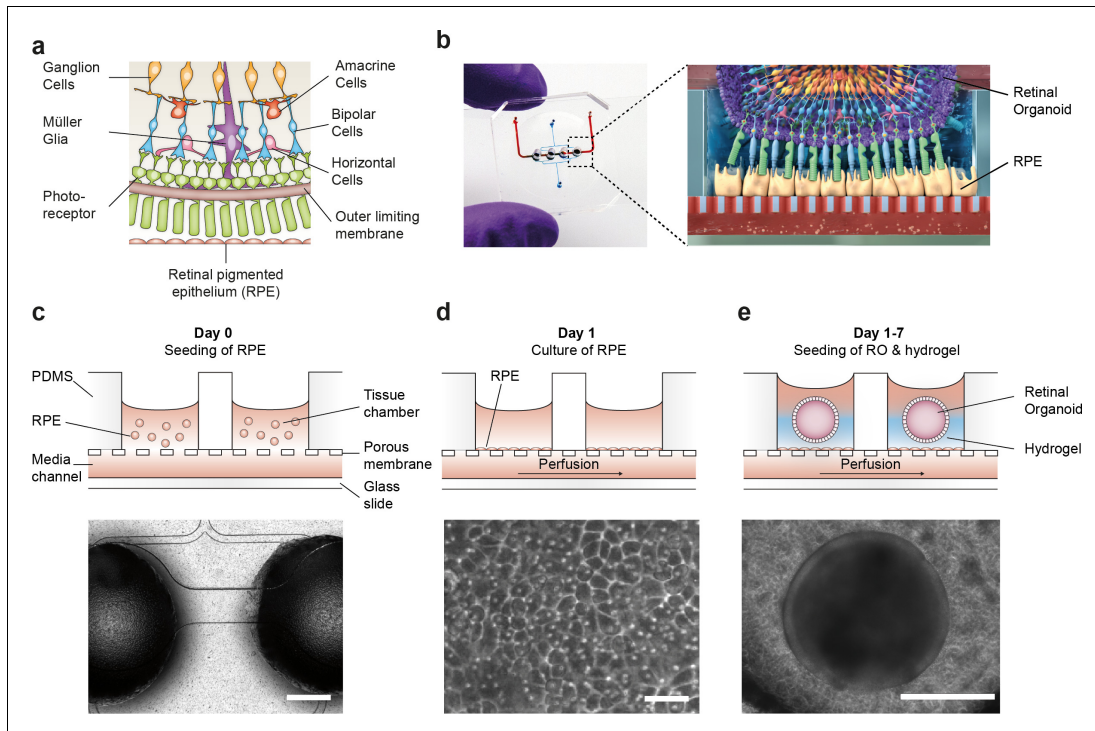


**Figure 3.** Microfluidic RoC. (a) Schematic representation of the human retinal composition and cell types in vivo. (b) Photo (left) of the RoC and (right) representation of the RO photoreceptor and RPE interaction. (c) RPE cells are seeded into the device, (d) forming a densely packed monolayer after 24 hr of culture. (e) ROs and the hyaluronic acid-based hydrogel are directly loaded from the top into the well and onto the RPE. Bars indicate (c) 500 μm, (d) 80 μm, (e) 400 μm.

DOI: <https://doi.org/10.7554/eLife.46188.005>

The following figure supplement is available for figure 3:

**Figure supplement 1.** Long-term culture of RoC.

DOI: <https://doi.org/10.7554/eLife.46188.006>

physiological structure (Figure 2b). Each RoC features four identical micro-tissues connected via a microchannel and is comprised of two transparent and biocompatible polymer layers. The top layer features the compartments for the ROs and RPE, whereas the bottom layer provides a channel for a vasculature-like perfusion enabling a constant supply of nutrients and compounds. Both layers are separated by a thin porous membrane mimicking the endothelial barrier and shielding the tissues from shear forces while simultaneously enabling the exchange of nutrients and metabolites (Figure 3b). The tissue compartments are accessible from above for the initial seeding process and sealed during the subsequent culture process to avoid evaporation and contamination. A stable tissue comprising ROs and RPE was achieved by first seeding hiPSC-derived RPE cells at a defined density into each tissue compartment (Figure 3c) and subsequent culture for 24 hr (Figure 3d). This step was followed by injection of ROs embedded in a hyaluronic acid-based hydrogel (representing the major component of the interphotoreceptor matrix between RPE and PRC) into the tissue compartments (Figure 3e). This led to the formation of a thin hydrogel layer, generating a defined distance between RPE cells and the outer limiting membrane of the ROs. Thereby, a direct contact

and, thus, an uncontrolled outgrowth of cells from the ROs during culture was successfully avoided. ROs and RPE were cultured in the system for at least 3 days prior to further functionality assessment or experimentation. The controlled culture conditions enabled a stable culture of the RoC for at least 21 days (*Figure 3—figure supplement 1*).

### Specific marker expression and polarization of retinal pigment epithelial cells in the RoC

A polarized and functional RPE is crucial for the survival of photoreceptors *in vivo* and a vital part of the visual cycle shuttling retinoids between the RPE and photoreceptor outer segments (*Kevany and Palczewski, 2010; Marmorstein, 2001*). Therefore, the RPE in the RoC was thoroughly tested for its marker expression and polarization (*Figure 4, Figure 4—figure supplement 1*). Expression of RPE markers PAX6 and MITF can be observed after 7–14 days in the chip (*Figure 4a–b*). Mature RPE inside the chip displayed cobble stone-like morphology and tight-junction formation visualized by ZO-1 staining (*Figure 4c*). The melanosome and pigmentation marker Melanoma gp100 (also called

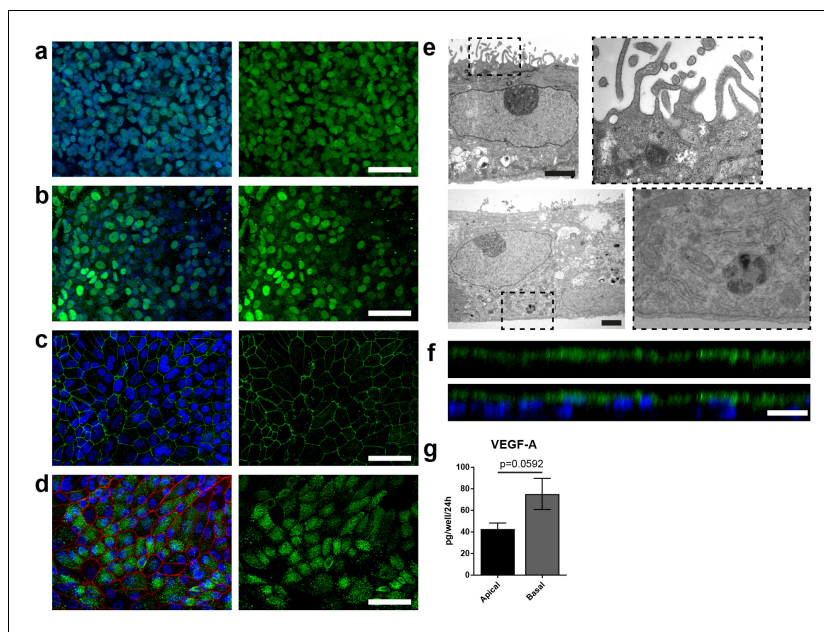


**Figure 4.** Specific marker expression and polarization of retinal pigment epithelial cells in the RoC. (a–d) Evaluation of RPE cells cultured for 14 days in the RoC by immunostaining of relevant RPE markers: a) RPE cells stained for MITF (green), (b) PAX6 (green), (c) ZO-1 (green) and (d) Melanoma gp100 (green), ZO-1 (red). (e) Electron microscopic image of polarized RPE cells. RPE cells display apical microvilli (top row) and a basal membrane (bottom row). (f) Apical microvilli formation is shown using confocal microscopy (orthogonal view of a z-stack) and immunohistochemical staining for ezrin (green). (g) Fluorescent quantification of VEGF-A secretion using ELISA comparing medium collected from a basal and apical channel in a specialized version of the RoC (n = 3 chips). Bars indicate a–d) (left) 50  $\mu$ m, e) 2  $\mu$ m, f) 20  $\mu$ m. Blue: DAPI. Error Bars: S.E.M. p=p value (Two-sided student's t-test). DOI: <https://doi.org/10.7554/eLife.46188.007>

The following source data and figure supplements are available for figure 4:

**Source data 1.** Source data for *Figure 4a*.

DOI: <https://doi.org/10.7554/eLife.46188.010>

**Figure supplement 1.** Characterization of dish and chip cultured human iPSC-derived RPE.

DOI: <https://doi.org/10.7554/eLife.46188.008>

**Figure supplement 1—source data 1.** Source data for *Figure 4—figure supplement 1 a*.

DOI: <https://doi.org/10.7554/eLife.46188.009>

PMEL17 or *Silver* locus protein) (Berson et al., 2001; Theos et al., 2005) was highly expressed in chip-cultured RPE (Figure 4d) indicating a strong pigmentation. Conclusive evidence for the maturation and proper functionality of RPE is its state of polarization (Marmorstein, 2001; Sonoda et al., 2009). Electron microscopy analysis revealed not only the strong pigmentation of the RPE but also the presence of apical microvilli as well as a basal membrane already after 7 days of on-chip culture (Figure 4e). Further, we observed the polarized expression of ezrin, an apical microvilli marker (Kivelä et al., 2000) (Figure 4f). Finally, polarized RPE displayed basal secretion of VEGF-A, which could be measured on-chip by using a double-channel chip in which basal and apical medium could be collected separately (Figure 4g). The VEGF-A concentration was higher in the basal channel than in the apical (70 vs 40 pg per chip in 24 hr). Taken together, the RPE in the RoC is strongly pigmented, polarized, and expresses respective RPE markers.

### Physiological secretion kinetics into the vasculature-mimicking channels

The vasculature-like perfusion in the media channels enables both, the precisely controllable delivery of defined media and compounds to the tissue as well as the transport of secreted factors away from the tissue, allowing for a time-resolved sampling of the secretion kinetics. In order to analyze and characterize the fluid flow as well as the transport of diluted species in the RoC, we performed computational fluid dynamics simulations: Due to the fluidic resistance of the porous membrane, the convective fluid flow is confined to the media channels (Figure 5a). At the same time, nutrients, compounds, and further dissolved molecules are transported to the tissue chamber via diffusion. This rapid process enables a precisely controllable delivery (Figure 5b) as well as a controlled washout. In order to verify this, we conducted a proof of concept experiment during which we switched from a colorless liquid to a colored one and observed a complete distribution of the dye within 300 s (flow rate of 20  $\mu\text{l/hr}$ ) (Figure 5—figure supplement 1). Subsequent injection of a colorless liquid again demonstrated a washout in the same time frame (see Video 1 and 2).

To further elucidate the advantages of the vasculature-like perfusion, we injected media supplemented with 10 ng/ml TGF- $\beta$ 1 over 24 hr and subsequently washed the stimulant out again. By sampling the effluent from the media outlets of the RoC, we were able to measure the VEGF-A kinetics before and during the stimulation as well as after the washout (Figure 5c). Already after 2 hr, we could observe a 2-fold increase of VEGF-A levels in the effluent medium relative to the baseline level at 0 hr. After this initial peak, the VEGF-A levels decreased over time resting above the baseline level. Finally, after 24 hr a second peak was reached. The subsequent washout of TGF- $\beta$ 1 using normal media led to a steady decrease of VEGF-A levels at the 36 and 48 hr time-point, respectively. In summary, the vasculature-like perfusion in the RoC enabled the controlled delivery and washout of the stimulant TGF- $\beta$ 1 without disturbing the culture conditions as well as time-resolved monitoring of physiological VEGF-A secretion kinetics.

### Enhanced outer segment formation in the RoC

The close proximity and the precisely orchestrated interaction of photoreceptors and the RPE layer is fundamental for vision, ensuring the phagocytosis and processing of shed photoreceptor outer segments (POS) as well as a supply of nutrients and oxygen (Elman et al., 1976). The RoC device allows the establishment of a defined interaction site between the segment structures of the RO and RPE cells without impairing neither structure nor viability of the organoid (Figure 6—figure supplements 1–2). Live cell imaging in the chip was enabled by transducing RPE cells with an IRBP-GFP viral vector and by marking the surface structures of the organoids with PNA lectin coupled to Alexa Fluor 568 prior to on-chip culture (Figure 6a). By measuring the distance between lectin-marked segment tips and GFP-labeled RPE, we found a distance of approximately  $5 \pm 3.19 \mu\text{m}$  over different experiments (Figure 6c). Subsequently, immunostaining using rhodopsin (rod outer segments) and phalloidin (cytoskeleton of the RPE and the RO including tight junctions) revealed that the segment structures and RPE cells are in close apposition on-chip (Figure 6b).

To further study the mechanically delicate interaction site between ROs and RPE in cryosections, we performed immunofluorescence analysis using a specifically tailored chip version (Figure 6d). After 7 days of on-chip culture, the close proximity of RPE and RO was preserved and no indication of cell outgrowth or general loss of integrity of the continuous OLM, labeled by the actin-cytoskeleton marker phalloidin, was observed (Figure 6d). Further, the hydrogel-filled space between the

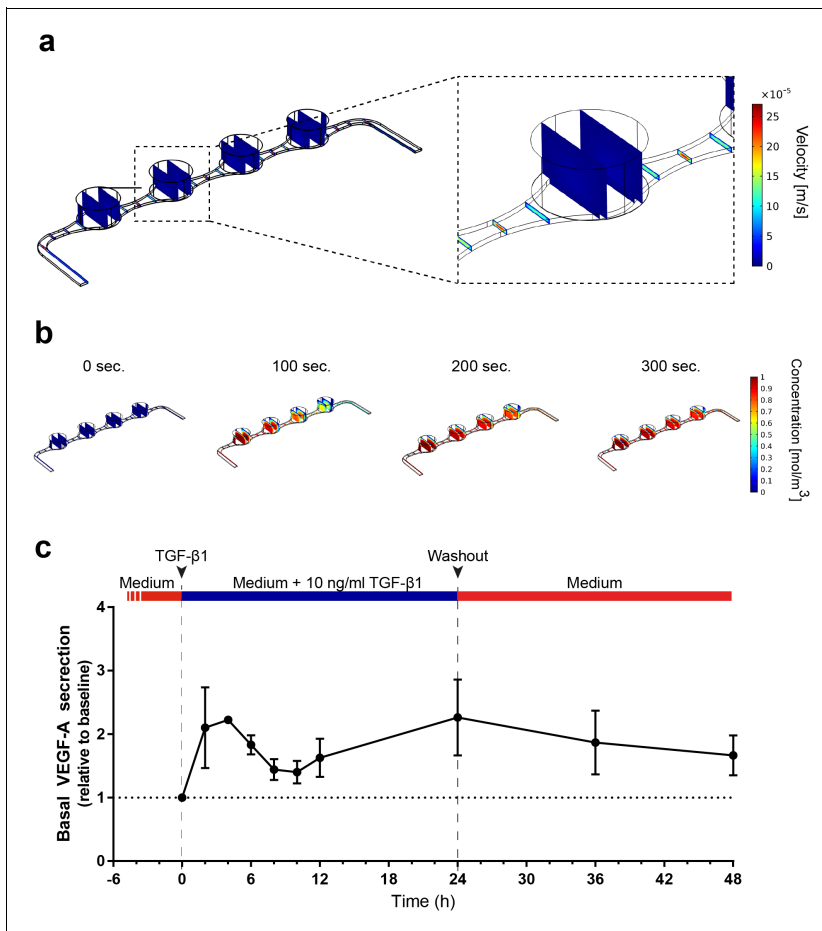


**Figure 5.** Precisely controllable delivery of stimulants and time-resolved secretion kinetics. (a-b) Analysis of the free and porous media flow and the transport of diluted species in the RoC: (a) Convective flow is confined to the vasculature-like media compartments and (b) compounds are delivered rapidly into the tissue chambers via diffusion. (c) Time-resolved monitoring of the secretion of VEGF-A before and after media supplemented with 10 ng/ml TGF- $\beta$ 1 was injected into RoCs ( $n = 3$ ). After 24 hr, TGF- $\beta$ 1 was washed out using a normal medium. VEGF-A secretion in individual RoCs was normalized to the baseline secretion at 0 hr. Error bars: S.E.M.

DOI: <https://doi.org/10.7554/eLife.46188.011>

The following source data and figure supplement are available for figure 5:

**Source data 1.** Source data for **Figure 5c**.

DOI: <https://doi.org/10.7554/eLife.46188.013>

**Figure supplement 1.** Perfusion-enabled precisely controllable injection and washout.

DOI: <https://doi.org/10.7554/eLife.46188.012>

RPE monolayer and the RO was strongly invaded by rhodopsin and ROM1 (outer segment marker)-positive clusters indicating an increased and cumulated presence of inner and outer segment-like structures (**Figure 6d**). A detailed analysis of the interaction site via electron microscopy confirmed the formation of numerous inner segments with clusters of mitochondria as well as the maintenance

of the OLM (*Figure 6e*). The distance of outer segment tips and RPE microvilli in this exemplary image is around 5  $\mu\text{m}$  (*Figure 6e*), which is in accordance with the data shown above.

Next, we examined whether the formation and preservation of outer segment-like structures are improved in the RoC in comparison to an RO cultured in the chip without RPE and conventional dish cultured ROs (*Figure 6f*). Using electron microscopy, we could find outer segment-like structures in all conditions (*Figure 6f*), displaying distinct disk formation (*Figure 6g*, exemplarily). However, in the RoC system (RoC), the number of outer segment structures was about three times higher than in RO chips without RPE (RoC w/o RPE) and in dish cultured ROs (*Figure 6h*). Interestingly, there was no difference observed in the RoC chip without RPE and dish culture, indicating a positive effect of the RPE on outer segment formation and preservation. In summary, the RoC increases the formation of outer segment-like structures on the RO without disturbing the normal survival and makeup of the organoid structure.

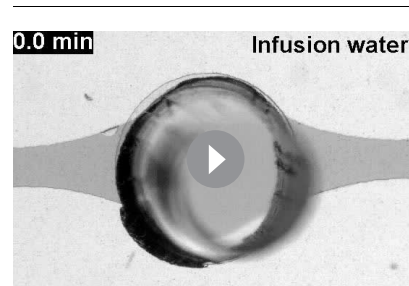
### Modeling key functionalities of the visual cycle

To assess whether the ROs and the RPE can reproduce principle retinal functionality on-chip, we first assessed the ability of the RO photoreceptors to produce an *in vivo* like calcium flux. Calcium ions ( $\text{Ca}^{2+}$ ) are fundamentally important for the function of photoreceptors and involved in many processes ranging from photodetection, transduction and synaptic transfer (reviewed in *Krizaj and Copenhagen, 2002*). To be able to monitor calcium transients and investigate photoreceptor metabolism and functionality, we established on-chip calcium imaging as an easy-to-perform read-out method. By loading RO and RPE on-chip with the calcium dye fura-2-AM, we were able to image calcium dynamics for individual photoreceptors or RPE cell ROIs over an extended timespan (*Figure 7—figure supplement 1*).

Second, we focused on one of the main functions of RPE, the phagocytosis of substances and cell remnants in the form of membrane stacks produced by the photoreceptors. The general capability of the hiPSC-RPE to perform phagocytosis was initially verified using bovine retinal outer segments (*Figure 7—figure supplement 2*). In the RoC platform, RPE cells were labeled by a promoter-driven GFP to mark cell bodies. By labeling the organoids with PNA lectin before the RoC was set up, segment structures were labeled and visualized (as described in *Figure 6a*). Already after 1 day in culture, PNA lectin-positive structures were found within the RPE cell bodies, indicating ongoing digestion of segment particles (*Figure 7a*). The composition of these particles was examined by immunostaining for rhodopsin (*Figure 7b*). This revealed that many of the lectin-positive particles found in the RPE cells were positive for rhodopsin. Next, we examined whether the particles taken up by the RPE are found in the early endosomes, which, in a later step, fuse to phagolysosomes for a full digestion. We labeled RPE cells prior to setting up the RoC with a GFP construct visualizing early endosome complexes (*Figure 7c*, red). After on-chip immunostaining of rhodopsin, specific colocalization of GFP-labeled early endosomes with rhodopsin-positive fragments was detected (*Figure 7c*).



**Video 1.** Bright field microscopy movie depicting the infusion of a colored liquid into a RoC previously perfused with color-less liquid (flow rate 20  $\mu\text{l/hr}$ ).  
DOI: <https://doi.org/10.7554/eLife.46188.014>



**Video 2.** Bright field microscopy movie depicting the wash-out of the colored liquid via perfusion with color-less liquid (flow rate 20  $\mu\text{l/hr}$ ).  
DOI: <https://doi.org/10.7554/eLife.46188.015>

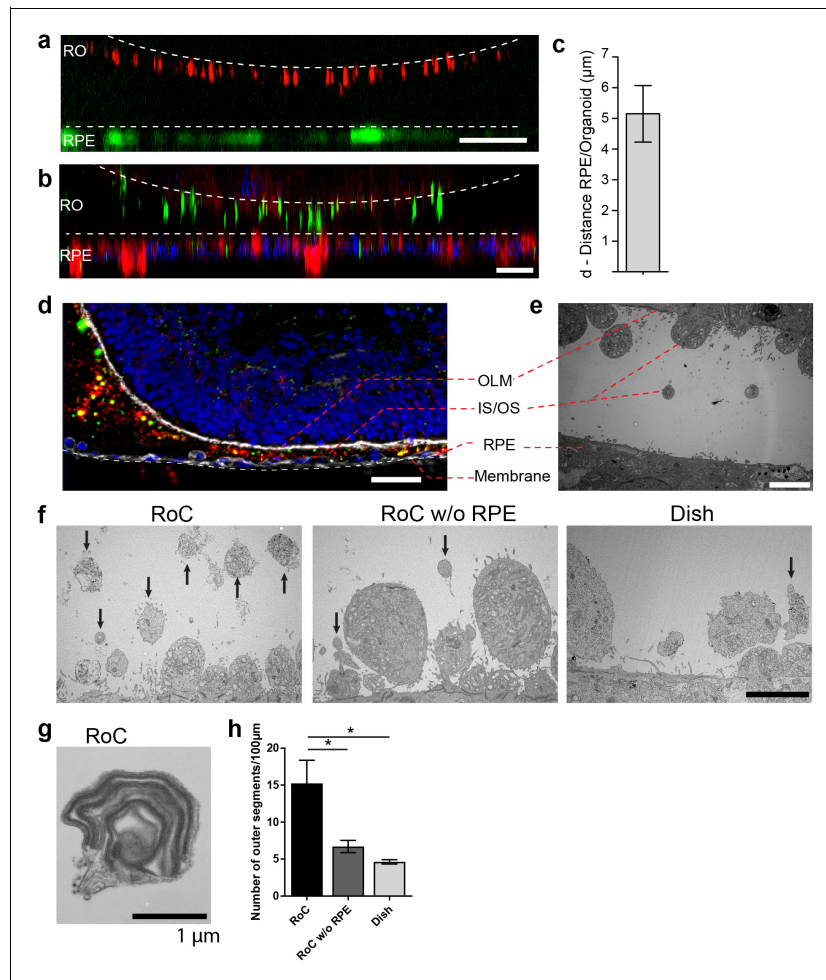


**Figure 6.** RO-RPE interaction enhances the outer segment number at the connection site. (a) For live-cell observation of RoCs, hiPSC-RPE was labeled with a pJG-IRBP-GFP viral vector prior co-culture (green); hiPSC-derived RO-ROPCs were labeled with PNA lectin Alexa Fluor 568 (red). RO-RPE interaction site is illustrated as an orthogonal view (b) Orthogonal view of RO (Day 181) and RPE co-cultured for 7 days in the RoC and subsequently stained in situ for rhodopsin (green) and phalloidin (red). c) Distance between GFP-labeled RPE and PNA lectin-stained segment tips in a) was assessed by measurement using orthogonal images (n = 12 chip compartments). (d) Representative cryosection from 7 days co-cultured day 260 ROs and hiPSC-RPE. Sections were immunostained with ROM1 (green; outer segment marker), phalloidin (white; cytoskeleton) and rhodopsin (red; rods). (e) Electron microscopic image of a day 190 organoid facing RPE cultured in the RoC. (f) Representative electron microscopic images of inner and outer segments on the surface of day 181 ROs cultured for 7 days in f1) the RoC, f2) the RoC without RPE and f3) dish-cultured ROs. Black arrows indicate outer segments identified by stack formation. (g) Exemplary high magnification image of an outer segment-like structure containing organized membrane disks found in day 181 ROs cultured for 7 days in the RoC with RPE. (h) Number of segments/100 μm RO circumference comparing RoC, RoC without RPE and dish cultured RO. In the RoC, only the RPE facing side was analyzed (n = 3 RoC, 4 RoC w/o RPE and 3 dish cultured ROs were analyzed). Bars indicate (a-b) 40 μm, (d) 40 μm, (e-f) 5 μm, (g) 1 μm. Blue: DAPI. IS = inner segment, OS = outer segment. Error Bars: S.E.M. \*p-value<0.05.

DOI: <https://doi.org/10.7554/eLife.46188.016>

The following source data and figure supplements are available for figure 6:

**Source data 1.** Source data for Figure 6c.

Figure 6 continued on next page

Figure 6 continued

DOI: <https://doi.org/10.7554/eLife.46188.019>

**Source data 2.** Source data for **Figure 6h**.

DOI: <https://doi.org/10.7554/eLife.46188.020>

**Figure supplement 1.** Comparison of dish and chip cultured human iPSC-derived retinal organoids.

DOI: <https://doi.org/10.7554/eLife.46188.017>

**Figure supplement 1—source data 1.** Source data for **Figure 6—figure supplement 1b**.

DOI: <https://doi.org/10.7554/eLife.46188.021>

**Figure supplement 2.** Comparison of cell death in RO cultured in the RoC or dish.

DOI: <https://doi.org/10.7554/eLife.46188.018>

Finally, we visualized the RPE endosomes in the RoC using electron microscopy. We examined day 7 RoCs, identifying indigested outer segment-like structures in the RPE (**Figure 7d**). Here, we found several membrane stack-structures in the RPE below the RO. These structures displayed multi-membrane formation (red arrow) as well as small round membrane structures, both strongly reminiscent of similar features found in outer segment-like structures in ROs (**Figure 7d**, right). Taken together, this strongly indicates functional indigestion of segment structures by the RPE, which is a major prerequisite for a functional visual cycle and therefore a physiological RPE-photoreceptor model.

### Evaluation of drug-induced retinopathy

In order to highlight the RoC's applicability for drug development and toxicology assessment, we exposed the system to the anti-malaria drug chloroquine (CQ) and the antibiotic gentamicin (GM), which both were previously shown to have pathological side effects on the retina (*Elman et al., 1976; Ding et al., 2016; Yusuf et al., 2017; Zemel et al., 1995; McDonald et al., 1986*).

After 3 days of on-chip culture, retinal tissue was exposed to two different concentrations of CQ (20  $\mu\text{g/ml}$  and 80  $\mu\text{g/ml}$ ) for three additional days. Concentrations were chosen based on previously described effects of CQ on cell viability using the RPE cell line ARPE-19 (*Chen et al., 2011*), and preliminary experiments using hiPSC-RPE for CQ treatment (**Figure 8—figure supplement 1**). Subsequent to the treatment, the RoCs were stained with propidium iodide (PI) to assess cell death (**Figure 8a**). Additionally, they were co-stained with the lysosomal marker protein LAMP2 (**Figure 8c**) since lysosomal dysfunction is involved in the pathophysiology of CQ (*Chen et al., 2011; Mahon et al., 2004; Rosenthal et al., 1978*). When RoCs were exposed to 20  $\mu\text{g/ml}$  CQ, no significant impact on cell viability (**Figure 8b**) and only a minor increase in LAMP2 signal (**Figure 8c**) were observed. However, at a concentration of 80  $\mu\text{g/ml}$ , cell viability was clearly impacted as shown by a significantly stronger PI staining (**Figure 8a,b**) compared to controls without CQ treatment. Furthermore, after exposure to 80  $\mu\text{g/ml}$  CQ, a strong LAMP2 signal was visible (**Figure 8c**), indicating an enlargement of lysosomes where the drug is accumulating and leading to lysosomal dysfunction. The increase in LAMP2 was not limited to the RPE but was also very pronounced in the RO (**Figure 8c**).

To assess the effect of GM, the antibiotic was added for 6 days to the RoC and to RoC without RPE (**Figure 8d,e**). In RoCs without RPE, an increase in cell death was observed at a GM concentration of 0.5 mg/ml (**Figure 8f**) and even more prominent in RoCs exposed to a 5-fold higher GM concentration (2.5 mg/ml), which was significant in comparison to the controls. In the complete RoC (RO and RPE), similar effects became apparent: The low GM concentrations led to a profound yet not significant increase in the PI signal, whereas the high concentration of 2.5 mg/ml GM led to a significant strong increase (**Figure 8g**). Since the quantified PI signal was a combined signal from cells in RPE and RO, we investigated whether the RO was affected differently by the drug when comparing the conditions with and without RPE (RoC and RoC w/o RPE). For that purpose, we subtracted the PI signal localized in the RPE from the calculated values of the entire RoC in the 0.5 mg/ml treated chips (**Figure 8h**). Interestingly, we found an increase of PI in the condition without RPE, but an unchanged PI signal in the RoC-cultured RO. This is in contrast to the results from the RoC without RPE, where a robust increase was observed when treating the chip with 0.5 mg/ml GM (**Figure 8h**). This could indicate a barrier or even protective function of the RPE, shielding the organoid from the drug and decreasing the toxic effects of the drug on the organoid.

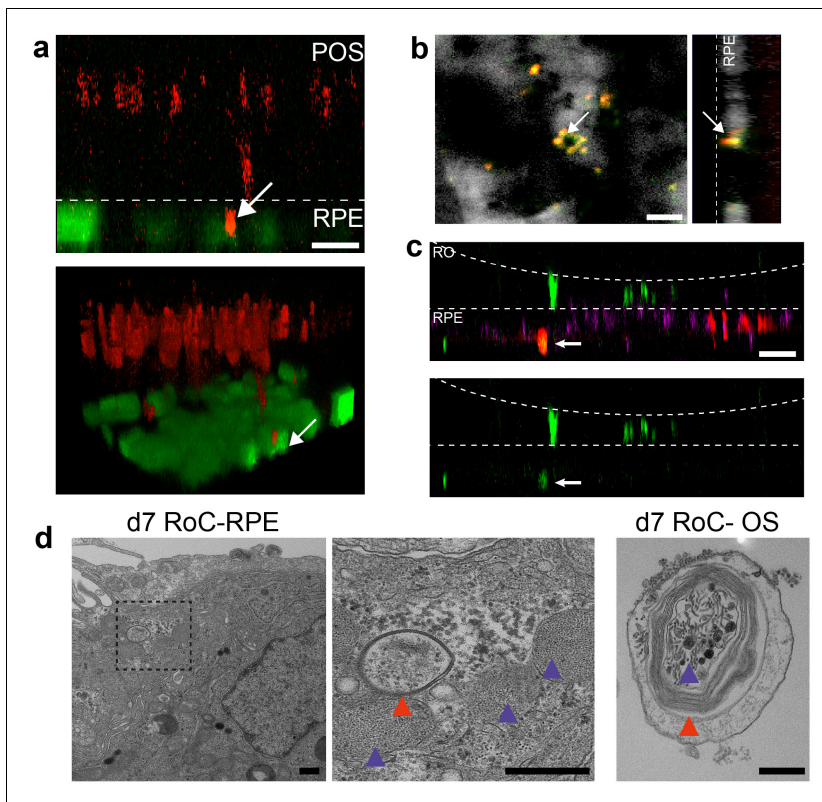


**Figure 7.** Interaction of RO and RPE in the RoC displays phagocytosis of outer segment-like structures. (a) Orthogonal view (x-z projection) and 3D reconstruction (bottom) of live-cell-monitored ROs and RPE at day 1 of RoC (RoC) culture. RO (red) and RPE (green) marked as described in [Figure 6a](#). Arrow indicates PNA lectin stained photoreceptor segment fragment internalization by RPE cells. (b) Samples, as described in a) stained with rhodopsin antibody (red) and PNA lectin (green). RPE (white). Arrows indicate PNA lectin-marked fragments which perfectly co-localize with rhodopsin. The left image shows a top-view; right image shows an orthogonal y-z projection (c) Immunofluorescence imaging of RoC (ROs at day 190 of differentiation). Previously to the chip culture, RPE cells were labeled with an early endosome-GFP construct (red). Chips were thereafter immunostained for rhodopsin (green). (d) Electron microscopic images of day 7 RoC. d1) shows RPE situated underneath the RO. d2) magnification of d1) as indicated by the dotted black square. d3) Outer segment-like structure in a day 7 RoC. Red and blue arrows indicate segment-disk structures within the RPE (d2) and the corresponding structures found in an RO outer segment (d3). Scale bars: (a) 10  $\mu\text{m}$ , (b) 10  $\mu\text{m}$ , (c) 50  $\mu\text{m}$ , (d) 500 nm Blue: DAPI.

DOI: <https://doi.org/10.7554/eLife.46188.022>

The following figure supplements are available for figure 7:

**Figure supplement 1.** Phagocytosis assay in dish cultured hiPSC-derived RPE.

DOI: <https://doi.org/10.7554/eLife.46188.023>

**Figure supplement 2.** Calcium-imaging in the RoC (at 370 nm) with ratiometric calcium indicator dye Fura-2.

DOI: <https://doi.org/10.7554/eLife.46188.024>

## Discussion

Microphysiological OoC platforms have the potential to revolutionize drug development and may provide new fundamental insights into development and disease. Over the last decade, bioengineering approaches have led to the development of functionally and structurally highly advanced MPSs for a variety of organs and tissues. To study degenerative retinal diseases and investigate retinal

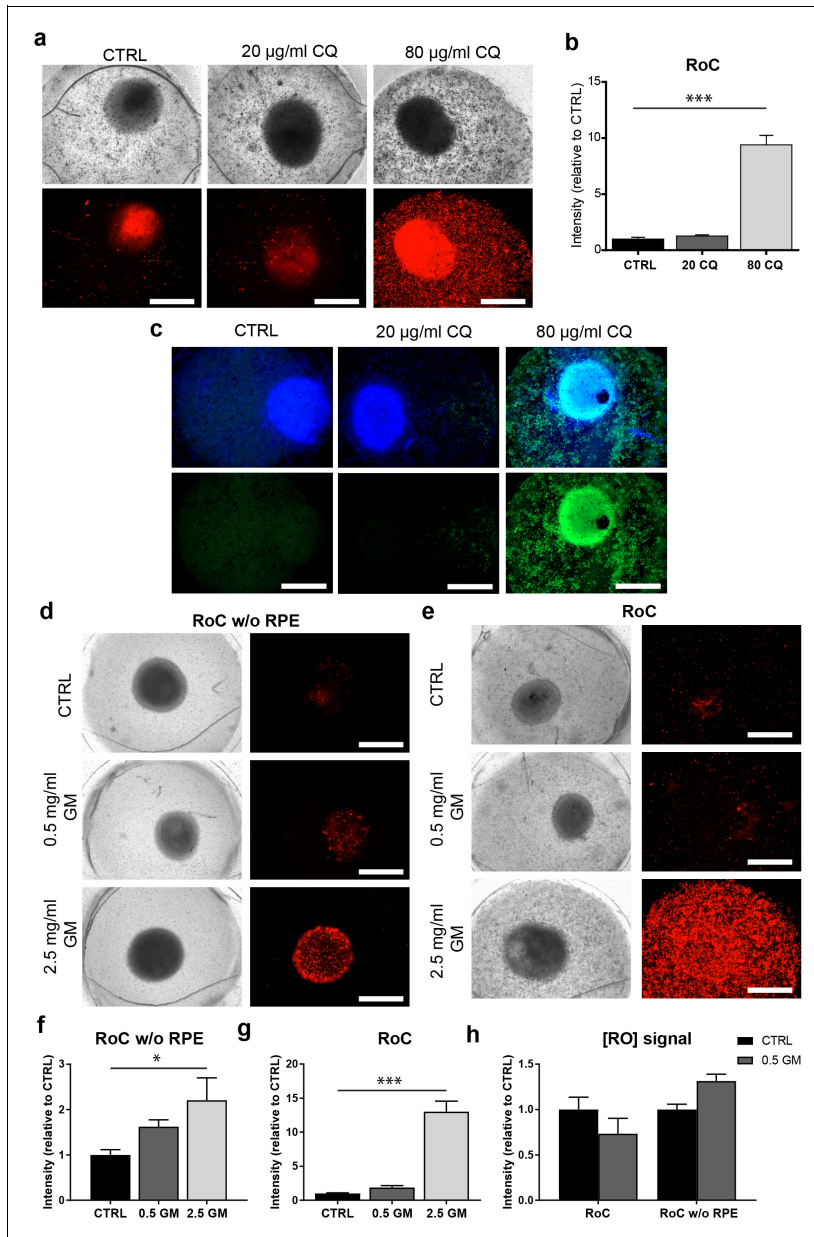


**Figure 8.** The RoC as a pharmacological testing platform. (a) Representative bright-field and fluorescence images of day 243–260 RO cultured in the RoC with RPE on day three after treatment with chloroquine (CQ). RoC were either not treated with chloroquine as control (CTRL), treated with 20  $\mu\text{g/ml}$  CQ or treated with 80  $\mu\text{g/ml}$  CQ for 3 days. On day 3, chips were stained with propidium iodide (PI) (red; cell death). (b) Quantification of fluorescence intensities of PI staining, relative to controls ( $n = 6\text{--}11$  chip compartments in three independent experiments). (c) Immunostaining with GM. *Figure 8 continued on next page*

Figure 8 continued

LAMP2 (green, lysosomes) and HOECHST (blue) after 3 days of drug testing of untreated RoCs (CTRL) and RoCs treated with 20  $\mu$ g/ml CQ or 80  $\mu$ g/ml CQ. (d) Representative bright-field and fluorescence images of day 202 RO cultured in the RoC without RPE. Cells were treated for 6 days with 0.5 mg/ml gentamicin, 2.5 mg/ml gentamicin or H<sub>2</sub>O (CTRL). On day 6, RoCs were stained with propidium iodide (PI) (red, cell death). (e) Representative bright-field and fluorescence images of day 202 RO cultured in the RoC. Cells were treated for six days with 0.5 mg/ml gentamicin, 2.5 mg/ml gentamicin or H<sub>2</sub>O (CTRL). On day 6, RoCs were stained with propidium iodide (PI) (red, cell death). (f) Quantification of fluorescence intensities of the PI signal of RO chip compartments without RPE relative to controls (n = 3 chip compartments per conditions). (g) Quantification of fluorescence intensities of the PI signal in the co-culture RoC relative to controls (n = 9 chips compartments per condition). (h) Comparison of the fluorescence intensities of PI staining of RO cultured in the RoC with (left bars) and without RPE (right bars) treated for 6 days with gentamicin (0.5 mg/ml) relative to their individual controls (CTRL). CQ = Chloroquine, GM = Gentamicin. HOECHST (blue; nuclei). Scale bars: 500  $\mu$ m. Error bars: S.E.M. \*p<0.05, \*\*\*p<0.001.

DOI: <https://doi.org/10.7554/eLife.46188.025>

The following source data and figure supplement are available for figure 8:

**Source data 1.** Source data for **Figure 8b**.

DOI: <https://doi.org/10.7554/eLife.46188.027>

**Source data 2.** Source data for **Figure 8f**.

DOI: <https://doi.org/10.7554/eLife.46188.028>

**Source data 3.** Source data for **Figure 8g**.

DOI: <https://doi.org/10.7554/eLife.46188.029>

**Source data 4.** Source data for **Figure 8h**.

DOI: <https://doi.org/10.7554/eLife.46188.030>

**Figure supplement 1.** Chloroquine applied on dish cultured hiPSC-RPE.

DOI: <https://doi.org/10.7554/eLife.46188.026>

toxicities, an MPS integrating physiologically relevant retinal tissue is of utmost importance. However, it is extremely challenging if not almost impossible to recapitulate the complex stratified (and interconnected) tissue architecture of the human retina solely using engineering approaches, commonly applied in the field. To create a 3D RoC, we addressed this challenge by combining the biological self-assembly capabilities of ROs with the precisely controllable assembly in microfabricated modules provided by engineering strategies. This combination of interdisciplinary approaches enabled us to successfully create a complex multi-layer structure that includes all cell types and layers present in the neuroretinal ROs, connected to an RPE layer. All integrated cell types were thereby derived from the same hiPSCs. For the first time, we demonstrate a retina model successfully recapitulating the precisely orchestrated interaction between photoreceptors and RPE in vitro. This interaction is one of the key characteristics of the visual cycle, and the RPE is essential for the normal function and survival of photoreceptors, for example via an active phagocytic uptake of photoreceptor outer segments (POS) (Kevany and Palczewski, 2010). In addition, the microfluidic concept of the RoC adds a further important aspect, the vasculature-like perfusion. The precisely controllable perfusion enables the generation of a physiological transport (both towards and away from the tissue) of nutrients, compounds, and metabolic products, the maintenance of stable, constant conditions over long time-periods (e.g. nutrient and metabolites levels/gradients), as well as the capability to probe the secretome and metabolome in a time-resolved manner. Moreover, it makes the system amenable for the interconnection with further organ-systems enabling the study of for example systemic effects. The applicability of the RoC for compound screening and toxicological studies was demonstrated by i) the successful recapitulation of side-effects of the anti-malaria drug chloroquine and ii) the mimicry of gentamicin-induced retinopathy revealing a protective effect of the RPE barrier. Both the tight barrier function of the RPE layer as well as the melanin-binding of GM (known to be protective in ocular pigmented vs. albino animals (Zemel et al., 1995) could be the source of this protective effect.

In comparison to the conventionally employed retinal model system, the introduced RoC features a variety of advantages and novel potential:

Traditional monolayer cell culture assays have been of limited value in retinal research as they solely include certain cell subtypes, thereby providing a restricted physiological relevance. The more complex ROs solved this issue partially (Zhong et al., 2014), but were still limited due to the absence of functional interaction with the RPE. Attempts in recreating the retinal niche in the past have failed to recapitulate the precise RPE-PR arrangement, and thus, did not yield matured

photoreceptors with large formations of membrane disk-containing outer segments. The RoC platform is able to mimic this particular niche and a physiological interaction of RPE and photoreceptor outer segments (POS), by embedding ROs and RPE in the hyaluronic-based hydrogel in specifically tailored microfluidic chambers. This arrangement is much more physiological and controlled than previous approaches employing an unpredictable and unorganized RPE formation during RO generation. This interphotoreceptor matrix in the RoC provides mechanical stability for the small and fragile developing POS, which would otherwise either be damaged or prevented from outgrowth as in conventional suspension cultures. In the RoC, hence, numerous outer segments facing towards the RPE were formed. The flexible and highly controlled tissue assembly paves the way for the modeling of a variety of disease states, for example by combining ROs derived from patients suffering from retinal diseases with RPE derived from the same or healthy donors.

Post-mortem human retinal explants are the only human models that are currently available and achieve a comparable level of complexity. Those ex-vivo models are, however, greatly limited in terms of supply, with respect to long-term culture, and due to inter-patient variability. Moreover, they are not applicable for studies targeting developmental aspects. The introduced RoC system is entirely based on hiPSCs that are easy to expand and to cryo-conserve. This not only avoids the problem of limited supply but also provides the capability to create a multitude of genetically identical systems and sets the foundation for a scale-up to higher throughput systems, provided an appropriate framework and an automated process landscape is established (Probst *et al.*, 2018). The hiPSC technology further paves the way for the generation of disease-specific as well as patient-specific models opening up future applications in disease modeling and personalized medicine. Additionally, hiPSC derived ROs exhibit the ability to stay viable for more than a year in vitro. This is a crucial aspect in terms of answering developmental aspects, studying disease initialization and progression as well as assessing long-term effects or side effects of drugs.

Both current in vitro and ex vivo models share one major limitation, the lack of vascularization or vasculature-like perfusion. This aspect of the microfluidic RoC adds a further dimension of physiological relevance and advantage over the conventional models as described above.

Animal models are so far the only model systems that feature a blood circulation as well as a structural tissue complexity. Yet, besides issues of ethical concerns, results from animal models are often not translatable to humans as none of the small animals used in the field of retina research is able to fully represent the human retinal system. The human genetic background and recapitulation of human retinal tissue structure, hence, provide the potential for the RoC model to overcome those translation hurdles. Animal models, however, still possess structural elements of the visual systems, for example, optical nerve and inner blood-retinal barrier, which cannot be re-created in vitro, so far.

Taken together, the introduced RoC represents a highly advanced in vitro model, which is not hampered by many of the limitations of conventional (in vitro, ex vivo, in vivo) model systems and which can be the first step towards the reduction and replacement of animal models in the field of ophthalmology. Further development will target challenges of innervation (addition of an optical nerve), incorporation of blood-retinal barriers, the integration into multi-organ platforms, as well as the generation of disease-specific systems.

### Summary

The scarce availability of physiologically relevant in vitro models of the human retina and the limited capability of animal models to recapitulate physiological human responses have i) hampered the development of potential new drugs to treat degenerative diseases such as Stargardt disease, age-related macular degeneration or retinitis pigmentosa and ii) prevented the detection of retinal toxicities early in the drug pipeline. By combining hiPSC-ROs and -RPE cells in a microphysiological environment, the introduced human RoC system provides a physiologically relevant model system that recapitulates key functionalities of the human retina, which are impaired in patients suffering from retinal degeneration. Due to a toolbox of in situ and ex-situ analysis options, the platform is extremely versatile and features potential applications for drug development, toxicity screening, disease modeling, and personalized medicine.

Materials and methods

Key resources table

Reagent type (species) or resource	Designation	Source or reference	Identifiers	Additional information
Antibody	Donkey anti-Mouse IgG Secondary Antibody Alexa Fluor 488, polyclonal	ThermoFisher Scientific	Cat.# R37114 RRID:AB_2556542	IHC(1:1000)
Antibody	Donkey anti-Mouse IgG Secondary Antibody Alexa Fluor 568, polyclonal	ThermoFisher Scientific	Cat.# A10037 RRID:AB_2534013	IHC(1:1000)
Antibody	Donkey anti-Mouse IgG Secondary Antibody Alexa Fluor 647, polyclonal	ThermoFisher Scientific	Cat.# A-31571 RRID:AB_162542	IHC(1:1000)
Antibody	Donkey anti-Goat IgG Secondary Antibody Alexa Fluor 488, polyclonal	ThermoFisher Scientific	Cat.# A-11055 RRID:AB_2534102	IHC(1:1000)
Antibody	Donkey anti-Goat IgG Secondary Antibody Alexa Fluor 568, polyclonal	ThermoFisher Scientific	Cat.# A-11057 RRID:AB_142581	IHC(1:1000)
Antibody	Donkey anti-Goat IgG Secondary Antibody Alexa Fluor 647, polyclonal	ThermoFisher Scientific	Cat.# A-21447 RRID:AB_141844	IHC(1:1000)
Antibody	Donkey anti-Rabbit IgG Secondary Antibody Alexa Fluor 488, polyclonal	ThermoFisher Scientific	Cat.# R37118 RRID:AB_2556546	IHC(1:1000)
Antibody	Donkey anti-Rabbit IgG Secondary Antibody Alexa Fluor 568, polyclonal	ThermoFisher Scientific	Cat.# A10042 RRID:AB_2534017	IHC(1:1000)
Antibody	Donkey anti-Rabbit IgG Secondary Antibody Alexa Fluor 647, polyclonal	ThermoFisher Scientific	Cat.# A-31573 RRID:AB_2536183	IHC(1:1000)
Antibody	Mouse anti-AP2 $\alpha$ , monoclonal	Santa Cruz Biotechnology	Cat.# sc-12726 RRID:AB_667767	IHC(1:100)
Antibody	Goat anti-Arrestin 3 (Cone Arrestin), polyclonal	Santa Cruz Biotechnology	Cat.# sc-54355 RRID:AB_2060084	IHC(1:50)
Antibody	Goat anti-Brn-3b, polyclonal	Santa Cruz Biotechnology	Cat.# sc-31989 RRID:AB_2167523	IHC(1:50)
Antibody	Goat anti-Chx10, polyclonal	Santa Cruz Biotechnology	Cat.# sc-21690 RRID:AB_2216006	IHC(1:200)
Antibody	Mouse anti-CRALBP, monoclonal	Abcam	Cat.# ab15051 RRID:AB_2269474	IHC(1:250)
Antibody	Mouse anti-EEA1, monoclonal	ThermoFisher Scientific	Cat.# 14-9114-80 RRID:AB_2572928	IHC(1:500)
Antibody	Rabbit anti-Ezrin, polyclonal	Cell Signaling	Cat.# 3145S RRID:AB_2100309	IHC(1:200)
Antibody	Mouse anti-LAMP2, monoclonal	Santa Cruz Biotechnology	Cat.# sc18822 RRID:AB_626858	IHC(1:50)
Antibody	Mouse anti-Melanoma-gp100, monoclonal	Abcam	Cat.# ab787 RRID:AB_306146	IHC(1:100)
Antibody	Mouse anti-MITF, monoclonal	Exalpha Biologicals	Cat.# X1405M	IHC(1:500)
Antibody	Rabbit anti-Pax-6, polyclonal	Covance	Cat.# PRB-278P-100 RRID:AB_291612	IHC(1:100)
Antibody	Rabbit anti-PKC $\alpha$ , polyclonal	Santa Cruz Biotechnology	Cat.# sc-208 RRID:AB_2168668	IHC(1:500)

Continued on next page

Continued

Reagent type (species) or resource	Designation	Source or reference	Identifiers	Additional information
Antibody	Mouse anti-Rhodopsin, monoclonal	Santa Cruz Biotechnology	Cat.# sc-57432 RRID:AB_785511	IHC(1:200)
Antibody	Rabbit anti-ROM1, polyclonal	Proteintech	Cat.# 21984-1-AP	IHC(1:200)
Antibody	Mouse anti-RPE65, monoclonal	Abcam	Cat.# ab78036 RRID:AB_1566691	IHC(1:100)
Antibody	Rabbit anti-Opsin, blue, polyclonal	Merck Millipore	Cat.# ab5407 RRID:AB_177457	IHC(1:200)
Antibody	Rabbit anti-ZO-1, polyclonal	ThermoFisher Scientific	Cat.# 61-7300 RRID:AB_138452	IHC(1:100)
Commercial assay or kit	TUNEL Assay (Click-iT TUNEL Alexa Fluor 488 Imaging Assay)	ThermoFisher Scientific	Cat.# C10245	
Commercial assay or kit	CellLight Early Endosomes-GFP, BacMam 2.0	ThermoFisher Scientific	Cat.# C10586	
Commercial assay or kit	VEGF-A Human ELISA Kit	ThermoFisher Scientific	Cat.# BMS277-2	
Chemical compound, drug	Alexa Fluor 647 Phalloidin	ThermoFisher Scientific	Cat.# A12379	1:500
Chemical compound, drug	PNA lectin-Alexa Fluor 568	ThermoFisher Scientific	Cat.# L32458	20 µg/ml
Chemical compound, drug	PNA lectin-Alexa Fluor 647	ThermoFisher Scientific	Cat.# L32460	20 µg/ml
Chemical compound, drug	Recombinant Human TGF-β1	Peptotech	Cat.# 100-21	
Chemical compound, drug	HOECHST 33342	ThermoFisher Scientific	Cat.#H3570	1:2000
Chemical compound, drug	Chloroquine	Sigma-Aldrich	Cat.#C6628	
Chemical compound, drug	Gentamicin	Sigma-Aldrich	Cat.#G1397	
Recombinant DNA reagent	pJG-IRPB-eGFP	Department of Biological Structure, University of Washington ( <a href="https://faculty.washington.edu/tomreh/">https://faculty.washington.edu/tomreh/</a> )		
Software, algorithm	COMSOL Multiphysics	COMSOL Multiphysics	RRID:SCR_014767	
Software, algorithm	Prism	GraphPad	RRID:SCR_002798	
Software, algorithm	FIJI		RRID:SCR_002285	

### Fabrication of retina MPS

The RoC consists of two Polydimethylsiloxane (PDMS) layers and a porous Polyethylene terephthalate (PET) membrane in between, bonded to a thin glass slide (170 µm). First, PDMS master molds were fabricated. For the media channel mold, SU8-50 photoresist (MicroChem, USA) was spin-coated onto a previously cleaned 4" silicon wafer to obtain a height of 100 µm. To create the desired structure, the substrate was exposed to 350 mJ/cm<sup>2</sup> of UV light, followed by development in SU-8 developer (Microresist Technology GmbH, Germany) for 6 min. Finally, the wafer was rinsed with isopropanol and blow-dried using nitrogen. The second wafer for RO and RPE culture was fabricated in two steps. Initially, a base layer of 25 µm for the membrane insert was fabricated by spin-coating a first layer of photoresist SU8. The exposure to UV light, in this case, was 200 mJ/cm<sup>2</sup>. Subsequently,

the wafer was developed in SU-8 developer for 4 min, rinsed in isopropanol and blow-dried with nitrogen. Next, the wafer was coated with a second layer of SU-8-3025 to fabricate the tissue channels with a height of 40  $\mu\text{m}$ . The wafer was exposed to UV light at 250  $\text{mJ}/\text{cm}^2$  for 10 s and developed for 4 min. Afterward, both master molds were silanized with chlorotrimethylsilane (Sigma-Aldrich, Germany). Subsequently, Sylgard 184 PDMS (Dow Corning, USA) was mixed at a 10:1 ratio of prepolymer to curing agent and molded by using the wafers as a negative master mold. The layer for the media supply was made by exclusion molding followed by curing overnight at 60°C. The RO/RPE culture layer was fabricated by pouring 25 g of the PDMS mixture onto the master mold and curing it overnight at 60°C. Next, the PDMS slabs were peeled off the wafers and the media-supply layers were bonded to a glass slide previously cleaned by a 30 s exposure to oxygen plasma at 50 Watts. Inlets and outlets were punched using a biopsy puncher with a diameter of 0.75 mm. To culture the cells and organoids, four chambers were punched out of the PDMS with a biopsy puncher of 2 mm diameter. Semipermeable membranes with a diameter of 20 mm, made from PET (Sabeu GmbH, Germany) with a pore diameter of 3  $\mu\text{m}$  and a thickness of 10–20  $\mu\text{m}$ , were functionalized using bis-[3-trimethoxysilypropyl]amine (Sigma-Aldrich, Germany). Before assembly, both PDMS layers were cleaned with isopropanol and Scotch tape to remove dust particles. Afterwards, both layers were treated with oxygen plasma at 50 W for 30 s. Then, the membrane was placed into the inlay of the RO/RPE culture layer. Finally, both layers were aligned to each other using a stereo microscope and baked overnight at 60°C to stabilize bonding.

## Cell culture

### iPSC Culture

All hiPSC cell lines were derived from healthy donors as previously described (Linta *et al.*, 2012) and tested for stem cell markers and germ-layer differentiation potential. HiPSCs were cultured on Matrigel (hESC-qualified, BD Biosciences, USA)-coated plates with FTDA medium (Frank *et al.*, 2012). Cells were passaged every 6–7 days using Dispase (Stemcell Technologies, Canada). Differentiated colonies were removed manually by scraping. All procedures were in accordance with the Helsinki convention and approved by the Ethical Committee of the Eberhard Karls University Tübingen (Nr. 678/2017BO2). Control persons gave their written consent.

### Retinal organoid culture

HiPSC-derived RO were differentiated based on a protocol by Zhong *et al.* (2014) with some modifications. Briefly, for embryoid body (EB) formation,  $2.88 \times 10^6$  hiPSCs were detached on day 0 using TrypLE (ThermoFisher Scientific, USA) and dissociated to single cells. Cells were then mixed with PeproGrow (PeproTech, USA) medium, 10  $\mu\text{M}$  Y-27632 (ROCK-inhibitor, Ascent Scientific, USA) and 10  $\mu\text{M}$  blebbistatin (Sigma-Aldrich, USA) and distributed to 96 untreated v-shaped 96-wells (Sarstedt, Germany). For re-aggregation, the plate was centrifuged at 400 g for 4 min. On day 1, 80% of the medium was removed and replaced with N2 medium (DMEM/F12 (1:1)+Glutamax supplement (ThermoFisher Scientific, USA), 24 nM sodium selenite (Sigma-Aldrich, USA), 16 nM progesterone (Sigma-Aldrich, USA), 80  $\mu\text{g}/\text{ml}$  human holotransferrin (Serologicals, USA), 20  $\mu\text{g}/\text{ml}$  human recombinant insulin (Sigma-Aldrich), 88  $\mu\text{M}$  putrescine (Sigma-Aldrich, USA), 1x minimum essential media-non essential amino acids (NEAA, ThermoFisher Scientific, USA), 1x antibiotics-antimycotics (AA, ThermoFisher Scientific, USA)). Medium was changed again on day 4. On day 7, EBs were plated on Growth-Factor-Reduced Matrigel (BD Biosciences, USA)-coated six well plates at a density of 32 EBs/well and medium was changed daily. On day 16, medium was switched to a B27-based Retinal differentiation medium (BRDM) (DMEM/F12 (3:1) with 2% B27 (w/o vitamin A, ThermoFisher Scientific, USA), 1x NEAA and 1x AA). On day 24, eye fields were detached using 10  $\mu\text{l}$  tips and collected in 10 cm bacterial petri dishes (Greiner Bio One, Germany) with BRDM, adding 10  $\mu\text{M}$  ROCK-Inhibitor Y-27632 for one day. After completed formation, ROs were selected and if necessary detached from non-retinal spheres using microscissors. From day 40 onwards, ROs in BRDM were supplemented with 10% fetal bovine serum (FBS, Thermo Fisher Scientific, USA) and 100  $\mu\text{M}$  taurine (Sigma-Aldrich, USA). From day 70–100, BRDM with FBS and taurine was further supplemented with 1  $\mu\text{M}$  retinoic acid (Sigma-Aldrich, USA), which was reduced to 0.5  $\mu\text{M}$  during days 100–190 and removed afterwards.

### Differentiation of retinal pigment epithelial cells

RPE cells were derived as a product from RO differentiation following (slightly adapted) procedures of *Zhong et al. (2014)* and *Ohlemacher et al. (2015)*. For this purpose, pigmented areas or spheres were removed from ROs using microscissors under an inverted microscope. The pigmented areas were collected in 1.5 ml Eppendorf tubes (Eppendorf, Germany) and washed once with Dulbecco's phosphate-buffered saline (PBS, no calcium, no magnesium, Thermo Fisher Scientific, USA). To dissociate the RPE into single cells for adhesion culture, the pigmented spheres were treated with Accumax (Sigma-Aldrich, USA) for 90 min at 37°C and 5% CO<sub>2</sub> and resuspended every 30 min using a 100 µl pipette. The reaction was stopped using BRDM with 10% FBS followed by centrifugation at 1500 rpm for 2 min. The derived single RPE-cells were plated on 6-well plates or coverslips in 24-well plates, treated with a 0.01% Poly-L-Ornithine Solution (Sigma-Aldrich, USA) for 30 min at room temperature and 20 µg/ml Laminin (Roche, Switzerland) for 4 hr at 37°C and 5% CO<sub>2</sub>. For the plating of the cells, BRDM was supplemented with 20 µg/ml EGF (Cell Guidance Systems, United Kingdom), 20 µg/ml FGF2 (Cell Guidance Systems, United Kingdom), 2 µg/ml heparin (Sigma-Aldrich, USA), and 10 µM Y-27632 (ROCK-inhibitor, Ascent Scientific, USA) (*Ohlemacher et al., 2015; Croze et al., 2014*). In addition, for the first 24 hr, 10% FBS (Thermo Fisher Scientific, USA) was added to achieve adherence of the cells. When cells had reached confluence, medium was switched to BRDM without supplementation.

### Transduction of RPE cells

To generate green fluorescent iPSC-RPE lines, adherent RPE cultures were incubated with lentiviral particles generated from pJG-IRPB-eGFP plasmids (*Lamba et al., 2010*) (Gift from Deepak Lamba, Thomas Reh) in BRDM + 10% FBS for one day, washed three times with PBS and further cultivated in BRDM.

### RoC culture

Individual systems were sterilized via oxygen plasma treatment for 3 min at 50 Watts and placed into PBS-filled 50 ml tubes to displace the air in the channels. Before seeding hiPSC-RPE cells into the MPS, each system was removed from the tube, carefully dried with a paper towel and placed into a 10 cm dish. Each well was coated for 2 hr with 50 µg/ml Laminin in DMEM/F12 at 37°C and 5% CO<sub>2</sub>. RPE cells were detached and dissociated using Accumax at 37°C and 5% CO<sub>2</sub> for 10–40 min, depending on the adherence and passage of the cells. To remove cell agglomerates, a 70 µm cell strainer was used. As a next step, each well was seeded with RPE at a density of 27 000 cells in a volume of 4.5 µl BRDM supplemented with 10% FBS. RoC were incubated for at least 2 hr at 37°C and 5% CO<sub>2</sub> to allow RPE cells to adhere to the semipermeable membrane. The medium was changed every day for 1–3 days prior ROs were loaded into the RoCs. ROs were placed onto the RPE covered membrane. Hyaluronic acid-based hydrogel HyStem-C (ESI Bio, USA) was prepared according to the manual and added to the well by pipetting. During culture, the chambers were covered by a sterile adhesive tape (optical adhesive covers, Thermo Fisher Scientific, USA) to avoid evaporation. BRDM supplemented with 100 µM taurine and 10% FBS was supplied at a constant flow rate of 20 µl/h by syringe pump.

### Drug treatment

RPE and ROs were seeded into the RoC as described above. Subsequently, ROs and RPE were either treated for three days with 20 and 80 µg/ml chloroquine (Sigma-Aldrich, USA) in BRDM using a syringe pump at a flow rate of 30 µl/h or with 0.5 mg/ml and 2 mg/ml Gentamicin (Sigma-Aldrich, USA) for 6 days. For every treatment, control RoCs were also used, without addition of equal amounts of the solvent (H<sub>2</sub>O). After 3 days of treatment, cells in the RoCs were stained using HOECHST (Thermo Fisher Scientific, USA) and 3 µM propidium iodide (PI, Sigma Aldrich, USA) to assess cell death. RoCs were washed twice with PBS using a syringe and fixed with 4% PFA for immunohistochemical staining of LAMP2.

### Phagocytosis assay using bovine ROS

Bovine rod outer segments were isolated as previously described (*Vogt et al., 2013*). For the phagocytosis assay out-of-the-chip, hiPSC-RPE was plated on cover slips after coating with 0.01% Poly-L-Ornithine Solution and Laminin as described above. For the phagocytosis assay in the RPE-

chip, RPE was loaded as described above into the Laminin-coated wells. On the next day, hiPSC-RPE on coverslips or in the chip were incubated with bovine photoreceptor outer segments (POS) at a density of 10 POS/RPE in BRDM for 2 hr at 37°C, then washed with PBS 3x and cultivated for additional 2 hr in BRDM and then fixed with 4% paraformaldehyde (Carl Roth, Germany) and 10% sucrose (Carl Roth, Germany) in PBS for 20 min at room temperature for immunohistochemistry.

### VEGF-A secretion assays

Specialized double-channel RoCs were generated for apical and basal secretion measurement. These chips were identical with the previously described setup, except that an additional channel was included (apical channel) connecting the compartments, with an additional in- and outlet that allows media flow above the RPE layer, in addition to the media flow below. These double-channel chips were loaded with RPE cells as described and then cultivated for 14 days using a syringe pump. Effluent from the upper and lower-channel outlet were collected after 24 hr. The apical and basal media were analyzed from three different chips and initial volumina were noted for calculation of the total substance quantity per chip on the apical or basal side.

Stimulation of VEGF-A secretion was measured in regular RoC platforms. To acquire comparable samples, the effluent was collected over 2 hr resulting in 100  $\mu$ l volumes (flow rate of 50  $\mu$ l/h). The effluent was collected once before TGF- $\beta$ 1 exposure to measure the baseline secretion of VEGF-A. Subsequently, the RoCs were perfused with medium containing 10 ng/ml TGF- $\beta$ 1 (PeproTech, USA). Samples were collected every 2 hr for 12 hr and once after 24 hr. After 24 hr, TGF- $\beta$ 1 was removed from the medium and samples were collected at the 36 and 48 hr time-points, 12 and 24 hr after starting the washout, respectively.

The collected samples were immediately frozen at  $-20^{\circ}\text{C}$ . The concentration of VEGF-A was measured after defrosting the samples using the VEGF-A Human ELISA Kit (Thermo Fisher Scientific, USA). The assay was performed according to the manufacturer's protocol and absorbance was measured at 450 nm.

### Live cell labeling of hiPSC retinal organoids

For live cell labeling of RO photoreceptor segments, ROs were incubated in a reaction tube for 30 min in BRDM containing 20  $\mu$ g/ml PNA lectin-Alexa Fluor 568 (Thermo Fisher Scientific, USA) or PNA lectin-Alexa Fluor 647 (Thermo Fisher Scientific, USA) followed by washing with medium four times, prior to the transfer into the RoC.

### Live cell endocytosis and phagocytosis assay

For live cell endocytosis experiments, RPE cells were infected overnight with 10 particles/cell of Cell-Light Early-Endosomes GFP (BacMam 2.0, Thermo Fisher Scientific, USA) prior to the seeding of RPE into the RoC. Endosome labeling could be detected for >5 days.

### Production of agarose RoCs and cryoembedding

Agarose RoCs were produced from an in-house fabricated mold using 4% Agarose/BRDM + 10% FBS containing four separate compartments and a semipermeable membrane (as described in the MPS section) at the bottom of each well. RPE and ROs were loaded into the agarose RoCs as already described. For fixation, agarose RoCs were fixed in 4% paraformaldehyde in 0.1 M phosphate buffered saline (pH 7.4) (Polysciences, Warrington Pa., USA) for 2 hr. ROs from classic dish culture were washed with PBS and fixed with 4% paraformaldehyde and 10% sucrose in PBS for 20 min at room temperature, then kept in PBS at 4°C.

After rinsing in PBS, agarose RoCs or RO were cryoprotected in graded sucrose/PBS (10% for 30 min, 20% for 1 hr, 30% overnight), embedded in cryomatrix (Tissue-Tek O.C.T. Compound, Sakura, Netherlands) and frozen in liquid nitrogen. Cryosections (14  $\mu$ m) were cut on a Leica CM 3050 s Cryocut, mounted on Superfrost glass slides, and stored at  $-20^{\circ}\text{C}$ .

### Transmission electron microscopy

For transmission electron microscopy, agarose RoCs with ROs and RPE were fixed in the chambers with Karnovsky buffer (2.5% glutaraldehyde, 2% paraformaldehyde, 0.1 M sodium cacodylate buffer, pH 7.4) (Electron Microscopy Sciences, Germany) for 12 hr at 4°C. After fixation, the samples were

rinsed three times in 0.1 M sodium cacodylate buffer (pH 7.4, Electron Microscopy Sciences, Germany) for a total of 30 min, and postfixed in 1% OsO<sub>4</sub> (Electron Microscopy Sciences, Germany) for 1.5 hr at room temperature. After three additional washes in cacodylate buffer and dehydration in 50% ethanol, tissues were counterstained with 6% uranyl acetate dissolved in 70% ethanol (Serva, Germany) followed by graded ethanol concentrations of ethanol (80% and 96% for 15 min each, 100% for two times 10 min, acetone 100%, 15 min). The dehydrated samples were incubated in a 2:1 and 1:1 mixture of acetone and Epon resin (Serva, Germany) for 1 hr each, on a shaker. Finally, organoids were infiltrated with pure Epon and polymerized by overnight incubation at 60°C. The next day, ROs and RPE were punched out of the chambers. Upon punches containing RPE-filter and ROs were embedded in fresh resin in flat molds (Science Services, Germany) and cured 12 hr at 60°C followed by 2 hr at 90°C.

Ultrathin sections (50 nm) were cut on a Reichert Ultracut S (Leica, Germany), collected on copper grids and counterstained with Reynolds lead citrate. Sections were analyzed with a Zeiss EM 900 transmission electron microscope (Zeiss, Germany) equipped with a 2k × 2k CCD camera.

Images were used for quantification of outer segment density using an image analysis software (iTEM, Olympus Soft Imaging Solutions, Germany). To calculate the ratio of outer segments per μm organoid surface, a line was drawn and measured along the outer limiting membrane of the organoid and outer segment structures visible along the line were counted.

### Immunohistochemistry

For in situ chip staining, whole-mount staining was performed using a blocking solution of 5% or 10% normal donkey serum (Millipore, USA) with 0.2% triton-X (Carl Roth, Karlsruhe, Germany) for permeabilization, twice for 1 hr. Primary antibodies were added to the blocking solution for 1 or 2 days at 4°C, then secondary antibodies were added in blocking solution overnight at 4°C. Next, ROs were counterstained with HOECHST 33342 for 10 min at room temperature (1:2000, Thermo Fisher Scientific, USA). Washing steps to remove residual antibodies were performed with PBS, three times for 2 hr at room temperature after incubation of primary and secondary antibodies, as well as after HOECHST staining.

Cryosections from agarose-chips and ROs were rehydrated in PBS for 15 min and incubated in a blocking solution of 10% normal donkey serum in PBS with 0.2% triton-X for 1 hr. Wholemount ROs were incubated in a blocking solution of 10% normal donkey serum in PBS with 0.2% triton-X for 1 hr. Primary antibodies were diluted in blocking solution and incubated overnight at 4°C. Secondary antibodies were diluted in 1:1 blocking solution:PBS and incubated for 2 hr at room temperature. Mounting was performed with ProLong Gold Antifade Reagent with DAPI (Thermo Fisher Scientific, USA). Washing steps to remove residual antibodies were performed with PBS, three times for 3 min at room temperature after primary and secondary antibodies.

Cells grown on glass coverslip were washed with PBS and fixed with 4% paraformaldehyde and 10% sucrose in PBS for 20 min at room temperature, then kept in PBS at 4°C. For blocking and permeabilization, cover slips were incubated with 5% normal donkey serum and 0.2% triton-X for 1 hr. Primary antibodies were diluted in blocking solution and incubated overnight at 4°C. Secondary antibodies were diluted in blocking solution and incubated for 2 hr at room temperature. Mounting was performed with ProLong Gold Antifade Reagent with DAPI (Thermo Fisher Scientific, USA). Washing steps to remove residual antibodies were performed with PBS, three times for 5 min at room temperature after primary and secondary antibodies.

For LAMP-2 stainings, 0.5% saponin (Millipore, USA) was used instead of Triton-X and washing steps were performed using 0.1% saponin in PBS instead of using only PBS.

Antibodies used were:

Secondary Antibodies:

- Donkey anti-Mouse Alexa Fluor 488 (1:1000, R37114, Thermo Fisher Scientific, USA)
- Donkey anti-Mouse Alexa Fluor 568 (1:1000, A10037, Thermo Fisher Scientific, USA)
- Donkey anti-Mouse Alexa Fluor 647 (1:1000, A-31571, Thermo Fisher Scientific, USA)
- Donkey anti-Goat Alexa Fluor 488 (1:1000, A-11055, Thermo Fisher Scientific, USA)
- Donkey anti-Goat Alexa Fluor 568 (1:1000, A-11057, Thermo Fisher Scientific, USA)
- Donkey anti-Goat Alexa Fluor 647 (1:1000, A-21447, Thermo Fisher Scientific, USA)
- Donkey anti-Rabbit IgG (H + L) Alexa Fluor 488 (1:1000, R37118, Thermo Fisher Scientific, USA)

- Donkey anti-Rabbit IgG (H + L) Alexa Fluor 568 (1:1000, A10042, Thermo Fisher Scientific, USA)
- Donkey anti-Rabbit IgG (H + L) Alexa Fluor 647 (1:1000, A12379, Thermo Fisher Scientific, USA)

## Primary:

- Alexa Fluor 647 Phalloidin (1:500, A12379, Thermo Fisher Scientific, USA)
- AP2 $\alpha$  (1:100, sc-12726, Santa Cruz Biotechnology, USA)
- Arrestin 3 (Cone Arrestin, 1:50, sc-54355, Santa Cruz Biotechnology, USA)
- Brn-3b (1:50, sc-31989, Santa Cruz Biotechnology, USA)
- CHX10 (1:200, sc-21690, Santa Cruz Biotechnology, USA)
- CRALBP (1:250, ab15051, Abcam, USA)
- EEA1 (1:500, 14-9114-80, eBioscience, Thermo Fisher Scientific, USA)
- EZRIN (1:200, 3145S, Cell Signaling, USA)
- LAMP2 (1:50, sc18822, Santa Cruz Biotechnology, USA)
- Melanoma gp100 (1:100, ab787, Abcam, USA)
- MITF (1:500, X1405M, Exalpha Biologicals, USA)
- PAX6 (1:100, PRB-278P-100, Covance, USA)
- PKC $\alpha$  (1:500, sc-208, Santa Cruz Biotechnology, USA)
- Rhodopsin (1:200, sc-57432, Santa Cruz Biotechnology, USA)
- ROM1 (1:200, 21984-1-AP, Proteintech, USA)
- RPE65 (1:100, ab78036 Abcam, USA)
- Anti-Opsin, blue (1:200, AB5407, Merck Millipore, USA)
- ZO-1 (1:100, 61-7300, Thermo Fisher Scientific, USA)

**TUNEL assay**

TUNEL Assay (Click-iT TUNEL Alexa Fluor 488 Imaging Assay; Thermo Fisher Scientific, USA) was performed according to the manufacturer's manual.

**Gene expression analysis using Fluidigm qRT-PCR**

Total RNA isolation and gene expression analysis was performed as previously described (Raab *et al.*, 2017). For quantification of the gene expression of the genes of interest, Taqman assays were purchased from Thermo Fisher Scientific, USA.

**Calcium imaging**

RoCs were incubated overnight with BRDM containing 9-cis-Retinal (Sigma-Aldrich, USA), 0.27  $\mu$ M Fura-2-AM and 0.1% pluronic acid (Invitrogen, USA) at 37°C and 5% CO<sub>2</sub>. Afterwards, the RoCs were perfused with BRDM (5 ml) to wash out the excess dye. Ratiometric calcium-imaging recordings were performed utilizing an upright fluorescence microscope (BX50WI, Olympus, Germany) equipped with a 40x water immersion objective (LUMPlan FL, 40X/0.80W,  $\infty/0$ , Olympus), a polychromator (VisiChrome, Till Photonics, Germany) and a CCD camera (RETIGA-R1, 1360  $\times$  1024 pixel, 16 bit). During the calcium-imaging recordings, stacks (single-plane two-channel) of the Fura-2 fluorescence at the focal plane of the ROs photoreceptors were acquired at 10 Hz ( $\lambda_{exc}$  = 340 and 380 nm; Olympus U-MNU filter set, 30 milliseconds exposure time, 8-pixel binning) using the VisiView software (Till Photonics, Germany). The calcium-imaging ratio-stacks were generated by dividing the fluorescence images recorded at the excitation wavelengths of F340 and F380 (ImageJ, RatioPlus, <https://imagej.nih.gov/>). To detect the calcium signals in the RoCs, fluorescent-labeled cells were manually encircled by regions of interest (ROIs) and the obtained ROIs coordinates were used to extract corresponding calcium traces from the ratio-stacks. Average frames of pre- and post-stimulus frames substituted ratio frames during the light stimulation period (using the ImageJ building function Z-projection ('Average intensity')).

**Fluorescence intensity quantification**

The fluorescence intensity of the propidium iodid signal was quantified using ImageJ (<https://imagej.nih.gov/>) before and after PI labeling using ROI selection and mean intensity pixel values. Signal intensities of images taken before PI labeling were considered as background and subtracted from

the measured PI values. The mean PI fluorescence intensity of only the RO in the RoC ( $I_{RO}$ ) was calculated via:

$$I_{RO} = I_{RO+RPE} - I_{RPE}$$

where by  $I_{RO+RPE}$  is the mean PI signal intensity in the RO area ( $A_{RO}$ ) from both RO as well as RPE and  $I_{RPE}$  is the mean PI signal intensity of solely the RPE.  $I_{RPE}$  was thereby calculated via:

$$I_{RPE} = \frac{I_{RoC} \times A_{RoC} - I_{RO+RPE} \times A_{RO}}{A_{RoC} - A_{RO}}$$

with  $I_{RoC}$  representing the mean PI intensity of the entire RoC area ( $A_{RoC}$ ).

### Microscopy

All microscopic images were as indicated in the individual panels either taken by an Imager.M2 Apo-tome1 (Carl Zeiss, Germany), LSM 710 Confocal microscope (Carl Zeiss, Germany) or by the EVOS FL Imaging System.

### Simulation of the fluidic transport processes

The free and porous fluid flow, as well as the transport of diluted species, was modeled according to work previously described (Loskill *et al.*, 2017). Briefly, we created a simplified model of the RoC consisting of the media channel and the four tissue chambers, each with a diameter of 2 mm and a height of 1 mm. The porous PET membrane, between the media channel and tissue chambers, was modeled with a thickness of 10  $\mu\text{m}$ . The incompressible stationary free fluid flow was modeled by the Navier-Stokes equation with the properties of water (dynamic viscosity  $\mu = 1 \times 10^{-3} \text{ m}^2/\text{s}$ , density  $\rho = 1000 \text{ kg/m}^3$ ) and a flow rate of 20  $\mu\text{l/h}$ . Fluid flow from the media channel through the isoporous membrane into the tissue channel was modeled using Darcy's law (porosity = 0.056, hydraulic permeability  $\kappa = 1.45 \times 10^{-14} \text{ m}^2$ ). The transport of diluted species was described by the time-dependent convection-diffusion with a diffusion coefficient  $1 \times 10^{-9} \text{ m}^2/\text{s}$  and an initial concentration of 1 mol/ $\text{m}^3$ .

### Statistical analysis

To analyze differences between samples conditions, the two-sided student's t-test (Figure 4g), the one-way-ANOVA with a Bonferroni post-hoc test (Figure 6h), the one-way-ANOVA with a Dunnett post-hoc test (Figure 8b,f,g) or a two-way-ANOVA with a Bonferroni post-hoc test (Figure 8h) was used. Statistical analysis was performed with GraphPad Prism 7.04 (San Diego, California). Data are presented as mean  $\pm$  S.E.M. p-value is indicated in the respective graphs.

### Data availability

The authors declare that the main data supporting the findings of this study are available within the article and its Supplementary Information files.

### Acknowledgements

This work was supported in part by the Fraunhofer-Gesellschaft Internal program Attract 601543 (PL), has received funding from the European Union's Horizon 2020 research and innovation programme under grant agreement No 766884 (PL), the DFG (DFG LI 2044/4-1 and DFG LI 2044/5-1 to SL, SCHE701/14-1 to KSL), the Ministry of Science, Research and the Arts of Baden-Württemberg (Az: 7542.2-501-1/13/6 to PL and Az: 33-729.55-3/214-8 to KS-L), the NC3Rs CrackIT scheme (PL and SL) and the Hector Fellow Academy grant to WH. The authors thank Dr. Murat Ayhan for advice on the statistical analysis.

## Additional information

### Funding

Funder	Author
Fraunhofer-Gesellschaft	Peter Loskill
Deutsche Forschungsgemeinschaft	Katja Schenke-Layland Stefan Liebau
Horizon 2020 Framework Programme	Peter Loskill
Ministerium für Wissenschaft, Forschung und Kunst Baden-Württemberg	Katja Schenke-Layland Peter Loskill
National Centre for the Replacement, Refinement and Reduction of Animals in Research	Stefan Liebau Peter Loskill
Hector Fellow Academy	Wadood Haq

The funders had no role in study design, data collection and interpretation, or the decision to submit the work for publication.

### Author contributions

Kevin Achberger, Christopher Probst, Jasmin Haderspeck, Investigation, Methodology, Writing—original draft, Writing—review and editing; Sylvia Bolz, Wadood Haq, Investigation, Methodology; Julia Rogal, Johanna Chuchuy, Marina Nikolova, Virginia Cora, Lena Antkowiak, Investigation; Nian Shen, Katja Schenke-Layland, Marius Ueffing, Conceptualization, Writing—review and editing; Stefan Liebau, Peter Loskill, Conceptualization, Funding acquisition, Methodology, Writing—original draft, Project administration, Writing—review and editing

### Author ORCIDs

Kevin Achberger  <https://orcid.org/0000-0001-5706-6201>

Christopher Probst  <https://orcid.org/0000-0002-1380-0117>

Peter Loskill  <https://orcid.org/0000-0002-5000-0581>

### Decision letter and Author response

Decision letter <https://doi.org/10.7554/eLife.46188.033>

Author response <https://doi.org/10.7554/eLife.46188.034>

## Additional files

### Supplementary files

- Transparent reporting form

DOI: <https://doi.org/10.7554/eLife.46188.031>

### Data availability

The authors declare that the main data supporting the findings of this study are available within the article and its supplementary information files.

## References

- Achberger K, Haderspeck JC, Kleger A, Liebau S. 2019. Stem cell-based retina models. *Advanced Drug Delivery Reviews* **140**:33–50. DOI: <https://doi.org/10.1016/j.addr.2018.05.005>, PMID: 29777757
- Agarwal A, Goss JA, Cho A, McCain ML, Parker KK. 2013. Microfluidic heart on a chip for higher throughput pharmacological studies. *Lab on a Chip* **13**:3599–3608. DOI: <https://doi.org/10.1039/c3lc50350j>, PMID: 23807141

- Berson JF, Harper DC, Tenza D, Raposo G, Marks MS. 2001. Pmel17 initiates premelanosome morphogenesis within multivesicular bodies. *Molecular Biology of the Cell* **12**:3451–3464. DOI: <https://doi.org/10.1091/mbc.12.11.3451>, PMID: 11694580
- Bhise NS, Manoharan V, Massa S, Tamayol A, Ghaderi M, Miscuglio M, Lang Q, Shrike Zhang Y, Shin SR, Calzone G, Annabi N, Shupe TD, Bishop CE, Atala A, Dokmeci MR, Khademhosseini A. 2016. A liver-on-a-chip platform with bioprinted hepatic spheroids. *Biofabrication* **8**:014101. DOI: <https://doi.org/10.1088/1758-5090/8/1/014101>, PMID: 26756674
- Blanks JC, Johnson LV. 1984. Specific binding of peanut lectin to a class of retinal photoreceptor cells: A species comparison. *Investigative Ophthalmology & Visual Science* **25**:546–557. PMID: 6715128
- Buch H, Vinding T, la Cour M, Appleyard M, Jensen GB, Vesti Nielsen N. 2004. Prevalence and causes of visual impairment and blindness among 9980 scandinavian adults. *Ophthalmology* **111**:53–61. DOI: <https://doi.org/10.1016/j.ophtha.2003.05.010>
- Chen PM, Gombart ZJ, Chen JW. 2011. Chloroquine treatment of ARPE-19 cells leads to lysosome dilation and intracellular lipid accumulation: possible implications of lysosomal dysfunction in Macular degeneration. *Cell & Bioscience* **1**:10. DOI: <https://doi.org/10.1186/2045-3701-1-10>, PMID: 21711726
- Chen LJ, Ito S, Kai H, Nagamine K, Nagai N, Nishizawa M, Abe T, Kaji H. 2017. Microfluidic co-cultures of retinal pigment epithelial cells and vascular endothelial cells to investigate choroidal angiogenesis. *Scientific Reports* **7**:3538. DOI: <https://doi.org/10.1038/s41598-017-03788-5>, PMID: 28615726
- Croze RH, Buchholz DE, Radeke MJ, Thi WJ, Hu Q, Coffey PJ, Clegg DO. 2014. ROCK inhibition extends passage of pluripotent stem Cell-Derived retinal pigmented epithelium. *STEM CELLS Translational Medicine* **3**:1066–1078. DOI: <https://doi.org/10.5966/sctm.2014-0079>, PMID: 25069775
- Datta P, Allamargot C, Hudson JS, Andersen EK, Bhattarai S, Drack AV, Sheffield VC, Seo S. 2015. Accumulation of non-outer segment proteins in the outer segment underlies photoreceptor degeneration in Bardet-Biedl syndrome. *PNAS* **112**:E4400–E4409. DOI: <https://doi.org/10.1073/pnas.1510111112>, PMID: 26216965
- Ding HJ, Denniston AK, Rao VK, Gordon C. 2016. Hydroxychloroquine-related retinal toxicity. *Rheumatology* **55**:957–967. DOI: <https://doi.org/10.1093/rheumatology/kev357>, PMID: 26428520
- Dodson KH, Echevarria FD, Li D, Sappington RM, Edd JF. 2015. Retina-on-a-chip: a microfluidic platform for point access signaling studies. *Biomedical Microdevices* **17**:1–10. DOI: <https://doi.org/10.1007/s10544-015-0019-x>, PMID: 26559199
- Elman A, Gullberg R, Nilsson E, Rendahl I, Wachtmeister L. 1976. Chloroquine retinopathy in patients with rheumatoid arthritis. *Scandinavian Journal of Rheumatology* **5**:161–166. DOI: <https://doi.org/10.3109/03009747609165456>, PMID: 981992
- Fine SL, Berger JW, Maguire MG, Ho AC. 2000. Age-related macular degeneration. *New England Journal of Medicine* **342**:483–492. DOI: <https://doi.org/10.1056/NEJM200002173420707>, PMID: 10675430
- Frank S, Zhang M, Schöler HR, Greber B. 2012. Small molecule-assisted, line-independent maintenance of human pluripotent stem cells in defined conditions. *PLOS ONE* **7**:e41958. DOI: <https://doi.org/10.1371/journal.pone.0041958>, PMID: 22860038
- Huh D, Matthews BD, Mammoto A, Montoya-Zavala M, Hsin HY, Ingber DE. 2010. Reconstituting organ-level lung functions on a chip. *Science* **328**:1662–1668. DOI: <https://doi.org/10.1126/science.1188302>, PMID: 20576885
- Jeon J, Hotaling N, Zamani M, Dejene R, Ingber D, Bharti K. 2016. Tissue engineered human Blood-Retinal Barrier-on-a-Chip. *Investigative Ophthalmology & Visual Science* **57**:5325.
- Kevany BM, Palczewski K. 2010. Phagocytosis of retinal rod and cone photoreceptors. *Physiology* **25**:8–15. DOI: <https://doi.org/10.1152/physiol.00038.2009>, PMID: 20134024
- Kivelä T, Jääskeläinen J, Vaheri A, Carpén O. 2000. Ezrin, a membrane-organizing protein, as a polarization marker of the retinal pigment epithelium in vertebrates. *Cell and Tissue Research* **301**:217–223. DOI: <https://doi.org/10.1007/s004410000225>, PMID: 10955717
- Krizaj D, Copenhagen DR. 2002. Calcium regulation in photoreceptors. *Frontiers in Bioscience* **7**:d2023–d2044. DOI: <https://doi.org/10.2741/A896>, PMID: 12161344
- Lamba DA, McUsic A, Hirata RK, Wang PR, Russell D, Reh TA. 2010. Generation, purification and transplantation of photoreceptors derived from human induced pluripotent stem cells. *PLOS ONE* **5**:e8763. DOI: <https://doi.org/10.1371/journal.pone.0008763>, PMID: 20098701
- Linta L, Stockmann M, Kleinhans KN, Böckers A, Storch A, Zaehres H, Lin Q, Barbi G, Böckers TM, Kleger A, Liebau S. 2012. Rat embryonic fibroblasts improve reprogramming of human keratinocytes into induced pluripotent stem cells. *Stem Cells and Development* **21**:965–976. DOI: <https://doi.org/10.1089/scd.2011.0026>
- Loskill P, Sezhan T, Tharp KM, Lee-Montiel FT, Jeeawoody S, Reese WM, Zushin PH, Stahl A, Healy KE. 2017. WAT-on-a-chip: a physiologically relevant microfluidic system incorporating white adipose tissue. *Lab on a Chip* **17**:1645–1654. DOI: <https://doi.org/10.1039/C6LC01590E>, PMID: 28418430
- Mahon GJ, Anderson HR, Gardiner TA, McFarlane S, Archer DB, Stitt AW. 2004. Chloroquine causes lysosomal dysfunction in neural retina and RPE: implications for retinopathy. *Current Eye Research* **28**:277–284. DOI: <https://doi.org/10.1076/ceyr.28.4.277.27835>, PMID: 15259297
- Marmorstein AD. 2001. The polarity of the retinal pigment epithelium. *Traffic* **2**:867–872. DOI: <https://doi.org/10.1034/j.1600-0854.2001.21202.x>, PMID: 11737824
- Mathur A, Loskill P, Shao K, Huebsch N, Hong S, Marcus SG, Marks N, Mandegar M, Conklin BR, Lee LP, Healy KE. 2015. Human iPSC-based cardiac microphysiological system for drug screening applications. *Scientific Reports* **5**:8883. DOI: <https://doi.org/10.1038/srep08883>, PMID: 25748532

- McDonald HR, Schatz H, Allen AW, Chenoweth RG, Cohen HB, Crawford JB, Klein R, May DR, Snider JD. 1986. Retinal toxicity secondary to intraocular gentamicin injection. *Ophthalmology* **93**:871–877. DOI: [https://doi.org/10.1016/S0161-6420\(86\)33648-0](https://doi.org/10.1016/S0161-6420(86)33648-0), PMID: 3763130
- Mishra S, Thakur A, Redenti S, Vazquez M. 2015. A model microfluidics-based system for the human and mouse retina. *Biomedical Microdevices* **17**:107. DOI: <https://doi.org/10.1007/s10544-015-0002-6>, PMID: 26475458
- Nakano T, Ando S, Takata N, Kawada M, Muguruma K, Sekiguchi K, Saito K, Yonemura S, Eiraku M, Sasai Y. 2012. Self-formation of optic cups and storable stratified neural retina from human ESCs. *Cell Stem Cell* **10**:771–785. DOI: <https://doi.org/10.1016/j.stem.2012.05.009>, PMID: 22704518
- Nakao Y, Kimura H, Sakai Y, Fujii T. 2011. Bile canaliculi formation by aligning rat primary hepatocytes in a microfluidic device. *Biomicrofluidics* **5**:022212. DOI: <https://doi.org/10.1063/1.3580753>
- Ohlemacher SK, Iglesias CL, Sridhar A, Gamm DM, Meyer JS. 2015. Generation of highly enriched populations of optic vesicle-like retinal cells from human pluripotent stem cells. *Current Protocols in Stem Cell Biology* **32**:1H.8.1–1H.8.20.
- Penha FM, Rodrigues EB, Maia M, Furlani BA, Regatieri C, Melo GB, Magalhães O, Manzano R, Farah ME. 2010. Retinal and ocular toxicity in ocular application of drugs and chemicals—part II: retinal toxicity of current and new drugs. *Ophthalmic Research* **44**:205–224. DOI: <https://doi.org/10.1159/000316695>, PMID: 20699625
- Probst C, Schneider S, Loskill P. 2018. High-throughput organ-on-a-chip systems: current status and remaining challenges. *Current Opinion in Biomedical Engineering* **6**:33–41. DOI: <https://doi.org/10.1016/j.cobme.2018.02.004>
- Puleo CM, McIntosh Ambrose W, Takezawa T, Elisseeff J, Wang TH. 2009. Integration and application of vitrified collagen in multilayered microfluidic devices for corneal microtissue culture. *Lab on a Chip* **9**:3221–3227. DOI: <https://doi.org/10.1039/b908332d>, PMID: 19865728
- Raab S, Klingenstein M, Möller A, Illing A, Tosic J, Breunig M, Kuaes G, Linta L, Seufferlein T, Arnold SJ, Kleger A, Liebau S. 2017. Reprogramming to pluripotency does not require transition through a primitive streak-like state. *Scientific Reports* **7**:16543. DOI: <https://doi.org/10.1038/s41598-017-15187-x>, PMID: 29185460
- Renouf DJ, Velazquez-Martin JP, Simpson R, Siu LL, Bedard PL. 2012. Ocular toxicity of targeted therapies. *Journal of Clinical Oncology* **30**:3277–3286. DOI: <https://doi.org/10.1200/JCO.2011.41.5851>, PMID: 22649132
- Rosenthal AR, Kolb H, Bergsma D, Huxsoll D, Hopkins JL. 1978. "Chloroquine retinopathy in the rhesus monkey, ". *Investigative Ophthalmology & Visual Science* **17**:1158–1175. PMID: 102610
- Shintani K, Shechtman DL, Gurwood AS. 2009. Review and update: current treatment trends for patients with retinitis pigmentosa. *Optometry - Journal of the American Optometric Association* **80**:384–401. DOI: <https://doi.org/10.1016/j.optm.2008.01.026>, PMID: 19545852
- Sonoda S, Spee C, Barron E, Ryan SJ, Kannan R, Hinton DR. 2009. A protocol for the culture and differentiation of highly polarized human retinal pigment epithelial cells. *Nature Protocols* **4**:662–673. DOI: <https://doi.org/10.1038/nprot.2009.33>, PMID: 19373231
- Su PJ, Liu Z, Zhang K, Han X, Saito Y, Xia X, Yokoi K, Shen H, Qin L. 2015. "Retinal synaptic regeneration via microfluidic guiding channels, ". *Scientific Reports* **5**:13591. DOI: <https://doi.org/10.1038/srep13591>, PMID: 26314276
- Theos AC, Truschel ST, Raposo G, Marks MS. 2005. The silver locus product Pmel17/gp100/Silv/ME20: controversial in name and in function. *Pigment Cell Research* **18**:322–336. DOI: <https://doi.org/10.1111/j.1600-0749.2005.00269.x>, PMID: 16162173
- Vogt A, Fuerholzner B, Kinkl N, Boldt K, Ueffing M. 2013. Isotope coded protein labeling coupled immunoprecipitation (ICPL-IP): a novel approach for quantitative protein complex analysis from native tissue. *Molecular & Cellular Proteomics* **12**:1395–1406. DOI: <https://doi.org/10.1074/mcp.O112.023648>, PMID: 23268931
- Wikswjo JP. 2014. The relevance and potential roles of microphysiological systems in biology and medicine. *Experimental Biology and Medicine* **239**:1061–1072. DOI: <https://doi.org/10.1177/1535370214542068>
- Wilmer MJ, Ng CP, Lanz HL, Vulto P, Suter-Dick L, Masereeuw R. 2016. Kidney-on-a-Chip technology for Drug-Induced nephrotoxicity screening. *Trends in Biotechnology* **34**:156–170. DOI: <https://doi.org/10.1016/j.tibtech.2015.11.001>, PMID: 26708346
- Yin X, Mead BE, Safaee H, Langer R, Karp JM, Levy O. 2016. Stem cell organoid engineering. *Cell Stem Cell* **18**:25–38. DOI: <https://doi.org/10.1016/j.stem.2015.12.005>
- Yusuf IH, Sharma S, Luqmani R, Downes SM. 2017. Hydroxychloroquine retinopathy. *Eye* **31**:828–845. DOI: <https://doi.org/10.1038/eye.2016.298>
- Zemel E, Loewenstein A, Lei B, Lazar M, Perlman I. 1995. "Ocular pigmentation protects the rabbit retina from gentamicin-induced toxicity, ". *Investigative Ophthalmology & Visual Science* **36**:1875–1884. PMID: 7635661
- Zhang B, Korolj A, Lai BFL, Radisic M. 2018. Advances in organ-on-a-chip engineering. *Nature Reviews Materials* **3**:257–278. DOI: <https://doi.org/10.1038/s41578-018-0034-7>
- Zhong X, Gutierrez C, Xue T, Hampton C, Vergara MN, Cao LH, Peters A, Park TS, Zambidis ET, Meyer JS, Gamm DM, Yau KW, Canto-Soler MV. 2014. Generation of three-dimensional retinal tissue with functional photoreceptors from human iPSCs. *Nature Communications* **5**:4047. DOI: <https://doi.org/10.1038/ncomms5047>, PMID: 24915161



Publication [5]

## **WAT-on-a-chip integrating human mature white adipocytes for mechanistic research and pharmaceutical applications**

**J. Rogal**, C. Binder, E. Kromidas, S. Schneider, C. Probst, K. Schenke-Layland, P. Loskill  
*Sci. Rep.* 10, 6666 (2020), <https://dx.doi.org/10.1038/s41598-020-63710-4>

### **Abstract:**

Obesity and its numerous adverse health consequences have taken on global, pandemic proportions. White adipose tissue (WAT) – a key contributor in many metabolic diseases – contributes about one fourth of a healthy human’s body mass. Despite its significance, many WAT-related pathophysiological mechanisms in humans are still not understood, largely due to the reliance on non-human animal models. In recent years, Organ-on-a-chip (OoC) platforms have developed into promising alternatives for animal models; these systems integrate engineered human tissues into physiological microenvironment supplied by a vasculature-like microfluidic perfusion. Here, we report the development of a novel OoC that integrates functional mature human white adipocytes. The WAT-on-a-chip is a multilayer device that features tissue chambers tailored specifically for the maintenance of 3D tissues based on human primary adipocytes, with supporting nourishment provided through perfused media channels. The platform’s capability to maintain long-term viability and functionality of white adipocytes was confirmed by real-time monitoring of fatty acid uptake, by quantification of metabolite release into the effluent media as well as by an intact responsiveness to a therapeutic compound. The novel system provides a promising tool for wide-ranging applications in mechanistic research of WAT-related biology, in studying of pathophysiological mechanisms in obesity and diabetes, and in R&D of pharmaceutical industry.

OPEN

# WAT-on-a-chip integrating human mature white adipocytes for mechanistic research and pharmaceutical applications

Julia Rogal<sup>1,2</sup>, Carina Binder<sup>1</sup>, Elena Kromidas<sup>1,2</sup>, Julia Roosz<sup>1</sup>, Christopher Probst<sup>1</sup>, Stefan Schneider<sup>1</sup>, Katja Schenke-Layland<sup>2,3,4</sup> & Peter Loskill<sup>1,2\*</sup>

Obesity and its numerous adverse health consequences have taken on global, pandemic proportions. White adipose tissue (WAT) – a key contributor in many metabolic diseases – contributes about one fourth of a healthy human's body mass. Despite its significance, many WAT-related pathophysiological mechanisms in humans are still not understood, largely due to the reliance on non-human animal models. In recent years, Organ-on-a-chip (OoC) platforms have developed into promising alternatives for animal models; these systems integrate engineered human tissues into physiological microenvironment supplied by a vasculature-like microfluidic perfusion. Here, we report the development of a novel OoC that integrates functional mature human white adipocytes. The WAT-on-a-chip is a multilayer device that features tissue chambers tailored specifically for the maintenance of 3D tissues based on human primary adipocytes, with supporting nourishment provided through perfused media channels. The platform's capability to maintain long-term viability and functionality of white adipocytes was confirmed by real-time monitoring of fatty acid uptake, by quantification of metabolite release into the effluent media as well as by an intact responsiveness to a therapeutic compound. The novel system provides a promising tool for wide-ranging applications in mechanistic research of WAT-related biology, in studying of pathophysiological mechanisms in obesity and diabetes, and in R&D of pharmaceutical industry.

The global obesity pandemic poses one of today's biggest challenges to public health. Each year, 2.8 million people die from causes related to overweight or obesity<sup>1</sup>. Since the 1970s, the worldwide prevalence of obesity has nearly tripled, also leading to an upsurge in associated comorbidities such as type 2 diabetes (Fig. 1a)<sup>2</sup>. Future projections reveal the gravity of this public health crisis: the prevalence rates of childhood obesity are increasing at an alarming pace<sup>3</sup>, and by 2030, more than 50% of U.S. adults are predicted to be obese<sup>4</sup>. White adipose tissue (WAT) is the principal organ in obesity. In healthy human adults, WAT comprises approximately 20–25% of the total body mass, thus constituting the second largest organ, after the skin. In obese individuals, WAT's contribution to the total body mass may become as high as 50% (Fig. 1b)<sup>5</sup>.

WAT is tightly involved in the two most important functions of an organism – energy homeostasis and reproduction<sup>6</sup>. In energy homeostasis, not only does WAT act as the main storage site of excess dietary energy (Fig. 1c), it also performs crucial endocrine and metabolic functions (Fig. 1d)<sup>7,8</sup>. WAT can sense the body's energy status, and respond appropriately, either by storing fuel, in the form of triacylglycerides, or by releasing it as glycerol and fatty acids, for ultimate delivery to organs in need. While this classically described role of WAT already entailed extensive crosstalk between WAT and other organs, its inter-organ communications extend beyond simple feedback loops activated by fed- or fasted states. Endocrine functions of white adipocytes, and other WAT-resident cells in the stromal vascular fraction, are performed by the release of a variety of adipokines (adipose-associated

<sup>1</sup>Fraunhofer Institute for Interfacial Engineering and Biotechnology IGB, Nobelstrasse 12, 70569, Stuttgart, Germany. <sup>2</sup>Department of Women's Health, Research Institute for Women's Health, Eberhard Karls University, Calwerstrasse 7, 72076, Tübingen, Germany. <sup>3</sup>NMI Natural and Medical Sciences Institute at the University of Tübingen, Markwiesenstr. 55, 72770, Reutlingen, Germany. <sup>4</sup>Department of Medicine/Cardiology, Cardiovascular Research Laboratories, David Geffen School of Medicine at UCLA, 675 Charles E. Young Drive South, MRL 3645, Los Angeles, CA, USA. \*email: [peter.loskill@igb.fraunhofer.de](mailto:peter.loskill@igb.fraunhofer.de)

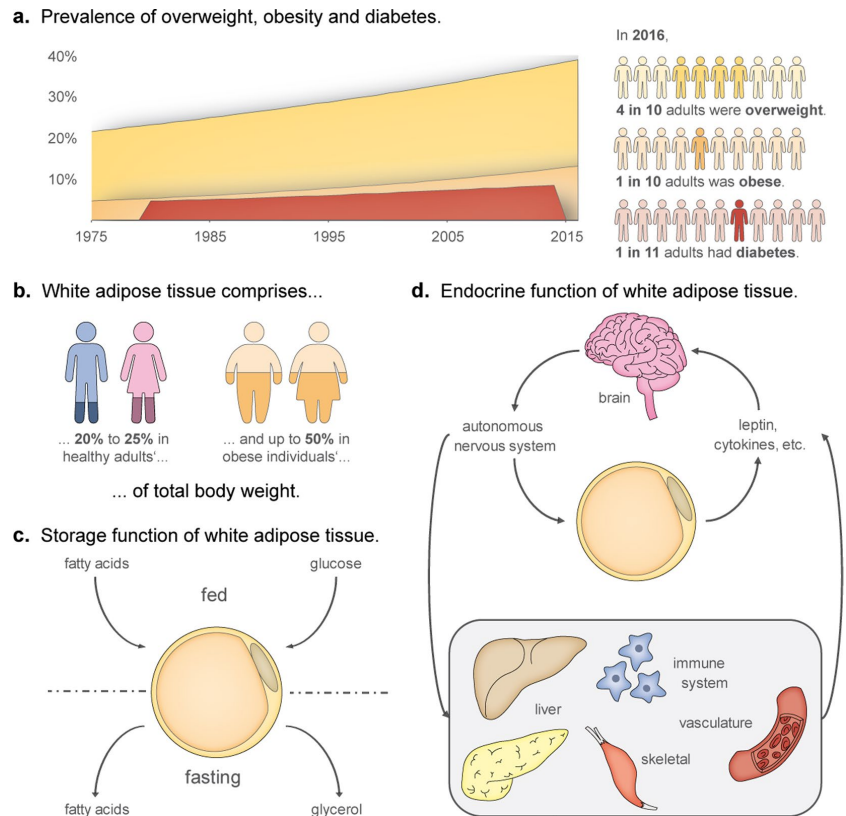


**Figure 1.** Relevance of research on WAT. (a) The worldwide prevalence of obesity has nearly tripled since 1975; in 2016, almost 40% of adults aged 18 and over could be classified as overweight, 13% of them were even obese. This developments has coincided with a rising prevalence of diabetes, which in 2016 affected approximately 9% of adults worldwide. T2DM – the most prevalent form of diabetes – often develops during chronic positive energy balance, e.g., by a combination of excessive energy intake and physical inactivity<sup>1,2</sup>. (b) WAT’s contribution to body mass is 20–25% in healthy individuals, and up to 50% in the obese<sup>5</sup>. (c) Traditional view of WAT as an organ primarily for energy storage. (d) Additional, modern-day concepts of WAT functionality, including extensive endocrine functions.

cytokines) which affect the functioning of the brain, liver, pancreas and immune system<sup>9</sup>. Besides managing nutritional homeostasis, WAT contributes to the regulation of the hypothalamic-pituitary-gonadal axis by secreting and metabolizing sex steroids<sup>7</sup>. Especially adipose tissue intracrinology, i.e., the modulation of sex steroid levels by significant numbers of locally expressed enzymes that activate, convert, or inactivate circulating steroid hormones, plays important roles in human reproductive function<sup>7,10,11</sup>. Given its prominent endocrine functions and extensive cross-talk with other organs, it comes as little surprise that abnormal amounts, or altered functioning of WAT may result in wide-ranging disorders, including hepatic and cardiovascular diseases<sup>12,13</sup>, diabetes and cancer<sup>14–16</sup>.

In line with its important roles in metabolism, inflammation and cancer, WAT has emerged as a drug target with major therapeutic potential for a variety of diseases<sup>17–19</sup>. Additionally, storage metabolism by WAT can have a major impact on the efficacy of drug therapies, such as those for cardiovascular diseases and cancer<sup>20,21</sup>. For instance, adipocytes may metabolize and inactivate the chemotherapeutic Daunorubicin<sup>21</sup>, which strongly affects the efficacy of this anticancer therapeutic. Furthermore, the capacity of WAT to sequester hydrophobic compounds, gives the tissue a prominent role in absorption, distribution, metabolism, and excretion (ADME) processes.

Even though WAT plays such a significant role in many diseases, surprisingly little is known about pathophysiological processes of WAT, especially when considering the ever-increasing prevalence of obesity and its co-morbidities. An important reason for this lacking insight is that mechanistic studies in humans often involve

unacceptable health risks. Hence, most research depends on clinical observation, genome-wide association studies (GWAS) as well as animal studies<sup>22</sup>. Although animal models have led to many insights in obesity and diabetes, they often are lacking in predictive validity for human body functioning, first because of important species differences in nutrition and metabolism, and second because the distinct, unique physiological and pathophysiological roles of WAT in humans<sup>23</sup>. Alternatively, conventional, cell culture-based *in vitro* models have been widely utilized and are significantly less controversial ethically. Typically, researchers have used a variety of cell sources, ranging from (immortalized) murine, to primary human (pre-)adipocytes, each featuring distinct advantages and limitations<sup>24</sup>. *In vitro* differentiation of adipogenic progenitor cells, i.e., either pre-adipocytes or multipotent stem cell lines, or (induced) pluripotent stem cells, is often the method of choice due to the availability of donor-specific information, and the capacity of these cells to undergo expansion and cryopreservation while retaining their characteristic fat depot. Yet, the *in vitro* use of differentiated adipocytes has two major drawbacks: unlike their *in situ* matured congeners, (i) their lipid contents never reach a state of unilocularity, but remain distributed among multiple small lipid vacuoles, and (ii) their gene expression and secretome differs significantly in the relative proportions of adipose-associated hormones<sup>25–27</sup>. Both phenomena reflect a pre-mature state of the *in vitro* differentiated adipocytes, which strongly suggests that mature human adipocytes provide the best recapitulation of a mature human adipocyte physiology. Yet, the *ex vivo* culture of primary human adipocytes is extremely challenging, due to issues with the cells' buoyancy, fragility and de-differentiation, which so far have hindered development of robust protocols for long-term culturing. Similarly, studies using whole WAT explants are restricted to short culture durations. Additionally, inter-individual variability complicates the interpretation of study results based on samples from different donors<sup>28</sup>.

Overall, it is of utmost importance to develop microscale platforms that provide microphysiological environments for the long-term culture of white adipocytes in structures that may recapitulate *in vivo* physiology, and functionality based on a minimal amount of cells. By combining modern techniques in microfabrication, biomaterials and tissue engineering, organ-on-a-chip technology has enabled the construction of promising platforms for mechanistic and pharmaceutical studies, that have great potential for disease modeling as well as the optimization of personalized medical treatments of obesity and diabetes<sup>29–32</sup>. The integration of tissues with *in vivo*-like structure and functionality in perfused microenvironments is of particular interest when studying endocrine tissues and multi-factorial diseases, due to the possibility to combine individual chips into multi-organ systems<sup>33,34</sup>. However, although organ-on-a-chip research has burgeoned in recent years, and numerous platforms have been developed for many organs and tissues, WAT appears to have been largely overlooked, and only a few relevant efforts have been undertaken<sup>25</sup>. Several research groups injected pre-adipocytes from murine<sup>35,36</sup> or human<sup>37–39</sup> sources into microfluidic chambers, and were able to subsequently induce adipogenesis. Others directly introduced primary adipocytes from mice into mesoscopic, perfused reservoirs<sup>40</sup>. In a recently introduced elegant approach, Harms *et al.* cultured mature human white adipocytes in multiwell plates underneath membranes in a transwell format<sup>41</sup>. All of these innovative approaches, however, did not enable the generation of human white adipose tissue-like structures with *in vivo*-like physiology.

Here, we present the first OoC platform that integrates human primary mature adipocytes into a perfused microfluidic chip. The human WAT-on-a-chip consists of multiple, tissue-specific chambers that are fluidically connected to a vasculature-like microchannel, while being shielded from the shear forces of the perfusion fluid. Using specifically tailored isolation and injection protocols, 3D microtissues based on freshly isolated adipocytes are generated inside a series of individual chambers. Thus, a large number of independent replicate cell cultures from individual donors can be produced and kept viable – as well as functional – for over one month. By analyzing media effluents and taking advantage of the optical accessibility of the tissue chambers, the patency of cells as well as key cell-physiological aspects, e.g., fatty acid metabolism and drug responsiveness, could be monitored successfully.

## Materials and Methods

**Fabrication and characterization of microfluidic platforms.** *Chip fabrication by soft lithography and replica molding.* The microfluidic platform is a custom-designed three-layered hybrid device featuring two micro-patterned polydimethylsiloxane (PDMS; Sylgard 184, Dow Corning, USA) layers, which are separated by an isoporous semipermeable membrane. The media channel and tissue chamber microstructures in the PDMS slabs were generated using two differently patterned master wafers that served as positive molding templates. The intricately structured masters were fabricated by commonly used photolithographic processes described previously<sup>36</sup>. The chips' PDMS structures were created using two different molding techniques: standard molding to obtain thicker slabs with closed structures, and exclusion molding to obtain thin layers with open structures (cf. "Replica molding of PDMS parts" in the supplements section). To prepare the semipermeable membranes, commercially available polyethylene terephthalate (PET) membranes ( $r_p = 3 \mu\text{m}$ ;  $\rho_p = 8 \times 10^5$  pores per  $\text{cm}^2$ ; TRAKETCH® PET 3.0 p S210  $\times$  300, SABEU GmbH & Co. KG, Northeim, Germany) were functionalized by a plasma-enhanced, chemical vapor deposition (PECVD) process (cf. "Membrane functionalization" in the supplements section). In a final step, chips were assembled in three subsequent  $\text{O}_2$ -plasma activation (15 s, 50 W; Diener Zepto, Diener electronic GmbH + Co. KG, Ebhausen, Germany) and bonding steps, followed by an overnight exposure to 60 °C for bonding enhancement (cf. "Chip assembly" in the supplements section).

*Chip preparation for experiments.* On the day before cell injection, chips were  $\text{O}_2$ -plasma sterilized (60 s, 50 W) and subsequently filled with Dulbecco's phosphate-buffered saline without  $\text{MgCl}_2$  and  $\text{CaCl}_2$  ( $\text{PBS}^-$ ; Sigma-Aldrich Chemie GmbH, Steinheim, Germany), under sterile conditions. Then, the  $\text{PBS}^-$  filled chips were kept overnight at 4 °C in  $\text{PBS}^-$  to allow evacuation of residual air from the channel systems.

**Numerical modeling.** To model fluid flow and transport of a diluted species, COMSOL Multiphysics (COMSOL, Stockholm, Sweden) software was used. The process was based on a numerical model which was previously published for our previous murine WAT-on-a-chip<sup>36</sup>. Briefly, the incompressible stationary free fluid flow was modeled by the Navier-Stokes equation with the properties of water (dynamic viscosity  $\mu = 1 \times 10^{-3} \text{ m}^2/\text{s}$ , density  $\rho = 1000 \text{ kg/m}^3$ ) at a flow of  $20 \mu\text{l/h}$ . Fluid flow from the media channel through the isoporous membrane into the tissue channel was modeled using Darcy's law (porosity = 0.056, hydraulic permeability  $\kappa = 1.45 \times 10^{-14} \text{ m}^2$ ). The transport of diluted species was described by the time-dependent convection-diffusion with a diffusion coefficient  $1 \times 10^{-9} \text{ m}^2/\text{s}$  and an initial concentration of  $1 \text{ mol/m}^3$ .

**Diffusive transport.** To visualize diffusion of compounds from the media microchannels over the isoporous membrane into the tissue chamber inside the microfluidic platform, we monitored the perfusion of a  $0.5 \text{ mg/ml}$  fluorescein isothiocyanate-dextran (FITC-dextran;  $150 \text{ kDa}$ , 46946, Sigma-Aldrich Chemie GmbH) solution in PBS<sup>-</sup> in the system. Prior to the diffusion experiment, the tissue chambers were filled with the collagen hydrogel matrix commonly used to encapsulate the adipocytes (cf. "Injection of human mature adipocytes into the microfluidic platform"). The flow rate was set to  $40 \mu\text{l/h}$  and the fluorescence intensity was measured every  $6.2 \text{ s}$  for three positions in the chip – the media channel, the top of the underlying tissue chamber, as well as the bottom of the same tissue chamber.

**Isolation and culture of primary human adipocytes.** *Human tissue samples.* Human adiposetissue biopsies were obtained from plastic surgeries performed by Dr. Ulrich E. Ziegler (Klinik Charlottenhaus, Stuttgart, Germany), approved by the local medical ethics committee: Patients gave an informed consent according to the permission of the "Landesärztekammer Baden-Württemberg" (IRB#: F-2012-078; for normal skin from elective surgeries). All procedures were carried out in accordance with the rules for medical research of human subjects, as defined in the Declaration of Helsinki. All primary mature adipocytes were isolated from biopsies that were taken from female, pre-obese donors (BMI  $25.0 - 29.9$ , as per the WHO classification), aged 45 to 55.

*Isolation of primary human adipocytes.* Primary mature adipocytes were isolated from subcutaneous adipose tissue samples. The isolation protocol was performed as previously described<sup>42,43</sup>, with slight modifications. In brief, the subcutaneous adipose tissue was rinsed twice with Dulbecco's phosphate buffered saline with  $\text{MgCl}_2$  and  $\text{CaCl}_2$  (PBS<sup>+</sup>; Sigma-Aldrich Chemie GmbH), and visible blood vessels, as well as connective-tissue structures, were thoroughly removed. The remaining adipose tissue was cut into fine pieces of approximately  $1 \text{ cm}^3$ , and digested with a collagenase solution [ $0.13 \text{ U/ml}$  collagenase type NB4 (Serva Electrophoresis GmbH, Heidelberg, Germany) in Dulbecco's Modified Eagle Medium (DMEM/Ham's-F12; Thermo Fisher Scientific, Waltham, USA), with  $1\%$  bovine serum albumin (BSA; Sigma-Aldrich Chemie GmbH)] for  $60 \text{ min}$  at  $37^\circ\text{C}$  on a rocking shaker ( $50 \text{ cycles/min}$ ; Polymax 1040, Heidolph Instruments GmbH & CO. KG, Schwabach, Germany). Next, the digested tissue was passed through cell strainers (mesh size:  $500 \mu\text{m}$ ), and subsequently washed three times with DMEM/Ham's-F12. For each washing step, adipocytes and medium were mixed, and left to rest for  $10 \text{ min}$  to allow separation of the buoyant adipocytes and the medium; this was followed by aspiration of the liquid media from underneath the packed layer of adipocytes.

*Injection of human mature adipocytes into the microfluidic platform.* Immediately after the isolation of white adipocytes from tissue samples, the adipocytes were prepared for injection into the microfluidic platforms. Sixty  $\mu\text{l}$  of densely packed adipocytes were mixed with  $24 \mu\text{l}$  of a dispersion of  $10 \text{ mg/ml}$  collagen type 1 (from rat tail, provided by Fraunhofer IGB),  $6 \mu\text{l}$  neutralization buffer [DMEM/Ham's F-12 ( $10\times$ ); Biochrom GmbH, Berlin, Germany), and  $50 \text{ mM}$  NaOH in Aqua dest ( $1:1$ ) with  $0.2 \text{ M}$   $\text{NaHCO}_3$  and  $0.225 \text{ M}$  HEPES (Carl Roth GmbH + Co. KG, Karlsruhe, Germany)] and immediately injected into the chip's tissue-chamber system by manual pressure. Each system of connected tissue chambers was loaded individually at a steady pace, to ensure that the collagen hydrogel reached the tissue chambers before the onset of gelation.

*On-chip culture of adipose tissue.* During on-chip culturing, the WAT-chips were maintained in a humidified incubator at  $37^\circ\text{C}$  and a  $5\% \text{ CO}_2$  atmosphere. The adipocytes were supplied with a  $20\text{--}40 \mu\text{l/h}$  flow of Subcutaneous Adipocyte Maintenance Medium (AM-1; BioCat GmbH, Heidelberg, Germany) maintained by positive pressure from an automated syringe pump (LA-190, Landgraf Laborsysteme HLL GmbH, Langenhagen, Germany). Under sterile conditions, media reservoirs were re-filled with fresh media every other day, and the media effluents were collected from the media-systems' outlets once every  $1\text{--}2$  days (depending on the experiment), and stored at  $-80^\circ\text{C}$  for subsequent analysis of metabolites.

**Structural and functional characterization of on-chip adipose tissues.** *Fluorescent double staining of intracellular lipid vacuoles and nuclei.* To visualize the structure of on-chip adipose tissues, intracellular lipid vacuoles and nuclei were stained using the neutral lipid stain BODIPY<sup>TM</sup> 493/503 (4,4-Difluoro-1,3,5,7,8-Pentamethyl-4-Bora-3a,4a-Diaza-s-Indacene; D3922, Thermo Fisher Scientific) and 4',6-Diamidin-2-phenylindol (DAPI; D8417, Sigma-Aldrich Chemie GmbH). All fixation- and staining solutions were flushed through the chip at a rate of  $80 \mu\text{l/h}$  by a syringe pump. The in-chip adipocytes were fixed overnight with  $4\%$  phosphate-buffered formaldehyde solution (Roti<sup>®</sup>-Histofix  $4\%$ , P087, Carl Roth GmbH + Co. KG). Next, permeabilization was achieved by flushing the chip for  $3 \text{ h}$  with PBST [PBS<sup>+</sup> with  $0.1\%$  Tween-20 (P7949, Sigma-Aldrich Chemie GmbH)]. Then, the fluorescence staining solution – PBST with  $1 \mu\text{g/ml}$  BODIPY<sup>TM</sup> 493/503 and  $1 \mu\text{g/ml}$  DAPI – was pumped through the system for  $2 \text{ h}$ , and finally washed out with PBS<sup>+</sup> for at least  $30 \text{ min}$  to remove residual staining solution. To stain explants, chunks of approximately  $100 \text{ mm}^3$  were cut off from the biopsy, washed with PBS<sup>+</sup> twice and fixed for  $1 \text{ h}$  with  $4\%$  phosphate-buffered formaldehyde solution.

Afterwards, the fixed explants were washed with PBS<sup>+</sup>, permeabilized and stained as described above (1 h of incubation time for each step). Finally, the explants were washed three times in PBS<sup>+</sup> to remove residual staining solution and stored in PBS<sup>+</sup> until imaging.

Imaging of the stained adipocytes was performed and processed by a laser scanning microscope (Zeiss LSM 710, Carl Zeiss, Oberkochen, Germany) with specialized software (ZEN 2012 SP1 (black edition), Release Version 8.1)).

**Live/dead staining of integrated white adipose tissue.** To assess the viability of the adipocytes on-chip, a live/dead-assay based on fluorescein diacetate (FDA; F1303, Thermo Fisher Scientific) and propidium iodide (PI; P3566, Thermo Fisher Scientific) was performed. Prior to staining, the culture medium was removed from the chip by flushing the media channels with PBS, using gravitational flow. The staining solution containing FDA (final concentration 27 µg/ml) and PI (final concentration 135 µg/ml) diluted in PBS, was flushed into the media channel by gravitational flow, and incubated for 25 min in a humidified incubator at 37 °C and 5% CO<sub>2</sub>. The staining solution was then removed by flushing PBS through the media channels using gravitational flow. Right after that, imaging was performed by an inverted fluorescence microscope (Leica DMi8, LEICA Microsystems GmbH, Wetzlar, Germany).

**Monitoring and analysis of fatty acid uptake and release.** For online monitoring of fatty acid uptake by the adipocytes, 4 µM of the fluorescently-labeled fatty acid analog, BODIPY<sup>TM</sup> 500/510 C1, C12 (4,4-Difluoro-5-Methyl-4-Bora-3a,4a-Diaza-s-Indacene-3-Dodecanoic Acid; D3823, Thermo Fisher Scientific), was added to the culture medium for a duration of 60 min and pumped through the media systems at 80 µl/h via positive pressure provided by a syringe pump. Next, the culture medium was switched to AM-1 only, to visualize the release of the fluorescent fatty acid analog. During the experiment, the chips were placed under complete darkness in an incubator chamber that was fitted to the microscope stage, and set to 37 °C. Imaging was performed using the inverted Leica DMi8 fluorescence microscope. During the 120 min running time of the experiment, images of both bright-field (BF) and FITC-channels were captured every two minutes from each tissue chamber on the chip. As a reference, each position was imaged at time point 0 min (t<sub>0</sub>).

To quantify the patterns of fluorescence intensity during the uptake and release of the fluorescent fatty acid analog, the mean gray value of the fluorescence of the individual tissue chambers and the fluorescence of the background were measured for each time point using ImageJ 1.50i software (National Institute of Health, Bethesda, USA). After subtracting the background levels from the fluorescence intensities measured in the chambers, the offset was calculated by setting the intensity measured at t<sub>0</sub> to a fluorescence intensity of 0 A.U. Then, the intensities for each chamber were expressed as a percentage of the highest recorded intensity from that chamber during the experiment. Note: Normalization on the chamber-level was considered to be necessary, because the amount of injected adipocytes varied between the chambers with the used WAT-chip design.

**Responsiveness to β-adrenoreceptor agonistic drugs.** To assess the effect of β-adrenergic agonist drugs on fatty acid metabolism, AM-1 medium was supplemented with 10 µM isoproterenol hydrochloride (I6504, Sigma-Aldrich Chemie GmbH). Fluorescence intensity was measured for 60 min with, and then for 60 min without addition of 4 µM BODIPY<sup>TM</sup> 500/510 C1, C12 to the conditioned medium at 37 °C with an inverted fluorescence microscope (LEICA DMi8, LEICA Microsystems GmbH) to assess the dynamics of fatty acid uptake and release. Measurement and analysis of fluorescence was performed as described above.

**Non-invasive analysis of cytotoxicity from media effluents.** The release of lactate dehydrogenase (LDH) was quantified from the media effluents to non-invasively assess the adipocytes' on-chip viability. The medium effluents were collected for a sampling time of 24 h on different days of on-chip culture. For analysis of the medium effluents, we used the CytoTox 96<sup>®</sup> Non-Radioactive Cytotoxicity Assay (G1780; Promega GmbH, Walldorf, Germany) and followed the manufacturer's instructions for performing the assay in a 384-well plate format. This assay allows for colorimetric detection of necrotic and late-stage apoptotic cells. For a Target Cell Maximum LDH Release Control, adipocytes were injected into two chips as described above. After injection, the adipocytes were perfused with lysis buffer for 2 h until all adipocytes were lysed. The mean of the acquired absorbance was assumed to be the maximum LDH release possible for the given experimental setup including chip design and adipocyte donor. All other acquired LDH data were normalized to this value.

**Analysis of adipose-associated metabolites.** The non-esterified fatty acid (NEFA) contents of medium effluents were determined by enzymatic analysis, using the ACS-ACOD-MEHA method (NEFA-HR(2) Assay, FUJIFILM Wako Chemicals Europe GmbH, Neuss, Germany). Effluents were thawed and centrifuged at 10,000 × g for 10 min. Then, 25 µl of sample [i.e. the effluents' supernatant, or AM-1 as blank, or oleic acid for a standard curve (270-77000, FUJIFILM Wako Chemicals Europe GmbH)] were supplemented with 100 µl of the R1 solution (434-91795, FUJIFILM Wako Chemicals Europe GmbH) and 50 µl of the R2 solution (436-91995, Wako Chemicals GmbH), incubating 10 min at 37 °C after each addition. NEFA concentrations were determined by measuring absorbance at 550 nm (Infinite<sup>®</sup> 200 PRO, Tecan Trading AG, Switzerland). To assess the influence of albumin on NEFA release, 0.2% human serum albumin (HSA; A1653, Sigma-Aldrich Chemie GmbH) was added to the culture medium for 24 h. To ensure that increases in the measured NEFA concentrations could not be attributed to the presence of HSA during assay performance, we performed NEFA-measurements on the oleic acid standard with and without HSA. No differences were observed in the detected NEFA-concentration between the two conditions (Fig. S4).

As another readout for lipolysis, glycerol concentrations were determined using a colorimetric assay. Media effluents were thawed and centrifuged at 10,000 × g for 10 min. Then, 40 µl of sample [i.e. the effluents' supernatants, or AM-1 as blank, or Glycerol Standard Solution for a standard curve (G7793, Sigma-Aldrich Chemie

GmbH)] were supplemented with 60  $\mu\text{l}$  of the Free Glycerol Reagent (F6428, Sigma-Aldrich Chemie GmbH). After a 5-min incubation at 37 °C, absorbance at 540 nm was recorded.

**Statistical analysis.** All graphs show raw data means  $\pm$  standard deviation (unless otherwise indicated). We annotated or sample size  $n$  as follows:

- For analyses pertaining to data at tissue chamber level (e.g. from fatty acid transport assays),  $n$  denotes the number of tested tissue chambers.
- For analyses pertaining on tissue system level only, i.e., the collectivity of eight chambers connected via one media channel, (e.g. metabolite measurements),  $n$  denotes the number of tested tissue systems.

For statistical analysis of differences, we performed independent two-sample  $t$ -tests using OriginPro 2018 software (OriginLab, Northampton, MA, USA). Unless otherwise indicated, a  $p$ -value threshold for significance of 0.05 was used.

## Results and Discussion

**Concept and characterization of the microfluidic platform.** In order to generate a microphysiological environment capable of generating a human WAT-model, and maintaining tissue viability and functionality during long-term culture, we developed a specifically tailored microfluidic platform featuring a footprint comparable to the size of a stamp ( $2 \times 2$  cm). The essential features of the platform, depicted in Fig. 2a, are 3D-tissue chambers and perfusable microchannels that are separated by an isoporous membrane. Each chip platform houses two identical, independent systems each featuring eight individual tissue chambers. All tissue chambers are located at the end of individual branches of a main channel, which can be accessed via a common inlet for cell injection. The tissue chambers are specifically designed to accommodate adipose tissue, particularly its large-sized, fragile and buoyant adipocytes: they are cylindrical structures with a diameter of 720  $\mu\text{m}$  and a height of 200  $\mu\text{m}$ . The tissue-chamber microstructures are encased by transparent glass (cover slip or microscope slide) at the bottom, enabling easy visual inspection of the tissues with most current types of microscope, and by an isoporous membrane on the top side. The membrane was specifically functionalized (Supplement S2) to ensure a tight sealing of chip components, and to provide a porous barrier to the adjacent media microchannels. The channels can be connected to external devices (e.g. syringe- or peristaltic pumps), to achieve a vasculature-like perfusion with media. This allows for a precisely controllable convective transport of nutrients, metabolites, and other dissolved molecules towards, as well as away from, the tissue chambers, mimicking the *in vivo* circulation of blood. It also opens up the possibility to administer compounds with high temporal resolution. The membrane further ensures that convective transport is restricted to the media channels, thereby shielding the tissue chambers from non-physiological shear forces (Fig. 2b). Through the micropores, dissolved molecules may diffuse quickly in and out of the tissue chambers, as confirmed by computational modeling and by dynamic tracking of a fluorescent dye in different channel- and chamber locations (Fig. 2b). In sum, the membrane constitutes an endothelial-like barrier that separates perfused media from the chip-embedded tissues. Although this artificial barrier admittedly does not recapitulate active transport processes occurring *in vivo*, it does provide a potential scaffold for the inclusion of endothelial cells in future generations of the platform.

**Generation and functional validation of human white adipose tissue on-chip.** Two major difficulties of mature adipocytes – their buoyancy and fragility – have traditionally hampered the *in vitro* culture of WAT. We developed specifically optimized cell-isolation and -injection protocols to enable the integration of freshly isolated, mature primary adipocytes from humans into the tissue chambers of our microphysiological platform. By suspending the isolated cells into a collagen hydrogel before injection, their viability and integrity could be preserved. The use of the hydrogel ensures both the protection and the 3D arrangement of the fragile cells during the formation of the microtissue. Moreover, the hydrogel and the location of the cell-injection inlets on the bottom of the tissue chambers (Figs. 2a and 3) help to overcome the issue of adipocyte buoyancy. Successful cell loading generates 8 independent, parallel 3D WAT-like microtissues per system (and 16 per platform).

Due to the microscale footprints of chambers and platform, only a small number of cells are required per chamber. This is of particular importance, as the tissues are based on primary, non-proliferating cells, and multiple chips (independent replicates) can be loaded with cells from a single biopsy, enabling testing under multiple experimental and control conditions of microtissues from the same donor. This is of crucial advantage when dealing with inter-donor variability, while it also enables patient-specific experiments.

**Structural analysis of adipocytes on-chip.** To investigate the structural arrangement of the generated adipose tissue, we established a staining protocol that enabled the on-chip visualization of intracellular lipid vacuoles using a neutral lipid stain. After six days of on-chip culturing, confocal imaging confirmed the formation of dense, 3D tissues composed of large unilocular adipocytes (Fig. 3a). The observable, mature phenotype of adipocytes suggests that the tissue-generation and -culture methods were capable of creating and maintaining physiological microenvironments and conditions. Inappropriate culture conditions have been frequently reported to induce cell dedifferentiation<sup>43,44</sup> which would lead to highly proliferative dedifferentiated fat cells (DFAT) with multilineage character<sup>45</sup>. One of the first hallmarks of dedifferentiation is the re-organization of lipids into multiple lipid droplets (i.e., a multilocular phenotype) and an increased rate of lipolysis<sup>44</sup>.

Moreover, we analyzed the microfluidic platform for a potential selectivity in terms of adipocyte structure by comparing the size of the lipid vacuoles of adipocytes on-chip to that of the respective donor-specific explants (Fig. 3b). Due to the unilocularity of mature adipocytes, determining lipid droplet size is an indirect measure for the adipocytes' size. The quantitative analysis revealed that both average size as well as the distribution of

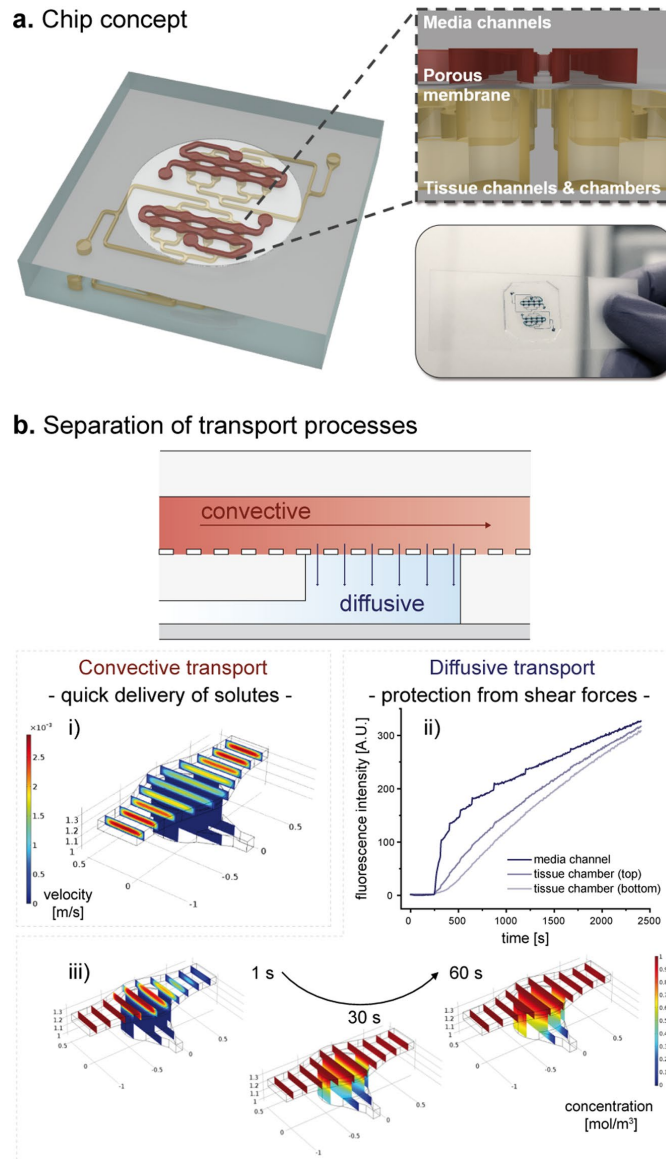


**Figure 2.** Concept of the microphysiological platform and microfluidic perfusion. **(a)** Schematic of the chip platform featuring two independent systems with eight tissue chambers each. As shown in the cross-sectional zoom-in, tissue chambers, which feature tissue channel inlets at the bottom, are located right below the perfusable media channels, and separated from them by a microporous membrane. **(b)** During flow, the chip's circuitry imposes a separation of the two transport processes, convection and diffusion. Convective flow is confined to the vasculature-like media channels, as confirmed by computational modeling (i). The tissue chambers are supplied by a diffusive transport as confirmed by observable diffusion of a fluorescent dye from the media channel into a hydrogel-filled tissue chamber (ii), as well as by computational modeling (iii).

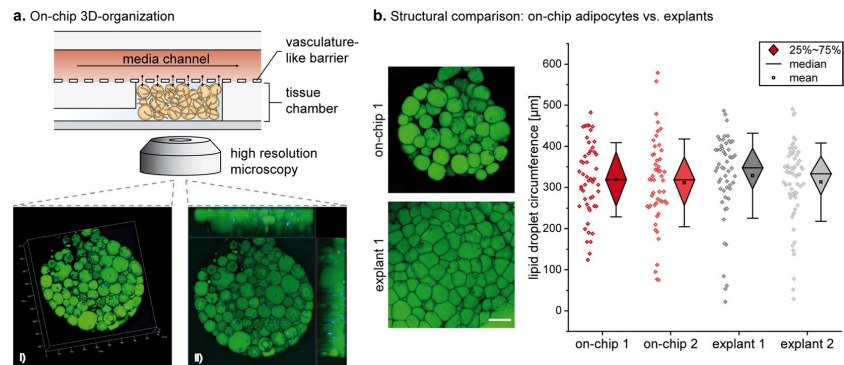


**Figure 3.** Structural characterization of human WAT-on-a-chip. **(a)** On day 6 of on-chip culture, intracellular lipid vacuoles (green; neutral lipid stain BODIPY™ 493/503) and nuclei (blue; DAPI) were visualized by confocal imaging. As shown by a 3D-rendered Z-stack of one WAT-chamber (i) (steps on the scale in 100 μm) and the corresponding maximum intensity projection with two sectional planes (ii), the individual adipocytes were unilocular and formed a densely packed 3D microtissue throughout the tissue chamber. **(b)** Comparison of lipid vacuole size of adipocytes on-chip versus explants (two replicates per condition). Scale bar equals 150 μm.

individual cell sizes are very similar between explant and on-chip culture. This indicates that the WAT-on-a-chip does indeed recapitulate the morphological heterogeneity of mature adipocytes in WAT *in vivo*.

**Validation of adipocyte functionality on-chip.** To assess the capability of the WAT-on-a-chip system to maintain viability and functionality of the integrated tissues, we deployed a comprehensive toolbox of chip-specific, functional readout methods. First, the viability and integrity of the vast majority of cells after eight days of on-chip culture was confirmed using a FDA/PI-based live/dead-staining protocol tailored specifically for the chip's configuration (Fig. 4a). In addition, to verify that the objective of any microphysiological OoC system – the recapitulation of *in vivo* functionality – was indeed attained, we examined multiple functional endpoints. Taking advantage of the optical accessibility and continuous medium perfusion through our system, we performed non-invasive imaging and analysis of media effluents under several conditions.

To monitor fatty acid metabolism in real-time, we added the fluorescently tagged fatty dodecanoic acid (C<sub>12</sub>H<sub>24</sub>O<sub>2</sub>) analog (BODIPY™ 500/510 C1, C12) to the perfusion medium, and characterized the dynamics of fatty acid influx into, and efflux from, the WAT-model. This assay represents a powerful tool that allows non-invasive assessment of the cellular uptake of fatty acids, their accumulation in intracellular lipid vacuoles, and their release from adipocytes when the fatty-acid analog is removed from the medium. Utilizing time-resolved fluorescence microscopy, we were able to observe these characteristic uptake and secretion kinetics in the adipocytes cultured on-chip (Fig. 4b).

The continuous, convective transport by the perfusion flow of metabolized and secreted factors away from the tissues, provides opportunities for effluent sampling in a time-resolved manner, allowing the dynamics of e.g. metabolism, secretion, and endocrine functionality to be measured. Using colorimetric assays, we characterized the levels of oleic acid, a representative of non-esterified fatty acids (NEFAs), and of glycerol in the effluent medium, and found that their concentrations remained very stable for several days of culturing (Fig. 4c). The measured NEFA and glycerol levels were comparable to levels from human subcutaneous adipose tissue explants immediately after biopsy<sup>46</sup>. In a similar approach, we examined the impact on fatty acid release of a 0.2 (w/v)% supplementation of the perfusion medium with human serum albumin (HSA). After 24 h of perfusion, we observed a significant increase of NEFA levels in the effluent (Fig. 4d). Thus, in our system, effluent sampling provided a powerful, non-invasively obtained readout of secretome and metabolome dynamics with high temporal resolution (depending on the sensitivity of the employed assay). This constitutes an effective link for the cross-correlation with clinical data and biomarker development. The general applicability of effluent sampling, however, is restricted by the base material PDMS, which is utilized for the majority of microfluidic platforms and also for our WAT-on-a-chip. The major limitation of many polymers and especially PDMS is the absorption of small hydrophobic molecules, which is especially an issue in microfabricated devices due to the large surface-to-volume ratio<sup>47</sup>. Hence, many hormones as well as adipokines can partition into the polymer leading to an uncontrolled reduction of their concentration in the effluent down to undetectable amounts. This is, for instance, the case for the important adipokine adiponectin (Supplement S5). To account for this, future generations of the WAT-chip are envisioned to employ alternative materials or surface coatings.

**Long-term functionality of integrated white adipose tissue.** One of the main challenges of conventional adipocyte *in vitro* culture is the long-term maintenance of functional stability. As discussed above, issues related to buoyancy, fragility and de-differentiation of adipocytes typically limit the duration of integrity of *in vitro* cultures to a couple of days at most<sup>46,48</sup>. Our structural and functional characterization of the

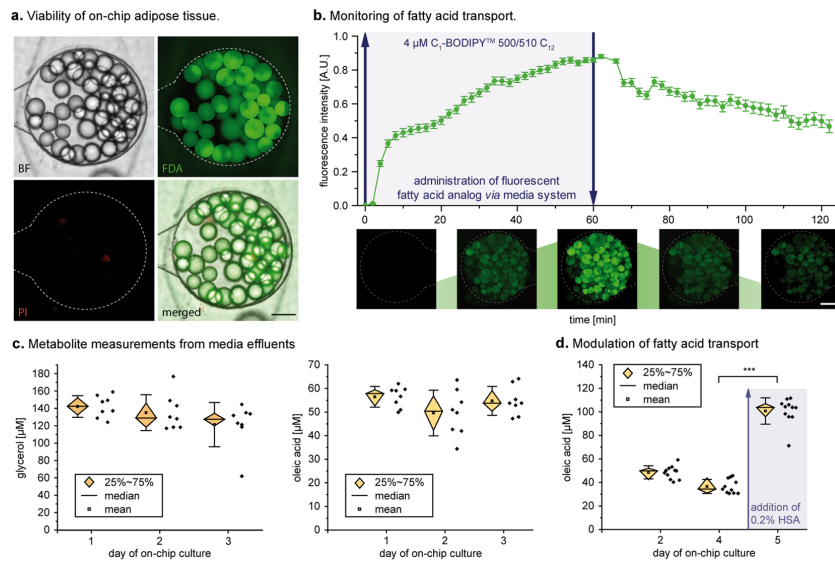


**Figure 4.** Functional validation of the human WAT-on-a-chip. **(a)** Live/dead-staining of adipocytes on day 8 of on-chip culture. FDA (green) marks live adipocytes by confirming membrane integrity and esterase activity in the vast majority of the integrated adipocytes. PI (red) staining indicates a very low number of apoptotic/necrotic and dead adipocytes. Scale bar equals 150 μm. **(b)** On-line monitoring of fatty acid transport on day 6. Monitoring of fatty acid uptake and accumulation was realized by the addition of a fluorescent fatty acid analog (4 μM BODIPY™ 500/510 C1, C12) to the perfused medium for one hour, followed by measurement of the mean fluorescence intensity. Upon removal of the fatty acid analog from the medium, fatty acid release could be observed (n = 47 individual tissue chambers). Scale bar equals 150 μm. **(c)** Evaluation of fatty acid metabolites in media effluents. Using colorimetric assays, glycerol and oleic acid (representative of non-esterified fatty acids) concentrations were found to be stable for the first three days of on-chip culture (n = 8 systems with 8 tissue chambers each). **(d)** Upon addition of 0.2% w/v human serum albumin (HSA) to the culture medium for 24 h, fatty acid release significantly increased compared to that during previous days (p < 0.005; n = 11 systems with eight tissue chambers each).

WAT-on-a-chip indicated that this microphysiological platform is capable of maintaining stable culture conditions over prolonged time periods. However, to investigate the potential of the platform to support a robust, long-term culture, we non-invasively monitored cell viability for a culture time of 36 days (Fig. 5a) by analyzing the release of lactate dehydrogenase (LDH) to the medium effluents. Throughout the culture, LDH levels were below 5% of LDH levels measured in the target cell maximum LDH release control (positive control) indicating a good overall on-chip viability. These findings were further supported by a live/dead-staining performed as an endpoint analysis of the long-term culture. To additionally investigate the long-term functionality, we performed fatty acid uptake assays on the tissues after 6 days, as well as after 36 days of on-chip culture (Fig. 5b). We observed that even after more than a month of *in vitro* culture, adipocytes still showed functional uptake and accumulation of fatty acids. Interestingly, a difference in initial uptake rates emerged, which might be related to size limitation of the “long-term-fed” cells on day 36. Still, these findings highlight that the WAT-on-a-chip is indeed capable of maintaining the functionality of adipose tissue for much longer periods than are conventional methods. This brings within reach a variety of novel opportunities for *in vitro* studies, e.g. of long-term effects of nutrition, repeated exposure of potential toxicants, or of long-term endocrine dynamics<sup>49</sup>.

**Applicability of WAT-on-a-chip for drug testing.** Since an important area of application for the organ-on-a-chip technology is drug development, we conducted a proof of concept compound test to assess the applicability of our WAT-on-a-chip for pharmaceutical research. After 6 days of on-chip culture, we exposed the WAT-chip to the β-adrenergic agonist isoproterenol, which is known to induce lipolysis. By additionally supplementing the medium with the fluorescently tagged fatty acid analog (BODIPY™ 500/510 C1, C12) for 60 minutes, we were able to monitor isoproterenol-related effects on fatty acid uptake and release by adipocytes, using standard fluorescence microscopy (Fig. 6). While media with fluorescently tagged fatty acids was perfused, the normalized fluorescent intensity in the isoproterenol-treated systems increased significantly more slowly than in non-treated control systems. After switching to media without the fluorescently tagged fatty acid analog, the fluorescent intensity decreased much quicker in the isoproterenol-treated systems. Taken together, this means that the isoproterenol exposure induced a reduction of the net uptake rate of fatty acids and an increase of their release rate. Both findings are in line with the expected lipolysis-inducing effect of isoproterenol.

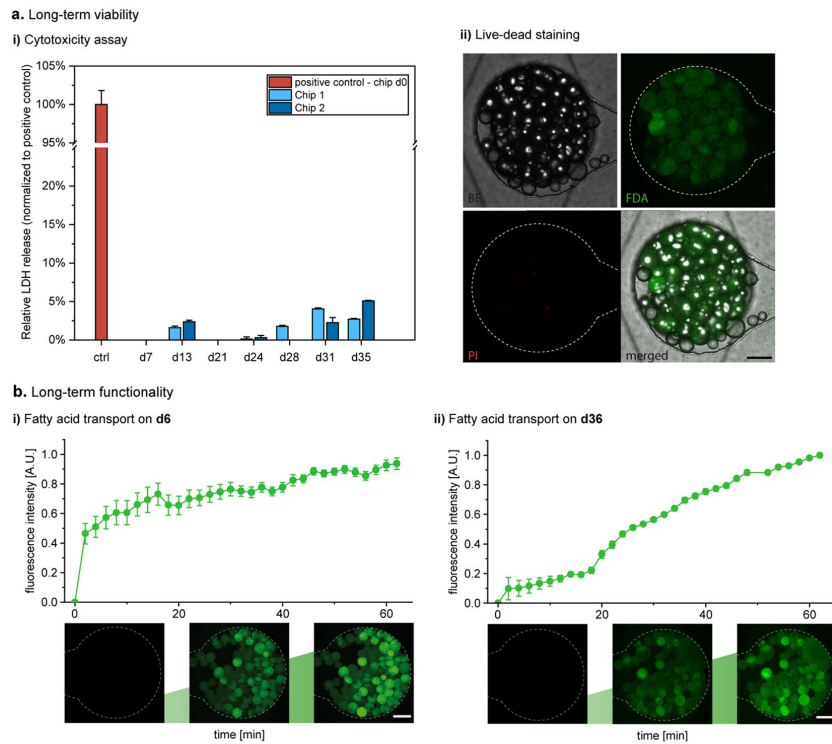


**Figure 5.** Long-term viability and functionality of the human WAT-on-a-chip. **(a)** Long-term viability determined via **(a.i)** non-invasive measurement of LDH release from medium effluents (absence of bars indicates no detectable difference to 0) as well as **(a.ii)** live/dead staining at day 36. Scale bar equals 150  $\mu\text{m}$ . **(b)** Dynamic measurement of the normalized fluorescence intensity in tissue chambers perfused with medium containing a fluorescent fatty acid analog (4  $\mu\text{M}$  BODIPY<sup>TM</sup> 500/510 C1, C12) revealed functional fatty acid uptake and accumulation in the WAT-model after **(b.i)** 6 as well as **(b.ii)** 36 days of on-chip culture ( $n=6$  individual tissue chambers). Scale bars equal 150  $\mu\text{m}$ .

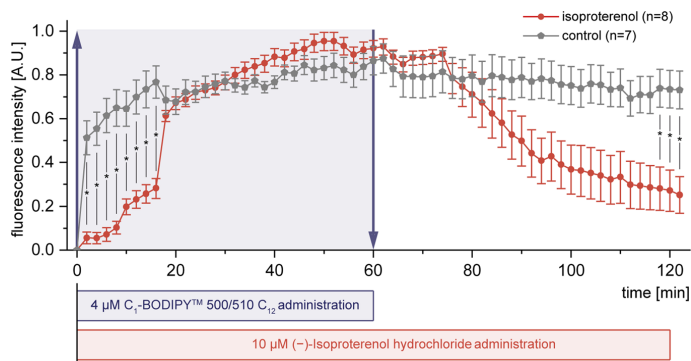


**Figure 6.** Applicability for drug testing illustrated by the effect of isoproterenol on fatty acid uptake and release. Normalized mean fluorescence intensity obtained by time-lapse fluorescence microscopy of WAT-on-a-chip systems perfused with medium supplemented with the fluorescently tagged fatty acid analog (4  $\mu\text{M}$  BODIPY<sup>TM</sup> 500/510 C1, C12) during the first 60 minutes. Kinetics in systems exposed to 10  $\mu\text{M}$  Isoproterenol (red circles) show significant differences to non-treated controls (grey polygons) ( $n=7$  and  $n=8$  individual tissue chambers; mean fluorescence intensities  $\pm$  SEM are presented).

Evidently, the used approach based on standard microscopy provides facile and non-invasive read-outs for drug screening, with a very high time-resolution, which is amenable for massive parallelization and automation. One noteworthy limitation is the requirement for normalization of readings from individual tissue chambers. Absolute quantitative values would provide even more information and potential for cross-correlation; it is, therefore, planned to address this in future generations of chips and readout-infrastructure. Overall, the successful proof of concept highlights the applicability of the WAT-on-a-chip system for screening purposes and the potential the system can have for drug development purposes.

### Conclusion

Due to the lack of suitable experimental human model systems, research in adipose tissue biology and obesity has so far relied mostly on animal models, non-physiological *in vitro* systems, GWAS studies and (clinical) epidemiology. The first two approaches have major limitations in terms of their translatability to humans; the latter two require complex statistical analyses of large data sets and do not permit strong conclusions on pathophysiological mechanisms or efficacy of therapeutic interventions in individuals. The human WAT-on-a-chip platform presented here provides a novel tool that enables the maintenance, monitoring and manipulation of human adipocytes in a durably stable, tissue-like microphysiological environment. As an engineered model system, there are naturally still differences compared to complex *in vivo* tissue, which could be further reduced in the future, e.g. by the integration of WAT-resident immune cells and further cells from the stromal vascular fraction. Nevertheless, the vasculature-like perfusion provides opportunities for biomarker evaluation and “liquid biopsies” that can be cross-correlated with clinical endpoints, as well as a potential connection link for integration with other organ-on-a-chip platforms<sup>34</sup>. Multi-organ-chips integrating WAT-models are likely to be of major interest e.g. for ADMET, diabetes or non-alcoholic steatohepatitis (NASH) studies.

Overall, the introduced WAT-on-a-chip system offers new perspectives and opportunities in mechanistic studies, pharmaceutical development and testing, as well as in personalized medicine.

Received: 17 May 2019; Accepted: 31 March 2020;

Published online: 20 April 2020

### References

- World Health Organization (WHO), *Obesity*, <https://www.who.int/news-room/facts-in-pictures/detail/6-facts-on-obesity> (accessed 16 February 2019).
- World Health Organization (WHO), *Global Health Observatory (GHO) data*, <https://www.who.int/gho/en/> (accessed 16 February 2019).
- World Health Organization (WHO), *Facts and figures on childhood obesity*, <https://www.who.int/end-childhood-obesity/facts/en/> (accessed 16 February 2019).
- Wang, Y., Beydoun, M. A., Liang, L., Caballero, B. & Kumanyika, S. K. Will All Americans Become Overweight or Obese? Estimating the Progression and Cost of the US Obesity Epidemic. *Obesity* **16**, 2323–2330 (2008).
- Young, B., O’Dowd, G. & Woodford, P. *Wheater’s Functional Histology*, Churchill Livingstone, 6th Edition, ISBN 9780702047473 (2014).
- Rosen, E. D. & Spiegelman, B. M. What We Talk About When We Talk About Fat. *Cell* **156**, 20–44 (2014).
- Kershaw, E. E. & Flier, J. S. Adipose Tissue as an Endocrine Organ. *J. Clin. Endocrinol. Metab.* **89**, 2548–2556 (2004).
- Scherer, P. E. Adipose Tissue: From Lipid Storage Compartment to Endocrine Organ. *Diabetes* **55**, 1537–1545 (2006).
- Fasshauer, M. & Blüher, M. Adipokines in health and disease. *Trends Pharmacol. Sci.* **36**, 461–470 (2015).
- Bélangier, C., Luu-The, V., Dupont, P. & Tchernof, A. Adipose Tissue Intracrinology: Potential Importance of Local Androgen/Estrogen Metabolism in the Regulation of Adiposity. *Horm. Metab. Res.* **34**, 737–745 (2002).
- Mayes, J. S. & Watson, G. H. Direct effects of sex steroid hormones on adipose tissues and obesity. *Obes. Rev.* **5**, 197–216 (2004).
- Marra, F. & Bertolani, C. Adipokines in liver diseases. *Hepatology* **50**, 957–969 (2009).
- Berg, A. H. & Scherer, P. E. Adipose tissue, inflammation, and cardiovascular disease. *Circ. Res.* **96**, 939–949 (2005).
- Zhang, Z. & Scherer, P. E. Adipose tissue: The dysfunctional adipocyte — a cancer cell’s best friend. *Nat. Rev. Endocrinol.* **14**, 132–134 (2018).
- Hajer, G. R., van Haefen, T. W. & Visseren, F. L. J. Adipose tissue dysfunction in obesity, diabetes, and vascular diseases. *Eur. Heart J.* **29**, 2959–2971 (2008).
- Pérez-Hernández, A. I., Catalán, V., Gómez-Ambrosi, J., Rodríguez, A. & Frühbeck, G. Mechanisms linking excess adiposity and carcinogenesis promotion. *Front. Endocrinol. (Lausanne)* **5**, 65 (2014).
- Nawrocki, A. R. & Scherer, P. E. Keynote review: the adipocyte as a drug discovery target. *Drug Discov. Today* **10**, 1219–1230 (2005).
- Kusminski, C. M., Bickel, P. E. & Scherer, P. E. Targeting adipose tissue in the treatment of obesity-associated diabetes. *Nat. Rev. Drug Discov.* **15**, 639 (2016).
- Haas, B., Schlinkert, P., Mayer, P. & Eckstein, N. Targeting adipose tissue. *Diabetol. Metab. Syndr.* **4**, 43 (2012).
- Sankaralingam, S., Kim, R. B. & Padwal, R. S. The Impact of Obesity on the Pharmacology of Medications Used for Cardiovascular Risk Factor Control. *Can. J. Cardiol.* **31**, 167–176 (2015).
- Sheng, X. *et al.* Adipocytes Sequester and Metabolize the Chemotherapeutic Daunorubicin. *Mol. Cancer Res.* **15**, 1704–1713 (2017).
- Kleinert, M. *et al.* Animal models of obesity and diabetes mellitus. *Nat. Rev. Endocrinol.* **14**, 140 (2018).
- King, A. & Bowe, J. Animal models for diabetes: Understanding the pathogenesis and finding new treatments. *Biochem. Pharmacol.* **99**, 1–10 (2016).
- Poulos, S. P., Dodson, M. V. & Hausman, G. J. Cell line models for differentiation: preadipocytes and adipocytes. *Exp. Biol. Med.* **235**, 1185–1193 (2010).
- Li, X. & Easley, C. J. Microfluidic systems for studying dynamic function of adipocytes and adipose tissue. *Anal. Bioanal. Chem.* **410**, 791–800 (2018).
- Mandrup, S., Loftus, T. M., MacDougald, O. A., Kuhajda, F. P. & Lane, M. D. Obese gene expression at *in vivo* levels by fat pads derived from sc implanted 3T3-F442A preadipocytes. *Proc. Natl. Acad. Sci. U.S.A.* **94**, 4300–5 (1997).
- Volz, A.-C., Omengo, B., Gehrke, S. & Kluger, P. J. Comparing the use of differentiated adipose-derived stem cells and mature adipocytes to model adipose tissue *in vitro*. *Differentiation* **110**, 19–28 (2019).
- Abbott, R. D. *et al.* Variability in responses observed in human white adipose tissue models. *J. Tissue Eng. Regen. Med.* **12**, 840–847 (2017).
- Rogal, J., Zbinden, A., Schenke-Layland, K. & Loskill, P. Stem-cell based organ-on-a-chip models for diabetes research. *Adv. Drug Deliv. Rev.* **140**, 101–128 (2019).

30. Esch, E. W., Bahinski, A. & Huh, D. Organs-on-chips at the frontiers of drug discovery. *Nat. Rev. Drug Discov.* **14**, 248–260 (2015).
31. Ahadian, S. *et al.* Organ-On-A-Chip Platforms: A Convergence of Advanced Materials. *Cells, and Microscale Technologies. Adv. Healthc. Mater.* **7**, 1700506 (2018).
32. Berg, A. V. D., Mummery, C. L., Passier, R. & Van Der Meer, A. D. Personalised organs-on-chips: functional testing for precision medicine. *Lab Chip* **19**, 198–205 (2019).
33. Esch, M. B. *et al.* Multi-Organ toxicity demonstration in a functional human *in vitro* system composed of four organs. *Adv. Drug Deliv. Rev.* **69–70**, 158–169 (2014).
34. Rogal, J., Probst, C. & Loskill, P. Integration concepts for multi-organ chips: how to maintain flexibility?! *Futur. Sci. OA FSO180* (2017).
35. Dugan, C. E. & Kennedy, R. T. *Measurement of lipolysis products secreted by 3T3-L1 adipocytes using microfluidics*, Elsevier Inc., 1st edn., vol. 538 (2014).
36. Loskill, P. *et al.* WAT-on-a-chip: a physiologically relevant microfluidic system incorporating white adipose tissue. *Lab Chip* **17**, 1645–1654 (2017).
37. Abbott, R. D. *et al.* Long term perfusion system supporting adipogenesis. *Methods* **84**, 84–89 (2015).
38. Liu, Y. *et al.* Adipose-on-a-chip: a dynamic microphysiological *in vitro* model of the human adipose for immune-metabolic analysis in type II diabetes. *Lab Chip* **19**, 241–253 (2019).
39. Kongsuphol, P. *et al.* *In vitro* micro-physiological model of the inflamed human adipose tissue for immune-metabolic analysis in type II diabetes. *Sci. Rep.* **9**, 4887 (2019).
40. Godwin, L. A. *et al.* A microfluidic interface for the culture and sampling of adiponectin from primary adipocytes. *Analyst* **140**, 1019–1025 (2015).
41. Harms, M. J. *et al.* Mature Human White Adipocytes Cultured under Membranes Maintain Identity, Function, and Can Transdifferentiate into Brown-like Adipocytes. *Cell Rep.* **27**, 213–225.e5 (2019).
42. Zhang, H. H., Kumar, S., Barnett, A. H. & Eggo, M. C. Surface Proteins of Gram-Positive Bacteria and How They Get There. *J. Endocrinol.* **164**, 119–128 (2000).
43. Huber, B. *et al.* Integration of Mature Adipocytes to Build-Up a Functional Three-Layered Full-Skin Equivalent. *Tissue Eng. Part C Methods* **22**, 756–764 (2016).
44. Sugihara, H., Yonemitsu, N., Miyabara, S. & Yun, K. Primary cultures of unilocular fat cells: characteristics of growth *in vitro* and changes in differentiation properties. *Differentiation* **31**, 42–49 (1986).
45. Matsumoto, T. *et al.* Mature adipocyte-derived dedifferentiated fat cells exhibit multilineage potential. *J. Cell. Physiol.* **215**, 210–222 (2008).
46. Decaunes, P., Bouloumié, A., Ryden, M. & Galitzky, J. *Ex vivo* Analysis of Lipolysis in Human Subcutaneous Adipose Tissue Explants. *Bio-protocol* **8**, 1–12 (2018).
47. Toepke, M. W. & Beebe, D. J. PDMS absorption of small molecules and consequences in microfluidic applications. *Lab Chip* **6**, 1484–1486 (2006).
48. Maurizi, G. *et al.* Human white adipocytes convert into “rainbow” adipocytes *in vitro*. *J. Cell. Physiol.* **232**, 2887–2899 (2017).
49. Nawroth, J., Rogal, J., Weiss, M., Brucker, S. Y. & Loskill, P. Organ-on-a-Chip Systems for Women's Health Applications. *Adv. Healthc. Mater.* **1700550** (2017).

### Acknowledgements

The authors thank Dr. Ziegler (Klinik Charlotenhaus, Stuttgart) for the kind provision of human adipose tissue from plastic surgery, Dr. Jakob Barz for help with the PECVD coating process, and Silvia Kolbus-Hernandez, Elena Rubiu as well as Luisa Merz for their assistance with cell culture and chip fabrication. We further thank Prof. Andreas Stahl and Pete Zushin for helpful discussions and Joost Overduin for language-editing. The research was supported in part by the Fraunhofer-Gesellschaft internal programs Talenta Start (to J.R.) and Attract (601543), the DAAD funded by the Bundesministerium für Bildung und Forschung (BMBF) (PPP USA 2018, 57387214) (all to P.L.), as well as the Ministry of Science, Research and the Arts of Baden-Württemberg (Az: 7542.2-501-1/13/6 to P.L. and Az: 33-729.55-3/214-8 to K.S.-L.).

### Author contributions

J.R. and P.L. designed the device. J.R. and C.B. fabricated the device. J.R., C.B., E.K. and J.Rz. performed and analyzed the experiments. S.S. performed membrane characterization. C.P. performed simulations. K.S.-L. gave biological advice. J.R., K.S.-L. and P.L. wrote the manuscript. J.R. and P.L. designed the study.

### Competing interests

The authors declare no competing interests.

### Additional information

**Supplementary information** is available for this paper at <https://doi.org/10.1038/s41598-020-63710-4>.

**Correspondence** and requests for materials should be addressed to P.L.

**Reprints and permissions information** is available at [www.nature.com/reprints](http://www.nature.com/reprints).

**Publisher's note** Springer Nature remains neutral with regard to jurisdictional claims in published maps and institutional affiliations.



**Open Access** This article is licensed under a Creative Commons Attribution 4.0 International License, which permits use, sharing, adaptation, distribution and reproduction in any medium or format, as long as you give appropriate credit to the original author(s) and the source, provide a link to the Creative Commons license, and indicate if changes were made. The images or other third party material in this article are included in the article's Creative Commons license, unless indicated otherwise in a credit line to the material. If material is not included in the article's Creative Commons license and your intended use is not permitted by statutory regulation or exceeds the permitted use, you will need to obtain permission directly from the copyright holder. To view a copy of this license, visit <http://creativecommons.org/licenses/by/4.0/>.

© The Author(s) 2020



Publication [7]

## **Isolation, Integration, and Culture of Human Mature Adipocytes Leveraging Organ-on-Chip Technology**

**J.Rogal**<sup>#</sup>, J. Roosz<sup>#</sup>, P.Loskill

*Methods Mol. Biol.*, in press (2021), [https://dx.doi.org/10.1007/978-1-0716-1693-2\\_18](https://dx.doi.org/10.1007/978-1-0716-1693-2_18)

### **Abstract:**

Research on white adipose tissue (WAT), which constitutes one-fifth to one-half of the total body mass of a human's body, has gained more and more interest and attention in the era of "diabesity." In vitro research on mature human WAT is hampered by many challenges and, hence, a majority of WAT-related research is conducted using animal models as well as clinical observations and genome-wide association studies (GWAS), both featuring limitations in terms of translatability and potential for experimental interventions, respectively. Here, we describe methods to isolate primary mature human adipocytes from biopsies and to fabricate tailored organ-on-chip platforms for the long-term culture of WAT constructs.

# Chapter 18 1

## Isolation, Integration, and Culture of Human Mature Adipocytes Leveraging Organ-on-Chip Technology 2 3

Julia Rogal, Julia Roosz, and Peter Loskill 4

### Abstract 5

Research on white adipose tissue (WAT), which constitutes one-fifth to one-half of the total body mass of a human's body, has gained more and more interest and attention in the era of "diabesity." In vitro research on mature human WAT is hampered by many challenges and, hence, a majority of WAT-related research is conducted using animal models as well as clinical observations and genome-wide association studies (GWAS), both featuring limitations in terms of translatability and potential for experimental interventions, respectively. Here, we describe methods to isolate primary mature human adipocytes from biopsies and to fabricate tailored organ-on-chip platforms for the long-term culture of WAT constructs. 6  
7  
8  
9  
10  
11  
12

**Keywords** Organ-on-chip, Microphysiological systems, Primary adipocytes, Microfluidics, White adipose tissue, Fat-on-chip, WAT-on-chip 13  
14  
15

---

### 1 Introduction 16

White adipose tissue (WAT) makes up one-fifth to one-fourth of a healthy adult human's body mass [1]. In obese individuals, WAT can even amount to half of the total body mass. As a highly specialized organ, it is not only responsible for storage and release of energy but it is also a key regulator of metabolism in its endocrine function. An abnormal amount and/or function of WAT, as is the case in obesity, for instance, predisposes the affected individuals to developing a myriad of severe comorbidities including metabolic diseases, especially type 2 diabetes mellitus (T2DM) [2], cardiovascular diseases [3], and cancer [4]. Therefore, it comes as no surprise that, especially in the era of "diabesity," with 1.9 billion people worldwide being overweight and 422 million being affected by diabetes [5, 6], research on WAT has gained more and more interest and attention within the past few decades. 17 AU1  
18  
19  
20  
21  
22  
23  
24  
25  
26  
27  
28  
29  
30

---

Julia Rogal, Julia Roosz contributed equally to this work.

Marco Rasponi (ed.), *Organ-on-a-Chip: Methods and Protocols*, Methods in Molecular Biology, vol. 2373, [https://doi.org/10.1007/978-1-0716-1693-2\\_18](https://doi.org/10.1007/978-1-0716-1693-2_18), © Springer Science+Business Media, LLC, part of Springer Nature 2021

Julia Rogal et al.

Due to the unique characteristics of adipocytes including their large size, fragility as well as buoyancy in aqueous solutions, in vitro research on mature human WAT is hampered by many challenges. This is why, to date, most of the gained insights on (patho)-physiology of WAT are based on (1) animal studies as well as (2) clinical observations and genome-wide association studies (GWAS). The latter enable the analysis of systemic interdependencies rather than molecular or cellular mechanisms and pathways. Animal models, on the other hand, enable mechanistic research on a (sub)cellular level; findings, however, are often not translatable to human physiology because of massive interspecies differences when it comes to metabolism.

To study human WAT in vitro, the sources for cells range from immortalized cell lines and adipose progenitor cells to primary human stem cells and mature adipocytes. In vitro differentiated adipocytes show a premature state, which does not recapitulate physiological conditions; especially with regard to the unilocularity of their lipid contents as well as their gene expression and secretome, which differ significantly in the relative proportions of adipose-associated hormones. Therefore, the best choice of cells for studying human mature WAT remain human primary mature adipocytes—despite their rather complicated handling requirements.

Biopsies of WAT are easily available from plastic surgery as resections of excessive skin and subcutaneous WAT, enabling the isolation of primary mature adipocytes. To overcome the scarcity of suitable culture conditions, fluidic platforms providing a microenvironment with physiological cues can enable the long-term culture and studies of WAT in the context of pathomechanisms and compound testing. Those organ-on-chip platforms combine microfabrication, biomaterials and tissue engineering to embed mature adipocytes in a microphysiological environment. WAT-on-chip platforms, for example, in the form of disease models hold great potential for mechanistic and pharmaceutical studies as well as the optimization of personalized medical treatments of obesity and diabetes [7–9].

Here we present detailed methods for the isolation of human mature adipocytes and their integration into a tailored perfused microphysiological platform amenable for long-term culture [10]. The WAT-on-chip is based on a polydimethylsiloxane (PDMS) microfluidic platform comprising multiple, tissue-specific chambers and a vasculature-like microchannel. The chambers are fluidically connected to the constantly perfused channels via a porous membrane, allowing for a diffusive supply of soluble factors while shielding the cells from the shear forces of the perfused liquid. The specifically tailored isolation and injections protocols enable creation of 3D microtissues based on freshly isolated mature adipocytes. The microtissues can be kept viable on chip for over

Isolation, Integration, and Culture of Human Mature Adipocytes Leveraging...

1 month. Optical accessibility and analyzing of effluents allow for monitoring the patency of the cells as well as key cell-physiological aspects, for example, fatty acid trafficking and drug responsiveness.

<b>2</b>	<b>Materials</b>	82
<b>2.1</b>	<b>Chip Fabrication</b>	
	1. Photoresist (e.g., SU-8 50 and SU-82010).	83
	2. Photoresist developer (e.g., SU-8 developer).	84
	3. Wafer: 4" Si-Wafer; test grade.	85
	4. Silane: chlorotrimethylsilane.	86
	5. PDMS: Polydimethylsiloxane.	87
	6. Desiccator.	88
	7. Glass slides: 76 × 26 mm, height 1 mm.	89
	8. PET membranes: TRAKETCH® PET 3.0 p S210x300 (SABEU GmbH & Co. KG); SiO <sub>x</sub> coated via plasma-enhanced, chemical vapor deposition (PECVD).	90 91 92
	9. Biopsy punch: diameter of 0.75 mm.	93
	10. Release liner: (3 M Scotchpak™ 1022 Release Liner Fluoropolymer Coated Polyester Film, 3 M ID 70000200280).	94 95
	11. Plasma cleaner.	96
	12. UV exposure unit.	97
	13. Hot plate.	98
	14. Spin coater.	99
	15. Foldback clamps.	100
	16. Stainless steel tweezers.	101
	17. Isopropanol for cleaning.	102
	18. Acetone for cleaning.	103
	19. Pressurized N <sub>2</sub> -gas for blow drying.	104
	20. Household adhesive tape.	105
	21. Ethanol 70% (v/v).	106 107
<b>2.2</b>	<b>Adipocyte Isolation</b>	
	1. Transportation box for biopsy.	108
	2. <i>Transportation buffer for biopsy</i> : Dulbecco's phosphate-buffered saline with MgCl <sub>2</sub> and CaCl <sub>2</sub> (PBS <sup>+</sup> ) containing 1% (v/v) Penicillin/Streptomycin (10.000 U/ml).	109 110 111
	3. <i>Enzymatic digestion solution</i> : DMEM/Ham's F-12 (1:1), 1% (w/v) Bovine Serum Albumin (BSA) and 0.13 U/ml collagenase ( <i>see Note 1</i> ).	112 113 114
	4. <i>Strainer</i> (pore size 500 μm).	115

Julia Rogal et al.

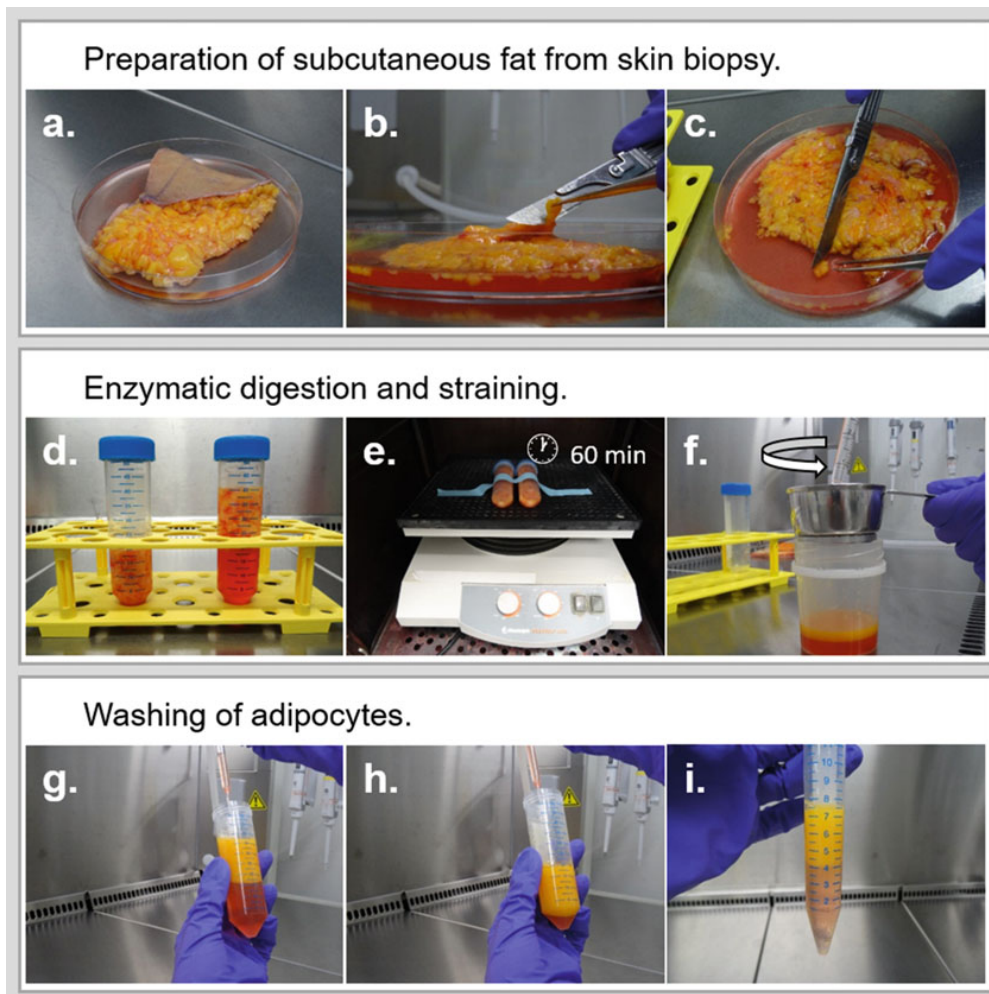


**Fig. 4** Overview of the main steps in adipocyte isolation, using resected skin with subcutaneous adipose tissue as cell source. Collecting and dissecting of WAT (depicted in a–c), digestion of collagen in WAT by enzymatic digestion (d, e), followed by straining of digested WAT (f), washing off of remaining enzymatic digestion solution (g, h). Prior to injection of the adipocytes into the microfluidic platform, the cells are transferred to a 15 ml conical tube (i) as it creates a higher packed layer of adipocytes and thereby facilitates adipocyte handling

5. *Reservoir cup* with matching diameter to strainer (depicted in Fig. 4f). 116
6. *Petri dishes*. 117
7. *Stainless steel tweezers*. 118
8. *Scalpel*. 119
9. *Conical falcon tubes*. 120

Isolation, Integration, and Culture of Human Mature Adipocytes Leveraging . . .

	10. Plate shaker.	122
	11. Incubator.	123
		124
<b>2.3 Adipocyte Injection</b>	1. 10 mg/ml Collagen Type I (see Note 2).	125
	2. Neutralization buffer for collagen dispersion (see Note 3).	126
	3. Blunt pipette tips for transferring of adipocytes (see Note 4).	127
	4. Stainless steel plugs: diameter 0.7 mm, length approximately 8 mm (see Note 5).	128
		129
	5. Microcentrifuge tube.	130
		131
<b>2.4 Adipocyte on-Chip Culture</b>	1. Adipocyte culture medium: AM-1 (BioCat GmbH) containing 1% (v/v) penicillin–streptomycin (10.000 U/ml).	132
		133
	2. Tubing: 0.762 × 2.286 mm.	134
	3. Connector needles: 21 GA needle (see Note 6).	135
	4. Syringes.	136
	5. Syringe pump (see Note 7).	137
		138
<hr/>		
<b>3 Methods</b>		139
<b>3.1 Chip Fabrication</b>	The WAT-on-chip is specifically designed to accommodating human mature white adipocytes and is fabricated via UV lithography and replica molding [11]. The microfluidic platform is made from two PDMS pieces featuring media channels and tissue chambers respectively and a isoporous TRAKETCH® PET-membrane sandwiched in-between. To facilitate microscopic accessibility, the tissue compartments of the chips are bonded to conventional glass slides. To avoid including particles or lint throughout the chip fabrication process, all steps should be carried out in a clean room or on clean benches.	140
		141
		142
		143
		144
		145
		146
		147
		148
		149
		150
<b>3.1.1 Chip Design and Wafer Fabrication</b>	To obtain the two PDMS pieces, two microstructured master wafers are required. The layouts were designed using a CAD software (Fig. 1a) and then converted into photomasks by an external service. The wafers are produced via a two-step UV lithography process (Fig. 1b), described in details for the tissue layer wafer in the following:	151
		152
		153
		154
		155
		156
	1. Clean the silicon wafers (4 in.) first with acetone and then with isopropanol for 2 min each and subsequently dehydrate them for 15 min on a hot plate (150 °C).	157
		158
		159
	2. Spin coat the first layer of photoresist to generate 100 μm (10 μm for media wafers) thick layers using the parameters provided by the photoresist manufacturer.	160
		161
		162

Julia Rogal et al.

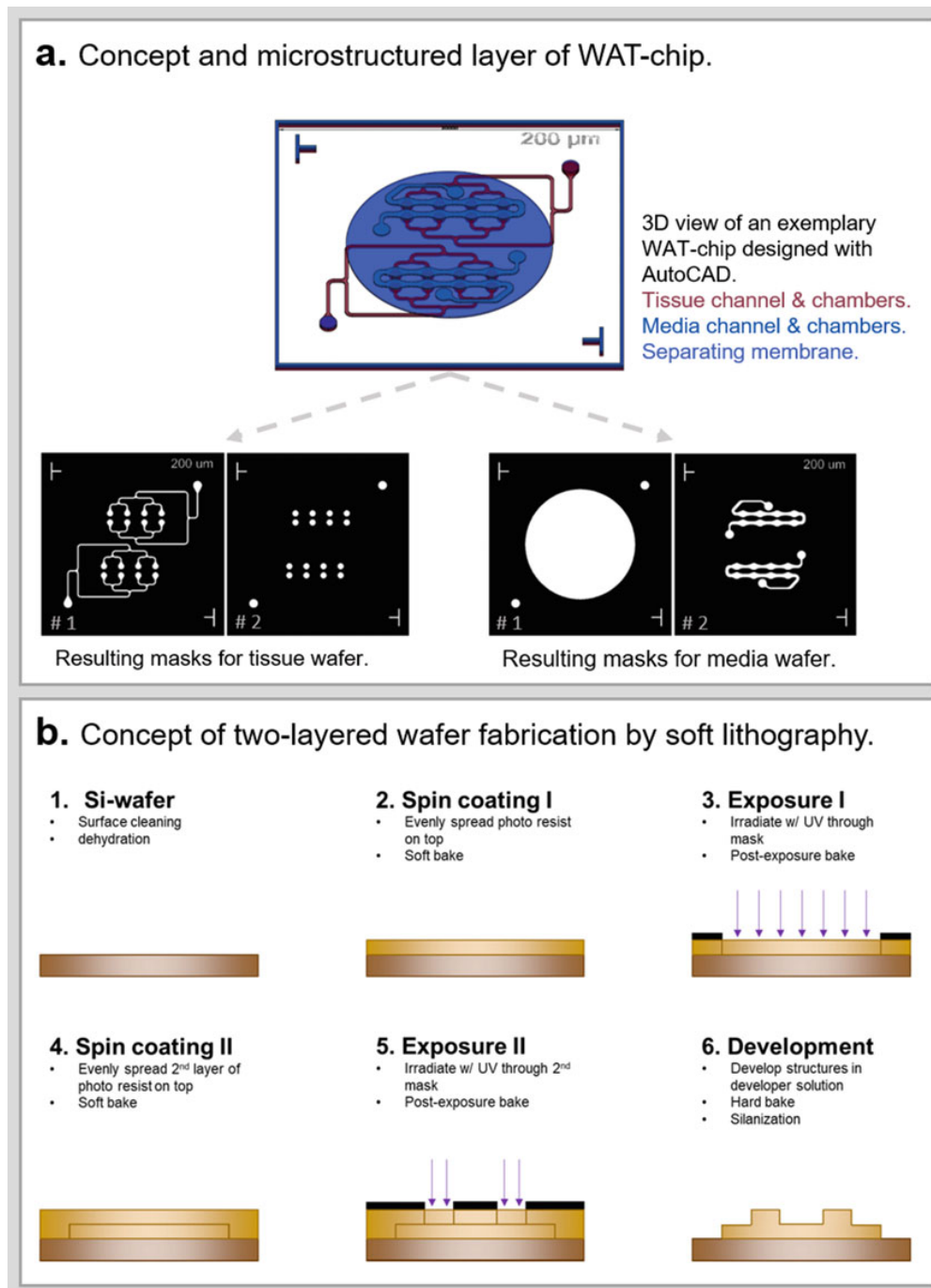


**Fig. 1** Master wafer fabrication. (a) Chip and mask designs. (b) Microfabrication process using two-step UV lithography

Isolation, Integration, and Culture of Human Mature Adipocytes Leveraging...

	3. Bake the wafer for 10 min at 65 °C and 30 min at 95 °C (solely 3 min at 95 °C for media wafers) on a hot plate and then let it cool down at RT.	163 164 165
	4. Place the wafer and the respective mask #1 under the exposure unit and expose according to the photoresist manufacturer's specification.	166 167 168
	5. Bake the wafer for 1 min at 65 °C and 10 min at 95 °C (solely 4 min at 95 °C for media wafers) on a hot plate and then let it cool down at RT.	169 170 171
	6. Repeat <b>steps 1–5</b> to pattern the second layer of 100 µm height (85 µm for media wafer) using the respective mask #2.	172 173
	7. Immerse the wafer for 10 min (8 min for media wafers) in photoresist developer and then twice in isopropanol for 2 min.	174 175
	8. Bake overnight at 150 °C on a hot plate.	176
	9. Functionalize the wafers with chlorotrimethylsilane via vapor-deposition by placing them together with 200 µl of silane in an evacuated desiccator for 2 h.	177 178 179 180
3.1.2 PDMS Mixture Preparation	1. Pour 30 g of prepolymer and 3 g of curing agent (included in the PDMS box kit) in a cup.	181 182
	2. Thoroughly mix pre-PDMS mixture using a plastic stirrer.	183
	3. Degas the pre-PDMS mixture with a desiccator until all air bubbles are removed ( <i>see Note 8</i> ).	184 185 186
3.1.3 Replica Molding of the Media Layer	The PDMS layer featuring the media channels seals the chip to the top leaving only access through the ports. The PDMS media layer is produced by <i>standard molding</i> (Fig. 2a; <i>see Note 9</i> ):	187 188 189
	1. Pour 25 g of the prepared PDMS mixture on top of the media wafer ( <i>see Note 10</i> ).	190 191
	2. Make sure the PDMS covers the entire surface of the wafer by tilting it ( <i>see Note 11</i> ).	192 193
	3. Cure the PDMS in a convection oven set to 60 °C overnight by placing the wafer on a levelled surface.	194 195
	4. On the next day, let the PDMS-wafer complex cool down to room temperature.	196 197
	5. Peel the PDMS off the wafer.	198
	6. Using a scalpel, cut the individual pieces ( <i>see Note 12</i> ) and punch the access ports at the indicated positions using a 0.75 mm-diameter biopsy punch ( <i>see Note 13</i> ).	199 200 201 202
3.1.4 Replica Molding of the Tissue Layer	The chip's tissue layer is an open-structured PDMS piece, which is bonded to a glass coverslip. This ensures maximal optical accessibility of the on-chip tissues as the only distance to be overcome when	203 204 205

Julia Rogal et al.

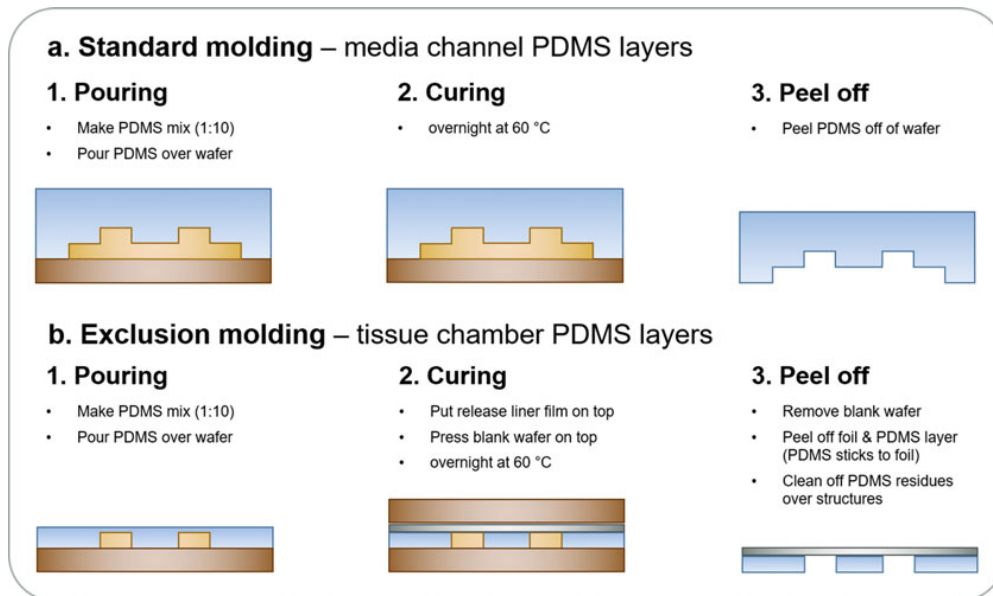


**Fig. 2** Replica molding of PDMS pieces. **(a)** The media layer is produced by standard molding. PDMS structures are closed to the top. **(b)** The tissue chamber PDMS layers are produced by exclusion molding. This process leaves open PDMS structures. (Reproduced from Rogal et al. [10] CC BY 4.0)

imaging with an inverted microscope is the coverslip thickness (*see* 206  
**Note 14**). To produce the tissue layer pieces, PDMS is *exclusion-* 207  
*molded* (Fig. 2b). 208

1. Pour ~1.25 g of the prepared PDMS mixture on top of the 209  
media wafer. 210
2. Thoroughly spread the PDMS across the wafer until all struc- 211  
tures are covered by gently rotating and tilting it. 212
3. Degas the PDMS on the wafer by applying vacuum in a desic- 213  
cator for a few minutes. 214
4. Cut release liner to the size of the wafer and carefully lower it 215  
with the treated surface facing the PDMS onto the wafer. Make 216  
sure to not include air bubbles. 217
5. Clamp the ensemble between two smooth surfaces (e.g., 218  
unpatterned wafers or Plexiglas discs) by applying even pres- 219  
sure using clamps. 220
6. Cure the PDMS in a convection oven set to 60 °C overnight. 221
7. On the next day, let the clamped PDMS–wafer ensemble cool 222  
down to room temperature. 223
8. Remove the clamps and clamping surfaces. 224
9. Peel off the PDMS (it will adhere to the release liner) from the 225  
wafer. 226

Isolation, Integration, and Culture of Human Mature Adipocytes Leveraging . . .

	10. Using scissors cut the individual pieces and microscopically examine if all structures are opened. Remove residues of PDMS adhering to the foil closing off the open structures using tweezers. Be thorough to open up the chambers entirely. Leftover PDMS pieces in the chambers will disturb on-chip cell culture.	227 228 229 230 231 232 233
3.1.5 Chip Assembly	Chip assembly includes cleaning of all parts, three subsequent bonding steps as well as finishing and quality control (Fig. 3):	234 235
	1. Thoroughly clean all PDMS parts, the membrane as well as the coverslip by rinsing with isopropanol and blow-drying with pressurized N <sub>2</sub> . (The tissue layer still adheres to the release liner. It is only removed in <b>step 5</b> .)	236 237 238 239
	2. Clean all PDMS pieces further by repeated pressing and peeling with strips of household adhesive tape.	240 241
	3. <i>Bonding step 1</i> : Activate the PDMS-side of the tissue layer–release liner ensemble as well as the surface of the coverslip with O <sub>2</sub> -plasma (15 s, 50 W). Immediately after activation, press the activated surfaces together. Enhance the bonding by clamping the bonded part between two glass slides using fold-back clips and place it in a 60 °C convection oven for 30 min. Afterward, let the part cool down to room temperature before using it in bonding <b>step 3</b> .	242 243 244 245 246 247 248 249
	4. <i>Bonding step 2</i> : Activate one side of a SiO <sub>x</sub> -coated PET-membrane as well as the structured surface of the standard-molded media layer (O <sub>2</sub> -plasma—15 s, 50 W). Immediately after activation, insert the membrane into the designated inlay and press the activated surfaces together. Directly proceed with bonding <b>step 3</b> .	250 251 252 253 254 255
	5. <i>Bonding step 3</i> : Remove the release liner from the exclusion-molded tissue layer. Activate the PDMS surface of the exclusion-molded tissue layer on the coverslip as well as the membrane–media layer ensemble (O <sub>2</sub> -plasma—15 s, 50 W). Immediately after activation, align structures carefully and press the activated surfaces together. To enhance bonding, clamp the chip between two glass slides using foldback clips and place it in a 60 °C convection oven overnight. Afterward, let the part cool down to room temperature before quality check.	256 257 258 259 260 261 262 263 264 265
	6. Test the bonding and fluidic continuity of the chip by injecting 70% EtOH into the chip using a blunt 21 GA needle connected to a syringe. Since the tissue system has no outlet, start flushing the chip through the tissue port. Check if the liquid exits the chip through the media ports only. If liquid leaks anywhere else, the chip is defective. Place chips in the 60 °C convection oven to allow for a fast evaporation of the 70% EtOH.	266 267 268 269 270 271 272

Julia Rogal et al.

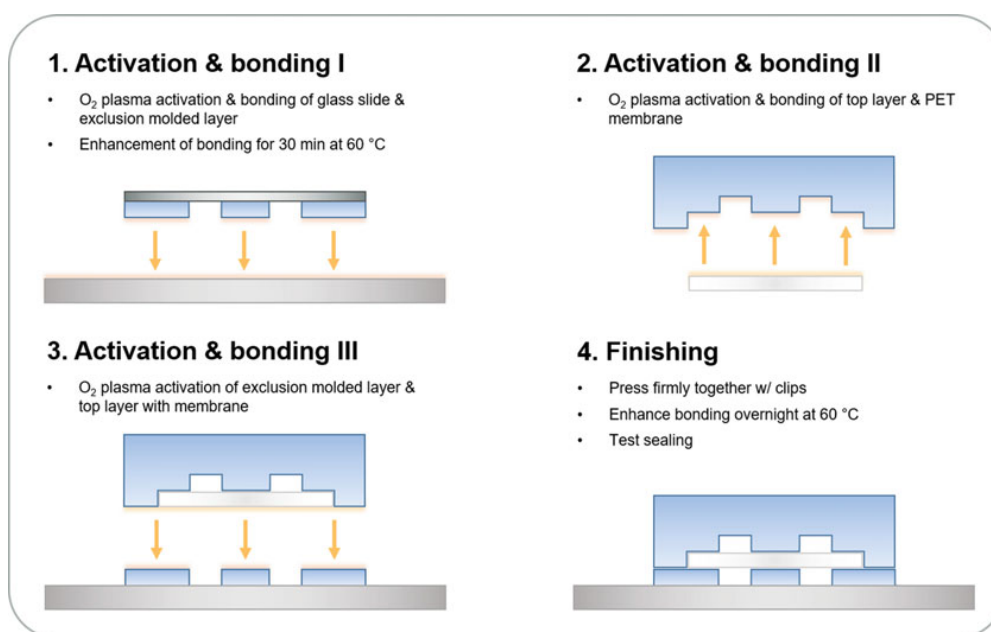


**Fig. 3** Overview of chip assembly workflow. Chip assembly involves three subsequent O<sub>2</sub>-plasma-activation steps. After finishing, a quality control should occur. (Reproduced from Rogal et al. [10] CC BY 4.0)

### 3.2 Adipocyte Isolation

Isolation and culture of primary cells requires sterile practice and is therefore conducted in a laminar flow bench using sterile materials (see Note 15). The primary mature human adipocytes are isolated from subcutaneous adipose tissue in two key steps: enzymatic digestion as well as straining and washing of singularized mature adipocytes (Fig. 4).

273  
275  
276  
277  
278  
279  
280  
281  
282  
283  
284  
285  
286  
287  
288  
289  
290  
291  
292  
293  
294  
295

#### 3.2.1 Enzymatic Digestion

1. Prewarm custom-made enzymatic digestion solution and DMEM/Ham's F-12 (1:1) in a water bath at 37 °C.
2. Transfer a piece of the biopsy from transport container to petri dish and rinse twice with Dulbecco's phosphate-buffered saline with MgCl<sub>2</sub> and CaCl<sub>2</sub> (PBS<sup>+</sup>) (see Note 16).
3. Remove the subcutaneous fat from the skin by cutting it off using tweezers and scalpel.
4. Cut adipose tissue into fine pieces with approximate size of 1 cm<sup>3</sup> and transfer the pieces to a 50 ml conical tube. Per conical tube, collect 20 ml of adipose tissue pieces.
5. Add 20 ml custom-made enzymatic digestion solution to the adipose tissue pieces (1:1) and incubate horizontal on plate shaker (50 cycles/min) in a humidified (95% rH) incubator at 37 °C and 5% CO<sub>2</sub> (see Notes 17 and 18).

Isolation, Integration, and Culture of Human Mature Adipocytes Leveraging...

3.2.2	<i>Straining and Washing of Adipocytes</i>	1. Put the 500 $\mu\text{m}$ strainer on the reservoir and pass suspension through the sieve, stirring slightly with a 10 ml plastic pipette ( <i>see Note 19</i> ).	296 297 298
		2. Transfer suspension to a 50 ml conical tube and wait for 5 min to allow phase separation of buoyant adipocytes (upper phase) and enzymatic digestion solution (lower phase).	299 300 301
		3. Aspirate off lower phase to discard enzymatic digestion solution by using a glass Pasteur pipette as depicted in Fig. 4g, h.	302 303
		4. To wash off residual collagenases, add DMEM/Ham's F-12 (1:1) to adipocytes, wait for phase separation and aspirate off lower phase.	304 305 306
		5. Repeat <b>steps 3</b> and <b>4</b> two more times.	307
		6. Immediately proceed with adipocyte injection ( <i>see Notes 20</i> and <b>21</b> ).	308 309 310
3.3	<b>Adipocyte Injection</b>	On the day before cell injection, the microfluidic platform is sterilized and fully degassed.	311 312
3.3.1	<i>Chip Preparation Prior to Injection</i>	1. Sterilize the chips by placing them ports facing up into $\text{O}_2$ -plasma (60 s, 50 W). After this step, handle the chips under sterile conditions at all times.	313 314 315
		2. Fill the chips with Dulbecco's phosphate-buffered saline without $\text{MgCl}_2$ and $\text{CaCl}_2$ ( $\text{PBS}^-$ ) by pipetting the liquid through the tissue inlet. The $\text{PBS}^-$ should then exit the chip through both of the media ports.	316 317 318 319
		3. Transfer the $\text{PBS}^-$ -filled chips to 50 ml centrifuge tubes filled with $\text{PBS}^-$ . Make sure the chip is fully submerged.	320 321
		4. Keep the chips in the centrifuge tube overnight at 4 $^\circ\text{C}$ in $\text{PBS}^-$ to allow evacuation of residual air from the channel systems ( <i>see Note 22</i> ).	322 323 324 325
3.3.2	<i>Tubing Preparation</i>	To connect the chips to a media perfusion, inlet and outlet tubings need to be prepared beforehand. Two different types of 21 GA needles are used: (1) stainless steel plastic hub dispensing needles and (2) bare blunt 21 GA needle (for connecting the ports of the chip).	326 327 328 329 330
		1. To prepare the inlet tubing, a blunt 21 GA needle is pushed into a 75 cm piece of Tygon tubing (0.762 $\times$ 2.286 mm, e.g., Tygon <sup>®</sup> ND 100-80 Medical Tubing). A 21 GA dispensing needle is inserted into the other end of the tubing.	331 332 333 334
		2. For the outlet tubing, a bare blunt 21 GA needle is inserted into a 10 cm piece of Tygon tubing.	335 336
		3. Prior to use, the tubing is sterilized by autoclaving.	337 338

Julia Rogal et al.

3.3.3	Potential residues of the enzymatic digestion solution among the adipocytes need to be washed off as it can lead to bursting of the fragile cells. Set free oils will disturb culture of adipocytes in the microfluidic platform and need to be removed.	339 340 341 342
<i>Adipocyte Preparation Prior to Injection</i>	<ol style="list-style-type: none"> <li>1. Transfer isolated adipocytes in DMEM/Ham's F-12 (1:1) to 15 ml falcon tube to obtain packed layer of adipocytes.</li> <li>2. If injection does not follow subsequently to isolation, wash adipocytes to discard free collagenases, burst adipocytes and oil as described before (cf. adipocyte isolation <b>steps 3</b> and <b>4</b>).</li> <li>3. Additionally, aspirate burst adipocytes and remove oils from surface.</li> </ol>	343 344 345 346 347 348 349 350
3.3.4 <i>Injection</i>	<p>Chip injection should occur directly after the isolation of cells. Due to the limited timeframe caused by hydrogel gelation, we recommend injecting only 1–2 chips at a time when learning the injection process (as described below). With more practice, injection of up to 6 systems at a time can be possible. Repeat the following steps until all chips are filled with cells.</p> <ol style="list-style-type: none"> <li>1. Remove one chip submerged in PBS<sup>-</sup> and gently dry the bottom of the chip as well as the coverslip with a lab wipe. Do not dry the upper surface of the chip to prevent air from entering the channels. Check if there are air pockets in the tissue structures of the chip despite the overnight submersion in PBS<sup>-</sup> (<i>see Note 22</i>).</li> <li>2. Place a pipette tip filled with approximately 50 µl PBS<sup>-</sup> into one of the media ports (<i>see Note 23</i>). By gently applying pressure onto the pipette tip with your thumb, push liquid through the chip until a liquid droplet is covering the tissue inlet (<i>see Note 24</i>). Repeat for the other system.</li> <li>3. In a microcentrifuge tube, thoroughly mix 60 µl of the prepared adipocytes from the packed adipocyte layer (<i>see Note 25</i>) with 24 µl of the 10 mg/ml collagen type 1 (<i>see Note 2</i>) dispersion by gently pipetting up and down.</li> <li>4. Add 6 µl neutralization buffer (<i>see Note 3</i>) to the adipocyte–collagen mixture and thoroughly mix by gently pipetting up and down. At this point, it is crucial to work quickly to inject the adipocyte–collagen mixture before the collagen gels entirely.</li> <li>5. Take 20 µl of the adipocyte–collagen–neutralization buffer mixture into a pipette tip. Remove the tip from the pipette, and create a droplet of the mixture at the tip of the pipette tip using your thumb.</li> <li>6. Let the PBS<sup>-</sup> droplet over the tissue inlet port and the droplet at the pipette tip's tip coalesce. Then gently push the pipette tip into the tissue inlet (<i>see Note 23</i>).</li> </ol>	351 352 353 354 355 356 357 358 359 360 361 362 363 364 365 366 367 368 369 370 371 372 373 374 375 376 377 378 379 380 381 382 383

Isolation, Integration, and Culture of Human Mature Adipocytes Leveraging...

7. Creating a steady pace, gentle manual pressure onto the pipette tip's top with your thumb, push the adipocyte-hydrogel mixture into the first tissue system until the chambers are filled evenly (*see Note 26*). Move on to the next system or prepare a new adipocyte-collagen-neutralization buffer mixture if the hydrogel is too solid already. 384-389
8. Using tweezers, gently plug the tissue inlet using the sterile metal plugs (*see Note 5*). 390-391
9. Intermediately, supply the on-chip adipocytes with AM-1 medium by inserting an empty pipette tip into the media outlet port and a tip filled with 100 µl medium into the media inlet port. 392-395
10. Keep the injected chips in a humidified (95% rH) incubator at 37 °C and 5% CO<sub>2</sub> until they are connected to constant media perfusion after all systems were injected. 396-399

**3.4 Connection to Media Perfusion and on-Chip Culture**

Constant perfusion of the chip is realized via pushing the culture medium through tubing which connects the microfluidic platform to a syringe mounted to a syringe pump. Perfused media is exiting the platform through the outlet tubing in the outlet port and collected as effluent in microcentrifuge tubes. The flow rate is set to 20 µl/h. 400-405

1. Fill syringes with prewarmed AM-1 medium containing 1% (v/v) penicillin-streptomycin (10.000 U/ml) (*see Notes 27 and 28*). 406-408
2. Connect tubing via needle hub to Luer Lock™ adaptor of the syringe and fill tubing with media from the syringe, creating a droplet of media at the outlet of the tubing (*see Note 29*). 409-411
3. Insert needle carefully into media inlet port through the droplet of media to avoid introduction of air to the system. 412-413
4. If connected correctly, very slight pressure on the plunger of the syringe creates drop of media on the outlet port of the media channel. Insert outlet tubing through the liquid droplet. Place end of tubing into microcentrifuge tube to collect effluent (*see Notes 30 and 31*). 414-418
5. Mount the syringe to the syringe pump, set flow rate, syringe diameter for the specific syringe being used and incubate microfluidic platform over culturing period in a humidified (95% rH) incubator at 37 °C and 5% CO<sub>2</sub> (*see Note 32*). 419-423

**4 Notes**

1. For preparation of the enzymatic digestion solution, weigh 1% (w/v) of bovine serum albumin (BSA) and slowly add 425-426

Julia Rogal et al.

- DMEM/Ham's F-12 (1:1). Incubate on a plate shaker with slow agitation to facilitate dissolving of BSA. As soon as BSA is dissolved, add 0.13 U/ml collagenase and incubate on plate shaker again until collagenase is dissolved. The solution can be stored at  $-20\text{ }^{\circ}\text{C}$ ; we recommend preparing a stock solution in aliquots of 40 ml.
2. For encapsulating the singularized adipocytes prior to injection, a highly concentrated collagen type I dispersion is required (we use an in-house made collagen dispersion with concentration of 10 mg/ml, commercially available is, for example, Corning<sup>®</sup> Collagen I, High Concentration, Rat Tail).
  3. Neutralization buffer for collagen dispersion: DMEM/Ham's F-12 (10 $\times$ ) and 50 mM NaOH in aqua dest (1:1) with 0.2 M NaHCO<sub>3</sub> and 0.225 M HEPES.
  4. For gentle transfer of adipocytes cut tips should be used. To achieve a wider opening of the tips, the ends of 100  $\mu\text{l}$  pipette tips are cut off too. This will minimize shear stress on the adipocytes during transfer. Prior to use, cut tips are sterilized by autoclaving.
  5. Plugs for closing the injection ports of the chips are cut from a stainless steel alloy wire with a diameter of 0.7 mm to a length of approximately 8 mm using pliers. Prior to use, plugs are sterilized by autoclaving.
  6. Bare blunt needles can be purchased or made from the dispensing needles by removing the plastic hub after dissolving the glue overnight in a 70% ethanol solution.
  7. Controlled media perfusion is realized by connecting the injected chips to a syringe pump, such as a 12-channel pump using the prepared tubings and Luer Lock<sup>™</sup> style syringes.
  8. After degassing, be very gentle when opening the valve for ventilation to prevent PDMS spilling and breaking of wafers due to the sudden change in pressure.
  9. For standard molding, we clamp the wafers in custom-made 3D printed molds.
  10. Prevent formation of air bubbles while pouring PDMS by having the opening of the mixing cup close to the wafer and a wide stream of PDMS, instead of far away and a thin stream of PDMS.
  11. If air bubbles are created around the structures of the wafer during PDMS pouring, degas the PDMS on the wafer before curing.
  12. When cutting PDMS, use a ruler or a glass slide as a cutting guidance. For nice edges, do not cut entirely through the

## Isolation, Integration, and Culture of Human Mature Adipocytes Leveraging...

- PDMS but make a shallow incision only. Then bend the PDMS along the incisions to break the pieces apart. 470  
471
13. We recommend examining suited pipette tips for the ports punched beforehand. Usually 100–200  $\mu$ l pipette tips should fit nicely into 0.75 mm-diameter ports. However, we experienced significant variations in the tip diameters depending on manufacturer. Note that tips that are too wide for the port might rupture the port and cause leakages. 472  
473  
474  
475  
476  
477
  14. We recommend bonding the PDMS pieces to glass coverslips to enable best conditions for imaging of the on-chip tissue. However, the coverslips are extremely fragile and might easily break throughout the fabrication, injection and culture steps. We therefore suggest to fix a coverslip to a standard glass slide by applying scotch tape at the two shorter edges of the slides. This technique facilitates handling of the chip. For high quality imaging, the tape and the glass slide can be easily removed from underneath the coverslip. 478  
479  
480  
481  
482  
483  
484  
485  
486
  15. Isolation should occur on the day of surgery. Storing of biopsies overnight at 4 °C leads to solidifying of the fat tissue and thereby dying of adipocytes. 487  
488  
489
  16. If the resected biopsy is too big to put in a petri dish, lifting it out of transport box using tweezers with teeth and cutting suitable piece off with scissors can be helpful. 490  
491  
492
  17. Adipocytes need to be handled carefully without shaking and rigorous pipetting, as they are fragile and burst easily, which, in turn, leads to unwanted oils set free among them. 493  
494  
495
  18. Sealing off the lids of conical tubes containing fat and enzymatic digestion solution with Parafilm avoids spilling during the incubation time on the plate shaker. 496  
497  
498
  19. To facilitate the straining of the adipocytes after collagen digestion, the sieve can be tilted slightly so that stirring and flow of the sieved suspension can be observed. 499  
500  
501
  20. If injection to microfluidic platform is not performed subsequent to adipocyte isolation, transfer adipocytes in DMEM/Ham's F-12 (1:1) to cell culture flask (75 cm<sup>2</sup>) and incubate in a humidified (95% rH) incubator at 37 °C and 5% CO<sub>2</sub>. The maximum culture period of isolated adipocytes in flasks should not exceed overnight periods. 502  
503  
504  
505  
506  
507
  21. When not needed, the isolated adipocytes should be kept at 37 °C during the injection process. If the injection process takes a long time, we recommend intermediate extra washing steps to maintain the cells' viability. 508  
509  
510  
511
  22. If there are air pockets remaining in the chips' tissue chambers despite the overnight submersion in PBS<sup>-</sup>, it can help to centrifuge the chips in the centrifuge tubes. 512  
513  
514

Julia Rogal et al.

23. Be careful to not rupture the PDMS around the ports when pushing liquids/the adipocyte–hydrogel mixture into the system using manual pressure. We recommend holding the tip between index and middle finger ensuring to not push the tip itself further into the chip. 515  
516  
517  
518  
519
24. Introduction of air into microfluidic platforms needs to be avoided at any time. 520  
521
25. For transferring the adipocytes, we recommend to prepare pipette tips with cutoff tips. This will minimize shear forces on the adipocytes during pipetting. Moreover, pipet very slowly from the adipocyte layer to collect as many adipocytes as possible. We usually take 30–60 s to take up the 60  $\mu$ l of adipocyte suspension needed for the injection mixture. If pipetting occurs too fast, there is a high risk to take up more medium than adipocytes. If there is a lot of oil on top of the adipocyte layer, aspirate it off to not contaminate the outside of the pipette tip with the oil. 522  
523  
524  
525  
526  
527  
528  
529  
530  
531
26. To control the injection process of the adipocyte–collagen–neutralization buffer mixture, we recommend either monitoring filling status of the chambers using a bright field microscope (preferred option), or placing the chip toward a dark background for contrast enhancement to make the injection macroscopically visible. 532  
533  
534  
535  
536  
537
27. One source of air bubbles could be syringes if the air is not removed from the syringes prior to connection of tubing. Therefore filling the syringe with media already takes caution. Ventilate syringe, place in media reservoir and try to aspirate in media without perturbation and aspirating air in. Wet inside of the barrel of syringe by tilting movements. Hold syringe vertically with plunger facing toward your working bench. Air bubbles will accumulate in upper region of the barrel. By pressing plunger in and holding the syringe still vertically, air will escape through the opening. Tipping on side of the barrel can move air bubble to the center and ease their removal. 538  
539  
540  
541  
542  
543  
544  
545  
546  
547  
548
28. Installing more than one syringe in the same syringe pump requires same volume in each syringe. Pulling out plungers for making them fit into pump will result in introducing air into the platform. 549  
550  
551  
552
29. Inlet tubing need to be filled completely with media prior inserting into the platform. Coalescing droplets of media on inserting needle and inlet port assures that no air is introduced by connecting tubing to port. 553  
554  
555  
556
30. As collection tubes for effluents, holes with size of outlet tubing can be drilled into caps of microcentrifuge tubes. This will diminish evaporation of sampled effluents. 557  
558  
559

Isolation, Integration, and Culture of Human Mature Adipocytes Leveraging...

- 31. For ease of handling, molds with storage space for platforms and racks for collection tubes can be 3D-printed in a customized manner. 560-562
- 32. Length of tubing needs should be adjusted to given conditions (e.g., if pump can be placed inside the incubator or needs to be stored outside the incubator). 563-565

567 **References**

569	1. Young B, O'Dowd G, Woodford P (2014)	7. Rogal J, Zbinden A, Schenke-Layland K et al	588
570	Wheater's functional histology: a text and colour atlas. Churchill Livingstone/Elsevier, Philadelphia, PA	(2019) Stem-cell based organ-on-a-chip models for diabetes research. <i>Adv Drug Deliv Rev</i> 140:101–128	589
571		8. van den Berg A, Mummery CL, Passier R et al	590
572		(2019) Personalised organs-on-chips: functional testing for precision medicine. <i>Lab Chip</i> 19:198–205	591
573	2. Kahn SE, Hull RL, Utzschneider KM (2006)	9. Marx U, Akabane T, Andersson TB et al	592
574	Mechanisms linking obesity to insulin resistance and type 2 diabetes. <i>Nature</i> 444:840–846	(2020) Biology-inspired microphysiological systems to advance patient benefit and animal welfare in drug development. <i>ALTEX</i> 37:364–394	593
575		10. Rogal J, Binder C, Kromidas E et al (2020) WAT-on-a-chip integrating human mature white adipocytes for mechanistic research and pharmaceutical applications. <i>Sci Rep</i> 10:6666	594
576		11. Xia Y, Whitesides GM (1998) Soft lithography. <i>Annu Rev Mater Sci</i> 28:153–184	595
577	3. Berg AH, Scherer PE (2005) Adipose tissue, inflammation, and cardiovascular disease. <i>Circ Res</i> 96:939–949		596
578			597
579			598
580	4. Zhang Z, Scherer PE (2018) Adipose tissue: the dysfunctional adipocyte—a cancer cell's best friend. <i>Nat Rev Endocrinol</i> 14:132–134		599
581			600
582			601
583	5. WHO Obesity and overweight. <a href="https://www.who.int/news-room/fact-sheets/detail/obesity-and-overweight">https://www.who.int/news-room/fact-sheets/detail/obesity-and-overweight</a>		602
584			603
585			604
586	6. WHO Diabetes, <a href="https://www.who.int/news-room/fact-sheets/detail/diabetes">https://www.who.int/news-room/fact-sheets/detail/diabetes</a>		605
587			606

Uncorrected Proof

Publication [8]

## Integration of electrospun membranes into low-absorption thermoplastic organ-on-chip

J. Chuchuy, **J. Rogal**, T. Ngo, K. Stadelmann, L. Antkowiak, S. Liebau, K. Schenke-Layland, P. Loskill.

*ACS Biomater. Sci. Eng.* **7**, 3006–3017 (2021),

<https://dx.doi.org/10.1021/acsbmaterials.0c01062>

### Abstract:

In recent years, organ-on-chip (OoC) systems have provoked increasing interest among researchers from different disciplines. OoCs enable the recreation of in vivo-like microenvironments and the generation of a wide range of different tissues or organs in a miniaturized way. Most commonly, OoC platforms are based on microfluidic modules made of polydimethylsiloxane (PDMS). While advantageous in terms of biocompatibility, oxygen permeability, and fast prototyping amenability, PDMS features a major limitation as it absorbs small hydrophobic molecules, including many types of test compounds, hormones, and cytokines. Another common feature of OoC systems is the integration of membranes (i) to separate different tissue compartments, (ii) to confine convective perfusion to media channels, and/or (iii) to provide mechanical support for cell monolayers. Typically, porous polymer membranes are microstructured using track-etching (e.g., polyethylene terephthalate; PET) or lithography (e.g., PDMS). Although membranes of different biomechanical properties (rigid PET to elastic PDMS) have been utilized, the membrane structure and material remain mostly artificial and do not resemble in vivo conditions (extracellular matrix). Here, we report a method for the reliable fabrication and integration of electrospun membranes in OoC modules, which are made of laser-structured poly(methyl methacrylate) (PMMA). The choice of PMMA as base material provides optical parameters and biocompatibility similar to PDMS while avoiding the absorption problem. Using electrospinning for the generation of 3D membranes, microenvironments resembling the native extracellular matrix (ECM) can be generated. We tested two different kinds of electrospun membranes and established processes for a tight integration into PMMA modules. Human (microvasculature) endothelial as well as (retinal pigment) epithelial cell layers could be successfully cultured inside the systems for up to 7 days, while being either directly exposed to (endothelial cells) or protected

(epithelial cells) from the shear flow. Our novel method enables the versatile fabrication of OoC platforms that can be tailored to the native environment of tissues of interest and at the same time are applicable for the testing of compounds or chemicals without constraints.

## Integration of Electrospun Membranes into Low-Absorption Thermoplastic Organ-on-Chip

Johanna Chuchuy, Julia Rogal, Tran Ngo, Kathrin Stadelmann, Lena Antkowiak, Kevin Achberger, Stefan Liebau, Katja Schenke-Layland, and Peter Loskill\*

 Cite This: *ACS Biomater. Sci. Eng.* 2021, 7, 3006–3017

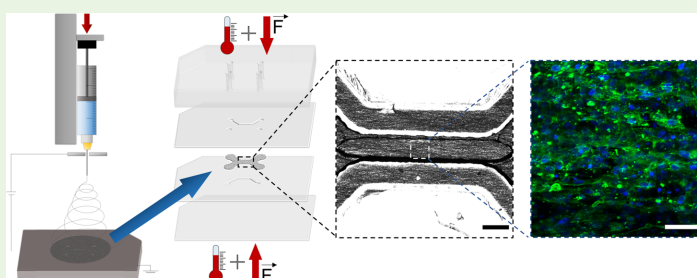
 Read Online

ACCESS |

 Metrics & More

 Article Recommendations

 Supporting Information



**ABSTRACT:** In recent years, organ-on-chip (OoC) systems have provoked increasing interest among researchers from different disciplines. OoCs enable the recreation of *in vivo*-like microenvironments and the generation of a wide range of different tissues or organs in a miniaturized way. Most commonly, OoC platforms are based on microfluidic modules made of polydimethylsiloxane (PDMS). While advantageous in terms of biocompatibility, oxygen permeability, and fast prototyping amenability, PDMS features a major limitation as it absorbs small hydrophobic molecules, including many types of test compounds, hormones, and cytokines. Another common feature of OoC systems is the integration of membranes (i) to separate different tissue compartments, (ii) to confine convective perfusion to media channels, and/or (iii) to provide mechanical support for cell monolayers. Typically, porous polymer membranes are microstructured using track-etching (e.g., polyethylene terephthalate; PET) or lithography (e.g., PDMS). Although membranes of different biomechanical properties (rigid PET to elastic PDMS) have been utilized, the membrane structure and material remain mostly artificial and do not resemble *in vivo* conditions (extracellular matrix). Here, we report a method for the reliable fabrication and integration of electrospun membranes in OoC modules, which are made of laser-structured poly(methyl methacrylate) (PMMA). The choice of PMMA as base material provides optical parameters and biocompatibility similar to PDMS while avoiding the absorption problem. Using electrospinning for the generation of 3D membranes, microenvironments resembling the native extracellular matrix (ECM) can be generated. We tested two different kinds of electrospun membranes and established processes for a tight integration into PMMA modules. Human (microvasculature) endothelial as well as (retinal pigment) epithelial cell layers could be successfully cultured inside the systems for up to 7 days, while being either directly exposed to (endothelial cells) or protected (epithelial cells) from the shear flow. Our novel method enables the versatile fabrication of OoC platforms that can be tailored to the native environment of tissues of interest and at the same time are applicable for the testing of compounds or chemicals without constraints.

**KEYWORDS:** organ-on-chip, microphysiological systems, electrospinning, membranes, PMMA, biomaterials, microfabrication, microfluidics, microvascular endothelial cells, hiPS RPE

### INTRODUCTION

Culturing complex human 3D tissues embedded in a microphysiological environment and nourished through a continuous laminar media flow can be achieved by using advanced novel microfluidic tissue platforms, also known as organ-on-chip (OoC).<sup>1</sup> Every platform can be individually tailored to the specific tissue microenvironment and requirements. To achieve this, the systems normally comprise tissue

**Special Issue:** Beyond PDMS and Membranes: New Materials for Organ-on-a-Chip Devices

**Received:** July 17, 2020

**Accepted:** February 5, 2021

**Published:** February 16, 2021



channels and media channels, which are often separated by microchannels or porous membranes with or without cell lining, mimicking a vascular-like barrier or the extracellular matrix (ECM).<sup>2</sup> To be able to generate a physiologically relevant microenvironment for the cells, the properties of the membrane are pivotal. Up to now, most OoC systems integrate polymeric porous membranes, such as polydimethylsiloxane (PDMS), polycarbonate (PC), or polyethylene terephthalate (PET) membranes.<sup>2</sup> These membranes are commonly used because of their commercial availability (PC and PET), flexible fabrication processes (PDMS membranes), as well as the easy integration into PDMS-based chips. However, due to their 2D planar surfaces, these membranes lack dimensionality and structure to mimic the physiological 3D environment of the native ECM. Furthermore, their surfaces usually have to be pretreated or coated to facilitate cell adhesion.<sup>2</sup> A further current challenge of OoC platforms is the common choice of PDMS as base material. PDMS shows many advantages such as its biocompatibility, transparency, and flexibility and can be easily structured by replica molding to fabricate microfluidic systems.<sup>3</sup> Yet, PDMS is also known to absorb small molecules because of its hydrophobic polymer network.<sup>4</sup> The absorption behavior of OoC base materials is important because many pharmacological compounds and chemicals that are to be tested are hydrophobic, but also crucial factors in the medium to promote cell nutrition and functionality can have a hydrophobic character. Uncontrolled, unspecific absorption into the PDMS leads to highly variable compound levels and limited system robustness, impeding the generation of dose–response curves and leading to potential underestimation of toxicities.<sup>5,4</sup> As a result, the field of OoC development has begun to shift away from PDMS and toward exploring alternative materials.<sup>5</sup> PMMA is a promising alternative for OoC fabrication, overcoming the disadvantages of PDMS while featuring similar optical parameters and biocompatibility.

To address the disadvantages of conventionally used porous membranes, electrospun membranes offer great potential. Electrospun membranes are scaffolds of micro- or nanofibers that are randomly stacked onto each other to form a 3D structure with a high surface-area-to-volume ratio.<sup>6</sup> These characteristics enable the creation of microenvironments with structural, biochemical, and biophysical properties highly similar to the native ECM.<sup>7</sup> Electrospun scaffolds can therefore facilitate physiological cell–cell and cell–ECM crosstalk, enhancing tissue functionality closer to the native tissue.<sup>8</sup> Properties, such as fiber diameter, porosity, mechanical strength, and thickness can easily be tailored to the requirements of the native ECM specific to the respective tissue.<sup>9</sup> Another advantage is the possibility to blend the polymer solution for electrospinning with proteins to avoid the necessity for subsequent coating procedures and to enable location-specific cell attachment.<sup>10,11</sup> So far, electrospun scaffolds are widely utilized for tissue engineering applications,<sup>7</sup> such as vascular grafts<sup>12</sup> and nerve regeneration guidance conduits.<sup>13</sup> Moreover, electrospinning has also been applied to guide neurite outgrowth,<sup>14</sup> bone and cartilage tissue generation,<sup>15</sup> for repairing tendons and ligaments,<sup>16</sup> as well as wound dressings,<sup>17</sup> just to list a few. Despite the advantages over conventional membranes, only few OoC platforms integrate electrospun membranes so far. This might be due to difficulties in the integration and bonding of membranes into microfluidic chips to achieve a tight sealing without any leakages.<sup>18</sup> In recent years, however, a number of promising

first approaches have been introduced: Kim et al.,<sup>19</sup> for instance, recently developed a microfluidic chip containing a bottom chamber for the integration of 3D electrospun constructs prepared from polycaprolactone (PCL) to emulate the ECM's *in vivo*-like environment for human liver hepatocellular carcinoma cells. The chip was designed with an open well, which was sealed after insertion of the electrospun scaffold. With the culture of Hep2G cells for 14 days, they showed the successful generation of engulfed aggregates, indicating the 3D culture-specific morphology. In 2018, Yang et al. created a lung-on-chip with a poly(lactic-co-glycolic acid) (PLGA) electrospun membrane directly spun onto a PDMS-slab incorporating an open channel.<sup>20</sup> The attachment of the fiber mat onto the PDMS chip not only sealed the channel, but the electrospun membrane also served as an air–liquid interface, important for the recapitulation of the lung alveoli. To analyze whether the adhesion of the fibers to the PDMS during the electrospinning process evoked sufficient bonding to tightly seal the chip, a rhodamine dye was flushed into the channel, and subsequently, the channel was imaged. However, no data regarding the long-term stability of the chip sealing was provided. Furthermore, Budhwani et al. developed a so-called blood-vessel “lab-on-a-brane”.<sup>21</sup> There, three different kinds of electrospun membranes based on either a synthetic material (Nylon), a biological material (collagen), or a hybrid combination of collagen and poly-L-lactide (PLA) were integrated into a PDMS platform containing two chambers. The membranes were either directly spun onto the PDMS or integrated at a later stage of the chip fabrication process. The aim of this project was to establish *in vivo*-like vessel-tissue physiology, whereby the success was evaluated by showing barrier functionality of a coculture of smooth muscle cells and endothelial cells. Finally, Moghadas et al. developed an electrospun membrane from a blend of PDMS and poly(methyl methacrylate) (PMMA) for an easy and tight bonding process into PDMS chips.<sup>18</sup> Although the study established a robust fabrication process, the membrane showed some restrictions for cell adhesion because of its hydrophobic character.

The common theme of all introduced approaches to integrate electrospun membranes into OoC platforms is that they are based on PDMS-platforms, which feature several limitations as discussed above. To address both the challenge of unspecific absorption as well as the physiological representation of the microenvironment, we established a novel fabrication process to incorporate electrospun membranes into PMMA-based OoC platforms. The produced PMMA-chips integrate different types of electrospun membranes in a tightly sealed manner and show greatly reduced absorption of hydrophobic molecules. As a proof-of-concept, we demonstrated that the chips are amenable for both in-flow as well as shear-force protected culture of cell layers, using human primary microvasculature endothelial cells (mvECs) and human induced pluripotent stem cell (iPSC)-derived retinal pigment epithelial cells (RPE). In the future, the system could serve as platform for barrier models such as pulmonary air–liquid interfaces, blood–brain barriers, and blood–retinal barriers. The versatile and robust fabrication process could also be applied to generate further types of *in vivo*-like microenvironments tailored to cell or tissue needs offering a promising alternative to conventionally used membranes in OoC devices.

## MATERIALS AND METHODS

**Chip Fabrication.** *Chip Design.* The developed chip was designed using the CorelCAD 2018 software. The chip consists of four layers in total. The three bottom layers—floor plate, lower and upper channel layers—were cut out from a 175  $\mu\text{m}$  thick PMMA sheet (PLEXIGLAS Resist, 99524 GT, Evonik). Both channels feature a width of 300  $\mu\text{m}$ , and the central area with both channels overlapping has a length of 2300  $\mu\text{m}$ . The top layer, cut from a 3 mm thick PMMA plate (0133466, Modulor), seals the chip and provides accesses to the in- and outlets of both channels. In- and outlet ports are designed with a diameter of 1.36 mm to accurately fit Tygon tubing (VERNAAD04103, VWR international GmbH). All PMMA layers were structured using a lasercutter with a 10 W CO<sub>2</sub>-laser (Universal Laser Systems, VLS2.30) and the following laser parameters: The 175  $\mu\text{m}$  PMMA layers were cut twice with 10% power, 10% speed, and 1000 pixel per inch (PPI), while the 3 mm PMMA was cut using 100% power, 2% speed, and 1000 PPI.

*Membrane Fabrication.* The membranes were fabricated using either bare PLA or PLA with gelatin methacryloyl (PLA-GM<sub>2</sub>). 12% w/v PLA (81273, Sigma-Aldrich) and a 12% w/v blend of PLA with GM<sub>2</sub> (90:10% w/w) (GM<sub>2</sub>, generated as described previously by Hoch et al.<sup>23</sup>) were dissolved in 1,1,1,3,3,3-Hexafluoro-2-propanol (HFIP, 105228, Sigma-Aldrich) overnight using a magnetic stirrer. The membranes were electrospun using a device from IME medical electrospinning (EC-CLI apparatus). The distance between needle and collector was 18 cm. A small needle with a diameter of 0.4 mm (4657705, B. Braun) was used during the spinning process to generate thin fibers. A 1 mL syringe was filled with polymer solution and constantly pumped with a flow rate of 1.5 mL h<sup>-1</sup> for 2.5 minutes at ambient conditions of 23 °C and humidity of 30%. Different voltages were set depending on the polymer solution: +16/−0.5 kV for PLA and +18/−4 kV for PLA-GM<sub>2</sub>. The membranes were directly spun onto the PMMA layer that was attached to the collector together with a PDMS piece below ensuring even fiber distribution. Before electrospinning, the PMMA and PDMS parts were wrapped together in aluminum foil with the majority of the material on the left and right side of the chip to create a localized conductivity. Subsequently, a scalpel was soaked with HFIP and guided along the edge of the PMMA and aluminum foil. The chips were then placed in a fume hood overnight. In the last step, the lasercutter was used to weld the membrane with the PMMA by cutting around the channel outline with low laser power settings (parameters: 2% power, 10% speed, 1000 PPI; repeated twice).

*Chip Assembly.* For the assembly of the chips with the membrane, all individual layers were aligned on top of each other and fixed with scotch tape on two edges of the chip to avoid a misalignment of the chip during the subsequent bonding steps. For thermal fusion bonding, the chip was placed in between two conventional glass slides and clamped with two small foldback clips (2141999; Jakob Maul GmbH) on each side and then placed for 15 minutes in a convection oven that was preheated to 130 °C. Subsequently, the chip was allowed to cool down to room temperature (RT) at which point the clips and glass slides were removed.

*Chip Characterization. Membrane Characterization.* Scanning electron microscopy (SEM, ZEISS Auriga 40) was used to examine the effects of temperature and pressure on membrane characteristics and fiber morphology during chip fabrication. From the SEM images, the fiber diameter and the pore size were analyzed by using the software ImageJ 1.52p (National Institute of Health, Bethesda, MD). The diameter of at least 40 fibers was measured manually, and afterward, the mean diameter and standard deviation were calculated. To appraise the values for the pore sizes, thresholding was applied, and the pores were then analyzed using particle analysis from three images per membrane.

*Chip Sealing and Absorption Characterization.* To assess absorption of hydrophobic molecules, the fully assembled PMMA chip was compared to a control chip made from PDMS. Since the goal was to assess the absorption into the bulk chip material, the PDMS chip did not contain any membranes. The PDMS chip was

prepared by, first, fabricating two negative masters—one from the PMMA bottom channel layer and another from the top channel layer, which were adhered onto conventional Petri dishes. PDMS (Sylgard 184, Dow Corning) was mixed in a ratio 10:1 base to curing agent and degassed prior to pouring the mixture into the Petri dishes. The PDMS polymer was added until the layers were completely covered. Then, the polymer was cured in the oven at 60 °C overnight. On the next day, the PDMS masters were removed and coated with chlorotrimethylsilane (386529, Sigma-Aldrich) for 2 hours by vapor deposition. The chlorotrimethylsilane coating allows the treated PDMS to be used as master molds for replica molding with fresh PDMS. Therefore, the treated PDMS was placed into fresh Petri dishes, and again PDMS molds were produced from the master molds by pouring PDMS onto them and curing. The slabs were peeled off, and the edges of the PDMS slabs were cut with a scalpel to the chip size. Then, the PDMS layer containing the top channel layer was punched at the locations of the in- and outlets with a biopsy punch (504529 World Precision Instruments) to be able to access the channels. Both parts were cleaned with isopropanol and scotch tape to remove the remaining dust and then bonded to each other by activating the surfaces with O<sub>2</sub> plasma (15 s, 50 W; Zepto, Diener) and placing them into the oven for at least 4 hours to stabilize bonding.

For the diffusion experiment, a solution of Rhodamine B (83689, Sigma-Aldrich) at a concentration of 5 mg/mL in distilled water was prepared and further diluted to 1:100 in PBS, similar to the protocol from Virumbrales-Muñoz et al.<sup>23</sup> Pipette tips, filled with a volume of 50  $\mu\text{L}$  of the working solution were placed into the inlets, while empty pipette tips were placed at the outlets to collect waste. Both the control PDMS chip and the developed PMMA chip incorporating the electrospun membrane were tested at the same time for direct comparison. After the chips were connected to Rhodamine B-filled pipette tips, images were taken every 10 minutes for 2 hours using an inverted fluorescence microscopy (Leica DMI8, LEICA Microsystems GmbH) at a 10 $\times$  magnification, capturing the overlapping area of both channels. ImageJ was used to analyze the mean gray intensity of a selected square with even representing area of the channel and of the bonded region of the chip. The background of each mean gray value measurement was subtracted, and the relative region of interest (ROI) mean intensity was plotted as a function over time using Origin 2019 (OriginLab).

To investigate the absorption behavior of the PLA membranes, the chips were exposed for 2h with Rhodamine B solution as described above. Subsequently, the chips were washed by flushing 12  $\times$  50  $\mu\text{L}$  of PBS through the channel. Right after exposure as well as after 6 and 12 flushes respectively, defined channel sections of the chips were imaged using constant microscope settings. For analysis, the mean gray value of the channel intensity was measured, and the background was subtracted from each image using the software ImageJ. The graph was then plotted using Origin 2019 (OriginLab).

*Cell Culture. MvECs Isolation and Culture.* Human skin-derived microvascular endothelial cells (mvECs) were isolated from human skin tissue biopsies. The biopsies were obtained from plastic surgeries performed by Dr. Ulrich E. Ziegler (Klinik Charlottenhaus, Stuttgart, Germany), approved by the local medical ethics committee. Patients gave an informed consent according to the permission of the "Landesärztekammer Baden-Württemberg" (IRB#: F-2012-078; for normal skin from elective surgeries). All procedures were carried out in accordance with the rules for medical research of human subjects, as defined in the Declaration of Helsinki. All mvEC-related experiments utilized cells harvested from the same donor (abdomen skin tissue of a 53-year old female; BMI of 29).

The isolation of mvECs from the human skin biopsies was conducted as follows: First, the subdermal layer comprising adipose tissue and connective tissue was carefully removed from the cutis. Then, the cutis was cut into 1–2 mm wide strips and incubated in a dispase solution (2 U/mL in PBS<sup>-</sup>, Serva Electrophoresis) at 4 °C overnight. On the next day, the epidermis was removed, and the dermis strips were digested in 0.05% trypsin in EDTA (59418C, Sigma-Aldrich; 15040033, ThermoFisher) at 37 °C for 40 minutes.

The reaction was stopped by adding 1% v/v fetal calf serum (FCS, SH3006603, ThermoFisher) to the trypsin/EDTA solution. Using a cell scraper, mvECs were scratched off of the dermis into prewarmed endothelial cell growth medium (ECGM, C-22010, PromoCell) supplemented with 1% gentamicin (15710049, ThermoFisher). The resulting cell suspension was filtered twice through cell strainers (mesh sizes: 100 and 70  $\mu\text{m}$ ) and then centrifuged at 209g for 5 minutes. The cells were then resuspended in ECGM and seeded into T175 culture flasks at a density of  $(4\text{--}5) \times 10^4$  cells/cm<sup>2</sup>. During the first week of culture, the cells were rinsed with PBS<sup>-</sup> and subsequently treated with the EDTA-solution (15040033, ThermoFisher) (6–10 minutes at 37 °C) every 2 days to detach any remaining fibroblasts from the culture.

**hiPSC-RPE Culture.** Retinal pigment epithelial (RPE) cells differentiated from human induced pluripotent stem cells (hiPSC) were kindly provided by the Institute of Neuroanatomy at the University of Tübingen. Details regarding the cell differentiation protocol for the cells can be found in a previous publication from Achberger et al.<sup>24</sup> All procedures followed the Helsinki convention and were approved by the Ethical Committee of the Eberhard Karls University Tübingen (Nr. 678/2017BO2). Cells were cultured using B27-based retinal differentiation medium (BRDM) (Dulbecco's modified Eagle's medium (DMEM) (41965039, ThermoFisher): DMEM/F12 (10565018, ThermoFisher) (1:1) with 2% B27 (w/o vitamin A, 12587-010, ThermoFisher), 1X minimum essential medium essential amino acids (NEAA, 11140-050, ThermoFisher), and 1X antibiotics-antimycotics (AA, 15240-062, ThermoFisher)).

**T-Cell Isolation.** The cell sourcing follows the Helsinki convention and was approved by the ethical Committee of the Eberhard Karls University Tübingen (Nr. 495/2018-BO02 for the isolation of PBMCs from whole blood). Primary human PBMCs (peripheral blood mononuclear cells) were isolated from whole blood collected up to 1 hour before isolation using standard density gradient centrifugation (Biocoll, Merck), according to manufacturer instructions. After isolation, PBMCs were stained with CellTracker Deep Red Dye (ThermoFisher Scientific) at 1  $\mu\text{M}$  in X-vivo medium (Lonza) for 45 minutes, at 37 °C, protected from light. The PBMCs were cultured at the concentration of  $0.5 \times 10^6$  cells/mL for both chip perfusion and plate controls, in the total volume of 1 mL. T cell activation was achieved with anti-CD3/CD28 antigens using 10  $\mu\text{L}$  of TransAct (Milteny Biotec) per  $0.5 \times 10^6$  cells.

**On-Chip Culture.** Prior to cell seeding, all chips were sterilized by flushing with 70% EtOH and subsequently washed with PBS. To enhance cell attachment to the PLA membranes, a coating protocol was adapted from Achberger et al.<sup>24</sup> Briefly, a 0.01% poly-L-ornithine solution (P4957, Sigma-Aldrich) was injected into the chips for 30 minutes at RT, following by a wash with PBS. Next, the PLA membranes were coated with laminin (11243217001, Roche) at a concentration of 50  $\mu\text{g}/\text{mL}$  in cell culture medium (DMEM/F12 for RPE and ECGM for mvECs) for 2 hours in the incubator (37 °C, 5% CO<sub>2</sub>, 95% humidity).

RPE was detached and singularized using Accumax (A7089-100 ML, Sigma-Aldrich). For the static culture, the RPE cells were cultured in a supplemented BRDM medium containing 20  $\mu\text{g}/\text{mL}$  EGF (GFH26-100, Cell Guidance Systems), 20  $\mu\text{g}/\text{mL}$  FGF2 (GFH146-50, Cell Guidance Systems), 2  $\mu\text{g}/\text{mL}$  heparin (H3149, Sigma-Aldrich), 10  $\mu\text{M}$  ROCK-inhibitor Y-27632 (S1049, Selleck Chem) and 10% FCS (SH3006603, ThermoFisher). For the perfusion, medium was replaced again by BRDM without supplementation.

The mvECs were detached by rinsing the flask with PBS<sup>-</sup> and incubating with 0.05% trypsin in EDTA (S9418C, Sigma-Aldrich; 15040033, ThermoFisher) at 37 °C for 3–5 minutes. The enzymatic reaction was stopped by adding 1% v/v FCS (SH3006603, ThermoFisher). The cell suspension was then centrifuged at 209g for 5 minutes, and the cell pellet was resuspended in ECGM + 1% penicillin/streptomycin (P/S; 15140-122, ThermoFisher) to reach the desired cell concentration. For on-chip culture, ECGM + 1% P/S medium was perfused.

Both cell types were adjusted to a final concentration of 1 000 000 cells/mL in cell-specific medium. Prior to on-chip seeding, three empty pipet tips were placed in the two outlet ports of both channels and at the inlet of the lower channel. The fourth pipet tip was used to load 100  $\mu\text{L}$  of the mvECs or RPE suspension into the upper channel's inlet. After incubating for 2 hours, the cell suspension had equilibrated to the same filling level in the four pipet tips. To ensure a proper nutrition of the cells for 2 days of static culture, each pipet tip was filled up to a volume of 100  $\mu\text{L}$ /pipet tip. To connect the chips to external pumps, all pipet tips were removed, and the in- and outlet of the not-perfused channel were sealed with a piece of sterile PCR tape (EN83.1, Carl Roth). The chip was perfused in push mode using a syringe pump (LA-190 Landgraf HLL). For the mvECs, it was important to set a very low flow rate at the beginning and to slowly ramp up the flow as the cells were directly exposed to the applied flow. Therefore, for mvEC chips, the pump rate was set to 5  $\mu\text{L}/\text{h}$  for the first 24 hours and ramped up to a flow rate of 10  $\mu\text{L}/\text{h}$  after 48 h. Finally, after 96 hours, the pump was set to a constant flow of 20  $\mu\text{L}/\text{h}$ . For the RPE cells, a constant flow rate of 20  $\mu\text{L}/\text{h}$  was used from the beginning.

**On-Chip Viability Assay.** Live/dead staining solution was prepared by diluting fluorescein diacetate (FDA, 1 mg/mL in acetone, F7378 Sigma-Aldrich) and propidium iodide (PI, 1 mg/mL in PBS<sup>-</sup>, P4170, Sigma-Aldrich) in PBS<sup>-</sup> in a ratio of 3:8:100. One of the chips in each experimental round was used as control while the other chips were connected to the pump. The control chips were filled with 20  $\mu\text{L}$  of live/dead-staining solution by placing a pipet tip in the upper channel inlet, resulting in a hydrostatic pressure driven flow. After 15 minutes of incubation, the channels were washed with PBS<sup>-</sup> and then imaged. Images were taken with a laser scanning microscopy (Zeiss LSM 710, Carl Zeiss). Maximum intensity projections of the images were generated with the software ImageJ.

**Cell Morphology and Phenotype Analysis.** To analyze the morphology of the mvEC layer, the cells were stained with an anti-CD31 antibody on day 7 of on-chip culture. Thereto, the chips were washed with PBS<sup>-</sup> once and then incubated for 15 minutes at RT with a CD31-APC conjugated antibody (REA730, Milteny Biotec), which was diluted 1:50 in PBS<sup>-</sup> + 0.5% bovine serum albumin (BSA, A9418, Sigma-Aldrich). Afterward, the chips were washed with PBS<sup>-</sup> twice, fixed at RT for 10 minutes with 4% solution of Roti-Histofix (P087, Carl Roth), and then washed again twice with PBS<sup>-</sup>. For each staining step, the pipet tips in the endothelial channel were gently removed from the ports. An empty tip was inserted into the outlet and a tip containing 20  $\mu\text{L}$  of the step-specific solution was placed into the inlet of the channel.

For the characterization of the cell phenotype of the RPE tissues, the cells were fixed with 4% solution of Roti-Histofix (P087, Carl Roth) on day 4 at RT for 20 minutes. The tissues were blocked and permeabilized with 3% bovine serum albumin (BSA, A9418, Sigma-Aldrich) and 0.1% Triton X-100 (28314, ThermoFisher) for 1 hour, followed by a washing step with PBS. The chips were then incubated with a solution of phalloidin for staining actin filaments (A22283, invitrogen, 1:50 in PBS<sup>-</sup>) and DAPI (1 mg/mL stock solution; D9542 Sigma-Aldrich; diluted to working solution of 1:500 in PBS<sup>-</sup>) for 1 hour at RT and washed with PBS<sup>-</sup>.

Finally, Z-stack images of both cell layer types were obtained with the LSM. Maximum intensity projections of the images were generated with the software ImageJ. In the experiment, three chips of each experimental setup were stained, of which representative images are shown. To assess cell alignment, images were analyzed using the ImageJ plugin OrientationJ.

**Immune Cell Migration On-Chip.** To prepare them for the immune cell migration experiments, the chips were first sterilized and flushed with PBS<sup>-</sup> as described above. To stimulate migration, we filled the bottom channel with a hyaluronan-based hydrogel (Hystem-C, CellSystems GmbH) containing the chemoattractant CCL19 (CCL19/MIP-3 $\beta$ , R&D Systems) in a final concentration of 250 ng/mL and Lipopolysaccharide (LPS, eBioScience, ThermoFischer, 500 $\times$ , added 1:1000 to the hydrogel). To add the hydrogel, the in- and outlets of the top channels were sealed using sterile tape. Then,

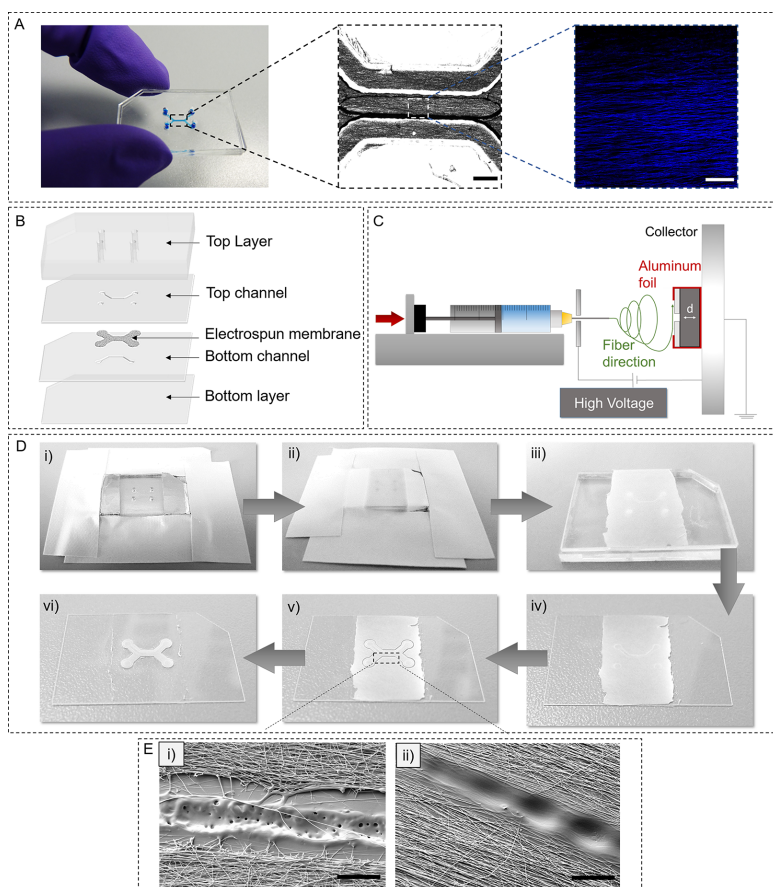


**Figure 1.** Chip design and fabrication: (A) left: photograph of a PLA-GM<sub>2</sub> chip; center: bright field microscopy image of the membrane (scale bar: 500  $\mu\text{m}$ ); right: confocal image of the autofluorescence (DAPI channel) of the fibers on-chip (scale bar: 50  $\mu\text{m}$ ); (B) Schematic of all layers of the chip design; (C) Electrospinning process showing the fiber deposition setup featuring an additional distance created by nonconductive PDMS pieces indicated by “d” for the creation of a flat membrane above the substrate. (D) Chronological sequence of images during the membrane fabrication: (i) Packing of the structured PMMA-piece (together with a PDMS-slab below) into aluminum foil. Aluminum foil is located on the sides to create a fiber orientation along the channel; (ii) Membrane spun onto the entire part; (iii) Membrane after having been cut along the interface of the PMMA part with the aluminum foil using a scalpel wetted with HFIP, thereby creating a localized bonding of the membrane to the PMMA; (iv) Membrane on structured PMMA after removing PDMS; (v) Membrane after lasercutting around the channels; (vi) Final geometry of membrane for bonding process with the minimal necessary membrane size; (E) Effect of the lasercutting process to the fibers; (i) PLA membrane; (ii) PLA-GM<sub>2</sub> membrane (scale bars: 100  $\mu\text{m}$ ).

20  $\mu\text{L}$  of the hydrogel was pushed through the bottom channel until it reached the outlet. The pipet tips were removed, and the chips were placed in the incubator for 15 minutes to allow the hydrogel to cross-link. After 15 minutes, the tape was removed from the in- and outlets of the top channels, and the bottom channel inlets were sealed in return. To prevent clogging of the top channel, it was briefly flushed with 20  $\mu\text{L}$  of sterile PBS<sup>-</sup>. Tubing was connected to the channel outlet while a filter pipet tip with 150  $\mu\text{L}$  of PBMC suspension (cell concentration 500,000 cells/mL) was inserted into the inlet. To generate a defined flow, the cell suspension was drawn through the channel by a syringe pump in “pull mode” with a flow rate of 5  $\mu\text{L}/\text{h}$ . After 17 hours, the pump was stopped, and the chips were fixed, permeabilized, and stained for DAPI as described above. For

evaluation, z-stacks with an LSM were recorded and plotted using the software ZEN Black (version 2.1).

## RESULTS AND DISCUSSION

**1. Chip Concept and Fabrication.** We developed a novel microphysiological system (MPS) that incorporates an electrospun membrane to mimic an *in vivo*-like surface for cell growth. The chip is made from PMMA as the main material, which displays a lower absorption of hydrophobic molecules compared to the broadly used alternative PDMS.<sup>25</sup> The chip consists of multiple PMMA layers that feature two parallel straight channels (width of 300  $\mu\text{m}$ , height of 175  $\mu\text{m}$ )

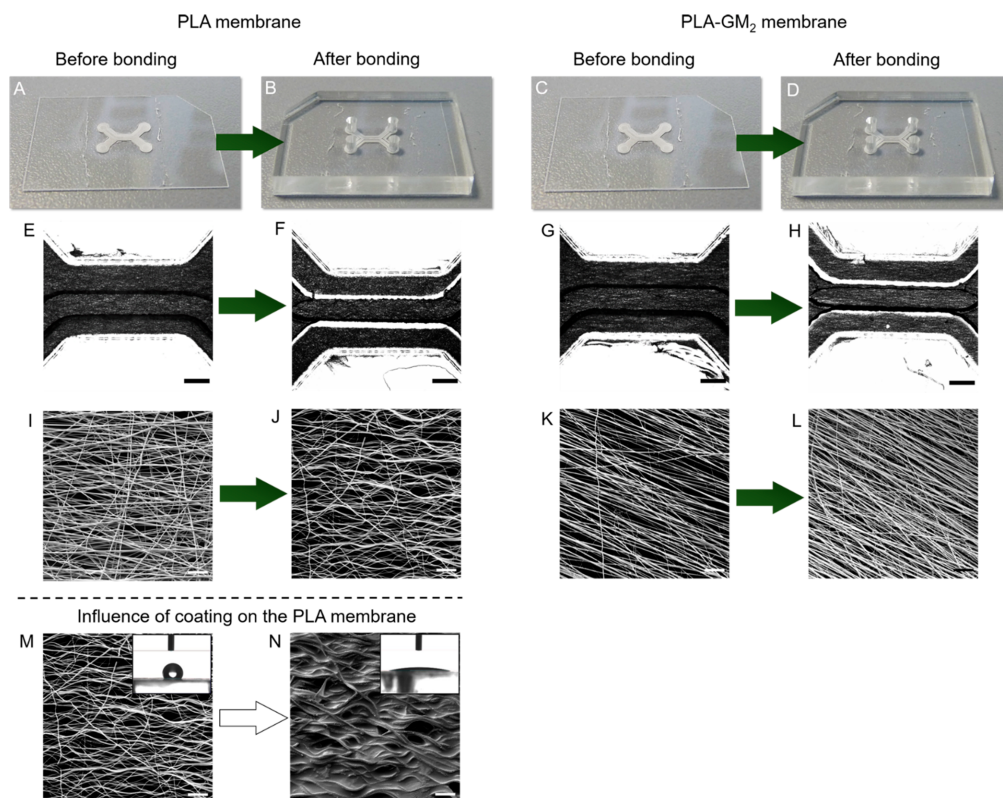


**Figure 2.** Morphological changes of the membrane during the chip preparation: (A,C) Representative image of PMMA layer with electrospun membranes before bonding; (B,D) Representative image of PMMA chip after bonding; (E) Brightfield microscopy of the PLA membrane before and (F) after bonding; (G) Brightfield microscopy of the PLA-GM<sub>2</sub> membrane before and (H) after bonding; (I) SEM image of the morphology of the PLA membrane before and (J) after temperature treatment; (K) SEM image of the morphology of the PLA-GM<sub>2</sub> membrane before and (L) after temperature treatment; (M,N) Changes in morphology and contact angle of the PLA membranes due to coating: (M) Before coating, featuring high hydrophobicity; (N) After coating, featuring low hydrophobicity; Microscopy images; scale bar: 500  $\mu\text{m}$  (E–H); SEM images; scale bar: 20  $\mu\text{m}$  (I–N).

separated by an electrospun membrane over a length of 2300  $\mu\text{m}$  (Figure 1A,B). This chip design serves as proof of concept model for the integration of electrospun membranes into OoC platforms and can be further adapted to the tissue of interest in a flexible way.

To generate thin and homogeneously distributed membranes in between the channels, we established the following procedure: membranes were spun directly onto the bottom side of the layers containing the top channels (refer to Figure 1B). As the layer is very thin (175  $\mu\text{m}$ ) and has open channel structures, an additional nonconductive material, a 2 mm thick square PDMS slab, was placed below prior to electrospinning to prevent locally focused conductivity in the channel structures (Figure 1C). Further, the PMMA module was covered with aluminum foil on the left and right side of the layer to produce a membrane with a directional fiber orientation along the channel direction (Figure 1D (ii)).<sup>26</sup> To avoid excessive spinning beyond the chip area, the edges of the chip were covered with a nonconductive tape.

During the electrospinning process, fibers are directed from the needle tip toward the conductive collector when an electric field is applied. Therefore, the fibers tend to be located wherever conductive material can be reached. The nonconductive PDMS slab, hence, played an important role in the electrospinning process: Without it, the fibers were located and highly concentrated inside the channel, because the cut structures provided a direct path to the collector. As a result, it was not possible to create a homogeneous fiber mat on the PMMA layers. The separation provided by the PDMS slab, however, facilitated the fabrication of homogeneous membranes.

After the spinning process, we could successfully remove excess fibers by guiding a scalpel briefly soaked in HFIP along the border of PMMA and aluminum foil. The HFIP solvent fused the membrane edges into the PMMA layer; otherwise, the membrane would be lifted off the smooth PMMA surface during the subsequent removal of aluminum foil and PDMS slab (Figure 1D (iii) and (iv)).

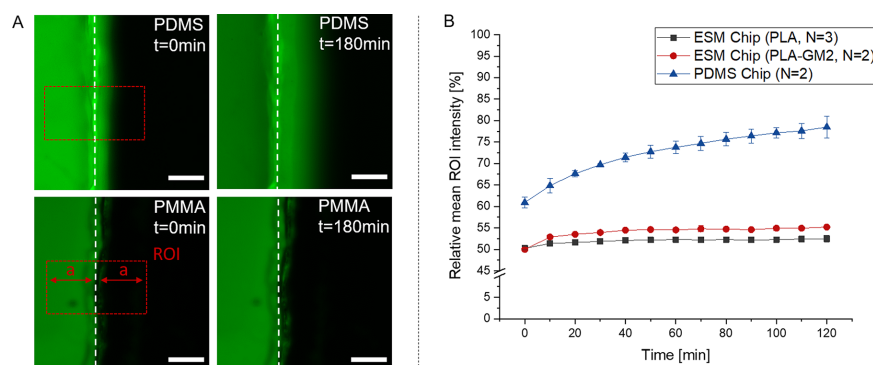


**Figure 3.** Diffusion profile of Rhodamine B in the PMMA chips in comparison to control chips made from PDMS; (A) Fluorescence microscopy images of the diffusion of the dye at the start and end of the experiment (scale bars: 100  $\mu\text{m}$ ); (B) Relative mean ROI intensity over a period of 120 minutes; The values (mean values w/standard deviation) were obtained from rectangular regions that were centrally positioned at the edge between channels and bulk material, whereby half of the rectangle covered the inside of the channel and the other half the outside of the channel. Thus, the starting value was 50% intensity.

In a last step of the membrane fabrication, an engraved line that melted both materials with each other surrounding the channels was generated to reduce the size of the membranes to the necessary minimum (Figure 1D (v)). Thereby, the fibers of the membrane were melted with the PMMA material and the surrounding fibers could be easily removed with a wipe (Figure 1D (vi)). Depending on the material of the electrospun membranes, the welded structures can look slightly different (Figure 1E). However, we did not observe any effects of these differences in terms of chip sealing or membrane integrity. Finished chips were obtained by assembling, aligning and then thermally bonding all the layers (cf. Figure 1B).

Membranes based on two different polymer solutions were integrated: PLA and a blend of PLA-GM<sub>2</sub>. PLA was chosen for several reasons: First, it is known as a biocompatible material that has already been used for the fabrication of electrospun scaffolds with endothelial cell adhesion and growth.<sup>27</sup> In addition, the material has a low degradation time because of its strong hydrophobic character. Further, PLA has a high melting point of 180 °C,<sup>28</sup> which was crucial to prevent melting of the membranes during the thermal bonding step.

Lastly, PLA has been approved by the US Food and Drug Administration (FDA) for biomedical applications, such as a surgical suture material.<sup>29</sup> However, as the hydrophobicity of the material may lead to poor cell adhesion, subsequent treatments of the membrane are usually necessary. One possible treatment procedure is to coat the membrane with a natural ECM component prior to cell seeding. Another elegant and time-saving method is to prepare a blended polymer solution containing a natural polymer alongside the PLA to reduce the hydrophobicity and add cell recognition sites on the fibers.<sup>11</sup> For this reason, a solution of PLA was prepared in combination with a biopolymer component. As high temperatures are applied on the membranes during the fabrication process (130 °C, 15 minutes), gelatin methacryloyl (GM) was chosen as biopolymer. Gelatin has already been exposed to high temperatures during its fabrication through the partial denaturation of native collagen and is accordingly considered to be stable in the bonding step. Furthermore, gelatin features a very high protein content of 85–92% making it a suitable

material for the insertion of several cell recognition sites into the membrane.<sup>30</sup> It has been shown earlier that GM can be successfully electrospun and shows improved cell viability compared to conventional gelatin.<sup>31</sup> Moreover, an improved cell density on the fiber mat could also be achieved by blending with uncross-linked GM.<sup>32</sup> Therefore, GM<sub>2</sub> with a 2-fold excess of methacrylic anhydride was chosen, as UV-cross-linking was not planned to be performed on these membranes. However, when cross-linking the fibers, a GM with a higher amount of methacrylic anhydride could be chosen.<sup>22</sup>

**2. Platform Characterization. Membrane Characterization.** To analyze the effect of thermal fusion bonding on the membrane fiber morphology, bright field microscopy and SEM images were taken before and after the bonding step (Figure 2A–D). The bright field images show that the channel remains covered by a homogeneous fiber mat, and the membranes are not damaged. Along the interfaces between membrane and PMMA module, a white border becomes apparent after bonding, indicating a tight sealing of the chip (Figure 2E–H). Comparing the images before and after bonding, it can be clearly seen that the PLA membranes start to slightly wrinkle during this bonding process by forming curled fibers (Figure 2I, J). The analysis of the fiber diameter revealed that the membranes consist of nanofibrous constructs with median fiber diameter of  $0.6 \pm 0.2 \mu\text{m}$  and  $0.6 \pm 0.3 \mu\text{m}$  for the PLA membranes and the hybrid membranes with gelatin, respectively. Interestingly, prior to heat and pressure treatment, the membranes had a larger fiber diameter of  $3 \pm 1 \mu\text{m}$  and  $2.1 \pm 0.8 \mu\text{m}$  for PLA and PLA-GM<sub>2</sub> respectively. During the heat treatment, the membranes become slightly wavy as the temperature is above the glass transition temperature; therefore, the fibers are stretched, resulting in the reduction of fiber size and a curved structure, which was predominantly observed for the PLA-membranes. In comparison, the membranes with gelatin did not seem to be affected by heat or pressure treatment as shown by the fibers that stay linear during the bonding process (Figure 2K, L). However, the reduced fiber size indicated the morphological change and a slight sagging of the membranes. In general, the fibers are preferentially aligned in one direction because of the

anisotropic placement of the aluminum foil covers. In cases where nonaligned fibers are desired, simply covering all sides of the chips with aluminum will be sufficient (Supplementary Figure S1).

Further, the pore size of the membranes is important as it determines if the fiber constructs are dense enough to support the cells. Measurement of pore sizes using image analysis revealed that PLA membranes had an average pore size of 5  $\mu\text{m}$ , while the PLA-GM<sub>2</sub> membranes had a slightly smaller average pore size of about 1  $\mu\text{m}$ . In suspension, endothelial cells have a diameter of 13–14  $\mu\text{m}$ ,<sup>33</sup> and human retinal pigmented epithelial cells have a similar cell center-to-center spacing of 14–15  $\mu\text{m}$  measured on excised retinas<sup>34</sup>). With consideration of the cells' shape, the fiber mat seems to be dense enough to capture the cells. When comparing with other conventionally used cell culture membranes, the achieved pore sizes of the electrospun membranes are in a similar range. However, it has to be noted that the analysis of the fiber mat via image analysis is not very precise as the pores are not conventional circular pores but measured as a result of a batch of stacked nanofibers. Therefore, this measurement solely gives an orientation whether the membranes are dense enough to capture the cells. In addition, by coating the PLA membranes with laminin, the surface becomes more homogeneous and the pores are filled with the coating substance (Figure 2M,N).

**Chip Sealing and Absorption Behavior.** The leakage of solutes from microfluidic channels can occur via two routes: leakage of the entire media due to nonproper chip sealing or the absorption of the solute into the bulk chip material. A proper chip sealing is particularly an issue when integrating membranes into thermoplastic chips.<sup>18</sup> The absorption of hydrophobic molecules is particularly a problem of PDMS-based systems<sup>4</sup> but can occur in other polymers too. To confirm the tightness of our chip as well as the low absorption characteristics, we incubated a hydrophobic fluorescent dye (Rhodamine B) containing media for several hours inside the chip as described previously.<sup>23</sup> As a control for the absorption aspect, a conventional PDMS chip was treated the same way as the PMMA chip. In the fully assembled PMMA chip, the fluorescent intensity at the border of the channel remained constant over a period of 2 hours of exposure with the fluorescent dye (Figure 3). This indicated both that the PMMA chips are tightly sealed and that the chip material itself does not absorb the dye molecules. The lack of a fluorescent signal outside the channel revealed that no liquid entered the joint between PMMA layers and membrane, indicating a bonding between PMMA and membrane strong enough to create a proper tightness. Additionally, it demonstrated that no absorption of the fluorescent dye into the bulk PMMA is occurring, which is especially apparent when compared to the rapid partitioning into the PDMS control, similar to observations in previous work.<sup>23,35</sup>

Since PLA constitutes the basis for the electrospun membranes and is a hydrophobic polymer as well, we also assessed the absorption of Rhodamine B into the PLA fibers. Indeed fluorescent dye remained in the membranes after 2 hours of incubation but was released quickly by subsequently flushing the channel with PBS<sup>-</sup> (Supplementary Figure S2). However, compared to the use of PDMS as a bulk chip material featuring a large volume and small surface-to-volume ratio, the bulk absorption by the PLA nanofibers featuring a much smaller total volume and higher surface-to-volume ratio is negligible.

In summary, these experiments demonstrate a proper PMMA chip sealing while highlighting the prevention of small molecules absorption into the bulk chip material.

**3. On-Chip Cell Culture.** To evaluate the suitability of the PMMA-chips with integrated electrospun membranes for cell and tissue culture, two different cell types were injected into the microfluidic channels: Both human skin-derived primary mvECs and hiPSC-derived RPE were seeded into chips with two types of membranes, PLA-only and PLA-GM<sub>2</sub>. The limited transparency of the membranes provides a challenge for cell monitoring using brightfield microscopy; however, using fluorescence microscopy, it was possible to image cells on either sides of the membrane. Special attention had to be paid to the oxygen supply, since, unlike PDMS, PMMA is not oxygen permeable leaving the tissues on-chip dependent on oxygen supply via the media (perfusion). This is especially critical during the initial seeding and layer formation step, during which only a static media supply and no perfusion yet is applied. Hence, to assess cell viability on-chip after 2 days with static media supply, the chips were stained for FDA and PI (Figure 4). For both mvECs as well as RPE, the live/dead

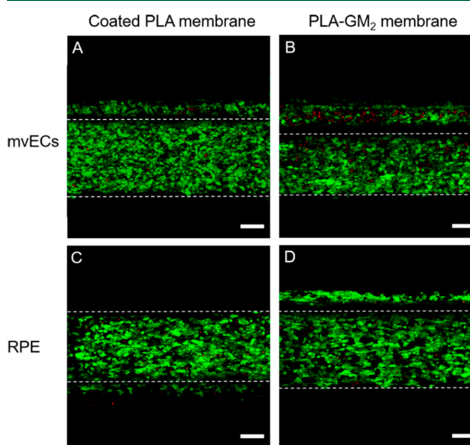


**Figure 4.** Live/dead staining of different cell types cultured on membranes prior to onset of perfusion; green (FDA - indicating viable cells); red (PI - indicating dead cells); white dotted lines mark the area where both channels are overlapping; the cells beyond channel overlap are due to misalignment of the chips; A: mvECs on a PLA-membrane; B: mvECs on a PLA-GM<sub>2</sub> membrane; C: RPE on a PLA-membrane; D: RPE on a PLA-GM<sub>2</sub> membrane (scale bars: 100  $\mu\text{m}$ ).

assay revealed dense layers on both membrane types, showing a predominantly viable (green) cell layer with only a few dead (red) cell nuclei. These findings indicated that even without perfusion, sufficient oxygen supply is ensured. To demonstrate the suitability for both in-flow as well as shear-force protected culture of cell layers, two different culture configurations were chosen for RPE and mvECs.

Since endothelial cells *in vivo* are constantly exposed to shear flow and shear forces, the mvECs were injected into the same channel as assigned for the perfusion during culture (Figure 5A). Following the initial static cell attachment and layer formation step, the media flow was slowly ramped up in three steps to avoid cell detachment. Subsequently, the flow rate was

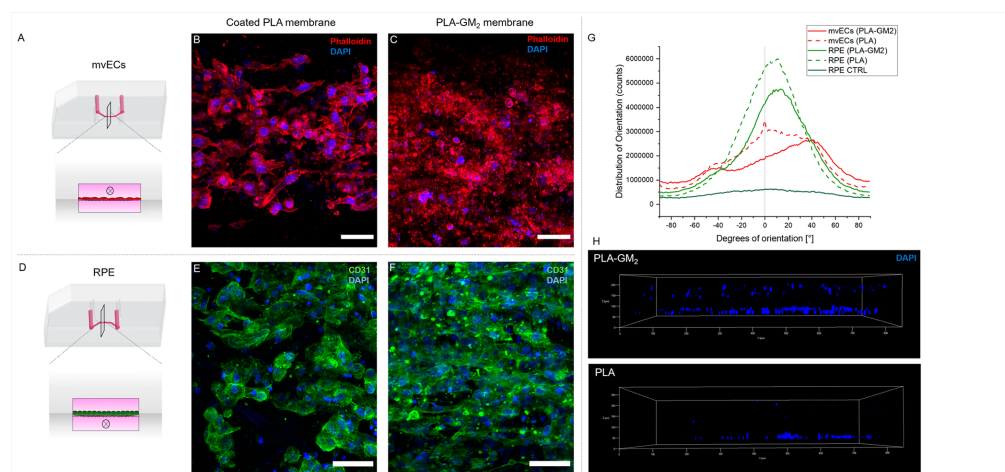


**Figure 5.** Chips cultured with perfusion. (A) Schematic of mvEC-perfusion: Flow and shear forces are directly applied onto cell layer, perfused channel is showed in the cross section and indicated by the circle. (B) mvECs onto PLA-membrane after 7 days of on-chip culture (C) mvECs onto PLA-GM<sub>2</sub> membrane after 7 days of on-chip culture (red: CD31; blue: DAPI); (D) Schematic of RPE-perfusion: cells are protected from direct shear forces through the membrane; (E) RPE onto PLA membrane after 4 days of on-chip culture (green: phalloidin; blue: DAPI; scale bars: 50  $\mu$ m); (F) RPE onto PLA-GM<sub>2</sub> membrane after 4 days of on-chip culture (green: phalloidin; blue: DAPI; scale bars: 50  $\mu$ m); (G) Distribution of cell orientation depending on material and cell type showing a preferred orientation along the fiber direction (0°); (H) Confocal microscopy z-stacks of the lower hydrogel filled channel (175  $\mu$ m height) after perfusing immune cells through the upper channels, revealing cell migration through the membranes (both PLA-GM<sub>2</sub> and PLA).

kept constant at 20  $\mu$ L/h. Immunofluorescence staining for PECAM-1 (CD31) after 7 days of on-chip culture revealed the preservation of the cell layer and of the phenotype of the endothelial cells (Figure 5B,C). Moreover, the cells appeared to be preferentially aligned with the fiber orientation, which was especially evident for less dense cell layers (cf. Supplementary Figure S3A). Image analysis of the distribution of the cell orientation confirmed this observation (Figure 5G). This is consistent with previous studies that showed that endothelial cell orientation can be guided using electrospun substrates.<sup>36</sup>

Contrary to endothelial tissue, most epithelial tissue is protected from shear flow and forces *in vivo*. Hence, we cultured the RPE in the nonperfused channel, separated from the media flow by the electrospun membrane (Figure 5D). As this configuration also avoids the danger of flow-induced cell detachment, the media perfusion through the RPE-chips was initiated 2 days after the seeding without ramping up the flow rate. Immunofluorescence staining of the F-actin in epithelial cells with phalloidin after 4 days showed that RPE cell layers maintained intact (Figure 5E,F). Even after 2 weeks of on-chip culture, RPE cells maintained viability (Supplementary Figure S3B), demonstrating the applicability of the chips for long-term culture. In general, for RPE cells, electrospun membranes have been employed previously to mimic the Bruch's membrane below the RPE and found to be an appropriate substrate for tissue transplantation.<sup>37–39</sup> Research groups have mostly focused on the suitability of these membranes for implantation to patients with a damaged RPE. Popelka et al.,<sup>38</sup> for instance, used a membrane produced from PLA to show a successful *in vitro* cell attachment.

To analyze whether cells can migrate through the membranes, immune cells were perfused through one of the

channels, and their infiltration in the other channel was assessed. PBMCs isolated from fresh human whole blood and activated via anti-CD3/CD28 antigens were flushed through chips featuring a chemoattractant containing hyaluronan-based hydrogel in the nonperfused channel. After 17 hours, it can be clearly seen that cells migrated through the membranes and infiltrated the hydrogel in the bottom layer (Figure 5H), highlighting that both types of membranes are porous enough for cells to migrate through.

Comparing the two different membranes types, we did not observe any fundamental differences in the cell migration behavior and in cell attachment, neither for mvECs nor for RPE. However, the PLA-membranes had to be coated prior to cell seeding; otherwise, they were strongly hydrophobic and did not present any recognition sites for cell adhesion. Coating with cell type-specific matrix component is a reliable method often employed to promote cell adhesion. It is, however, a time-consuming process that requires several working steps prior to cell seeding. Moreover, the coating does usually not exclusively cover the membrane but the entire channel. Consequently, the cells can adhere not only to the membrane but also to the channel walls. Depending on the targeted configuration, this can limit the accuracy of the emulation of certain tissues. Unlike the PLA membranes, the PLA-GM<sub>2</sub> membranes intrinsically contain cell recognition sites as a modified gelatin was already integrated into the membranes during the fabrication process. These membranes can, hence, overcome the disadvantages of a conventional coating process and provide a facile way of providing localized adhesion areas for cells.

## CONCLUSIONS

For many years, electrospinning techniques have been employed to create *in vivo*-like scaffolds, especially for regenerative medicine. In the field of OoC, however, electrospinning has been barely applied, and the few existing approaches are PDMS-based systems. Since the use of PDMS as a chip material becomes more and more limiting owing to the material's absorption of small hydrophobic molecules, we have developed an alternative fabrication process to generate PMMA-platforms integrating two different types of electrospun membranes with a PLA backbone. The fabricated systems showed the feasibility of producing, customizing, and incorporating different kinds of electrospun membranes into thermoplastic-based OoCs. Further, it presents a tunable and flexible fabrication process to create an adaptable environment for the cells by adjusting (visco)elasticity or porosity of the membranes along with the application of natural materials (e.g., native proteins of the ECM).

The principle suitability of this approach to serve as a basis for OoC systems was demonstrated by the integration of two different cell types—mvECs and RPEs. Both indicated good viability. mvECs also expressed cell-specific markers in on-chip culture. One essential advantage of electrospun membranes is its morphology as a 3D stack of fibers; therefore, the cells can adhere, integrate into the membrane, and eventually remodel the microenvironment. Looking ahead, diseases could be initiated, such as the formation of choroidal neovascularization, where blood vessels start growing in an uncontrolled way, migrate toward the epithelial barrier, and finally disrupt the epithelial layer. In contrast, with a conventional membrane, this could not be emulated as no membrane disruption could happen through the rigid membrane with defined pore sizes. From the technical perspective, this robust fabrication method for the integration of electrospun membranes into OoCs is a promising approach to overcome the disadvantages of synthetic, rigid membranes and to create an improved cell environment emulating several ECM-properties.

## ASSOCIATED CONTENT

### Supporting Information

The Supporting Information is available free of charge at <https://pubs.acs.org/doi/10.1021/acsbomaterials.0c01062>.

SEM images of the two types of scaffolds with different fiber alignment; characterization of absorption of fluorescent dye by membranes; cell viability on chip for low cell density conditions and long-term culture (PDF)

## AUTHOR INFORMATION

### Corresponding Author

**Peter Loskill** – *Fraunhofer Institute for Interfacial Engineering and Biotechnology IGB, 70569 Stuttgart, Germany; Department of Women's Health, Research Institute for Women's Health, Eberhard Karls University of Tübingen, 72076 Tübingen, Germany; [orcid.org/0000-0002-5000-0581](https://orcid.org/0000-0002-5000-0581); Email: [peter.loskill@uni-tuebingen.de](mailto:peter.loskill@uni-tuebingen.de)*

### Authors

**Johanna Chuchuy** – *Fraunhofer Institute for Interfacial Engineering and Biotechnology IGB, 70569 Stuttgart, Germany; Department of Women's Health, Research Institute*

*for Women's Health, Eberhard Karls University of Tübingen, 72076 Tübingen, Germany*

**Julia Rogal** – *Fraunhofer Institute for Interfacial Engineering and Biotechnology IGB, 70569 Stuttgart, Germany; Department of Women's Health, Research Institute for Women's Health, Eberhard Karls University of Tübingen, 72076 Tübingen, Germany*

**Tran Ngo** – *Fraunhofer Institute for Interfacial Engineering and Biotechnology IGB, 70569 Stuttgart, Germany; [orcid.org/0000-0002-4093-7004](https://orcid.org/0000-0002-4093-7004)*

**Kathrin Stadelmann** – *NMI Natural and Medical Sciences Institute at the University Tübingen, 72770 Reutlingen, Germany*

**Lena Antkowiak** – *Institute of Neuroanatomy & Developmental Biology INDB, Eberhard Karls University of Tübingen, 72074 Tübingen, Germany*

**Kevin Achberger** – *Institute of Neuroanatomy & Developmental Biology INDB, Eberhard Karls University of Tübingen, 72074 Tübingen, Germany*

**Stefan Liebau** – *Institute of Neuroanatomy & Developmental Biology INDB, Eberhard Karls University of Tübingen, 72074 Tübingen, Germany*

**Katja Schenke-Layland** – *Department of Women's Health, Research Institute for Women's Health, Eberhard Karls University of Tübingen, 72076 Tübingen, Germany; NMI Natural and Medical Sciences Institute at the University Tübingen, 72770 Reutlingen, Germany; Department of Medicine/Cardiology, Cardiovascular Research Laboratories, David Geffen School of Medicine at UCLA, Los Angeles, California 90095, United States; [orcid.org/0000-0001-8066-5157](https://orcid.org/0000-0001-8066-5157)*

Complete contact information is available at: <https://pubs.acs.org/10.1021/acsbomaterials.0c01062>

## Notes

The authors declare no competing financial interest.

## ACKNOWLEDGMENTS

The authors thank Dr. Ziegler (Klinik Charlottenhaus, Stuttgart) for the provision of skin biopsies from plastic surgery, Lisa Rebers for the provision of the gelatin methacryloyl, Julia Roosz for the mvEC isolation and culture, Claudia Teufel for the immune cell isolation, and Verena Holzmüller for her assistance with RPE cell culture and chip fabrication. The research was supported in part by the Ministry of Science, Research and the Arts of Baden-Württemberg (Az: 7542.2-501-1/13/6) and the Friedrich Naumann Foundation for Freedom.

## ABBREVIATIONS

OoC, organs-on-chip; ECM, extracellular matrix; PDMS, polydimethylsiloxane; PMMA, poly(methyl methacrylate); PC, polycarbonate; PET, polyethylene terephthalate; PCL, polycaprolactone; PLA, poly-L-lactide; PLGA, poly(lactic-co-glycolic acid); GM, gelatin methacryloyl; GM2, gelatin methacryloyl with a 2-fold excess of methacrylic anhydride; HFIP, 1,1,1,3,3,3-hexafluoro-2-propanol; RT, room temperature; SEM, scanning electron microscopy; ROI, region of interest; mvECs, microvascular endothelial cells; hiPS, human induced pluripotent stem; RPE, retinal pigment epithelium; MPS, microphysiological system; FDA, Food and Drug

Administration; PBS<sup>-</sup>, phosphate-buffered saline; DAPI, 4',6-diamidin-2-phenylindol; CO<sub>2</sub>, carbon dioxide

## REFERENCES

- (1) Marx, U.; Andersson, T. B.; Bahinski, A.; Beilmann, M.; Beken, S.; Cassee, F. R.; Cirit, M.; Daneshian, M.; Fitzpatrick, S.; Frey, O.; Gaertner, C.; Giese, C.; Griffith, L.; Hartung, T.; Heringa, M. B.; Hoeng, J.; De Jong, W. H.; Kojima, H.; Kuehl, J.; Leist, M.; Luch, A.; Maschmeyer, I.; Sakharov, D.; Sips, A. J. A. M.; Steger-Hartmann, T.; Tagle, D. A.; Tonevitsky, A.; Tralau, T.; Tsyb, S.; Van De Stolpe, A.; Vandebriel, R.; Vulto, P.; Wang, J.; Wiest, J.; Rodenburg, M.; Roth, A. Biology-Inspired Microphysiological System Approaches to Solve the Prediction Dilemma of Substance Testing. *ALTEX* **2016**, *33* (3), 272–321.
- (2) Pasman, T.; Grijpma, D.; Stamatialis, D.; Poot, A. Flat and Microstructured Polymeric Membranes in Organs-on-Chips. *J. R. Soc. Interface* **2018**, *15* (144), 20180351.
- (3) Bhatia, S. N.; Ingber, D. E. Microfluidic Organs-on-Chips. *Nat. Biotechnol.* **2014**, *32* (8), 760–772.
- (4) Ahadian, S.; Civitarese, R.; Bannerman, D.; Mohammadi, M. H.; Lu, R.; Wang, E.; Davenport-Huyer, L.; Lai, B.; Zhang, B.; Zhao, Y.; Mandla, S.; Korolj, A.; Radisic, M. Organ-On-A-Chip Platforms: A Convergence of Advanced Materials, Cells, and Microscale Technologies. *Adv. Healthcare Mater.* **2018**, *7* (2), 1700506.
- (5) Bovard, D.; Iskandar, A.; Luettich, K.; Hoeng, J.; Peitsch, M. Organs-on-a-Chip: A New Paradigm for Toxicological Assessment and Preclinical Drug Development. *Toxicol. Res. Appl.* **2017**, *1*, 239784731772635.
- (6) Wang, X.; Hsiao, B. S. Electrospun Nanofiber Membranes. *Curr. Opin. Chem. Eng.* **2016**, *12*, 62–81.
- (7) Khorshidi, S.; Solouk, A.; Mirzadeh, H.; Mazinani, S.; Lagaron, J. M.; Shariif, S.; Ramakrishna, S. A Review of Key Challenges of Electrospun Scaffolds for Tissue-engineering Applications. *J. Tissue Eng. Regen. Med.* **2016**, *10* (9), 715–738.
- (8) Pampaloni, F.; Reynaud, E. G.; Stelzer, E. H. K. Air-Liquid Interface Growth Medium Apoptosis/Anoikis Aggregation Polarization Differentiation. *Nat. Rev. Mol. Cell Biol.* **2007**, *8* (10), 839–845.
- (9) Zhang, X.; Reagan, M. R.; Kaplan, D. L. Electrospun Silk Biomaterial Scaffolds for Regenerative Medicine. *Adv. Drug Delivery Rev.* **2009**, *61* (12), 988–1006.
- (10) Meng, Z. X.; Wang, Y. S.; Ma, C.; Zheng, W.; Li, L.; Zheng, Y. F. Electrospinning of PLGA/Gelatin Randomly-Oriented and Aligned Nanofibers as Potential Scaffold in Tissue Engineering. *Mater. Sci. Eng., C* **2010**, *30* (8), 1204–1210.
- (11) Oh, S. H.; Lee, J. H. Hydrophilization of Synthetic Biodegradable Polymer Scaffolds for Improved Cell/Tissue Compatibility. *Biomed. Mater.* **2013**, *8* (1), 014101.
- (12) Hasan, A.; Memic, A.; Annabi, N.; Hossain, M.; Paul, A.; Dokmeci, M. R.; Dehghani, F.; Khademhosseini, A. Electrospun Scaffolds for Tissue Engineering of Vascular Grafts. *Acta Biomater.* **2014**, *10* (1), 11–25.
- (13) Xie, J.; Macewan, M. R.; Liu, W.; Jesuraj, N.; Li, X.; Hunter, D.; Xia, Y. Nerve Guidance Conduits Based on Double-Layered Scaffolds of Electrospun Nanofibers for Repairing the Peripheral Nervous System. *ACS Appl. Mater. Interfaces* **2014**, *6* (12), 9472–9480.
- (14) Koppes, A. N.; Zaccor, N. W.; Rivet, C. J.; Williams, L. A.; Piselli, J. M.; Gilbert, R. J.; Thompson, D. M. Neurite Outgrowth on Electrospun PLLA Fibers Is Enhanced by Exogenous Electrical Stimulation. *J. Neural Eng.* **2014**, *11* (4), 046002.
- (15) Holmes, B.; Castro, N. J.; Zhang, L. G.; Zussman, E. Electrospun Fibrous Scaffolds for Bone and Cartilage Tissue Generation: Recent Progress and Future Developments. *Tissue Eng., Part B* **2012**, *18* (6), 478–486.
- (16) Sill, T. J.; von Recum, H. A. Electrospinning: Applications in Drug Delivery and Tissue Engineering. *Biomaterials* **2008**, *29* (13), 1989–2006.
- (17) Schneider, A.; Wang, X. Y.; Kaplan, D. L.; Garlick, J. A.; Egles, C. Biofunctionalized Electrospun Silk Mats as a Topical Bioactive Dressing for Accelerated Wound Healing. *Acta Biomater.* **2009**, *5* (7), 2570–2578.
- (18) Moghadas, H.; Saidi, M. S.; Kashaninejad, N.; Nguyen, N. T. A High-Performance Polydimethylsiloxane Electrospun Membrane for Cell Culture in Lab-on-a-Chip. *Biomicrofluidics* **2018**, *12* (2), 024117.
- (19) Kim, J. H.; Park, J. Y.; Jin, S.; Yoon, S.; Kwak, J. Y.; Jeong, Y. H. A Microfluidic Chip Embracing a Nanofiber Scaffold for 3D Cell Culture and Real-Time Monitoring. *Nanomaterials* **2019**, *9* (4), 588.
- (20) Yang, X.; Li, K.; Zhang, X.; Liu, C.; Guo, B.; Wen, W.; Gao, X. Nanofiber Membrane Supported Lung-on-a-Chip Microdevice for Anti-Cancer Drug Testing. *Lab Chip* **2018**, *18* (3), 486–495.
- (21) Budhwani, K. I.; Thomas, V.; Sethu, P. Lab-on-a-Brane: Nanofibrous Polymer Membranes to Recreate Organ-Capillary Interfaces. *J. Micromech. Microeng.* **2016**, *26* (3), 035013.
- (22) Hoch, E.; Hirth, T.; Tovar, G. E. M.; Borchers, K. Chemical Tailoring of Gelatin to Adjust Its Chemical and Physical Properties for Functional Bioprinting. *J. Mater. Chem. B* **2013**, *1* (41), 5675–5685.
- (23) Virumbrales-Muñoz, M.; Livingston, M. K.; Farooqi, M.; Skala, M. C.; Beebe, D. J.; Ayuso, J. M. Development of a Microfluidic Array to Study Drug Response in Breast Cancer. *Molecules* **2019**, *24* (23), 4385.
- (24) Achberger, K.; Probst, C.; Haderspeck, J. C.; Bolz, S.; Rogal, J.; Chuchuy, J.; Nikolova, M.; Cora, V.; Antkowiak, L.; Haq, W.; Shen, N.; Schenke-Layland, K.; Ueffing, M.; Liebau, S.; Loskill, P. Merging Organoid and Organ-on-a-Chip Technology to Generate Complex Multi-Layer Tissue Models in a Human Retina-on-a-Chip Platform. *eLife* **2019**, *8*, 1–26.
- (25) Jodat, Y. A.; Kang, M. G.; Kiaee, K.; Kim, G. J.; Martinez, A. F. H.; Rosenkranz, A.; Bae, H.; Shin, S. R. Human-Derived Organ-on-a-Chip for Personalized Drug Development. *Curr. Pharm. Des.* **2019**, *24* (45), 5471–5486.
- (26) Hu, T.; Li, Q.; Dong, H.; Xiao, W.; Li, L.; Cao, X. Patterning Electrospun Nanofibers via Agarose Hydrogel Stamps to Spatially Coordinate Cell Orientation in Microfluidic Device. *Small* **2017**, *13* (3), 1602610.
- (27) Xu, C.; Inai, R.; Kotaki, M.; Ramakrishna, S. Electrospun Nanofiber Fabrication as Synthetic Extracellular Matrix and Its Potential for Vascular Tissue Engineering. *Tissue Eng.* **2004**, *10* (7–8), 1160–1168.
- (28) Ahmed, J.; Varshney, S. K. Polylactides-Chemistry, Properties and Green Packaging Technology: A Review. *Int. J. Food Prop.* **2011**, *14* (1), 37–58.
- (29) Xu, J.; Zhang, J.; Gao, W.; Liang, H.; Wang, H.; Li, J. Preparation of Chitosan/PLA Blend Micro/Nanofibers by Electrospinning. *Mater. Lett.* **2009**, *63* (8), 658–660.
- (30) Schrieber, R.; Gareis, H. *Gelatine Handbook*; Wiley-VCH Verlag GmbH & Co. KGaA: Weinheim, 2007. DOI: 10.1002/9783527610969.
- (31) Sun, X.; Lang, Q.; Zhang, H.; Cheng, L.; Zhang, Y.; Pan, G.; Zhao, X.; Yang, H.; Zhang, Y.; Santos, H. A.; Cui, W. Electrospun Photocrosslinkable Hydrogel Fibrous Scaffolds for Rapid In Vivo Vascularized Skin Flap Regeneration. *Adv. Funct. Mater.* **2017**, *27* (2), 1–12.
- (32) Lobo, A. O.; Afewerki, S.; de Paula, M. M. M.; Ghannadian, P.; Marciano, F. R.; Zhang, Y. S.; Webster, T. J.; Khademhosseini, A. Electrospun Nanofiber Blend with Improved Mechanical and Biological Performance. *Int. J. Nanomed.* **2018**, *13*, 7891–7903.
- (33) Wagner, W. H.; Henderson, R. M.; Hicks, H. E.; Banas, A. J.; Johnson, G. Differences in Morphology, Growth Rate, and Protein Synthesis between Cultured Arterial and Venous Endothelial Cells. *J. Vasc. Surg.* **1988**, *8* (4), 509–519.
- (34) Roorda, A.; Zhang, Y.; Duncan, J. L. High-Resolution in Vivo Imaging of the RPE Mosaic in Eyes with Retinal Disease. *Invest. Ophthalmol. Visual Sci.* **2007**, *48* (5), 2297–2303.
- (35) Toepke, M. W.; Beebe, D. J. PDMS Absorption of Small Molecules and Consequences in Microfluidic Applications. *Lab Chip* **2006**, *6* (12), 1484–1486.

(36) Ma, Z.; He, W.; Yong, T.; Ramakrishna, S. Grafting of Gelatin on Electrospun Poly(Caprolactone) Nanofibers to Improve Endothelial Cell Spreading and Proliferation and to Control Cell Orientation. *Tissue Eng.* **2005**, *11* (7-8), 1149.

(37) Warnke, P. H.; Alamein, M.; Skabo, S.; Stephens, S.; Bourke, R.; Heiner, P.; Liu, Q. Primordium of an Artificial Bruch's Membrane Made of Nanofibers for Engineering of Retinal Pigment Epithelium Cell Monolayers. *Acta Biomater.* **2013**, *9* (12), 9414–9422.

(38) Popelka, S.; Studenovská, H.; Abelová, L.; Ardan, T.; Studený, P.; Straňák, Z.; Klíma, J.; Dvoránková, B.; Kotek, J.; Hodan, J.; Rypáček, F. A Frame-Supported Ultrathin Electrospun Polymer Membrane for Transplantation of Retinal Pigment Epithelial Cells. *Biomed. Mater.* **2015**, *10* (4), 045022.

(39) Chan, S. Y.; Chan, B. Q. Y.; Liu, Z.; Parikh, B. H.; Zhang, K.; Lin, Q.; Su, X.; Kai, D.; Choo, W. S.; Young, D. J.; Loh, X. J. Electrospun Pectin-Polyhydroxybutyrate Nanofibers for Retinal Tissue Engineering. *ACS Omega* **2017**, *2* (12), 8959–8968.

## Publication [10]

**Peristaltic on-chip pump for tunable media circulation and whole blood perfusion in PDMS-free organ-on-chip and organ-disc systems**

S. Schneider, M. Bubeck, **J. Rogal**, H. Weener, C. Rojas, M. Weiss, M. Heymann, A. D. van der Meer, P. Loskill

*Lab Chip* Ahead of Print (2021) <https://dx.doi.org/10.1039/D1LC00494H>

**Abstract:**

Organ-on-chip (OoC) systems have become a promising tool for personalized medicine and drug development with advantages over conventional animal models and cell assays. However, the utility of OoCs in industrial settings is still limited, as external pumps and tubing for on-chip fluid transport are dependent on error-prone, manual handling. Here, we present an on-chip pump for OoC and Organ-Disc systems, to perfuse media without external pumps or tubing. Peristaltic pumping is implemented through periodic compression of a flexible pump layer. The disc-shaped, microfluidic module contains four independent systems, each lined with endothelial cells cultured under defined, peristaltic perfusion. Both cell viability and functionality were maintained over several days shown by supernatant analysis and immunostaining. Integrated, on-disc perfusion was further used for cytokine-induced cell activation with physiologic cell responses and for whole blood perfusion assays, both demonstrating the versatility of our system for OoC applications.

# Lab on a Chip

**PAPER**
[View Article Online](#)  
[View Journal](#)


Cite this: DOI: 10.1039/d1lc00494h

## Peristaltic on-chip pump for tunable media circulation and whole blood perfusion in PDMS-free organ-on-chip and Organ-Disc systems†

 Stefan Schneider,<sup>a</sup> Marvin Bubeck,<sup>ab</sup> Julia Rogal,<sup>ac</sup> Huub J. Weener,<sup>ad</sup> Cristhian Rojas,<sup>e</sup> Martin Weiss,<sup>ef</sup> Michael Heymann,<sup>b</sup> Andries D. van der Meer,<sup>d</sup> and Peter Loskill<sup>id \*aceg</sup>

Organ-on-chip (OoC) systems have become a promising tool for personalized medicine and drug development with advantages over conventional animal models and cell assays. However, the utility of OoCs in industrial settings is still limited, as external pumps and tubing for on-chip fluid transport are dependent on error-prone, manual handling. Here, we present an on-chip pump for OoC and Organ-Disc systems, to perfuse media without external pumps or tubing. Peristaltic pumping is implemented through periodic compression of a flexible pump layer. The disc-shaped, microfluidic module contains four independent systems, each lined with endothelial cells cultured under defined, peristaltic perfusion. Both cell viability and functionality were maintained over several days shown by supernatant analysis and immunostaining. Integrated, on-disc perfusion was further used for cytokine-induced cell activation with physiologic cell responses and for whole blood perfusion assays, both demonstrating the versatility of our system for OoC applications.

 Received 4th June 2021,  
 Accepted 23rd August 2021

DOI: 10.1039/d1lc00494h

[rsc.li/loc](https://rsc.li/loc)

### Introduction

Microfluidic organ-on-chip (OoC) systems can be used to culture cells under vasculature-like perfusion in a precisely controllable microenvironment to achieve physiological relevant *in vitro* models of human tissues and organs.<sup>1</sup> Several on-chip organ and tissue models have been introduced and provide alternatives to ethically challenging animal testing and non-physiological 2D cell culture, for more efficient drug development and personalized medicine.<sup>2–5</sup> Especially OoCs featuring unidirectional, circulatory pumping that recapitulate human vascular flows are highly sought after.

External pumps are able to achieve microfluidic, closed-loop perfusion: i) peristaltic pumps allow for a circulatory, unidirectional fluid flow when connected in-line with a shared reservoir for ingoing and outgoing media.<sup>6</sup> ii) Pressure pumps that combine multiple external valves and air-pressurized reservoirs can also sustain unidirectional circulation.<sup>7,8</sup> However, external pumps are often bulky and require tubing to couple fluids into the chips, which increases the required manual handling, risk of leakage, dead volumes and unspecific surface-binding of small molecules.<sup>9</sup>

External pumps and tubing can be avoided, for instance, by using gravity-driven pumping, whereby flow is induced by hydrostatic pressure difference of fluid levels in connected reservoirs. Fluid levels and hence the pressure gradient can be maintained over a longer period by tilting of the chip.<sup>10</sup> Gravity-driven, unidirectional circulation, however, requires considerable adaptations to the chip and the overall process as *e.g.* including a bypass between reservoirs,<sup>11,12</sup> limiting unidirectional flow to a short-cut channel<sup>13</sup> or pumping effluent back to inlet reservoirs.<sup>14</sup>

Therefore, the integration of peristaltic pumps on-chip is popular when flexibility in chip design and application are important. Here, fluid is displaced by mechanically actuating a film or flexible channel structure. A popular method for actuating on-chip peristaltic pumps is using pneumatics, as *e.g.* implemented in a perfused multiwell system<sup>15</sup> or multi-OoC platform.<sup>16,17</sup> Such pneumatic actuation of a flexible

<sup>a</sup> Fraunhofer Institute for Interfacial Engineering and Biotechnology IGB, Stuttgart, Germany

<sup>b</sup> Institute of Biomaterials and Biomolecular Systems, University of Stuttgart, Stuttgart, Germany

<sup>c</sup> Department of Biomedical Engineering, Faculty of Medicine, Eberhard Karls University Tübingen, Tübingen, Germany. E-mail: peter.loskill@uni-tuebingen.de

<sup>d</sup> Applied Stem Cell Technologies, University of Twente, Enschede, The Netherlands

<sup>e</sup> NMI Natural and Medical Sciences Institute at the University of Tübingen, Reutlingen, Germany

<sup>f</sup> Department of Women's Health, Faculty of Medicine, Eberhard Karls University Tübingen, Tübingen, Germany

<sup>g</sup> 3R-Center for *in vitro* Models and Alternatives to Animal Testing, Eberhard Karls University Tübingen, Tübingen, Germany

† Electronic supplementary information (ESI) available. See DOI: 10.1039/d1lc00494h



film requires multiple lines to supply external pressure to switch periodically between different pressure levels on-chip. Alternatives for pneumatic actuation, directly integrated or in close proximity to the chip, are braille pins,<sup>18</sup> piezoelectric discs,<sup>19</sup> electromagnets<sup>20,21</sup> or permanent magnets.<sup>22</sup> Especially magnets are attractive for peristaltic pump actuation, as they allow implementation of relatively simple systems, such as *e.g.* magnetically dragged steel balls for fluid displacement.<sup>23,24</sup>

Peristaltic on-chip pumping requires a flexible material, such as the elastomer polydimethylsiloxane (PDMS), to allow for mechanical fluid displacement. PDMS continues to be a popular material for microfluidic devices due to ease of fabrication.<sup>25</sup> However, PDMS-related absorption of small hydrophobic molecules,<sup>26</sup> high water vapor permeability<sup>27</sup> and leaching of uncured PDMS-components<sup>28</sup> is popularizing alternative materials, especially for cell-based and OoC applications.<sup>29</sup> A promising alternative to PDMS is thermoplastic elastomer (TPE), which combines thermoplastic and elastic characteristics.<sup>30</sup> TPE can be structured *e.g.* by hot embossing<sup>31,32</sup> and allows for thermal fusion bonding to other thermoplastic substrates.<sup>32–34</sup> TPE subtypes based on styrenic block copolymer formulations without oil additives show reduced absorption of small molecules as well as lower water permeability in comparison to PDMS and provide a biocompatible chip material.<sup>32,35</sup>

In this study, we present a novel TPE-based on-chip pumping technology for microfluidic cell culture and OoC applications. Advancing the capabilities of the recently introduced organ-on-a-disc technology,<sup>36</sup> we integrated a compact peristaltic pump on the “Organ-Disc”. Avoiding suboptimal chip materials such as PDMS and providing compatibility to industry-scale fabrication processes, our disc consists of microstructured, thermoplastic foils and hot embossed, flexible TPE films. For media perfusion through our platform, steel balls compress flexible pump channels in the central TPE pump module and are rolled around the central disc axis by a magnetic actuator underneath the disc. Media is stored in a reservoir on top of the disc, perfused through the disc cell culture channels, and transported back into the same reservoir compartment. Thereby, we introduce an entirely new approach that allows cultivation of microphysiological tissues under a closed-loop media perfusion with tunable, unidirectional flow and continuous access to the supernatant for further analysis. Paving the way for automated workflows and increased throughput, our platform features multiple independent systems per disc that run in parallel and eliminates the need for external pumps and error-prone tubing connections. We demonstrate the utility of this technology through microphysiological perfusion experiments culturing endothelial cells under controllable shear stress. Leveraging the simple access to the circulating media throughout the cultivation, evaporative media loss as well as cell metabolism was monitored over several days. Cytokine-induced activation of endothelial cells resulted in physiologic cell responses and demonstrated the

functionality of cells cultured under on-disc perfusion. Finally, we showed the applicability of our platform for perfusion of endothelial lined channels with human whole blood and monitoring of platelet adhesion to the endothelium.

## Materials and methods

### Disc materials

Discs were fabricated from several layers of approx. 750  $\mu\text{m}$  thick thermoplastic elastomer (TPE; Mediprene OF400M, based on oil-free styrene-ethylene/butylene-styrene elastomer, HEXPOL TPE AB) extruded by an external service provider (Fraunhofer Institute for Process Engineering and Packaging IVV) and 175  $\mu\text{m}$  polymethyl methacrylate foils (PMMA; PLEXIGLAS Film 99 524, Röhm). Each disc consists of TPE-based “pump” and “pump support” layers and PMMA-based “port”, “cell channel” and “bottom” layers (Fig. 1a). Reservoirs for media storage were made from polypropylene (PP), fabricated by an external service provider (CNCTeile24) and connected to discs with laser cut (VLS2.30, Universal Laser Systems) biocompatible, double-sided adhesive tape (ARcare 90 106, Adhesives Research).

### Epoxy master fabrication

The epoxy master fabrication started with the generation of SU-8 (SU-8 2075, Kayaku Advanced Materials) microstructures on 150 mm silicon wafers (Siegert Wafer) by standard ultraviolet (UV) light lithography. SU-8 was spin coated with a final speed of 1500 rpm at room temperature and soft baked (7 min at 65 °C then 30 min at 95 °C). Photomasks were designed (CorelCAD 2018, Corel Corporation) and purchased from an external provider (KOPP-desktopmedia). SU-8 layers were exposed to UV light (275 mJ cm<sup>-2</sup>, ABM Series 60 Exposure Systems, ABM, Inc.) using the photomask, post-exposure baked (5 min at 65 °C then 12 min at 95 °C) developed for 16 min (SU-8 developer, Kayaku Advanced Materials), washed with isopropanol and hard baked (30 min at 160 °C). Subsequently, wafers were treated using 100  $\mu\text{L}$  trichloro(1*H*,1*H*,2*H*,2*H*-perfluorooctyl)silane (448 931, Sigma-Aldrich) in a desiccator overnight at reduced pressure.

Fluoroelastomer-based O-rings (138  $\times$  2 mm FPM 75, Dichtelemente arcus) were placed concentrically on the wafers, both clamped between two 5 mm thick PMMA plates (Oroglass cast acrylic glass, Trinseo) and 50 mL syringes (BD Plastipak, BD) connected to the upper PMMA plate featuring two ports. PDMS (Sylgard 184, Dow Corning) was mixed (10 : 1 base:curing agent mass ratio), degassed and injected into the cavity above the SU-8 microstructures. For this, PDMS was filled into one syringe without plunger connected to the upper PMMA plate while pulling the plunger of the other syringe and generating a small vacuum for PDMS injection into the cavity. Subsequently, PDMS was cured overnight at 60 °C (Universal Oven UN110, Memmert), peeled off of both PMMA plates and the wafer, cleaned with isopropanol and blow-dried with compressed nitrogen.



## Lab on a Chip

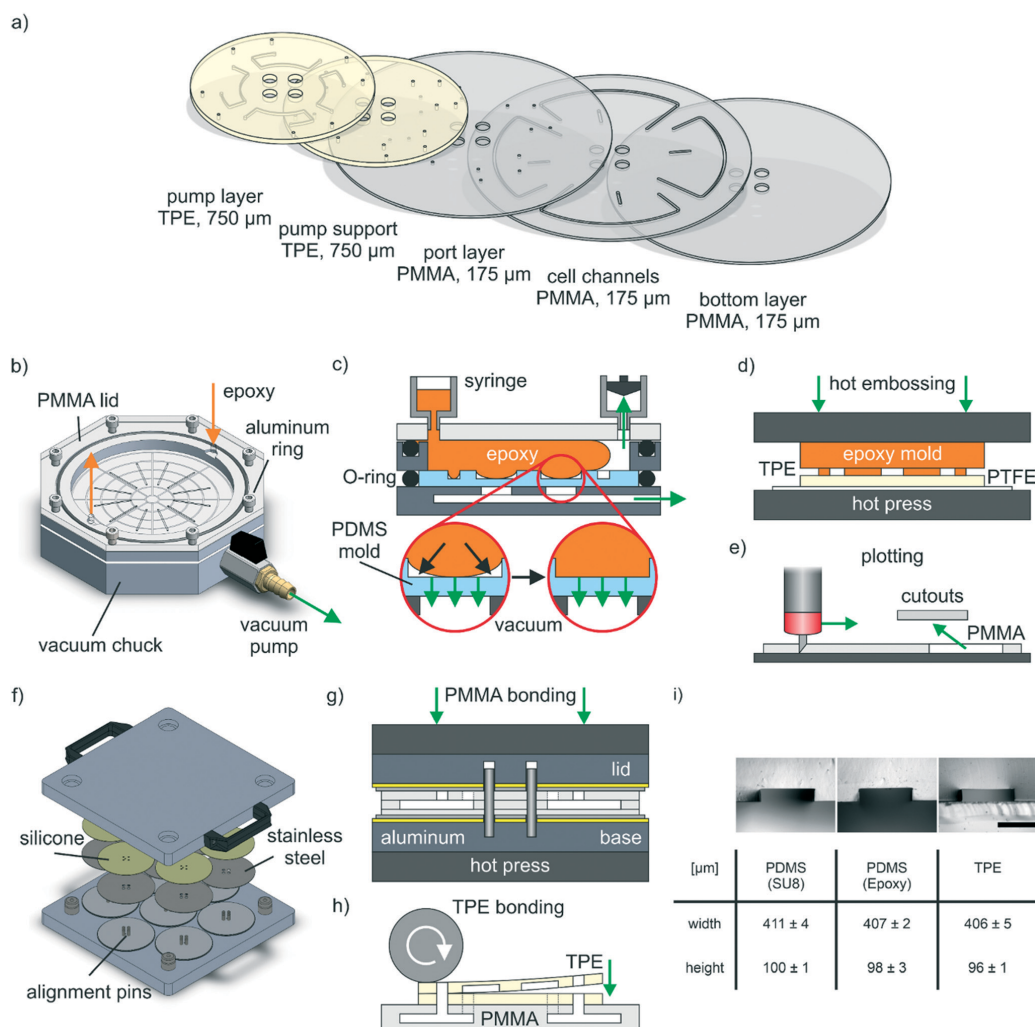


**Fig. 1** Microfluidic disc design and fabrication. a) Individual disc layers: pump and pump support layer are based on 750 μm thick, flexible TPE, while port, cell channel and bottom layer are fabricated from 175 μm thick PMMA foils. b-d) Epoxy mold based hot embossing: b) custom tool designed for transferring structures from PDMS molds into epoxy. c) Application of vacuum underneath the PDMS mold removes trapped air and allows for complete cavity filling. d) Epoxy molds were used for structuring of TPE layers using a hot press. e) Plotting: PMMA layers were structured by cutting with a drag knife. f and g) Thermal fusion bonding: f) custom bonding tool for bonding of up to seven stacks of thermoplastic materials; each having a 10 cm diameter footprint. g) PMMA layers are stacked into the tool featuring pins for correct alignment, which is afterwards transferred into a hot press for bonding. h) TPE bonding: after thermal fusion bonding of PMMA layers, TPE layers are bonded one after each other on top by plasma activation, lamination and subsequent thermal bonding in an oven. i) Precise TPE structuring: microscopy images and measured dimensions of channel side cuts of PDMS-molds both from initial SU-8 structures and from epoxy stamp as well of the respective TPE after hot embossing. For imaging purposes, the flexible TPE is supported on a microscope slide. Scale bar: 300 μm.  $N = 4$  channels, two analyzed cross sections per channel.

An aluminum-based molding tool was designed (Solidworks 2019, Dassault Systèmes) and manufactured by an external service provider (CNCTeile24). The base plate of the tool has an integrated vacuum chuck structure and a

hose connector for connecting a vacuum pump (Fig. 1b) allowing for vacuum-assisted fixation of the mold and removal of air bubbles trapped during epoxy injection (Fig. 1c).



For epoxy molding, the replica molded PDMS was placed onto the vacuum chuck with a pump ( $\geq 100$  mbar max. absolute pressure, LABOPORT N 86 KN.18, KNF) constantly generating a contact vacuum. An aluminum-ring, defining the dimensions of the final epoxy master (8 mm height, 110 mm diameter), was placed onto the PDMS mold and an O-ring (120 × 2 mm FPM 75, Dichtelemente arcus) was placed around the PDMS. A 5 mm PMMA plate (Oroglass cast acrylic glass, Trinseo) with two ports for syringe connection was screwed onto the aluminum ring and sealed with an O-ring (125 × 2 mm FPM 75, Dichtelemente arcus).

A two-component (“part A” and “part B”) epoxy resin (EpoxAcast 670 HT, Smooth-On) modified with an epoxy thinner (Epic Epoxy Thinner, Smooth-on) reducing the viscosity was mixed (part A:thinner:part B = 100:10:17.6 mass ratio), degassed in a desiccator at reduced pressure for 3 min and placed in an ultrasound bath (JP-031S, RS PRO) for another 10 min.

Identically to the described PMDS injection, the epoxy mixture was flushed into the tool using syringes connected to the PMMA plate. After partial curing for 24 h at room temperature and constantly applied contact vacuum, the tool was disconnected from the pump and transferred to an oven for 24 h at 60 °C (Universal Oven UN110, Memmert) for complete curing. Afterwards, the cured epoxy was removed from the tool and tempered in an oven (Universal Oven UN30, Memmert) for 2 h at 80 °C followed by 3 h at 150 °C and slowly cooled to room temperature overnight in the closed, switched off, oven.

Vacuum-assisted air bubble removal by gas diffusion through the PDMS mold, was exemplary visualized by filling de-ionized water into the molding cavity with the vacuum pump turned on and imaged with a USB microscope (UM038, Conrad Electronic SE).

#### TPE hot embossing

TPE layers (11 × 11 cm<sup>2</sup>) were laminated on a 250 μm thick polytetrafluoroethylene (PTFE) foil (High-tech-flon films and fabrics) as temporary support layer using a handheld pressure roller (Steinel). The epoxy master was placed in the center of the TPE sheet and both were transferred on a 150 mm silicon wafer (Siegert Wafer) into a preheated hot press (LabManual 300, Fontijne Presses) (Fig. 1d).

At a plate temperature of 140 °C, the epoxy was pressed into the TPE at a pressure of 0.4 MPa for 10 min, then the plates were water cooled below 40 °C in 4–5 min before opening the press. The TPE was peeled off of the epoxy and PTFE with a few drops of isopropanol. TPE layers were then cut to the respective size, ports were either punched (504 647, World Precision Instruments) or drilled (1.2 mm, RoNa Werkzeuge), cleaned with isopropanol and blow-dried with compressed nitrogen.

#### Plotting

PMMA-based channels were fabricated with a vinyl cutter (Graphtec CE6000-40 Plus, Graphtec) by 2D-structuring

(Fig. 1e). After plotting, all cutouts were removed and the PMMA layers were cleaned with isopropanol and blow-dried with compressed nitrogen.

#### Thermal fusion bonding

An aluminum-based bonding tool was designed (Solidworks 2019, Dassault Systèmes) and manufactured by an external service provider (MAAS Vorrichtungsbau) (Fig. 1f). Two aluminum plates build the basis of the tool with the bottom plate featuring pins (DIN 427 M5 screws, Reidl) for the alignment of PMMA layers. For a homogenous pressure distribution, 1 mm thick silicone mats (Elastomer plate VMQ 50 Shore A, Angst+Pfister) were placed between aluminum plates and mirror polished stainless steel plates (0.8 mm, TGA GmbH). For bonding, the respective PMMA layers were stacked between the polished steel plates and the tool was transferred into a preheated hot press (LabEcon 150, Fontijne Presses) (Fig. 1g). PMMA layers were bonded in two steps: first 20 min at 103 °C and 0.18 MPa and then 30 min at 103 °C at 1.9 MPa. Afterwards, the tool was removed from the hot press, slowly cooled down to room temperature overnight and then opened for removing the bonded PMMA modules.

#### TPE bonding

Both TPE layers were bonded after each other on the thermal fusion bonded PMMA modules. For each bonding step, the respective TPE layer was oxygen (O<sub>2</sub>) plasma treated (1 min, <2 mbar, 3.3 sccm O<sub>2</sub>, 50 W; Zepto, Diener) and laminated on top of PMMA or previously added TPE using a handheld pressure roller (Steinel) (Fig. 1h). Afterwards, a fluoropolymer coated polyester film (3M Scotchpak 1022 Release Liner, 3M) was temporarily laminated on the TPE and a small weight placed (2–5 kg or 6–15 kPa) on top during subsequent bonding at 95 °C for 1 h in an oven (Universal Oven UN30, Memmert).

#### Burst pressure test

For bonding strength assessment, burst pressure tests using compressed nitrogen gas were conducted. Epoxy glue (UHU PLUS ENDFEST, UHU) was used for both attaching luer connectors (BDMFTLL-9, Nordson MEDICAL) to channel inlets and sealing the channel outlets. After at least 24 h for complete curing of the epoxy glue, a nitrogen line was attached to the luer connectors and the disc submerged in water for monitoring gas leakage. A manual pressure controller (DR 022-00-3, Landefeld Druckluft und Hydraulik) was used for increasing the nitrogen gas pressure until either the disc layers delaminated or the maximum output pressure (3.5 bar) of the controller was reached.

#### Microstructure analysis

For microstructure analysis, side cuts from channel structures in various materials (specified in each case) were obtained by cutting with scalpels or scissors. The cross

sections were imaged using a stereomicroscope (SteREO Discovery.V8, Carl Zeiss MicroImaging) and analyzed with Fiji (ImageJ version 1.53c).<sup>37</sup>

### Pumping setup

For peristaltic pumping, discs were placed on a PMMA rack equipped with a stepper motor (SY42STH38-1684A, Pololu Corporation). A PMMA-based magnet holder with eight magnets (S-10-05-N52N, maximum adhesion 32.4 N, remanence 1.42–1.47 T, Webcraft) was connected to the motor to rotate underneath the mounted disc. The pumping setup was placed in an incubator (Heraeus BBD 6220, Thermo Scientific) for perfused on-disc cell culture. All other electronic components required for controlling the motor remained outside the incubator and were connected with a thin cable to the motor. The stepper motor was controlled by a motor driver (2128, Pololu Corporation) and a microcontroller (ATmega328P Board, Eckstein) with a display (I2C 16 × 2 LCD Display Module, Eckstein) and a rotary encoder (KY-040, reichelt elektronik) user interface to set motor parameters. On top of the disc, eight steel balls (diameter 5 mm, stainless steel 1.4034, HSI-Solutions) were placed above the magnets. A grooved ring of a thrust ball bearing (S51204, CQ GmbH) and another PMMA-based magnet holder with another eight, less strong, magnets (S-05-05-N, maximum adhesion 9.22 N, remanence 1.32–1.37 T, Webcraft) were placed on top of the steel balls. The magnets on top were less strong than the magnets connected to the motor shaft, which provided a suitable compromise between sufficient compression and an acceptable level of friction between steel balls and disc.

### Flow rate measurements

Flow rate measurements were conducted at room temperature within a period of three days using de-ionized water supplemented with watercolor (Ecoline Liquid Watercolour, Royal Talens) for improved visualization. Luer connectors (BDMFTLL-9, Nordson MEDICAL) were connected to the inlet and outlet using 2 mm thick, laser cut (VLS2.30, Universal Laser Systems) PMMA (Oroglass cast acrylic glass, Trinseo) adapters equipped with adhesive tape (ARcare 90106, Adhesives Research). Syringes with volume scale (1 mL, Omnifix-F, B. Braun Melsungen) were attached to the luer connectors, filled with equal amounts of liquid. Using a 5 s ramp time to the respective, final motor speed, the time needed for changing the volume in both syringes (0.05 mL per measurement) was taken. The volume flow rate was averaged from in total two systems from independent discs, each system was measured three times.

### Cell culture

Commercially available, cryopreserved human umbilical vein endothelial cells (HUVEC), from pooled donors were acquired from Lonza (C2519A) and cultured in endothelial cell growth medium (EGM-2 BulletKit, CC-3162, Lonza) with 1% (v/v) gentamicin (10 ng mL<sup>-1</sup>, Gibco). HUVECs at passage three were

thawed and seeded in 175 cm<sup>2</sup> filter cap cell culture flasks (CELLSTAR, Greiner Bio-One). After 24 h, the cell culture media was exchanged and the HUVECs were expanded for the following 3 days before cell loading into the disc.

For generating a cell suspension for subsequent cell loading, adherent cells were washed with PBS (Dulbecco's phosphate buffered saline w/o calcium w/o magnesium, Biowest), detached by a 3 min incubation step at 37 °C using 0.05% (v/v) trypsin (Trypsin-EDTA Solution 10×, SIGMA Life Science) in Versene solution (Versene 1:5000 1×, Gibco). The cell suspension was transferred into a centrifuge tube (50 mL CELLSTAR polypropylene tube, Greiner Bio-One), trypsin inactivated by adding 10% (v/v) fetal bovine serum (FBS; Thermo Fisher Scientific) and centrifuged for 5 min at 1000 rpm or 216g (Multifuge 3S-R, Heraeus). Cells were counted using trypan blue (trypan blue 4 g l<sup>-1</sup> in aqueous solution, VWR chemicals) using a hemocytometer (C-Chip Neubauer improved DHC-N01, NanoEnTek).

### Cell loading and cell channel lining

Discs were sprayed with 70% (v/v) ethanol and plasma activated (4 min, <2 mbar, 3.3 sccm O<sub>2</sub>, 50 W; Zepto, Diener) after drying. Each system of a disc was flushed using 100 μL of 70% (v/v) ethanol and then three times using 100 μL of PBS for the removal of ethanol.

For cell adhesion, channels were coated using 100 μL of 0.1 mg mL<sup>-1</sup> collagen-I (FibriCol, Catalog #5133, Advanced BioMatrix) in PBS for 1 h at 37 °C. Subsequently, channels were flushed using 100 μL of PBS and afterwards filled with cell culture media.

For cell seeding, pipette tips containing 75 μL of cell suspension with 6 × 10<sup>6</sup> cells per mL were connected to each cell channel. To prevent cells from entering the pump channel during injection, they were introduced through the outlet of the system in opposite direction of media perfusion. Brightfield microscopy (Leica DMi1, Leica Microsystems) was used to confirm that cells did not enter into the TPE module.

Unless otherwise specified, discs were turned upside down after cell injection for 1 h at 37 °C to promote cell adhesion to the cell channel ceiling. The seeding density for the cell channel with a volume of 15 μL and 84 mm<sup>2</sup> large ceiling is approx. 1000 cells per mm<sup>2</sup>. Afterwards, the discs were turned reservoir side up, and each reservoir compartment was filled with 5 mL cell culture media, sealed with a breathable tape (Z380059, Sigma-Aldrich) and HUVECs were cultured for 72 h at 10 revolutions per hour (rph) motor speed under standard cell culture conditions (37 °C, 95% humidity, 5% CO<sub>2</sub>, Heraeus BBD 6220, Thermo Scientific) for complete channel lining with cells. Before conducting experiments, the motor was stopped, the tape removed, media exchanged and a new breathable tape applied to seal the reservoir.

### Ion, glucose and lactate measurements

Cell loading and initial on-disc culture for cell attachment for solute analysis differed slightly compared to standard cell



injection. After collagen-I coating and cell injection (day -1), each reservoir compartment was filled with 5 mL cell culture media, sealed with a breathable tape (Z380059, Sigma-Aldrich) and cells were kept under static conditions for 1 h for cell adherence. Subsequently, the motor was ramped slowly to 100 rph over a period of 4 h. After 24 h (day 0), the cell culture media was exchanged to remove all non-adhering cells and to provide a reference base line for subsequent supernatant monitoring.

Subsequently, every 24 h a 110  $\mu\text{L}$  sample from the supernatant of each system was taken and stored at  $-80\text{ }^\circ\text{C}$  until further analysis. The withdrawn sample volume was replaced with an equal amount of cell culture media. Every 72 h (day 3 and day 6), the cell culture media was exchanged completely in all reservoir compartments. For media exchange or sampling, the motor was stopped, the breathable tape replaced and the motor ramped up to 100 rph again in 1 h.

For sample analysis, a bioanalyte analyzer was used (Vi-CELL MetaFLEX, Beckman Coulter): potassium ( $\text{K}^+$ ), sodium ( $\text{Na}^+$ ), chloride ( $\text{Cl}^-$ ) and calcium ( $\text{Ca}^{2+}$ ) concentrations were analyzed in samples from a system without HUVECs ("reference system") for evaporation monitoring. Glucose and lactate concentrations were analyzed in five systems culturing HUVECs. For day 1 and day 2, one sample was excluded from the analysis due to a sensor response error reported from the bioanalyte analyzer (day 1 and 2:  $N = 4$ , all others:  $N = 5$ ). Fresh cell culture media was identically analyzed for measuring the concentrations of all considered components ( $N = 4$ ).

#### CD31/nuclei staining

Each channel was washed three times using 100  $\mu\text{L}$  PBS+ (Dulbecco's phosphate buffered saline with  $\text{MgCl}_2$  and  $\text{CaCl}_2$ , Sigma-Aldrich). Afterwards, channels were filled with fixation solution (Roti-Histofix 4%, Carl Roth). After 15 min of incubation at room temperature, channels were washed again with PBS.

"Permeabilization/diluent buffer" containing 30  $\text{mg mL}^{-1}$  bovine serum albumin (BSA; A9647, Sigma-Aldrich), 0.1% (v/v) Triton X-100 (Sigma-Aldrich) in PBS was used for cell permeabilization, blocking of unspecific binding and as diluent for antibodies and dyes. For cell permeabilization and blocking, channels were filled with this buffer and incubated for 15 min at room temperature. Subsequently, primary CD31 antibody (M0823, mouse anti-human, Agilent Technologies), diluted 1:50, was injected into cell channels and washed out after 2 h incubation at room temperature using PBS. Staining solution containing secondary antibody (A-11003, goat anti-mouse, Alexa Fluor 546, Invitrogen), diluted 1:100, and 1  $\mu\text{g mL}^{-1}$  of Hoechst (62249, Hoechst 33342, Thermo Scientific) was flushed into cell channels, incubated for 1 h at room temperature and subsequently washed three times using 100  $\mu\text{L}$  of PBS.

Stained HUVECs were imaged using a confocal laser-scanning-microscope (LSM 710, Carl Zeiss MicroImaging).

Tile scan images were stitched with ZEN (ZEN black edition 2.3 SP1, Carl Zeiss Microscopy). Z-stacks were transferred into maximum intensity projections using Fiji (ImageJ version 1.53c)<sup>37</sup> and into 3D renders using Fiji in combination with the Volume Viewer plugin (Volume Viewer 2.01.2, [https://github.com/fiji/Volume\\_Viewer](https://github.com/fiji/Volume_Viewer)).

#### Live/dead staining

Before live/dead staining, channels were washed three times using 100  $\mu\text{L}$  PBS+. Afterwards, 100  $\mu\text{L}$  of staining solution with 27  $\mu\text{g mL}^{-1}$  of fluorescein diacetate (FDA; F7378, Sigma-Aldrich) for labeling viable cells and 135  $\mu\text{g mL}^{-1}$  of propidium iodide (PI; P4170, Sigma-Aldrich) for labeling dead cells in PBS+ was filled into the channels. The staining solution was incubated for 5 min at  $37\text{ }^\circ\text{C}$ . Chips were washed three times using 100  $\mu\text{L}$  PBS+ and imaged immediately. Images of stained HUVECs were acquired at  $37\text{ }^\circ\text{C}$  using a fluorescence microscope with heated enclosure (Leica DMi8, Leica Microsystems).

#### Endothelial cell activation and readout of cytokine secretion

After cell loading and 48 h of perfusion at 10 rph motor speed for cell channel lining, media was exchanged to determine baseline cytokine secretion to the supernatant over a 24 h period ("pre-treatment" condition,  $N = 8$ ). Subsequently, perfusion media was replaced by cell culture media containing either 20  $\text{ng mL}^{-1}$  ("24 h treated" condition,  $N = 4$ ) or no ("24 h untreated" condition,  $N = 4$ ) tumor necrosis factor alpha (TNF- $\alpha$ ; SRP3177, Sigma-Aldrich) and perfused for another 24 h at 10 rph motor speed.

Subsequently, HUVECs were stained for CD106 to visualize endothelial activation. For this, cell channels were first flushed using 100  $\mu\text{L}$  PBS+ with 10  $\text{mg mL}^{-1}$  BSA. Subsequently, channels were filled with conjugated CD106 antibody (130-104-164, CD106 Antibody, anti-human, REAfinity, APC, Miltenyi Biotec), diluted 1:10 in PBS+ with 10  $\text{mg mL}^{-1}$  BSA, and incubated for 30 min at  $37\text{ }^\circ\text{C}$ . After washing three times using 100  $\mu\text{L}$  PBS+, HUVECs were imaged at  $37\text{ }^\circ\text{C}$  using a fluorescence microscope with heated enclosure (Leica DMi8, Leica Microsystems).

To determine cytokine content from supernatants, samples of the supernatant were taken for all conditions at the respective time points, centrifuged for 5 min at 3000 rpm or 1942g (Multifuge 3S-R, Heraeus) for removal of debris and then stored at  $-80\text{ }^\circ\text{C}$  until further analysis. We quantified concentrations of the proinflammatory cytokines interleukin 6 (IL-6), interleukin 8 (IL-8) and angiotensin-2 (Ang-2) under baseline conditions as well as in response to inflammatory stimulation using a fluorescent bead-based multiplex sandwich immunoassay (LEGENDplex Human Angiogenesis Panel 1, 740697, BioLegend) read by flow cytometry (Guava easyCyte 8HT, Merck) following the manufacturer's manual. In short, the stored supernatants were thawed and, in technical duplicates for each condition, incubated with a cocktail of target-specific capture beads with unique



respective sizes and internal fluorescence for 2 h. Subsequently, biotinylated detection antibodies were added for 1 h to allow formation of capture bead-analyte-detection antibody sandwiches. By finally incubating the captured and detected analytes with streptavidin-phycoerythrin, the amount of bound cytokines was quantified *via* fluorescence signal intensities. To correlate fluorescence signal intensity

to cytokine concentration, a standard curve for all analyzed cytokines was generated in the same assay. Flow cytometry data were analyzed using the LEGENDplex cloud-based data analysis software suite (BioLegend). All gates were adjusted manually to find optimal differentiation between capture bead populations, and the same gating strategy applied to all assay runs.

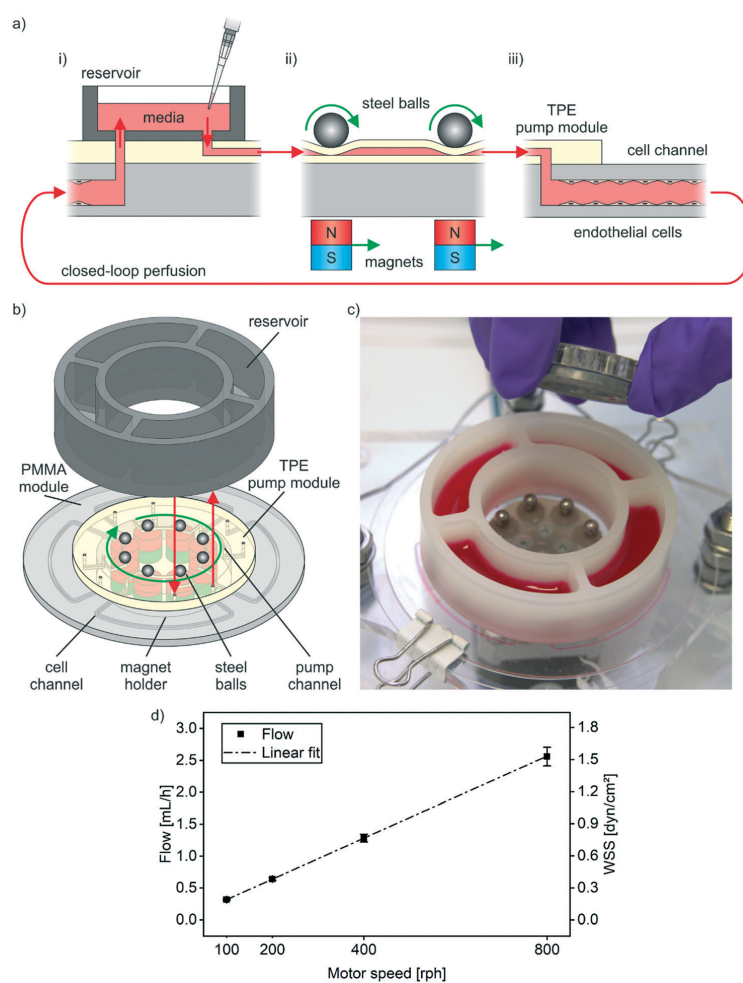


**Fig. 2** Integrated, peristaltic pumping. a) Circular closed-loop perfusion concept: i) media from the reservoir enters the TPE pump module. ii) Steel balls rolling over flexible channels pump media from the reservoir and push it further to the cell channel. iii) Endothelial cells lining the inner walls of the cell channel are cultured under constant media perfusion. Media exiting a cell channel, is pumped back into the reservoir creating a closed loop media perfusion. b) Pumping mechanism: magnets moving underneath the disc pull down and drag steel balls over microchannels in the TPE pump module. Thereby, liquid is pushed through the connected PMMA module. A reservoir with individual compartments for each system on the disc is connected on top. c) Pumping setup: photograph of a disc with steel balls, bottom and top magnet holder and connected reservoir filled with colored liquid. For pumping, the disc is mounted on a spinner featuring a stepper motor for rotation of the bottom magnet holder underneath the disc. d) Tunable perfusion: flow rate measurements and calculated wall shear stress (WSS) at different motor speeds. Data from two systems from independent discs, each measured three times using de-ionized water.

### Whole blood perfusion and analysis of platelet adhesion

Collection of whole blood was carried out in accordance with the rules for investigation of human subjects as defined in the Declaration of Helsinki. Patients gave a written agreement according to the permission of the ethical Committee of the Eberhard Karls University Tübingen (Nr. 495/2018-BO02).

Blood was collected in tubes with sodium citrate (VACUETTE TUBE 9 mL 9NC Coagulation sodium citrate 3.2%, Greiner Bio-One), supplemented with 1% (v/v) conjugated CD41 antibody (MHCD4104, CD41 Monoclonal Antibody, PE, Invitrogen) for fluorescent platelet labeling and kept at room temperature for 10 min in the dark. Prior to blood perfusion, 1% (v/v) of HEPES (4-(2-hydroxyethyl)-1-piperazineethanesulfonic acid, 1 M, Gibco) containing 63.2 mM CaCl<sub>2</sub> (Sigma-Aldrich) and 31.6 mM MgCl<sub>2</sub> (Invitrogen) was added to the blood sample in order to add ions required for blood coagulation.

Experiments were performed using cell channels lined with HUVECs cultured for 96 h at 10 rph motor speed for media perfusion before blood perfusion experiments. Empty pipette tips (300  $\mu$ L, Greiner Bio-One) and pipette tips filled with 300  $\mu$ L blood were connected to the inlet and outlet of the reservoir, respectively. Cell culture media was filled in the reservoir compartments for the subsequent flushing of the blood out of the channels. For linear blood perfusion from the blood-filled pipette tip to the empty pipette tip, the motor was ramped up in 1 min to a final speed of 800 rph maintained for 5 min. Fresh blood was refilled during this initiation step to avoid draining of the blood-filled pipette tip. For flushing blood out from the channels, all pipette tips were removed while the motor was kept running for another 5 min to displace blood with the media previously loaded into the reservoir compartments. During flush-out, 1 mL of cell culture media was exchanged. Subsequently, the motor was stopped, and the channels were additionally flushed manually using PBS+.

After complete blood removal, HUVECs were fixed and stained for CD31 and nuclei as described previously, however, applying overnight incubation at 4 °C for the primary antibody and using a different secondary antibody for fluorescent labeling of CD31 (A32723, goat anti-mouse, Alexa Fluor 488 Plus, Invitrogen). After washing with PBS, stained HUVECs and platelets were imaged using a fluorescence microscope (Leica DMI8, Leica Microsystems).

### Data presentation and statistical analysis

If not stated otherwise, data is presented as mean  $\pm$  standard deviation in text and diagrams with sample sizes stated in each case. OriginPro (Version 2021, OriginLab Corporation) in combination with OriginPro's Paired Comparison Plot plugin (version 3.6) was used for testing statistical significance of different cytokine concentrations using Tukey's range test. OriginPro was also used for linear

regression of measured flow rates produced by on-disc pumping.

## Results and discussion

### Design, fabrication and pumping mechanism

The peristaltic Organ-Disc features an integrated on-disc pump and is constructed from a total of five polymer layers: TPE pump and pump support layers as well as PMMA port, cell channel and bottom layers (Fig. 1a). Each disc features four individual microfluidic networks symmetrically arranged around its central axis. The TPE pump layer contains 400  $\mu$ m wide and 100  $\mu$ m high channels and forms the basis for the integrated peristaltic pump together with the pump support layer (*cf.* Fig. S1† showing the complete 2D Organ-Disc layout). Three PMMA layers (175  $\mu$ m thick) enclose the cell channels (1000  $\mu$ m wide) in a similar configuration as the previously reported centrifugal organ-on-a-disc system.<sup>36</sup>

Hot embossing of microstructures into TPE layers uses custom epoxy stamps fabricated by replica molding.<sup>38,39</sup> Our custom injection-molding tool allows for the fabrication of temperature stable epoxy stamps *via* replica molding from PDMS masters.<sup>32</sup> Air bubbles trapped in-between microstructures during injection of the epoxy can be removed by vacuum-assisted gas diffusion through the PDMS mold (*cf.* Video S1† demonstrating the process using water). Side cuts obtained from PDMS-molds of both the initial SU-8 structures and the epoxy stamp as well as the final TPE, confirmed a precise transfer of microstructure dimensions (Fig. 1i). After complete curing and tempering, the epoxy molds can be used for a large number of hot embossing cycles; this is a considerable advantage over hot embossing directly using SU-8 structures, which typically brake off the silicon wafer already after few cycles.

PMMA layers are structured by plotting and thermal fusion bonding. For robust and high-throughput thermal fusion bonding, a custom bonding tool was used to align and bond up to seven stacks of thermoplastic foils (footprint of a 4" wafer) simultaneously. A general challenge for thermal fusion bonding of thermoplastics is the optimization of heat, pressure and bonding time. If heat and pressure are too low, an insufficient bonding is achieved, whereas too high temperatures and forces lead to channel distortion.<sup>40</sup> For the PMMA used in this study, bonding 10 °C below the material's glass transition ( $T_G = 113$  °C) with 1.9 MPa of pressure allows for stable bonds with minimal impact on microchannels: the PMMA bonds withstood a nitrogen pressure of at least 3.5 bar (maximum pressure of the used gas pressure controller) without channel failure ( $N = 3$  discs). After bonding, the channel height was reduced only by 2.7%, from original 175  $\mu$ m (thickness of the PMMA foil) to  $170 \pm 15$   $\mu$ m. Similarly, the channel width was only reduced by 3.7% from 1000  $\mu$ m (CAD design) to  $963 \pm 28$   $\mu$ m ( $N = 4$  channels).

After thermal fusion bonding of the PMMA layers, the flexible TPE layers were added on top. TPE already displays good but reversible adhesion to PMMA at room temperature.

Open Access Article. Published on 25 August 2021. Downloaded on 8/31/2021 8:03:14 PM.  
This article is licensed under a Creative Commons Attribution-NonCommercial 3.0 Unported Licence.



To achieve robust and stable bonding, TPE surfaces were plasma activated<sup>41</sup> and bonded to PMMA under heat and pressure (95 °C and 15 kPa for 1 h). Burst pressure tests of fully assembled discs resulted in a failure at the TPE-TPE interface at  $3.1 \pm 0.3$  bar of nitrogen pressure ( $N = 3$  discs; cf. Fig. S2† showing cross sections of a PMMA cell channel and a TPE pump channel after bonding).

To enable on-disc pumping, a peristaltic pumping mechanism was implemented allowing for a closed-loop perfusion through the system (Fig. 2a): medium is pumped from the reservoir into the pumping module, then pushed further into the cell culture channel and subsequently back into the reservoir. Steel balls on top of the pump module are pulled into the pump channels by magnets underneath the disc (Fig. 2b). This results in localized channel collapse and sealing. To perfuse liquid through the channels, the magnets are rotated around the central axis by a stepper motor. Thereby, the steel balls roll over the pump channels and push liquid through the system; whereby, the flow rate is controlled by the rotation speed of the steel balls. An open, PP-based cell culture media reservoir with one compartment for each system is added on top of the disc (Fig. 2c). A grooved ring from a thrust ball bearing and further magnets integrated in a PMMA ring are added on top during operation for better positioning of the steel balls and to sustain higher compression forces.

#### Closed-loop perfusion for cell culture and cell monitoring

**Tunable perfusion rate.** During peristaltic, on-disc pumping, eight steel balls travel sequentially over a pump channel and push liquid through the system. Volume displacement over time was quantified by recording syringe volume changes of syringes attached to in- and outlets. We observed a linear relationship between motor speed and resulting flow rate with a coefficient of determination close to one ( $R^2 = 0.99999$ ) (Fig. 2d). Rotation speeds of 100–800 rph induced average flow rates of 0.32–2.6 mL h<sup>-1</sup>. Observed flow rates were in good agreement with theoretical flow rate calculations (Fig. S3†), which allow for an estimation of the peristalsis of the Organ-Disc pump (Fig. S4†). Flow measurements indicated a good pump channel compression and an appropriate sealing by the steel balls preventing back flow. (Fig. S5†). Flow measurements were conducted on three consecutive days with comparable flow rates over this period (Fig. S6†). Throughout long-term cultures under closed-loop, peristaltic perfusion, we checked the peristaltic pump every day by attaching a pipette tip to the reservoir outlet-port. Thereby, we tested the presents of fluid flow by a rising media level in the pipette tip.

The wall shear stress (WSS)  $\tau$  generated in the cell channel with width  $W$  and height  $H$  can be estimated by

$$\tau = \frac{6\eta Q}{H^2 W},$$

with viscosity  $\eta$  (= 1 mPa s for water at RT) and laminar flow rate  $Q$ . In the Organ-Disc, average flow rates of 0.32–2.6 mL

h<sup>-1</sup> translated in 0.19–1.5 dyn cm<sup>-2</sup> at 100–800 rph motor speed respectively. In our system, the ratio  $H/W$  equals 0.18 for the cell channel (cf. Table S1†). In principle, the applied relation for WSS is only valid for flow between infinite parallel plates. Therefore, WSS will not be completely homogenous over the full cell channel and slightly higher in the channel center. Theoretically, the WSS can be increased up to 14% in the channel center for  $H/W = 0.18$  if the influence of the channel side walls is considered as well.<sup>42</sup> Further information about the hydraulic resistance, pressure drop and Reynolds number of our system are provided in the ESI† (Table S2).

**Evaporation monitoring.** Standard cell culture at 37 °C proceeds in a humidified environment to limit evaporation from cell culture dishes or plates. However, preventing evaporative loss in microwell plates or microfluidic systems with open reservoirs can be challenging, due to high surface-to-volume ratios.<sup>43</sup> In the presented disc, evaporative loss can occur *via* diffusion of water vapor through the gas permeable reservoir tape cover, or through the microchannel walls. To quantify evaporation, ion concentrations were measured in a long-term disc perfusion experiment (100 rph or 0.32 mL h<sup>-1</sup>) without cells (Fig. 3a). Media exchange and supernatant sampling for analysis were the only processes that affected total solute amounts in the media. Monitoring of ion concentrations therefore quantifies media volume changes (ESI†). In average, the total media volume in the reference system was reduced by  $4.4 \pm 2.5\%$  ( $N = 4$  ions) per day. This amounted to about  $13.2 \pm 3.0\%$  in total volume loss (approx. 0.66 mL) during a three day window, which was hence set as the critical incubation time for media exchange.

Evaporation estimates were based on the average evaporation taking all types of ions into account. Calculated evaporations differed slightly depending on which type of ion was considered. Quantified rates were as high as 6.3% per day for potassium, as low as 2.7% per day for calcium and about 4.2% and 4.3% per day for sodium and chloride respectively. A similar divergence was observed previously when evaporative loss was monitored *via* salt concentrations during cell culture.<sup>44</sup>

Condensation on the reservoir sealing tape can also affect cell-culture media concentrations as small volumes are inevitably removed together with the tape during reservoir sampling. Sampling, including removal of the sealing tape, is conducted the same way for all conditions; therefore, the accompanying impact on solute concentrations is comparable. A continued three-day media exchange regiment results in an overall sawtooth profile, around a desired steady state throughout the experimental run.

**Monitoring of cell metabolism.** Levels of metabolite and nutrients, such as glucose and lactate, were monitored in discs containing endothelial cells (HUVECs). Beginning 24 h after onset of perfusion, a reduction in glucose concentration was clearly detectable for all time points (Fig. 3b, upper panel). Repeated media exchanges resulted in a characteristic sawtooth kinetic profile with substrate glucose and the



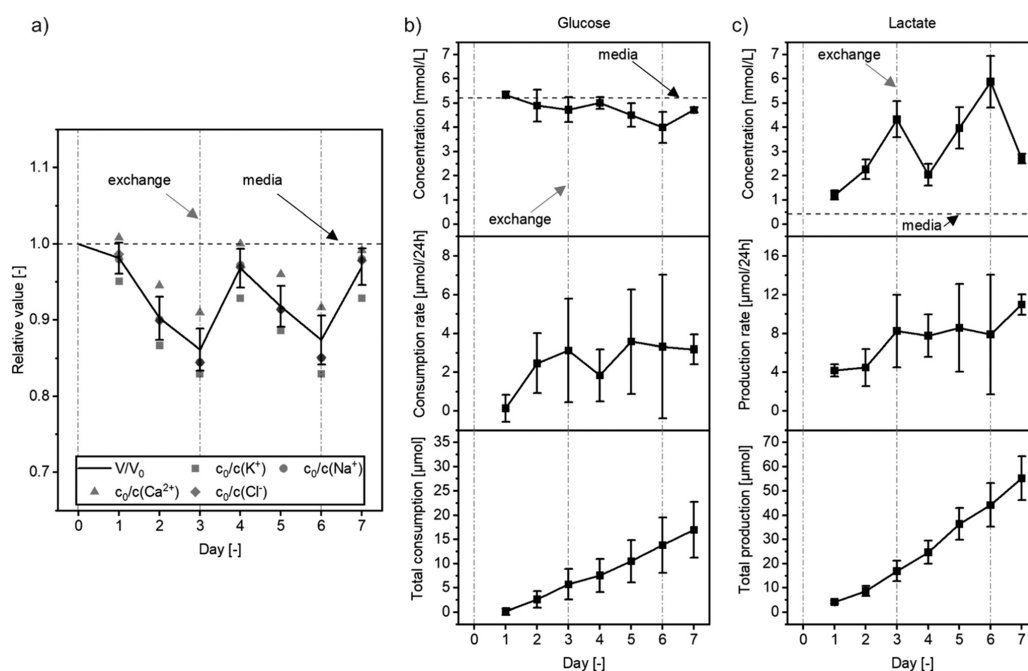


**Fig. 3** On-disc perfusion with cell culture media. a–c) Monitoring of metabolic activity of HUVECs cultured under flow (media exchanged every three days, marked by the “exchange” label and a dash-dotted, grey line. Dashed, black line with the label “media” refers to the fresh cell culture media): a) evaporation monitoring: symbols refer to ion concentrations in relation to fresh media for four different types of ions in a perfused, reference system without cells. Black line shows the mean, relative volume of media in a reservoir compartment calculated from ion concentrations. b and c) Monitoring of cell metabolism during culture by measuring b) glucose and c) lactate concentrations in the perfused media: the derived media volume and concentration kinetics (raw data; upper panels) allow for calculation of glucose consumption and lactate production for each day (rate; central panels) or cumulative over the full culture period (cumulative; lower panels) that are not falsified by evaporation (day 1 and 2:  $N = 4$ , all others:  $N = 5$ ).

product lactate following inverted trajectories (Fig. 3c, upper panel). Cells can produce lactate either through glycolysis under aerobic or anaerobic conditions.<sup>45</sup> Aerobic glycolysis is reported for tumor cells or proliferating cells, as a result of the so-called Warburg effect.<sup>46</sup> Endothelial cells have been shown to be highly glycolytic even when in contact with sufficient oxygen levels.<sup>47</sup> Furthermore, complete anaerobic conditions are not expected in our disc as the gas permeable sealing tape on top of the reservoir can accommodate gas exchange.<sup>48–51</sup> However, oxygen concentrations in proximity to the cells are unknown. Given the short dwell time of media in the channel of approx. 4.5 min at  $0.32 \text{ mL h}^{-1}$ , oxygen depletion should be minimal (*cf.* Table S3†). Future disc generations, could integrate oxygen sensors<sup>52</sup> to allow for simultaneous monitoring of oxygen levels and cell metabolism.

To derive actual glucose and lactate consumption and production rates, we normalized the measured concentrations against the salt ion derived evaporative water loss quantifications (Fig. 3b and c, central and lower panel). Total amounts of nutrients and metabolites are balanced the

same way as for the reference system making the same assumptions of homogenous mixing and representative sampling. Absolute amounts  $N$  of solutes  $i$  are calculated as

$$N_i(t) = V_t c_i(t)$$

with  $V$  being the salt ion derived total media volume and  $c$  being the concentration of  $i$  in the drawn sample at day  $t$ . Comparing absolute solute changes within  $\Delta t = 24 \text{ h}$  using

$$\frac{|N_i(t) - N_{t-1}(t)|}{\Delta t}$$

results in a production or consumption rate per day. The cumulative production or consumption over time then is

$$\frac{|N_i(t) - N_0(t)|}{t \Delta t}$$

Average glucose consumption was  $2.5 \pm 2.2 \mu\text{mol}$  per day, while  $7.5 \pm 3.5 \mu\text{mol}$  per day lactate was produced. Each molecule of glucose can at most form two lactate molecules. For HUVECs, a



glycolytic index of 1.74 was reported previously, which is the ratio of produced lactate molecules for each consumed glucose molecule.<sup>53</sup> Hence, resulting rates are in reasonable agreement, considering the standard deviation. The discrepancy between the calculated consumption and production stems from the measured nutrient and metabolite concentrations. Overall high glucose content in the media results in absolute concentration changes close to the standard deviation, whereas, fresh media is almost lactate-free and, hence, already small changes to lactate content clearly observable. Additionally, the media volume  $V_c$  strongly affects the calculated solute amounts as it is also subject to measurement errors and therefore leads to error propagation. However, at the same time, this demonstrates the importance of monitoring evaporation in microfluidic cell culture and organ-on-chip systems.

#### Confluent endothelial cell lining of disc channels

Endothelial cells (HUVECs) were injected into the disc with sub-confluent seeding densities and cultured for 72 h while gently circulating media (10 rph, corresponding to approx.  $30 \mu\text{L h}^{-1}$  or  $0.02 \text{ dyn cm}^{-2}$ ). During this period, HUVECs expanded, adhered to all inner channel surfaces and reached confluency.

Using the tunable on-disc perfusion, the flow rate was subsequently raised to either  $2.6 \text{ mL h}^{-1}$  or  $0.32 \text{ mL h}^{-1}$  (shear stress of  $1.5 \text{ dyn cm}^{-2}$  or  $0.19 \text{ dyn cm}^{-2}$  respectively) for varying shear stress on endothelial cell lined channels during another 24 h. Fluorescence microscopy revealed a confluent lining of all channel walls with endothelial layers positive for CD31 (platelet endothelial cell adhesion molecule 1, PECAM1) over the entire length of the channels (Fig. 4a and b). Endothelial layers cultured in the higher shear rate condition ( $1.5 \text{ dyn cm}^{-2}$ ) displayed more cell-cell contacts than layers cultured with the 8-fold lower shear stress (Fig. 4b). Nevertheless, under both flow conditions, cells were viable as confirmed by live/dead staining with only minimal amount of PI-positive cells (FDA/PI, Fig. 4c). No distinct cell alignment in flow direction was observed. This is in agreement with previous reports of HUVEC alignment under shear-flows of  $7.2 \text{ dyn cm}^{-2}$  and higher.<sup>54–56</sup> Flow rates required for shear stress induced HUVEC alignment can in principle be achieved by the peristaltic on-disc pump, either through increased motor speeds or suitably configured pump channel layouts. However, a common problem of peristaltic pumping is the friction associated with high actuation speeds. In our case, pumping at rotation speeds higher than 800 rph resulted in premature TPE degradation and pump failure. Channel designs that increase the actuated volume per duty cycle without increasing mechanical stresses on the disc hence seems to be the more attractive approach to achieve higher flow and shear rates.

#### Tumor necrosis factor alpha (TNF- $\alpha$ )-induced endothelial cell activation

Physiological function of the endothelium on-disc can be accessed by monitoring the response to stimulation. Thereto,

after 72 h of culture with gentle media circulation (approx.  $30 \mu\text{L h}^{-1}$  or  $0.02 \text{ dyn cm}^{-2}$ ), the HUVEC-lined channels were perfused with  $20 \text{ ng mL}^{-1}$  TNF- $\alpha$  for another 24 h without changing the flow rate. TNF- $\alpha$  treated cells show an increased presence of vascular cell adhesion protein 1 (VCAM1, CD106) compared to non-treated cells (Fig. 4d), at comparable channel cell density. This response is in agreement with previous studies showing an increased CD106 expression due to TNF- $\alpha$  treatment.<sup>57,58</sup>

In addition to analysis of CD106 expression, cytokines released into the perfused media in response to endothelial activation were monitored. Analysis of cytokines in the effluent before and after the 24 h TNF- $\alpha$  treatment demonstrated a significant increase in IL-6, IL-8 and Ang-2 levels (Fig. 4e). Compared to untreated systems, the concentration of IL-6 was increased 12-fold, of IL-8 38-fold, and of Ang-2 2.5-fold, respectively. Media from non-treated systems before and after 24 h incubation showed stable levels of all tested cytokines.

Increased IL-6 and IL-8 release from HUVECs upon TNF- $\alpha$  stimulation is well characterized;<sup>59,60</sup> therefore, demonstrating the physiological response to stimulation of an endothelium cultured in our system. Similarly, the upregulation of Ang-2 expression in HUVECs after TNF- $\alpha$  activation has been reported previously.<sup>61</sup> Fiedler *et al.* showed that Ang-2 is stored in Weibel-Palade bodies of endothelial cells and released after stimulation into the media.<sup>62</sup> Interestingly, Fiedler *et al.* did not detect Ang-2 in the supernatant after TNF- $\alpha$  stimulation; however, the authors performed only short-term release experiments. In our case, cytokines were released over 24 h into circulating media containing TNF- $\alpha$  and accumulated over time. Therefore, the disc configuration is suitable to investigate circulating stimuli treatments over longer periods and time-dependent cell response assessments.

#### On-disc perfusion of whole blood and platelet adhesion

Lining the microchannels with confluent endothelial layers minimizes the exposure of the perfused media to the polymeric chip material and enables artificial, blood-perfused capillaries.<sup>63,64</sup> Demonstrating an important step for on-disc blood perfusion, we injected fresh human whole blood into discs featuring HUVEC-lined channels (pre-cultured on-disc for 96 h at approx.  $30 \mu\text{L h}^{-1}$  or  $0.02 \text{ dyn cm}^{-2}$ ). Immediately prior to injection, whole blood collected in citrate tubes was supplemented with ions required for coagulation processes and CD41 antibody for fluorescent labeling of platelets.

In contrast to previous closed-loop media circulation, blood was directly passed from inlet to outlet pipette tips that were attached to the respective ports in the reservoir compartment (Fig. 4f, Video S2†). Subsequent pumping of cell culture media evacuated the perfused blood from the cell culture channel (Video S3†). All four channels remained structurally intact and no blood clots or clogging formed.



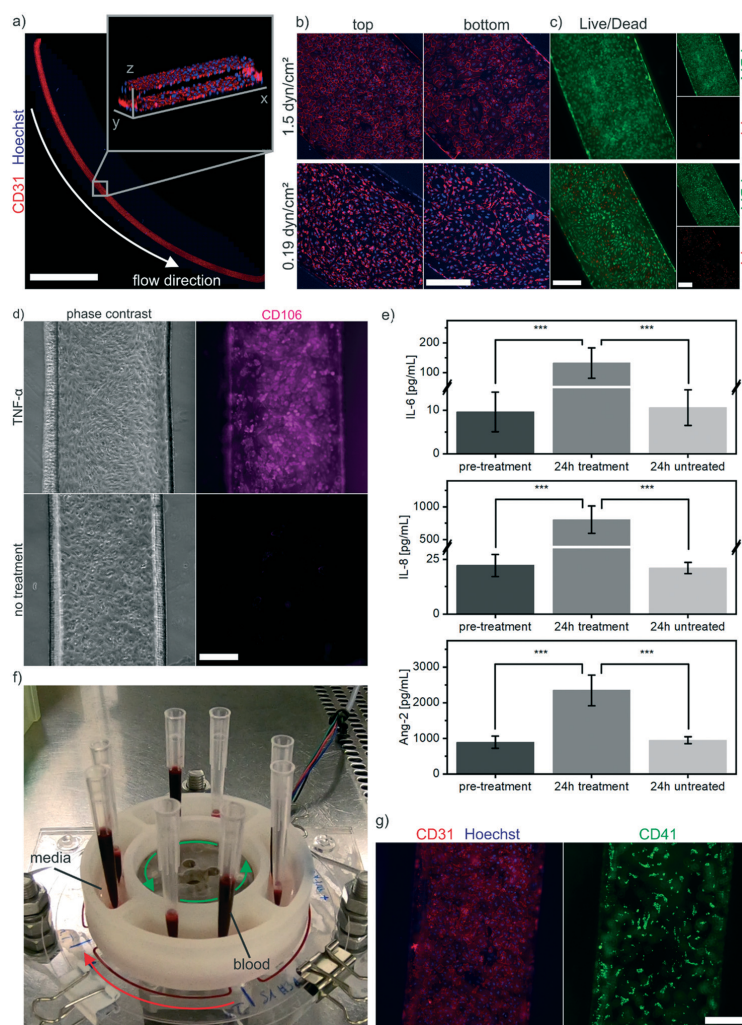


**Fig. 4** On-disc perfusion of endothelial cell-lined microchannels. a) Confocal microscopy images of entire channels lined with endothelial layers stained with CD31 antibody and Hoechst ( $1.5 \text{ dyn cm}^{-2}$  condition). Maximum intensity projection, scale bar: 10 mm. Inset with a 3D render obtained from a z-stack acquired in the channel center. b) Fluorescence microscopy images of endothelial monolayers lining top and bottom of cell channels labeled with CD31 antibody and Hoechst for different flow rate conditions. Maximum intensity projection, scale bar: 300  $\mu\text{m}$ . c) Monitoring of viability via fluorescence microscopy imaging of endothelial layers labeled with FDA and PI (viable and dead cells respectively) for different flow rate conditions. Scale bars: 300  $\mu\text{m}$ . d) Phase contrast image and CD106 antibody staining of endothelial layers treated for 24 h with TNF- $\alpha$  and untreated control. Scale bar: 300  $\mu\text{m}$ . e) Cytokine measurement by flow cytometry: after 24 h of TNF- $\alpha$  treatment ( $N = 4$ ) concentrations of IL-6, IL-8 and Ang-2 in the perfused medium are significantly ( $p < 0.001$ ) higher compared to cytokine concentrations in samples taken before the treatment ( $N = 8$ ) or from untreated systems ( $N = 4$ ). f) Photograph of set-up enabling perfusion of fresh whole blood through the discs by attaching pipette tips to in- and outlets of the reservoir ports. Media is filled in the reservoir compartments for subsequent flush-out of blood when pipette tips are removed. g) Fluorescence microscopy images of channels after perfusion of blood featuring fluorescently labeled platelets (CD41, right) and (left) labeled with CD31 antibody and Hoechst. Scale bar: 300  $\mu\text{m}$ .

Antibody staining revealed a strong CD31 signal at cell-cell contacts indicating an intact cell morphology after 96 h of culture and whole blood perfusion (Fig. 4g). Fluorescent

CD41 labeling revealed domains of platelets adhering to the endothelium. Platelet adhesion is an important process during thrombosis and stroke.<sup>65</sup> The capability of the

## Lab on a Chip

## Paper

presented platform to both generate a functional endothelium and to provide an integrated, tunable perfusion paves the way for further microphysiological experiments. As we demonstrated that whole blood perfusion is possible in our systems, future applications could aim at the study of platelet adhesion under blood flows of different shear stress<sup>66</sup> and automated platelet aggregation monitoring.<sup>67</sup>

## Conclusion

We engineered an Organ-Disc with integrated peristaltic pumping for parallelized culturing of lumen-like endothelial cell structures. Disc materials and fabrication readily translate to scaled industrial settings. PDMS is completely avoided and TPE is instead used for soft and flexible layers and thermoplastic PMMA as highly transparent, rigid material. The used microstructuring methods, plotting and hot embossing, as well as the bonding processes are precise, parallelizable and result in a highly robust microfluidic system.

The integrated, peristaltic pump of our disc achieves accurate perfusion and supersedes expensive, external pumps or problematic tubing connections. Media stored in a reservoir and circulating through the system is easily accessible throughout the whole experiment and allows for user-friendly analysis. Ion, nutrient and metabolite concentrations were assessed over multiple days of on-disc HUVEC culture to monitor cell metabolism as well as evaporation, an important yet often ignored aspect of microfluidic engineering.

The proof-of-concept of our integrated platform technology for Organ-Disc and OoC systems is achieved through generating and culturing lumen-like structures of HUVECs and conducting several on-disc experiments: we demonstrate perfusion under varying shear stress, *in vitro* recapitulation of endothelial activation and response to inflammatory stimuli, as well as whole blood perfusion. Furthermore, our system allows for versatile adaptations: *e.g.* transfer to other chip geometries, programmable motor settings for oscillatory flow patterns or co-culture applications. Overall, the presented platform provides a user-friendly and automatable perfusion technology for microphysiological systems and will help to advance the field of OoC research.

## Conflicts of interest

The authors declare no conflicts of interest.

## Acknowledgements

The research was supported in part by the Ministry of Science, Research and the Arts of Baden-Württemberg (Az: 33-7542.2-501-1/30/9).

## References

- 1 S. N. Bhatia and D. E. Ingber, Microfluidic Organs-on-Chips, *Nat. Biotechnol.*, 2014, 32(8), 760–772, DOI: 10.1038/nbt.2989.
- 2 B. Zhang, A. Korolj, B. F. L. Lai and M. Radisic, Advances in Organ-on-a-Chip Engineering, *Nat. Rev. Mater.*, 2018, 3(8), 257–278, DOI: 10.1038/s41578-018-0034-7.
- 3 B. Zhang and M. Radisic, Organ-on-a-Chip Devices Advance to Market, *Lab Chip*, 2017, 17(14), 2395–2420, DOI: 10.1039/C6LC01554A.
- 4 A. van den Berg, C. L. Mummery, R. Passier and A. D. van der Meer, Personalised Organs-on-Chips: Functional Testing for Precision Medicine, *Lab Chip*, 2019, 19(2), 198–205, DOI: 10.1039/C8LC00827B.
- 5 N. Franzen, W. H. van Harten, V. P. Retèl, P. Loskill, J. van den Eijnden-van Raaij and M. IJzerman, Impact of Organ-on-a-Chip Technology on Pharmaceutical R&D Costs, *Drug Discovery Today*, 2019, 24(9), 1720–1724, DOI: 10.1016/j.drudis.2019.06.003.
- 6 S. Deinhardt-Emmer, K. Rennert, E. Schicke, Z. Cseresnyés, M. Windolph, S. Nietzsche, R. Heller, F. Siwczak, K. F. Haupt, S. Carlstedt, M. Schacke, M. T. Figge, C. Ehrhardt, B. Löffler and A. S. Mosig, Co-Infection with Staphylococcus Aureus after Primary Influenza Virus Infection Leads to Damage of the Endothelium in a Human Alveolus-on-a-Chip Model, *Biofabrication*, 2020, 12(2), 025012, DOI: 10.1088/1758-5090/ab7073.
- 7 C. G. M. van Dijk, M. M. Brandt, N. Poulis, J. Anten, M. van der Moolen, L. Kramer, E. F. G. A. Homburg, L. Louzao-Martinez, J. Pei, M. M. Krebber, B. W. M. van Balkom, P. de Graaf, D. J. Duncker, M. C. Verhaar, R. Luttge and C. Cheng, A New Microfluidic Model That Allows Monitoring of Complex Vascular Structures and Cell Interactions in a 3D Biological Matrix, *Lab Chip*, 2020, 20(10), 1827–1844, DOI: 10.1039/D0LC00059K.
- 8 T. Qian, D. A. Gil, E. Contreras Guzman, B. D. Gastfriend, K. E. Tweed, S. P. Palecek and M. C. Skala, Adaptable Pulsatile Flow Generated from Stem Cell-Derived Cardiomyocytes Using Quantitative Imaging-Based Signal Transduction, *Lab Chip*, 2020, 20(20), 3744–3756, DOI: 10.1039/D0LC00546K.
- 9 K. Renggli and O. Frey, Chapter 12 - Design and Engineering of Multiorgan Systems, in *Organ-on-a-chip*, ed. J. Hoeng, D. Bovard and M. C. Peitsch, Academic Press, 2020, pp. 393–427, DOI: 10.1016/B978-0-12-817202-5.00012-7.
- 10 C. Lohasz, N. Rousset, K. Renggli, A. Hierlemann and O. Frey, Scalable Microfluidic Platform for Flexible Configuration of and Experiments with Microtissue Multiorgan Models, *SLAS Technol.*, 2019, 24(1), 79–95, DOI: 10.1177/2472630318802582.
- 11 M. B. Esch, H. Ueno, D. R. Applegate and M. L. Shuler, Modular, Pumpless Body-on-a-Chip Platform for the Co-Culture of GI Tract Epithelium and 3D Primary Liver Tissue, *Lab Chip*, 2016, 16(14), 2719–2729, DOI: 10.1039/C6LC00461J.
- 12 D. W. Lee, N. Choi and J. H. Sung, A Microfluidic Chip with Gravity-Induced Unidirectional Flow for Perfusion Cell Culture, *Biotechnol. Prog.*, 2019, 35(1), e2701, DOI: 10.1002/btpr.2701.
- 13 Y. I. Wang and M. L. Shuler, UniChip Enables Long-Term Recirculating Unidirectional Perfusion with Gravity-Driven



- Flow for Microphysiological Systems, *Lab Chip*, 2018, **18**(17), 2563–2574, DOI: 10.1039/C8LC00394G.
- 14 H. Azizgolshani, J. R. Coppeta, E. M. Vedula, E. E. Marr, B. P. Cain, R. J. Luu, M. P. Lech, S. H. Kann, T. J. Mulhern, V. Tandon, K. Tan, N. J. Haroutunian, P. Keegan, M. Rogers, A. L. Gard, K. B. Baldwin, J. C. de Souza, B. C. Hoeffler, S. S. Bale, L. B. Kratchman, A. Zorn, A. Patterson, E. S. Kim, T. A. Petrie, E. L. Wiertel, C. Williams, B. C. Isenberg and J. L. Charest, High-Throughput Organ-on-Chip Platform with Integrated Programmable Fluid Flow and Real-Time Sensing for Complex Tissue Models in Drug Development Workflows, *Lab Chip*, 2021, **21**(8), 1454–1474, DOI: 10.1039/D1LC00067E.
  - 15 I. Maschmeyer, A. K. Lorenz, K. Schimek, T. Hasenberg, A. P. Ramme, J. Hübner, M. Lindner, C. Drewell, S. Bauer, A. Thomas, N. S. Sambo, F. Sonntag, R. Lauster and U. Marx, A Four-Organ-Chip for Interconnected Long-Term Co-Culture of Human Intestine, Liver, Skin and Kidney Equivalents, *Lab Chip*, 2015, **15**(12), 2688–2699, DOI: 10.1039/C5LC00392J.
  - 16 K. Domansky, W. Inman, J. Serdy, A. Dash, M. H. M. Lim and L. G. Griffith, Perfused Multiwell Plate for 3D Liver Tissue Engineering, *Lab Chip*, 2010, **10**(1), 51–58, DOI: 10.1039/B913221J.
  - 17 C. D. Edington, W. L. K. Chen, E. Geishecker, T. Kassis, L. R. Soenksen, B. M. Bhushan, D. Freake, J. Kirschner, C. Maass, N. Tsamandouras, J. Valdez, C. D. Cook, T. Parent, S. Snyder, J. Yu, E. Suter, M. Shockley, J. Velazquez, J. J. Velazquez, L. Stockdale, J. P. Papps, I. Lee, N. Vann, M. Gamboa, M. E. LaBarge, Z. Zhong, X. Wang, L. A. Boyer, D. A. Lauffenburger, R. L. Carrier, C. Communal, S. R. Tannenbaum, C. L. Stokes, D. J. Hughes, G. Rohatgi, D. L. Trumper, M. Cirit and L. G. Griffith, Interconnected Microphysiological Systems for Quantitative Biology and Pharmacology Studies, *Sci. Rep.*, 2018, **8**(1), 4530, DOI: 10.1038/s41598-018-22749-0.
  - 18 W. Gu, X. Zhu, N. Futai, B. S. Cho and S. Takayama, Computerized Microfluidic Cell Culture Using Elastomeric Channels and Braille Displays, *Proc. Natl. Acad. Sci. U. S. A.*, 2004, **101**(45), 15861–15866, DOI: 10.1073/pnas.0404353101.
  - 19 B. Husband, M. Bu, A. G. R. Evans and T. Melvin, Investigation for the Operation of an Integrated Peristaltic Micropump, *J. Micromech. Microeng.*, 2004, **14**(9), S64–S69, DOI: 10.1088/0960-1317/14/9/011.
  - 20 J. R. Coppeta, M. J. Mescher, B. C. Isenberg, A. J. Spencer, E. S. Kim, A. R. Lever, T. J. Mulhern, R. Prantil-Baun, J. C. Comolli and J. T. Borenstein, A Portable and Reconfigurable Multi-Organ Platform for Drug Development with Onboard Microfluidic Flow Control, *Lab Chip*, 2017, **17**(1), 134–144, DOI: 10.1039/C6LC01236A.
  - 21 V. Tandon, W. S. Kang, T. A. Robbins, A. J. Spencer, E. S. Kim, M. J. McKenna, S. G. Kujawa, J. Fiering, E. E. L. Pararas, M. J. Mescher, W. F. Sewell and J. T. Borenstein, Microfabricated Reciprocating Micropump for Intracochlear Drug Delivery with Integrated Drug/Fluid Storage and Electronically Controlled Dosing, *Lab Chip*, 2016, **16**(5), 829–846, DOI: 10.1039/C5LC01396H.
  - 22 T. Pan, S. J. McDonald, E. M. Kai and B. Ziaie, A Magnetically Driven PDMS Micropump with Ball Check Valves, *J. Micromech. Microeng.*, 2005, **15**(5), 1021–1026, DOI: 10.1088/0960-1317/15/5/018.
  - 23 L. Yobas, K.-C. Tang, S.-E. Yong and E. Kye-Zheng Ong, A Disposable Planar Peristaltic Pump for Lab-on-a-Chip, *Lab Chip*, 2008, **8**(5), 660, DOI: 10.1039/b720024b.
  - 24 M. Du, X. Ye, K. Wu and Z. Zhou, A Peristaltic Micro Pump Driven by a Rotating Motor with Magnetically Attracted Steel Balls, *Sensors*, 2009, **9**(4), 2611–2620, DOI: 10.3390/s90402611.
  - 25 D. C. Duffy, J. C. McDonald, O. J. A. Schueller and G. M. Whitesides, Rapid Prototyping of Microfluidic Systems in Poly(Dimethylsiloxane), *Anal. Chem.*, 1998, **70**(23), 4974–4984, DOI: 10.1021/ac980656z.
  - 26 M. W. Toepke and D. J. Beebe, PDMS Absorption of Small Molecules and Consequences in Microfluidic Applications, *Lab Chip*, 2006, **6**(12), 1484, DOI: 10.1039/b612140c.
  - 27 Y. S. Heo, L. M. Cabrera, J. W. Song, N. Futai, Y.-C. Tung, G. D. Smith and S. Takayama, Characterization and Resolution of Evaporation-Mediated Osmolality Shifts That Constrain Microfluidic Cell Culture in Poly(Dimethylsiloxane) Devices, *Anal. Chem.*, 2007, **79**(3), 1126–1134, DOI: 10.1021/ac061990v.
  - 28 K. J. Regehr, M. Domenech, J. T. Koepsel, K. C. Carver, S. J. Ellison-Zelski, W. L. Murphy, L. A. Schuler, E. T. Alarid and D. J. Beebe, Biological Implications of Polydimethylsiloxane-Based Microfluidic Cell Culture, *Lab Chip*, 2009, **9**(15), 2132, DOI: 10.1039/b903043c.
  - 29 S. B. Campbell, Q. Wu, J. Yazbeck, C. Liu, S. Okhovatian and M. Radisic, Beyond Polydimethylsiloxane: Alternative Materials for Fabrication of Organ-on-a-Chip Devices and Microphysiological Systems, *ACS Biomater. Sci. Eng.*, 2021, **7**(7), 2880–2899, DOI: 10.1021/acsbomaterials.0c00640.
  - 30 E. Roy, J.-C. Galas and T. Veres, Thermoplastic Elastomers for Microfluidics: Towards a High-Throughput Fabrication Method of Multilayered Microfluidic Devices, *Lab Chip*, 2011, **11**(18), 3193, DOI: 10.1039/c1lc20251k.
  - 31 D. Brassard, L. Clime, K. Li, M. Geissler, C. Miville-Godin, E. Roy and T. Veres, 3D Thermoplastic Elastomer Microfluidic Devices for Biological Probe Immobilization, *Lab Chip*, 2011, **11**(23), 4099, DOI: 10.1039/c1lc20714h.
  - 32 S. Schneider, E. J. S. Brás, O. Schneider, K. Schlünder and P. Loskill, Facile Patterning of Thermoplastic Elastomers and Robust Bonding to Glass and Thermoplastics for Microfluidic Cell Culture and Organ-on-Chip, *Micromachines*, 2021, **12**(5), 575, DOI: 10.3390/mi12050575.
  - 33 J. Lachaux, C. Alcaine, B. Gómez-Escoda, C. M. Perrault, D. O. Duplan, P.-Y. J. Wu, I. Ochoa, L. Fernandez, O. Mercier, D. Coudreuse and E. Roy, Thermoplastic Elastomer with Advanced Hydrophilization and Bonding Performances for Rapid (30 s) and Easy Molding of Microfluidic Devices, *Lab Chip*, 2017, **17**(15), 2581–2594, DOI: 10.1039/C7LC00488E.
  - 34 M. D. Borysiak, K. S. Bielawski, N. J. Sniadecki, C. F. Jenkel, B. D. Vogt and J. D. Posner, Simple Replica Micromolding of Biocompatible Styrenic Elastomers, *Lab Chip*, 2013, **13**(14), 2773, DOI: 10.1039/c3lc50426c.



- 35 K. Domansky, J. D. Sliz, N. Wen, C. Hinojosa, G. Thompson, J. P. Fraser, T. Hamkins-Indik, G. A. Hamilton, D. Levner and D. E. Ingber, SEBS Elastomers for Fabrication of Microfluidic Devices with Reduced Drug Absorption by Injection Molding and Extrusion, *Microfluid. Nanofluid.*, 2017, 21(6), 107, DOI: 10.1007/s10404-017-1941-4.
- 36 S. Schneider, F. Erdemann, O. Schneider, T. Hutschalik and P. Loskill, Organ-on-a-Disc: A Platform Technology for the Centrifugal Generation and Culture of Microphysiological 3D Cell Constructs Amenable for Automation and Parallelization, *APL Bioeng.*, 2020, 4(4), 046101, DOI: 10.1063/5.0019766.
- 37 J. Schindelin, I. Arganda-Carreras, E. Frise, V. Kaynig, M. Longair, T. Pietzsch, S. Preibisch, C. Rueden, S. Saalfeld, B. Schmid, J.-Y. Tinevez, D. J. White, V. Hartenstein, K. Eliceiri, P. Tomancak and A. Cardona, Fiji: An Open-Source Platform for Biological-Image Analysis, *Nat. Methods*, 2012, 9(7), 676–682, DOI: 10.1038/nmeth.2019.
- 38 J. S. Jeon, S. Chung, R. D. Kamm and J. L. Charest, Hot Embossing for Fabrication of a Microfluidic 3D Cell Culture Platform, *Biomed. Microdevices*, 2011, 13(2), 325–333, DOI: 10.1007/s10544-010-9496-0.
- 39 E. W. K. Young, E. Berthier, D. J. Guckenberger, E. Sackmann, C. Lamers, I. Meyvantsson, A. Huttenlocher and D. J. Beebe, Rapid Prototyping of Arrayed Microfluidic Systems in Polystyrene for Cell-Based Assays, *Anal. Chem.*, 2011, 83(4), 1408–1417, DOI: 10.1021/ac102897h.
- 40 C.-W. Tsao and D. L. DeVoe, Bonding of Thermoplastic Polymer Microfluidics, *Microfluid. Nanofluid.*, 2009, 6(1), 1–16, DOI: 10.1007/s10404-008-0361-x.
- 41 S. Yu, S. P. Ng, Z. Wang, C. L. Tham and Y. C. Soh, Thermal Bonding of Thermoplastic Elastomer Film to PMMA for Microfluidic Applications, *Surf. Coat. Technol.*, 2017, 320, 437–440, DOI: 10.1016/j.surfcoat.2016.11.102.
- 42 B. J. Chung, A. M. Robertson and D. G. Peters, The Numerical Design of a Parallel Plate Flow Chamber for Investigation of Endothelial Cell Response to Shear Stress, *Comput. Struct.*, 2003, 81(8–11), 535–546, DOI: 10.1016/S0045-7949(02)00416-9.
- 43 N. Scott Lynn, C. S. Henry and D. S. Dandy, Evaporation from Microreservoirs, *Lab Chip*, 2009, 9(12), 1780–1788, DOI: 10.1039/B900556K.
- 44 V. Wiegmann, C. B. Martinez and F. Baganz, A Simple Method to Determine Evaporation and Compensate for Liquid Losses in Small-Scale Cell Culture Systems, *Biotechnol. Lett.*, 2018, 40(7), 1029–1036, DOI: 10.1007/s10529-018-2556-x.
- 45 M. J. Rogatzki, B. S. Ferguson, M. L. Goodwin and L. B. Gladden, Lactate Is Always the End Product of Glycolysis, *Front. Neurosci.*, 2015, 9, 22, DOI: 10.3389/fnins.2015.00022.
- 46 M. G. Vander Heiden, L. C. Cantley and C. B. Thompson, Understanding the Warburg Effect: The Metabolic Requirements of Cell Proliferation, *Science*, 2009, 324(5930), 1029–1033, DOI: 10.1126/science.1160809.
- 47 K. De Bock, M. Georgiadou, S. Schoors, A. Kuchnio, B. W. Wong, A. R. Cantelmo, A. Quaegebeur, B. Ghesquière, S. Cauwenberghs, G. Eelen, L.-K. Phng, I. Betz, B. Tembuysier, K. Brepoels, J. Welti, I. Geudens, I. Segura, B. Cruys, F. Bifari, I. Decimo, R. Blanco, S. Wyns, J. Vangindertael, S. Rocha, R. T. Collins, S. Munck, D. Daelemans, H. Imamura, R. Devlieger, M. Rider, P. P. Van Veldhoven, F. Schuit, R. Bartrons, J. Hofkens, P. Fraisl, S. Telang, R. J. DeBerardinis, L. Schoonjans, S. Vincier, J. Chesney, H. Gerhardt, M. Dewerchin and P. Carmeliet, Role of PFKFB3-Driven Glycolysis in Vessel Sprouting, *Cell*, 2013, 154(3), 651–663, DOI: 10.1016/j.cell.2013.06.037.
- 48 J. Börner, S. Buchinger and D. Schomburg, A High-Throughput Method for Microbial Metabolome Analysis Using Gas Chromatography/Mass Spectrometry, *Anal. Biochem.*, 2007, 367(2), 143–151, DOI: 10.1016/j.ab.2007.04.036.
- 49 V. Hsiao, E. L. C. de los Santos, W. R. Whitaker, J. E. Dueber and R. M. Murray, Design and Implementation of a Biomolecular Concentration Tracker, *ACS Synth. Biol.*, 2015, 4(2), 150–161, DOI: 10.1021/sb500024b.
- 50 F. Pinto, E. L. Thornton and B. Wang, An Expanded Library of Orthogonal Split Inteins Enables Modular Multi-Peptide Assemblies, *Nat. Commun.*, 2020, 11(1), 1529, DOI: 10.1038/s41467-020-15272-2.
- 51 F. Seyfarth, S. Schliemann, P. Elsner and U.-C. Hipler, Antifungal Effect of High- and Low-Molecular-Weight Chitosan Hydrochloride, Carboxymethyl Chitosan, Chitosan Oligosaccharide and N-Acetyl-d-Glucosamine against *Candida Albicans*, *Candida Krusei* and *Candida Glabrata*, *Int. J. Pharm.*, 2008, 353(1–2), 139–148, DOI: 10.1016/j.ijpharm.2007.11.029.
- 52 B. Müller, P. Sulzer, M. Walch, H. Zirath, T. Buryška, M. Rothbauer, P. Ertl and T. Mayr, Measurement of Respiration and Acidification Rates of Mammalian Cells in Thermoplastic Microfluidic Devices, *Sens. Actuators, B*, 2021, 334, 129664, DOI: 10.1016/j.snb.2021.129664.
- 53 B. Kim, J. Li, C. Jang and Z. Arany, Glutamine Fuels Proliferation but Not Migration of Endothelial Cells, *EMBO J.*, 2017, 36(16), 2321–2333, DOI: 10.15252/embj.201796436.
- 54 E. Tkachenko, E. Gutierrez, M. H. Ginsberg and A. Groisman, An Easy to Assemble Microfluidic Perfusion Device with a Magnetic Clamp, *Lab Chip*, 2009, 9(8), 1085, DOI: 10.1039/b812184b.
- 55 E. Tkachenko, E. Gutierrez, S. K. Saikin, P. Fogelstrand, C. Kim, A. Groisman and M. H. Ginsberg, The Nucleus of Endothelial Cell as a Sensor of Blood Flow Direction, *Biol. Open*, 2013, 2(10), 1007–1012, DOI: 10.1242/bio.20134622.
- 56 U. M. Sonmez, Y.-W. Cheng, S. C. Watkins, B. L. Roman and L. A. Davidson, Endothelial Cell Polarization and Orientation to Flow in a Novel Microfluidic Multimodal Shear Stress Generator, *Lab Chip*, 2020, 20(23), 4373–4390, DOI: 10.1039/D0LC00738B.
- 57 L. Osborn, C. Hession, R. Tizard, C. Vassallo, S. Luhowskyj, G. Chi-Rosso and R. Lobb, Direct Expression Cloning of Vascular Cell Adhesion Molecule 1, a Cytokine-Induced Endothelial Protein That Binds to Lymphocytes, *Cell*, 1989, 59(6), 1203–1211, DOI: 10.1016/0092-8674(89)90775-7.



## Paper

- 58 S. Lechleitner, J. Gille, D. R. Johnson and P. Petzelbauer, Interferon Enhances Tumor Necrosis Factor-Induced Vascular Cell Adhesion Molecule 1 (CD106) Expression in Human Endothelial Cells by an Interferon-Related Factor 1-Dependent Pathway, *J. Exp. Med.*, 1998, **187**(12), 2023–2030, DOI: 10.1084/jem.187.12.2023.
- 59 S.-I. Yamagishi, Y. Inagaki, K. Nakamura, R. Abe, T. Shimizu, A. Yoshimura and T. Imaizumi, Pigment Epithelium-Derived Factor Inhibits TNF- $\alpha$ -Induced Interleukin-6 Expression in Endothelial Cells by Suppressing NADPH Oxidase-Mediated Reactive Oxygen Species Generation, *J. Mol. Cell. Cardiol.*, 2004, **37**(2), 497–506, DOI: 10.1016/j.yjmcc.2004.04.007.
- 60 S. Yamagishi, Y. Inagaki, K. Nakamura and T. Imaizumi, Azelnidipine, A Newly Developed Long-Acting Calcium Antagonist, Inhibits Tumor Necrosis Factor- $\alpha$ -Induced Interleukin-8 Expression in Endothelial Cells through Its Anti-Oxidative Properties, *J. Cardiovasc. Pharmacol.*, 2004, **43**(5), 724–730.
- 61 I. Kim, J.-H. Kim, Y. S. Ryu, M. Liu and G. Y. Koh, Tumor Necrosis Factor- $\alpha$  Upregulates Angiopoietin-2 in Human Umbilical Vein Endothelial Cells, *Biochem. Biophys. Res. Commun.*, 2000, **269**(2), 361–365, DOI: 10.1006/bbrc.2000.2296.
- 62 U. Fiedler, M. Scharpfenecker, S. Koidl, A. Hegen, V. Grunow, J. M. Schmidt, W. Kriz, G. Thurston and H. G. Augustin, The Tie-2 Ligand Angiopoietin-2 Is Stored in and Rapidly Released upon Stimulation from Endothelial Cell Weibel-Palade Bodies, *Blood*, 2004, **103**(11), 4150–4156, DOI: 10.1182/blood-2003-10-3685.
- 63 P. F. Costa, H. J. Albers, J. E. A. Linssen, H. H. T. Middelkamp, L. van der Hout, R. Passier, A. van den Berg, J. Malda and A. D. van der Meer, Mimicking Arterial Thrombosis in a 3D-Printed Microfluidic in Vitro Vascular Model Based on Computed Tomography Angiography Data, *Lab Chip*, 2017, **17**(16), 2785–2792, DOI: 10.1039/C7LC00202E.
- 64 Y. Zheng, J. Chen, M. Craven, N. W. Choi, S. Totorica, A. Diaz-Santana, P. Kermani, B. Hempstead, C. Fischbach-Teschl, J. A. López and A. D. Stroock, In Vitro Microvessels for the Study of Angiogenesis and Thrombosis, *Proc. Natl. Acad. Sci. U. S. A.*, 2012, **109**(24), 9342–9347, DOI: 10.1073/pnas.1201240109.
- 65 B. Nieswandt, I. Pleines and M. Bender, Platelet Adhesion and Activation Mechanisms in Arterial Thrombosis and Ischaemic Stroke: Platelet Adhesion and Activation Mechanisms, *J. Thromb. Haemostasis*, 2011, **9**, 92–104, DOI: 10.1111/j.1538-7836.2011.04361.x.
- 66 D. Meza, S. K. Shanmugavelayudam, A. Mendoza, C. Sanchez, D. A. Rubenstein and W. Yin, Platelets Modulate Endothelial Cell Response to Dynamic Shear Stress through PECAM-1, *Thromb. Res.*, 2017, **150**, 44–50, DOI: 10.1016/j.thromres.2016.12.003.
- 67 H. J. Albers, R. Passier, A. van den Berg and A. D. van der Meer, Automated Analysis of Platelet Aggregation on Cultured Endothelium in a Microfluidic Chip Perfused with Human Whole Blood, *Micromachines*, 2019, **10**(11), 781, DOI: 10.3390/mi10110781.





## Publication [11]

**Autologous human immunocompetent white adipose tissue-on-chip**

**J. Rogal**, R. Xu, J. Roosz, C. Teufel, M. Cipriano, W. Eisler, M. Weiss, K. Schenke-Layland, P. Loskill

*under review* (available at bioRxiv <https://dx.doi.org/10.1101/2021.08.08.455559>)

**Abstract:**

Obesity and associated diseases, such as diabetes, have reached epidemic proportions globally. In the era of 'diabesity' and due to its central role for metabolic and endocrine processes, adipose tissue (specifically white adipose tissue; WAT) has become a target of high interest for therapeutic strategies. To gain insights in cellular and molecular mechanisms of adipose (patho-)physiology, researchers traditionally relied on animal models since *in vitro* studies on human WAT are challenging due to the large size, buoyancy, and fragility of mature white adipocytes. Leveraging the Organ-on-Chip technology, we introduce a next-generation microphysiological *in vitro* model of human WAT based on a tailored microfluidic platform featuring vasculature-like perfusion. The platform integrates a 3D tissue comprising all major WAT-associated cellular components in an autologous manner, including not only mature adipocytes but also organotypic endothelial barriers and stromovascular cells featuring tissue-resident innate immune cells, specifically adipose tissue macrophages. This microphysiological tissue model recapitulates pivotal WAT functions, such as energy storage and mobilization as well as endocrine and immunomodulatory activities. The combination of all individual cell types with extra cellular matrix-like hydrogels in a precisely controllable bottom-up approach enables the generation of a multitude of replicates from the same donors circumventing issues of inter-donor variability and paving the way for personalized medicine. Moreover, it allows to adjust the model's degree of complexity to fit a specific purpose via a flexible mix-and-match approach with different cell component modules. This novel WAT-on-chip system constitutes a human-based, autologous and immunocompetent *in vitro* model of adipose tissue that recapitulates almost full tissue heterogeneity. In the future, the new WAT-on-chip model can become a powerful tool for human-relevant research in the field of metabolism and its associated diseases as well as for compound testing and personalized- and precision medicine applications.

bioRxiv preprint doi: <https://doi.org/10.1101/2021.08.08.455559>; this version posted August 8, 2021. The copyright holder for this preprint (which was not certified by peer review) is the author/funder, who has granted bioRxiv a license to display the preprint in perpetuity. It is made available under a [CC-BY-NC-ND 4.0 International license](#).

Human immunocompetent WAT-on-chip  
Rogal et al. 2021

### **Autologous human immunocompetent white adipose tissue-on-chip**

Julia Rogal<sup>a,b</sup>, Raylin Xu<sup>b,c</sup>, Julia Rooszd<sup>d</sup>, Claudia Teufel<sup>a</sup>, Madalena Cipriano<sup>a,b</sup>, Wiebke Eisler<sup>e</sup>, Martin Weiss<sup>d,f</sup>, Katja Schenke-Layland<sup>a,d,f,g,h</sup>, Peter Loskill<sup>a,b,d,i</sup> #

<sup>a</sup> Department of Biomedical Engineering, Eberhard Karls University Tübingen, Österbergstr. 3, 72074 Tübingen, Germany

<sup>b</sup> Fraunhofer Institute for Interfacial Engineering and Biotechnology IGB, 70569 Stuttgart, Germany

<sup>c</sup> Harvard Medical School (HMS), Boston, MA, USA

<sup>d</sup> NMI Natural and Medical Sciences Institute at the University of Tübingen, Markwiesenstr. 55, 72770 Reutlingen, Germany

<sup>e</sup> Clinic for Plastic, Reconstructive, Hand and Burn Surgery, BG Trauma Center, Eberhard Karls University Tübingen, Tübingen, Germany.

<sup>f</sup> Department of Women's Health, Eberhard Karls University Tübingen, Silcherstrasse Calwerstrasse 7/1, 72076 Tübingen, Germany

<sup>g</sup> Department of Medicine/Cardiology, Cardiovascular Research Laboratories, David Geffen School of Medicine at UCLA, 675 Charles E. Young Drive South, MRL 3645, Los Angeles, CA, USA

<sup>h</sup> Cluster of Excellence iFIT (EXC2180) "Image-Guided and Functionally Instructed Tumor Therapies", Eberhard Karls University Tuebingen; Tuebingen, Germany

<sup>i</sup> 3R-Center for *In vitro* Models and Alternatives to Animal Testing, Eberhard Karls University Tübingen, Tübingen, Germany

Prof. Dr. Peter Loskill

Department of Biomedical Engineering, Eberhard Karls University Tübingen

Österbergstr. 3, 72074 Tübingen, Germany

Phone: +49 7071-29-85293 | E-Mail: [peter.loskill@uni-tuebingen.de](mailto:peter.loskill@uni-tuebingen.de)

bioRxiv preprint doi: <https://doi.org/10.1101/2021.08.08.455559>; this version posted August 8, 2021. The copyright holder for this preprint (which was not certified by peer review) is the author/funder, who has granted bioRxiv a license to display the preprint in perpetuity. It is made available under aCC-BY-NC-ND 4.0 International license.

Human immunocompetent WAT-on-chip  
Rogal et al. 2021

## **Abstract**

Obesity and associated diseases, such as diabetes, have reached epidemic proportions globally. In the era of ‘diabesity’ and due to its central role for metabolic and endocrine processes, adipose tissue (specifically white adipose tissue; WAT) has become a target of high interest for therapeutic strategies. To gain insights in cellular and molecular mechanisms of adipose (patho-)physiology, researchers traditionally relied on animal models since *in vitro* studies on human WAT are challenging due to the large size, buoyancy, and fragility of mature white adipocytes. Leveraging the Organ-on-Chip technology, we introduce a next-generation microphysiological *in vitro* model of human WAT based on a tailored microfluidic platform featuring vasculature-like perfusion. The platform integrates a 3D tissue comprising all major WAT-associated cellular components in an autologous manner, including not only mature adipocytes but also organotypic endothelial barriers and stromovascular cells featuring tissue-resident innate immune cells, specifically adipose tissue macrophages. This microphysiological tissue model recapitulates pivotal WAT functions, such as energy storage and mobilization as well as endocrine and immunomodulatory activities. The combination of all individual cell types with extra cellular matrix-like hydrogels in a precisely controllable bottom-up approach enables the generation of a multitude of replicates from the same donors circumventing issues of inter-donor variability and paving the way for personalized medicine. Moreover, it allows to adjust the model’s degree of complexity to fit a specific purpose via a flexible mix-and-match approach with different cell component modules. This novel WAT-on-chip system constitutes a human-based, autologous and immunocompetent *in vitro* model of adipose tissue that recapitulates almost full tissue heterogeneity. In the future, the new WAT-on-chip model can become a powerful tool for human-relevant research in the field of metabolism and its associated diseases as well as for compound testing and personalized- and precision medicine applications.

## **Keywords:**

adipose tissue-on-chip, mature adipocytes, microfluidics, endothelial barrier, immunometabolism, adipokines, ATMs

bioRxiv preprint doi: <https://doi.org/10.1101/2021.08.08.455559>; this version posted August 8, 2021. The copyright holder for this preprint (which was not certified by peer review) is the author/funder, who has granted bioRxiv a license to display the preprint in perpetuity. It is made available under aCC-BY-NC-ND 4.0 International license.

Human immunocompetent WAT-on-chip  
Rogal et al. 2021

### **Introduction**

Obesity, defined by a body mass index (BMI) of 30 or above, has reached epidemic proportions globally. About 13% of the world's adult population was obese in 2016 (World Health Organization, 2021) – and this number has continued to rise. Marked by a state of low-grade chronic inflammation, obesity is a well-recognized risk factor for a myriad of co-morbidities, amongst them type 2 diabetes mellitus (T2DM), cardiovascular and neurodegenerative diseases, at least 13 different types of cancer (National Cancer Institute at the National Institutes of Health, 2020), and infectious diseases [e.g. COVID19 (Andrade et al., 2021; Hornung et al., 2021)]. Moreover, being obese directly impacts the immune system's ability to respond to infections (Alarcon et al., 2021; Hornung et al., 2021). Therefore, in the era of 'diabesity' and due to its central role for metabolic and endocrine processes, adipose tissue has become a target of high interest for therapeutic strategies against various diseases.

Adipose tissues can be categorized into white adipose tissue (WAT), brown adipose tissue (BAT), brite/beige adipose tissue, and pink adipose tissue. Each tissue type is morphologically distinct and performs unique functions (Corrêa et al., 2019). In this study, we focus on WAT. White adipocytes are integral components of WAT and highly specialized to lipid metabolism. Unlike any other cell type, they can take up and store vast amounts of lipids without being damaged. Moreover, white adipocytes are well equipped to sense and govern the body's energy status. These cells make up about 90% of WAT volume but less than 50% of cellular content (Corvera, 2021). The remaining WAT-associated cell populations are broadly pooled as stromal vascular fraction (SVF). These stromovascular cells include adipose-derived mesenchymal stem cells (AdMSCs), adipocyte and vascular progenitors, fibroblasts, as well as tissue-resident immune cells. Crosstalk between stromovascular cells and adipocytes considerably contributes to modulation of immune responses (Morigny et al., 2021; Sun et al., 2011). Dysfunction of both storage and endocrine WAT activity can have systemic consequences. The close connection between WAT and the immune system comes as no surprise. The most frequent immune cell populations in WAT are adipose tissue macrophages (ATMs), eosinophils, innate lymphoid cells, T cells, and B cells (Eberl et al., 2015; Guzik et al., 2017; Han et al., 2017; Patel et al., 2020; Srikakulapu and McNamara, 2020). Typically, adipose tissue immune cells control integrity and hormone sensitivity of adipocytes (Reilly and Saltiel, 2017). Yet, in response to overnutrition, adipocytes expand in number (hyperplasia) and size (hypertrophy) and eventually unleash a cascade of inflammatory events. Alongside adipocyte-associated functional changes, such as disturbed fatty acid (FA) metabolism or increased insulin resistance, this adipose tissue inflammation is marked by an accelerated immune cell infiltration. For instance, ATMs constitute about 5%-10% of the SVF in healthy humans but up to 50% in obesity (Russo and Lumeng, 2018; Weisberg et al., 2003). Consequently, WAT has become highly relevant for studies on systemic immunometabolism (Lercher et al., 2020).

Gaining human-relevant cellular and molecular insights in adipose (patho-)physiology, however, has traditionally been limited by several aspects: (i) *in vivo* human studies on mechanistic pathways usually entail unacceptable health risks. Thus, a large part of our understanding regarding human WAT function builds on clinical, mostly systemic, observations and genome-wide association studies (GWAS). (ii) Even though *in vivo* animal models allow for more flexibility regarding depth of biological level and degree of experimental interventions, their predictive value for humans is limited. There are major discrepancies between mice and humans, especially when it comes to metabolism and immunology (Greek and Menache, 2013; Mestas and Hughes, 2004; Reitman, 2018; Remick, 2005; van der Worp et al., 2010). (iii) *In vitro* studies on human WAT can be challenging due to the large size, buoyancy, and fragility of mature white adipocytes; rendering conventional cell culture methods unsuitable. Additionally, studies using WAT explants frequently encounter difficulties caused by hypoxia or inflammation (Fain et al., 2010; Gesta et al., 2003). Thus, many adipose *in vitro* studies utilized *in vitro* differentiation of adipocyte progenitors. However, so far, the maturity of these differentiated adipocytes does not adequately reflect the biology and functionality of mature adipocytes (Bahmad et al., 2020; Li and Easley, 2018; Volz et al., 2019).

As a consequence, compared to other organ systems, research on *in vitro* adipose tissue models has been rather sparse. Additionally, the predominant intention behind adipose tissue engineering has been the development of large-scale tissue grafts for regenerative medicine, rather than studies on adipose (patho-)physiological mechanisms. Still,

bioRxiv preprint doi: <https://doi.org/10.1101/2021.08.08.455559>; this version posted August 8, 2021. The copyright holder for this preprint (which was not certified by peer review) is the author/funder, who has granted bioRxiv a license to display the preprint in perpetuity. It is made available under aCC-BY-NC-ND 4.0 International license.

Human immunocompetent WAT-on-chip  
Rogal et al. 2021

several efforts have been made to come up with advanced long-term tissue culture models that can circumvent the restraints in mature adipocyte handling and culturability. 3D biomaterial scaffolds are often utilized to provide protection and a certain degree of structural stability (Abbott et al., 2018, 2016b, 2016a; Huber et al., 2016; Louis et al., 2019). Along the same line, structurally supported *in vitro* cultures have been achieved via sandwiching strategies, trapping mature adipocytes between SVF cell sheets (Lau et al., 2018), and sophisticated versions of ceiling cultures taking advantage of adipocyte buoyancy (Harms et al., 2019). While these approaches considerably contributed to the longevity of mature adipocytes *in vitro*, they still fall short on recapitulating key aspects of the adipose tissue microenvironment including vascular perfusion, cell-cell interactions as well as immune components.

In recent years, the Organ-on-Chip (OoC) technology has become a powerful tool for building *in vitro* culture systems that are reflective of human physiology. Combining microfabrication techniques and tissue engineering, OoCs emulate *in vivo* functionality of a certain organ or tissue at the smallest possible scale in a microfluidic platform. Alongside organ-specific 3D microenvironments, physiological cell-cell and cell-matrix interactions, one of the key features of OoCs is the vasculature-like perfusion; an aspect that is especially important for WAT *in vitro* culture, in view of its high metabolic and endocrine activity. Nevertheless, the current landscape of WAT-on-chip models is still scarce and shaped by *in vitro* differentiated adipocytes (Bahmad et al., 2020; Li and Easley, 2018; McCarthy et al., 2020). Despite some efforts to reflect insulin resistance or WAT immunoregulatory function, almost all WAT-on-chip models turn to differentiating AdMSCs/pre-adipocytes (Kongsuphol et al., 2019; Liu et al., 2019; Yang et al., 2021, 2020) or even murine preadipocytes as fundamental cellular components (Loskill et al., 2017; Tanataweethum et al., 2021, 2018; Zhu et al., 2018). Notably, there is a variety of microanalytical fluidic systems, which aim to interrogate adipocyte functionality using microfluidics approaches (Godwin et al., 2015; Hu et al., 2020; Li et al., 2018). While these analytical platforms integrate mature adipocytes and are powerful means to assess highly time-resolved adipocyte secretions, they are less suited for long-term culture of adipose tissue. To our best knowledge, the only OoC system, which is based on mature human adipocytes and adapted for long-term culture, is our previously published adipocyte-on-chip model (Rogal et al., 2020). Yet, this model integrates only adipocytes and thereby falls short on reflecting WAT's full heterogeneity and consequent endocrine activities.

Here, we introduce a next-generation human WAT-on chip platform, which integrates all major WAT-associated cellular components in an autologous manner (figure 1). Mature adipocytes, together with stromovascular cells, or tissue-resident immune cells extracted from SVF, were encapsulated in a hydrogel matrix and injected into the microfluidic device's tissue chambers. Media-perfused channels supplying the tissue chambers via diffusive exchange across a porous membrane were lined with tight layers of endothelium and served as travelling route for circulating immune cells (figure 1a). Besides the holistic reflection of the cellular composition of WAT, most importantly its immunocompetency, a key feature of our system is its fully autologous character (figure 1b). From skin biopsies with subcutaneous fat, we isolated mature adipocytes, SVF as well as microvascular endothelial cells (mvECs). In a further step, CD14<sup>+</sup>-cells, i.e., monocytes and macrophages, were separated from the SVF using magnetic activated cell sorting (MACS). For experiments on immune cell infiltration, T cells and CD14<sup>+</sup>-cells were derived from peripheral blood mononuclear cells (PBMCs), which were isolated from the biopsy donors' blood. The individual cell types enabled us to build up a WAT model via a precisely controllable bottom-up approach that recapitulates pivotal WAT functions, such as energy storage and mobilization as well as endocrine and immunomodulatory activities. To adjust the model's degree of complexity to fit a specific purpose, we introduce a flexible mix-and-match WAT-on-chip with different cell component modules.

bioRxiv preprint doi: <https://doi.org/10.1101/2021.08.08.455559>; this version posted August 8, 2021. The copyright holder for this preprint (which was not certified by peer review) is the author/funder, who has granted bioRxiv a license to display the preprint in perpetuity. It is made available under aCC-BY-NC-ND 4.0 International license.

Human immunocompetent WAT-on-chip  
Rogal et al. 2021

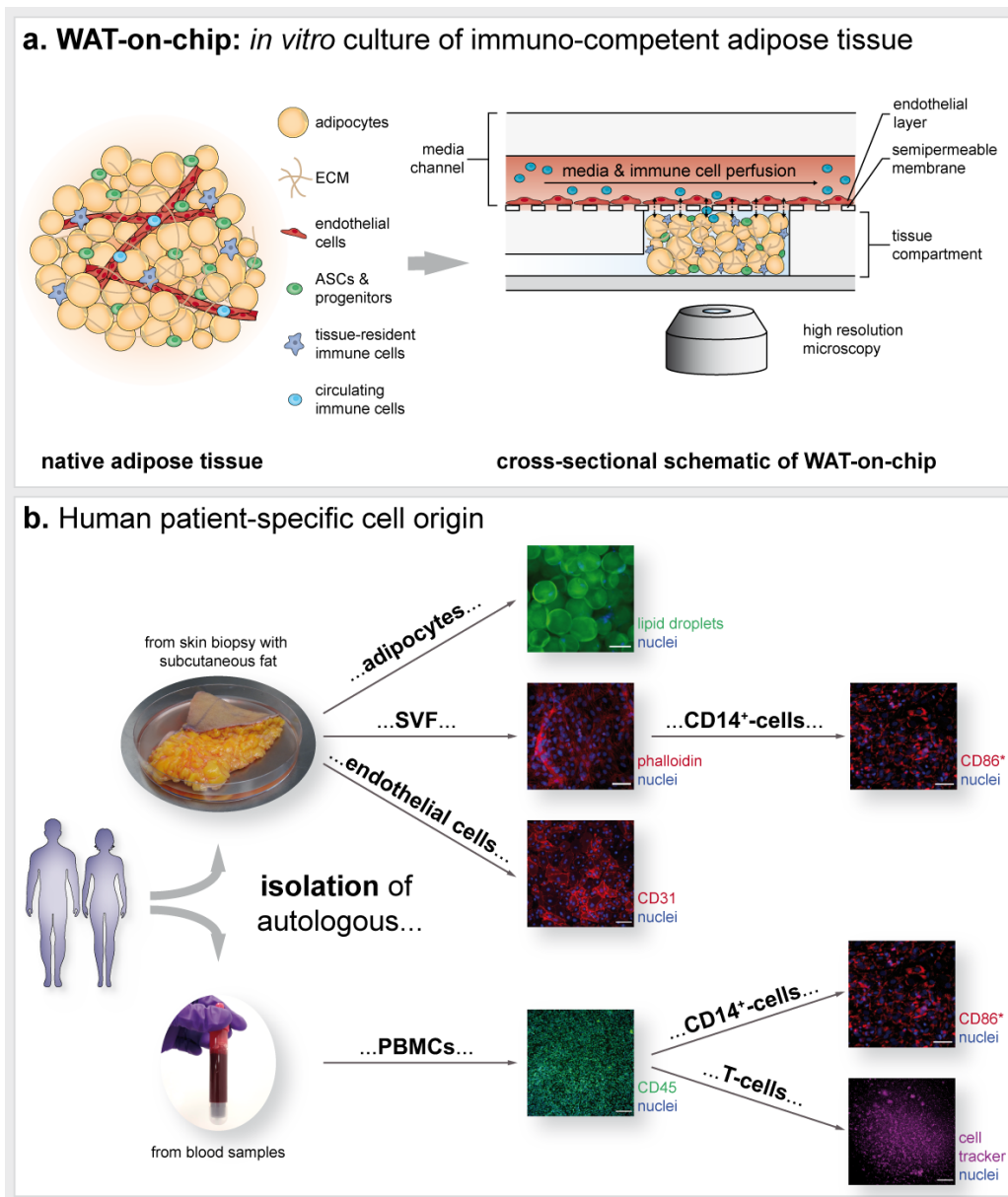


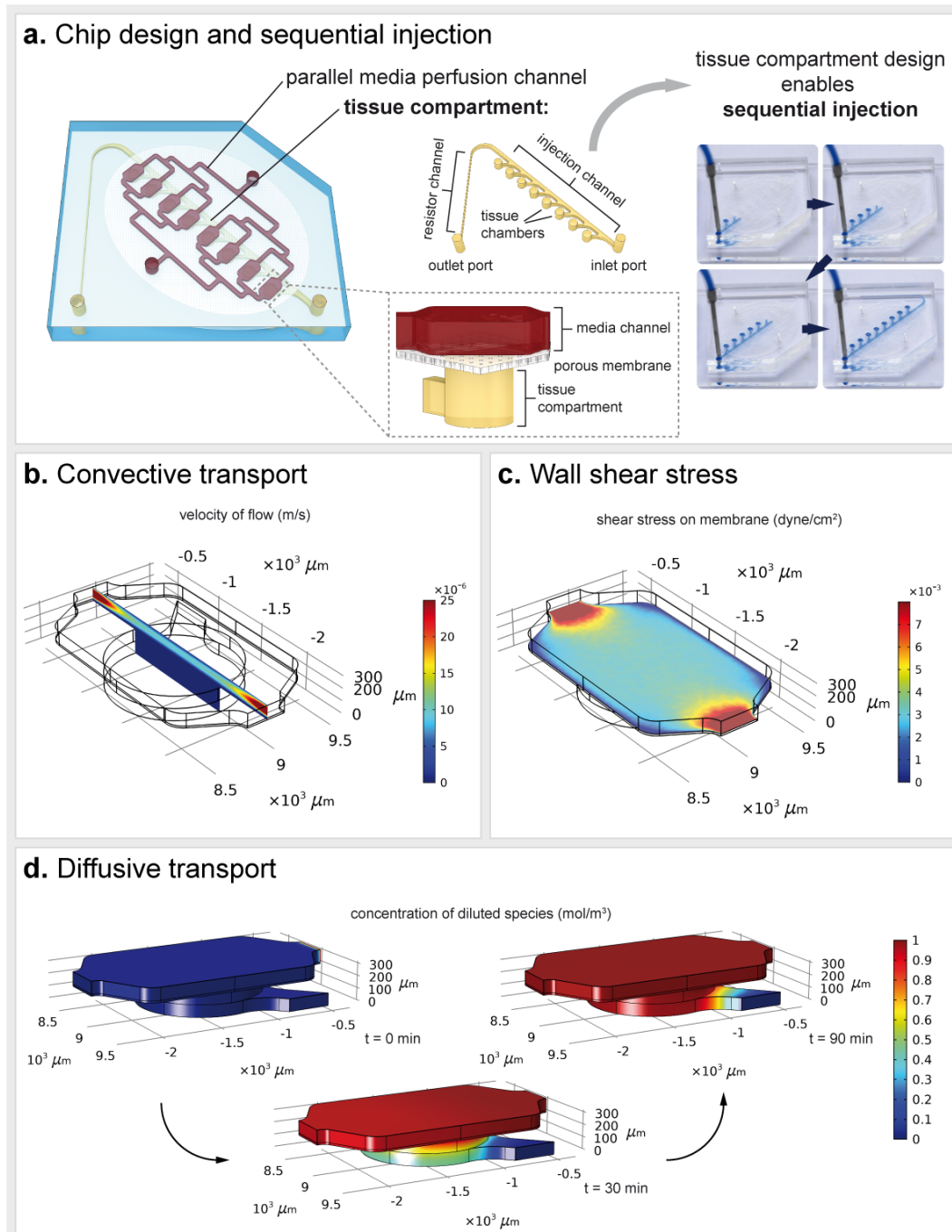
**Figure 1. Concept of the human patient-specific WAT-on-chip model.** (a) Schematic of WAT *in vivo* anatomy and integration of all cellular components into the microfluidic platform: Mature adipocytes, progenitors, stem cells, and tissue-resident immune cells are encapsulated in a hydrogel and cultured in the chips' tissue compartment. Microvascular endothelial cells (mvECs) are seeded via the media channel onto the membrane shielding tissue chambers from the constant perfusion. To study immune cell recruitment, circulating immune cells were perfused through the media channels. (b) Patient-specific cell sources for building the WAT-on-chip model: Mature human adipocytes, mvECs as well as cells from the stromal vascular fraction (SVF), including tissue-resident immune cells such as CD14<sup>+</sup>-cells, are isolated from skin biopsies with subcutaneous fat. Circulating immune cells, such as T-cells, are retrieved by isolating PBMCs from the patients' blood. Scale bars equal 100  $\mu$ m (adipocytes, CD31, CD45 and T cell visualization) or 50  $\mu$ m (SVF and CD14<sup>+</sup>-cell visualization). \*CD14<sup>+</sup>-cells are isolated using magnetic activated cell sorting (MACS) and could therefore not be stained for CD14 but for CD86, another marker expressed on macrophages.

bioRxiv preprint doi: <https://doi.org/10.1101/2021.08.08.455559>; this version posted August 8, 2021. The copyright holder for this preprint (which was not certified by peer review) is the author/funder, who has granted bioRxiv a license to display the preprint in perpetuity. It is made available under aCC-BY-NC-ND 4.0 International license.

Human immunocompetent WAT-on-chip  
Rogal et al. 2021

## Results and Discussion

### *Microfluidic platform specifically tailored to accommodate adipose tissue*



6

bioRxiv preprint doi: <https://doi.org/10.1101/2021.08.08.455559>; this version posted August 8, 2021. The copyright holder for this preprint (which was not certified by peer review) is the author/funder, who has granted bioRxiv a license to display the preprint in perpetuity. It is made available under a [CC-BY-NC-ND 4.0 International license](#).

Human immunocompetent WAT-on-chip  
Rogal et al. 2021

**Figure 2. Characterization of the microfluidic platform.** (a) Key characteristics of the WAT-on-chip platforms are (i) a parallel media perfusion channel to ensure equal media supply for each tissue chamber and (ii) a tissue compartment with eight separate tissue chambers. The design of the tissue compartment enables sequential injection of the tissue chambers. Computational fluid dynamic modeling revealed (b) a convective flow confined to the media channel, (c) low shear forces ( $\sim 0.002 - 0.006 \text{ dyn/cm}^2$ ) on the membrane and (d) ensured diffusion of diluted species from the media flow into the tissue chambers. For all simulations, the flow rate was set to  $2.5 \mu\text{L/h}$  per parallel channel, which results in  $20 \mu\text{L/h}$  total flow rate, and the tissue compartment was assumed to be filled with a hydrogel.

The microfluidic platform used in this study is a customized system specifically tailored to the integration of WAT (cf. figures 1a and 2a). The device was fabricated from two microstructured polydimethylsiloxane (PDMS) layers that are separated by a semipermeable, porous polyethylene terephthalate (PET) membrane. The lower PDMS layer was patterned with channel- and chamber microstructures to form the tissue compartment. It is comprised of eight individual tissue chambers branching off a common injection channel at a  $45^\circ$  angle and a thin, high-resistance channel towards the outlet port of the tissue compartment. Via the micropores in the PET membrane, the tissue chambers are connected to a constant media perfusion through media channels molded into the upper PDMS layer (media compartment). To the other side, the tissue chambers are encased by glass coverslips to enable optimal visual accessibility of on-chip tissues. The tissue chambers are 1 mm in diameter and feature a height of 0.2 mm each, resulting in a total tissue volume of  $1.26 \mu\text{l}$  for the eight tissue chambers (for detailed dimensions cf. table 1, Materials and Methods section). In addition to the cylindrical shape of the tissue chambers, all edges in the tissue compartment were rounded to avoid cell damage. The media perfusion was realized by a parallel arrangement of media channels bifurcating from a common media inlet port that later merge to meet in a common media outlet port. We chose a parallel media perfusion over a serial media perfusion to avoid crosstalk among the individual chambers.

Besides housing the media channel compartment, the upper PDMS layer contains ports for tissue loading as well as media in- and outlet ports. Through the connection to an external syringe pump, we were able to precisely control the convective transport of substances, i.e., nutrients or drugs/compounds, to the tissue chambers as well as removal of metabolites or waste products from the on-chip tissues.

A key design feature of the platform is the architecture of the tissue compartment system, which enables a sequential injection procedure (figure 2a). Upon injecting the cell suspension through the tissue compartment's inlet port, the chambers fill one after another following the path of lowest resistance (figure 2a); provided that the ports of the media compartment above are open. These injection properties are particularly favorable for handling human mature adipocytes: Owing to their large size and high lipid contents, these cells are extremely fragile. The sequential loading process prevents "overloading" of tissue chambers. Thereby, it protects the adipocytes from high pressures and potential damage during injection. Moreover, the technique facilitates a uniform loading and equal filling states among the chambers. The outlet of the tissue compartment is not only essential to the sequential injection principle; it also enables a clearing of the injection channel from surplus cells that did not fit into the tissue chambers anymore. For these remnant cells, a sufficient media supply could not be guaranteed, and cell death signals secreted by these remnant cells could negatively impact the perfused cells in the tissue chambers.

The separation of tissue chambers from the constant flow in the media channels by the porous membranes shields the tissue compartment from shear forces, as confirmed by computational fluid dynamics (CFD) modelling (figure 2b). The wall shear stress (WSS) on top of the membrane, above the hydrogel-filled tissue chambers, ranges between  $3 \times 10^{-3} - 4 \times 10^{-3} \text{ dyn/cm}^2$  (figure 2c). Yet, despite the membrane's warding the tissue chambers from shear stress, sufficient nutrients reach the entire tissue chamber through diffusive transport across the membrane (figure 2c).



bioRxiv preprint doi: <https://doi.org/10.1101/2021.08.08.455559>; this version posted August 8, 2021. The copyright holder for this preprint (which was not certified by peer review) is the author/funder, who has granted bioRxiv a license to display the preprint in perpetuity. It is made available under a [CC-BY-NC-ND 4.0 International license](#).

Human immunocompetent WAT-on-chip  
Rogal et al. 2021

LCFA n=16) and its dependency on glucose (on d4-d5) (no glucose n=3; high glucose n=6) (i). We further analyzed (ii) basal adipokine secretion (on d4) (donor 1 n=4; donor 2 n=6) as well as (iii) the adipocytes' response to  $\beta$ -adrenergic stimulation (on d4-d5). (c) Cytokine release in response to proinflammatory stimulation for 24 h with TNF- $\alpha$  (20 ng/ml) or LPS (100 ng/ml) on d5. Cytokine secretion is depicted relative to the secretion determined for the 24 h-period before stimulation (two independent chips per donor for each condition).

After a general characterization of the microfluidic platform per se, we sought to investigate its suitability for the integration of human mature adipocytes suspended in a hydrogel matrix.

Human mature adipocytes were isolated from skin biopsies with subcutaneous adipose tissue and cultured overnight in flask-format. Prior to injection, the adipocytes were suspended in a hydrogel matrix and then injected into the tissue compartment. The hydrogel added a protective surrounding during injection and prevented buoyant adipocytes from floating to the top of the tissue chambers. Importantly, the integration of an adipocyte-surrounding matrix is physiologically relevant: *in vivo*, alterations in adipose tissue extracellular matrix (ECM) can lead to metabolic changes. An excess deposition of ECM, as is the case in obesity, was found to lead to an aggravation of insulin sensitivity (Lin et al., 2016), for instance. In our model, a synthetic hydrogel was used to achieve higher control and reproducibility compared to natural alternatives. Since collagens comprise the main ECM component in adipose tissue (Ruiz-Ojeda et al., 2019), we chose the HyStem<sup>®</sup>-C hydrogel, which is rich in denatured collagens providing cell attachment sites. Moreover, as a recent study reported that adipocytes in stiffer 3D matrices had increased pro-fibrotic gene expression profiles (Di Caprio and Bellas, 2020), we decreased the stiffness of the resulting hydrogel matrix by tailoring ratios of its components.

We characterized the adipocytes' viability, morphology and functionality on-chip at different time points. Furthermore, we studied their response to  $\beta$ -adrenergic- as well as pro-inflammatory stimulation. To assess impact of donor-variability, we also compared how cells from different donors (table 2, Materials and Methods) perform in the same experimental set-up.

The viability of adipocytes on-chip was assessed non-invasively via monitoring the release of lactate dehydrogenase (LDH) into the media effluents (supplementary figure S1). Therefore, effluents were collected every 24 h over a 12-day culture. While at the beginning of the culture low levels of LDH were detected (below 10% relative to expected maximum release), LDH was not detectable after d5 anymore. These findings indicated a good overall on-chip viability of adipocytes. Culture monitoring via bright field microscopy further backed the evidence of a stable adipocyte long-term culture on-chip (supplementary figure S2).

To characterize the morphology of adipocytes further, we stained lipid droplets (with a BODIPY neutral lipid stain), perilipin A (via immunofluorescence staining) and nuclei on d5 of on-chip culture (figure 3a). Confocal imaging of this staining revealed a dense, 3-dimensional arrangement of adipocytes throughout the entire chamber. Moreover, it confirmed the preservation of key morphological features of adipocyte maturity such as (i) unilocularity (i.e., storage of lipid content in one larger lipid vacuole instead of several smaller lipid vacuoles) and (ii) expression of the lipid droplet-coating protein perilipin A.<sup>1</sup>

Unilocularity is a vital hallmark of the mature adipocyte phenotype. Many mature adipocyte *in vitro* culture methods, such as different variants of ceiling cultures (Sugihara et al., 1989; Zhang et al., 2000; Fernyhough et al., 2004), eventually induce a dedifferentiation of adipocytes to fibroblast-like progenitor states. Along the dedifferentiation process, the adipocytes undergo intracellular reorganization such as loss of the large lipid droplet, instead being multilocular, and spreading of cytoplasm (Côté et al., 2019). The dedifferentiation might be induced by an exposure to physical stressors (Yiwei Li et al., 2020), such as the presence of an adhesion surface as in the case of ceiling culture. The readiness of mature adipocytes to dedifferentiate has high potential for regenerative medicine (Côté et al., 2019),

---

<sup>1</sup> Notably, conventional 3D volumetric imaging is particularly complicated for adipose tissue. Since obscuring effects from light scattering majorly occur at lipid-aqueous interfaces, imaging of adipocytes is highly susceptible to these effects, especially in deeper layers of the tissue.

bioRxiv preprint doi: <https://doi.org/10.1101/2021.08.08.455559>; this version posted August 8, 2021. The copyright holder for this preprint (which was not certified by peer review) is the author/funder, who has granted bioRxiv a license to display the preprint in perpetuity. It is made available under aCC-BY-NC-ND 4.0 International license.

Human immunocompetent WAT-on-chip  
Rogal et al. 2021

and elucidation of the underlying mechanisms of de- and redifferentiation is of utmost importance for understanding tumor progression (Yiwei Li et al., 2020, p.). Yet, this change in cell identity would be more than unfavorable when studying mechanisms of adipose tissues. Perilipin A, also called PLIN1, is expressed abundantly in mature adipocytes. It functions as a stabilizer of larger lipid droplets (usually < 10  $\mu\text{m}$ ) and plays an important role in hormone-induced lipolysis (Itabe et al., 2017). More recent studies in mice even suggest a major contribution of PLIN1 to anti-inflammatory processes and prevention of insulin resistance by restricting uncontrolled lipolysis (Sohn et al., 2018).

Adipocyte function on-chip was confirmed by analyzing its energy storage and mobilization capacities (figure 3bi). Upon administering fluorescently tagged fatty acids (FAs) to the adipocytes via the media perfusion, FAs were taken up by the adipocytes as indicated by an increase in intracellular fluorescence intensity. This uptake was monitored in real-time by imaging the individual tissue chambers every 3 minutes and quantified by plotting the fluorescence intensities against time of FA administration. Both fluorescent analogs of dodecanoic acid, also called lauric acid [with 12 carbon (C) atoms a representative of a medium-chain fatty acid (MCFA), BODIPY-C<sub>12</sub>], and hexadecanoic acid, also called palmitic acid [with 16 C atoms a representative of a long-chain fatty acid (LCFA), BODIPY-C<sub>16</sub>], were administered to capture potentially different FA uptake mechanisms. While short-chain fatty acids and MCFAs can freely diffuse across the cell membrane into the cytosol, the uptake of LCFAs, which are the most abundant among the three FA types, appears to be more complex (Schönfeld and Wojtczak, 2016). Despite still being under discussion, LCFA uptake might be realized through combination of passive diffusion and protein-accelerated entry into the membrane as well as desorption at the inner side of the membrane (Glatz and Luiken, 2020; Jay et al., 2020; Thompson et al., 2010).

Of note, the MCFA analog has two fluorophores attached (in positions C1 and C12), as compared to the LCFA analog, which has the BODIPY-fluorophore only in the C16 position. Therefore, the higher final fluorescence intensity signal obtained when feeding the MCFA analog could be attributed to the double amount of fluorophore. It is noteworthy that through the attachment of these two fluorophores, the MCFA analog might be comparable to a LCFA regarding its size. Hence, its trafficking properties could resemble that of a LCFA as well (Kolahi et al., 2016).

Leveraging the established FA uptake assay, we further investigated the dependency of BODIPY-C<sub>12</sub> uptake rates on glucose concentration in the perfused medium. We found FA uptake rates to be higher, when the medium contained a high glucose concentration (17.5 mM) as compared to medium with no glucose added (except for glucose contained in fetal calf serum). These findings are in line with the need for glucose to form glycerol-3-phosphate for the backbone of triacylglycerides (TAGs) in lipogenesis (Morigny et al., 2021). Another reason might be the inhibition of fatty acid release by glucose uptake (Wolfe, 1998).

Furthermore, basal lipolytic activity during on-chip culture was determined by measuring glycerol concentration in media effluents for three different adipocyte donors. While a release of glycerol was detected for all donors, we found considerable inter-donor variations concerning the released concentrations (supplemental figure S3). These variations were found to be higher than intra-donor variations on different days of analysis as well as variations from different independent chips of the same donor on the same day of analysis.

This donor-specific cell behavior was also present when we determined basal adipokine release from the on-chip adipocytes (figure 3bii). While the release of retinol binding protein 4 (RBP4) was similar between the two donors, the secretion of adiponectin varied. Generally, the adipokine release by the adipocytes on-chip demonstrates an endocrine functionality in addition to the metabolic functionality. Interestingly, adiponectin and leptin release into media effluents was not detectable for our adipocyte-only on-chip cultures; in co-culture with other WAT cell components, however, the release of these two important adipokines could be verified (cf. Autologous full complexity WAT-on-chip). Of note, adipose endocrine signaling occurs not only through peptides, such as adipokines and other cytokines but also through fatty acids ('lipokines') as well as exosomal microRNAs (Morigny et al., 2021; Scheja and Heeren, 2019).

The findings from our adipocyte-only chip culture experiments indicate that the platform is well suited for the culture of this demanding cell type. Adipocyte buoyancy and fragility is managed by encapsulation in a hydrogel matrix for cell

bioRxiv preprint doi: <https://doi.org/10.1101/2021.08.08.455559>; this version posted August 8, 2021. The copyright holder for this preprint (which was not certified by peer review) is the author/funder, who has granted bioRxiv a license to display the preprint in perpetuity. It is made available under a [CC-BY-NC-ND 4.0 International license](#).

Human immunocompetent WAT-on-chip  
Rogal et al. 2021

anchorage and by very gentle injection and culture properties (sequential injection and protection from shear). Through a range of assays, we could show that a mature adipocyte phenotype as well as key *in vivo* functions were preserved in our *in vitro* model. Importantly, our on-chip culture concept was able to capture inter-donor differences concerning general adipocyte function, which could also be observed when studying responsiveness to external stimulations.

Next, we sought to study the adipocytes' drug responsiveness. Due to its lipolytic effects, we selected the  $\beta$ -adrenoreceptor agonist isoproterenol and administered 1-100  $\mu$ M via the media perfusion (figure 3biii). As other catecholamines, this synthetic noradrenaline-derivative induces the breakdown of TAGs and its release from adipocytes. When introducing the drug after feeding the tissues with the BODIPY-C<sub>12</sub> FA, we observed different FA release rates. The higher the isoproterenol concentration, the faster the intracellular fluorescence intensity signal from the BODIPY-C<sub>12</sub> decreased. Another readout backing the adipocytes' lipolytic response to  $\beta$ -adrenergic stimulation was the determination of glycerol secretion during a 24 h drug treatment, which revealed a dose-dependent response; higher glycerol levels associated with higher doses of the drug.

Finally, we evaluated the adipocytes' proinflammatory response to an acute 24 h TNF- $\alpha$  or LPS stimulation (figure 3c). We observed an increase in monocyte chemoattractant protein-1 [MCP-1, alternatively CC-chemokine ligand 2 (CCL2)], interleukin-8 [IL-8, alternatively C-X-C motif chemokine ligand 8 (CXCL8)] and interleukin-6 (IL-6) secretion for both TNF- $\alpha$  and LPS treatment. These findings were expected since adipocytes are responsive to both TNF- $\alpha$  and LPS, and have been shown to produce any of the three analyzed cytokines (Bruun et al., 2001; Hoch et al., 2008; Meijer et al., 2011). Again, we performed this experiment for two different adipocyte donors and found considerable differences in the degree of response as well as between the two stimulants. We further investigated the impact of inflammatory stimulation on adipocytes' FA uptake as well as glycerol release; using the abovementioned methods, no difference in the examined properties were registered (data not shown).

bioRxiv preprint doi: <https://doi.org/10.1101/2021.08.08.455559>; this version posted August 8, 2021. The copyright holder for this preprint (which was not certified by peer review) is the author/funder, who has granted bioRxiv a license to display the preprint in perpetuity. It is made available under aCC-BY-NC-ND 4.0 International license.

Human immunocompetent WAT-on-chip  
Rogal et al. 2021

**Characterization of on-chip endothelial barrier from mvECs**

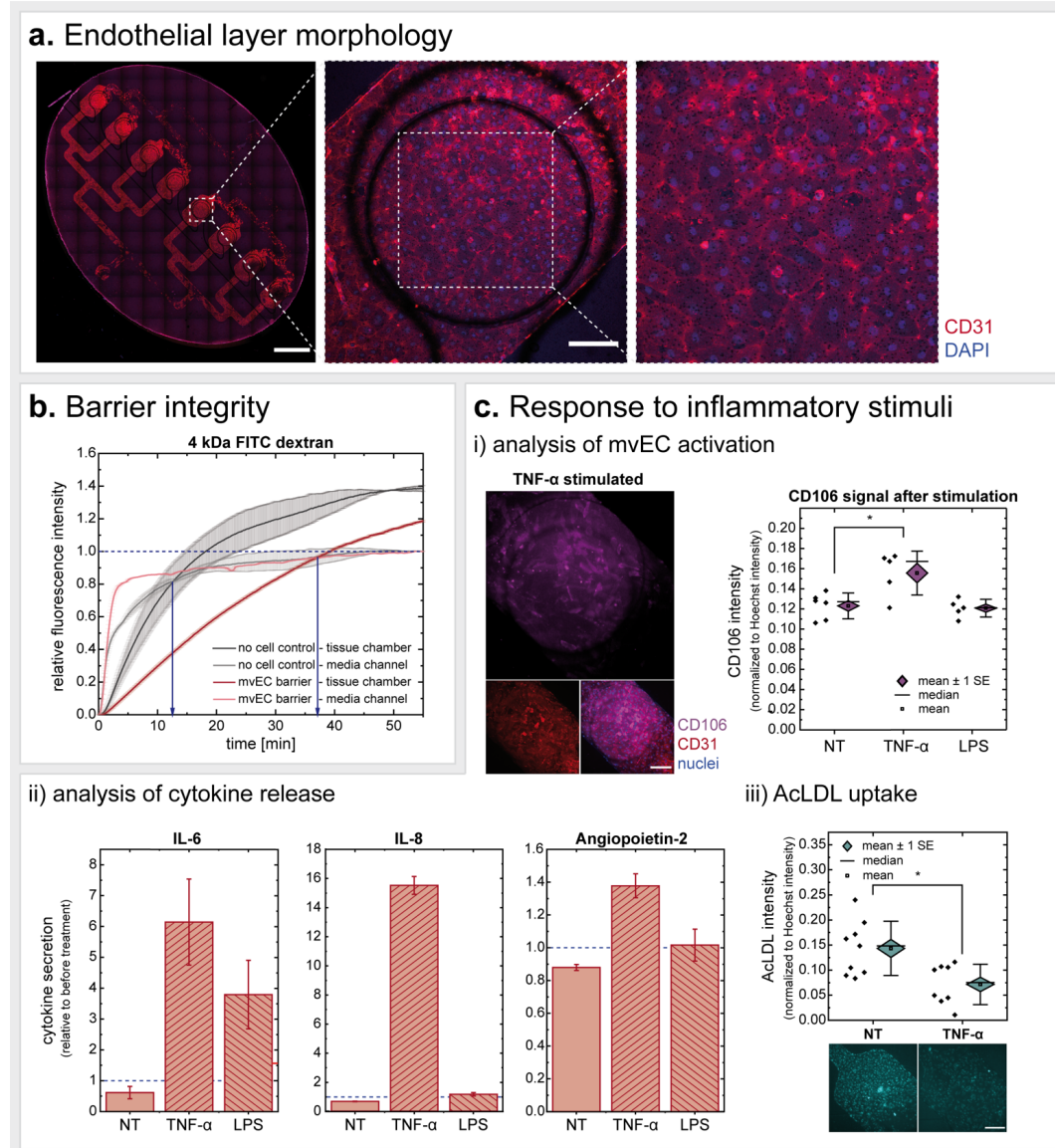


**Figure 4. Characterization of on-chip endothelial barrier.** (a) Microvascular endothelial cells (mvECs) seeded onto the membrane in the medium channel formed uniform, tight monolayers as visualized by CD31 staining (fixed on d7). Scale bars equal 2 mm (tile scan of entire chip) and 200  $\mu$ m (one-chamber view). (b) Endothelial barrier integrity determined by fluorescence macromolecule tracing. We measured time difference in 4 kDa FITC-dextran signal equilibria in tissue chambers vs. media channels for chips with endothelial barrier vs. chips without endothelial barrier. Endothelial barriers were less permeable than plain, acellularized membranes. (c) Exposure of the on-chip endothelial barrier to inflammatory stimuli lead to (i) a significant increase in CD106 expression for TNF- $\alpha$  stimulation (unpaired *t* test with *p*-value  $\leq 0.05$ ; scale bar equals 200  $\mu$ m), (ii) altered inflammatory cytokine secretion (*n*=2 for each stimulus) and (iii) decreased uptake/intracellular retention of acetylated low-density lipoprotein (AcLDL) (unpaired *t* test with *p*-value  $\leq 0.05$ ; scale bar equals 200  $\mu$ m).

12

bioRxiv preprint doi: <https://doi.org/10.1101/2021.08.08.455559>; this version posted August 8, 2021. The copyright holder for this preprint (which was not certified by peer review) is the author/funder, who has granted bioRxiv a license to display the preprint in perpetuity. It is made available under a [CC-BY-NC-ND 4.0 International license](#).

Human immunocompetent WAT-on-chip  
Rogal et al. 2021

Next, we established protocols to line the perfused media channels, particularly the membrane forming the interface to the tissue chambers, with endothelium [microvascular endothelial cells (mvECs)]. Through this step, the transport from the media channel across the membrane into the tissue compartment was upgraded from passive diffusion to dynamic transport regulated by endothelial cells.

To characterize this on-chip endothelial barrier, we ran a series of experiments with endothelial barrier-only chips, i.e., no other cell type included in the tissue chambers. However, to maintain on-chip mechanical properties, the tissue compartment was filled with the hydrogel matrix prior to mvEC seeding into the media channels. After seeding, the cells were allowed to adhere overnight (under static, diffusion-driven nutrient supply) before connecting the chips to constant media perfusion. The flow rate was then ramped up to the final flow rate (20  $\mu\text{L}/\text{h}$ ) in a stepwise manner (increase by 5  $\mu\text{L}/\text{h}$  every 2 h) to avoid mvEC detachment.

The mvECs quickly formed a dense monolayer that remained viable for at least one week of on-chip culture (figure S4a). We confirmed endothelial identity by verifying the expression of CD31 [alternatively platelet endothelial cell adhesion molecule 1 (PECAM1); a junctional molecule highly expressed on the surface of ECs] (figure 4a) as well as CD309 [alternatively vascular endothelial growth factor receptor 2 (VEGFR-2) or kinase insert domain-containing receptor (KDR)] and endothelial nitric oxide synthase [eNOS; alternatively nitric oxid synthase 3 (NOS3)] (figure S4b). Besides confirming EC identity, the anti-CD31 staining also demonstrates the formation of tight endothelial barriers with pronounced intercellular junctions throughout the entire chip. CD31 functions as a mechano-sensor, controls leukocyte trafficking and maintains the integrity of EC junctions (Privratsky and Newman, 2014). However, we did not observe any alignment of the mvECs in the direction of flow. This can be attributed to the shear forces on the membrane being considerably lower than *in vivo* (figure 2c) [here  $\sim 3 \times 10^{-3}$ - $4 \times 10^{-3}$   $\text{dyn}/\text{cm}^2$ , figure 2c, *in vivo* usually 0.1–60  $\text{dyn}/\text{cm}^2$  (Park et al., 2011)]. An increase in flow rate was not possible: a flow rate higher than 20  $\mu\text{L}/\text{h}$  diluted metabolites and messenger molecules secreted by the adipocytes into the effluent media to a concentration below detection limits of determination assays used in this study.

The permeability of the mvEC barrier was tested by analyzing the transport of a fluorescently labeled dextran across the endothelial barrier in comparison to an acellular membrane (figure 4b and figure S4c). We found that 4 kDa FITC-dextran (figure 4b) are retained longer in the medium channel in the presence of a vascular barrier; in chips without this barrier, an equilibrium in fluorescence signal between media channel and tissue chamber was reached notably faster. Repeating this permeability assay using 40 kDa and 150 kDa FITC-dextran suggested similar differences in macromolecule transport across the endothelial barrier (figure S4c).

Finally, we investigated the response of the endothelium to pro-inflammatory stimuli (figure 4c). We found, that the CD106 [alternatively vascular cell adhesion molecule 1 (VCAM-1)] expression by mvECs was significantly increased in response to  $\text{TNF-}\alpha$ , but not to LPS. Compliant with this result, we found the endothelial release of proinflammatory cytokines (IL-6, IL-8 and angiopoietin 2) after stimulation to be most increased after the  $\text{TNF-}\alpha$  treatment. While the LPS treatment induced an increased release of IL-6, releases of IL-8 and angiopoietin 2 were minimally increased by the proinflammatory challenge. Moreover,  $\text{TNF-}\alpha$  stimulation affected the uptake (or intracellular retention) of acetylated low-density lipoprotein (Ac-LDL) by the endothelial cells resulting in almost twice as high fluorescence intensity.

Overall, these findings show that a tight endothelial barrier could be successfully established on-chip and key endothelial functions maintained for at least one week of culture. The vasculature is a dynamic barrier that can rapidly respond to changes in the circulation. Amongst other ways of such response, ECs take the part of metabolic gate keepers. They regulate and adjust transport rates of nutrients and hormones, including FAs, glucose and insulin, from the vessel lumen into tissues (Hasan and Fischer, 2021). Another important aspect of the endothelial barrier is its role as traveling route for immune cells and, potentially, recruiters thereof.

Besides the systemic endothelial tasks, ECs also contribute to organ-specific functions depending on their site of operation. Generally, owing to the adipose tissue's enormous plasticity, adipogenesis is strongly dependent on

---

bioRxiv preprint doi: <https://doi.org/10.1101/2021.08.08.455559>; this version posted August 8, 2021. The copyright holder for this preprint (which was not certified by peer review) is the author/funder, who has granted bioRxiv a license to display the preprint in perpetuity. It is made available under aCC-BY-NC-ND 4.0 International license.

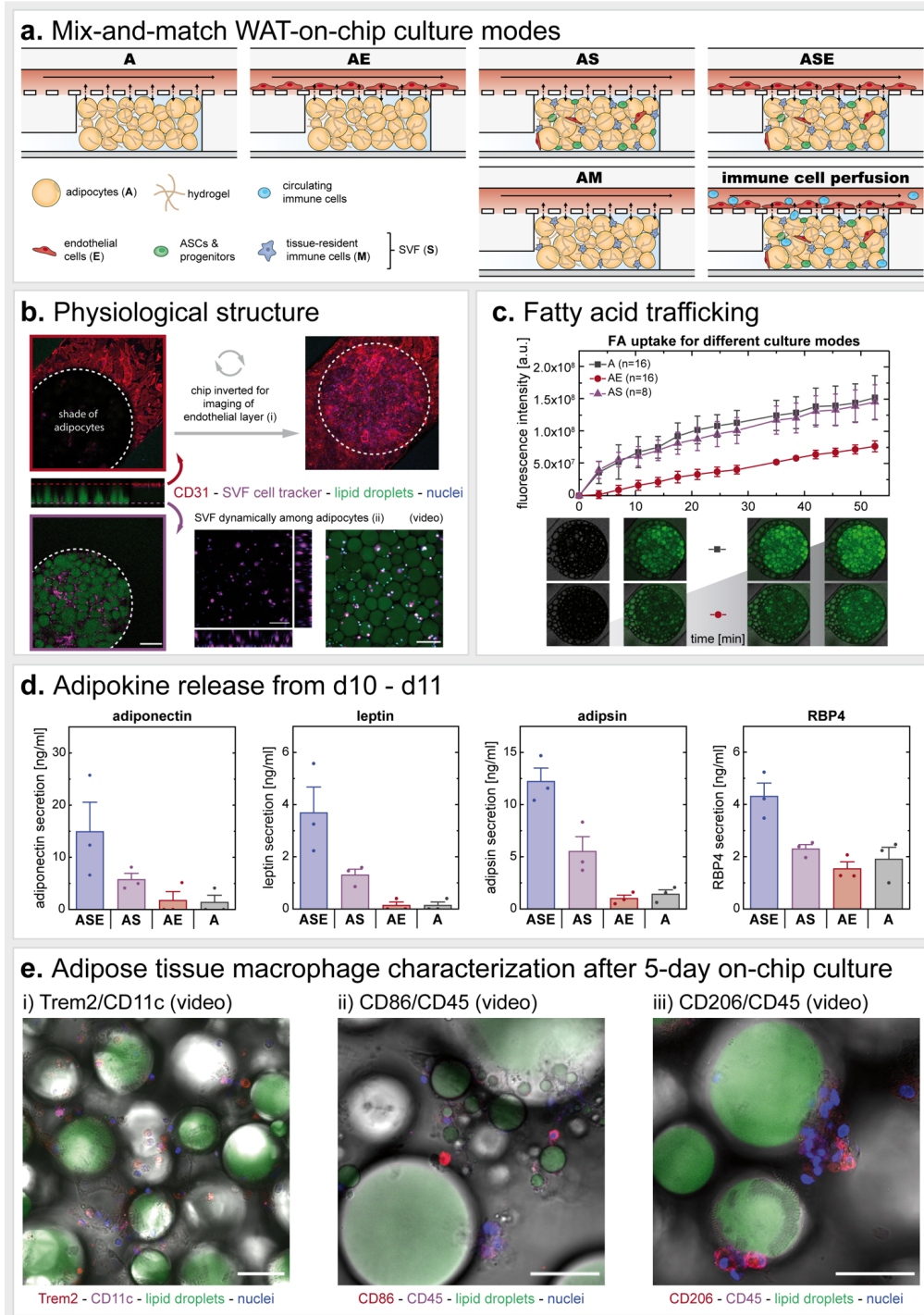
Human immunocompetent WAT-on-chip  
Rogal et al. 2021

angiogenesis (Augustin and Koh, 2017). Yet, the quiescent endothelium is as important as the active one: Adipose mvECs, for instance, were shown to directly crosstalk with adipocytes to regulate peroxisome proliferator activated receptor  $\gamma$  (PPAR $\gamma$ ) pathways and thereby the adipocytes' ability to take up and store lipids (Gogg et al., 2019). Notably, even though adipose mvECs take up lipids as well, they cannot undergo a full adipogenic differentiation when exposed to cues of adipose differentiation (Gogg et al., 2019). In this project dermal instead of adipose-derived mvECs were used owing to the limited amount of subcutaneous adipose tissue, which had to serve as a source for adipocytes, general SVF as well as tissue-resident immune cells. These dermal mvECs were isolated from the dermis of the skin/fat biopsy. Yet, despite the difference in origin tissue, it was shown previously that skin-derived and adipose-derived mvECs are very similar: they showed the same expression of endothelial markers, migration and sprouting behavior as well as response to inflammatory stimulation (Monsuur et al., 2016).

bioRxiv preprint doi: <https://doi.org/10.1101/2021.08.08.455559>; this version posted August 8, 2021. The copyright holder for this preprint (which was not certified by peer review) is the author/funder, who has granted bioRxiv a license to display the preprint in perpetuity. It is made available under aCC-BY-NC-ND 4.0 International license.

Human immunocompetent WAT-on-chip  
Rogal et al. 2021

**Autologous full complexity WAT-on-chip: fit-for-purpose mix-and-match toolbox**



bioRxiv preprint doi: <https://doi.org/10.1101/2021.08.08.455559>; this version posted August 8, 2021. The copyright holder for this preprint (which was not certified by peer review) is the author/funder, who has granted bioRxiv a license to display the preprint in perpetuity. It is made available under aCC-BY-NC-ND 4.0 International license.

Human immunocompetent WAT-on-chip  
Rogal et al. 2021

**Figure 5.** Modular mix-and-match toolbox to build fit-for-purpose autologous WAT-on-chip models. (a) To create WAT-on-chip models specifically tailored to certain scientific questions, we propose a spectrum of on-chip culture conditions with varying degrees of complexity ranging from simple adipocyte-only systems (A) to highly complex full WAT-on-chip models (ASE). (b) Structural characterization of the full WAT-on-chip model (ASE) on d12. Anti-CD31 immunofluorescence staining showed a tight endothelial barrier on the chip's membrane. To visualize the membrane area over the adipocyte-filled tissue chambers, the chip had to be inverted (i). Adipocytes were displayed by staining of their lipid droplets. To uncover stromovascular cells, SVF was labelled with a cell tracker prior to injection into the chip. SVF was 3-dimensionally distributed among the adipocytes in the tissue chamber (adipocytes not shown for better visibility of SVF) (ii; orthogonal view). Moreover, a tracking of SVF motion within the first 6 h after injection revealed dynamic migration for some of the labelled cells while others remained stationary (ii; video). Scale bars equal 200  $\mu\text{m}$  (one-chamber view) and 100  $\mu\text{m}$  (zoomed-in orthogonal view and video). (c) Monitoring of FA trafficking properties for A, AS and AE systems uncovered noticeable differences in FA uptake comparing A and AS to AE. Representative images of A and AE conditions at time points 0 min, 10.5 min, 38.5 min and 52.5 min. (d) Comparison of adipokine release by different co-/multi-culture WAT-on-chips from the same patient, measured from media effluents collected for 24 h from d10 to d11 of on-chip culture. Even though the analyzed adipokines are exclusively produced by adipocytes, there were considerable differences in their release regarding the models' cellular composition. (e) Identification of on-chip ATMs by visualizing CD11c and Trem2 (i), CD86 and CD45 (ii) and CD206 and CD45 (iii) expression. Lipid scavenging properties and formation of crown-like structures were visualized. Z-stack imaging data are represented as videos to ensure full elucidation of all events in one stack. Frames of videos are individual planes of acquired Z-stacks. Scale bars equal 50  $\mu\text{m}$ .

To further enhance the physiological relevance of our model, we sought to integrate stromovascular cells in addition to the adipocytes and endothelial barrier. The SVF is a dynamic, heterogeneous cell population with variable degrees of maturity and varying functions. It is the sum of all adipose tissue nucleated cells except for adipocytes themselves, and it includes mesenchymal stem cells, adipocyte and vascular progenitors, mature vascular cells as well as fibroblasts and various types of immune cells. Since the cellular composition was reported to change greatly when culturing and passaging SVF (Nunes et al., 2013; Sun et al., 2019; Szöke et al., 2012), we injected the cells together with the adipocytes the day after isolation.

Notably, combining patient-specific adipocytes and mvECs presented a bigger logistical challenge: while adipocytes cannot be cultured properly in conventional cell culture formats and need to be injected into the microfluidic platform within 24 h after isolation, the mvEC yield after isolation is not sufficient for prompt injection. Instead, mvECs need to be expanded and purified from other cell types, such as fibroblasts, in adherent cell culture for at least seven days. Therefore, adipocytes were (co-)cultured with or without SVF/CD14<sup>+</sup>-cells on-chip for one week before ECs were set for seeding on d7 (figure 7, Materials and Methods section).

We created a physiologically relevant, autologous *in vitro* model of human WAT by integrating adipocytes, SVF and mvECs, all derived from the same tissue donor. To provide a fit-for-purpose model that allows researchers to choose the cell types of interest and the level of complexity depending on the actual research question, we established the following co- and multi-culture models (figure 5a): adipocyte-only systems (culture condition hereinafter dubbed "A"), adipocyte-endothelial co-culture systems ("AE"), adipocyte-SVF multi-culture systems ("AS") and adipocyte-SVF-endothelial multi-culture systems ("ASE"). Due to the high importance of adipose-immune interactions, we further established a method to build adipocyte-CD14<sup>+</sup> cell co-culture systems ("AM") to enable directed studies on adipocyte-monocyte/macrophage crosstalk. To characterize the various co- and multi-culture WAT models, we analyzed on-chip viability, physiological structure, cytokine release as well as FA trafficking properties.

The platform was able to maintain good overall viability of all cell types for at least 12 days of on-chip culture, as demonstrated by low LDH release into the media effluents (figure S1).

To confirm a physiological tissue structure, we fluorescently stained and imaged an ASE-chip after 12 days of on-chip culture (figure 5b). Endothelial cells – marked by an anti-CD31 staining – formed an interconnected monolayer (figure 5bi), comparable to our endothelial-only experiments (figure 4a). Adipocytes in the ASE chip also displayed large unilocular lipid droplets indicating preservation of adipocyte maturity. Because of their heterogeneity, there is no single specific marker to identify SVF. The location of the stromovascular cells could, nevertheless, be monitored by labelling them with a cell tracker prior to injection, demonstrating a homogeneous distribution across the tissue chamber among the adipocytes (figure 5bii). Moreover, tracing of SVF migration on-chip for 6 h after injection revealed

16

bioRxiv preprint doi: <https://doi.org/10.1101/2021.08.08.455559>; this version posted August 8, 2021. The copyright holder for this preprint (which was not certified by peer review) is the author/funder, who has granted bioRxiv a license to display the preprint in perpetuity. It is made available under aCC-BY-NC-ND 4.0 International license.

Human immunocompetent WAT-on-chip  
Rogal et al. 2021

that some cells moved dynamically throughout the tissue chamber while most cells appeared to have settled in defined locations, pointing to the heterogeneity in function (figure 5bii video).

Characterization of FA transport properties via the BODIPY-C<sub>12</sub> FA uptake assay showed similar uptake rates between A and AS conditions. The AE systems, however, displayed a noticeably (approx. 50%) lower fluorescence intensity (figure 5c), hinting at a lower FA uptake and/or actively controlled transport through the EC barrier. From the results of the EC barrier integrity characterization using a 4 kDa FITC-dextran (10x bigger than the BODIPY-C<sub>12</sub> FA analog; figure 4b), a convergence of fluorescence intensity signals would have been expected within the duration of the assay, assuming comparable intracellular FA uptake by adipocytes across the three conditions and merely passive transendothelial transport of the BODIPY-C<sub>12</sub> FA analog. Yet, after 50 min, the fluorescence intensity signal for AE was still at approx. 50% of the one for A and AS. This suggests that either the FA uptake is downregulated by the interaction of ECs and adipocytes or that the endothelial-mediated FA transport is not passive, diffusive transport but an actively controlled process. Indeed, in its function as metabolic gatekeeper, the endothelium is presumed to actively adjust its barrier function in order to regulate FA and lipoprotein transport by involving a complex signaling machinery (Mehrotra et al., 2014; Pi et al., 2018). Furthermore, in line with previous reports (Gogg et al., 2019), the increased background fluorescence signal for the AE condition, as compared to A/AS, indicates an uptake of FAs by ECs.

Next, we compared the adipokine (adiponectin, leptin, adiponectin and RBP4) release from four different culture systems (figure 5c). Interestingly, the ASE condition showed the highest release for all four adipokines. On the contrary, for AE and A, adipokine release was overall much lower than for ASE: adiponectin and leptin release was hardly detectable while adiponectin and RBP4 levels were only approx. 8-10% and 35-45%, respectively. This outcome highlights how crucial the contribution of the other cell populations in adipose tissue is to adipocyte function and how important it is to integrate them to model adipose tissue: each of the analyzed factors has been reported to be predominantly produced by adipocytes (except for RBP4, which is also produced by hepatocytes); no other adipose-associated cell type was described to release any of the four cytokines in significant amounts (Scheja and Heeren, 2019). Hence, given the four adipokines are indeed exclusively secreted by the adipocytes, the increase in secretion for the ASE condition stems from the interaction of the adipocytes with the other cell types.

Finally, we established an adipose-on-chip model that integrates solely adipocyte and macrophages (AM) amenable for studies specifically targeted at the interaction of these two cell types. We visualized immune cell phenotypes on d5 after injecting a mixture of adipocytes and CD14<sup>+</sup> cells isolated from patient-specific SVF (figure 5e). CD14 is a co-receptor to the LPS receptor and is strongly expressed on monocytes and macrophages. Adipose tissue macrophages (ATMs) exhibit a great phenotypic plasticity, that is much more complex than the binary M1/pro-inflammatory- vs. M2/anti-inflammatory classification and include populations such as metabolically activated ATMs (MMe) or oxidized ATMs (Mox) (Yunjia Li et al., 2020; Russo and Lumeng, 2018). Additionally, a new subset of lipid-associated macrophages (LAMs), highly expressing the lipid receptor Trem2, was found in adipose tissue from obese humans. Trem2 was discovered to be essential for LAMs to exert their protective functions such as counteracting adipocyte hypertrophy and inflammation. (Jaitin et al., 2019) Moreover, many macrophages have a mixed activation state and harbor both M1 and M2 markers, such as the hybrid CD11c<sup>+</sup> (classically M1) CD206<sup>+</sup> (classically M2) ATMs associated with insulin resistance (Wentworth et al., 2010).

After five days of on-chip culture, we could observe ATMs in the tissue expressing the commonly occurring markers of human ATMs CD11c, CD206 as well as CD86, the general leukocyte marker CD45 as well as LAM-specific marker Trem2 (figure 5e). The ATMs were positioned in 3D among the adipocytes with clusters of ATMs frequently attaching to individual adipocytes or even wrapping around them as crown-like structures (e.g., video 5e). Visualization of lipid droplets via both neutral lipid staining and bright field microscopic imaging, moreover, revealed an uptake of lipids by ATMs indicating a lipid scavenging activity (e.g., video 5e). We also investigated monocyte/macrophage phenotypes under inflammatory stimulation: Via immunofluorescence staining, we did not observe any obvious differences in ATM marker expression between the stimulation conditions (LPS, TNF- $\alpha$ , NT). Effluent analysis with respect to secretion of

bioRxiv preprint doi: <https://doi.org/10.1101/2021.08.08.455559>; this version posted August 8, 2021. The copyright holder for this preprint (which was not certified by peer review) is the author/funder, who has granted bioRxiv a license to display the preprint in perpetuity. It is made available under aCC-BY-NC-ND 4.0 International license.

Human immunocompetent WAT-on-chip  
Rogal et al. 2021

pro-inflammatory cytokines, however, revealed an upregulation of several typical pro-inflammatory cytokines during TNF- $\alpha$  or LPS treatment (figure S5).

This capacity of the model to integrate ATMs is of particular importance, since with WAT's recognition as an endocrine, immunoregulatory organ, adipose tissue immune cells, specifically ATMs, have become a prominent research topic. As described above, ATMs are extremely plastic and adapt to different adipose tissue physiological states. In the healthy state, they regulate tissue homeostasis while in diseased conditions, such as obesity, ATMs play a major role in the low-grade, chronic inflammation and dysregulated metabolism (Caslin et al., 2020). Their tasks are as multifaceted as their appearance, but one of the main ATM functions seems to be engulfing dead adipocytes. Being under severe metabolic stress predisposes hypertrophic adipocytes to pyroptosis (i.e., a pro-inflammatory form of programmed cell death), a process attracting macrophages (Giordano et al., 2013). Aside from ingesting entire cells, ATMs are attributed to fulfill substrate buffering activities: Given their ability to handle variable substrate loads throughout their lifetime, ATMs can incorporate lipids, catecholamines and iron to modulate the availability of and protect other cell types from a surplus of these substances in the adipose tissue microenvironment (Caslin et al., 2020; Caspar-Bauguil et al., 2015).

There is also evidence for an active, direct crosstalk between adipocytes and ATMs. Adipocyte-derived FAs are an important modulator of macrophage metabolism; for instance, ATM uptake of FAs was found to be coupled to lysosome biogenesis (Xu et al., 2013). Moreover, adipocytes were found to release exosome-sized, lipid-laden vesicles (AdExos) that were found to induce a differentiation of macrophage precursors into ATMs. Hence, AdExos might not only be an alternative lipid release mechanism from adipocytes but also a directed technique for adipocytes to modulate macrophage function. (Flaherty et al., 2019) Another important example of adipocyte-macrophage crosstalk is the recently discovered intercellular transfer of mitochondria: in an *in vivo* rodent study, mitochondria were found to be transferred from adipocytes to neighboring macrophages, potentially to support the survival of metabolically compromised cells (Brestoff et al., 2021).

While adipocytes' dysregulated metabolism still appears to be the main drivers of WAT immune responses (Morigny et al., 2021), ATM contributions should not in the least be disregarded; their close and manifold crosstalk with the adipocytes still makes them key players of all adipose-associated pathologies and therefore a potential therapeutic target. Here, we have shown that our WAT-on-chip model can incorporate ATMs that maintain physiological phenotypes even after five days of on-chip culture and recapitulate key ATM functions such as scavenging lipids and phagocytosing adipocytes and thereby serve as a powerful platform to further enlighten adipocyte-ATM interactions.

Human immunocompetent WAT-on-chip  
Rogal et al. 2021

**Immunocompetency of the WAT-on-chip**

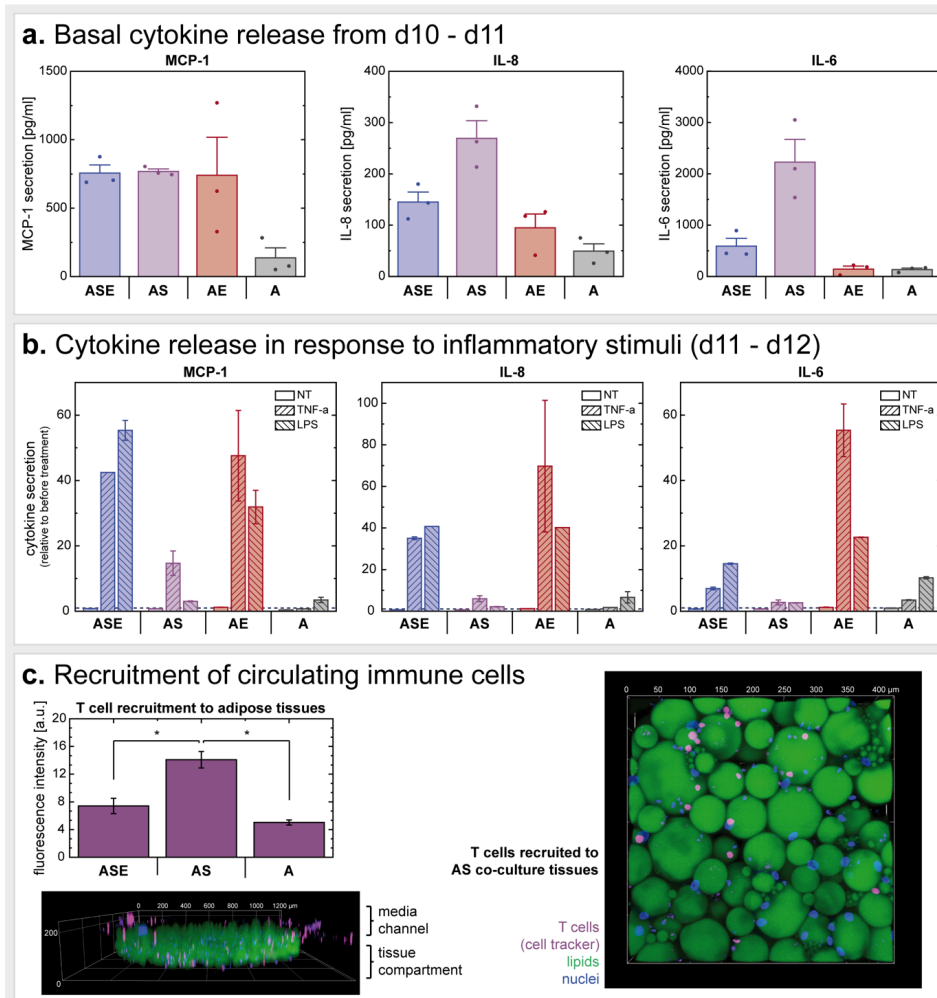


**Figure 6.** Immunocompetency of different WAT-on-chip culture conditions. (a) Baseline (i.e., non-stimulated) cytokine release from culture conditions ASE, AS, AE and A measured for 24 h from d10-d11. (b) Cytokine release in response to pro-inflammatory challenge (with TNF- $\alpha$  or LPS) for 24 h from d11-d12 on-chip. Cytokine concentrations are presented relative to the respective baseline cytokine release for each individual chip. (c) Recruitment of autologous T-cells perfused through the media channels for 18 h from d12-d13 of on-chip culture. Prior to perfusion, T cells were labeled with a cell tracker. Within the 18 h, T cells infiltrated the tissue chambers from the media channels, shown exemplarily in 3D renderings of an entire tissue chamber (side view) and of a zoom-in (top view). Recruitment was quantified by comparing fluorescence intensity in the tissue chambers (unpaired t test with  $p$ -value  $\leq 0.05$ ). Both fluorescence images show T-cell recruitment into AS chambers. All experiments were conducted simultaneously and with cells from the same donor.

After verification of the WAT-chip's suitability to integrate macrophages, we expanded experiments on immunocompetency by elucidating immunomodulatory cytokine release and responsiveness to inflammatory threats. As already addressed, on-chip adipocytes and endothelial barriers respond to TNF- $\alpha$  as well as LPS stimulation by ramping up their release of pro-inflammatory cytokines (figures 3c and 4cii). Here, we examine the participation of (i) the other adipose tissue components and (ii) intercellular crosstalk in immune responses. Intriguingly, we already

bioRxiv preprint doi: <https://doi.org/10.1101/2021.08.08.455559>; this version posted August 8, 2021. The copyright holder for this preprint (which was not certified by peer review) is the author/funder, who has granted bioRxiv a license to display the preprint in perpetuity. It is made available under aCC-BY-NC-ND 4.0 International license.

Human immunocompetent WAT-on-chip  
Rogal et al. 2021

registered differences in basal (i.e., unstimulated) cytokine release between the different culture modes although all cells for all modes were derived from the same donor to maximize comparability (figure 6a). Generally, cytokine expression was lowest from adipocyte-only chips, indicating major contributions of the other adipose tissue-associated cells. While the MCP-1 concentration was comparable between ASE, AS and AE, IL-8 and IL-6 concentrations were highest for AS. It is surprising that the interleukin secretion from ASE is lower than the secretion from AS, since ASE contains the same number of adipocytes and SVF as the AS condition. This points to a damping impact of EC presence regarding IL-6 and IL-8 release into the medium compartment in the ASE condition and might be an example of the necessity for a holistic view when modeling intercellular communication. Overall, the measured cytokine concentrations fall in the same range as determined for other *in vitro* studies. WAT is a main source of circulating IL-6, with an about 35% contribution to basal circulating IL-6 (Wueest and Konrad, 2020). Besides adipocytes, adipose-derived mesenchymal stem cells were previously found to produce loads of IL-6, too (Blaber et al., 2012); hence, the elevated IL-6 release for the ASE and AS on-chip conditions is not surprising. While IL-6 has a context-dependent role and can act both pro- and anti-inflammatory, IL-8 and MCP-1 secretion is usually associated with inflammation and obesity (Cimini et al., 2017; Kim et al., 2006). Surprisingly, we still detected a basal release of both cytokines in the supposedly 'healthy' condition, which could lead back to the tissue origin – fat-removal procedures often occur in case of donor obesity. However, when adding external inflammatory stimuli their secretion was massively (up to 70-fold) increased (figure 6b). Hence, it remains obscure whether the registered 'basal' cytokine release is already, to some extent, shifted into an inflammatory state due to an obesogenic ground state of donor cells, or whether IL-8 and MCP-1 are released from adipose tissue in moderation in a healthy state as well.

As anticipated, in response to proinflammatory stimulation, cytokine release was upregulated in all culture conditions in comparison to non-treated systems (figure 6b). The increase of cytokine secretion relative to the 24 h period before treatment is highest for the ASE and particularly AE conditions implying a strong involvement of ECs to the inflammatory reaction. Moreover, the ASE and A chips appeared to respond stronger to the LPS treatment while AS and AE tended to release higher concentrations of the cytokines when stimulated with TNF- $\alpha$ . Notably, the temporal resolution of cytokine measurement in response to stimulation (here 24 h) could in the future be increased by sampling effluents, e.g., every 30 min to capture secretion kinetics.

Finally, we evaluated the suitability of our WAT-on-chip platform for studying immune cell perfusion and recruitment to adipose tissue. From d12-d13, autologous CD3/CD28 co-stimulated and fluorescently labelled T cells were perfused through the media channels of different adipose tissue culture mode chips for 18 h (figure 6c). By confocal imaging, we could confirm the infiltration of cell tracker-labelled cells into the adipose tissue compartment. This analysis indicated a significantly higher recruitment to the AS condition compared to both ASE multi-culture chips and A culture chips. A potential reason for this finding might be the elevated IL-8 and IL-6 release we registered from the AS cultures; both interleukins were shown to locally mediate T cell attraction (Bruun et al., 2001; McLoughlin et al., 2005; Taub et al., 1996; Weissenbach et al., 2004).

Additionally, we investigated the recruitment of PBMC-derived CD14<sup>+</sup>-cells to on-chip adipocytes upon perfusion through the media channels. While perfused CD14<sup>+</sup>-cells were not able to transmigrate through 3  $\mu$ m pore-sized membranes, we were able to register scarce CD14<sup>+</sup>-cell infiltration into adipocyte-only systems when using 5  $\mu$ m pore-sized membranes instead (figure S6). A potential reason for the low recruitment compared to T cell recruitment might be that the chemotactic cues produced by adipocytes were too low to attract monocyte-masses. However, these are just preliminary findings, and they would require more in-depth analysis.

Generally, these findings show that our platform is well suited to recapitulate T cell infiltration into adipose tissue. Importantly, it is not only the tissue-resident immune cells that seem to provide the necessary chemotactic cues; mature adipocytes themselves were able to attract T cells, too, which is in line with previous findings (Poloni et al., 2015). Incorporating T cells in adipose tissue models is of importance since T cells were recently discovered to play a major role in immunometabolism. WAT has been implicated in serving as a reservoir for tissue-resident memory T cells, which have distinct functional and metabolic profiles (Han et al., 2017). Furthermore, obesity has been associated

bioRxiv preprint doi: <https://doi.org/10.1101/2021.08.08.455559>; this version posted August 8, 2021. The copyright holder for this preprint (which was not certified by peer review) is the author/funder, who has granted bioRxiv a license to display the preprint in perpetuity. It is made available under aCC-BY-NC-ND 4.0 International license.

Human immunocompetent WAT-on-chip  
Rogal et al. 2021

with increased T cell populations, particularly adaptive CD8<sup>+</sup> T cells, residing in WAT (Wang et al., 2021). Obesity might cause adipose tissue T-cell exhaustion (Porsche et al., 2021) and lead to unusual, T-cell mediated pathogenesis upon infection (Misumi et al., 2019).

### **Conclusion**

Here, we introduce, to the best of our knowledge, the first human, fully autologous immunocompetent WAT-on-chip platform integrating almost all in vivo WAT-associated cell types in mature states. Given the high complexity and associated logistical requirements, which accompany a full WAT in vitro model, we propose a mix-and-match WAT-on-chip toolbox that allows researchers to build a flexible, fit-for-purpose platform. As key component, mature human adipocytes are combined with patient-specific stromovascular cells, endothelium and/or different types of immune cells. The developed system enables long-term culture of human WAT in vitro while it preserves key functional features of not only adipocytes but at all other WAT-associated cellular components. More precisely, the system enabled a preservation of mature phenotypes alongside key responsibilities such as energy storage and mobilization functions, and basal endocrine activity. We further confirmed the on-chip WAT's drug- and inflammatory responsiveness, and suitability for studies on immune cell infiltration.

The system is based on a specifically tailored microfluidic platform integrating several injection and on-chip culture features, such as the sequential loading and shielding from shear stress, that make it particularly favorable for the integration of human WAT. Thereby, the system is well equipped to overcome two major difficulties arising from working with human mature adipocytes: buoyancy and fragility. In the future, technological refinements could aim at scale-up and sensor integration: To achieve parallelized platforms with increased throughput, a combination with enabling technologies might be worthwhile; e.g., the WAT-on-chip design could be transferred to the organ-on-disc platform (Schneider et al., 2020; Stefan Schneider et al., 2021). To enable in-line monitoring of adipose tissue secretions, on-chip sensors based on different technologies could be integrated (Fuchs et al., 2021; Hu et al., 2020; Zhu et al., 2018, 2021).

To set up the WAT model, we established protocols and processes that allow to source all the different cell types from one individual donor; more specifically, from tissue samples of subcutaneous adipose tissue with skin that are readily available in most hospitals. The choice of a human cell source is an integral part for human-centered research. Even though findings from animal models have shed light into many aspects of WAT (patho-)physiology in the past, they are stretched to their limits regarding human-relevant mechanisms with increasing frequency. Despite efforts on humanization of animal models, there are still dominant discrepancies between rodents and humans, especially when it comes to studying metabolism and functioning of the immune system (Greek and Menache, 2013; Mestas and Hughes, 2004; van der Worp et al., 2010). Moreover, the capability to isolate all cell types from one individual, the bottom-up approach of tissue generation and the microscopic footprint of the WAT-on-Chip, enable not only fully autologous models but also the creation of a large number of tissue models from one donor; the latter allows circumventing the challenge of inter-donor differences as well as the study of patient-specific WAT responses, paving the way for future applications in personalized medicine.

When addressing patient-specificity, an aspect that is of particular interest is the immune system, which is closely interwoven with adipose tissue biology. Here, the autologous character of our WAT-on-Chip is of notable relevance especially when studying the adaptive immune system. The findings on WAT immunomodulatory functions on-chip back the suitability of our platform for research on adipose tissue inflammation and its underlying mechanisms. Especially the precisely controllable administration of inflammatory agents and the potential for highly time-resolved readouts of tissue response make our platform a powerful tool to study immune responses.

Besides demonstrating its competency to build a WAT-on-chip with highest physiological relevance integrating almost all cell types existing in in vivo WAT, we introduced a modular WAT-on-chip toolbox. When deciding on a suitable model for probing a specific scientific question, the rule should always be "as simple as possible but as complex as necessary". In other words, the full WAT-on-chip model might be too complex for certain questions, and complexity

21

---

bioRxiv preprint doi: <https://doi.org/10.1101/2021.08.08.455559>; this version posted August 8, 2021. The copyright holder for this preprint (which was not certified by peer review) is the author/funder, who has granted bioRxiv a license to display the preprint in perpetuity. It is made available under aCC-BY-NC-ND 4.0 International license.

Human immunocompetent WAT-on-chip  
Rogal et al. 2021

might generate noise and off-target signals. The modular approach allows for an adjustable degree of complexity and enables end users to select those cellular components required for their specific question creating a fit-for-purpose, customized WAT-on-chip. For proof-of-principle, we characterized several combinations of mature adipocytes with stromovascular cells, ECs, and tissue-resident innate immune cells. Interestingly, we did not encounter any differences in adipocytes' phenotype or energy storage function when comparing the different multi-culture conditions, but their endocrine function appeared to be strongly impacted by the co-culture with other cell types. Adipokines, presumably exclusively produced by adipocytes themselves, were found in highest concentrations in the full WAT model – notably higher than in the adipocyte-only condition. Furthermore, we found the response to proinflammatory threats modulated by influence of other adipose tissue-associated cells. Overall, the outcome of our study indicates that the full WAT model with all in vivo components indeed reflects adipocyte endocrine function best.

In conclusion, our novel WAT-on-chip system provides a human-based, autologous and immunocompetent in vitro model of WAT. It recapitulates almost full tissue heterogeneity by integrating not only mature adipocytes but also organotypic endothelial barriers and stromovascular cells, with optional separation of tissue-resident innate immune cells, specifically ATMs. Therefore, the new WAT-on-chip model can be a powerful tool for future, human-relevant research in the field of metabolism and its associated diseases as well as for compound testing and personalized- and precision medicine applications.

## Materials and methods

### Chip fabrication and characterization

#### Chip design and dimensions

The microfluidic platform used for integrating human WAT and associated immune components is a custom-made device consisting of two layers of micro-patterned polydimethylsiloxane (PDMS; Sylgard 184, Dow Corning, USA) sandwiching an isoporous, semipermeable polyethylene terephthalate (PET)-membrane (3  $\mu\text{m}$  poresize:  $r_p = 3 \mu\text{m}$ ;  $\rho_p = 8 \times 10^5$  pores per  $\text{cm}^2$ ; TRAKETCH<sup>®</sup> PET 3.0 p S210  $\times$  300, or 5  $\mu\text{m}$  poresize:  $r_p = 4.6 \mu\text{m}$ ;  $\rho_p = 0.6 \times 10^5$  pores per  $\text{cm}^2$ ; TRAKETCH<sup>®</sup> PET 5.0 p S210  $\times$  300, SABEU GmbH & Co. KG, Northeim, Germany). While the lower micro-patterned PDMS layer accommodates human WAT, the upper PDMS-layer, separated from the lower one by the membrane, serves as media compartment for constant media perfusion. To assure best optical accessibility of the tissues, the tissue compartment is secured to a glass coverslip (AN-21-000627; 25 mm  $\times$  75 mm, thickness 1, Langenbrinck GmbH, Emmendingen, Germany). The architecture of the microstructures in the PDMS layers was specifically designed to house human mature adipocytes, and it was drafted using CorelCAD [Corel Corporation, Ottawa, Ontario, Canada]. Table 1 and figure 2a provide an overview of the most important chip dimensions and resulting volumes.

**Table 1: Dimensions of microfluidic WAT-on-chip platform.**

Tissue compartment		
Entire compartment	Area [ $\text{mm}^2$ ]	21.59
	Volume [ $\mu\text{l}$ ]	2.80
Dimensions of one chamber	Radius [mm]	0.50
	Area [ $\text{mm}^2$ ]	0.79
	Height [mm]	0.20
	Volume [ $\mu\text{l}$ ]	0.16
Sum of eight chambers	Area [ $\text{mm}^2$ ]	6.28
	Volume [ $\mu\text{l}$ ]	1.26
Media compartment		
Entire compartment	Area [ $\text{mm}^2$ ]	39.81
	Height [mm]	0.10
	Volume [ $\mu\text{l}$ ]	3.98

#### Chip fabrication by soft lithography and replica molding

The microfluidic platforms were fabricated using the soft lithographic as well as replica molding protocols described in our previous publications (Loskill et al., 2017; Rogal et al., 2020, 2021). In brief, media channel- and tissue chamber microstructures in the PDMS layers were generated by using two differently patterned master wafers functioning as positive molding templates. These master wafers were produced by common soft lithography techniques first introduced by Xia and Whitesides (Xia and Whitesides, 1998). To achieve different heights for injection channels and tissue chambers in the tissue compartment layer, or a membrane inlay with media channel on top in the media compartment layer, respectively, each of the two master wafers was fabricated in two consecutive patterning steps. We recently described our procedures for a two-step master wafer fabrication in detail (Rogal et al., 2021). The PDMS layers were then generated by deploying two different replica molding techniques: (i) To create thin tissue layers with chambers and injection port structures opened to both sides, we used a technique called ‘exclusion molding’. By placing a release liner [Scotchpak™ 1022 Release Liner Fluoro- 94 polymer Coated Polyester Film; 3M, Diegem, Belgium] onto the uncured PDMS on the wafer and applying uniform pressure onto the construct, curing of the PDMS resulted in 200  $\mu\text{m}$ -high PDMS layers, as defined by the 200  $\mu\text{m}$  tissue chamber height. Consequently, microstructures were open to both sides. (ii) The PDMS layer patterned with the media compartment was generated by standard replica molding; the amount of PDMS yielding a layer of approximately 5 mm was poured onto the master wafer and released after curing. Then, the PDMS slabs resulting from the molding processes were cut to the size of the chip and ports to access the chips were pierced using a biopsy punch (Disposable Biopsy Punch, 0.75 mm diameter; 504529; World

bioRxiv preprint doi: <https://doi.org/10.1101/2021.08.08.455559>; this version posted August 8, 2021. The copyright holder for this preprint (which was not certified by peer review) is the author/funder, who has granted bioRxiv a license to display the preprint in perpetuity. It is made available under aCC-BY-NC-ND 4.0 International license.

Human immunocompetent WAT-on-chip  
Rogal et al. 2021

Precision Instruments, Friedberg, Germany). To enable O<sub>2</sub>-plasma-based bonding of the PET-membrane, commercially available membranes were functionalized by a plasma-enhanced, chemical vapor deposition (PECVD) process (Rogal et al., 2020). In a three-step O<sub>2</sub>-plasma activation- (each 15 s, 50 W, 0.2 cm<sup>3</sup>m<sup>-1</sup> O<sub>2</sub>; Diener Zepto, Diener electronic GmbH + Co. KG, Ebhausen, Germany) and bonding sequence, the chip was assembled: (i) bonding of exclusion-molded tissue compartment layer to a glass coverslip, (ii) bonding of functionalized PET-membrane into membrane inlay of media compartment layer, and (iii) full chip assembly by bonding the media compartment layer with membrane to the tissue compartment layer on the coverslip. To enhance bonding, the assembled chips were kept at 60°C overnight. To assure quality of bonding, chips were then flushed with DI-water and observed for any leakages or discontinuities in liquid flow. One day prior to cell injections, the chips were sterilized and hydrophilized by a 5-minute O<sub>2</sub>-plasma treatment. Under sterile conditions, they were then filled with PBS<sup>-</sup> and kept overnight fully immersed in Dulbecco's phosphate buffered saline without MgCl<sub>2</sub> and CaCl<sub>2</sub> (PBS<sup>-</sup>; Merck KGaA) to allow for any residual air to evacuate from the channel system.

### Numerical modeling

To model fluid flow, its associated shear forces as well as transport of diluted species, we used COMSOL Multiphysics (COMSOL Vers.5.5, Stockholm, Sweden). The numerical model was based on simulations we previously published for our murine as well as our precursor adipocyte-on-chip models (Loskill et al., 2017; Rogal et al., 2020). In brief, we coupled the Free and Porous Media Flow and Transport of Diluted Species in Porous Media physics modules. We included the presence of hydrogel in the tissue compartment for all simulations since it significantly affects the convective and diffuse flow regimes. We used the Navier-Stokes equation with the properties of water (dynamic viscosity  $\mu = 1 \times 10^{-3}$  m<sup>2</sup>/s, density  $\rho = 1000$  kg/m<sup>3</sup>) to model incompressible stationary free fluid flow at a general flow rate of 20  $\mu$ l/h (equivalent to a flow rate of 2.5  $\mu$ l/h in each of the eight parallel media channels over the tissue chambers). To model fluid flow from the media channel through the porous PET-membrane into the tissue chamber as well as through the hydrogel, Darcy's law was used (membrane - porosity = 0.056, hydraulic permeability  $\kappa = 1.45 \times 10^{-14}$  m<sup>2</sup>; hydrogel - porosity = 0.99, hydraulic permeability  $\kappa = 1.5 \times 10^{-16}$  m<sup>2</sup> (McCarty and Johnson, 2007)). Using the time-dependent convection-diffusion with diffusion coefficients of  $1 \times 10^{-9}$  m<sup>2</sup>/s (water) and  $1 \times 10^{-11}$  m<sup>2</sup>/s (hydrogel) and an initial concentration of 1 mol/m<sup>3</sup>, we described transport of diluted species.

### ***Isolation and culture of primary adipose tissue- and blood-derived cells***

#### Human tissue samples

All cell types [i.e., adipocytes ('A'), cells from SVF ('S'), microvascular endothelial cells ('E'), different types of immune cells (CD14<sup>+</sup>-cells, i.e., monocytes/macrophages 'M', and PBMCs activated towards T-cells 'T')] used in experiments for this publication are human primary cells which were isolated from subcutaneous skin biopsies and donor-specific blood samples. In case of co- and multi-cultures, experiments were always conducted in an autologous manner. Table 2 provides an overview of patient demographics and relevant medical records. Weight statuses were ranked according to World Health Organization (World Health Organization, n.d.).

**Table 2. Overview of cell source and donor demographics itemized per experiment.**

Figure	Donor sex	Donor age	Source of biopsy	BMI at time of surgery	Weight status according to WHO	BMI at highest	Weight status according to WHO	Diagnosed metabolic disease (incl. diabetes)
3a morphology	F	39	Thigh	29.33	Pre-obese	N/A	N/A	N/A
3b i MCFAs/LCFA uptake	F	30	Abdomen	23	Normal	44.9	Obesity class III	Not diagnosed
3b i glucose-dependent FA uptake	F	57	Upper arm	31.2	Obesity class I	58.3	Obesity class III	Not diagnosed

24

bioRxiv preprint doi: <https://doi.org/10.1101/2021.08.08.455559>; this version posted August 8, 2021. The copyright holder for this preprint (which was not certified by peer review) is the author/funder, who has granted bioRxiv a license to display the preprint in perpetuity. It is made available under a [CC-BY-NC-ND 4.0 International license](#).

Human immunocompetent WAT-on-chip  
Rogal et al. 2021

3b i glycerol release over time donor 1	M	33	Gluteal	21	Normal	N/A	N/A	Not diagnosed
3b i glycerol release over time donor 2	F	29	Inner thigh	29.71	Pre-obesity	N/A	N/A	Not diagnosed
3b i glycerol release over time donor 3	F	48	Upper arm	40	Obesity class III	N/A	N/A	Not diagnosed
3b ii endocrine function & 3c donor 1	f	43	Abdomen	25.39	Pre-obesity	45.44	Obesity class III	Not diagnosed
3b ii endocrine function & 3c donor 2	F	43	Thigh	21	Normal	N/A	N/A	Not diagnosed
3b iii β-adrenergic stimulation FA release	F	57	Upper arm	31.2	Obesity class I	58.3	Obesity class III	Not diagnosed
3b iii β-adrenergic stimulation glycerol release	F	39	Thigh	29.33	Pre-obese	N/A	N/A	N/A
3c cytokine release donor 1	F	43	Abdomen	25.39	Pre-obesity	45.44	Obesity class III	Not diagnosed
3c cytokine release donor 2	F	43	Thigh	21	Normal	N/A	N/A	Not diagnosed
4 all data	F	53	Abdomen	29	Pre-obese	N/A	N/A	N/A
5bi ASE staining	F	50	Back	29.74	Pre-obese	61.01	Obesity class III	N/A
5bii SVF tracking	F	41	Abdomen	29	Pre-obese	29.74	Pre-obese	Not diagnosed
5c FA trafficking	F	37	Thigh	30.86	Obesity class I	57.52	Obesity class III	Not diagnosed
5e Trem2/CD11c	F	43	Thigh	21	Normal	N/A	N/A	Not diagnosed
5e CD45/CD86 CD45/CD206	F	42	Thigh	26	Pre-obese	N/A	N/A	N/A
6 all data	F	43	Thigh	21	Normal	N/A	N/A	Not diagnosed

Human subcutaneous skin and adipose tissue biopsies were obtained from plastic surgeries performed by Dr. Wiebke Eisler (BG Klinik Tübingen, Tübingen, Germany) and Dr. Ulrich E. Ziegler (Klinik Charlottenhaus, Stuttgart, Germany), approved by the local medical ethics committee: Patients gave an informed consent according to the permission of the "Landesärztekammer Baden-Württemberg" (No. 495/2018BO2 and F-2020-166). All procedures were carried out in accordance with the rules for medical research of human subjects, as defined in the Declaration of Helsinki. Collection of human whole blood samples was performed in accordance with the Declaration of Helsinki. Healthy blood donors and patients gave informed consent as approved by the Ethical Committee of the Eberhard Karls University Tübingen (No. 495/2018-BO02 for the isolation of PBMCs from whole blood).

Throughout the isolation, injection and chip culture processes, different cell-type specific cell culture media were used. All media, except for the endothelial cell medium, are defined compositions. Table 3 provides an overview of the different types of cell culture media used for cell-type specific isolations, pre-chip and on-chip cultures.

**Table 3. Overview of different types of enzymatic digestion solutions and cell culture media used in this study.**

Name of solution/medium	Use	Ingredients
Adipose tissue digestion solution	- Digestion of adipose tissue for adipocyte and SVF isolation	DMEM/F-12 + 0.13 U/ml collagenase type NB4 + 1% (w/v) BSA

bioRxiv preprint doi: <https://doi.org/10.1101/2021.08.08.455559>; this version posted August 8, 2021. The copyright holder for this preprint (which was not certified by peer review) is the author/funder, who has granted bioRxiv a license to display the preprint in perpetuity. It is made available under aCC-BY-NC-ND 4.0 International license.

Human immunocompetent WAT-on-chip  
Rogal et al. 2021

A wash medium	<ul style="list-style-type: none"> <li>- Wash adipocytes during isolation</li> <li>- Wash adipocytes prior to injection</li> </ul>	DMEM/F-12 + 100 U/mL Pen/Strep
A base medium	<ul style="list-style-type: none"> <li>- Overnight flask culture of adipocytes (A) between isolation and chip injection</li> </ul>	DMEM/F-12 (incl. glutamine) + 10% (v/v) FCS + 10 µM HEPES + 100 U/mL Pen/Strep
S/M base medium	<ul style="list-style-type: none"> <li>- Overnight flask culture of SVF/CD14<sup>+</sup> cells between isolation and chip injection</li> <li>- First seeding of PBMC-derived CD14<sup>+</sup>-cells</li> </ul>	<i>A base medium</i> + 10 ng/mL GM-CSF
Skin digestion solution	<ul style="list-style-type: none"> <li>- Digestion of dissected skin for mvEC isolation</li> </ul>	PBS+ 2.0 /mL Dispase II
mvEC expansion medium	<ul style="list-style-type: none"> <li>- Expansion of isolated mvECs in cell culture flask format</li> </ul>	ECGM + 10 mg/mL Gentamicin
PBMC culture medium	<ul style="list-style-type: none"> <li>- For PBMC thawing process</li> </ul>	X-VIVO™ 15 + 10% (v/v) autologous serum + 100 U/mL Pen/Strep
PBMC freezing medium	<ul style="list-style-type: none"> <li>- For freezing PBMCs after isolation</li> </ul>	10% (v/v) dimethylsulfoxid (DMSO) in FCS
PBMC thawing medium	<ul style="list-style-type: none"> <li>- Overnight plate culture of thawed PBMCs</li> </ul>	<i>PBMC culture medium</i> + 10 U/ml IL-2
T cell activation medium	<ul style="list-style-type: none"> <li>- In plate culture medium for activation of thawed PBMCs prior to chip loading</li> </ul>	<i>PBMC culture medium</i> + 1% (v/v) T Cell TransAct™ human
2X Monocyte/macrophage culture medium	<ul style="list-style-type: none"> <li>- Maintenance of PBMC-derived CD14<sup>+</sup> cells for 5 days</li> </ul>	<i>A base medium</i> + 20 ng/mL GM-CSF
A medium	<ul style="list-style-type: none"> <li>- On-chip cultures of adipocyte (A)-only chips</li> </ul>	<i>A base medium</i> + 60 nM Insulin + 100 nM Rosiglitazone
E medium	<ul style="list-style-type: none"> <li>- On-chip cultures of mvEC (E) layer-only chips</li> </ul>	ECGM + 100 U/mL Pen/Strep
E TNF-α stimulation medium	<ul style="list-style-type: none"> <li>- 24 h pro-inflammatory stimulation with TNF-α of mvEC (E) layer-only chips</li> </ul>	<i>E medium</i> + 20 ng/mL TNF-α
E LPS stimulation medium	<ul style="list-style-type: none"> <li>- 24 h pro-inflammatory stimulation with LPS of mvEC (E) layer-only chips</li> </ul>	<i>E medium</i> + 100 ng/mL LPS
AE co-culture medium	<ul style="list-style-type: none"> <li>- On-chip co-cultures of adipocytes (A) and endothelial layer (E)</li> </ul>	<i>A medium</i> : <i>E medium</i> 1:1
AS/AM co-culture medium	<ul style="list-style-type: none"> <li>- On-chip co-cultures of adipocytes (A) and SVF (S) or CD14<sup>+</sup>-cells (M)</li> <li>- Perfusion of monocytes</li> </ul>	<i>A medium</i> + 10 ng/mL GM-CSF
ASE multi-culture medium	<ul style="list-style-type: none"> <li>- On-chip multi-culture of adipocytes (A), endothelial layer (E) and SVF (S)</li> </ul>	<i>AE co-culture medium</i> + 10 ng/mL GM-CSF
A TNF-α stimulation medium	<ul style="list-style-type: none"> <li>- 24 h pro-inflammatory stimulation with TNF-α of adipocyte (A)-only chips</li> </ul>	<i>A base medium</i> + 20 ng/mL TNF-α
AS/AM TNF-α stimulation medium	<ul style="list-style-type: none"> <li>- 24 h pro-inflammatory stimulation with TNF-α of on-chip co-cultures of adipocytes (A) and SVF (S) or CD14<sup>+</sup>-cells (M)</li> </ul>	<i>A base medium</i> + 10 ng/mL GM-CSF + 20 ng/mL TNF-α

bioRxiv preprint doi: <https://doi.org/10.1101/2021.08.08.455559>; this version posted August 8, 2021. The copyright holder for this preprint (which was not certified by peer review) is the author/funder, who has granted bioRxiv a license to display the preprint in perpetuity. It is made available under a [CC-BY-NC-ND 4.0 International license](#).

Human immunocompetent WAT-on-chip  
Rogal et al. 2021

ASE TNF- $\alpha$ stimulation medium	- 24 h pro-inflammatory stimulation with TNF- $\alpha$ of on-chip multi-culture of adipocytes (A), endothelial layer (E) and SVF (S)	<i>A base medium:E medium</i> 1:1 + 10 ng/mL GM-CSF + 20 ng/mL TNF- $\alpha$
A LPS stimulation medium	- 24 h pro-inflammatory stimulation with LPS of adipocyte (A)-only chips	<i>A base medium</i> + 100 ng/mL LPS
AS/AM LPS stimulation medium	- 24 h pro-inflammatory stimulation with LPS of on-chip co-cultures of adipocytes (A) and SVF (S) or CD14 <sup>+</sup> -cells (M)	<i>A base medium</i> + 10 ng/mL GM-CSF + 100 ng/mL LPS
ASE LPS stimulation medium	- 24 h pro-inflammatory stimulation with LPS of on-chip multi-culture of adipocytes (A), endothelial layer (E) and SVF (S)	<i>A base medium:E medium</i> 1:1 + 10 ng/mL GM-CSF + 100 ng/mL LPS
T-cell perfusion medium	- Overnight perfusion of circulating immune cells	X-VIVO 15 + 100 U/mL Pen/Strep

### Isolation and pre-chip culture of mature adipocytes

Primary mature adipocytes were isolated from human skin and subcutaneous adipose tissue biopsies on the same day of surgery. We recently described our isolation process at length in a methodical book chapter (Rogal et al., 2021). In brief, the skin was separated from the subcutaneous adipose tissue and used for isolation of endothelial cells. The adipose tissue was then rinsed with Dulbecco's phosphate buffered saline with MgCl<sub>2</sub> and CaCl<sub>2</sub> (PBS<sup>-</sup>; Merck KGaA, Darmstadt, Germany) twice, and macroscopically visible blood vessels and connective tissue structures were carefully removed. The remaining adipose tissue was cut into small pieces of approximately 1 cm<sup>3</sup> and subsequently enzymatically digested by incubation in a collagenase solution (*adipose tissue digestion solution*) for 60 min at 37°C on a rocking shaker (50 cycles/min; Polymax 1040, Heidolph Instruments GmbH & CO. KG, Schwabach, Germany). Finally, the digested adipose tissue was strained through a mesh size of 500  $\mu$ m and washed three times with DMEM/F-12, no phenol red (21041025; Thermo Fisher Scientific Inc., Waltham, MA) with 100 U/mL Penicillin/Streptomycin (Pen/Strep) (*A wash medium*). For each washing step, adipocytes and medium were gently mixed, and left to rest for 10 min. After separation of the buoyant adipocytes and the medium, the liquid medium from underneath the packed layer of adipocytes was aspirated. Adipocyte isolation was performed on the day before injection into the chips. The freshly isolated adipocytes were cultured overnight, by adding equal volumes of packed adipocytes and *A base medium* to a culture flask kept in a humidified incubator at 37°C and a 5% CO<sub>2</sub> atmosphere.

### Isolation and pre-chip culture of mvECs

Human microvascular endothelial cells (mvECs) were isolated from resected skin from plastic surgeries. A piece of approximately 8 cm<sup>2</sup> was washed and submersed in Phosphate Buffered Saline without calcium chloride and magnesium chloride (PBS<sup>-</sup>; L0615; Biowest, Nuaille, France). Subcutaneous fat as well as big blood vessels were removed, and the remaining skin was cut in strips of approximately 4 cm length and 1 mm width and finally incubated in 10 ml *skin digestion solution* (2.0 U/mL dispase D4693, Merck KGaA, in PBS<sup>-</sup>) at 4°C overnight. The following day, the epidermis was peeled off using tweezers and the remaining strips of dermis were washed twice in PBS<sup>-</sup>. After a short incubation in Versene Solution (15040066; Thermo Fisher Scientific Inc.), dermis strips were incubated for 40 min in 0.05% Trypsin in EDTA Solution (59418C; SAFC) at 37 °C [trypsin reaction stopped by adding 10% Fetal Calf Serum (10326762; HyClone™, Cytiva Europe GmbH, Freiburg, Germany)] to loosen the cells from the tissue. The strips were transferred to the lid of a petri dish containing 10 mL pre-warmed PBS<sup>-</sup>. Processing each dermis strip at a time, the dissociated cells were scraped out with a scalpel. After each strip was scraped for at least 8 times, the resulting cell suspension was strained (mesh size 70  $\mu$ m) into a centrifuge tube and the petri dish lid was rinsed two more times with PBS<sup>-</sup>. To obtain a cell pellet, the cell solution in the centrifuge tube was centrifuged at 209 rcf for 5 minutes. The supernatant was discarded, and the pellet was resuspended in pre-warmed 10 mL Endothelial Cell Growth Medium (ECGM; C-22010, PromoCell GmbH, Heidelberg, Germany) with 10 mg/mL Gentamicin (*mvEC expansion medium*),

27

bioRxiv preprint doi: <https://doi.org/10.1101/2021.08.08.455559>; this version posted August 8, 2021. The copyright holder for this preprint (which was not certified by peer review) is the author/funder, who has granted bioRxiv a license to display the preprint in perpetuity. It is made available under aCC-BY-NC-ND 4.0 International license.

Human immunocompetent WAT-on-chip  
Rogal et al. 2021

seeded into two T25 cell culture flasks and incubated at 37°C, 5% CO<sub>2</sub> and 95% rH overnight. On the next day, dead cells and debris were washed off by rinsing with PBS<sup>-</sup> followed by addition of fresh *mvEC expansion medium*.

To remove fibroblasts from the expansion flask, the cells were washed with PBS<sup>-</sup> and incubated in Versene Solution at 37°C, 5% CO<sub>2</sub> and 95% rH until the fibroblasts detached. Following the aspiration of the Versene Solution, the cells were washed once again with PBS<sup>-</sup> and pre-warmed *mvEC expansion medium* was added. Versene treatment was repeated accordingly throughout the first days of culture when needed. Else, media was changed every 3 days until the cells were injected into the microfluidic platform.

To (i) achieve sufficient cell count for chip injection and to (ii) purify isolated mvECs from fibroblast contamination as described above, mvECs must be expanded in flask format for at least 6 days after isolation. For experiments on endothelial layer-only chips (no donor-specificity required), mvECs from one donor were cryopreserved and re-used for the whole series of the experiment.

#### Isolation and pre-chip culture of SVF

Stromal vascular fraction (SVF) was isolated from human subcutaneous adipose tissue biopsies on the same day of surgery. The adipose tissue sample was rinsed with PBS<sup>-</sup> twice, large blood vessels were carefully removed and then cut into small pieces of approximately 1 cm<sup>3</sup>. The adipose tissue pieces were then enzymatically digested by incubation in *adipose tissue digestion solution* (in equal volumes of adipose tissue and digestion solution) for 30 min at 37°C on a rocking shaker. After digestion, the tissue was passed through a strainer (mesh size: 500 µm) and left to rest for 10 min to allow for a separation of buoyant mature adipocytes, medium and non-buoyant cells. The packed layer of adipocytes was carefully aspirated, and the remaining cell suspension centrifuged for 5 min at 350 rcf. To lyse erythrocytes, supernatant was carefully decanted, and the cell pellet was gently re-suspended in Red Blood Cell Lysis Solution (freshly prepared according to manufacturer's instruction; 130-094-183; Miltenyi Biotec B.V. & Co. KG, Bergisch Gladbach, Germany) which was incubated for 3 min at room temperature. Then, the cell suspension was strained through a 100 µm mesh size, collecting the filtrate in a centrifuge tube, and centrifuged for 5 min at 350 rcf. After decanting the supernatant, the cell pellet was resuspended in *S/M base medium* and cells were counted using Trypan blue and a hemocytometer. Cells from the SVF were cultured overnight in flask format in *S/M base medium* (seeding density of ~1x10<sup>5</sup> cells/cm<sup>2</sup>) or directly sorted *via* MACS to isolate CD14<sup>+</sup>-cells.

#### Peripheral blood mononuclear cell (PBMC) isolation, freezing and autologous serum collection

Isolation of fresh human PBMCs was initiated within 1 h after blood collection using Histopaque<sup>®</sup> 1077 (10771; Merck KGaA) and standard density centrifugation (800 rcf, 20 min, no brakes). After centrifugation, PBMCs were washed twice in PBS<sup>-</sup> supplemented with 0.1% BSA and 2 mM EDTA. PBMCs were used directly for isolation of CD14<sup>+</sup>-cells or immediately frozen at 10x10<sup>6</sup> cells/mL in *PBMC freezing medium* using a CoolCell<sup>®</sup> Container (Corning).

For collection of autologous serum, whole blood was collected in S-Monovettes<sup>®</sup> containing serum gel with clotting activator (Sarstedt) followed by serum separation through centrifugation.

#### Isolation and pre-chip culture of CD14<sup>+</sup>-cells from SVF or PBMCs

CD14 is a co-receptor to the LPS receptor (lacking a cytoplasmatic domain, antibody binding, such as the MACS antibody, to CD14 alone does not provoke signal transduction) and is strongly expressed on monocytes and macrophages. To maintain cell identity and promote a monocyte-to-macrophage differentiation, we supplemented the cell culture medium with granulocyte-macrophage colony-stimulating factor (GM-CSF) for the entire culture period. CD14<sup>+</sup>-cells were isolated by magnetic activated cell sorting (MACS) with positive selection using CD14 MicroBeads (130-050-201; Miltenyi Biotec B.V. & Co. KG) from freshly isolated SVF or PBMCs according to supplier's instructions. In brief, MACS buffer was prepared freshly before each isolation by diluting MACS BSA Stock Solution (130-091-376; Miltenyi Biotec B.V. & Co. KG) 1:20 in autoMACS Rinsing Solution (130-091-222; Miltenyi Biotec B.V. & Co. KG). For degassing, the MACS buffer was sonicated for 10 min. Counted, freshly isolated cell suspension from SVF (cf. Isolation and pre-chip culture of SVF) or from PBMCs was centrifuged for 10 min at 350 rcf at 4°C to avoid activation

28

Human immunocompetent WAT-on-chip  
Rogal et al. 2021

of monocytes. Then, the supernatant was aspirated completely, and the cell pellet was resuspended in 80  $\mu$ l of MACS buffer and 20  $\mu$ l of CD14 MicroBeads per  $\leq 1 \times 10^7$  total cells. After incubating for 15 min at 4°C, the cells were washed by adding 2 ml of MACS buffer per  $\leq 1 \times 10^7$  total cells and centrifuged for 10 min at 350 rcf at 4°C. In the meantime, an LS column (130-042-401; Miltenyi Biotec B.V. & Co. KG) was placed into the magnetic field of an QuadroMACS Separator (130-090-976; Miltenyi Biotec B.V. & Co. KG) and primed by rinsing with 3 ml of MACS buffer. Flow-through was collected in a 15 ml centrifuge tube underneath the column. For separation, the cell pellet was resuspended in 500  $\mu$ l of MACS buffer per  $\leq 1 \times 10^8$  total cells and applied onto the column. Unlabeled cells were collected by subsequently washing the column by adding 3x 3 ml of MACS buffer. Then, the column was removed from the magnetic field and placed onto a new collection tube, 5 ml of MACS buffer were added onto the column, and magnetically labeled cells were flushed out by firmly pushing the plunger into the column. The cell suspension was centrifuged for 10 min at 350 rcf at 4°C. SVF-derived CD14<sup>+</sup>-cells were resuspended in *S/M base medium*, cells were counted and seeded at a density of  $\sim 1 \times 10^6$  cells/cm<sup>2</sup> for overnight culture. PBMC-derived CD14<sup>+</sup>-cells were resuspended in *S/M base medium* and cultured at a density of  $\sim 3 \times 10^5$  cells/cm<sup>2</sup>. Every two days, 50 % of medium was exchanged with *2X Monocyte/macrophage culture medium*.

#### Thawing of PBMCs and activation of T-cells prior to chip culture

To thaw frozen PBMCs, cryopreserved cells were shortly placed at 37 °C, resuspended in prewarmed *PBMC culture medium* (X-VIVO™ 15 medium (BE02-060F; Lonza Group AG, Basel, Switzerland) supplemented with 10% autologous serum and 100U/mL Pen/Strep), centrifuged and cultured at  $\sim 1.5 \times 10^6$  cells/cm<sup>2</sup> in *PBMC thawing medium* overnight. PBMCs were washed and cultured in *PBMC culture medium* at a density of 0.5 – 1x10<sup>6</sup> cells/mL in a total volume of 1 ml. CD3/CD28-mediated activation of T cells was conducted by using 10  $\mu$ l of T cell TransAct™ (130-111-160; Miltenyi Biotec B.V. & Co. KG) according to manufacturer's instructions (*T cell activation medium*). T cells were activated for 3 days prior to injection.

#### On-chip culture of adipose tissue

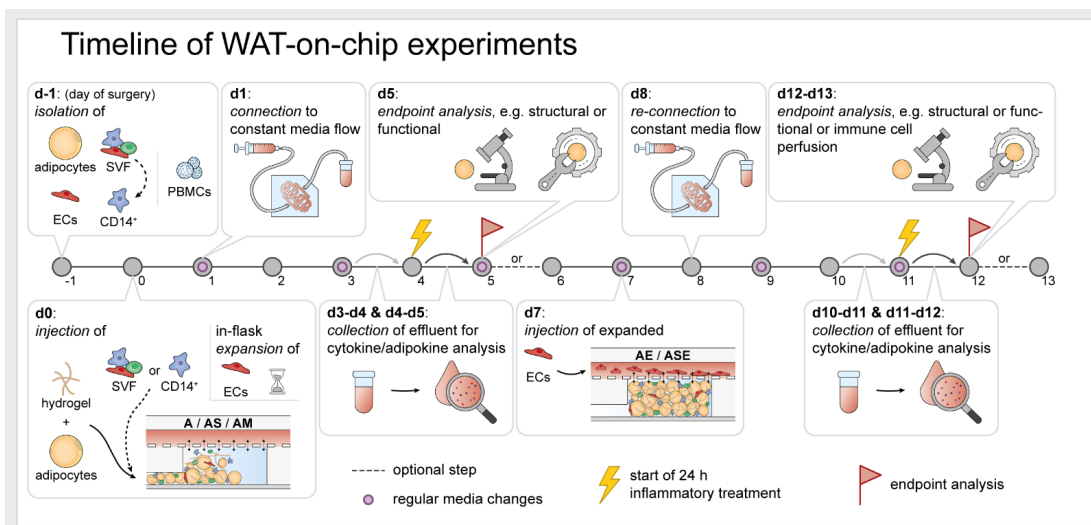


**Figure 7. Overview of WAT-on-chip experiment timeline.** On d-1, adipocytes, SVF and mvECs were isolated from skin/subcutaneous fat biopsies, and PBMCs were isolated from patients' blood samples. D0 denotes the day of adipocyte (plus tissue chamber-resident cell types) injection. mvECs had to be expanded in culture flasks and could only be seeded onto the chips' membranes on d7. After each injection, chips were supplied gravitationally overnight, before connecting to constant media perfusion on the next days. Media in pumping reservoirs were exchanged every other day. Most endpoint analyses were performed on d5 and d12.

bioRxiv preprint doi: <https://doi.org/10.1101/2021.08.08.455559>; this version posted August 8, 2021. The copyright holder for this preprint (which was not certified by peer review) is the author/funder, who has granted bioRxiv a license to display the preprint in perpetuity. It is made available under aCC-BY-NC-ND 4.0 International license.

Human immunocompetent WAT-on-chip  
Rogal et al. 2021

### General remarks on injection, handling and readouts

Figure 7 provides an overview of the general timeline of WAT-on-chip experiments. Adipocyte-only as well as adipocyte-SVF and adipocyte-CD14<sup>+</sup>-cell co-culture chips were injected on the day after isolation. Day of chip injection is defined as day 0 (d0) for all experiments. After injection, on-chip tissues were supplied with respective culture media (cf. table 3) via gravity-driven flow overnight. On d1, chips were then connected to constant media perfusion via an external syringe pumping system (LA-190, Landgraf Laborsysteme HLL GmbH, Langenhagen, Germany). For connecting the chips to the syringe pump, we used Tygon tubing (0.762 x 2.286 mm, e.g. Tygon® ND 100-80 Medical Tubing, Saint-Gobain Performance Plastics Pampus GmbH, Willich, Germany), 21 GA stainless steel plastic hub dispensing needles (e.g., KDS2112P, Weller Tools GmbH, Besigheim, Germany; connected to Luer Lok™ style syringes) and blunt 21 GA stainless steel needles (made from the dispensing needles by removing the plastic hub after dissolving the glue overnight in a 70% ethanol solution). Media perfusion was realized in push mode, flow rate set to 20 µL/h. Unless stated otherwise, medium was changed every other day by re-filling inlet tubing and syringe reservoirs with fresh, pre-warmed culture medium. Endpoint analyses were conducted on d5 (d6, respectively, for monocyte perfusion) or d12 (d13, respectively, for T cell perfusion). In the case of stimulation experiments, effluents were collected for the 24 h-period prior to stimulation in order to assess basal secretion for each chip. Stimulation then occurred for 24 h from d4 to d5, or from d11 to d12, respectively.

### Injection of adipose tissue into the microfluidic platform

Adipocytes were prepared by washing three times with *A wash medium* as described above (cf. Isolation and pre-chip culture of mature adipocytes). HyStem-C (GS313; CellSystems®, Troisdorf, Germany) hydrogel components were reconstituted and mixed according to manufacturer's instructions (except for the crosslinker). Chips were prepared as described above (cf. Chip fabrication by soft lithography and replica molding) on the day before adipose tissue injection. Prior to injection, the chips were removed from PBS<sup>-</sup> storage and a pipette tip filled with 100 µL PBS<sup>-</sup> was inserted into the tissue compartment's outlet to create a liquid droplet over the tissue inlet. Then, 60 µL of adipocytes from packed adipocytes layer were gently mixed with 25 µL of hydrogel components and 0.63 µL of Extralink (i.e., 40:1 hydrogel components:crosslinker). Then, 10 µL of the mixture were immediately injected into the chip's tissue-chamber system by manual pressure. To avoid inclusion of air, the PBS-droplet over the tissue inlet port and adipocyte-hydrogel mixture were let coalesce before inserting the pipette tip into the port. Each tissue compartment system was loaded individually at a steady pace, to ensure that the adipocyte-hydrogel mixture reached the tissue chambers before the onset of gelation. When all tissue chambers were filled with adipocyte-hydrogel mixture, the injection channel was flushed with hydrogel by mixing 25 µL of hydrogel components with 6.25 µL of Extralink (i.e., 4:1 hydrogel components:crosslinker) and injecting 10 µL/chip via the tissue inlet ports into the tissue system. The injection ports were then closed using plugs. On-chip adipocytes were intermediately supplied by a gravitational media perfusion: an empty pipette tip was inserted into the media outlet port and a pipette tip filled with 100 µL of *A medium* was inserted into the media inlet port. Approximately 50 µL were manually pushed through the chip immediately to avoid crosslinking of the hydrogel inside the media channel. Using the method described above, up to 8 chips could be injected with one mixture before gelation of the hydrogel occurred. After overnight gravitational media supply, chips were connected to constant media perfusion of 20 µL/h. Media changes were performed every 3 days unless otherwise stated.

For injection of adipocyte-SVF or adipocyte-CD14<sup>+</sup>-cell co-culture chips, the above protocol was slightly adapted: adherent cells (i.e., SVF or CD14<sup>+</sup>-cells) were detached (see instructions below) and cell pellets of 0.5x10<sup>6</sup> cells in 0.5 mL microcentrifuge tubes were prepared. Cell pellets were then resuspended in 25 µL of hydrogel components mix before adding 60 µL adipocytes and 0.63 µL of Extralink. Cell mixture injection, injection channel flushing, intermediate media supply and connection to constant media perfusion (using *AS/AM co-culture medium*) was done as described above for adipocyte-only chips.

Cells from the SVF were detached in sequential incubation steps with TrypLE™ Select Enzyme (1X) (12563011; Thermo Fisher Scientific Inc.): the growth area was rinsed once with PBS<sup>-</sup>. Then, the cell layer was incubated (37°C, 5% CO<sub>2</sub> and

bioRxiv preprint doi: <https://doi.org/10.1101/2021.08.08.455559>; this version posted August 8, 2021. The copyright holder for this preprint (which was not certified by peer review) is the author/funder, who has granted bioRxiv a license to display the preprint in perpetuity. It is made available under a [CC-BY-NC-ND 4.0 International license](#).

Human immunocompetent WAT-on-chip  
Rogal et al. 2021

95% rH) for 5 min with 1:1 TrypLE™:PBS; for 3 min with TrypLE™, and finally for another 8 min with TrypLE™. After each incubation step, the detachment solution was collected, and the enzymatic reaction was stopped by adding 10% (v/v) FCS to the cell suspension. Finally, the surface of the culture vessel was thoroughly rinsed to further detach cells. CD14<sup>+</sup>-cells were detached in a similar manner: 4 mg/mL lidocaine hydrochloride (L5647; Merck KGaA) were solved in Versene Solution freshly for each detachment. The growth surface was rinsed with PBS- once, and then the cells were detached by sequential incubation (37°C, 5% CO<sub>2</sub> and 95% rH) in lidocaine solution for 3 min and 15 min. After each incubation step, the culture vessel was gently tapped from the bottom, and then the detachment solution was collected. After cell detachment, collected cell suspensions were pooled per cell type and centrifuged at 350 rcf for 5 min. After resuspension in *S/M base medium*, cells were counted, and transferred to microcentrifuge tubes as mentioned above.

### Seeding of endothelial barriers in the microfluidic platform

Seven days after isolation, the mvECs were injected into the media channels of the microfluidic platforms to establish an endothelial barrier on the membrane separating tissue compartments from media perfusion.

For on-chip monoculture of endothelial layers, the chips' tissue compartments were filled with HyStem-C (GS313; CellSystems<sup>®</sup>, Troisdorf, Germany) prior to mvEC seeding. Chips were prepared as described above (cf. Chip fabrication by soft lithography and replica molding) on the day before mvEC seeding. Prior to seeding, hydrogel components were reconstituted and mixed according to manufacturer's instructions. The chips were removed from PBS- storage and a pipette tip filled with 100 µL PBS- was inserted into the tissue compartment's outlet to create a liquid droplet over the tissue inlet. Finally, 10 µL of hydrogel mixture were injected into the tissue compartment inlet port (to avoid enclosure of air during injection, liquid droplet over the inlet port and injection mixture were let coalesce before inserting the pipette tip into the PDMS). To avoid crosslinking of the hydrogel inside the media channel, 50 µL of PBS were flushed through the media compartment after hydrogel injection.

In case of multi-culture with other adipose tissue components, mvECs were added on d7 of adipocyte on-chip culture due to the required mvEC-expansion and -purification period described above. Immediately before EC injection into the co-culture systems, the media perfusion was disconnected by carefully removing the inlet and outlet tubing from the media ports of the system.

For mvEC detachment, medium was aspirated, and cells were washed with PBS-, and incubated with 0.05% Trypsin in EDTA solution (2 ml solution in T25 culture flask) for 5 min at 37°C, 5% CO<sub>2</sub> and 95% rH. After 5 min, the enzymatic reaction was stopped by adding 10% FCS and the cell suspension was transferred to a centrifuge tube. The cell culture flask was rinsed once with PBS-. The cell suspension was centrifuged for 5 min at 209 rcf and the cell pellet resuspended in pre-warmed *mvEC expansion medium*. The cells were counted manually using a hemocytometer and the cell concentration was adjusted to 4x10<sup>6</sup> cells/mL. A 100 µL filter tip was filled with 10 µL of the mvEC suspension and the tip was removed from the pipette. Carefully, the tip was inserted into the media inlet port of the chip. Introduction of air into the system was avoided by inserting the tip through a liquid droplet over the media inlet. An empty 100 µL filter tip was inserted into the media outlet and flow from the filled tip to the empty tip was ensured. The system was incubated for 2 h at 37°C to allow attachment of the mvECs. Within these 2 h, the mvEC suspension was gently moved inside the chip to increase membrane coverage by gently applying manual pressure on the pipette tips. After 2 h, the tips were removed carefully and 100 µL filter tips filled with 100 µL culture medium as defined by on-chip cell components (e.g., *E medium* for mvEC-only chips or *AE co-culture medium*) were inserted into media in- and outlet to provide static media supply at 37°C overnight. On the following day, the systems were (re-)connected to constant media perfusion. During the first 4 h, the media perfusion was ramped starting at 5 µL/h over the first 2 h, then 10 µL/h for 2 h, and finally set to 20 µL/h. Media changes were performed every 3 days unless otherwise stated.

### Inflammatory stimulation

Inflammatory stimulations were performed by treating the chips for 24 h from d4-d5 or d11-d12 with TNF- $\alpha$  (final concentration of 20 ng/mL; SRP3177; Merck KGaA) or LPS (final concentration of 100 ng/mL; 00-4976-93; Thermo

bioRxiv preprint doi: <https://doi.org/10.1101/2021.08.08.455559>; this version posted August 8, 2021. The copyright holder for this preprint (which was not certified by peer review) is the author/funder, who has granted bioRxiv a license to display the preprint in perpetuity. It is made available under aCC-BY-NC-ND 4.0 International license.

Human immunocompetent WAT-on-chip  
Rogal et al. 2021

Fisher Scientific Inc.) added to the respective media for each culture mode (table 3). To determine cytokine and metabolite concentrations in response to inflammatory stimulation, effluents were collected for the 24 h before treatment (baseline release for each chip) and after the 24 h-treatment.

#### Perfusion of immune cells

Activated T-cells were perfused for 18 h from d12-d13 of on-chip culture, and recruitment to different adipose tissue culture modes was studied (A, AS, ASE). T-cells were detached by (i) removing half of the culture medium, (ii) gently pipetting and collect already detached cells in a centrifuge tube, (iii) rinsing the growth surface with PBS, gently pipetting and collecting the cell suspension again. Then, the cell suspension was centrifuged at 300 rcf for 5 min. Before perfusion, T-cells were labeled with CellTracker™ Deep Red Dye (C34565; Thermo Fisher Scientific Inc.) by resuspending the cell pellet in CellTracker Solution (reconstituted according to manufacturer's instructions and further diluted to 2  $\mu$ M in DMEM + 100 U/mL Pen/Strep) and incubating for 60 min (37°C, 5% CO<sub>2</sub> and 95% rH). Labeled cells were then centrifuged at 300 rcf for 5 min, resuspended in X-VIVO™ 15 + 100 U/mL Pen/Strep, counted and adjusted to a cell concentration of 375,000 cells/mL ( $\rightarrow$  275  $\mu$ L/chip, i.e., circa 100,000 cells/chip). T-cells were perfused through the chips media channel by inserting a pipette tip containing 275  $\mu$ L cell suspension into the media outlet and withdrawing the suspension with a flow rate of 10  $\mu$ L/h. T cell recruitment to different adipose culture modes was quantified by determination of cell tracker fluorescence intensity in the tissue chambers.

Circulating monocytes derived from PBMCs were perfused for 24 h from d5-d6 of on-chip culture, and recruitment to one culture mode (A) was studied comparing 3  $\mu$ m- and 5  $\mu$ m membrane pore sizes. Before detachment, the CD14<sup>+</sup>-cells were labelled with CellTracker™ Deep Red Dye by incubating CellTracker Solution (reconstituted according to manufacturer's instructions and further diluted to 2  $\mu$ M in DMEM + 100 U/mL Pen/Strep) for 60 min (37°C, 5% CO<sub>2</sub> and 95% rH). Afterwards, cells were washed by adding *S/M base medium*. Detachment was performed as described above (cf. Injection of adipose tissue into the microfluidic platform), and the cell concentration was adjusted to 112,500 cells/mL (250  $\mu$ L/chip  $\rightarrow$  28,125 cells/chip) in *AS/AM co-culture medium*. CD14<sup>+</sup>-cells were perfused through the chips media channel by inserting a pipette tip containing 250  $\mu$ L cell suspension into the media outlet and withdrawing the suspension with a flow rate of 10  $\mu$ L/h.

### ***Structural characterization of adipose tissue components on-chip***

#### Endothelial barrier function assessment

Endothelial barrier integrity was assessed for the endothelial layer-only culture mode using a macromolecular tracer approach. For comparison, chips without endothelial barrier, only with a hydrogel gel-filled tissue compartment were measured. On d5 of on-chip culture, media supplemented with 100  $\mu$ g/mL FITC-dextran with sizes of 3-5 kDa (FD4; Merck KGaA) or 40 kDa (FD40; Merck KGaA) were perfused through the chip at a flow rate of 20  $\mu$ L/h for 60 min. Using a confocal Laser-Scanning-Microscope (LSM 710, Carl Zeiss Microscopy GmbH, Jena, Germany), fluorescence intensity was determined for 3 different focal planes (lower tissue chamber, upper tissue chamber and media channel) every 5 s. For analysis, we measured the mean grey value for each focal plane position for each time point using Fiji (Image J version 1.53c) (Schindelin et al., 2012), subtracted the background mean grey value and adjusted the offset in time it took for the tracer to reach the medium channel. Mean grey values were then normalized to the mean grey value measured at the final time point in the media channel.

#### Labelling for cell tracking

To trace and visualize the SVF, cells were labeled with a cell tracker prior to injection. Before detaching the cells, they were incubated in CellTracker™ Deep Red Dye solution (reconstituted according to manufacturer's instructions and further diluted to 2  $\mu$ M in DMEM + 100 U/mL Pen/Strep) for 60 min (37°C, 5% CO<sub>2</sub> and 95% rH). Afterwards, cells were washed by replacing the labelling solution by *S/M base medium*.

bioRxiv preprint doi: <https://doi.org/10.1101/2021.08.08.455559>; this version posted August 8, 2021. The copyright holder for this preprint (which was not certified by peer review) is the author/funder, who has granted bioRxiv a license to display the preprint in perpetuity. It is made available under aCC-BY-NC-ND 4.0 International license.

Human immunocompetent WAT-on-chip  
Rogal et al. 2021

**(Immuno-) staining**

A variety of (immuno-) staining procedures were performed on d5 or d6 (only for monocyte recruitment experiment), respectively, or d12 or d13 (only for T-cell recruitment experiment), respectively. We used conjugated and unconjugated antibodies.

All conjugated antibodies (table 4) were stained prior to fixation (except for CD11c and eNOS) by washing the chips once with PBS<sup>+</sup> and twice with PBS<sup>+</sup> with 0.5% (w/v) BSA. Then the antibody was diluted in PBS<sup>+</sup> with 0.5% (w/v) BSA and 20 µM Hoechst 33342 Solution (62249; Thermo Fisher Scientific Inc.) and incubated for 30 min (37°C, 5% CO<sub>2</sub> and 95% rh), followed by two washing steps with PBS<sup>+</sup> with 0.5% (w/v) BSA. Afterwards, chips were imaged within 45 min (Leica DMI8 with incubation unit, Leica Microsystems) or fixed directly for further staining. CD11c and eNOS conjugated antibodies were added to secondary antibody solutions at concentrations listed in table 4.

For all types of unconjugated staining, on-chip tissues were fixed, permeabilized and blocked prior to antibody incubation. In brief, the chips were washed by flushing the media channels three times with PBS<sup>+</sup> before fixing the on-chip tissues with ROTI<sup>®</sup>Histofix 4% (P087.6; Carl Roth GmbH + Co. KG, Karlsruhe, Germany) for 60 min at room temperature (RT) under gentle rocking on a rocking shaker. After fixation, the chips were washed three times with PBS<sup>+</sup>, permeabilized with 0.2% (w/v) Saponin in PBS<sup>+</sup> for 20 min at RT and blocked with 0.3% (v/v) Triton-X and 3% (w/v) BSA in PBS<sup>+</sup> for 30 min at RT. All primary and secondary antibodies were diluted in antibody diluent (S3022; Agilent Technologies, Inc, Santa Clara, CA) to concentrations listed in table 4. Primary antibodies were incubated at RT overnight. Secondary antibody solutions were supplemented with 1 µg/mL DAPI solution (MBD0015; Merck KGaA) and 1 µg/mL BODIPY<sup>™</sup> 493/503 dye (D3922; Thermo Fisher Scientific Inc.) and incubated for 1 h at RT. Finally, the chips were washed three times with PBS<sup>+</sup> and imaged within the next 48 h using a confocal Laser-Scanning-Microscope (LSM 710, Carl Zeiss MicroImaging). Importantly, to confirm endothelial coverage over the tissue chambers, the chips had to be inverted for imaging, or else the adipocytes in the tissue chamber obscured the EC barrier.

**Table 4. Overview of antibodies used for on-chip staining.**

Staining with unconjugated antibodies						
Primary antibody				Coupled with secondary antibody		
Staining target	Antibody	Specifics	Final concentration/dilution	Antibody	Specifics	Final concentration/dilution
Perilipin A	Anti-Perilipin A antibody produced in rabbit	P1998 [Merck KGaA]	12 µg/ml	F(ab') <sub>2</sub> -Goat anti-Rabbit IgG (H+L) Cross-Adsorbed Secondary Antibody, Alexa Fluor 555	A-21430 [Thermo Fisher Scientific Inc.]	20 µg/ml
CD31	Monoclonal Mouse Anti-Human CD31, Endothelial Cell (Dako Omnis)	M0823 [Agilent Technologies, Inc.]	1:50	Goat anti-Mouse IgG (H+L) Cross-Adsorbed Secondary Antibody, Alexa Fluor 546	A-11003 [Thermo Fisher Scientific Inc.]	20 µg/ml
CD68	Purified Mouse Anti-Human CD68	556059 Clone Y1/82A (RUO) [BD]	5 µg/ml	Goat anti-Mouse IgG (H+L) Cross-Adsorbed Secondary Antibody, Alexa Fluor 488	A-11001 [Thermo Fisher Scientific Inc.]	20 µg/ml
CD86	Recombinant Anti-CD86 antibody [EPR21962]	ab239075 [Abcam]	11.38 µg/ml	F(ab') <sub>2</sub> -Goat anti-Rabbit IgG (H+L) Cross-Adsorbed Secondary Antibody, Alexa Fluor 555	A-21430 [Thermo Fisher Scientific Inc.]	20 µg/ml
CD206	Recombinant Anti-Mannose Receptor antibody [EPR6828(B)]	ab125028 [Abcam]	3.6 µg/ml	F(ab') <sub>2</sub> -Goat anti-Rabbit IgG (H+L) Cross-Adsorbed Secondary Antibody, Alexa Fluor 555	A-21430 [Thermo Fisher Scientific Inc.]	20 µg/ml
Trem2	TREM2 Recombinant Rabbit Monoclonal	702886 [Thermo Fisher Scientific Inc.]	5 µg/ml	F(ab') <sub>2</sub> -Goat anti-Rabbit IgG (H+L) Cross-Adsorbed Secondary Antibody, Alexa Fluor 555	A-21430 [Thermo Fisher Scientific Inc.]	20 µg/ml

bioRxiv preprint doi: <https://doi.org/10.1101/2021.08.08.455559>; this version posted August 8, 2021. The copyright holder for this preprint (which was not certified by peer review) is the author/funder, who has granted bioRxiv a license to display the preprint in perpetuity. It is made available under aCC-BY-NC-ND 4.0 International license.

Human immunocompetent WAT-on-chip  
Rogal et al. 2021

	Antibody (9H4L26)				
Staining with conjugated antibodies					
	Antibody	Specifics	Final concentration/dilution	Staining prior to fixation	Staining post fixation
CD31	CD31 Antibody, anti-human, REAfinity™	130-110-807 [Miltenyi Biotec B.V. & Co. KG]	1:25	Yes	No
CD106	CD106 (VCAM-1) Antibody, anti-human, REAfinity™	130-104-164 [Miltenyi Biotec B.V. & Co. KG]	1:10	Yes	No
CD309	CD309 (VEGFR-2) Antibody, anti-human, REAfinity™	130-117-984 [Miltenyi Biotec B.V. & Co. KG]	1:35	Yes	No
eNOS	eNOS Antibody, anti-human, APC, REAfinity™	130-106-840 [Miltenyi Biotec B.V. & Co. KG]	1:10	No	Yes
CD45	CD45 Antibody, anti-human, APC, REAfinity™	130-110-771 [Miltenyi Biotec B.V. & Co. KG]	1:25 – 1:10	Yes	No
CD11c	CD11c Antibody, anti-human, APC, REAfinity™	130-114-110 [Miltenyi Biotec B.V. & Co. KG]	1:25	No	Yes

### Functional characterization of adipose tissue on-chip

#### Live-/dead staining

To evaluate the viability of the mvECS forming the vascular barrier on chip, a live-/dead staining was performed and imaged via fluorescence microscopy. The cytosol of living cells was stained with fluorescein diacetate (FDA) (F7378; Merck KGaA); the nuclei of dead cells with propidium iodide (PI) (P4170; Merck KGaA). A stock solution of FDA was prepared by dissolving the powder in acetone (1 mg/mL). PI powder was dissolved in PBS<sup>-</sup> (1 mg/mL). Stock solutions were stored protected from light and diluted right before the staining process. FDA and PI stocks were diluted in 838  $\mu$ L PBS<sup>+</sup>, adding 27  $\mu$ L of PI and 135  $\mu$ L of FDA. To stain the mvEC barrier-on-chip, the chip was disconnected from tubing and the media channel was flushed with PBS<sup>+</sup> via hydrostatic pressure created by inserting a filled pipette tip into the media inlet port and an empty tip into the media outlet port. After equilibration of the PBS<sup>+</sup> level in the tips, they were replaced by a tip filled with 50  $\mu$ L live-/dead-staining solution. After another incubation of 5 min at 37°C, 5% CO<sub>2</sub> and 95% rH, the tips were removed, and the media channel was flushed two times with PBS<sup>+</sup> as described above. Fluorescent imaging was conducted immediately after the staining using a Leica DMI8 (with incubation unit, Leica Microsystems, Wetzlar, Germany).

#### Fatty acid uptake monitoring of adipocytes

To assess fatty acid uptake properties of on-chip adipocytes, a medium-chain fatty acid (Dodecanoic Acid, C12; BODIPY™ 500/510 C1, C12; D3823, Thermo Fisher Scientific Inc.) or a long-chain fatty acid (Hexadecanoic Acid, C16; BODIPY™ FL C16, D3821, Thermo Fisher Scientific Inc.) were added at a concentration of 4  $\mu$ M to the culture medium as defined by culture mode (table 3). The uptake of the fatty acids was monitored in real-time using a fluorescence microscope with incubation (Leica DMI8 with incubation unit, Leica Microsystems) for 60 min. Fluorescence images were acquired every 3 min for each position. To quantify fatty acid uptake, for each time point per position, we measured mean grey values in the tissue chamber and in the plain media channel as background using Fiji software.

#### Responsiveness to $\beta$ -adrenoreceptor agonists

$\beta$ -adrenergic stimulation was performed by adding (-)-Isoproterenol hydrochloride (I6504; Merck KGaA) to culture medium as defined by culture mode (table 3). Final concentration ranged from 1  $\mu$ M to 100  $\mu$ M. For each final concentration, a corresponding 1000X stock solution was prepared by dissolving the isoproterenol in PBS<sup>-</sup>.

bioRxiv preprint doi: <https://doi.org/10.1101/2021.08.08.455559>; this version posted August 8, 2021. The copyright holder for this preprint (which was not certified by peer review) is the author/funder, who has granted bioRxiv a license to display the preprint in perpetuity. It is made available under a [CC-BY-NC-ND 4.0 International license](#).

Human immunocompetent WAT-on-chip  
Rogal et al. 2021

Isoproterenol responsiveness was read out after a 2 h feeding phase of on-chip adipocytes with the fluorescently labeled fatty acid (BODIPY™ 500/510 C1, C12; D3823, Thermo Fisher Scientific Inc.) by analyzing the release of fatty acids from the adipocytes. Moreover, glycerol secretion after 24 h of stimulation was determined (cf. Analyses of effluents).

### Acetylated low density lipoprotein (AcLDL) uptake by endothelial layer

Low Density Lipoprotein from Human Plasma, acetylated and coupled to a Dil complex (Dil AcLDL; L3484; Thermo Fisher Scientific Inc.) was added to *E medium* or *E TNF- $\alpha$  stimulation medium* (following a 24 h-stimulation) at a final concentration of 1  $\mu$ g/mL. Uptake solutions were pre-heated and administered to the chips via gravitational flow (empty pipette tip in media outlets, pipette tip filled with 50  $\mu$ L uptake solution in media inlets) for 3 h at 37°C, 5% CO<sub>2</sub> and 95% rH. Afterwards, nuclei were stained by adding Hoechst 33342 Solution (62249; Thermo Fisher Scientific Inc.) to the uptake solutions for 20 min at 37°C, 5% CO<sub>2</sub> and 95% rH. Uptake solutions were removed from the chips by gravitationally washing with *E medium* or *E TNF- $\alpha$  stimulation medium*. Uptake was imaged within 45 min (Leica DMi8 with incubation unit, Leica Microsystems).

### Analyses of effluents (cytotoxicity, glycerol release and cytokine secretion)

For all experiments involving analyses of effluents, we used chips without cells (but with hydrogel-filled tissue compartments) as negative controls. These chips were run in parallel to tissue-laden chips and handled identically. Media effluents were collected over 24 h periods.

After collection, effluents were centrifuged at 1942 rcf for 10 min. Supernatants after centrifugation were directly processed for viability assessment and afterwards stored at -80°C for up to 4 months. They were not thawed more than twice. Prior to performing assays, effluents from storage and all required assay reagents were brought to RT.

To quantitatively assess the on-chip tissues' viability, we measured the release of lactate dehydrogenase (LDH) into the media effluents using the CytoTox 96® Non-Radioactive Cytotoxicity Assay (G1780, Promega GmbH, Walldorf, Germany). The assay was performed in a 384-well plate according to the manufacturer's instructions. To determine a Target Cell Maximum LDH Release Control, we lysed the on-chip tissues for the different culture conditions (A, AS, ASE; biological duplicates per condition) by incubating 1X Lysis Solution in the respective culture media for 2 h. The mean of the measured absorbance values was assumed to be the maximal LDH release possible for the given experimental set-up and set to 100%.

For quantitative enzymatic determination of glycerol secretion, we used Free Glycerol Reagent (F6428; Merck KGaA), and Glycerol Standard Solution (G7793; Merck KGaA) for a standard curve. In technical duplicates, 60  $\mu$ L of effluent were mixed with 40  $\mu$ L of Free Glycerol Reagent in a 96-well plate. After 10 min incubation at 37°C, 5% CO<sub>2</sub> and 95% rH, absorption at 540 nm was measured using a plate reader (Infinite® 200 PRO, Tecan Trading AG, Männedorf, Switzerland). For each assay run, a standard curve was generated to correlate absorbances to glycerol concentrations. Cytokines were determined by fluorescent bead-based multiplex sandwich immunoassays (LEGENDplex™ Human Angiogenesis Panel 1, 740697 and LEGENDplex™ Human Adipokine Panel, 740196; BioLegend, Inc., San Diego, CA) read by flow cytometry (Guava easyCyte 8HT, Merck KGaA) following the manufacturer's manual. In brief, effluents were analyzed in technical duplicates and incubated with a cocktail of target-specific capture beads followed by an incubation with biotinylated detection antibodies and finally with streptavidin-phycoerythrin (SA-PE). For each assay run, a standard curve was generated to correlate fluorescence intensities to cytokine concentrations. Flow cytometry data were evaluated with the LEGENDplex Cloud-Based Data Analysis Software Suite (BioLegend). Gates were adjusted manually to find optimal differentiation between capture bead populations, and the same gating strategy applied to all assay runs.

### ***Image processing, data presentation and statistical analysis***

Images were processed using Fiji (Image J version 1.53c) (Schindelin et al., 2012) to adjust brightness and contrast, create maximum intensity projections or orthogonal views of Z-stacks and to insert scale bars. For 3D rendering and stitching of tile scans, we used the ZEN software (ZEN 2.3 (blue edition), Carl Zeiss Microscopy GmbH).

35

---

bioRxiv preprint doi: <https://doi.org/10.1101/2021.08.08.455559>; this version posted August 8, 2021. The copyright holder for this preprint (which was not certified by peer review) is the author/funder, who has granted bioRxiv a license to display the preprint in perpetuity. It is made available under a [CC-BY-NC-ND 4.0 International license](#).

Human immunocompetent WAT-on-chip  
Rogal et al. 2021

All data is presented as mean  $\pm$  SE if not stated otherwise with sample sizes (n) stated for each case individually. For quantifications feasible on chamber level, such as optical readout, n denotes number of chambers covered in analyses. For quantifications feasible on chip level only, such as all kinds of effluent analyses, for instance, n denotes number of chip replicates. Descriptive statistics and graphs were generated using OriginPro (Version 2021, OriginLab Corporation). For testing statistical significance, we performed unpaired *t* tests using the online *t* Test Calculator tool provided by GraphPad (<https://www.graphpad.com/quickcalcs/ttest1/?format=50>). P value and statistical significance are indicated for each case individually.

bioRxiv preprint doi: <https://doi.org/10.1101/2021.08.08.455559>; this version posted August 8, 2021. The copyright holder for this preprint (which was not certified by peer review) is the author/funder, who has granted bioRxiv a license to display the preprint in perpetuity. It is made available under a [CC-BY-NC-ND 4.0 International license](#).

Human immunocompetent WAT-on-chip  
Rogal et al. 2021

### **Acknowledgements**

The authors thank Dr. Ziegler (Klinik Charlotenhaus, Stuttgart) for the kind provision of human adipose tissue from plastic surgery, Cristhian Rojas, Dominic Baum, Lena Scheying and Verena Haug for their assistance with cell culture and chip fabrication.

The research was supported in part by the Fraunhofer-Gesellschaft internal programs Talenta Start (to J.R.) and Attract (601543, to P.L.), by the Federal Ministry of Education and Research (BMBF; 031L0247B to P.L.) as well as the European Union's Horizon 2020 research and innovation program under the Marie Skłodowska-Curie grant agreements no. 812954 (to P.L.) and no. 845147 (to M.C.).

### **Author contributions**

Author	Contribution										
	Conceptualization	Methodology	Investigation	Formal analysis	Resources	Writing—original draft	Writing—review & editing	Visualization	Supervision	Project administration	Funding acquisition
J.R.	x	x	x	x		x		x			x
R.X.		x	x				x				
J.Rz.		x	x				x				
C.T.	x		x				x				
M.C.	x						x		x		
M.W.					x						
W.E.					x						
K.S.-L.							x		x		
P.L.	x						x		x	x	x

bioRxiv preprint doi: <https://doi.org/10.1101/2021.08.08.455559>; this version posted August 8, 2021. The copyright holder for this preprint (which was not certified by peer review) is the author/funder, who has granted bioRxiv a license to display the preprint in perpetuity. It is made available under aCC-BY-NC-ND 4.0 International license.

Human immunocompetent WAT-on-chip  
Rogal et al. 2021

## References

- Abbott RD, Borowsky FE, Alonzo CA, Zieba A, Georgakoudi I, Kaplan DL. 2018. Variability in responses observed in human white adipose tissue models. *J Tissue Eng Regen Med* **12**:840–847. doi:10.1002/term.2572
- Abbott RD, Kimmerling EP, Cairns DM, Kaplan DL. 2016a. Silk as a Biomaterial to Support Long-Term Three-Dimensional Tissue Cultures. *ACS Appl Mater Interfaces* **8**:21861–21868. doi:10.1021/acsami.5b12114
- Abbott RD, Wang RY, Reagan MR, Chen Y, Borowsky FE, Zieba A, Marra KG, Rubin JP, Ghobrial IM, Kaplan DL. 2016b. The Use of Silk as a Scaffold for Mature, Sustainable Unilocular Adipose 3D Tissue Engineered Systems. *Adv Healthcare Mater* **5**:1667–1677. doi:10.1002/adhm.201600211
- Alarcon PC, Damen MSMA, Madan R, Deepe GS, Spearman P, Way SS, Divanovic S. 2021. Adipocyte inflammation and pathogenesis of viral pneumonias: an overlooked contribution. *Mucosal Immunol*. doi:10.1038/s41385-021-00404-8
- Andrade FB, Gualberto A, Rezende C, Percegoni N, Gameiro J, Hottz ED. 2021. The Weight of Obesity in Immunity from Influenza to COVID-19. *Front Cell Infect Microbiol* **11**:638852. doi:10.3389/fcimb.2021.638852
- Augustin HG, Koh GY. 2017. Organotypic vasculature: From descriptive heterogeneity to functional pathophysiology. *Science* **357**:eaal2379. doi:10.1126/science.aal2379
- Bahmad HF, Daouk R, Azar J, Sapudom J, Teo JCM, Abou-Kheir W, Al-Sayegh M. 2020. Modeling Adipogenesis: Current and Future Perspective. *Cells* **9**:2326. doi:10.3390/cells9102326
- Blaber SP, Webster RA, Hill CJ, Breen EJ, Kuah D, Vesey G, Herbert BR. 2012. Analysis of in vitro secretion profiles from adipose-derived cell populations. *J Transl Med* **10**:172. doi:10.1186/1479-5876-10-172
- Brestoff JR, Wilen CB, Moley JR, Li Y, Zou W, Malvin NP, Rowen MN, Saunders BT, Ma H, Mack MR, Hykes BL, Balce DR, Orvedahl A, Williams JW, Rohatgi N, Wang X, McAllaster MR, Handley SA, Kim BS, Doench JG, Zinselmeyer BH, Diamond MS, Virgin HW, Gelman AE, Teitelbaum SL. 2021. Intercellular Mitochondria Transfer to Macrophages Regulates White Adipose Tissue Homeostasis and Is Impaired in Obesity. *Cell Metabolism* **33**:270–282.e8. doi:10.1016/j.cmet.2020.11.008
- Bruun JM, Pedersen SB, Richelsen B. 2001. Regulation of Interleukin 8 Production and Gene Expression in Human Adipose Tissue in Vitro. *The Journal of Clinical Endocrinology & Metabolism* **86**:1267–1273. doi:10.1210/jcem.86.3.7264
- Caslin HL, Bhanot M, Bolus WR, Hasty AH. 2020. Adipose tissue macrophages: Unique polarization and bioenergetics in obesity. *Immunol Rev* **295**:101–113. doi:10.1111/imr.12853
- Caspar-Bauguil S, Kolditz C-I, Lefort C, Vila I, Mouisel E, Beuzelin D, Tavernier G, Marques M-A, Zakaroff-Girard A, Pecher C, Houssier M, Mir L, Nicolas S, Moro C, Langin D. 2015. Fatty acids from fat cell lipolysis do not activate an inflammatory response but are stored as triacylglycerols in adipose tissue macrophages. *Diabetologia* **58**:2627–2636. doi:10.1007/s00125-015-3719-0
- Cimini FA, Barchetta I, Porzia A, Mainiero F, Costantino C, Bertocchini L, Ceccarelli V, Morini S, Baroni MG, Lenzi A, Cavallo MG. 2017. Circulating IL-8 levels are increased in patients with type 2 diabetes and associated with worse inflammatory and cardiometabolic profile. *Acta Diabetol* **54**:961–967. doi:10.1007/s00592-017-1039-1
- Corrêa, Heyn, Magalhaes. 2019. The Impact of the Adipose Organ Plasticity on Inflammation and Cancer Progression. *Cells* **8**:662. doi:10.3390/cells8070662
- Corvera S. 2021. Cellular Heterogeneity in Adipose Tissues. *Annu Rev Physiol* **83**:257–278. doi:10.1146/annurev-physiol-031620-095446

bioRxiv preprint doi: <https://doi.org/10.1101/2021.08.08.455559>; this version posted August 8, 2021. The copyright holder for this preprint (which was not certified by peer review) is the author/funder, who has granted bioRxiv a license to display the preprint in perpetuity. It is made available under aCC-BY-NC-ND 4.0 International license.

Human immunocompetent WAT-on-chip

Rogal et al. 2021

Côté JA, Ostinelli G, Gauthier M-F, Lacasse A, Tchernof A. 2019. Focus on dedifferentiated adipocytes: characteristics, mechanisms, and possible applications. *Cell Tissue Res* **378**:385–398. doi:10.1007/s00441-019-03061-3

Di Caprio N, Bellas E. 2020. Collagen Stiffness and Architecture Regulate Fibrotic Gene Expression in Engineered Adipose Tissue. *Adv Biosys* **4**:1900286. doi:10.1002/adbi.201900286

Eberl G, Colonna M, Di Santo JP, McKenzie ANJ. 2015. Innate lymphoid cells: A new paradigm in immunology. *Science* **348**:aaa6566–aaa6566. doi:10.1126/science.aaa6566

Fain JN, Cheema P, Madan AK, Tichansky DS. 2010. Dexamethasone and the inflammatory response in explants of human omental adipose tissue. *Molecular and Cellular Endocrinology* **315**:292–298. doi:10.1016/j.mce.2009.10.004

Fernyhough ME, Vierck JL, Hausman GJ, Mir PS, Okine EK, Dodson MV. 2004. Primary Adipocyte Culture: Adipocyte Purification Methods May Lead to a New Understanding of Adipose Tissue Growth and Development. *Cytotechnology* **46**:163–172. doi:10.1007/s10616-005-2602-0

Flaherty SE, Grijalva A, Xu X, Ables E, Nomani A, Ferrante AW. 2019. A lipase-independent pathway of lipid release and immune modulation by adipocytes. *Science* **363**:989–993. doi:10.1126/science.aaw2586

Fuchs S, Johansson S, Tjell AØ, Werr G, Mayr T, Tenje M. 2021. In-Line Analysis of Organ-on-Chip Systems with Sensors: Integration, Fabrication, Challenges, and Potential. *ACS Biomater Sci Eng* acsbiomaterials.0c01110. doi:10.1021/acsbmaterials.0c01110

Gesta S, Lolmède K, Daviaud D, Berlan M, Bouloumié A, Lafontan M, Valet P, Saulnier-Blache JS. 2003. Culture of Human Adipose Tissue Explants Leads to Profound Alteration of Adipocyte Gene Expression. *Horm Metab Res* **35**:158–163. doi:10.1055/s-2003-39070

Giordano A, Murano I, Mondini E, Perugini J, Smorlesi A, Severi I, Barazzoni R, Scherer PE, Cinti S. 2013. Obese adipocytes show ultrastructural features of stressed cells and die of pyroptosis. *Journal of Lipid Research* **54**:2423–2436. doi:10.1194/jlr.M038638

Glatz JFC, Luiken JJFP. 2020. Time for a détente in the war on the mechanism of cellular fatty acid uptake. *Journal of Lipid Research* **61**:1300–1303. doi:10.1194/jlr.6192020LTE

Godwin LA, Brooks JC, Hoepfner LD, Wanders D, Judd RL, Easley CJ. 2015. A microfluidic interface for the culture and sampling of adiponectin from primary adipocytes. *Analyst* **140**:1019–1025. doi:10.1039/C4AN01725K

Gogg S, Nerstedt A, Boren J, Smith U. 2019. Human adipose tissue microvascular endothelial cells secrete PPARγ ligands and regulate adipose tissue lipid uptake. *JCI Insight* **4**:e125914. doi:10.1172/jci.insight.125914

Greek R, Menache A. 2013. Systematic Reviews of Animal Models: Methodology versus Epistemology. *Int J Med Sci* **10**:206–221. doi:10.7150/ijms.5529

Guzik TJ, Skiba DS, Touyz RM, Harrison DG. 2017. The role of infiltrating immune cells in dysfunctional adipose tissue. *Cardiovascular Research* **113**:1009–1023. doi:10.1093/cvr/cvx108

Han S-J, Glatman Zaretsky A, Andrade-Oliveira V, Collins N, Dzutsev A, Shaik J, Morais da Fonseca D, Harrison OJ, Tamoutounour S, Byrd AL, Smelkinson M, Bouladoux N, Bliska JB, Brenchley JM, Brodsky IE, Belkaid Y. 2017. White Adipose Tissue Is a Reservoir for Memory T Cells and Promotes Protective Memory Responses to Infection. *Immunity* **47**:1154–1168.e6. doi:10.1016/j.immuni.2017.11.009

Harms MJ, Li Q, Lee S, Zhang C, Kull B, Hallen S, Thorell A, Alexandersson I, Hagberg CE, Peng X-R, Mardinoglu A, Spalding KL, Boucher J. 2019. Mature Human White Adipocytes Cultured under Membranes Maintain Identity, Function, and Can Transdifferentiate into Brown-like Adipocytes. *Cell Reports* **27**:213–225.e5. doi:10.1016/j.celrep.2019.03.026

bioRxiv preprint doi: <https://doi.org/10.1101/2021.08.08.455559>; this version posted August 8, 2021. The copyright holder for this preprint (which was not certified by peer review) is the author/funder, who has granted bioRxiv a license to display the preprint in perpetuity. It is made available under aCC-BY-NC-ND 4.0 International license.

Human immunocompetent WAT-on-chip

Rogal et al. 2021

Hasan SS, Fischer A. 2021. The Endothelium: An Active Regulator of Lipid and Glucose Homeostasis. *Trends in Cell Biology* **31**:37–49. doi:10.1016/j.tcb.2020.10.003

Hoch M, Eberle AN, Peterli R, Peters T, Seboek D, Keller U, Muller B, Linscheid P. 2008. LPS induces interleukin-6 and interleukin-8 but not tumor necrosis factor- $\alpha$  in human adipocytes. *Cytokine* **41**:29–37. doi:10.1016/j.cyto.2007.10.008

Hornung F, Rogal J, Loskill P, Löffler B, Deinhardt-Emmer S. 2021. The Inflammatory Profile of Obesity and the Role on Pulmonary Bacterial and Viral Infections. *IJMS* **22**:3456. doi:10.3390/ijms22073456

Hu J, Li X, Judd RL, Easley CJ. 2020. Rapid lipolytic oscillations in ex vivo adipose tissue explants revealed through microfluidic droplet sampling at high temporal resolution. *Lab Chip* **20**:1503–1512. doi:10.1039/D0LC00103A

Huber B, Borchers K, Tovar GE, Kluger PJ. 2016. Methacrylated gelatin and mature adipocytes are promising components for adipose tissue engineering. *J Biomater Appl* **30**:699–710. doi:10.1177/0885328215587450

Itabe H, Yamaguchi T, Nimura S, Sasabe N. 2017. Perilipins: a diversity of intracellular lipid droplet proteins. *Lipids Health Dis* **16**:83. doi:10.1186/s12944-017-0473-y

Jaitin DA, Adlung L, Thaïss CA, Weiner A, Li B, Descamps H, Lundgren P, Bleriot C, Liu Z, Deczkowska A, Keren-Shaul H, David E, Zmora N, Eldar SM, Lubezky N, Shibolet O, Hill DA, Lazar MA, Colonna M, Ginhoux F, Shapiro H, Elinav E, Amit I. 2019. Lipid-Associated Macrophages Control Metabolic Homeostasis in a Trem2-Dependent Manner. *Cell* **178**:686–698.e14. doi:10.1016/j.cell.2019.05.054

Jay AG, Simard JR, Huang N, Hamilton JA. 2020. SSO and other putative inhibitors of FA transport across membranes by CD36 disrupt intracellular metabolism, but do not affect FA translocation. *Journal of Lipid Research* **61**:790–807. doi:10.1194/jlr.RA12000648

Kim C-S, Park H-S, Kawada T, Kim J-H, Lim D, Hubbard NE, Kwon B-S, Erickson KL, Yu R. 2006. Circulating levels of MCP-1 and IL-8 are elevated in human obese subjects and associated with obesity-related parameters. *Int J Obes* **30**:1347–1355. doi:10.1038/sj.ijo.0803259

Kolahi K, Louey S, Varlamov O, Thornburg K. 2016. Real-Time Tracking of BODIPY-C12 Long-Chain Fatty Acid in Human Term Placenta Reveals Unique Lipid Dynamics in Cytotrophoblast Cells. *PLoS ONE* **11**:e0153522. doi:10.1371/journal.pone.0153522

Kongsuphol P, Gupta S, Liu Y, Bhuvanendran Nair Gourikutty S, Biswas SK, Ramadan Q. 2019. In vitro micro-physiological model of the inflamed human adipose tissue for immune-metabolic analysis in type II diabetes. *Sci Rep* **9**:4887. doi:10.1038/s41598-019-41338-3

Lau FH, Vogel K, Lockett JP, Hunt M, Meyer A, Rogers CL, Tessler O, Dupin CL, St. Hilaire H, Islam KN, Frazier T, Gimble JM, Scahill S. 2018. Sandwiched White Adipose Tissue: A Microphysiological System of Primary Human Adipose Tissue. *Tissue Engineering Part C: Methods* **24**:135–145. doi:10.1089/ten.tec.2017.0339

Lercher A, Baazim H, Bergthaler A. 2020. Systemic Immunometabolism: Challenges and Opportunities. *Immunity* **53**:496–509. doi:10.1016/j.immuni.2020.08.012

Li X, Easley CJ. 2018. Microfluidic systems for studying dynamic function of adipocytes and adipose tissue. *Anal Bioanal Chem* **410**:791–800. doi:10.1007/s00216-017-0741-8

Li X, Hu J, Easley CJ. 2018. Automated microfluidic droplet sampling with integrated, mix-and-read immunoassays to resolve endocrine tissue secretion dynamics. *Lab Chip* **18**:2926–2935. doi:10.1039/C8LC00616D

Li Yiwei, Mao AS, Seo BR, Zhao X, Gupta SK, Chen M, Han YL, Shih T-Y, Mooney DJ, Guo M. 2020. Compression-induced dedifferentiation of adipocytes promotes tumor progression. *Sci Adv* **6**:eaax5611.

bioRxiv preprint doi: <https://doi.org/10.1101/2021.08.08.455559>; this version posted August 8, 2021. The copyright holder for this preprint (which was not certified by peer review) is the author/funder, who has granted bioRxiv a license to display the preprint in perpetuity. It is made available under a [CC-BY-NC-ND 4.0 International license](#).

Human immunocompetent WAT-on-chip  
Rogal et al. 2021

doi:10.1126/sciadv.aax5611

Li Yunjia, Yun K, Mu R. 2020. A review on the biology and properties of adipose tissue macrophages involved in adipose tissue physiological and pathophysiological processes. *Lipids Health Dis* **19**:164. doi:10.1186/s12944-020-01342-3

Lin D, Chun T-H, Kang L. 2016. Adipose extracellular matrix remodelling in obesity and insulin resistance. *Biochemical Pharmacology* **119**:8–16. doi:10.1016/j.bcp.2016.05.005

Liu Y, Kongsuphol P, Chiam SY, Zhang QX, Gourikutty SBN, Saha S, Biswas SK, Ramadan Q. 2019. Adipose-on-a-chip: a dynamic microphysiological in vitro model of the human adipose for immune-metabolic analysis in type II diabetes. *Lab Chip* **19**:241–253. doi:10.1039/C8LC00481A

Loskill P, Sezhan T, Tharp KM, Lee-Montiel FT, Jeeawoody S, Reese WM, Zushin P-JH, Stahl A, Healy KE. 2017. WAT-on-a-chip: a physiologically relevant microfluidic system incorporating white adipose tissue. *Lab Chip* **17**:1645–1654. doi:10.1039/C6LC01590E

Louis F, Kitano S, Mano JF, Matsusaki M. 2019. 3D collagen microfibers stimulate the functionality of preadipocytes and maintain the phenotype of mature adipocytes for long term cultures. *Acta Biomaterialia* **84**:194–207. doi:10.1016/j.actbio.2018.11.048

McCarthy M, Brown T, Alarcon A, Williams C, Wu X, Abbott RD, Gimble J, Frazier T. 2020. Fat-On-A-Chip Models for Research and Discovery in Obesity and Its Metabolic Comorbidities. *Tissue Engineering Part B: Reviews* **26**:586–595. doi:10.1089/ten.teb.2019.0261

McCarty WJ, Johnson M. 2007. The hydraulic conductivity of Matrigel. *Biorheology* **44**:303–317.

McLoughlin RM, Jenkins BJ, Grail D, Williams AS, Fielding CA, Parker CR, Ernst M, Topley N, Jones SA. 2005. IL-6 trans-signaling via STAT3 directs T cell infiltration in acute inflammation. *Proceedings of the National Academy of Sciences* **102**:9589–9594. doi:10.1073/pnas.0501794102

Mehrotra D, Wu J, Papangeli I, Chun HJ. 2014. Endothelium as a gatekeeper of fatty acid transport. *Trends in Endocrinology & Metabolism* **25**:99–106. doi:10.1016/j.tem.2013.11.001

Meijer K, de Vries M, Al-Lahham S, Bruinenberg M, Weening D, Dijkstra M, Kloosterhuis N, van der Leij RJ, van der Want H, Kroesen B-J, Vonk R, Rezaee F. 2011. Human Primary Adipocytes Exhibit Immune Cell Function: Adipocytes Prime Inflammation Independent of Macrophages. *PLoS ONE* **6**:e17154. doi:10.1371/journal.pone.0017154

Mestas J, Hughes CCW. 2004. Of Mice and Not Men: Differences between Mouse and Human Immunology. *J Immunol* **172**:2731–2738. doi:10.4049/jimmunol.172.5.2731

Misumi I, Starmer J, Uchimura T, Beck MA, Magnuson T, Whitmire JK. 2019. Obesity Expands a Distinct Population of T Cells in Adipose Tissue and Increases Vulnerability to Infection. *Cell Reports* **27**:514–524.e5. doi:10.1016/j.celrep.2019.03.030

Monsoon HN, Weijers EM, Niessen FB, Gefen A, Koolwijk P, Gibbs S, van den Broek LJ. 2016. Extensive Characterization and Comparison of Endothelial Cells Derived from Dermis and Adipose Tissue: Potential Use in Tissue Engineering. *PLoS ONE* **11**:e0167056. doi:10.1371/journal.pone.0167056

Morigny P, Boucher J, Arner P, Langin D. 2021. Lipid and glucose metabolism in white adipocytes: pathways, dysfunction and therapeutics. *Nat Rev Endocrinol* **17**:276–295. doi:10.1038/s41574-021-00471-8

National Cancer Institute at the National Institutes of Health. 2020. Obesity and Cancer Fact Sheet - National Cancer Institute. <https://www.cancer.gov/about-cancer/causes-prevention/risk/obesity/obesity-fact-sheet>

Nunes SS, Maijoub JG, Krishnan L, Ramakrishnan VM, Clayton LR, Williams SK, Hoying JB, Boyd NL. 2013. Generation of

41

bioRxiv preprint doi: <https://doi.org/10.1101/2021.08.08.455559>; this version posted August 8, 2021. The copyright holder for this preprint (which was not certified by peer review) is the author/funder, who has granted bioRxiv a license to display the preprint in perpetuity. It is made available under aCC-BY-NC-ND 4.0 International license.

Human immunocompetent WAT-on-chip  
Rogal et al. 2021

a functional liver tissue mimic using adipose stromal vascular fraction cell-derived vasculatures. *Sci Rep* **3**:2141. doi:10.1038/srep02141

Park JY, White JB, Walker N, Kuo C-H, Cha W, Meyerhoff ME, Takayama S. 2011. Responses of endothelial cells to extremely slow flows. *Biomicrofluidics* **5**:022211. doi:10.1063/1.3576932

Patel R, Varghese JF, Yadav UCS. 2020. Crosstalk Between Adipose Tissue, Macrophages, and Other Immune Cells: Development of Obesity and Inflammation-induced Metabolic Diseases In: Faintuch J, Faintuch S, editors. *Obesity and Diabetes*. Cham: Springer International Publishing. pp. 151–163. doi:10.1007/978-3-030-53370-0\_11

Pi X, Xie L, Patterson C. 2018. Emerging Roles of Vascular Endothelium in Metabolic Homeostasis. *Circ Res* **123**:477–494. doi:10.1161/CIRCRESAHA.118.313237

Poloni A, Maurizi G, Ciarlantini M, Medici M, Mattiucci D, Mancini S, Maurizi A, Falconi M, Olivieri A, Leoni P. 2015. Interaction between human mature adipocytes and lymphocytes induces T-cell proliferation. *Cytotherapy* **17**:1292–1301. doi:10.1016/j.jcyt.2015.06.007

Porsche CE, Delproposito JB, Geletka L, O'Rourke R, Lumeng CN. 2021. Obesity results in adipose tissue T cell exhaustion. *JCI Insight* **6**:e139793. doi:10.1172/jci.insight.139793

Privratsky JR, Newman PJ. 2014. PECAM-1: regulator of endothelial junctional integrity. *Cell Tissue Res* **355**:607–619. doi:10.1007/s00441-013-1779-3

Reilly SM, Saltiel AR. 2017. Adapting to obesity with adipose tissue inflammation. *Nat Rev Endocrinol* **13**:633–643. doi:10.1038/nrendo.2017.90

Reitman ML. 2018. Of mice and men - environmental temperature, body temperature, and treatment of obesity. *FEBS Lett* **592**:2098–2107. doi:10.1002/1873-3468.13070

Remick DG. 2005. Interleukin-8: *Critical Care Medicine* **33**:S466–S467. doi:10.1097/01.CCM.0000186783.34908.18

Rogal J, Binder C, Kromidas E, Roosz J, Probst C, Schneider S, Schenke-Layland K, Loskill P. 2020. WAT-on-a-chip integrating human mature white adipocytes for mechanistic research and pharmaceutical applications. *Sci Rep* **10**:6666. doi:10.1038/s41598-020-63710-4

Rogal J, Roost J, Loskill P. 2021. Isolation, Integration, and Culture of Human Mature Adipocytes Leveraging Organ-on-Chip Technology Organ-on-a-Chip - Methods and Protocols, *Methods in Molecular Biology*. Springer US. p. IV, 346.

Ruiz-Ojeda, Méndez-Gutiérrez, Aguilera, Plaza-Díaz. 2019. Extracellular Matrix Remodeling of Adipose Tissue in Obesity and Metabolic Diseases. *IJMS* **20**:4888. doi:10.3390/ijms20194888

Russo L, Lumeng CN. 2018. Properties and functions of adipose tissue macrophages in obesity. *Immunology* **155**:407–417. doi:10.1111/imm.13002

Scheja L, Heeren J. 2019. The endocrine function of adipose tissues in health and cardiometabolic disease. *Nat Rev Endocrinol* **15**:507–524. doi:10.1038/s41574-019-0230-6

Schindelin J, Arganda-Carreras I, Frise E, Kaynig V, Longair M, Pietzsch T, Preibisch S, Rueden C, Saalfeld S, Schmid B, Tinevez J-Y, White DJ, Hartenstein V, Eliceiri K, Tomancak P, Cardona A. 2012. Fiji: an open-source platform for biological-image analysis. *Nat Methods* **9**:676–682. doi:10.1038/nmeth.2019

Schneider S, Erdemann F, Schneider O, Hutschalik T, Loskill P. 2020. Organ-on-a-disc: A platform technology for the centrifugal generation and culture of microphysiological 3D cell constructs amenable for automation and parallelization. *APL Bioengineering* **4**:046101. doi:10.1063/5.0019766

Schönfeld P, Wojtczak L. 2016. Short- and medium-chain fatty acids in energy metabolism: the cellular perspective.

bioRxiv preprint doi: <https://doi.org/10.1101/2021.08.08.455559>; this version posted August 8, 2021. The copyright holder for this preprint (which was not certified by peer review) is the author/funder, who has granted bioRxiv a license to display the preprint in perpetuity. It is made available under a [CC-BY-NC-ND 4.0 International license](#).

Human immunocompetent WAT-on-chip  
Rogal et al. 2021

*Journal of Lipid Research* **57**:943–954. doi:10.1194/jlr.R067629

Sohn JH, Lee YK, Han JS, Jeon YG, Kim JI, Choe SS, Kim SJ, Yoo HJ, Kim JB. 2018. Perilipin 1 (Plin1) deficiency promotes inflammatory responses in lean adipose tissue through lipid dysregulation. *Journal of Biological Chemistry* **293**:13974–13988. doi:10.1074/jbc.RA118.003541

Srikakulapu P, McNamara CA. 2020. B Lymphocytes and Adipose Tissue Inflammation. *ATVB* **40**:1110–1122. doi:10.1161/ATVBAHA.119.312467

Stefan Schneider, Marvin Bubeck, Julia Rogal, Huub Weener, Cristhian Rojas, Martin Weiss, Michael Heymann, Andries D van der Meer, Peter Loskill. 2021. Peristaltic on-chip pump for tunable media circulation and whole blood perfusion in PDMS-free organ-on-chip and organ-disc systems. *Lab Chip in revision*.

Sugihara H, Funatsumaru S, Yonemitsu N, Miyabara S, Toda S, Hikichi Y. 1989. A simple culture method of fat cells from mature fat tissue fragments. *Journal of Lipid Research* **30**:1987–1995. doi:10.1016/S0022-2275(20)38195-5

Sun K, Kusminski CM, Scherer PE. 2011. Adipose tissue remodeling and obesity. *J Clin Invest* **121**:2094–2101. doi:10.1172/JCI45887

Sun Y, Chen S, Zhang X, Pei M. 2019. Significance of Cellular Cross-Talk in Stromal Vascular Fraction of Adipose Tissue in Neovascularization. *ATVB* **39**:1034–1044. doi:10.1161/ATVBAHA.119.312425

Szöke K, Beckstrøm KJ, Brinchmann JE. 2012. Human Adipose Tissue as a Source of Cells with Angiogenic Potential. *Cell Transplant* **21**:235–250. doi:10.3727/096368911X580518

Tanataweethum N, Zelaya A, Yang F, Cohen RN, Brey EM, Bhushan A. 2018. Establishment and characterization of a primary murine adipose tissue-chip. *Biotechnology and Bioengineering* **115**:1979–1987. doi:10.1002/bit.26711

Tanataweethum N, Zhong F, Trang A, Lee C, Cohen RN, Bhushan A. 2021. Towards an Insulin Resistant Adipose Model on a Chip. *Cel Mol Bioeng* **14**:89–99. doi:10.1007/s12195-020-00636-x

Taub DD, Anver M, Oppenheim JJ, Longo DL, Murphy WJ. 1996. T lymphocyte recruitment by interleukin-8 (IL-8). IL-8-induced degranulation of neutrophils releases potent chemoattractants for human T lymphocytes both in vitro and in vivo. *J Clin Invest* **97**:1931–1941. doi:10.1172/JCI118625

Thompson BR, Lobo S, Bernlohr DA. 2010. Fatty acid flux in adipocytes: The in's and out's of fat cell lipid trafficking. *Molecular and Cellular Endocrinology* **318**:24–33. doi:10.1016/j.mce.2009.08.015

van der Worp HB, Howells DW, Sena ES, Porritt MJ, Rewell S, O'Collins V, Macleod MR. 2010. Can Animal Models of Disease Reliably Inform Human Studies? *PLoS Med* **7**:e1000245. doi:10.1371/journal.pmed.1000245

Volz A-C, Omengo B, Gehrke S, Kluger PJ. 2019. Comparing the use of differentiated adipose-derived stem cells and mature adipocytes to model adipose tissue in vitro. *Differentiation* **110**:19–28. doi:10.1016/j.diff.2019.09.002

Wang Lina, Sun P, Wu Y, Wang Li. 2021. Metabolic tissue-resident CD8+ T cells: A key player in obesity-related diseases. *Obesity Reviews* **22**. doi:10.1111/obr.13133

Weisberg SP, McCann D, Desai M, Rosenbaum M, Leibel RL, Ferrante AW. 2003. Obesity is associated with macrophage accumulation in adipose tissue. *J Clin Invest* **112**:1796–1808. doi:10.1172/JCI200319246

Weissenbach M, Clahsen T, Weber C, Spitzer D, Wirth D, Vestweber D, Heinrich PC, Schaper F. 2004. Interleukin-6 is a direct mediator of T cell migration. *Eur J Immunol* **34**:2895–2906. doi:10.1002/eji.200425237

Wentworth JM, Naselli G, Brown WA, Doyle L, Phipson B, Smyth GK, Wabitsch M, O'Brien PE, Harrison LC. 2010. Pro-Inflammatory CD11c+CD206+ Adipose Tissue Macrophages Are Associated With Insulin Resistance in Human Obesity. *Diabetes* **59**:1648–1656. doi:10.2337/db09-0287

bioRxiv preprint doi: <https://doi.org/10.1101/2021.08.08.455559>; this version posted August 8, 2021. The copyright holder for this preprint (which was not certified by peer review) is the author/funder, who has granted bioRxiv a license to display the preprint in perpetuity. It is made available under aCC-BY-NC-ND 4.0 International license.

Human immunocompetent WAT-on-chip  
Rogal et al. 2021

Wolfe RR. 1998. Metabolic interactions between glucose and fatty acids in humans. *The American Journal of Clinical Nutrition* **67**:519S-526S. doi:10.1093/ajcn/67.3.519S

World Health Organization. 2021. Obesity. <https://www.who.int/news-room/facts-in-pictures/detail/6-facts-on-obesity>

World Health Organization. n.d. Body mass index - BMI. *Body mass index - BMI*.  
<https://www.euro.who.int/en/health-topics/disease-prevention/nutrition/a-healthy-lifestyle/body-mass-index-bmi>

Wuest S, Konrad D. 2020. The controversial role of IL-6 in adipose tissue on obesity-induced dysregulation of glucose metabolism. *American Journal of Physiology-Endocrinology and Metabolism* **319**:E607–E613.  
doi:10.1152/ajpendo.00306.2020

Xia Y, Whitesides GM. 1998. SOFT LITHOGRAPHY. *Annu Rev Mater Sci* **28**:153–184.  
doi:10.1146/annurev.matsci.28.1.153

Xu X, Grijalva A, Skowronski A, van Eijk M, Serlie MJ, Ferrante AW. 2013. Obesity Activates a Program of Lysosomal-Dependent Lipid Metabolism in Adipose Tissue Macrophages Independently of Classic Activation. *Cell Metabolism* **18**:816–830. doi:10.1016/j.cmet.2013.11.001

Yang F, Carmona A, Stojkova K, Garcia Huitron EI, Goddi A, Bhushan A, Cohen RN, Brey EM. 2021. A 3D human adipose tissue model within a microfluidic device. *Lab Chip* **21**:435–446. doi:10.1039/D0LC00981D

Yang F, Cohen RN, Brey EM. 2020. Optimization of Co-Culture Conditions for a Human Vascularized Adipose Tissue Model. *Bioengineering* **7**:114. doi:10.3390/bioengineering7030114

Zhang H, Kumar S, Barnett A, Eggo M. 2000. Ceiling culture of mature human adipocytes: use in studies of adipocyte functions. *Journal of Endocrinology* **164**:119–128. doi:10.1677/joe.0.1640119

Zhu J, He J, Verano M, Brimmo AT, Glia A, Qasaimeh MA, Chen P, Aleman JO, Chen W. 2018. An integrated adipose-tissue-on-chip nanoplasmonic biosensing platform for investigating obesity-associated inflammation. *Lab Chip* **18**:3550–3560. doi:10.1039/C8LC00605A

Zhu Y, Mandal K, Hernandez AL, Kawakita S, Huang W, Bandaru P, Ahadian S, Kim H-J, Jucaud V, Dokmeci MR, Khademhosseini A. 2021. State of the art in integrated biosensors for organ-on-a-chip applications. *Current Opinion in Biomedical Engineering* 100309. doi:10.1016/j.cobme.2021.100309